PAUL SCHERRER INSTITUT

ISSN 1423-7296
March 2000

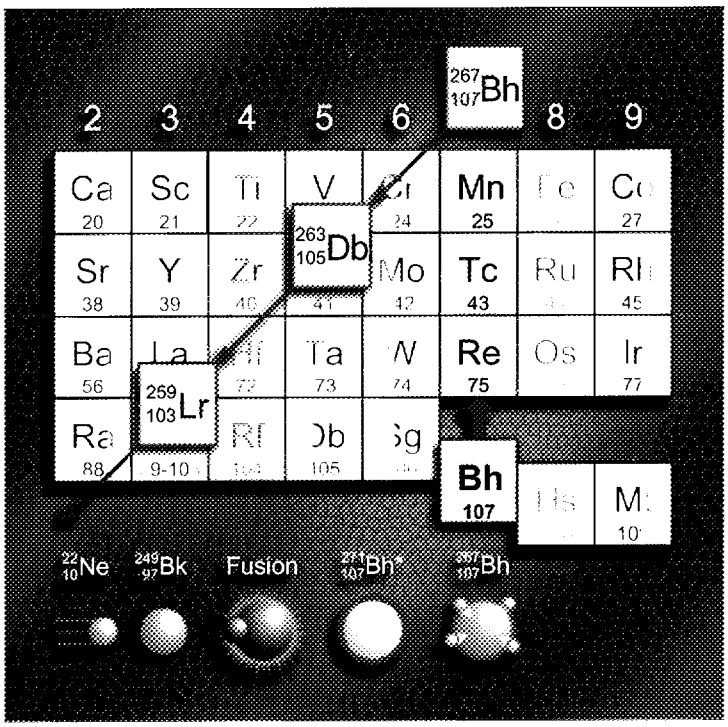

PSI • Scientific Report 1999 / Volume I

Particles and Matter

Cover Photo

An international collaboration of radiochemists led by the Laboratory for Radiochemistry and Environmental Chemistry of PSI and Bern University succeeded for the first time to experimentally investigate the chemical properties of bohrium (element 107) and to establish it as a member of group 7 of the Periodic Table. During a one-month long experiment, a total of only six bohrium atoms were gaschromatographically isolated in the form of volatile bohrium oxychloride molecules and identified by registering their unique decay sequence of alpha particle emissions via dubnium (element 105) to lawrencium (element 103). The short-lived bohrium atoms, decaying with a half-life of about 20 s, were produced by bombarding a very rare, highly radioactive berkelium target supplied by the US department of energy with an intense beam of neon ions at the PSI injector 1 cyclotron.

PAUL SCHERRER INSTITUT

ISSN 1423-7296
March 2000

Scientific Report 1999

Volume I

Particles and Matter

ed. by: J. Gobrecht, H. Gäggeler, D. Herlach, K. Junker, P.-R. Kettle, P. Kubik, A. Zehnder

CH-5232 Villigen PSI
Switzerland
Telephone: +41 56 310 21 11
Telefax: + 41 56 310 21 99
http://www.psi.ch

TABLE OF CONTENTS

Laboratory for Muon Spin Spectroscopy 45

Magnetism: Heavy Fermion Systems, Magnetic Ordering and Dynamics, Spin Glasses

Superconductivity

Semiconductors

Chemistry: Radicals, Reaction Kinetics, Charge Transfer

Other Topics

Experiments with Low Energy Muons

Experimental Techniques

INTRODUCTION

The highlight of research this year was the first-ever determination of the chemical properties of the superheavy element $^{107}Bohrium$ (see front cover). This was undertaken, by an international team led by H. Gäggeler of the **Laboratory for Radiochemistry**. Bohrium was produced by bombarding a Berkelium target with Neon ions from the Injector I cyclotron and six atoms were detected after having passed through an online gas chromatography device.

One important event in 1999 was the 25^{th} anniversary of the ring cyclotron. The original plan, in 1974, to extract a proton current of 100 μA was not without risk but could be achieved fairly soon after commissioning. The ring cyclotron performed so well that soon its current became limited by the Phillips injector cyclotron and in 1985 a new, more powerful injector was built. This year the ring routinely delivered 1.7 mA of proton beam and even higher currents of up to 3 mA are conceivable depending on further upgrades.

Although originally planned for fundamental research in nuclear physics, the particle beams of pions, muons, protons and neutrons are now used in a large variety of disciplines in both natural science and medicine. The beams at PSI have the world's highest intensities and therefore allow certain experiments to be performed, which would not be possible elsewhere.

At the **Laboratory for Particle Physics (LTP)** the focus has shifted from nuclear physics to elementary particle physics with about a fifty-fifty split between investigations of rare processes or particle decays using the high intensity muon, pion and recently also polarized neutron beams of PSI, and research at the highest energy frontier at CERN (Geneva) and DESY (Hamburg). The year 1999 was a year of accumulation of high statistics for the $\mu \rightarrow e$ conversion experiment on Titanium nuclei and for the pion beta decay experiment ($\pi^+ \rightarrow \pi^0 e^+ \nu$) as well others. Results are expected by the end of next year. Most crucial for the detector development of the large LHC experiments, especially for multi-strip gas chambers, was the continuous use of the high intensity test beams to study detector robustness in an environment of large particle fluxes.

The method of **Muon Spin Rotation (μSR)** has been used for investigations of problems in solid state physics from the beginning of era of the the ring cyclotron and is still a very active field. A high pressure cell for pressures up to 15'000 atmospheres was developed with the help of Geneva University and ETHZ and was installed this year to extend the capabilities of the existing instruments. For the low energy muon beam facility (a few keV, 100% polarized beam) a user group was founded and a user operation scheme was started.

Another highlight in December was the successful launch of the X-ray satellite XMM by an Ariane V rocket. The **Laboratory for Astrophysics (LAP)** was responsible for both the structure and thermal design of the reflection grating spectrometer (RGS) camera, built by Contraves Space. Yet another success story was the delivery, on time, of the HESSI solar satellite to NASA, again with substantial contributions from PSI. Large XMM science projects have been defined for a guaranteed time section, and several observing projects have been awarded to PSI through ESA's competitive guest observer programme. Similarly, preparations for HESSI data analysis efforts are under way.

With the new compact 500 keV accelerator, developed in the PSI **Laboratory for Ion Beams (LIP)** we were able to demonstrate the same sensitivity to ^{14}C as with the large tandem accelerator. This project opens new prospects for the efficient investigation of samples with much smaller and simpler instrumentation.

The **Laboratory for Micro and Nanotechnology (LMN)** continued to focus on research into molecular nanotechnology and SiGeC-nanostructures, the latter with the aim of producing silicon based optoelectronics. A third research field is now emerging in close collaboration with SLS, starting with new optical elements for X-ray optics (to be used initially at existing light sources such as ESRF, Hasylab, BESSY and eventually SLS) and further developments of nanoreplication techniques. Brainstorming has started, with respect to the production of nanostructures of the order of 10 nm feature size, over large areas (cm^2).

R. Eichler

Laboratory for Particle Physics

LABORATORY FOR PARTICLE PHYSICS

K. Gabathuler

1999, marked the 25^{th} anniversary of our pion factory. On this occasion a series of invited résumés were given at a special symposium during the twice-yearly held users meeting in July. The initiator of SIN and PSI, former Director Jean Pierre Blaser, recounted the "Origins and Early Days of the Ring Cyclotron" with personal recollections and anecdotes. Claude Joseph (Lausanne) and Florian Scheck (Mainz) summarized the achieved physics milestones in the strong interaction and electroweak sectors, respectively. Considering the more than 500 refereed publications in nuclear and particle physics collected in the last quarter-century, one sees that about three quarters of these deal with hadronic and nuclear physics, with peak numbers of publications in the early eighties. Since then, a handful of large and long-term precision experiments to test the standard model of particle physics represent the backbone of the experimental programme.

This trend should be enhanced in the future in accordance with the guide lines set by our authorities to concentrate the in-house programme on a few outstanding projects. Two new proposals have been submitted this year, which could become the centrepieces of the in-house programme in the next decade: a new search for the decay $\mu \rightarrow e + \gamma$ with a sensitivity down to 10^{-14}, and a source of ultra-cold neutrons allowing a 10 times more sensitive experiment on the electric dipole moment of the neutron. Both experiments are highly relevant searches for physics beyond the standard model and show, that our accelerator, with its very high intensity beams, can still make interesting contributions to particle physics research. However, these large initiatives, strongly promoted by H.K. Walter, the former head of the Laboratory for Particle Physics, will only be successful, if more collaborating groups from outside PSI contribute, with important financial and personnel resources.

Two other research proposals submitted to PSI in 1999 concern the new measurements of the muon lifetime to an accuracy of 1 part in 10^{-6}, which will yield a very precise value of the Fermi constant G_F, a fundamental parameter of the standard model. While an American collaboration plans to use a chopped muon beam, to be installed at PSI, to achieve this, their competitors from Europe plan to use a conventional beam with an extended active stopping target. The two complementary methods, with different systematic errors, could allow a cross check of these difficult experiments.

This year, there were two precision experiments which used a large fraction of the available beam time of πE5 (μ-e-conversion) and πE1 (π-β-decay). In both cases, data with very high statistics had to be collected . The shortening of target E from 6 cm to 4 cm in October was partially compensated for by an increased proton current. The excellent overall beam availability in 1999 was also very welcome. Since the running crews for these long-term experiments are rather small, they were forced to automate data-taking and detector control to a high degree, using the modern communication methods available today. Both experiments should complete their data-taking phases next year.

The search for an anomalous pion decay $\pi \rightarrow \mu X$, X being a hypothetical neutral particle of 33.9 MeV mass, was also completed in 1999. This process was suggested as an explanation for the unexpected structure in the time distribution of neutrino induced reactions observed at RAL. No evidence for this decay could be found at PSI, at a level of sensitivity on the branching fraction of a few 10^{-10}.

The construction of an ECR source, to be used as an X-ray calibration tool for the next generation of pionic hydrogen X-ray measurements, is well under way. The main component, a permanent sextupole magnet, to be installed in the cyclotron trap, has been ordered. The pionic hydrogen experiment aims at determining the line broadening due to the strong interaction, to an accuracy of 1% or better. To achieve this, Doppler broadening effects must be well understood. For this, the recently completed experiment, extracting the kinetic energy spectrum of the exotic atoms from time-of-flight measurements of the neutrons in the reaction $\pi^- p \rightarrow \pi^0 n$ provides a valuable input.

A new facility for neutron decay studies was commissioned in the summer, at SINQ. The large aperture and large momentum acceptance beam guide system delivers polarized cold neutrons ($\lambda \approx 5\mathring{A}$, polarization $\geq 97\%$) with a flux of $2 \times 10^8 n/cm^2/s/mA$. This is comparable with the best polarized neutron fluxes available at the ILL reactor. A first triple-vector experiment searching for T-violation in neutron decay, will start in 2000.

More than five years ago our laboratory joined the CMS Collaboration preparing its experiment at the future Large Hadron Collider at CERN. In September, one of the quarterly CMS-weeks, where the worldwide collaborators gather to discuss the detector design and construction, was organized by and held at PSI.

Avalanche photodiodes, foreseen as light sensors for the electromagnetic calorimeter in CMS, have been developed and their characteristics defined, in various stages, jointly by Hamamatsu Photonics and PSI. In 1999, an order for 180'000 APDs was placed with Hamamatsu by PSI, representing the CMS collaboration.

The R&D work for the CMS pixel detector, where PSI has overall responsibility, has concentrated on the design of the readout chip, with all necessary circuit parts now conceived. Next year will see the first assembly of the complete chip. The purchase of a new automatic wire bond station has also been approved for the Silicon detector laboratory.

High intensity pion test beams at PSI, closely simulating the expected difficult running conditions at LHC, have been used by many external groups preparing for experiments at LHC. This emphasizes the role of our laboratory at PSI: besides its being a userlab, it also acts as a baselab for experiments carried out elsewhere.

THEORY (I)

C. Alexandrou[2], A. Boriçi[3], A. Denner[1], St. Dürr[1], D. Graudenz[1], Th. Jensen[1], K. Junker[1], M. P. Locher[1], V. E. Markushin[1], M. Melles[1], St. Pozzorini[1], R. Rosenfelder[1], M. Roth[4], D. Wackeroth[5], O. Wigger[1]

PSI[1] – CYPRUS[2] – ETH ZÜRICH[3] – LEIPZIG[4] – ROCHESTER[5]

At present the Theory group is working mainly in the following fields: exotic atoms (nuclear, atomic and molecular effects), strong interaction physics at low energy (pions, mesonic resonances, antiprotons), nonperturbative methods in field theory like lattice gauge theory (algorithms, implementation of chiral symmetry) and the Standard Model of particle physics (collider physics, electroweak radiative corrections, deeply inelastic scattering, jets).

Below, and in the following contribution, a few examples are presented in more detail; for further topics see the detailed list of publications which also includes the work done in collaboration with visitors.

W-pair production

One of the most important tests of the electroweak Standard Model that is presently being performed is the investigation of W-pair production at LEP2. Owing to the very short lifetime of the W-bosons, the process $e^+e^- \to W^+W^- \to$ 4 fermions has to actually be studied. Figure 1 shows the present experimental data points for the corresponding cross section together with the Standard-Model prediction as obtained with the programme GENTLE. This programme contains besides the lowest-order contribution only the leading radiative corrections, i.e. the running of the electromagnetic coupling, the Coulomb singularity close to threshold, and the corrections associated with initial-state photon radiation. It is known that the missing corrections are of the order of 1–2% and tend to reduce the cross section. Accordingly, in Figure 1, the theoretical prediction is drawn as a band with a width of 2%. In view of the accuracy of the experimental data, a calculation of the missing corrections had become necessary. This calculation was performed at PSI and implemented into a Monte Carlo generator, called RACOONWW, during the last year. First results obtained with this generator have been published [1, 2]. Our results indeed show that the prediction of GENTLE is about 2% too high. The improved theoretical prediction gives a better agreement with experiment.

With the Monte-Carlo generator RACOONWW not only the total cross section but arbitrary distributions can be calculated. It provides, in particular, invariant-mass distributions, which are relevant for the experimental determination of the W-boson mass, and angular distributions, which are used to derive experimental limits to anomalous triple gauge-boson couplings. Furthermore, RACOONWW includes also the production of W pairs together with a photon, i.e. the process $e^+e^- \to W^+W^-(+\gamma) \to$ 4 fermions $+\gamma$ [3], which allows one to investigate quartic gauge-boson couplings. Moreover, our generator is not only applicable at LEP200 but also at higher energies which are relevant for a possible future linear electron–positron collider [4].

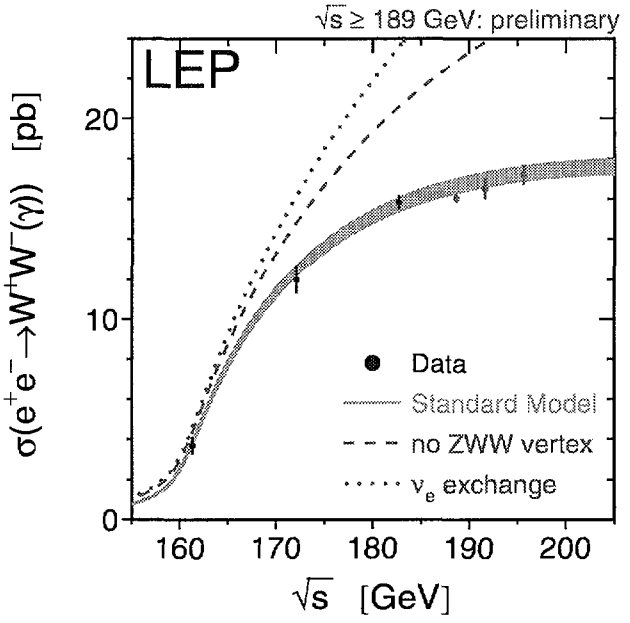

Figure 1: W-pair-production cross section at LEP

REFERENCES

[1] A. Denner, S. Dittmaier, M. Roth and D. Wackeroth, *$\mathcal{O}(\alpha)$ corrections to $e^+e^- \to W^+W^- \to 4$ fermions $(+\gamma)$: first numerical results from RacoonWW*, PSI-PR-99-29, hep-ph/9912261.

[2] A. Denner, S. Dittmaier, M. Roth and D. Wackeroth, *Four-fermion production with RacoonWW*, PSI-PR-99-30, hep-ph/9912290, to appear in the proceedings of the UK Phenomenology Workshop on Collider Physics, Durham, UK, 19–24 September, 1999.

[3] A. Denner, S. Dittmaier, M. Roth and D. Wackeroth, *Predictions for all processes $e^+e^- \to 4$ fermions $+\gamma$*, PSI-PR-99-10, hep-ph/9904472, Nucl. Phys. **B 560**, 33-65 (1999).

[4] A. Denner, S. Dittmaier, M. Roth and D. Wackeroth, *W-pair production at future e^+e^- colliders: precise predictions from* RACOONWW, PSI-PR-99-34, hep-ph/9912447.

THEORY (II)

C. Alexandrou[2], A. Boriçi[3], A. Denner[1], St. Dürr[1], D. Graudenz[1], Th. Jensen[1], K. Junker[1], M. P. Locher[1], V. E. Markushin[1], M. Melles[1], St. Pozzorini[1], R. Rosenfelder[1], M. Roth[4], D. Wackeroth[5], O. Wigger[1]

PSI[1] – CYPRUS[2] – ETH ZÜRICH[3] – LEIPZIG[4] – ROCHESTER[5]

Scalar mesons

The structure of light scalar mesons $J^{PC} = 0^{++}$, $I = 0$ has been studied in a dynamical coupled channel model [1]. The lightest state is shown to be the broad σ-meson which corresponds to the S-matrix pole at $(M_\sigma - i\Gamma_\sigma/2) = (0.4 - i0.2)$ GeV. This pole has a dynamical origin: it is produced by the attractive interaction in the $\pi\pi$-system. The σ-meson is fundamentally different from the $q\bar{q}$-resonances, in particular, it vanishes in the limit $N_c \to \infty$ where the $q\bar{q}$-resonances turn into narrow states.

The second state is the $f_0(980)$ near the $K\bar{K}$-threshold which corresponds to two S-matrix poles close to the physical region. This state is also of dynamical origin because it originates from a $K\bar{K}$ molecular-like state embedded into the $\pi\pi$-continuum. This state also vanishes in the limit $N_c \to \infty$ when the $K\bar{K}$-interaction becomes weak.

The genuine $q\bar{q}$-states and the scalar glueball are expected in the mass region $M > 1$ GeV where a number of $J^{PC} = 0^{++}$, $I = 0$ resonances have been found. The analysis of experimental data in the framework of the coupled–channel model shows that there is strong mixing between the different sorts of the scalar mesons leading to a significant violation of the OZI rule in the $J^{PC} = 0^{++}$, $I = 0$ channel.

Proton radius and muonic hydrogen

Traditionally elastic electron scattering data from the proton have been analyzed in the one-photon-exchange approximation since $Z\alpha \simeq 1/137$ was supposed to be small enough. In this way a root-mean-square charge radius of the proton $r_p = 0.862\,(12)$ fm has been deduced from elastic electron-proton scattering experiments at Mainz 20 years ago. This value superseded the nearly canonical value of 0.805(11) fm from Stanford which was based on an (invalid) $Q^2 \to 0$ extrapolation of the dipole form factor fitted to data at higher momentum transfer. In the last few years atomic Lamb shift measurements in hydrogen have become increasingly more accurate and are now very sensitive to the proton size. Assuming the validity of bound state QED calculations a value for the proton charge radius can be deduced from the Lamb shift; the most recent theoretical evaluation [3] leads to $r_p = 0.883\,(14)$ fm which is slightly higher than the electron scattering value. A possible reason for this discrepancy may be the distortion of the scattering waves in the electrostatic field of the proton which has recently been investigated [2]. In this work low-momentum-transfer scattering data from different experiments have been reanalyzed with Coulomb and recoil corrections included. This was done by calculating at each scattering angle and scattering energy the corresponding correction obtained from a partial wave analysis. The rms-radius was determined by a fit which allowed free normalization for each experiment. It turned out that the inclusion of Coulomb corrections into the analysis of electron scattering data lowers the χ^2 of the fit and increases the proton radius by about $(0.008 - 0.013)$ fm depending on the fit strategy. A value of $r_p = (0.880 \pm 0.015)$ fm has been obtained, which is now in excellent agreement with the one extracted from Lamb shift measurements.

Eventually, the muonic hydrogen experiment PSI-R-98-03 will yield this fundamental hadronic quantity with a tenfold higher accuracy than that obtained from electron scattering and the electronic Lamb shift. However, precision laser experiments only become feasible if a sizeable fraction of muonic hydrogen atoms end up in the $2S$-state with a sufficiently long lifetime. In liquid or gaseous hydrogen this lifetime is shortened considerably due to Stark mixing by μp-scattering on hydrogen followed by $2P \to 1S$ radiative transitions. A new detailed Monte Carlo kinetics calculation [4] has determined the surviving metastable fraction of the $(\mu p)_{2S}$ for a given initial kinetic energy of the muonic hydrogen atom (see Fig. 1). This calculation is based on cross sections obtained quantum mechanically in the coupled-channel approximation and provides a more reliable basis for estimating the important metastable $(\mu p)_{2S}$-fraction in the Lamb shift experiment.

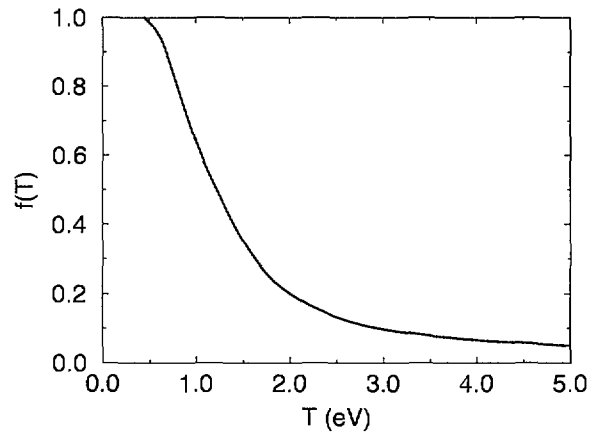

Figure 1: The metastable surviving fraction $f(T)$ of the $(\mu p)_{2S}$-states vs. the initial kinetic energy T at a hydrogen density of less than 10^{-2} of liquid hydrogen density

REFERENCES

[1] V. E. Markushin and M.P. Locher, *Structure of the light scalar mesons from a coupled channel analysis of the S-wave $\pi\pi - K\bar{K}$ scattering*, Frascati Physics Series Vol.XV (1999) 229-236, PSI-PR-99-15

[2] R. Rosenfelder, *Coulomb corrections to elastic electron-proton scattering and the proton charge radius*, PSI-PR-99-33, nucl-th/9912031

[3] K. Melnikov and T. van Ritbergen, hep-ph/9911277

[4] T.S. Jensen and V.E. Markushin, *Collisional quenching of the 2S state of muonic hydrogen*, PSI-PR-99-32, nucl-th/0001009

A PRECISE MEASUREMENT OF THE $\pi^+ \to \pi^0 e^+ \nu$ DECAY RATE

E. Frlež[1], J. E. Koglin[1], W. Li[1], R. C. Minehart[1], B. E. Norum[1], D. Počanić[1], S. Ritt[1,2], O. A. Rondon-Aramayo[1], L. C. Smith[1], W. A. Stephens[1], K. O. H. Ziock[1], W. Bertl[2], Ch. Broennimann[2], J. F. Crawford[2], M. Daum[2], R. Horisberger[2], D. Renker[2], D. Sawannakachorn[2], R. Schnyder[2], H. P. Wirtz[2], T. Kozlowski[3], B. G. Ritchie[4], V. A. Kalinnikov[5], N. V. Khomutov[5], A. S. Korenchenko[5], S. M. Korenchenko[5], N. P. Kravchuk[5], N. A. Kuchinsky[5], D. Mzhavia[6], Z. Tsamalaidze[6], I. Supek[7]

R-89-01.1, PIBETA Collaboration: VIRGINIA[1] – PSI[2] – SWIERK[3] – ARIZONA[4] – DUBNA[5] – TBILISI[6] – ZAGREB[7]

The PIBETA experiment aims to measure the pion beta decay ($\pi^+ \to \pi^0 e^+ \nu$) branching ratio to about 0.5 % in its current phase. The best experimental value at present has error limits of ~ 4 %, far exceeding the theoretical uncertainty of < 0.15 %.

During 1999, we have successfully completed the final commissioning of the PIBETA detector system and initiated production data-taking. Specifically, we have: (i) redesigned the trigger electronics around a new PSI-built fast LB500 logic module, (ii) introduced new trigger classes for beam diagnostics and monitoring, (iii) improved the beam passive and active collimation and tagging, as well as added the top plane of the cosmic veto house, (iv) implemented the domino sampling chip readout for the beam detectors, and (v) realized almost 100 % experiment automation, having the system run virtually free of human intervention.

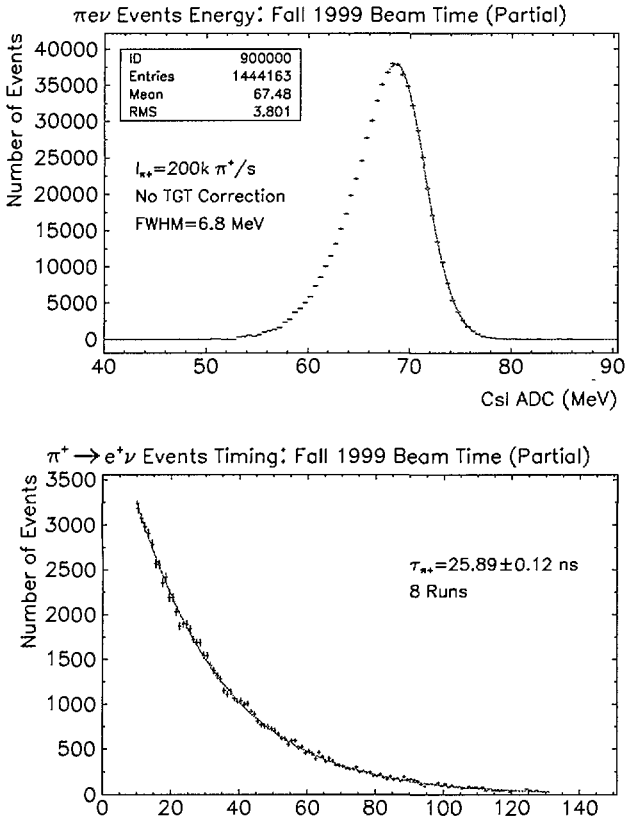

Figure 1: Typical preliminary $\pi \to e\nu$ calorimeter energy (top) and timing (bottom) spectra from our 1999 data.

Typical energy and timing spectra for the $\pi \to e\nu$ events used for the absolute π^+ beam normalization are displayed in Fig. 1.

The most important results of 1999 year's running period concern our pion beta ($\pi\beta$) decay data.

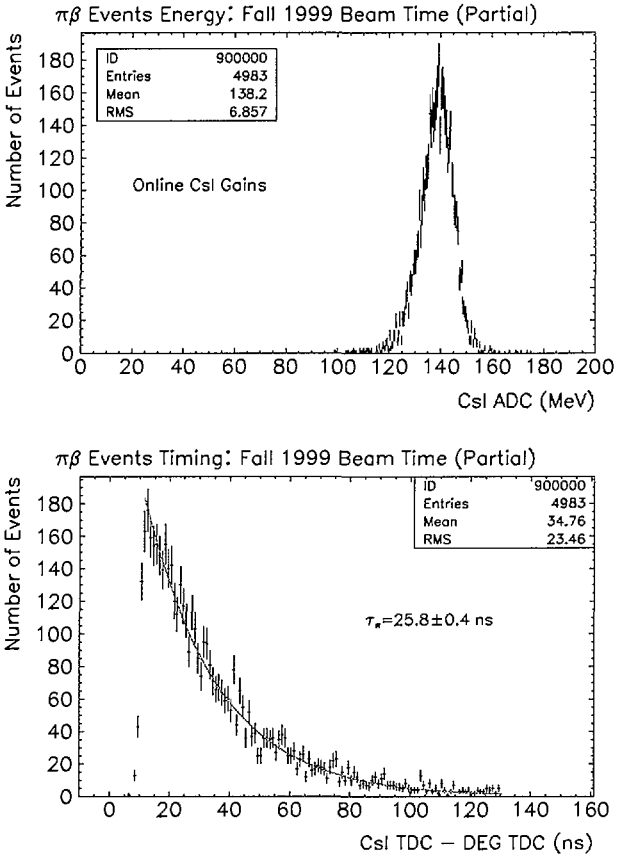

Figure 2: $\pi\beta$ calorimeter energy (top) and timing (bottom) spectra from about one half of the 1999 data set.

The top panel in Fig. 2 shows the spectrum of energy deposited in the CsI calorimeter by the two photons following the π^0 decay from $\pi^+ \to \pi^0 e^+ \nu$.

The bottom panel in Fig. 2 shows the timing difference spectrum between the CsI calorimeter hit and the π^+-stop. The spectrum is a clean exponential function consistent with the π^+-lifetime. At the statistical level of the current analysis there is no evidence of a non-pion decay background in the above histograms.

In summary, we have demonstrated that we can detect background free $\pi\beta$-events. The apparatus easily handled pion stopping rates of 1 MHz and lower, as designed. During 1999 we have recorded $\sim$10,000 $\pi\beta$-events which should enable us to extract the $\pi\beta$ branching ratio with about 1 % uncertainty, as was originally planned after the first year of operation.

MEASUREMENT OF THE TRANSVERSE POLARIZATION OF POSITRONS FROM THE DECAY OF POLARIZED MUONS

K. Bodek[1,2], A. Budzanowski[4], N. Danneberg[1], W. Fetscher[1], Ch. Hilbes[1], M. Janousch[1], L. Jarczyk[2], K. Kirch[1], St. Kistryn[2], J. Klement[1], K. Köhler[1], A. Kozela[1,4], J. Lang[1], M. Markiewicz[1], G. Llosa[1], X. Morelle[3], Th. Schweizer[1], J. Smyrski[2], J. Sromicki[1], E. Stephan[5], A. Strzałkowski[2], J. Zejma[2]

R 94 - 10.1, ETH[1] – J.U. CRACOW[2] – PSI[3] – INP. CRACOW[4] – KATOWICE[5]

This experiment aims at improving on the present limits [1] of the transverse positron polarization by one order of magnitude, to achieve better limits on non-standard couplings and time reversal invariance in weak interactions.

Polarized μ^+ arrive in bunches every 20 ns and are stopped in a beryllium target yielding a stop rate of $2 \cdot 10^7 s^{-1}$. They precess with a frequency of 50 MHz in a magnetic field of 0.3 T. The fact that the accelerator cycle (20 ns) is equal to the precession frequency (50 MHz) preserves the polarization of the muons. The decay positrons passing a start counter are tracked with drift chambers, and annihilate in a magnetized vacoflux foil which serves as a polarimeter. Two additional small chambers and veto counters ensure that the annihilation took place in the magnetized foil. The two annihilation photons are detected in the BGO calorimeter consisting of 127 hexagonal modules. Figure 1 shows the setup of the experiment.

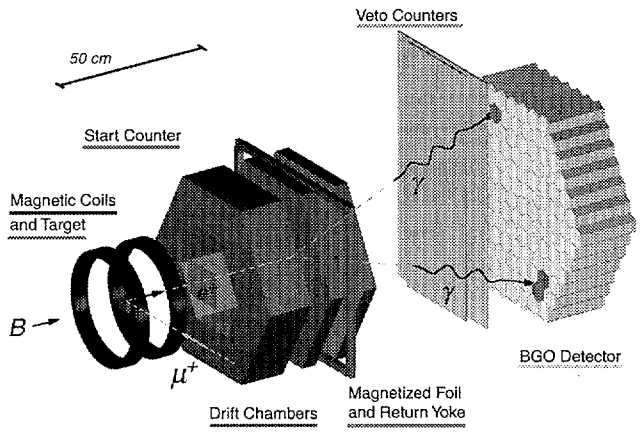

Figure 1: Setup of the μ_{P_T} experiment. Details are given in the text.

In 1999, data were taken with a complete experimental setup and a specially designed cluster recognition unit (CRU). This CRU selects events consisting of exactly two clusters on the BGO wall corresponding to the expected signature of annihilation events. The BGOs were calibrated online using cosmic rays.

Due to the μ-spin rotation, the effect of a transverse polarization component will manifest itself in a rotation of the photon intensity distribution on the BGO calorimeter. This time dependence can be written in the form

$$f(t) = 1 + A \cdot \sin(\omega t + \alpha) \quad (1)$$

where ω is the μSR frequency, t is the time between the accelerator cycle and muon decay, A and α are functions of the energy, position of the two photons and two orthogonal transverse polarization components P_1 and P_2. Equation 1 can be used to perform a log-likelihood parameter estimation of P_1 and P_2. Figure 2 shows the result of this fit to 1.6 Mio. annihilation events taken in August 1999 . Proper averaging of P_1 and P_2 over the energy dependence gives a preliminary result of $< P_1 >= 0.021 \pm 0.021$ and $< P_2 >= 0.022 \pm 0.021$. Using only this subset of the available data, both transverse polarization components are compatible with the standard model.

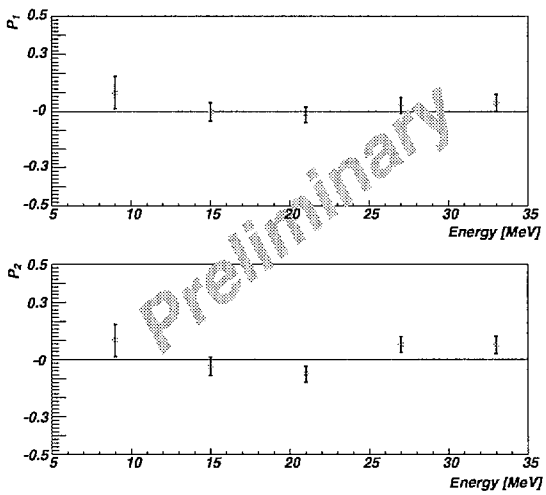

Figure 2: Transversal positron polarization components P_1 and P_2 as a function of the positron energy at the time of annihilation.

This project is supported in part by the Polish Committee for Scientific Research under Grant No. 2P03B05111.

REFERENCES

[1] H. Burkard et al., Phys. Lett. **B 160**, 343 (1985).

PARTICLE PHYSICS WITH POLARIZED COLD NEUTRONS AT SINQ

K. Bodek[1,4], P. Böni[1], N. Danneberg[1], W. Fetscher[1], W. Haeberli[5], Ch. Hilbes[1], A. Kharitonov[3], K. Kirch[1], K. Köhler[1], I. Krasnochtchekova[3], J. Lang[1], M. Lasakov[3], M. Lüthy[2], St. Kistryn[4], M. Markiewicz[1], E. Medvedev[3], V. Pusenkov[3], A. Schebetov[3], A. Serebrov[3], J. Sromicki[1,S], A. Vassiljev[3]

R-96-04, ETH ZÜRICH[1] – PSI[2] – GATCHINA[3] – CRACOW[4] – MADISON[5]

Neutron decay experiments are limited by counting statistics. With present day technology, the highest spatial density of free neutrons is obtained in a beam of *cold neutrons*. Recently, a new facility for particle physics has been installed at the spallation source SINQ. An experimental area has been constructed (Fig. 1) for a series of experiments fed by a high intensity, polarized cold neutron beam.

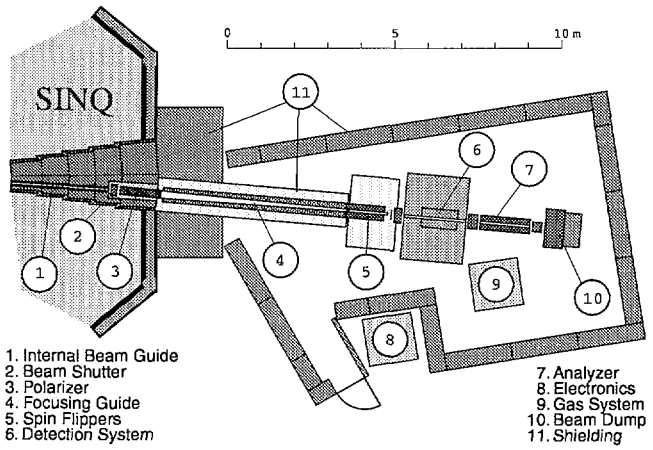

Figure 1: Layout of the Polarized Cold Neutron Facility.

The available neutron channel on the SINQ north-side has been equipped with a large aperture and large momentum acceptance beam guide. The guide is coated with ~450 layers of ($m \approx 3.3$) Ni/Ti supermirrors. The main neutron beam shutter is integrated into the SINQ biological shielding. The external part of the beamline [1] consists of a multi-slit supermirror polarizer and bender, a cold neutron beam stop, a focusing beam guide (tapering from 8×15 cm^2 down to 4×15 cm^2), radiofrequency spin flippers, a polarization analyzer system with a chopper for time-of-flight measurements, and two further cold neutron beam dumps placed downstream. The front section, including polarizer and bender, is mounted inside the SINQ shielding to contain radiation associated with the neutron capture reactions. The external part of the guide is enclosed by a sandwich-type radiation shielding (brass/ polyethylene/ iron/ lead) for fast neutrons penetrating the walls as well as secondary gamma rays. The whole beam tract is contained in a massive, biological shield.

Using the gold foil activation method a "thermal equivalent flux" of unpolarized neutrons of $3 \cdot 10^9$ (cm^2·s·mA)$^{-1}$ was determined at the entrance to the polarizer. With the same technique a flux of $6 \cdot 10^8$ (cm^2·s·mA)$^{-1}$ polarized neutrons was measured at the exit of the neutron guide, where the experiments will be located. The characteristic cold neutron spectrum and the wavelength dependence of the beam polarization was then determined (Fig. 2) using the time of flight technique. With this spectrum we estimate the "real" neutron flux of $2 \cdot 10^8$ (cm^2·s·mA)$^{-1}$. The total intensity of the polarized neutron beam available for experiments exceeds 10^{10} (s·mA)$^{-1}$. (At present the SINQ source operates routinely with a 1.2 mA proton beam; an upgrade of the beam current and spallation target is planned.) The average polarization in the central part of the beam exceeds 97% (Fig. 2). More detailed measurements of the neutron beam properties, e.g. the distributions of the flux, polarization and divergence, are in progress and will be reported elsewhere.

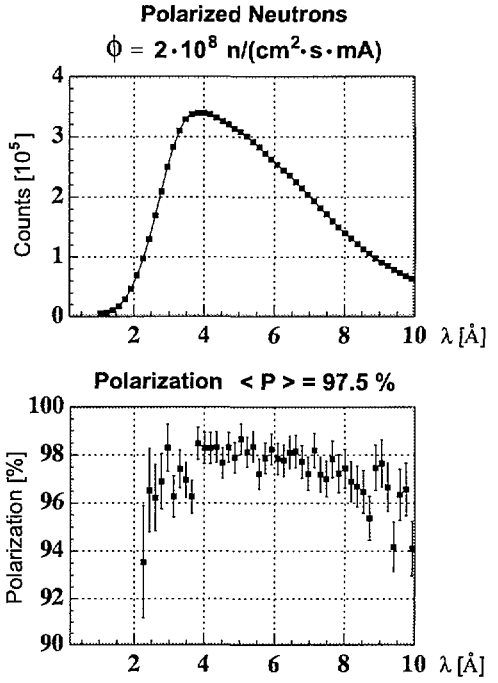

Figure 2: Upper part: Neutron spectrum measured using the TOF technique and a thin ^{3}He-detector. Lower part: Wavelength dependence of the beam polarization.

The physics program for this new facility will focus on free neutron decay studies, addressing mainly the questions of fundamental symmetries (time reversal and parity) and/or their violations in the weak interaction [2].

REFERENCES

[1] A. Schebetov, A. Serebrov, P. Böni, J. Sromicki et. al., *Polarizers with Condensers for Sector 50 at SINQ*, PNPI Report, 1998.

[2] I.C. Barnett, K. Bodek, J. Sromicki et. al., *Study of Fundamental Symmetries with Polarized Cold Neutrons at SINQ*, PSI Letter of Intent (BV-24, 1996) and Proposal (BV-26, 1997).

SEARCH FOR A NEUTRAL PARTICLE OF MASS 33.9 MEV IN PION DECAY

M. Daum[1], *M. Janousch*[3], *P.-R. Kettle*[1], *J. Koglin*[1,2], *D. Počanić*[2], *J. Schottmüller*[1], *C. Wigger*[1], *Z.G. Zhao*[4]

R-96-05.1, PSI[1] – VIRGINIA[2] – ETH ZÜRICH[3] – BEIJING[4]

We have searched for the rare pion decay

$$\pi^+ \to \mu^+ X, \qquad (1)$$

where X is a neutral particle of mass 33.9 MeV. This process was suggested by the KARMEN Collaboration to explain an anomaly in their observed time distribution of neutrino induced reactions [1]. The mass of X in decay (1) is very close to the mass difference between the charged pion and the muon. For a decay-in-flight experiment, this implies that the velocity of the decay muon is very similar to that of the original pion, and hence, $p_\mu \approx p_\pi \cdot m_\mu/m_\pi$.

In 1995, we measured the momentum spectrum of muons from π^+-decay in flight and placed an upper limit on the branching fraction η for this decay at $2.6 \cdot 10^{-8}$ (c.l. 95%) [2].

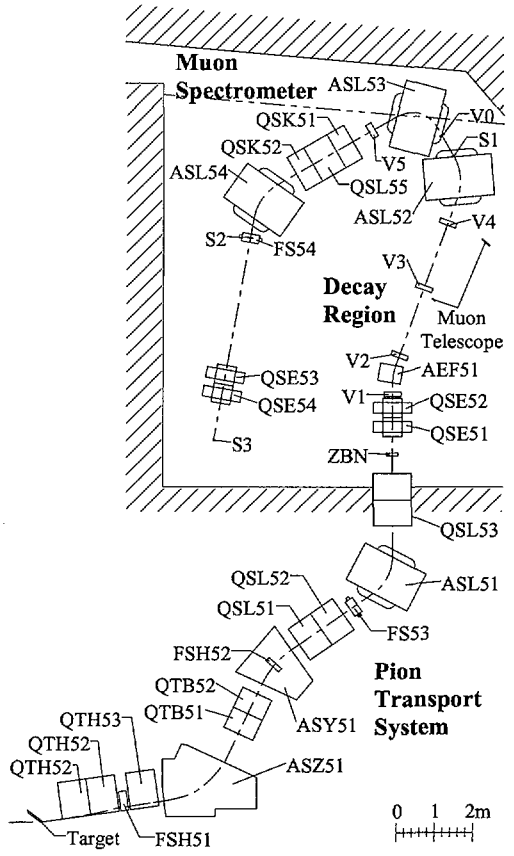

Figure 1: The beam-line consists of three parts: (i) the pion transport system up to and including the magnet AEF51; (ii) the pion decay region between the magnets AEF51 and ASL52; (iii) the muon spectrometer from the magnet ASL52 to the beam counter S3. ASZ, ASY, ASL, AEF: dipole magnets; QTH, QTB, QSL, QSE, QSK: quadrupole magnets; FSH, FS, ZBN: passive collimators; S1–S3: beam scintillation counters; V0–V5: active (scintillation counters) and passive (lead jaws) collimators.

In order to increase our sensitivity on η, a new experiment was started with various improvements made in suppressing the background. In 1999, we undertook our final run with an extra dipole magnet (ASL54) added to the muon spectrometer part of the beam-line, giving the final experimental setup shown in Fig. 1.

The pion transport system (see Fig. 1) was set to a momentum of 150 MeV/c. Muons from decay (1) are expected to have a momentum of approx. 113.5 MeV/c. By scanning the muon spectrometer part of the beam-line (see Fig. 1) from 103 MeV/c to 124 MeV/c, a muon momentum spectrum is obtained.

Our data are sub-divided into four data-sets, reflecting changes to the acceptance of the muon spectrometer during the experiment. One of these data-sets is displayed in Fig. 2. Clearly, no indication for the existence of the hypothetical decay (1) is evident in these data, nor is there any indication of its existence in the other data-sets. The expected level of background events originating from the radiative pion decay, $\pi^+ \to \mu^+ \nu_\mu \gamma$, is also indicated in Fig. 2.

From a preliminary analysis of all four data-sets, we estimate that we will be able to reach a sensitivity on η of a few 10^{-10} for the hypothetical decay (1).

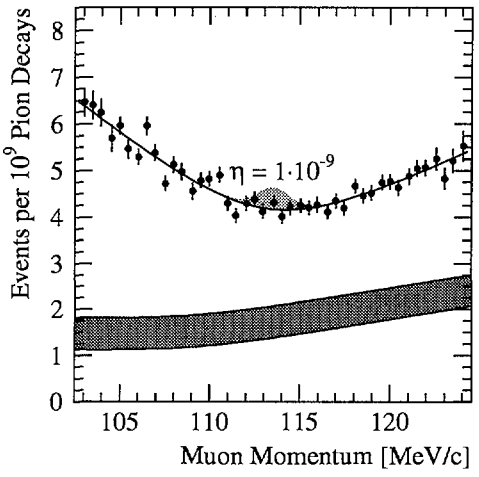

Figure 2: Experimental data-set. The solid curve shows the fit to the data (hyperbola plus Gaussian). The shaded peak shows the expected effect of the hypothetical decay (1) for $\eta = 1{\cdot}10^{-9}$. The shaded band shows the simulated background from the radiative pion decay, $\pi^+ \to \mu^+ \nu_\mu \gamma$, within computational uncertainties.

REFERENCES

[1] B. Armbruster et al., Phys. Lett. **B 348**, 19 (1995).

[2] M. Daum et al., Phys. Lett. **B 361**, 179 (1995).

A PRECISION MEASUREMENT OF THE MICHEL PARAMETER ξ" IN POLARISED MUON DECAY

P. Van Hove[1] , *J. Deutsch*[1] , *J. Govaerts*[1] , *P. Knowles*[1] , *R. Medve*[1] , *A. Ninane*[1] , *R. Prieels*[1] ,
N. Danneberg[2] , *W. Fetscher*[2] , *M. Hadri*[2] , *C. Hilbes*[2] , *K. Kirch*[2] , *M. Markiewicz*[2] , *J. Lang*[2] ,
O. Naviliat[2] , *T. Schweizer*[2] , *J. Sromicki*[2] ,
X. Morelle[3] , *J. Egger*[3] , *F. Foroughi*[3]

R-97-06, LOUVAIN[1] – ETH ZÜRICH[2] – PSI[3]

We describe briefly our final experimental setup and present the last results of the 1999 run concerning positron tracking in the spectrometer (Silicon detector) and the polarimeter. The experiment compares the energy dependence of the longitudinal polarization of positrons emited in polarized muon decay with the one of positrons from unpolarized muons. This will lead to a measurement of the Michel parameter ξ" with a precision of five per mille i.e. two orders of magnitude better than the precision obtained in [1].

Let us describe briefly the elements of the apparatus shown in figure 1. With a Wien filter to divert the numerous positrons at the end of the PIE3 beam line, we select highly polarized surface muons and stop them either in aluminium or in sulphur. The first target keeps the polarization, the second one destroys it. The muon polarization and rate are monitored using three telescopes (not shown in fig.1) viewing the muon stopping target at different angles. The most energetic positrons of the Michel spectrum are selected using a superconductor (TRAP) running at 2.5 Tesla and filled with collimators and shielding. An analysis of the positron momentum is performed with a resolution of 1 MeV/c by a silicon telescope array immersed in a homogeneous magnetic field of 2 Tesla, produced by the PSC Magnet. The positron polarimeter measures the rates of Bhabha scattering and Annihilation in flight of positrons on the polarized electrons of 2 Vacoflux foils with opposite magnetization. The magnetization can be reversed. Four wire chambers locate and identify the interaction. A fifth wire chamber followed by 2 hodoscopes and a wall of 127 BGO-crystals recognizes the two e+e- or $\gamma\gamma$ clusters and measures their energies. The full polarimeter is magnetically shielded by the Big Iron Box.

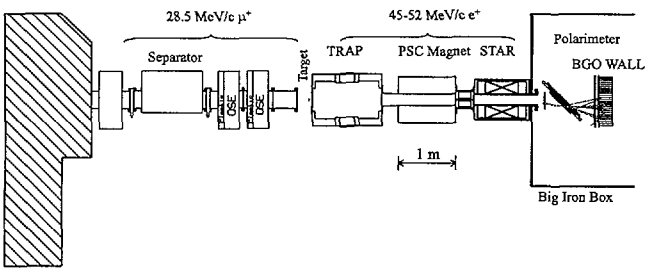

Figure 1: Full experimental setup.

Positron Spectrometry

In the March run, the positron tracker reached only 60% efficiency in energy reconstruction. New preamplifiers and a remote power supply to drive the bias voltages were installed, a new geometry of the Silicon units was chosen to avoid a too high concentration of positrons in the centre of the detector. The result was an increase of efficiency to 75% (95% efficiency in each of the 6 planes) and the possibility to obtain an on-line energy reconstruction with a simple mathematical algorithm. With this tool we could observe the difference in the positron energy spectrum from polarised and unpolarised muons. A preliminary analysis shows that the results are compatible with the Monte Carlo calculations. We are confident that the silicon spectrometer will deliver the desired resolution between 48 and 53 MeV.

Polarimeter

2 Vacoflux foils, 15 cm x 60 cm, are placed parallel to one another at an angle of 45° to the beam axis. Their opposite magnetization is generated by 2 coils giving a maximum of 2000 Ampere×turns. The 1mm thick foils, shaped to .75 mm in the positron beam region, were magnetically baked to have a high remnant field. The measured hysteresis curve shows that we keep more than 90% of the maximum possible polarization of the electrons in the foil without external current. This means that no external field can influence the BGO phototube amplification and produce systematic asymmetry when changing the direction of magnetization. The 4 chambers defining the nature and location of the Bhabha and Annihilation events are read-out with the same preamplifiers as the silicon detectors. With the shaping time of a few μs which we use, it is easy to get a high efficiency and bring these relatively compact chambers to work perfectly with a safe gas amplification. A fifth chamber, with groups of 32 wires read-out by one preamplifier, has to confirm the hits pattern of 2 hodoscopes each comprised of 7 plastic counters. The hodoscopes were included in the trigger to define event types by their multiplicity. The fifth chamber will also be included in the trigger for the next run, since the polarimeter Monte Carlo shows that it will efficiently reduce the number of wrong Bhabha triggers. The 127 BGO-crystals are calibrated with cosmic muons and their stability is controlled with 1 LED pulser on each BGO. The November test confirmed the quality of the magnetic shielding (the Big Iron Box): with all fields set, the gain changes of the phototubes can be corrected for by small changes in the HV. All fields are kept constant during the experiment except for the foil magnetization which does not produce any external magnetic field as explained above. A set of rate measurements was done with different foil materials and foil thickness. They perfectly reproduced the trigger rates given by the polarimeter Monte Carlo. The analysis of November's data is in progress.

REFERENCES

[1] H. Burkard et al., Phys. Lett. **B 150**, 242 (1985).

SEARCH FOR EXOTIC MUON DECAYS

R. Bilger[1], *K. Föhl*[2], *D. Branford*[2], *H. Clement*[1], *M. Cröni*[1], *A. Erhardt*[1], *R. Meier*[1], *A.N. Ostrowski*[2], *J. Pätzold*[1], *G.J. Wagner*[1]

R-99-01, TÜBINGEN[1] – EDINBURGH[2]

At the Rutherford Appleton Laboratory (RAL) the KARMEN collaboration is studying neutrino-nuclear reactions, induced from the decay products of positive pions, which are produced and stopped in the proton beam dump. In 1995, KARMEN reported [1] an anomaly in the time distribution of single prong events associated with the time interval corresponding to muon decay. Even with a much improved active detector shielding the anomaly has persisted in the new KARMEN data. This anomaly was suggested to originate from the observation of a hitherto unknown weakly interacting neutral and massive fermion, called x, produced in a rare pion decay process $\pi^+ \rightarrow \mu^+ \mathrm{x}$. The hypothetical decay $\pi^+ \rightarrow \mu^+ \mathrm{x}$ has been searched for, at PSI, in a series of experiments using magnetic spectrometers by studying muons from pion decay-in-flight [2, 3].

Very recently it has been proposed [4] that the observed time anomaly can also be explained by an exotic μdecay branch $\mu^+ \rightarrow \mathrm{e}^+\mathrm{X}$ resulting in the production of a new, weakly interacting neutral boson with mass $103.9\,\mathrm{MeV/c^2}$. The authors show that a second exponential in the KARMEN time distribution with a time constant corresponding to the muon lifetime and shifted by the flight-time of the X-particle $t_{\mathrm{TOF}} = 3.60\,\mu\mathrm{s}$ gives an acceptable fit to the KARMEN data.

In 1998, at the μE4 channel, we performed a first test measurement to search for the X particle by studying the low energy part of the Michel spectrum looking for a peak from mono-energetic positrons resulting from the two-body decay $\mu^+ \rightarrow \mathrm{e}^+\mathrm{X}$. The basic idea is to stop a μ^+-beam of momentum 60 MeV/c inside a germanium detector. The low energy decay positrons of interest also deposit their entire kinetic energy in the detector volume. For a sizeable fraction of events the subsequent annihilation radiation does not interact with the detector thus preserving the positron energy information. The detector setup consists of two plastic scintillator counters directly in front of a 9 mm thick planar high purity germanium (HPGe) detector with an area of $1900\,\mathrm{mm^2}$. In addition, we placed a 5 inch thick NaI(Tl) detector adjacent to the HPGe for detecting annihilation γ-rays. Results are shown in Fig. 1 and published in [5].

A further experiment to search for X using an improved detector setup, has been performed at the μE4 channel in 1999. By using a larger HPGe detector the maximum μ-stopping rate in the detector could be significantly increased. In addition, stopping the muons at a greater depth increased the energy deposition of high energy positrons in the crystal, thus shifting these 'background' events to higher energies resulting in more favourable background conditions. By using dedicated beam defining scintillators it was possible to use a larger area of the germanium detector as a sensitive area in the trigger. A flash ADC for the HPGe detector has been used with the aim to considerably improve on the positron identification efficiency and energy resolution. By placing two additional Ge detectors around the central HPGe detector it was possible to tag on the annihilation gamma rays with an improved energy resolution. Using the annihilation radiation and/or the information from the flash ADC it is possible to achieve a thresholdless measurement of the positron energy (down to the very end of the Michel spectrum).

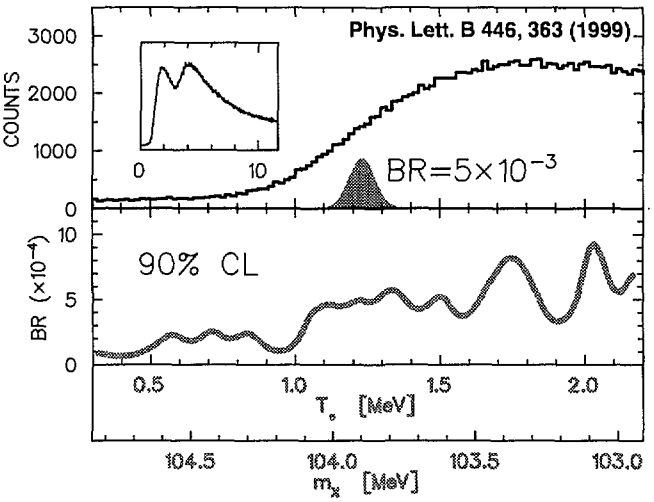

Figure 1: Plots showing the energy deposition during the delayed time gate in the HPGe detector (top and inset) and fit results leading to upper limits for the branching ratio for the decay $\mu^+ \rightarrow \mathrm{e}^+\mathrm{X}$ [5]. For the abscissa two corresponding scales are drawn, one is the positron kinetic energy $\mathrm{T_e}$, the other the X boson mass $\mathrm{m_X}$. In the graph at the top the Gaussian centered at 1.23 MeV gives the expected detector response if $\mu^+ \rightarrow \mathrm{e}^+\mathrm{X}$ would contribute with a branching ratio of $5 \cdot 10^{-3}$. The graph at the bottom gives the upper limit for a $\mu^+ \rightarrow \mathrm{e}^+\mathrm{X}$ decay branch at 90% confidence level by applying the Bayesian method to the fit results.

The analysis of the data is currently under way. With the improvements in the experimental setup as described above, we are confident that we are sensitive to a branching ratio of $1 \cdot 10^{-5}$ or smaller.

REFERENCES

[1] B. Armbruster et al., Phys. Lett. **B 348**, 19 (1995).

[2] R. Bilger et al., Phys. Lett. **B 363**, 41 (1995).

[3] M. Daum et al., Phys. Lett. **B 361**, 179 (1995).

[4] S. N. Gninenko and N. V. Krasnikov, Phys. Lett. **B 434**, 163 (1998).

[5] R. Bilger et al., Phys. Lett. **B 446**, 363 (1999).

ATMOSPHERIC PRODUCTION OF ^{26}AL

F. Kubo[1], V. Lazarev[1] W. Hajdas[2], E. Nolte[1]

R-94-08, MUNICH[1] – PSI[2]

The occurence of the long-lived radionuclide ^{26}Al in the atmosphere is due to two mechanisms: cosmogenic production on atmospheric argon and the influx of interplanetary dust containing ^{26}Al. To determine the atmospheric production of ^{26}Al, the cross sections of the reaction ^{40}Ar(p,6p9n) ^{26}Al were measured in the energy range from 100 to 590 MeV.

Argon gas targets were irradiated at the Proton Irradiation Facility (PIF). The target chambers were filled with gas at a pressure of 3 bar corresponding to $2 \cdot 10^{21}$ argon atoms per cm^2. Each target was irradiated with several 10^{13} protons. The produced ^{26}Al was absorbed on polypropylene foils at the inner walls of the chamber. The foils were placed into a hydrochloridic solution of ^{26}Al-free aluminium-standard. To precipitate $Al(OH)_3$ the acid was neutralized with NH_3OH. The $Al(OH)_3$ was oxidized at 900°C to Al_2O_3. The ratio ^{26}Al/Al was measured using AMS at the Garching accelerator laboratory. The measured cross sections are shown in Figure 1, together with previously measured cross sections by Reyss et al. [2].

To calculate the cross sections for the reaction ^{40}Ar(n,5p10n)^{26}Al a cascade-excitation-model (CEM 95) [4] was used. Using the differential flux of protons and neutrons in the atmosphere [3] the total average production rate of ^{26}Al could be calculated to be 0.69 atoms cm^{-2} sec^{-1}.

The influx of ^{26}Al by interplanetary dust can be estimated using measured cross sections on Mg, Al, Si, Fe and Ca [5] and the flux of the solar cosmic radiation at 1 A.U. With the assumption of an influx of 40 kt/d [6] and an elementary composition of the dust particles similar to C1-chondrites an influx of 0.17 ^{26}Al-atoms cm^{-2} sec^{-1} is obtained.

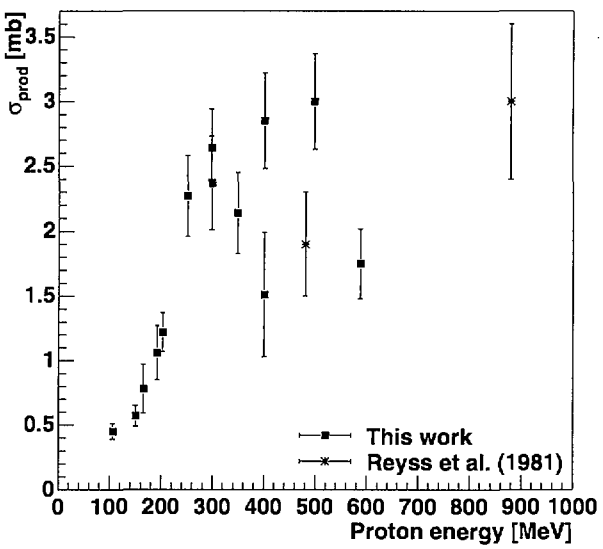

Figure 1: Measured cross sections for the ^{40}Ar(p,6p9n)^{26}Al-reaction. The points taken from [2] are from irradiation on liquid argon.

REFERENCES

[1] D. Lal and B. Peters, Handbuch der Physik, Springer, 1967, pp. 551-612

[2] J. Reyss, Y. Yokoyama, and F. Guichard, Earth and Planetary Sci. Lett. **53**, 203 (1981).

[3] V. Lazarev, Master thesis, St. Petersburg state tech. univ., 1998

[4] S. Mashnik, Izv. Ak. Nauk Ser. Phys. **60**, 73 (1996).

[5] T. Schiekel, Ph.D. thesis, Univesrität Köln, 1995

[6] S. Love and D. Brownlee, Science **262**, 550 (1993).

ANALYZING POWERS IN LOW ENERGY PION PROTON SCATTERING

R. Meier[1], R. Bilger[1], B. van den Brandt[2], J. Breitschopf[1], H. Clement[1], J. Comfort[3], M. Cröni[1], H. Denz[1], K. Föhl[5], E. Friedman[6], J. Gräter[1], P. Hautle[2], G.J. Hofman[4], J.A. Konter[2], S. Mango[2], J. Pätzold[1], M. Pavan[7], G.J. Wagner[1]

R-97-01, TÜBINGEN[1] – PSI[2] – ARIZONA[3] – COLORADO[4] – EDINBURGH[5] – JERUSALEM[6] – MIT[7]

The pion-nucleon system is the simplest hadronically interacting system that is easily accessible experimentally. Fundamental quantities can be extracted from data on pion-nucleon-scattering.

In recent years, extensive effort both by experimentalists and theorists has been aimed at fixing three of these quantities: the pion-nucleon coupling constant $f_{\pi NN}$, which determines the strength of the hadronic interaction, the degree of isospin breaking, which is connected to the mass ratio of the light quarks, and the σ-term, which gives access to the strangeness content of the nucleon.

Unfortunately, there is no agreement on the value of any of these quantities at present, mostly due to missing or inconsistent information in the πp scattering cross section database. Analyzing power (A_y) measurements in πp elastic scattering at low energies place important constraints on the phase shift analyses [1] and are able to resolve the inconsistencies in the cross section data base. Due to the difficulty of such measurements, only one A_y data-set at 68.3 MeV has been reported so far [2] in this energy region. The aim of our experiment is to substantially enhance the amount of A_y data. A novel scintillating polarized target is the key for solving the experimental problems.

These problems are caused by the structure of a dynamically polarized solid state target. The size of the polarized sample is typically comparable to the beam size. Therefore, the fraction of beam hitting it has to be monitored as it could change over time. Due to the heat shields and the vacuum vessel walls surrounding the target, as well as due to the magnetic field necessary to maintain polarization while measuring, the use of a beam definition counter is problematic. Another difficulty is caused by the target probe, which consists typically of frozen pieces of a material containing, in addition to the polarized protons, also carbon and oxygen, immersed in liquid helium, and cased in one or two brass containers. Events from πp elastic scattering must be separated from events due to background reactions on these materials. A very efficient method, the detection of the back-scattered proton in coincidence, is not suitable for measurements at low energies and small angles as the back-scattered proton does not leave the target. The energy straggling due to the material in the target region also limits the resolution that can be achieved with a pion detector for a kinematical separation of the various reactions.

A polarized active target helps to overcome these difficulties. It acts as a beam definition counter, rejecting reactions which take place outside it. Furthermore, the energy deposition in the target gives additional information on the interaction. Active polarized targets have been developed at PSI only recently [3]. The basic procedure for the production of polarizable scintillator consists in doping standard plastic scintillator with paramagnetic centres. This procedure is still being optimized for better polarizability and higher light output [4]. In the experiment described here proton polarizations of somewhat over 50% and light output of about 20% of the undoped scintillator were achieved.

The experiment was performed on the πE3 beam-line, using the Low Energy Pion Spectrometer LEPS as the pion detector. Data were taken with positively charged pions at 45, 51, 57, 68.3 and 87 MeV, at angles between Θ_{lab} =40° and 120°. The analysis is in progress. Preliminary results at 87 and 68.3 MeV are shown in Fig. 1 as solid points. The error bars include statistical errors only. The data are in good agreement with the previous measurement by Wieser et al. [2] at 68.3 MeV, shown as open data points. The results of the VPI SP99 and KH80 phase shift solutions are represented by solid and dashed lines. We plan to continue the measurements for π^-p elastic scattering. Here, data at 51 MeV and backward angles are of particular interest as an analysis has shown strong sensitivity of the analyzing power at this energy to the value of the σ-term [5].

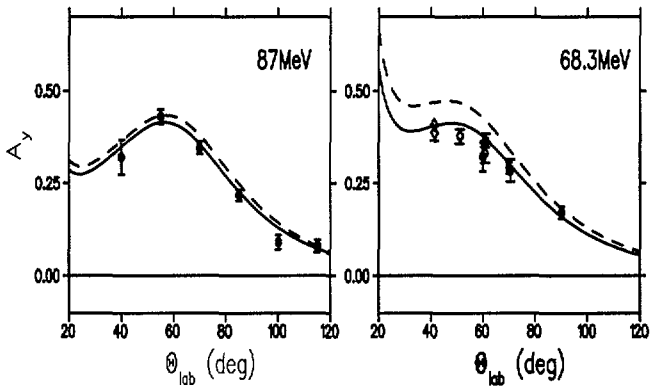

Figure 1: Preliminary results at 87 and 68.3 MeV are shown as solid data points. Open data points are from Wieser et al. [2]. The lines correspond to the VPI SP99 (solid) and KH80 (dashed) phase shift solutions.

REFERENCES

[1] M. E. Sainio, πN Newsletter **13**, 144 (1997).

[2] R. Wieser et al., Phys. Rev. **C 54**, 1930 (1996).

[3] B. van den Brandt et al., SPIN 96 Symposium Amsterdam (1996).

[4] H. Denz, Diploma Thesis, Univ. Tübingen (1998); J. Breitschopf, Diploma Thesis, Univ. Tübingen (1999).

[5] M. P. Locher, M. E. Sainio, Czech. J. Phys. **B 39** vol. 8, 934 (1989).

PRECISION MEASUREMENT OF SINGLET μP CAPTURE IN HYDROGEN

A. Adamczak[7], V.A. Andreev[1], D.V. Balin[1], T. Case[3], K.M. Crowe[3], J. Deutsch[5], P.U. Dick[2], A. Dijksman[2], J. Egger[2], A.A. Fetisov[1], V.A. Ganzha[1], J. Govaerts[5], F.J. Hartmann[4], W.D. Herold[2], V.I. Jatsioura[1], P. Kammel[3], A.G. Krivshich[1], E.M. Maev[1], O.E. Maev[1], V.E. Markushin[2], J. Martino[6], C. Petitjean[2], G.E. Petrov[1], R. Prieels[5], S.M. Sadetsky[1], G.N. Schapkin[1], R. Schmidt[2], W. Schöps[2], G.G. Semenchuk[1], A.A. Vorobyov[1], N.I. Voropaev[1]

R-97-05, GATCHINA[1] – PSI[2] – BERKELEY[3] – MUNICH[4] – LOUVAIN[5] – SACLAY[6] – CRACOW[7]

A new experiment has been set up to determine the capture rate in process $\mu p_{1s} \longrightarrow n + \nu_\mu$ to 1%, significantly exceeding the precision of previous experiments. This rate is sensitive to the weak form factors of the nucleon, in particular to the induced pseudoscalar coupling constant g_P. The measurement will be a rigorous test of modern effective field theories of low energy QCD [1].

Since direct observations of μp-capture by neutron measurement are limited to 5-10% accuracy we proposed to determine the capture rate from the difference of lifetimes τ_μ of $\mu^- p$ atoms versus that of the free μ^+. In order to achieve the planned precision, the μ^--measurement must be performed in ultraclean, deuterium depleted hydrogen gas at low density, about 1% of liquid H_2. Errors of τ below 10^{-5} must be achieved, requiring collection of at least 10^{10} good events. Any events from muon-stops outside the hydrogen gas must be carefully suppressed. To meet these challenges, we have developed a new hydrogen time projection chamber (TPC) of size 30x15x8 cm^3 surrounded by proportional chambers PC1-PC6, all placed inside a pressure vessel filled with 10 bar pure hydrogen.

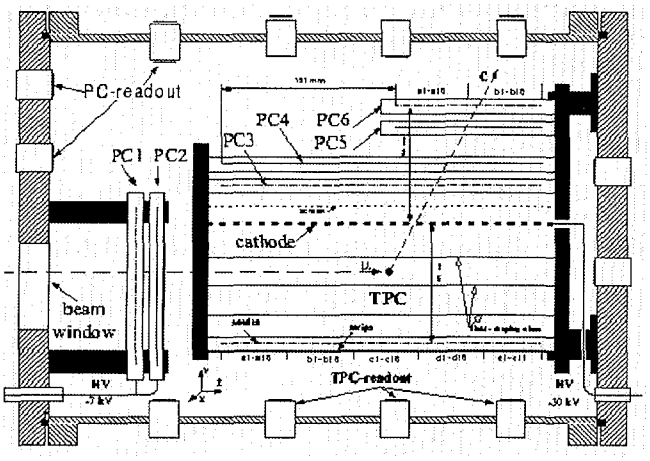

Figure 1: 1999 Setup of the hydrogen pressure vessel with TPC and PCs; for details see Refs. given in [2].

Figure1 shows the side view geometry of the hydrogen vessel with the chambers used in the 1999 test measurements. The system is designed to handle a muon beam of 50 kHz stopping in the TPC volume. The negative charges from ionizing particles drift in the TPC to a plane of 75 anode wires and 32 perpendicular cathode strips where they get amplified. The signals are digitized with 5 MHz in continuous mode and collected using custom-built deadtime-free TDCs. On-line tracking will be employed for data reduction to recordable levels. The concentrated track information is written to disc and tapes for later analysis.

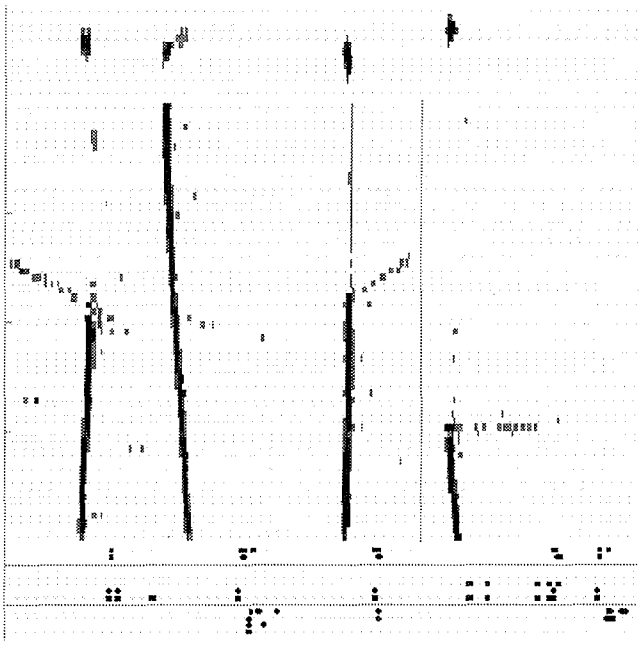

Figure 2: TDC display of μ- and e-tracks in the TPC. The horizontal axis gives the combined y-coordinate and drift time of tracks. Top: strip signals which show the x-position of the tracks (the tracks are very straight, so show up as spots.) Middle: anode signals which show the z-direction(beam) ; four long μ-tracks and and the associated e-tracks of three of them are seen. Bottom: wire chamber and external counter signals. When associated to TPC-tracks these give the entrance and decay times.

Figure 2 shows a small time section ($\sim 50\mu s$) of the continuous TDC display from the test run in December 1999. μ- and e-tracks can be easily distinguished by their different ionization density. Plastic counters, placed outside the pressure vessel and the wire chambers, act as independent detectors for muons and electrons allowing precise timing and tracking of single particles.

While test runs so far were made with normal hydrogen - unsuitable for the capture measurement - our chemistry group has already demonstrated production of ultra clean, deuterium depleted hydrogen with impurity levels below 10^{-8}.

REFERENCES

[1] V. Bernard et al., Phys. Rev. **D 50**, 6899 (1994); H.W. Fearing et al., Phys. Rev. **D 56**, 1783 (1997).

[2] PSI Ann. Rep. **1997, I**, 32; PSI Sci. Rep. **1998, I**, 20. P. Kammel et al., contribution to PANIC 99, Uppsala, to be published in Nucl. Phys. **A**.

MEASURING μD^3HE-FUSION

M. Augsburger[1], V.F. Boreiko[2], V.M. Bystritsky[2] S, W. Czapliński[5], A. Del Rosso[1], C. Donche–Gay[1], M. Filipowicz[5], O. Huot[1], P. Knowles[1], F. Mulhauser[1] S, V.N. Pavlov[2], F.M. Pen'kov[2], C. Petitjean[3], N.P. Popov[4], V.G. Sandukovsky[2], L.A. Schaller[1], H. Schneuwly[1], V.A. Stolupin[2], J. Woźniak[5]

R-98-02, FRIBOURG[1] – DUBNA[2] – PSI[3] – MUNICH[4] – CRACOW[5]

The goal of this experiment is to measure the fusion rate of the μd^{3}He molecule via the reactions

$$\mu d + {}^3\mathrm{He} \xrightarrow{\tilde{\lambda}_f} \mu + \alpha(3.7\,\mathrm{MeV}) + \mathrm{p}(14.6\,\mathrm{MeV}) \quad (1)$$

$$\xrightarrow{\tilde{\lambda}_{f\Gamma}} \mu^5\mathrm{Li} + \gamma + 16.4\,\mathrm{MeV}. \quad (2)$$

The main process, the production of 14.6 MeV protons, should lead to the determination of the fusion rate $\tilde{\lambda}_f$.

After the results of a two weeks test run in October 1997 [1, 2], we performed a 4 week run, one year later in October 1998 [3, 4]. This report will give an overview of our last experiment, performed in September 1999.

A scale drawing of the aluminum target is shown in Fig. 1. Details of the target and the gas supply system are found in Ref. [5]. The target entrance window flange, made of stainless steel, was covered by gold, in order to avoid muons stopping in the iron.

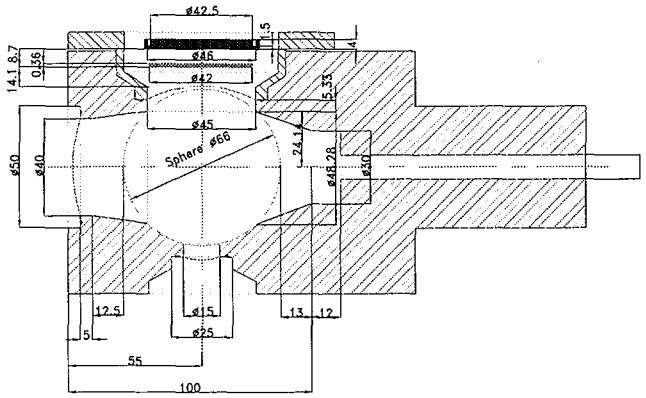

Figure 1: View of the target with a $(dE/dx - E)$–Si detector pair in the top flange.

Muons coming from the μE4 beam line are collimated by a 9 mm thick lead collimator with a 3.5 cm hole. The remaining muons are defined by a $4.2 \times 4.2 \times 0.1$ cm^3 plastic scintillator in anti–coincidence with a second scintillator, which has a 3.5 cm diameter aperture centred on the axis of the target and the lead collimator. Particular attention has been paid to the energy threshold of the muon scintillator, to ensure that every muon will give a signal, even if we accidently increase the pile–up rate by triggering on electrons.

The target was designed for the installation of three $(dE/dx - E)$–Si detector pairs, namely Si$_{UP}$, Si$_{DO}$, and Si$_{RI}$, located above, below, and to the right of the beam. The E–Si detectors are 4 mm thick, whereas the dE/dx–Si detectors have a thickness of 360 μm. Using these detector pairs protons could be separated from other charged particles, such as deuterons. They are located above (E$_{UP}$), below (E$_{DO}$), to the left (E$_{LE}$), and right (E$_{Ri}$) of the beam. They detect the muon decay electrons coming from the target.

We used three different Ge-detectors to measure different γ–ray energies. A 0.17 cm^3 Ge-detector was used for the measurement of the time distribution of the 6.85 keV X-rays emitted by the de–excitation of the μd^{3}He-molecule, a measurement which will provide the $\lambda_{\mu d}$ rate in the $D_2 + {}^3He$ mixture and a measure of the del$_e$ efficiency via the helium K_α line (the del$_e$ condition requires that the decay of the muon causing the event of interest is seen in a given time interval after the event, which proves that the muon was not destroyed in the event of interest). We simultaneously used a 75 cm^3 Ge-detector, to search for any impurities during each measurement. Finally, a 200 cm^3 Ge-detector has been tuned for an eventual measurement of hard fusion γ-rays at 16.4 MeV.

Measurements with pure deuterium, pure helium and mixtures of deuterium and 5% ^{3}He were performed. The pressure in the mixture was varied by a factor of three to obtain relative liquid hydrogen densities $\Phi = 0.0573$ and $\Phi = 0.168$. Data for a total of 1.2×10^{10} good muons for the low density measurement were collected. The very preliminary result for the fusion rate, based on the online analysis is $\tilde{\lambda}_f \leq 2(1) \times 10^4$ s^{-1}, a slightly lower limit than the existing one [6].

REFERENCES

[1] A. Del Rosso et al., PSI Ann. Rep. **1997, I,** 29.

[2] A. Del Rosso et al., Hyp. Interact. **118,** 177 (1999).

[3] A. Del Rosso et al., PSI Sci. Rep. **1998, I,** 21.

[4] F. Mulhauser et al., Progress Report to PSI Proposal R–98–02 (1999).

[5] V. F. Boreiko et al., Nucl. Instrum. Methods **A 416,** 221 (1998).

[6] E. M. Maev et al., Hyp. Interact. **118,** 171 (1999).

TOWARDS A MEASUREMENT OF THE LAMB SHIFT IN MUONIC HYDROGEN

F. Biraben [1], *C.A.N. Conde* [2], *C. Donche-Gay* [3], *T.W. Hänsch* [4], *F.J. Hartmann* [5], *P. Hauser* [6], *V.W. Hughes* [7], *O. Huot* [3], *P. Indelicato* [1], *P. Knowles* [3], *F. Kottmann* [8], *Y.-W. Liu* [7,6], *F. Mulhauser* [3], *F. Nez* [1], *C. Petitjean* [6], *R. Pohl* [6,8], *P. Rabinowitz* [9], *J.M.F. dos Santos* [2], *L.A. Schaller* [3], *H. Schneuwly* [3], *W. Schott* [5], *L.M. Simons* [6], *D. Taqqu* [6], *F. Trehin* [1], *J.F.C.A. Veloso* [2]

R-98-03, PARIS[1] – COIMBRA[2] – FRIBOURG[3] – MPQ GARCHING[4] – TU MUNICH[5] – PSI[6] – YALE[7] – ETH ZÜRICH[8] – PRINCETON[9]

Preparations for an experiment to measure the Lamb shift in muonic hydrogen, i.e. the μp(2S-2P) energy difference, started in 1999. The aim is to determine the proton charge radius with 10^{-3} relative precision and, in combination with precision spectroscopy of hydrogen atoms, to test bound-state QED on the sub-ppm level. Recent calculations of higher order vacuum polarization and other QED terms [1] as well as the proton polarizability contribution [2] determine the muonic hydrogen Lamb shift to 20 ppm, if terms depending on the proton radius are omitted.

Technical developments of the laser resonance experiment are proceeding at the collaborating institutes. A curved magnetic channel "MEK" ("Myonen-Extraktions-Kanal") operating at 0.15 Tesla was completed at PSI. It will be used to guide low-energy μ^- produced in the Cyclotron Trap to a 5 Tesla solenoid where the hydrogen gas target will be located. The 2-keV X-rays from the μp Lyman transitions will be detected by a xenon GPSC (gas proportional scintillation chamber) combined with a MSGC (micro-strip gas chamber) which acts as a detector for 170 nm photons. First tests with this new type of detector in a magnetic field showed that it operates reliably at 5 Tesla with an energy resolution of about 25% (FWHM) at 2.3 keV.

One of the main new components of the experiment is a short-pulsed Ti:Sa laser, tunable around 708 nm, which is under development at Paris. The excimer/dye laser combination to be used for pumping the Ti:Sa laser is currently set up at PSI.

The Lamb shift experiment is based on a sufficiently high population of long-lived μp(2S)-atoms. The 2S-state is known to be populated by $\sim$ 4% of all muons stopped in gaseous H_2 [3]. The longevity of the μp(2S)-atoms is assured when their kinetic energy is smaller than the quenching threshold of 0.31 eV. A detailed analysis of previous measurements of the μp kinetic energy distribution [4] is now available. The principle of this experiment was to measure the time-of-flight of μp-atoms, produced near the axis of a 20 cm long cylindrical gas target, to the gold-coated wall. The arrival time is given by the detection of MeV X-rays in a CsI scintillator produced by μAu-transitions after muon transfer. The combined analysis of the data taken at different gas pressures and target radii (7, 12, 20, and 58 mm) made it possible to determine the background time spectrum as well as effects from elastic μp+H_2 scattering and backscattering of μp-atoms from the gold surface. The TOF spectra were fitted with a superposition of Monte Carlo generated time spectra for individual initial kinetic energies (see fig. 1).

The initial μp(2S) kinetic energy distribution is practically identical to that of the μp(1S). Long-lived μp(2S)-atoms are either initially formed at a kinetic energy below quenching threshold, or they survive the process of slowing down from a higher initial kinetic energy to below threshold. The latter part has been worked out using a recent calculation of the 2S-2S elastic and 2S-2P inelastic cross sections [5]. The fraction of long-lived μp(2S)-atoms per muon stop is found to be $(1.58 \pm 0.11)\%$ and $(1.41 \pm 0.12)\%$ at 1 and 16 hPa gas pressure, respectively.

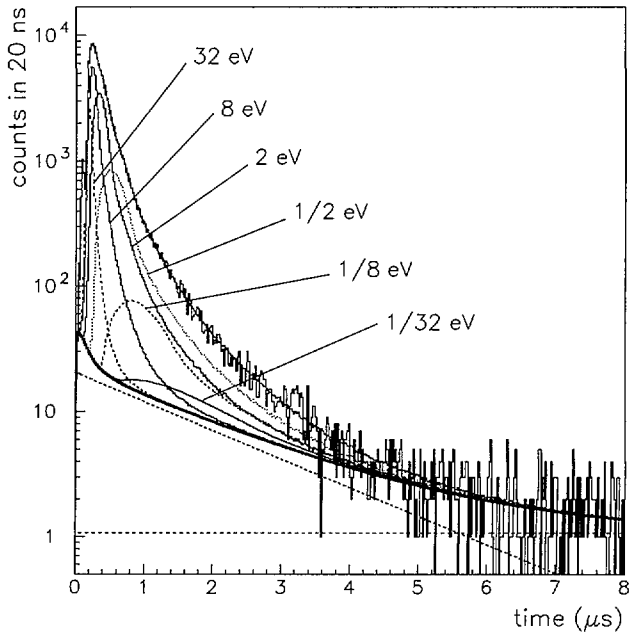

Figure 1: Fit of the μAu time spectrum taken at 16 hPa in the 7 mm target. For illustrative purposes only a reduced set of Monte Carlo generated time spectra was fitted. The individual contributions and the sensitivity of the data to low initial kinetic energies are clearly visible. The thick solid line is the total background. Also shown are the 'flat' time-uncorrelated background and the exponential background coming from muon stops in the target windows (lower dashed lines).

REFERENCES

[1] K. Pachucki, Phys. Rev. **A 60**, 3593 (1999).

[2] R. Rosenfelder, Phys. Lett **B 463**, 317 (1999).

[3] H. Anderhub et al., Phys. Lett. **B 143**, 65 (1984).

[4] F.J. Hartmann et al., PSI Sci. Rep. **1998, I**, 15.

[5] T.S. Jensen and V.E. Markushin, Preprint PSI-PR-99-32.

ACTIVATION ANALYSIS FOR STABLE ISOTOPES OF MOLYBDENUM AND GADOLINIUM

M.C. Cantone[1], *D.de Bartolo*[1], *A. Giussani*[1], *P. Roth*[2], *E. Werner*[2]

Z-94-07.1, MILAN[1] – NEUHERBERG[2]

The application of activation analysis to the determination of single stable isotopes in biological fields enables one to trace the biokinetics and metabolism of micronutrients, trace metals and potentially hazardous radionuclides, with their own stable isotopes. In comparison to the use of radiotracers, stable tracers provide less information, since only external sampling points (biological fluids, excreta) are available; their advantage lies in the fact that they are free from any undue radiation risk to the subjects investigated.

This technique has been applied to study absorption from the gastro- intestinal tract into the systemic circulation, internal biokinetics and excretion processes of the essential element molybdenum. Based on the results of preliminary investigations, a total of 54 new experiments has been conducted on 16 healthy human volunteers according to the protocol approved by the Ethics Committee of the Technische Universität München. Concentrations of the stable tracers in blood plasma and in urine were determined by means of activation analysis (AA), thermal ionization mass spectrometry (TIMS) and inductively coupled plasma mass spectrometry (ICPMS). AA and TIMS provide the most accurate results. ICPMS has a better sensitivity for elemental determination in aqueous solutions. Reliable measurements of isotopic concentrations in biological samples are however complicated by the appearance of external interferences and fractionation problems, which can be corrected for only to a limited extent.

In the following a preliminary evaluation of the results collected so far for 8 volunteers is presented. Intestinal absorption is strongly dependent from the mass administered: the absorbed fraction amounts to 0.93 +/- 0.04 after administration of 5.6 μg Mo/kg body weight, and it decreases to 0.63 +/- 0.09 after administration of 77 μg Mo/kg b.w. [1]. The form of administration also plays an important role, since absorption from liquids is about two times higher than from solid foods. The contemporary administration of absorption inhibitors, like the tannins present in black tea, for example, may reduce to one tenth the amount which passes into the systemic circulation. The biokinetics of molybdenum which has entered the systemic circulation is independent of the amount incorporated, although the fraction which is excreted into the urine is related to the body content of molybdenum: thus urinary excretion seems to be an active mechanism through which the body controls its own molybdenum status. These results are in good agreement with the findings of the early studies, and with other results present in the literature. They also confirm that the model for molybdenum radionuclides currently recommended by the International Commission on Radiological Protection ICRP contains several inaccuracies which prevent reliable estimates of the internal dose, after incorporation of radioactive Mo, to be obtained [2].

The application of activation analysis for determination of gadolinium isotopes has also been investigated [3]. This work has been conducted in cooperation with Prof. Yuri M. Tsipenyuk and co-workers of the P.L.Kapitzka Institute for Physical Problems in Moscow, Russia. In addition to the proton beam of the Injector 1 at PSI for charged particle activation, the possibility of using neutron activation analysis (using the neutron beam of the research reactor in Dubna) and photoactivation analysis (using the 30 MeV microtron at the P.L.Kapitzka Institute in Moscow) has been investigated. The following reactions have been chosen, since they give rise to the formation of a radioactive daughter suitable for measurements: ^{155}Gd(p,n)^{155}Tb, ^{156}Gd(p,n)^{156}Tb, ^{155}Gd(p,2n)^{154}Tb, ^{156}Gd(p,2n)^{155}Tb, ^{157}Gd(p,2n)^{156}Tb, ^{152}Gd(n,γ)^{153}Gd and ^{160}Gd(γ,n)^{159}Gd. Whereas more reaction channels are available using protons as projectiles, only one useful reaction was found for each of the other two techniques. Linearity response was checked using blood plasma samples doped with amounts of gadolinium ranging from 0.1 to 50 μg. All three techniques gave excellent results. With regard to sensitivity, neutron activation analysis provides the better results; considering activation with protons, (p,2n) reactions are a factor two better than (p,n). In conclusion, the three techniques can be considered as complementary, and can be used alternatively depending on the specific requirements.

REFERENCES

[1] E. Werner et al., Internal biokinetic behaviour of molybdenum studied with stable tracers, Jahrestagung der ASI, Göttingen, Germany, October 1999.

[2] A. Giussani et al., Internal dose for ingestion of molybdenum radionuclides based on a revised biokinetic model, Health Phys. **78**, 46-52 (2000).

[3] M.C. Cantone et al., Proton, photon and neutron activation analysis for the determination of stable isotopes of gadolinium in human blood plasma, J. Radioanal. Nucl. Chem. at press (2000).

RARE K^+ - DECAYS IN FLIGHT, AGS E865

R. Appel[4], G.S. Atoyan[8], B. Bassalleck[7], D.R. Bergmann[4], D.N. Brown[3], N. Cheung[3], S. Dhawan[4], H. Do[4], J. Egger[2], S. Eilerts[7], C. Felder[3], H. Fischer[7], M. Gach[3], W.D. Herold[2], V.V. Isakov[8], H. Kaspar[2,4], D.E. Kraus[3], D.M. Lazarus[1], P. Lichard[3], L. Leipuner[1], J. Lowe[7], J. Lozano[4], H. Ma[1], W. Menzel[5], S. Pislak[6,4], A.A. Poblaguev[8], V.E. Postoev[8], A. Proskurjakov[8], P. Rehak[1], P. Robmann [6], A. Sher [3], T.L. Thomas[7], J.A. Thompson[3], P. Truöl[6,4], A. Walid[4], H. Weyer[5,2], M.E. Zeller[4]

E-91-02.1, BNL[1] – NEW MEXICO[7] – PITTSBURGH[3] – YALE[4] – INR MOSCOW[8] – BASEL[5] – PSI[2] – ZÜRICH[6]

The final long data-taking run for experiment E865 at the Brookhaven AGS ended on New Years Eve 1998. Since then, the analysis of the data taken in 1996, 1997 and 1998, with a broad band charged particle spectrometer, equipped with a particle identification system for rare K^+ decays in-flight into multilepton final states, has progressed and been finalised for some channels.

Both the flavour changing neutral current decays $K^+ \to \pi^+e^+e^-$ ($K_{\pi ee}$) and $K^+ \to \pi^+\mu^+\mu^-$ ($K_{\pi\mu\mu}$) are known to be dominated in the Standard Model by long-distance effects involving one-photon exchange. Our published results for these decays not only include precise branching ratios [$(2.94 \pm 0.05(\text{stat}) \pm 0.13(\text{syst}) \pm 0.05(\text{theor})) \times 10^{-7}$ ($K_{\pi ee}$, [1]); $(9.22 \pm 0.60 \pm 0.49) \times 10^{-8}$ ($K_{\pi\mu\mu}$, [2])], but also establish firmly the vector nature of the interaction, and resolve the discrepancy of the older data with $e\mu$-universality. Furthermore the form factor parameters ($f_V(z) = a + bz + w^{\pi\pi}(z)$, $z = M_{ee}^2/m_K^2$) have been determined with $a = -0.587 \pm 0.010$ and $b = -0.655 \pm 0.044$, a result which points to a small but important contribution from the pion loop term $w^{\pi\pi}$, calculated in next-to-leading order chiral perturbation theory.

For the lepton flavour conservation violating decay $K^+ \to \pi^+\mu^+e^-$ the analysis of the 1996 data has ben completed [3, 4]. It yielded an upper 90% confidence limit for the branching ratio of 4×10^{-11}, which combined with our 1995 data and those from earlier experiments reduces to 2.9×10^{-11}. From our 1998 run we expect a sensitivity level of $\approx 5 \times 10^{-12}$. The first analysis pass of the 600 tapes with about 2×10^8 events recorded has recently finished. The second pass will further reduce the sample for the maximum likelihood method signal search. Figure 1 shows the results of such an analysis for the 1996 data.

As a by-product we have also reduced by at least an order of magnitude the limits on the following decays: $K^+ \to \pi^-\mu^+\mu^+$ ($< 3 \times 10^{-9}$) (previously $< 1.5 \times 10^{-4}$), $K^+ \to \pi^-e^+\mu^+$, $\pi^-e^+e^+$, $\pi^+e^+\mu^-$ (all $< 6 \times 10^{-10}$). A preliminary result for the S-wave $\pi\pi$ scattering length deduced from $K^+ \to \pi^+\pi^-e^+\nu_e$ (K_{e4}) decay (3×10^5 events observed, increasing available statistics by a factor 10) has also been reported [5]. Since a large number of theoretical calculations within the framework of chiral QCD perturbation theory exist, these results were eagerly awaited.

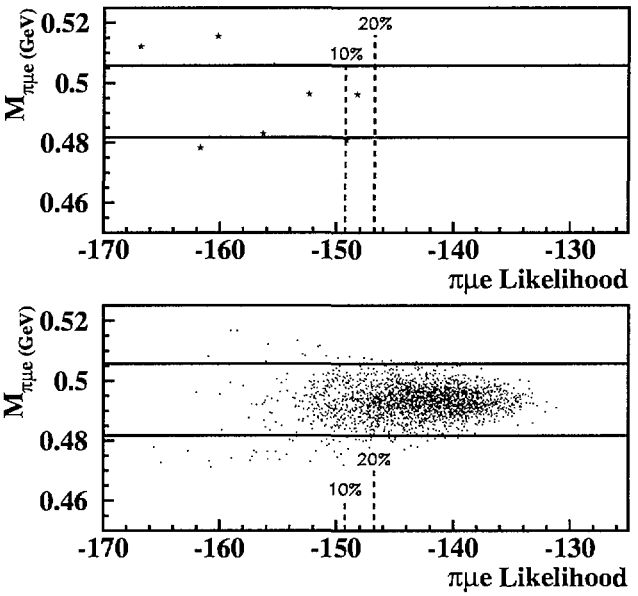

Figure 1: Scatter plot of the $\pi\mu e$ log-likelihood function versus the $\pi\mu e$ invariant mass for data (total 1996 sample, top) and Monte Carlo (expected signal, bottom). The horizontal lines indicate the acceptance in $\pi\mu e$-mass, while the dashed vertical lines mark the boundaries for an event having a 10% or 20% probability of being a signal event [3, 4].

REFERENCES

[1] R. Appel et al., Phys. Rev. Lett. **83**, 4482 (1999).

[2] H. Ma et al., Phys. Rev. Lett. **84** (2000), in print, hep-ex/9910047.

[3] *An Improved limit on the Decay* $K^+ \to \pi^+\mu^+e^-$, Hanh Do, Ph.D. Thesis, Yale University (1999).

[4] M. Zeller, Proc. of the Chicago Conference on Kaon Physics (KAON99), June 1999.

[5] S. Pislak, Miniproc. of the Workshop HadAtom99 on hadronic atoms, Bern, October 1999, eds. J. Gasser et al., hep-ph/9911339.

W-PAIR-PRODUCTION AT LEP2

A. J. Barczyk[1], *K. Deiters*[1], *M. Fabre*[1]

E-92-01, L3 COLLABORATION: PSI[1]

W-pairs are produced at LEP through three charged current processes contributing at tree level, denoted by CC03, with the decay of the W-bosons resulting in a four fermion final state.

The cross section measurement in every LEP experiment is performed simultaneously in all decay channels with a single maximum likelihood fit, using the Poisson probability function parametrized by the observed and expected number of events, as function of the total WW cross section and the W branching fractions, as well as the expected non-WW background, but also taking into accout cross-efficiencies between the channels. The results from the four experiments are then combined to yield LEP values, the cross section results being shown in Fig. 1 for $\sqrt{s} = 189$ GeV, where the collected luminosity per experiment amounts to about $175\mathrm{pb}^{-1}$.

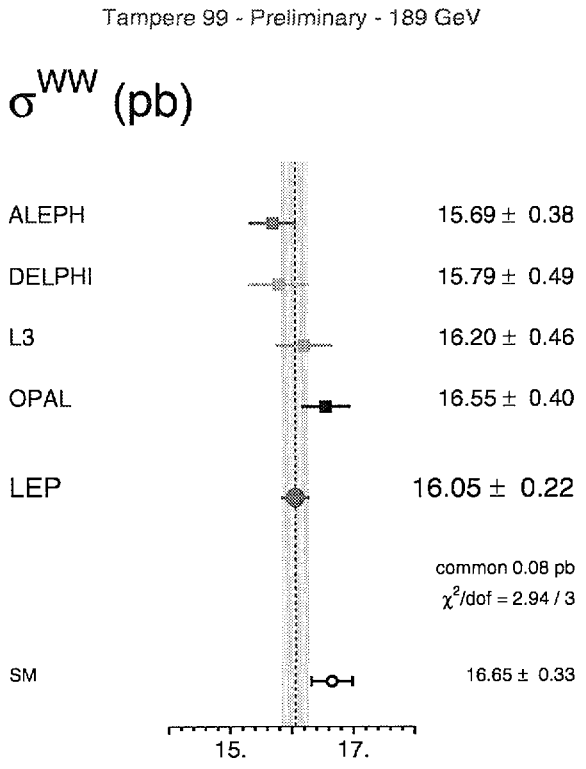

Figure 1: WW cross sections measured by the LEP experiments at $\sqrt{s} = 189$ GeV, and the combined value.

The measurements are in good agreement with the SM prediction calculated with GENTLE, using the world average $\mathrm{M_W} = 80.41 \pm 0.10$ GeV. A 2% error on the predicted value has been assigned, arising mainly from uncertainties in QED radiative corrections. In the theory group's contribution to this volume and in [1], a more precise MC study to overcome the missing corrections in GENTLE is discussed. Within the SM, and using the combined LEP measurement of the W branching ratios, the world average of the better known CKM matrix elements and $\alpha_s(M_W^2) = 0.121 \pm 0.002$, the value of $|V_{cs}|$ can be evaluated without assuming unitarity of the CKM matrix itself. The value resulting from the measurements quoted above gives $|V_{cs}| = 0.997 \pm 0.020$.

Through the mechanism of electroweak symmetry, mass is given to the W-boson, thus implying the existence of a third, longitudinal polarization state. Due to the V-A structure of weak decays, only the transverse W helicity states have been experimentally accessible in decays of light particles. In contrast to this, the amount of longitudinally polarized W-bosons in $\mathrm{e^+e^-} \to \mathrm{W^+W^-}$ is predicted to be $\sim 25\%$ at $\sqrt{s} = 190$ GeV [2]. In a recent L3 study performed at $\sqrt{s} = 183$ GeV and 189 GeV, the fraction of longitudinal polarization states was measured to be $29.5 \pm 11.4(stat.)\%$, and $25.2 \pm 5.7(stat.)\%$ at these two energies respectively [3], in agreement with the above prediction.

REFERENCES

[1] A. Denner, S. Dittmaier, M. Roth, and D. Wackeroth PSI-PR-99-34, hepph/9912447

[2] K.Hagiwara, K.Hikasa, R.D.Peccei, D.Zeppenfeld, Nucl. Phys. **B 282**, 253 (1987).

[3] L3 Collaboration, hep-ex/0001016, Submitted to Phys.Lett.B

HEAVY QUARK PRODUCTION AT HERA

S. Egli[2], R. Eichler[1,2], W. Erdmann[1], K. Gabathuler[2], J. Gassner[2], C. Grab[1], S. Hengstmann[3], M. Hilgers[1], R. Horisberger[2], H.C. Kästli[1], J. Kroseberg[3], U. Langenegger[1], S. Lüders[1], H. Niggli[1], P. Robmann[3], A. Schöning[1], F. Sefkow[3], U. Straumann[3], P. Truöl[3], Y. Tsipolitis[1], S. von Dombrowsky[3], R. Wallny[3], T. Walter[3]

E-93-01.1, H1-COLLABORATION: ETH ZÜRICH[1], – PSI[2], – ZÜRICH[3]

Results obtained by the Swiss part of the H1-collaboration on heavy quark production are presented. With the H1 detector at the ep-collider HERA, D^*-meson production cross sections have been measured in deep inelastic scattering with 4-momentum transfer $Q^2 > 2GeV^2/c^2$ and in photo-production at the photon-proton centre-of-mass energies $W_{\gamma p}$ ~88 and 194 GeV. Next-to-leading order QCD calculations are found to describe the differential cross sections quite well. Within the framework of these calculations, the gluon momentum distribution in the proton, $x_g g(x_g)$, has been extracted in the momentum fraction range of $7.5{\cdot}10^{-4} < x_g < 4{\cdot}10^{-4}$, at average scales $\mu^2 = \sqrt{4m_c^2 + p_\perp^2}$ of between 25 and 50 GeV^2/c^2. The gluon momentum fraction x_g has been approximately reconstructed from the measured kinematics of the scattered electron and the D^* meson final state. The results of this analysis [1] are shown in Figure 1, where the evolution with the scale is shown and compared with the parameterization in the Martin-Roberts-Stirling (MRST1) structure function set, obtained from deep inelastic scattering data.

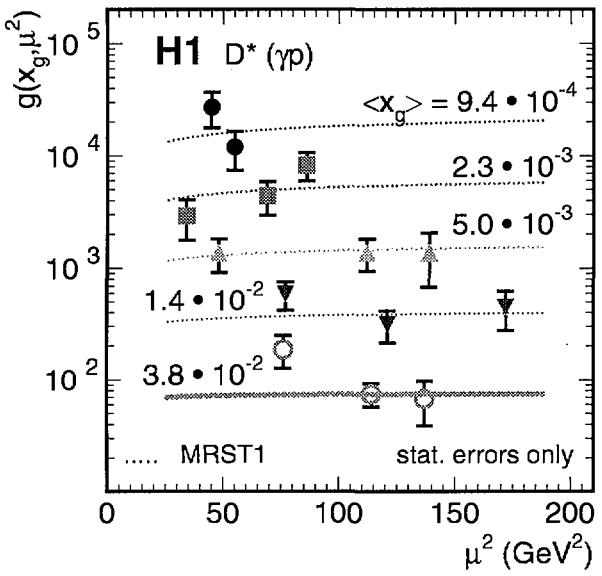

Figure 1: Gluon density distribution, measured in photoproduction as a function of the scale μ^2. Data are plotted as $g(x_g, \mu^2)$ to demonstrate the evolution with the scale. Each key symbol represents a different bin in x_g with the average value given in the figure. The error bars represent the statistical error only. The dotted lines represent the gluon density of the MRST1 shown as a function of scale μ^2 for the same set of x_g values.

The dominant contribution to $\sigma(ep \to b\bar{b}X)$ is due to the exchange of an almost real photon at a mean γp center-of-mass energy W = 200 GeV. Bottom quarks fragment into jets of particles containing a B-meson or B-baryon. To identify heavy quark decays the semileptonic decay into muons with transverse momentum p_t >2 GeV/c were used. Beauty and Charm events were separated on a statistical basis using the transverse momentum of the muon p_{rel}^T relative to the jet-axis (thrust axis). The larger b-quark mass enriches larger p_{rel}^T values. In the visible range of Q^2 <1 GeV^2, 0.1< y_{JB} <0.8 and p_t^μ > 2GeV/c we observe [2] $\sigma(ep \to b\bar{b}X) = 0.176 \pm 0.016(stat)^{+0.017}_{-0.008}(syst)pb$ with a value of $0.069 \pm 0.008pb$ expected in Leading Order and $0.104 \pm 0.017pb$ in Next-to-Leading Order QCD. The measured cross section is about a factor of two larger than expected as also observed at the Tevatron pp-collider and the energy dependence is depicted in figure 2.

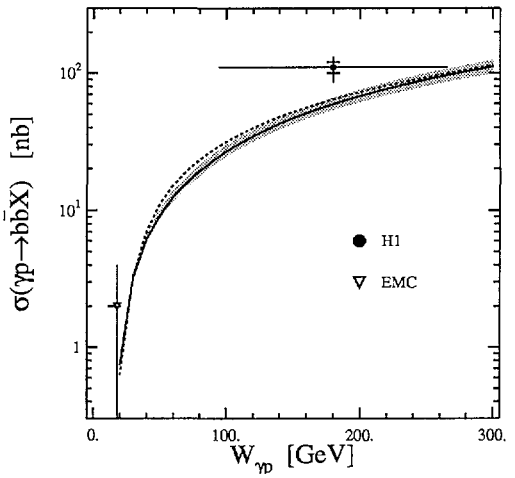

Figure 2: The total photoproduction cross section, $\sigma(\gamma p \to b\bar{b}X)$. The horizontal error bar represents the range of the measurement. The curves show expectations of NLO QCD calculations [3] with different structure function parameterizations. The shaded area corresponds to the uncertainty if the factorization scale changes by a factor 2.

A first signal of production and decay $D_s \to (\Phi \to KK)\pi$ could be seen by using the silicon vertex detector developed at PSI, ETHZ and University of Zürich. It was required that the charged tracks from the $KK\pi$ form a secondary vertex separated from the ep collision vertex by a distance $d/\sigma_d > 2$. A clear signal is observed and the ratio of D^* and D_s production agrees with expectations from fragmentation models.

REFERENCES

[1] H1-collaboration, Nucl.Phys. **B 545**, 21 (1999).

[2] H1-collaboration, Phys.Lett. **B 467**, 156 (1999).

[3] S. Frixione et al., Phys.Lett. **B 348**, 633 (1995).

THE COMPACT MUON SOLENOID (CMS) AT CERN'S LARGE HADRON COLLIDER LHC

M. Barbero[1,2], *R. Baur*[1], *W. Bertl*[1], *K. Deiters*[1], *P. Dick*[1], *A. Dijksmann*[1], *K. Gabathuler*[1], *J. Gobrecht*[1], *G. Heidenreich*[1], *R. Horisberger*[1], *Q. Ingram*[1], *R. Kaufmann*[1,3], *D. Kotlinski*[1], *R. Morf*[1], *D. Renker*[1], *R. Schnyder*[1], *D. Zuercher*[1,4]

E-94-09, CMS COLLABORATION: PSI[1] – BASEL[2] – ZÜRICH[3] – ETH ZÜRICH[4]

The CMS (Compact Muon Solenoid) detector will be one of the two large experiments at the 14 TeV Large Hadron Collider (LHC), due to come into operation at CERN in 2005. The headline physics goal of LHC is to find the Higgs particle postulated by the Standard Model. More generally formulated, the goal is to explore how the physics changes as one goes to energies where the Standard Model can no longer be valid in the perturbative form, satisfactory at LEP energies. Since we do not know how these changes will become evident (for example as signals of Super-Symmetry or a strongly interacting Higgs sector), the large experiments are conceived of as, not only Higgs hunters but also as general purpose detectors accessing as broad a range of physics as possible.

The CMS project is now entering into the construction phase, although R&D for some parts continues. Since the pixel detector, for which PSI has the project leadership, will be one of the last components to be installed, the R&D will continue for some time. PSI also has the leading role in the development of the avalanche photodiode read-out for the electromagnetic calorimeter's lead tungstate crystals. 1999 saw this R&D drawing to a close with the placing of a contract to purchase 130,000 diodes for CMS.

The detector is 14.6 metres in diameter and 21.6 metres long and is built around the largest solenoid magnet ever to be built: this is 6 metres in diameter and 13 metres long and will provide a field of 4 Tesla. All institutes participating in CMS contribute to the magnet purchase and construction. At an early stage PSI helped finance the design work, and the magnet group also provided technical advice. More recently, PSI has contributed to the contract to supply the return yoke and vacuum tank (for the superconducting coil) for the main, barrel-shaped, part of the detector. The contract was awarded in 1998, and in 1999 a major milestone was passed, the completion of the first of the five rings of which the yoke will be composed. Figure1 shows this assembled at the factory, on the occasion of a ceremony held to mark the event. It has since been dismantled again and transported to CERN where it will be reassembled.

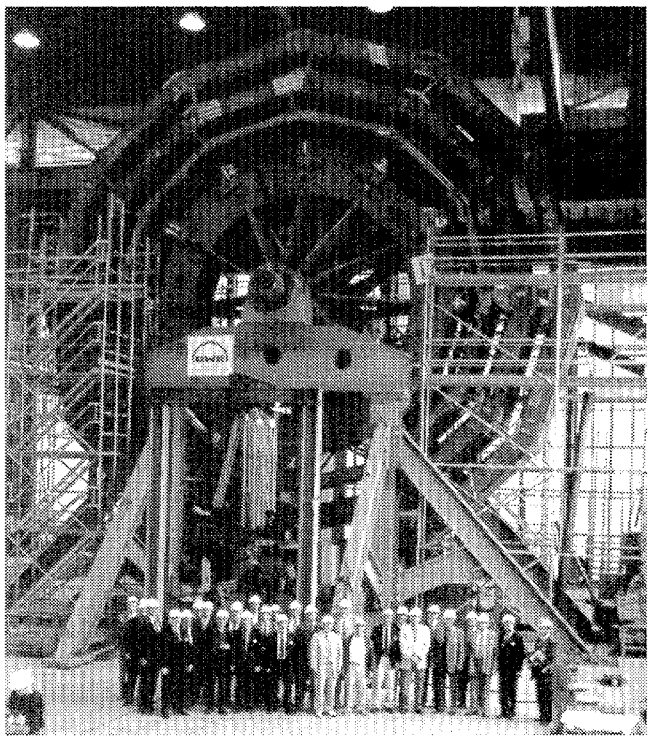

Figure 1: The first completed ring of the CMS magnet yoke. The height is 15.8 metres and it weighs nearly 1200 tonnes

DEVELOPMENT WORK FOR THE CMS PIXEL DETECTOR

C. Amsler[3], M. Barbero[4], R. Baur[1], W. Bertl[1], R. Eichler[1,2], W. Erdmann[2], K. Gabathuler[1], R. Horisberger[1], R. Kaufmann[3], D. Kotlinski[1], B. Meier[2], Ch. Regenfus[3], P. Riedler[3], R. Schnyder[1], S. Streuli[2], L. Tauscher[4]

E-94-09, SWISS CMS PIXEL COLLABORATION: PSI[1] – ETH ZÜRICH[2] – ZÜRICH[3] – BASEL[4]

The pixel detector as the innermost detector element in CMS has the task of tagging long-lived reaction products, e.g. b-quarks and τ-leptons, and to find secondary vertices. The pixel project is under the leadership of PSI, and the pixel barrel will be built essentially by a Swiss collaboration including PSI, ETHZ and the Universities of Basel and Zürich, with important contributions from the Österreichische Akademie der Wissenschaften Wien and RWTH Aachen. The pixel barrel modules consist of a Si-pixel sensor with 150 μm square pixels, which are read out by 16 frontend chips, bump-bonded in two rows of eight chips to the sensor. Before module production can start in the year 2002, extensive R&D work must be performed, the main part of it concerning the readout chip. All functional blocks have now been designed. The analogue stage has been redesigned and the peaking time could be improved from 44 ns to 28 ns (see Fig. 1). This is quite sufficient for the 25 ns bunch spacing at LHC. A first complete chip will be submitted to the foundry early in the year 2000.

A new concern has recently turned up namely, the chip logic and memory being disturbed by the heavy radiation exposure during the experiment (single event upset, SEU). This is caused by heavily ionizing fragments and recoils, which are produced in the chip by hadronic interactions and which deposit enough charge in a sensitive node to induce for example the state of a memory cell to flip. The sensitivity of an electronic device to SEU depends on the chip technology and is very difficult to predict.

Since the main hadronic component at the Large Hadron Collider (LHC) will consist of low energy pions, PSI is an ideal place to investigate SEU probabilities. The two radiation-hard chip technologies presently considered for the CMS pixel readout are the SOI processes of TEMIC (DMILL) and Honeywell (RIC-MOS IV). Shift register cells realized in both technologies have been placed in the high intensity πE1 beam of 200 MeV and upsets were monitored continuously. The results are shown in Table 1. The flux density expected at LHC can reach up to $5 \times 10^7\,\mathrm{cm^{-2}\,s^{-1}}$ for the innermost layer.

Supply voltage	2.5 V	4.0 V	5.0 V
DMILL ($\times 10^{13}$)	0.8	1.4	2.4
Honeywell ($\times 10^{13}$)	17	36	60

Table 1: Average pion fluence (π/cm^2) before a SEU occurs in DMILL and Honeywell memory cells for different supply voltages.

Each pixel unit cell has three trim bits which serve for setting the hit threshold. In the worst case (DMILL with 2.5 V supply voltage), one percent of the pixels in the innermost layer will be upset after 10 min. This means that in the chip design appropriate monitoring and download mechanisms must be foreseen which allow one to find and correct SEUs.

Concerning the sensors a first prototype batch has been received from CSEM and tests have started. A novel open atoll structure of p-stop rings around the n-pixels has been implemented (see insert in Figure 2). This provides a high resistive path between the pixels, which prevents the charging up of pixels where the bump bond fails. First tests show that the resistive network behaves as expected. Figure 2 shows the current between a pixel at 0.2 V and its grounded neighbours as a function of bias voltage. After full depletion a resistance of a few MΩ is reached. However, the conductivity will change after radiation damage, and this needs still to be investigated.

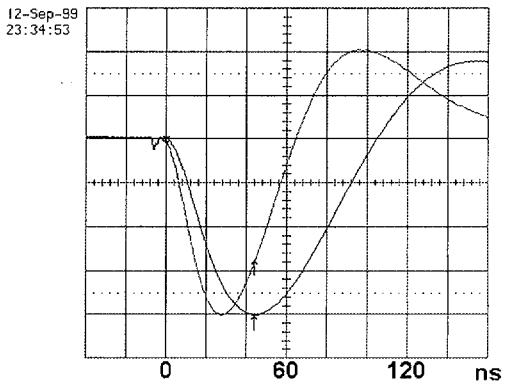

Figure 1: Pulse shapes of old and new analogue circuit

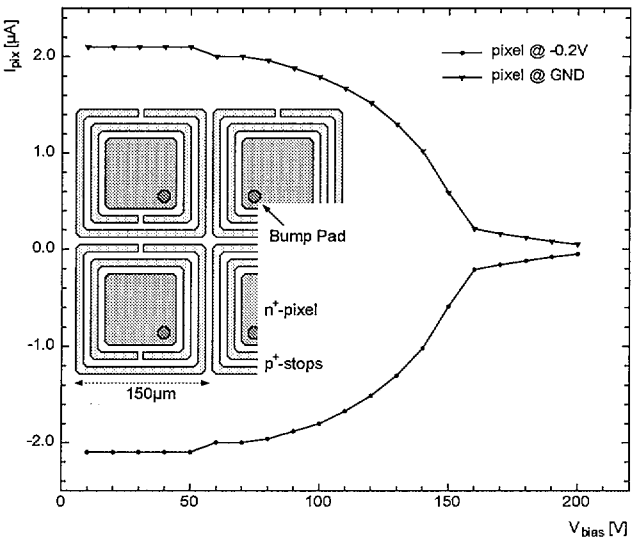

Figure 2: Interpixel current as a function of bias voltage. Around 160 V full depletion is reached (kink).

PROPERTIES OF THE AVALANCHE PHOTODIODES FOR THE CMS ELECTROMAGNETIC CALORIMETER

K. Deiters[1], *Q. Ingram*[1], *D. Renker*[1], *T. Sakhelashvili*[1], *D. Zurcher*[1]

E-94-09, CMS COLLABORATION: PSI[1]

The barrel of the electromagnetic calorimeter of the CMS detector at LHC will be made out of 61200 lead tungstate crystals. The design of the CMS detector and the operating conditions of LHC require that the photosensors operate in a magnetic field of 4 T and can withstand high radiation levels. In addition, since the crystals have a relatively low light yield, the photosensors need to have a comparably small electrical response to ionizing particles passing through them. During 1999, a seven year R&D programme with Hamamatsu Photonics to develop a suitable avalanche photodiode (APD) was brought to a succesful conclusion.

The Hamamatsu APDs are made by epitaxial growth on low resistivity n^+-type silicon followed by ion implantation and diffusion steps. Similar to a transistor, the APD has a *pn*-junction where the amplification takes place. Its depth is set at around 5 μm to minimize the sensitivity to ionizing radiation and to maximize the absorption of the blue light from the crystal.

Light releases electrons at the surface, in front of the *pn*-junction, and these are amplified in the avalanche at the junction. For electrons or positrons leaking through the rear of the crystals and passing through the APD, most of the energy deposited is behind the junction and the released electrons are not amplified. The effective thickness of the APDs, where released electrons are amplified, has been measured to be only 5.6 μm. This is very small compared to a PIN diode which has a thickness of 200 μm.

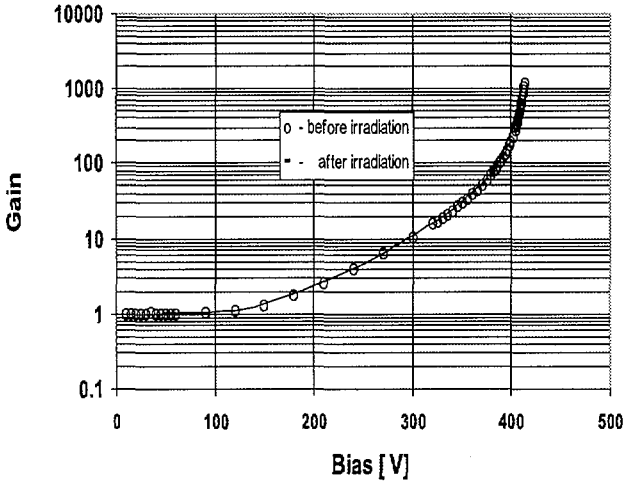

Figure 1: Gain (M) vs. bias voltage (V) before and after an irradiation with protons

To design the APDs with the necessary radiation hardness was perhaps the hardest aspect. The testing of the APDs for this was carried out at PSI. They were irradiated for about 2 hours with a 2 nA beam of 64 MeV protons (OPTIS). This dose corresponds to a fluence of about 2×10^{13} neutrons/cm^2, the expected total neutron fluence after 10 years of LHC operation in the central section of the calorimeter. During irradiation the APDs were operated at the planned gain (M) of 50.

Afterwards they were annealed for a week at a temperature of 90 ^oC, equivalent to the self-annealing during 10 years of LHC operation, and all parameters were re-measured. In Figure 1 measurements of the gain, taken before and after irradiation are compared; the bias voltage needed for a gain of 50 changes by only 1 Volt.

The dark current at gain 50 increases from 10 nA before irradiation to about $2\mu A$. All other parameters: the capacitance, series resistance, dM/dV, dM/dT and the quantum efficiency at gain 50 do not change during irradiation.

Active Area	$5 \times 5mm^2$
Op. Voltage	$\sim 380V$
Capacitance	70 pF
Series Resistance	3Ω
Dark Current	$< 10nA$
Quantum Efficiency	72% for 430nm
dM/dV x 1/M	3%/V
dM/dT x 1/M	-2.2%/^oC

Table 1: Parameters of recent APDs.

Table 1 summarizes the parameters of the APDs. *In situ* irradiation causes only a rise of the dark current while other parameters are stable. In the CMS detector the gain variation of 3%/V will require a good quality bias supply, but the demonstrated stability of the other APD parameters will help to keep the contribution from the APD to the calorimeter energy resolution small.

A related significant step was the decision on which optical glue to use to couple the APDs to the crystals. This must also be radiation hard, not detoriorate over 20 years, be transparent at wavelengths down to 350 nm or less and have as high a refractive index as possible. Further no component of the glue should attack the APD. The final choice was a microscopy mounting medium, Histomount, produced by National Diagnostics, with a refractive index of 1.63 at 430 nm.

Laboratory for Astrophysics

LABORATORY FOR ASTROPHYSICS

A. Zehnder

Space Instrumentation

For the Laboratory for Astrophysics the year 1999 was an exciting time with the smooth launch of the ESA cornerstone XMM (x-ray Multi Mirror Mission) aboard the Ariane 5 launcher on December 10. After 10 years of work on the two Reflection Grating Spectrometer (RGS) CCD cooling system, the mechanical housing and the front-end electronics, a decisive step had been successfully taken. The injection into its 2-day orbit and the instrument activation proceeded flawlessly. At the time of this writing both RGS instruments function as expected and promise a rich harvest of data for the next ten years.

The High Energy Solar Spectroscopic Imager HESSI was the other space instrument completed this year. HESSI is a US NASA Small Explorer Mission to observe impulsive high-energy events on the Sun with unprecedented energy, time and spatial resolution. We took the responsibility for the aspect systems and for the mechanical telescope structure, including the alignment of the delicate imaging grids. The hardware was delivered to UC Berkeley for integration into the spacecraft. Launch is foreseen for July 2000.

The PSI Proton Irradiation Facility PIF enables the study of radiation effects on electronic devices and materials. It was designed under contract by PSI and the European Space Agency ESA. In 1999, the PIF was extensively used. Sixteen groups from universities, space agencies and industrial firms performed about 35 different experiments. Most of the tests were devoted to characterize electronic components and devices for future satellite missions.

Scientific observation programs

The preparation phase for astrophysical observations using the XMM-RGS instruments were concluded in time. A comprehensive set of guaranteed observations was organized in co-operation with the other three RGS instrument institutes. PSI has taken partial responsibility for the planning of two RGS key projects on stellar atmospheres and plasma heating. The projects were formally submitted to ESA for consistency checks and are now an approved part of the observing program. Before the launch of XMM, scientific observations were performed with available X-ray spectroscopy satellites. Despite rather stiff competition, PSI won a considerable amount of XMM observing time, both guaranteed as well as open time available to guest observers world-wide. Four projects on stellar magnetic activity and star formation were approved with top ranking.

The proposed XMM-RGS observation of galactic cluster targets within the guaranteed time program has been definitively approved as well. Detailed simulation on several cluster properties, in particular cooling flows, has been carried out in order to prepare the XMM data analysis. The investigations on the dark matter problem have been pursued in different directions using both X-ray and microlensing data. The recent announcement of the first direct detection with the ISO satellite of cold H_2 clouds in the halo of the nearby NGC 891 galaxy lends additional strong support for the dark halo model we proposed some years ago.

Cryogenic Detectors

The cryogenic detector group is developing photon detectors with high sensitivity. We use the advantages of a low temperature environment together with the specific properties of superconductors. Very low temperatures are necessary to limit the creation of thermal and electrical excitations. Superconductors offer a rather low creation and/or detection threshold of the excess excitations, which are produced when the energy of a photon is absorbed in matter.

In 1999 we designed, fabricated, and tested microbolometer and superconducting tunneling thin film devices. A device made out of a superconducting strip acting as a photon absorber and two tunneling junctions at each end yielded the following results: an energy, a position, and time resolution of 48 eV at 6 keV, of a few microns, and of a microsecond, respectively.

We currently test the performances of our devices with visible light, and expect to obtain single photon sensitivity. Future imaging instruments will require the parallel read-out of several cryogenic pixels. The major obstacle to large pixel arrays remains the thermal load imposed by the leads contacting a device operating at very low temperature. For the future, we envisage the use of cryogenic devices in optical astronomy instrumentation.

XMM: FINAL SCIENCE PREPARATIONS AND LAUNCH

M. Audard[1], L. Grenacher[1], M. Güdel[1], Ph. Jetzer[1], P. Koch[4], D. Puy[1], H. Schild[2], W. Schmutz[2,3], K. W. Smith[1,2], K. Thomsen[1], A. Zehnder[1], and the RGS collaboration

PSI[1] – ETH ZÜRICH[2] – present address: PMOD/WRC, DAVOS[3] – ZÜRICH[4]

ESA's cornerstone XMM, the largest astrophysical X-ray observatory now in orbit, was successfully launched in December 1999. PSI has contributed to the Reflection Grating Spectrometers (RGS). Data and science issues related to early observations and the submission of additional guest observer proposals were in the spotlight during 1999.

Stellar Astrophysics Projects

About half of all detectable X-ray sources in the sky are stars. The presence of their hot, magnetized atmospheres is a major puzzle of astrophysics. In PSI's XMM science key project, we concentrate on i) coronal energy release and heating in active stars, and the relation with relativistic particles; ii) coronal magnetic structuring and abundances; iii) evolution of atmospheres of solar analogs; iv) magnetic activity in young stars; v) wind structure, composition, and location of X-ray sources in hot stars. Spectroscopy plays a central role in these investigations (temperature, density, pressure, and velocity determination from spectral line fluxes, shapes, and shifts). Two extensive guaranteed (GT) key projects have been worked out in the RGS Team under the lead of PSI and SRON. They comprise the largest section of the RGS guaranteed time (≈30% or 905 ks of on-source observing time for 26 stellar targets, with PSI acting as 'observing PI' on about half of them). During spring and summer 1999, we led small teams working on detailed instrument settings for each source (e.g., filter choice, optical monitor set-up, CCD windows, roll angles, detailed simulations, etc) to optimize the science use of XMM. We performed corresponding work for the calibration/performance verification targets; these will be observed and analyzed during the first 3 months by a small team in Utrecht, including two stellar astrophysicists of PSI.

To increase our science return, we also competed for the attractive first Guest Observer program. Four out of our five proposals were accepted, as well as four proposals on which we act as co-investigators. We concentrate on statistical flare physics, binary eclipses, and X-rays from T Tau stars.

Based on proposal requests, we have been awarded large amounts of observing time simultaneous with XMM, in particular with the VLA (148 hrs), the VLBA (≈100 hrs), EUVE (1 Msec), and the novel ASTRO-E (80 ksec, with high-resolution X-ray bolometers). A preparatory, long X-ray stellar spectroscopy observing campaign was conducted in 1999, using EUVE for 44 days together with BeppoSAX (10 days).

To exploit some spare time after the detector opening, we have proposed a long observation (≈2 weeks) of the active binary star HR1099, one of the strongest X-ray sources. This observation is now scheduled for late January 2000.

MG and MA became members of the *Chandra Emission Line Project* with the aim of contributing fundamental atomic data from deep XMM observations to new atomic data bases.

MG has worked as an organizer of the Y2000 Saas Fee Course in *High-Energy Spectroscopic Astrophysics* devoted to XMM and new X-ray missions. It aims at providing spectroscopy knowledge to interested scientists and students.

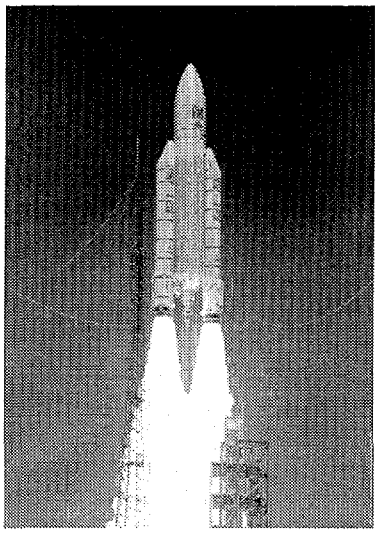

Figure 1: Launch of Ariane 5/XMM (photo: Arianespace).

Galaxy Cluster Project

Clusters of galaxies are the largest known structures in the universe and contain up to few thousands of galaxies. They are embedded in a vast cloud of hot gas, which is a strong source of X-rays. Accurate observations with XMM will allow to get temperature profiles and chemical composition of the hot gas. This information will for instance lead to a better determination of the total cluster masses and thus of their dark matter content, of the cooling flows and of other important cluster properties. In the RGS working group on clusters we have defined the instrument settings and performed extensive simulations for each of the selected galaxy clusters: nine clusters have been chosen for the GT program and two additional ones for the PV phase, corresponding to an observing time of more than 500 ks. We have also studied several aspects of astrophysical models for clusters, in particular the modelling of cooling flows. This knowledge is crucial for a correct interpretation of the observations with XMM.

Launch

After a smooth and flawless launch campaign during summer/fall 1999, XMM was launched with an Ariane 5 on December 10, 1999, from the ESA launch site in French Guyana. Shortly after a perfect insertion into a high orbit, the telescope doors opened, the solar panels unfolded, and the heaters were switched on. The commissioning phase will be continued in early January.

HYDRODYNAMIC FLARE SIMULATIONS: A TOOL FOR XMM AND HESSI STUDIES

M. Güdel

Introduction and Methods

Stellar and solar atmospheres are ideal laboratories to study the reaction of thin plasmas to explosive heating events. They are persistently heated to high temperatures ($>10^6$ K), testified by their strong X-ray emission. There is a lively debate on whether the energy is released in numerous stochastic, explosive events due to instabilities. XMM and HESSI both will address this problem. As a preparation, a hydrodynamic 1-D numerical simulation code has been devised.

The primary hydrodynamic simulation variables are the mass density ρ, the momentum density ρv, and the total energy density E. They obey the three conservation equations

$$\frac{\partial \rho}{\partial t} = -\frac{\partial(\rho v)}{\partial s} \tag{1}$$

$$\frac{\partial(\rho v)}{\partial t} = -\frac{\partial(\rho v^2)}{\partial s} - \frac{\partial P}{\partial s} - \rho g_{\|} + \frac{\partial}{\partial s}\left(\mu T^{5/2}\frac{\partial v}{\partial s}\right) \tag{2}$$

$$\begin{aligned}\frac{\partial E}{\partial t} &= -\frac{\partial(Ev)}{\partial s} - \frac{\partial(Pv)}{\partial s} - \rho g_{\|} v + \mu T^{5/2}\left(\frac{\partial v}{\partial s}\right)^2 \\ &+ v\frac{\partial}{\partial s}\left(\mu T^{5/2}\frac{\partial v}{\partial s}\right) + \frac{\partial}{\partial s}\left(\alpha\kappa T^{5/2}\frac{\partial T}{\partial s}\right) \\ &+ Q_{\rm eq}(s) + Q_{\rm var}(s,t) - \left(\frac{\rho}{m_{\rm H}}\right)^2 \Lambda(T)\end{aligned} \tag{3}$$

where s is the space variable, v the velocity, $g_{\|}$ the gravitational acceleration along s, P the thermal pressure, T the temperature, $\kappa = 9.2 \cdot 10^{-7}$[cgs] and $\mu = 1.25 \cdot 10^{-16}$[cgs] are constants of conduction and viscosity, respectively, in Spitzer's formulation. The heating terms Q_{eq} and Q_{var} refer to the equilibrium heating rate for a stable configuration, iteratively determined from the static equations ($\partial/\partial t \equiv 0 = v$), and to the time- and space-dependent additional heating, respectively. Finally, $\Lambda(T)$ is the plasma cooling function, and $m_{\rm H}$ is the mass of the proton. The equations are related through the equation of state and the energy relation

$$P = 2\frac{\rho}{m_{\rm H}}kT, \quad E = \frac{1}{2}\rho v^2 + \frac{P}{\gamma - 1} \tag{4}$$

where k is Boltzmann's constant, $\gamma = 5/3$ the ratio of the specific heats, and a hydrogen plasma has been assumed.

Equations (1)-(3) are solved in a split-time step procedure using Flux-Corrected Transport algorithms [1] on a time-dependent "adaptive" grid with its highest resolution region comoving with the transition region (steepest gradients of T, P, and ρ). The appropriate time step is calculated based on the Courant-Friedrichs-Lewy criterion and on the radiation and conduction time scales. The (nonlinear) viscosity term in Eq. (2) and the conduction term in Eq. (3) are solved using an implicit Euler scheme to maintain stability. The conductive flux $\kappa T^{5/2}\frac{\partial T}{\partial s}$ is corrected by a flux-dependent factor α derived from the treatment by Campbell [2] in order to smoothly connect from the (classical) Spitzer regime to saturation (electron free streaming limit). Phenomenological corrections for optical depths at low T are applied [3].

Applications and First Results

The code has been applied to stochastic sequences of energy pulses released into a half-circular rigid magnetic loop above a stellar surface. The energy distribution of the sample of events is a power-law as observed in solar flares (power-law index of -1.8).

The figures show the heating input function (top left), the reaction of the loop-top temperature (top right), and the modulation depth (bottom). The latter is defined here as the ratio between the standard deviation of the luminosity time series and the average luminosity, both referring to plasma within a given temperature interval (comprising a factor of 2 in T around the midpoints shown in the figures).

A characteristic increase of stochastic variability with temperature is noted; this is primarily due to the progressively smaller number of flares that heat to high temperatures. X-ray observations of solar and stellar coronal plasma have indeed indicated an increase of variability toward higher T [4,5] and confirm the hypothesis of the operation of a large number of unresolved heating events.

The code is presently being completed with the inclusion of ionization effects. It will then be applied to chromospheric evaporation processes as seen by XMM and HESSI in the soft and hard X-ray ranges.

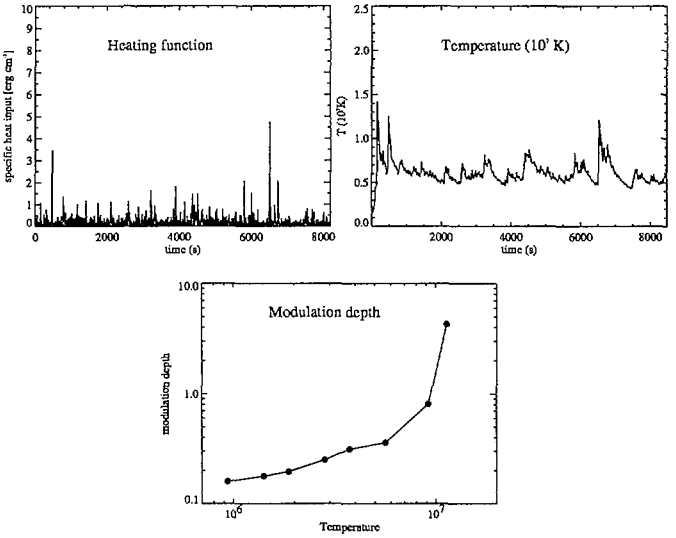

Figure 1: Stochastic energy input (top left), resulting loop top temperature (top right) and modulation depth (bottom).

REFERENCES

[1] J. P. Boris, D. L. Book, Meth. Comp. Phys. **16**, 85(1976)

[2] P. M. Campbell, Phys. Rev. **A 30**, 365(1984).

[3] F. Nagai Solar Phys. **68**, 351(1980).

[4] M. S. Giampapa, et al., ApJ **463**, 707(1996).

[5] T. Watanabe, et al., Solar Phys. **157**, 169(1995).

CORONAL HEATING OF ACTIVE STARS

M. Audard[1], *M. Güdel*[1], *J. J. Drake*[2], *V. Kashyap*[2], *E. F. Guinan*[3]

PSI[1] – Harvard-Smithsonian Center for Astrophysics, USA[2] – Villanova University, USA[3]

Active stars maintain hot, magnetically trapped plasmas above their photospheres. The mechanism of heating these corone is unknown. We have investigated the question of "flare heating" on several young active stars whose upper atmospheres are thought to be solar-like. We have further explored the link between flares and the stellar activity/rotation connection.

Astrophysical plasmas show various physical conditions that laboratory experiments cannot reproduce. The Sun (and its corona) is one of the nearest astrophysical plasmas available. However, coronae of active stars provide a much larger range of magnetic phenomena due to to their different ages, their various rotation periods and spectral types.

Flares on the Sun and stars are observed over a wide range of radiated energy. Large flares on the Sun emit on the order of 10^{30}-10^{32} ergs. Smaller-scale events, so-called 'microflares', reveal energies $\approx 10^6$ times smaller. The whole family of flares is thought to originate from energy released by reconnection of the magnetic field. The 'microflare' hypothesis proposes that the small events are responsible for a large fraction of the coronal heating because they would occur very often compared to the more energetic events. In a study of two young active solar analogs, we have found [1] flares to be distributed cumulatively in energy following power laws of the type $N(>E) = \int_E^\infty dN/dE\, dE \propto E^{-\alpha+1}$, with an index $\alpha = 2.2 \pm 0.2$. Hudson [2] has argued in the solar context that the radiated power of flares ($\int_{E_0}^\infty dN/dE E dE$) could be arbitrarily large for small E_0 and $\alpha > 2$. For these two young active stars, the microflare hypothesis for coronal heating may then be valid.

We have extended the study to a total of twelve young active stellar sources observed by the *Extreme Ultraviolet Explorer* (*EUVE*). These stars have solar-like coronae, and they show enhanced coronal and chromospheric activity. Using our statistical method to identify flares [1], we have constructed and fitted the flare occurence rate distributions with power laws (see Fig. 1). The power-law indices α cluster around a value of 2, although they may be different for different stellar spectral types. A trend for a flattening of the distributions with later spectral types is suggested in our data. We have further explored whether flares are correlated with some physical properties of stars, such as activity indicators and rotation parameters. One of the most interesting results is the correlation between the flare occurrence rate and the X-ray luminosity of a star (Fig. 2): X-ray bright stars show energetic flares more frequently than do X-ray faint stars. We have also found that the flare rate stays constant for stars of the same spectral type and in the saturation regime [3].

Flares can therefore provide a significant amount of energy to heat the coronae of active stars. The definite answer to which mechanism is responsible for the coronal heating is not yet available. Future observations with the new generation X-ray satellites (*XMM*, *Chandra*, and *ASTRO-E*) will hopefully solve part of the mystery.

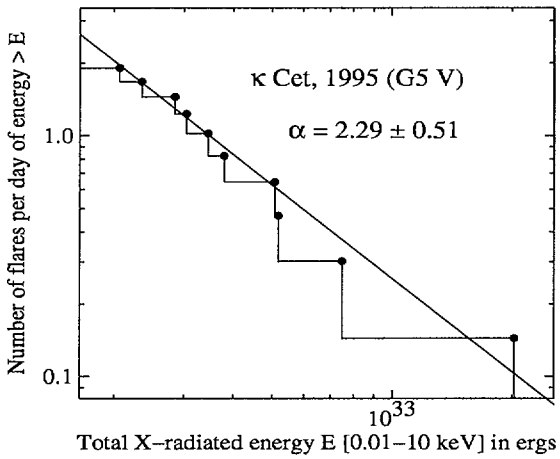

Figure 1: Example of a flare rate distribution.

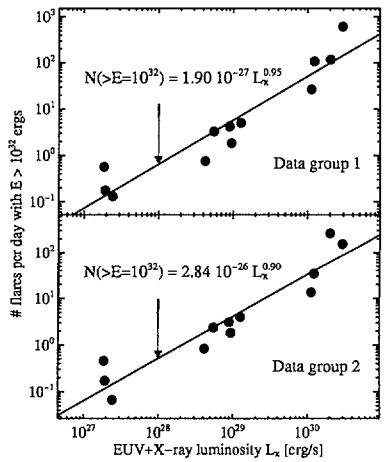

Figure 2: Flare occurrence rate vs. L_X. Data groups correspond to different fitting methods.

REFERENCES

[1] M. Audard, M. Güdel, & E. F. Guinan, Astrophys. J. **513**, L53(1999).

[2] H. S. Hudson, Sol. Phys. **133**, 357(1991).

[3] M. Audard, M. Güdel, J. J. Drake, V. Kashyap, & E. F. Guinan, Proc. of the Eleventh Workshop on Cool Stars, Stellar Systems, and the Sun, Oct. 4 – 8 (1999).

OBSERVATIONAL STUDIES OF YOUNG STELLAR OBJECTS AT VARIOUS WAVELENGTHS.

K. Smith[1], *M. Audard*[1], *A. Benz*[1], *I. Bonnell*[2], *J.P. Emerson*[3], *M. Güdel*[4], *T. Jenness*[5], *S. Skinner*[6]

ETH ZÜRICH[1] – ST. ANDREWS[2] – QUEEN MARY[3] – PSI[4] – JAC[5] – JILA[6]

Submillimetre studies of embedded YSO's

At submillimetre wavelengths, the thermal dust emission from molecular clouds is often optically thin, in contrast to optical or near infrared emission. Submillimetre studies can therefore reveal the morphology of embedded objects in the very earliest phases of star formation. We obtained SCUBA observations at 450μm and 850μm of the protomultiple system NGC1333/IRAS4. The high signal to noise of our maps allows deconvolution of the beam, which reveals a binary companion to one component. Simple considerations of binary dynamics suggest that this triple system is unstable and will probably not survive in its current form. Thus IRAS4 provides evidence that systems can evolve from higher to lower multiplicity as they move towards the main sequence. A map of spectral index suggests that the dense components have undergone grain evolution, and also that dust from the circumstellar environments is being entrained in a jet.

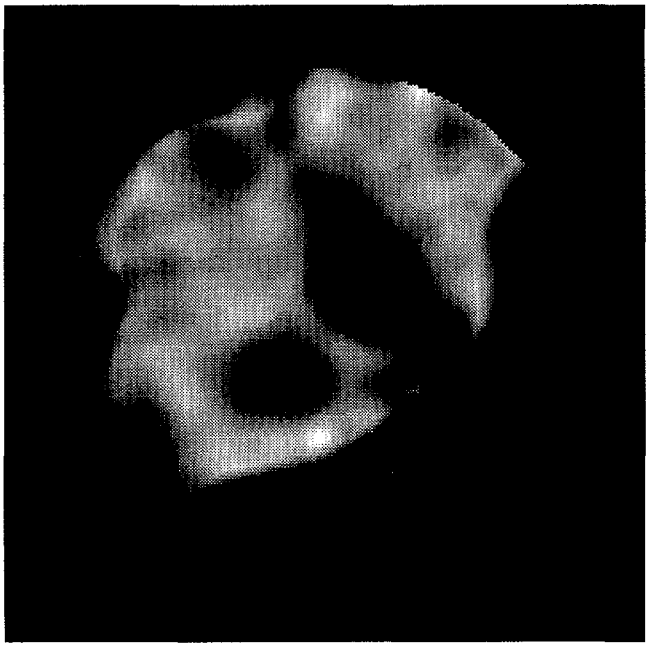

Figure 1: Spectral index map of IRAS4. The compact sources show up as dark regions, indicating grain evolution in dense dusty disks or envelopes. An elongated dark region runs through the main source from lower left to upper right. This is aligned with a known jet. This suggests that material from a disk close to the star is being entrained in the jet flow.

Prospects for YSO studies with XMM

As part of the XMM AO-1 round, we and our collaborators have prepared several proposals to study young stellar objects. All these proposals have been awarded time in AO-1.

X-ray spectroscopy of a Classical T Tauri star

We have been awarded 70 ksec of XMM open time to observe the spectrum of Sz 6, a CTTS in Chamaeleon, with the RGS. Classical T Tauri stars (CTTS) are pre-main-sequence objects which accrete material from a circumstellar disk. The central star possesses a strong magnetic field, which disrupts the disk and channels the material onto the stellar surface, where million-degree shocks are formed. Interaction between the field and disk is the most promising driving mechanism for collimated outflows and jets, which are driven out perpendicular to the disk plane. Flare-like events are typically seen in optical emission, and the objects are also variable at all wavelengths on timescales ranging from less than an hour up to decades. CTTS are known to be X-ray sources from previous X-ray missions, principally ROSAT. Various origins for this X-ray emission are envisaged. Firstly, the extreme magnetic activity presumably leads to coronal X-ray emission. Such a corona might differ significantly from known main-sequence coronae due to the high density of material present from the disk. Secondly, the accretion shock might give rise to soft X-rays (0.1-1 keV), although this region is also expected to be heavily obscured. Thirdly, the interaction between the magnetic field and the differentially rotating inner disk is expected to wind up the field, perhaps giving rise to violent reconnection zones above and below the disk.

The unprecedented sensitivity and spectral resolution of the RGS will allow us to isolate individual lines in the X-ray spectrum. Temperature and density indicators will allow us to deduce the physical conditions in the magnetosphere, and comparison with more conventional coronae will then be possible. Furthermore, the resolution of the RGS is sufficiently high that we will be able to discern gas motions of a few hundred kilometres per second - sufficient to observe either the orbital motion at the magnetosphere/disk boundary, or the inner part of the infalling accretion stream. Because of the unprecedented power of XMM, this will be the first opportunity to study the X-ray magnetosphere of a CTTS in such detail.

EPIC survey of star formation fields in Orion

Guaranteed time RGS observations of hot stars in Orion will result in the surrounding dense star fields being observed with EPIC. To complement these fields, we proposed further EPIC observations of surrounding areas of the Orion nebula. With these observations, we will conduct a survey of X-ray YSO sources, obtaining determinations of the X-ray luminosity function for faint objects as well as information regarding individual sources.

Deciphering the X-ray emission of the nearest Herbig star

The Herbig Ae/Be stars are the intermediate mass counterparts of the CTTS. As part of a collaboration with S. Skinner of JILA, we are involved in a successful proposal to obtain XMM EPIC observations of a nearby HAeBe star. This will allow the assessment of various shock models to explain the X-ray emission of Herbig stars.

ELECTRON FIREHOSE INSTABILITY AND ACCELERATION OF ELECTRONS IN SOLAR FLARES

G. Paesold[1,2] *and A.O. Benz*[1]

ETH ZÜRICH[1] – PSI[2]

An electron distribution with a temperature anisotropy $T_{\|}/T_{\perp} > 1$ can lead to the Electron Firehose instability (Here $\|$ and $\perp$ denote directions relative to the background magnetic field $\mathbf{B}_0$). Since possible particle acceleration mechanisms in solar flares exhibit a preference of energizing particles in parallel direction, such an anisotropy is expected during the impulsive phase of a flare.

Particle acceleration is a phenomenon occurring at many different sites throughout the universe. An important example of particle acceleration are solar flares, offering a wide range of observations that allow one to probe electron and ion acceleration.

Possible acceleration mechanisms can be divided into three main groups (for a detailed review see [3]) : 1.) *Shock Acceleration*, 2.) *Acceleration by parallel electric fields* and 3.) *Stochastic acceleration by MHD turbulence*. A preference for acceleration along the background magnetic field is a common feature of these acceleration models. Hence it is expected that the temperature in parallel direction of the according particle species increases during the acceleration process. In plasmas with a parallel pressure exceeding the perpendicular pressure the so-called Electron Firehose instability can occur [1]. In solar flares this instability is of interest for several reasons: 1.) Acceleration in parallel direction can be limited by the instability 2.) The excited waves could scatter particles to higher pitch angles which is required for most stochastic acceleration models to keep acceleration efficient.

In order to investigate the thresholds and growth rates of these waves in a flaring plasma the velocity distribution function of the electrons has been modeled by a bi-maxwellian with different temperatures $T_{\|}, T_{\perp}$ in parallel an perpendicular direction. An initial maxwellian plasma has been assumed and the thresholds have been derived by increasing only the parallel temperature.

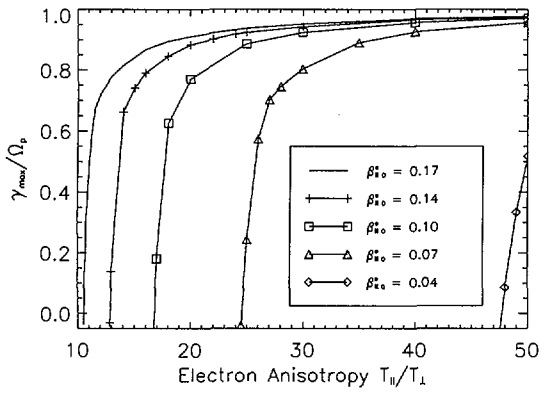

Figure 1: The maximum growth rate $\gamma_{\max}$ normalized to the proton gyrofrequency $|\Omega_p|$ versus the anisotropy $T_{\|}^e/T_{\perp}^e$ of the electrons; $T_{\perp}^p = T_{\|}^p$, $T_{\perp}^e = T_{\perp}^p$. The appropriate frequency is always of the order of $|\Omega_p|$. $\beta_{\|0}^e$ is the initial parallel plasma beta.

As it can be seen in Fig.1 instability occurs at initial betas of value ~ 0.01 at anisotropies of order ~ 30. These values are well within the expected ranges for solar flares ([2], [4]).

Additionally to this analysis of the known Electron Firehose instability a new wave mode propagating at oblique angles with respect to the background magnetic field has been found. It is excited by the same kind of anisotropy and exhibits much faster growth than the unstable modes described above. The preliminary results for this mode are depicted in Fig.2. Since this mode could be of much more importance than the Electron Firehose mode for limiting the acceleration in parallel direction, it will be a topic of future research.

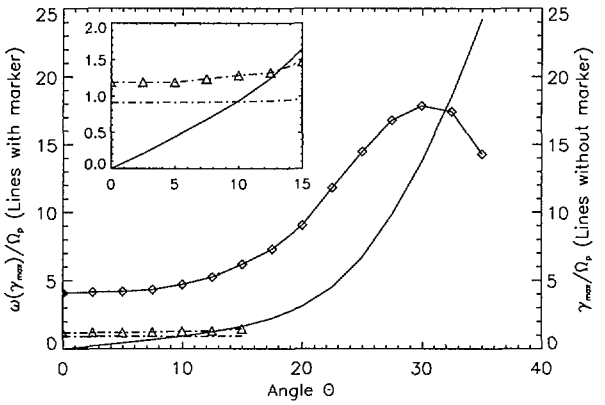

Figure 2: Frequency and the according growth rates vs. the propagation angle Θ with respect to the background magnetic field.The dashed lines indicate the branch of the parallel Electron Firehose instability. The solid lines show the oblique mode that exhibit much faster growth than the Electron Firehose instability.

REFERENCES

[1] J. V Hollweg, H. J. Völk, JGR **75/28**, 5297(1970)

[2] G. T. Lenters, J. A. Miller, ApJ **493**, 451 (1998)

[3] J. A. Miller, et al., JGR **102/A7**, 14631(1997)

[4] R. Pallavicini, S. Serio, G. S. Vaiana, ApJ **216**, 108(1977)

DARK MATTER IN THE UNIVERSE

Ph. Jetzer[1], *D. Puy*[1], *L. Grenacher*[1,2], *P. Kock*[2], *M. Strässle*[2], *F. De Paolis*[3], *G. Ingrosso*[3], *M. Roncadelli*[4]

PSI[1] – ZÜRICH[2] – LECCE[3] – PAVIA[4]

Recently the first direct detection with the ISO satellite of cold molecular clouds in the halo of the nearby NGC 891 galaxy has been announced. This gives strong additional support to our model for the dark halo, which we further improved. Moreover, we investigated several models for cooling flows in clusters of galaxies, in particular with respect to possible X-ray signatures. This work is of great importance for a correct analysis of the X-ray observations of galaxy clusters, which will be done with the XMM satellite. Using microlensing data towards the galactic centre we determined the mass function of the low mass stars which act as lenses and computed the expected number of events towards some spiral arm regions of our galaxy. This knowledge leads to important insight into the structure of the Galaxy.

Dark matter in the halo of our Galaxy

In collaboration with F. De Paolis, G. Ingrosso (Lecce University) and M. Roncadelli (Pavia University) we pursued the investigations on our scenario for dark matter in the halo of our Galaxy, according to which MACHOs (Massive Astrophysical Compact Halo Objects) are clumped into dark clusters along with large amount of cold H_2 clouds [1]. Recently, dutch astronomers using data of the Infrared Space Observatory (ISO) announced the first direct detection of cold molecular hydrogen clouds in the nearby galaxy NGC 891. The amount of detected molecular hydrogen is such that it makes up an important fraction if not all of the halo dark matter, at least within the radius corresponding to the optical disk of the galaxy. This discovery lends strong additional support to our model for the dark halo [1]. We, thus, made new more accurate computations on several aspects of the model. In particular we further improved on the expected γ-ray flux from the halo [2] (which is another distinctive feature of our model, that has already got possible confirmation from EGRET observations) and we started to investigate the infrared emission due to the molecular clouds, in order to be able to directly compare with the ISO measurements.

Cooling flows in clusters of galaxies

Cluster of galaxies are the largest known structures present in the Universe and contain up to a few thousand of galaxies. They are embedded in a vast cloud of hot gas, which is a strong source of X-rays, due to bremsstrahlung. From X-ray observations it is possible to get accurate estimates of the total cluster masses and of their dark matter content. The intracluster gas is densest in the core of the clusters where the cooling time due to X-ray emission is shortest. Indeed, if the cooling time is less than the age of the cluster a cooling flow is formed. There is nowadays strong evidence for the presence of cooling flows in the inner regions of many clusters. The ultimate fate of the cooling gas is, however, still unknown. Signatures of the cooling flows are best seen in X-ray observations. We have studied and improved several models for cooling flows, looking also at the possible distinctive signatures in the X-ray emission [3]. This work is also an important contribution to our activity in the framework of the working group on clusters of galaxies in the RGS team of XMM, which will analyse the scheduled galaxy cluster targets of the GT program.

Gravitational microlensing

In collaboration with F. De Paolis (Lecce University) we calculated the optical depth and the number of events due to gravitational microlensing towards the galactic bulge, the spiral arm directions γ Scutum, β Scutum, γ Normae, ϑ Muscae and some dwarf galaxies in the halo of the Galaxy [4]. Using the events found by the MACHO collaboration during their first year of observation towards Baade's Window we estimated the mass functions for the bulge and disk populations following the mass moment method. We find that the mass function can be described by a decreasing power-law with slope $\alpha \simeq 2.0$ in both cases and a minimal mass of $\sim 0.01\ M_\odot$ for the bulge and $\sim 0.02\ M_\odot$ for the disk, respectively. Assuming that the obtained mass function for the disk is also valid in the spiral arms, we find that the expected number of events towards the spiral arms is in reasonable agreement with the recent observations by the EROS collaboration [5]. Moreover, to study the influence of the Magellanic Clouds on the shape and the velocity dispersion in the halo we performed a N-body simulation. We found that their presence induces a slightly flattening of the halo. As a result the expected number of microlensing events towards some targets in the halo, such as the LMC or the SMC, decreases by about 20%, whereas due to the modification induced on the velocity dispersion the event duration increases.

REFERENCES

[1] F. De Paolis, G. Ingrosso, Ph. Jetzer and M. Roncadelli, Phys. Rev. Lett. **74**, 14(1995); Astron. and Astrophys. **295**, 567(1995).

[2] F. De Paolis, G. Ingrosso, Ph. Jetzer and M. Roncadelli, to appear in the New Journal of Physics

[3] P. Koch, *Cooling flows in clusters of galaxies*, Diploma Thesis ETH (1999)

[4] L. Grenacher, Ph. Jetzer, M. Strässle and F. De Paolis, Astron. and Astrophys. **351**, 775 (1999)

[5] F. Derue et al., to appear in Astron. and Astrophys., astro-ph/0001083

X-RAY PROPERTIES OF CLUSTERS OF GALAXIES

L. Grenacher[1,2], Ph. Jetzer[1], P. Koch[2], A. Obrist[2], D. Puy[1]
F. Melchiorri[3], Y. Rephaeli[4], S. Schindler[5], M. Signore[6]

PSI[1] - ZÜRICH[2] - ROME[3] - TEL AVIV[4] - LIVERPOOL[5] - OBS. of PARIS[6]

In many clusters of galaxies there is evidence for cooling flows which deposit large quantities of cool gas in the central regions. A fraction of this gas might accumulate as dense cool clouds. The most important heat source for molecular clouds in cooling flows is the X-ray bremsstrahlung emitted by the hot intracluster gas. In the successive fragmentation scenario this radiation is shielded by the presence of an attenuating column density. The balance between heating and cooling in the cluster environment leads to a thermal equilibrium inside the cooling flow region of the clusters. We investigated the coldest equilibrium achievable inside the cooling flow region. Moreover, we have analysed some aspects of the Sunyaev-Zel'dovich (SZ) effect which could lead to important constraints on cosmological models.

Cold molecular clouds and clusters of galaxies

In clusters of galaxies X-ray measurements show an excess absorption below $\sim$ 1 keV compared to a best fit bremsstrahlung model, which is interpreated as due to the presence of cold clouds. In a scenario with successive fragmentation of these clouds [1] we have calculated the molecular rotational line cooling due to HD and H_2 molecules and determined their minimum temperature T_{clump} achievable in equilibrium with the hot intracluster gas for some clusters [2] [3]:

Cluster	T_{clump} (in K)	T_{Kev} (in keV)
Centaurus	153	2.1
Hydra A	107	4.5
PKS 0745-191	92	8.6
Abell 262	119	2.5
Abell 426	83	6.3
Abell 478	228	7.1
Abell 496	58	4.8
Abell 576	102	2.9
Abell 1367	80	4.1
Abell 1795	136	5.3
Abell 2052	96	3.4
Abell 2151	256	2.9

Table 1: Equilibrium temperature T_{clump} and cluster temperature T_{keV} for different galaxy clusters.

Thus we find that an equilibrium is possible at low temperature in the cooling flow region and therefore especially nearby the clusters central galaxies. Indeed, the recent observation of the lowest pure rotational lines of H_2 in the spiral galaxy NGC 891 which is a direct detection of relatively warm (T=150-230 K) molecular clouds in the disk in addition to a massive cooler (80-90 K) component in the outer regions [4], supports the idea of the presence of important amount of cold gas, which could have formed in cooling flows.

Sunyaev-Zel'dovich effect

The SZ effect is one of the major sources of secondary anisotropies of the cosmic microwave background arising from inverse Compton scattering of the microwave photons by hot electrons in clusters of galaxies. By combining the SZ intensity change with the X-ray emission observations and solving for the number density distribution of the electrons responsible for both these effects and, moreover, assuming a certain geometrical shape, the angular diameter distance to galaxy clusters can be derived.This then leads to the determination of the Hubble constant.

The precise measurements of the SZ effect in the millimetric region for a selected sample of galaxy clusters is now performed by the group of F. Melchiorri, which has a dedicated telescope [5]. This observation will then be linked with the X-ray measurements of the clusters, which will be done by the XMM satellite. This work will be carried out in collaboration with the group of M. Signore and Y. Rephaeli.

Nevertheless, the SZ effect in the millimetric region is particularly difficult to measure due to systematic errors. For example, the shape and the geometry of clusters of galaxies, as well as projection effects can play a role. Our investigations [6] revealed, for instance, that asphericity can lead in some galaxy clusters to underestimate the Hubble constant by almost 14 %.

In collaboration with S. Schindler (John Moores Liverpool University) and M. Signore (Observatory of Paris) we started to model the density profiles for different clusters in order to evaluate their asphericity.

REFERENCES

[1] D. Puy, L. Grenacher, Ph. Jetzer, Astron. & Astrophys. **345**, 723(1999).

[2] L. Grenacher, Ph. Jetzer, D. Puy, astro-ph/9911203,(1999).

[3] L. Grenacher, Ph. Jetzer, D. Puy, astro-ph/9911438,(1999).

[4] E. Valentijn and P. Van der Werf, Astrophys. Journ. **522**, L29(1999).

[5] M. De Petris et al, New Astronomy **121**, 132(1996).

[6] A. Obrist, *Cosmology of the Sunyaev-Zel'dovich Effect*, Diploma Thesis 1999, University of Zürich

ANISOTROPIC PROTON FLUXES IN THE SAA

P. Bühler[1], *M. Kruglanski*[2], *E. Daly*[3], *A. Zehnder*[1]

PSI[1] – BIRA[2] – ESTEC[3]

During two years a Radiation Environment Monitor, REM [1] from PSI was mounted outside the Russian space station Mir and measured the charged particle fluxes of the environment. An outstanding result of this campaign was the measurement of the east-west effect of the protons in the South Atlantic Anomaly, SAA and its energy dependence.

The motion of a stably trapped particle in the earth's magnetosphere can be approximately described by its gyration around the local magnetic field line (the center of gyration is denoted as guiding center), its bounce motion along field lines between conjugate mirror points in the northern and southern hemisphere, and its drift around the earth. Its trajectory forms a shell which can be labeled by the so-called L-shell parameter, L, which in a dipole field approximation measures the distance between the center of the earth and the points where the shell crosses the magnetic equator.

At a given point D in space (see figure 1), the guiding centers GC1, GC2 of particles arriving from different directions have different locations. If the difference in guiding center position is large compared with the spatial flux gradient scale length then the observed flux distribution can be expected to be anisotropic [2]. The gyro-radius depends on

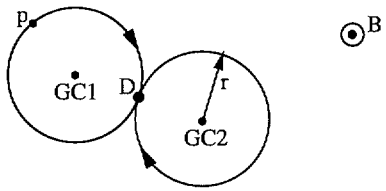

Figure 1: The difference in guiding center position GC1, GC2 of particles arriving from different directions at a given point D in space can cause anisotropic flux distributions.

the particle's mass, m and energy, E and on the magnetic field strength, B with
$r_{gyro} = p/(q \cdot B)$.

Since the effect scales with the gyro-radius, the anisotropy is best observed with high momentum particles at low magnetic fields. Mir encounters the minimum field strength of approximately 0.2 Gauss in the SAA. There the gyro-radius of 1 MeV electrons and 100 MeV protons (typical energies of particles detected by REM) are of the order of 100 m and 100 km, respectively. The SAA is also the place where the proton fluxes are high and the spatial flux gradients large - thus ideal for observing the anisotropy.

In order to extract the proton flux anisotropy in the Mir-REM data we binned the measurements in the SAA according to L, B, and pointing direction of the detector, and averaged the data in each bin over the entire Mir-REM lifetime.

In the upper panel of figure 2 the proton fluxes from east and west are compared for a number of B-L-bins. It shows the measured 100 MeV proton fluxes as function of L. The B-values correspond to the minimum values encountered by Mir at a given L. The fluxes from west are higher than those from east. The ratio is a function of L, is around 4 at L=1.1 earth radii and vanishes above L≈1.7 earth radii.

A similar behavior is found for the spectral hardness, as shown in the lower panel of figure 2, where the spectral indices γ (the proton spectra, $f_p(E)$ are fitted by a power law $f_p(E) = A_p \cdot (E/E_0)^{\gamma}$) are plotted versus L . The energy spectra of the protons coming from west are harder than those of the particles from east, and as for the fluxes, the difference vanishes above L≈1.7 earth radii.

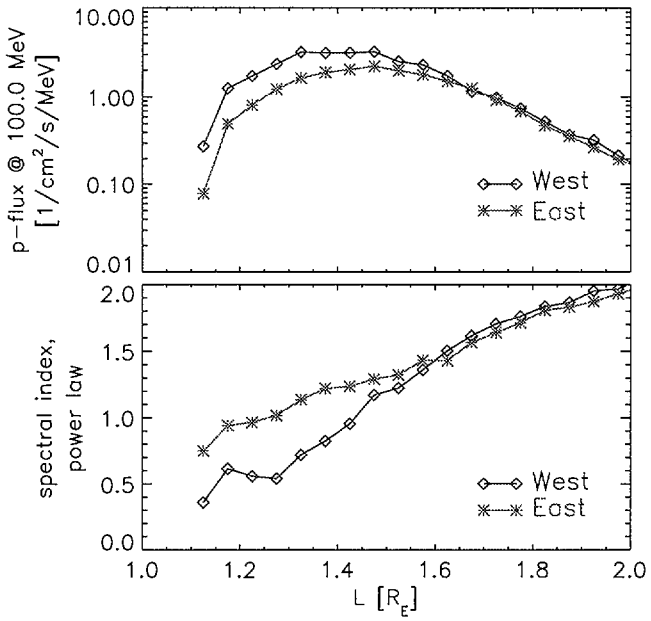

Figure 2: Comparison of proton fluxes from east and west in the SAA. The upper panel show the 100 MeV proton fluxes and the the lower panels the spectral power law indices as function of L.

The flux gradients in the SAA are mainly caused by the interaction of the protons with ambient atmospheric particles. The deeper an L-shell dips at the mirror points into the atmosphere the more the particles are absorbed. The fact that the high energy protons arriving from east at a given point in the SAA are members of L-shells dipping on average deepest into the atmosphere explains why the east fluxes are low and their spectra soft.

REFERENCES

[1] P. Bühler et al., Radiation Environment Monitor, *Nucl. Instr. and Meth. in Phys. Res.* **A 368**, 825(1996)

[2] M. Kruglanski et al., Proton anisotropy, *TREND-3 final report* **chapter 3**, BIRA-IASB, Belgium, 1998

ENERGY, POSITION AND TIME RESOLVING PHOTON SPECTROMETERS

Ph. Lerch[1], *E. C. Kirk*[1], *J. Olsen*[1], *J. Bialkowski*[1], *A. Zehnder*[1], *H. R. Ott*[2]

PSI[1] – ETH ZÜRICH[2]

The intrinsic energy resolution of a superconducting tunneling junction (STJ) device applied to the detection of photons is limited by the statistical fluctuations in the number of excess charge carriers (called quasiparticles) produced upon the absorption of energy [1] and by the fluctuations of tunneling processes through their barrier [2]. Both contributions are energy dependent so that we can write,

$$\Delta E_{fwhm} = 2.35\sqrt{\epsilon E_x(F + 1 + \frac{1}{< n >}] + \sigma^2_{elec}} \quad (1)$$

where $\epsilon \approx 2$ meV is the effective energy required to create excess charge carriers, F is the Fano factor [1], E_x is the photon energy, $< n >$ is the average number of tunnel processes per charge carrier and σ^2_{elec} is an energy independent electronic noise contribution.

The actual energy resolution obtained in the energy range of soft x-ray by state-of-the-art STJ devices is already a factor 3 better than that obtained with semiconducting devices. However, the limit set by Eq.1 is spoiled by a component reflecting uneven spatial response [3] of the devices to the deposition of energy, $\sigma^2_{spatial} \propto E^2$. There is vast experimental evidence that contact leads, device edges, interfaces, impurities within the materials, as well as sites of pinned magnetic flux lines are creating lower energy gap regions in the superconductor. These regions are responsible for the loss of quasiparticles and add complexity in the dynamical processses present in multilayered devices [4].

In order to study the dynamics of quasiparticles and to investigate separately several energy resolution degrading mechanisms, we microfabricated a series of x-ray spectrometers by instrumenting 2 STJs at the ends of 200 μm by 40 μm strips of epitaxial Ta. We determined their performances at 500 mK by illuminating devices with 5.9 and 6.4 keV photons without collimator. Photons absorbed in the Ta create quasiparticles which diffuse in either direction along the strip. Each Al-AlOx-Al-Nb devices collect a fraction of the total charge [5]. Coincidence data aquisition on both STJs allow the measurement of the energy, the position and the timing of every absorbed photons.

The figure shows the energy as a function of position measured by such a Ta-strip detector. The data was corrected for diffusion losses.

- the quasiparticle diffusion rate in an epitaxial film of Ta is rather slow, 8 cm^2/s
- the impurity content of the absorber as well as the quality of the interface within the layers of the device affect the energy resolution
- this detector concept yields an energy resolution of 50 eV at 6 keV, a position resolution of a few microns over an absorber size of 200 x 40 microns, and a timing resolution of 5 microseconds. The energy resolution at 6 keV is 3 times better than the one obtained for semiconducting devices.

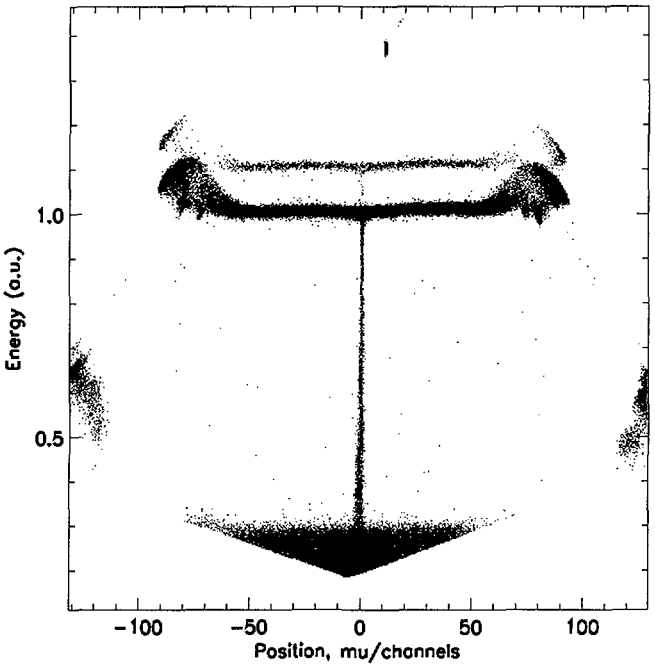

Figure 1: Energy vs position plot measured with a 2 junction spectrometer illuminated by 5.9 and 6.4 keV photons.

The large reponsivity of STJ devices, 500 e/eV, combined with the good absorption efficiency of the Ta absorber allows for energy resolved single photon detection at low energy (visible photons). We are testing our detectors with visible light and strongly envisage imaging applications in scientific instrumentation.

REFERENCES

[1] M. Kurakado and H. Mazaki, NIM **185**, 141 (1981).

[2] C.A. Mears *et al* Appl. Phys. Lett. **63**, 2961 (1993), and D.J. Goldie *et al* Appl. Phys. Lett. **64**, 3169 (1994).

[3] P. Verhoeve, N. Rando, J. Verveer, A. van Dordrecht, A. Peacok, P. Videler, M. Bavdaz, D.J. Goldie, T. Lederer, F. Scholze, G. Ulm, and R. Venn Phys. Rev. **B 53**, 809 (1996).

[4] A. Zehnder, Ph. Lerch, S.P. Zhao, Th. Nussbaumer, E. Kirk, H.R. Ott, Phys. Rev. **B 59**, 8875 (1999).

[5] H. Kraus, F. von Feilitzch, J. Jochum, R.L. Mössbauer, Th. Peterreins and F. Pröbst, Phys. Lett. **B 231**, 195(1989).

SMALL ARRAYS OF TRANSITION EDGE MICROCALORIMETERS

J. Olsen[1], *E. C. Kirk*[1], *Ph. Lerch*[1], *K. Thomsen*[1], *B. van den Brandt*[1], *M. Huber*[2], *G. C. Hilton*[2], *J. M. Martinis*[2], *A. Zehnder*[1], *S. Mango*[1], *H. R. Ott*[3]

PSI[1] – NIST - BOULDER[2] – ETH ZÜRICH[3]

Calorimetry, a standard technique, measures an absorbed photon (or particle) after its energy (or a fraction of it) has been converted to heat, by measuring a temperature rise $\Delta T \approx E/C_v$. E is the energy released by the event, and C_v is the heat capacity of the absorber/thermometer device. Impressive progress has been obtained since the technique is applied at millikelvin temperatures where many materials exhibit a very small heat capacity. Recently, individual photons were detected with an energy resolution of 0.15 eV between 0.3 eV and 3.5 eV [1] and 7.2 eV at 6 keV [2] with single pixel calorimeters fabricated with superconducting transition edge sensors (TES) as temperature - voltage transducers.

There are some specific advantages [3, 4, 5] to use a TES instead of a semiconducting thermistor as a thermometer in a calorimeter: a) the temperature of operation, which has to be above the base temperature of the cryogenic equipment, can be adjusted by using the proximity effect between two metals, b) the steep transition from the super- to the normal-conducting state, measured by the parameter $\alpha = (\delta log(R)/\delta log(T)$ where R is the resistance of the TES and T the temperature, increases the useful bandwidth, c) normal metals can be used as absorbers because the large value of α compensates for their larger heat capacity, and the design flexibility increases, d) the read-out of a large number of low impedance thermometers may be easier to achieve.

In this work we investigate multiple pixel devices in order to study the problems that need to be solved for future imaging instruments. Beyond the microfabrication of arrays, the important issues are related to the thermal crosstalk between devices and the electric and/or magnetic crosstalk in the read-out electronics.

We have developed a photolithographical fabrication process for the deposition of Mo/Au thermometers and Au absorbers on 250 nm thick silicon nitride membranes. The figure illustrates the resistive transition of one thermometer element. The small array chip is made with (3 x 4) 0.42 mm x 0.42 mm TES deposited on 0.8 mm x 0.8 mm membranes (1.14 mm x 1.14 mm on the back side) separated by a $\approx$ 1.6 mm pitch in the vertical and horizontal directions. The absorbers are 0.3 mm by 0.3 mm and placed in weak electrical contact in the center of the bilayers. The heat capacity of a 43 nm thick Mo and 123 nm thick Au bilayer is estimated to be $C_v \approx 0.52pJ/K$, a 1 μm thick Au absorber has $C_v \approx 0.78pJ/K$. The Si substrate acts as a primary heat sink linked to each thermometer by the nitride membrane which is designed to have a thermal coefficient $g \approx 2$ nW/K at 100 mK.

We built a dilution refrigerator with a cooling power of 60 μW at 100 mK and wired it for the read-out of two calorimeters. TES are low impedance devices and are best read-out by current sensitive amplifiers. We use superconducting quantum interference devices (SQUID) amplifiers [6] inductively coupled to an input coil placed in series with the TES. The calorimeters are operated around 100 mK, the SQUID amplifiers are operated at 2.2 K. A superconducting line is connecting each device to its SQUID.

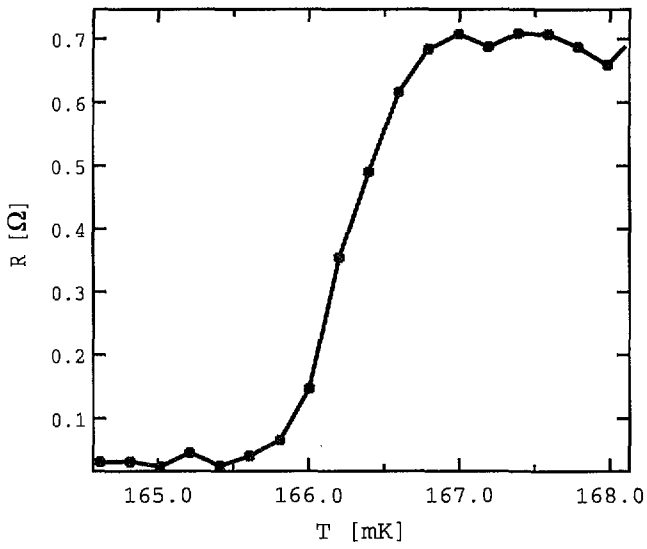

Figure 1: Resistive transition of 43 nm thick Mo and 123nm thick Au bilayer placed on a membrane and used as pixel thermometer element.

All the elements necessary for the operation of calorimeter devices were separately tested. We plan to perform experiments with synchrotron light.

REFERENCES

[1] B. Cabrera, R.M. Clarke, P. Cooling, A.J. Miller, S. Nam, R.W. Romani, Appl. Phys. Lett. **73**, 739(1998).

[2] D.A. Wollman, K.D. Irwin, G.C. Hilton, L.L. Dulcie, D.E. Newbury, J.M. Martinis, J. Microscopy **188**, 196(1997).

[3] J. Clarke, G.I. Hoffer, P.L Richards, N.H. Yeh, J. Appl. Phys. **48**, 4865(1985).

[4] P.L Richards, J. Clarke, R. Leoni, Ph. Lerch, S. Verghese, M.R. Beasley, T.H. Geballe, R.H. Hammond, P. Rosenthal, S.R. Spielman, Appl. Phys. Lett. **54**, 283(1989).

[5] K.D. Irwin, Appl. Phys. Lett. **66**, 1998(1995).

[6] R.P. Welty, J.M. Martinis, IEEE Trans. Mag **27**, 2924(1991).

BUILDING THE IMAGING SYSTEM OF THE HIGH-ENERGY SOLAR SPECTROSCOPIC IMAGER (HESSI)

F. Burri[1], R. Henneck[1], A. Mchedlishvili[1], P. Ming[1], K. Thomsen[1], A. Zehnder[1], A. Benz[2], et al.[3,4]

PSI[1] - ETH ZÜRICH[2] - GSFC[3] - DELFT[4]

HESSI is a NASA mission with a single instrument on a small spin-stabilized spacecraft in low earth orbit. The primary scientific aim of the mission is to explore the basic physics of particle acceleration and explosive energy release in Solar Flares. HESSI will produce hard X-ray images with an angular resolution as fine as 2 arc-seconds and a temporal resolution on the order of 10 ms; a detailed image can be obtained in 2 seconds. At the same time HESSI will provide energy resolution below 1 keV over the range from 3keV to 400 keV. For the first time HESSI will perform hard X-ray and gamma-ray imaging above 100 keV with an energy resolution of a few keV up to energies as high as 20 MeV.

The imaging capability of HESSI is based on a Fourier-transform technique using a set of 9 pairs of grids each spaced 1.55m. Transmission through a grid pair is modulated as the spacecraft rotates around its axis. The different grid pairs have different slit widths. For the finest grids an alignment and its stability to better than 20 arcsec is mandatory to yield sufficient modulation depth.

Given the exact timing of single photons together with the precise knowledge of the attitude of the imager it is possible to reconstruct an image of the source. The energy resolution of the instrument is achieved by using cooled Ge detectors.

HESSI will have the best angular and spectral resolution of any hard X-ray or gamma-ray instrument flown so far.

The main imager structure consists of a carbon fiber reinforced plastic (CFRP) tube with Titanium end- and center-rings. The winding layout of the CFRP tube has been optimized with respect to minimum twist as a possible result of variable environment conditions selecting a balanced symmetrical winding scheme. The titanium rings closely match with the CFRP in their coefficient of linear thermal expansion. On the end rings the grid bearing trays are mounted by means of flexible links. In a kinematic arrangement there are three mounts for each tray, two fixed ones and an adjustable one. The adjustable mounts allow for fine-tuning of the tray to tray twist.

Grids sit on individual grid mounts. They were delivered by NASA GSFC prealigned on their mounts. Fine adjustment of the finest grids was done on the coordinate measuring machine of the ETH in Zürich using their optical probe. Trays were mounted onto the imager tube on PSI's measuring machine.

After extensive verification of the alignment with the dedicated twist monitoring system (TMS) and vibrational and thermal acceptance testing the fully assembled flight hardware was sent to Berkeley for integration with the spacecraft.

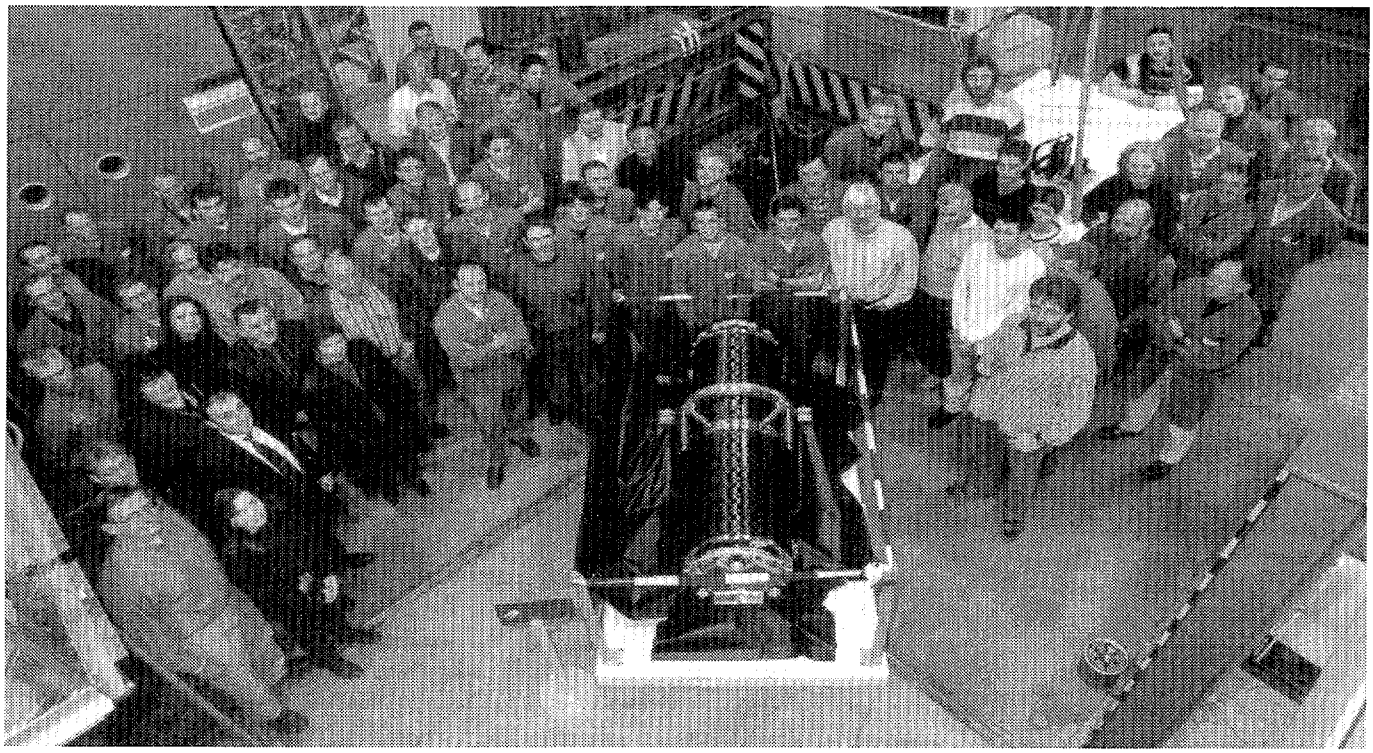

Figure 1: Most of the PSI contributors to the HESSI Imager structure

MODELLING HESSI RESPONSE - SCIENTIFIC OBJECTIVES

W. Hajdas[1], Ph. Jetzer[1], R. Henneck[1], A. Höchner[1], M. Fivian[1], M. Güdel[1], A. Zehnder[1], G. Schmid[1,2] D. Smith[3]

PSI[1] - ETH ZÜRICH[2] - UCB[3]

The complete mass model of the HESSI satellite was constructed. Together with Monte Carlo simulations of detector responses, it allows for an accurate analysis of the non-solar spectra with approximate source location and proper evaluation of the background. Solar and non-solar scientific goals for the HESSI mission were analysed. We identified several non-solar targets to be explored by HESSI, in particular gamma-ray bursts.

The primary scientific objective of the High Energy Solar Spectroscopic Imager HESSI is to study acceleration and energy release processes in the Sun's magnetised plasmas. The Sun and near-solar sources (e.g. Crab Nebula) will be measured in both spectroscopic and imaging modes. A large parts of the sky will be monitored in parallel in a non-imaging mode, for e.g. γ-ray bursts GBR, diffuse cosmic and terrestrial sources (e.g. aurora emission) or accreting black holes. Detector modelling is performed in Berkeley for the imaging mode and at PSI for the non-imaging one.

Response Computation – Mass Model

The total mass of the spacecraft is equal to 238 kg including 120 kg weight of the scientific payload. Payload instruments contain Ge spectrometer, imager, solar aspect and roll angle systems, and electronic modules. The spectrometer consists of 9 segmented Ge detectors (7.1⅄ x 8.5 cm^2) cooled by a cryostat. They provide 150 cm^2 effective area and wide field of view (60°-120°) perpendicularly to the sun direction. The UCB team delivered an exact model of the spectrometer and cryostat while PSI constructed models for imager and satellite structures.

The modelling was performed using conventions of the GEANT code (CERN). All essential parts of the satellite are included taking into account correct geometry, mass and chemical composition. For detector system and all parts in front of them, the description is minuteness. Other components and structures are included as accurately as possible, although with less detail. In general, parts far away from the spectrometer maintain their mass and composition while for geometry we utilise simplified shapes.

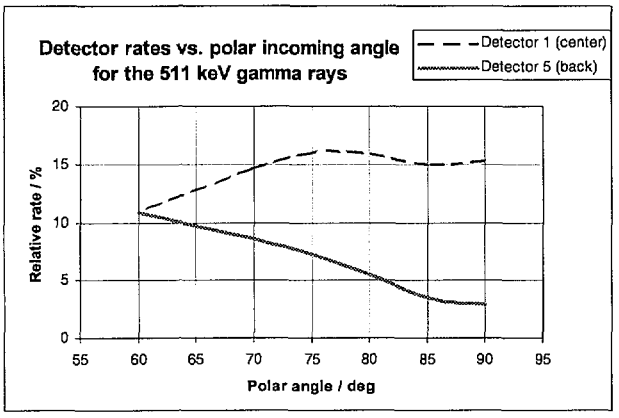

Figure 1 Normalised rates in selected detectors for gamma rays incoming angles θ from 60° to 90°.

The model provides a tool for determination of the detector response functions and studies of the background. It allows us to perform an accurate analysis of the X and gamma ray spectra collected from non-solar targets. In addition, it provides means to localise directions of the incoming photons utilising spacecraft rotation and detector occultations. Additional advantage comes from detector segmentation. First Monte Carlo tests were performed to study direction-resolving capabilities for a point gamma ray source. Initial results for both azimuth and polar angle are very promising as shown in Figure 1.

Solar Science

Our main interest in solar physics is in nuclear lines, in coronal evaporation processes, and in the sites of particle acceleration. HESSI is expected to contribute significantly to an understanding of these plasma physical and hydrodynamic mechanisms. We have been working on modelling of high-energy electrons trapped in coronal magnetic fields (collaboration with ETHZ). We have also contributed to the Hessi Data Center (HEDC) at ETHZ on science data format issues, data representation, science requirements, and software requirements. In a related effort, we have been planning the use of the SAS to measure variations of the solar diameter with varying magnetic activity through large statistical samples.

Gamma-Ray Bursts

Gamma Ray Bursts, first discovered in 1967, are short and intense bursts of MeV range γ-rays. Despite of significant observational advances in the last decade, GRBs still remain mysterious. An important issue to investigate is the presence of spectral features. HESSI's superior resolution can clearly resolve it and thus lead to substantial progress.

We estimated the number of GRBs, that could be detected with HESSI. Since the GRBs hit the detectors from all directions, HESSI's highest sensitivity covers the region from 30 keV to 2 MeV (10 keV – 20 MeV full range). Taking into account the expected background flux and assuming a best fit to the GRBs fluence, as observed by the BATSE instrument, we find that HESSI should be able to detect at least ~75 GRBs/yr. A major advantage of using HESSI for GRBs is its ability to detect lines due to the much better energy resolution as compared to present instruments. We thus made estimates for several lines, as for instance the electron-positron annihilation line at 511 keV or cyclotron lines that might be present in GRBs. We thus found is that the detection sensitivity for lines is much better at low energy than at high energy, given also the limited duration in time of the GRBs (less than 10^3 s).

Further Non-solar Objects

Among others, of particular interest for us are exact observations of the Crab Nebula with the highest spatial and energy resolution and studies of the ^{26}Al decay lines.

THE HESSI SOLAR ASPECT SYSTEM (SAS)

M. Fivian[1], *W. Hajdas*[1], *R. Henneck*[1], *A. Mchedlishvili*[1], *P. Ming*[1], *K. Thomsen*[1], *A. Zehnder*[1], *G. Hurford*[2], *D. Curtis*[2], *B. Dennis*[3]

PSI[1] – UC-BERKELEY[2] – GSFC-GREENBELT[3]

We describe the design and performance of the HESSI Solar Aspect System. It is based on the optical observation of the Sun image with 3 line CCDs and it will provide a position determination with accuracy $\leq$ 0.4 arcsec.

The Solar Aspect System (SAS) is part of the HESSI instrument [1] to be launched by mid-2000 at solar maximum. In order to reconstruct images with a resolution of 2 arcsec, the relative pointing of the imager has to be known with a precision of $\leq$ 0.4 arcsec (on a 1 σ level) at any time. The SAS consists of 3 identical lens/sensor subsystems (spaced at 120 degrees) and provides high bandwidth ($\leq$ 128 Hz) information on the solar pointing of the rotating spacecraft (15 rpm). Each SAS is based on focussing the Sun through a narrow bandwidth filter (at 670 nm) onto a 2048-element x (13 μm)^2 linear CCD. For each image, there are two limb crossings where the Sun image intersects the CCD. Integrating the image for $\approx$ 500 μs (programmable), a digital thresholding algorithm is used to select N pixels at the solar limb for inclusion in the telemetry. [2]

Ground based measurements

For calibration the imager with the integrated SAS subsystems was pointed directly at the Sun. Setting an initial pointing ahead of the Sun image motion, the drift of the Sun over the FOV ($\approx$ 1 degree) gives a well defined trajectory in the SAS image plane. Aquiring images for every integration cycle, Sun profiles were obtained (see Fig.1). Since the width of the solar limb (i.e. the angle over which the intensity raises from zero to about 50 % of the maximum intensity) is in the order of 1/100 arcsec, the measured width is a function of diffraction, chromatic aberation and environmental influences. Approaching the limbs the background is increasing gradually due to diffuse reflection from the CCD chip surface and subsequent back-reflection from the CCD window. Therefore the limbs were fitted with an error function adding a linear background. This fit provides a well defined width of the measured limb which turned out to be about 2.5 arcsec for a full diameter profile. Subtracting quadratically the width of the point spread due to the diffraction from the lens and the chromatic aberation a contribution of environmental influences to the point spread of about 1.7 arcsec is obtained. This is a realistic upper limit for 'seeing'. [3]

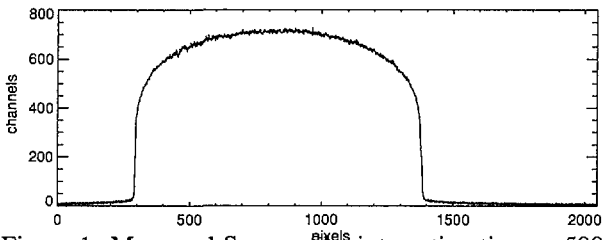

Figure 1: Measured Sun profile, integration time $\approx$ 500 μs. One pixel on the CCD corresponds to 1.73 arcsec.

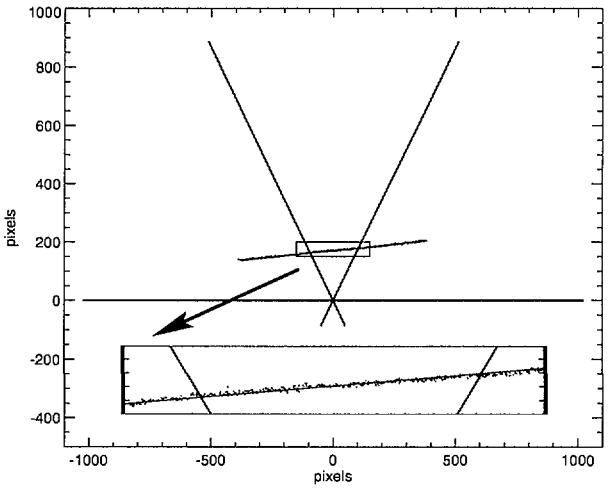

Figure 2: Drift of Sun over the SAS. The three 120 degrees spaced lines represent the three CCDs, the dots (in the blown-up diagram) with a linear fit represent the Sun centers for consecutive time intervals.

Reconstruction of the pointing

For ideal circumstances and with positions (lens optical center, CCD pixel location) known exactly, the mid-perpendiculars of the 3 chords would intersect in one point, the momentary Sun center position. Given the accuracy of our dimensional measuments ($\leq$ 5 μ for the lens optical center, $\approx$ 1 μ for the CCD pixels, $\approx$ 10 μ for the projection of the front tray on the rear tray) and given thermal and mechanical instabilities the mid-perpendiculars usually do not intersect in one point but form a residual triangle. The size and shape of the triangle depend sensitively on the position of the lenses and CCDs. In principle, we expect that from a model of this triangle, which will be measured every 10 ms, we will be able to calibrate these parameters independently. Nevertheless, the positions/dimensions measured on ground will make a good starting point. Without making any corrections to the nominal alignment an accuracy of the pointing of 0.7 arcsec (on a 1 σ level) is achieved (see Fig. 2). After rudimentary alignment corrections, a short term variation of the pointing of 0.4 arcsec has been measured (using 128Hz cadency).

REFERENCES

[1] R. P. Lin et al, SPIE Proc. **3442**, 2-12(1998).

[2] J. Bialkowski et al, PSI Ann. Report **1998**, Vol. I, 31.

[3] R. Henneck et al, SPIE Proc. **3765**, 518-523(1999).

THE HESSI ROLL ANGLE SYSTEM (RAS)

J. Bialkowski[1], F. Burri[1], M. Fivian[1], W. Hajdas[1], R. Henneck[1], A. Mchedlishvili[1], P. Ming[1], K. Thomsen[1], J. Welte[1], A. Zehnder[1], G. Hurford[2], D. Curtis[2], D. Pankow[2]

PSI[1] - UC BERKELEY[2]

We describe the design and performance of the HESSI Roll Angle System. Based on the observation of at least one star per satellite rotation, it will provide an absolute roll angle determination with accuracy ≤ 1 arcmin

The Roll Angle System (RAS) is part of the HESSI instrument [1] to be launched by NASA by mid-2000 at solar maximum. Its purpose is to provide information on the roll angle of the rotating spacecraft (15 rpm). Precise knowledge (1 arcmin at 1σ) of this angle is a necessary ingredient for image reconstruction. The RAS is a star camera which points out radially and observes stars at 75° from the sun direction. Stars within a field-of-view of 30° x 1.4° (parallel x orthogonal to satellite spin axis) are focussed by a lens onto a 2048 pixel line CCD. The passage of a star image over the CCD (orthogonally) will raise the signal in one or several pixels above threshhold and the timing of this signal defines the roll angle, once the star has been identified by comparing its pixel position and amplitude with a star map. During each passage of 16 ms duration we will measure typically 2 consecutive timeframes (without gap) with selectable integration time (~ 7 to 16 ms). Determination of the centroid of this time sequence will allow us to reconstruct the corresponding momentary roll angle with arcmin accuracy for a given object. Roll angles at intermediate times are inferred by assuming uniform rotation. More detail on the RAS concept and design is given in Refs.[2].

The originally selected CCD (Dalsa IL C6) was found to display unacceptably high timelag. Timelag is a consequence of incomplete charge transfer from the photosite into the shift register leading to a timeshift of the signal response with respect to an instantaneous light pulse. Correspondingly, the whole charge gets spread over several timeframes and hence reduces the maximum signal above threshold: in the case of the Dalsa IL C6 one loses a factor of 5 to 10 at small amplitudes. As a consequence we switched to the Dalsa TDI E1 CCD, which has 96 x 2048 pixels, each 13 by 13 μ. In the roll plane, i.e. along the 96 line, we exploit the full width of 1.25mm by binning over 48 or 96 pixels. This new type was fully characterized and already integrated into the flight board. The performance is as follows:

1. Noise 0.35 mV rms, independent of temperature and integration time between 7 and 16 ms.
2. No timelag
3. Dark current ~ 20 mV, constant between –10°C and –30C
4. Dynamical range about 1000

Since this CCD has no anti-blooming provisions the recovery time after exposure to very intense illumination represented a major problem. After the periodic exposure to Earth-reflected sunlight (every 4 s for about 2 s, intensity as much as 1000 times saturation level) the system should be sensitive with minimum deadtime. A special circuit with selectable 'Earth-shine' trigger level and accelerated reading for a programmable time period allowed us to reduce this deadtime to about 0.7 s. Given the increased sensitivity due to the longer integration times with the Dalsa TDI E1 we expect to trigger on $m_V = 4$ stars on-axis and should therefore still reach the specified goal of timing at least one star per revolution.

The TDI E1 was also radiation tested: after a passive, 6 krad Gamma-ray irradiation the dark current at room temperature is close to saturation level. However, for temperatures below –10°C the dark current is as for the non-irradiated samples.

The CCD is in very good thermal contact with the central RAS flange which supports the Leica Summilux, f/1.4, 50 mm lens and the optical baffle (see Fig.1). The latter also acts as a thermal radiator and is described seperately [3].

The flight system is in the last stages of integration and testing and awaits calibration with real stars on the Jungfraujoch observation platform in January 2000.

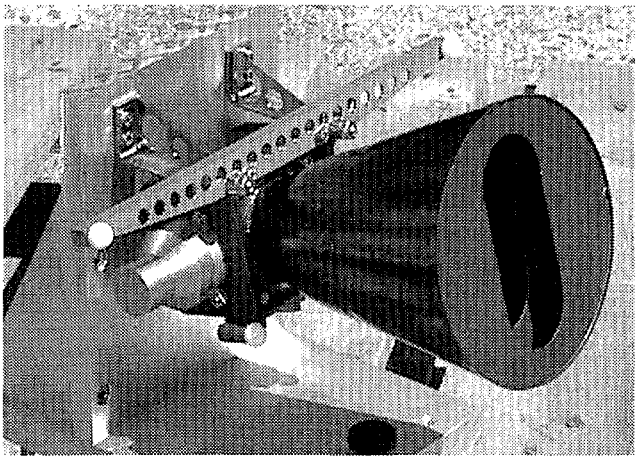

Fig. 2: Photograph of the RAS FM on its vibration support. The two top support struts are visible above the electronic housing and behind the alignment bar, which carries 2 tooling balls (in white, at a spacing of 280 mm). Another tooling ball is visible at the bottom of the central flange. The shiny cylinder on the left is the shutter pinpuller.

REFERENCES

[1] R.P Lin et al, SPIE Proc. **3442,** 2 - 12 (1998).

[2] R. Henneck et al, SPIE Proc. **3765,** 518-523 (1999), J. Bialkowski et al, Ann. Report PSI **1998, Vol.1,** p.32.

[3] F. Bürki et al, Ann. Report PSI **1999**, this volume.

AN OPTICAL BAFFLE MADE FROM THERMALLY CONDUCTIVE CARBON FIBRE

P. Bauer[1], F. Bürki[2], M. Dettwyler[2], P. Ermanni[2], R. Henneck[1], M. Konetschnig [2], P. Ming[1], K. Thomsen[1], J. Welte[1], A. Zehnder[1]

PSI[1] - ETH ZÜRICH[2]

We describe the design and performance of the optical baffle for the HESSI Roll Angle System. Based on a sandwich structure utilizing a core fibre with superior thermal conductivity and two cover layers of a mechanically robust fibre we achieve an effective conductivity along the fibre direction similar to that of Al

The Roll Angle System (RAS) is part of the HESSI instrument [1] and shall provide information on the roll angle of the rotating spacecraft (15 rpm). For details see Ref.[2].

The RAS is a star camera which points out radially and observes stars at 75° from the sun direction. Stars within a field-of-view of 30° x 1.4° (parallel x orthogonal to satellite spin axis) are focussed by a lens onto a 2048 pixel line CCD. The passage of a star image over the CCD (orthogonally) will produce a signal in at least one pixel and the timing of this signal defines the roll angle, once the star has been identified by comparing its pixel position and amplitude with a star map.

The optical system is protected from direct Sun illumination by the satellite instrument deck and from Earth-reflected light by an optical baffle for viewing angles ≥ 30° from the RAS optical axis. The baffle was designed for the specific case when HESSI is located exactly between Sun and Earth. This situation requires a straylight reduction of about $5*10^{-7}$. The design was based on extensive calculations with the ASAP/ APART straylight codes which considered the full optical path through the lens as well as the narrow FOV (± 0.7°) in the roll direction. The resulting design features 6 vanes with oblong apertures mounted in a cone with opening angle 30° (Fig.1). Nominally, it reduces the straylight to about 1.2 nW/mm² or 50% of a $m_v = 4$ star assuming that the star illuminates 2 pixels. In the calculation the vane knife-edges (nominally 50 μ radius and 0.2 total reflectivity) were found to be more critical than the baffle inside total reflectivity which was taken to be 0.06.

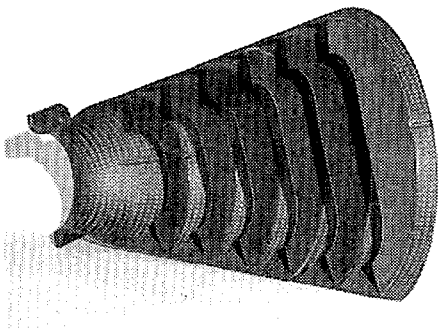

Fig.1: Cross sectional cut through the baffle. The fabric structure of the M60J 3K/954-2A can be clearly seen. The baffle length is 175 mm and the front vane diameter 150 mm.

For reasons of mass and mechanical stability the baffle was constructed from CFRP, containing a core of high-module fibers for thermal conductivity (K 1100 2K/954-2A, about 600 W/m/K along the fiber direction) and covering layers of medium-module fibers for mechanical strength (M60J 3K/954-2A fabric from Hexcel Composites). The vanes are made from the medium-module fibers alone. They are 0.5 mm thick with knife-edges of about 20 μ radius at a 45° bevel which were machined directly on a lathe with a conical cutter (see Fig.).

Fig.1: Cross section of a vane knife-edge machined out of a 0.3 mm thick CFRP vane. The edge radius is about 20 micron.

Total reflectivity measurements were done for several CFRP samples and it was found that CFRP structures lifted off a microbead-blasted replica surface have 'solar' reflectivities around 0.06, only about 50% higher than the best absorptive coatings. The baffle itself weighs about 150g.

The thermal properties of the whole system from the baffle via flange and CCD support to the CCD were measured in our 'cold space' simulation chamber for typical heat loads of the CCD and front-end electronics (1.5 W). We conclude that a CCD temperature of around -30°C to -40°C should be feasible, depending on what we assume for the temperature of the surroundings and for the view factors to cold space. The effective thermal conductivity of the composite baffle along the cone direction was evaluated to be about 200 W/m/K, i.e. similar to that of Al.

REFERENCES

[1] R.P Lin et al, SPIE Proc. **3442,** 2-12 (1998).

[2] R. Henneck et al, SPIE Proc. **3765,** 518-523 (1999).

OPERATING OF THE PROTON IRRADIATION FACILITY - CONCISE SUMMARY

W. Hajdas[1], K. Thomsen[1], A. Zehnder[1], R. Harboe-Sorensen[2] ()

PSI[1] - ESA-ESTEC[2]

In 1999, PIF experiments were conducted in both NA2 and OPTIS areas taking almost 80 shifts. About 35 different experiments were grouped into 23 beam blocks resulting in ca. 50 irradiation days. Proton tests were mainly devoted to qualify devices for very near satellite missions like HESSI, STRV-1c or INTEGRAL.

PIF particle beam experiments in 1999 covered, up to now, the biggest yearly period from 20 January to 14 December. They were arranged into 23 irradiation blocks of variable duration and resulted in ca. 50 days with the beam on target. More than 35 types of irradiation tests by 17 different groups of researchers were performed. In addition to standard PIF tests of electronics and detectors, two institutes used the facility for particle physics studies. Again, the required proton fluxes spanned greatly between 10^4 and 10^{10} /cm^2/sec and radial beam profiles covered the full available range from 16 to 100 mm FWHM. As in the 1998, there was a large interest in using the low energy protons in the OPTIS area.

Beam time and test area utilization by PIF

	NA2	OPTIS	^{60}Co	Total
Beam blocks	13	8	2	23
Shifts	65	12	2	79

IRRADIATION EXPERIMENTS

With evolving new technologies and devices, and advanced mission requirements, one can observe significant shift in types of PIF experiments in 1999. Several characteristic groups are shortly described below. The largest amount of beam time for ESA related activities, was used to calibrate and test the RADFET dosimeters. These devices will be used for total dose measurements on boards of e.g. STRV-1c, INTEGRAl and ISS missions. The next type is related with electronic qualification the HESSI satellite. Together with NASA-GSFC and Berkeley University the PSI, represented by Laboratory for Astrophysics, is preparing the HESSI launch in the year 2000. Large amount of the 1999 beam time was taken by particle/nuclear physicists to study the neutron production in Pb-Bi targets with future applications in SINQ. Industrial research teams also carried out two large experiments. The ABB tested sensitivity of power devices for upsets induced by ionizing particles on earth. The SIRA electronics irradiated optical fibers foreseen on telecommunication satellites. Several groups characterized different types of CCDs. They will be used e.g. on the ISS as an astronaut's hand camera or in HESSI's sun/star aspect systems.

Selected PIF experiments:

- RADFET dosimeter radiation response study
- ICARE particle monitor calibration
- SRAM/DRAMs proton SEU characterization
- Radiation damage of various CCDs
- Proton dose effects in photodiodes
- CCD, DSP, ADC total dose and SEE testing
- Damages in encoders and mirror coatings
- Optical fibers rad-hardness determination
- Activation measurement of Ta and Mo plates
- Radiation damage in infrared bolometers
- Radiation effects in power MOSFETs
- Proton production of neutrons in PbBi targets
- Performance studies of BGO veto detectors
- Full characterization of PROBA Star-tracker.

SYNOPSIS OF USERS AND COLLABORATIONS

Table: research groups involved in PIF experiments.

No	Research Institution
1	ESA/ESTEC, Nordwijk
2	PSI/GSFC/Berkeley University
3	LABEN, Alenia Spazio, Milano
4	Bosch-Telecom GmbH, Backnang
5	Carl Zeiss GmbH, Oberkochen
6	Contraves Space, Zürich
7	CNES, Toulouse
8	DIFESA Officine Galileo
9	SIRA Electro-Optics, Kent
10	ONERA-CERT, Toulouse
11	ABB Semiconductors, Lenzburg
12	Kopenhavn University
13	NMRC, Kork
14	SCK/CEN, Mol
15	SOREQ NRC, Yavne
16	SODERN ,Paris

FURTHER FACILITY DEVELOPMENT

- The PIF will move from NA2 to PKC2 area during constructions of the new PROSCAN cyclotron.
- The low energy facility in OPTIS will move into the NE-B area allowing for easier experimentation.
- Development of the new irradiation facility linked to the biomedical cyclotron is in the initial phase.

SENSITIVITY OF RADFET DOSIMETERS TO PROTONS AND GAMMAS

W. Hajdas[1], J. Bialkowski[1], U. Wyser[1], L. Adams[2], A. Mohammadzadeh[3], R.Nickson[3], B. O'Connell[4]

PSI[1] - BRUNEL[2] - ESTEC[3] - NMRC[4]

The Standard Radiation Environment Monitor SREM, designed by PSI-ESA-Contraves Space, will fly on board the STRV-1c satellite. The SREM will measure radiation doses deposited at various spacecraft locations using RADFET dosimeters. Their sensitivity to protons and gamma rays is characterised for various energies, dose rates and exposure geometries.

The SREM will detect cosmic radiation with a set of Si SBDs and measure dose depositions in different spacecraft locations using external RADFET dosimeters. Their very small dimensions, weight and low power consumption as well as simple operation make them attractive for spacecraft dose monitoring. As the STRV-1c radiation environment consists of different particles (mostly electrons and protons), this work was intended to characterise RADFETs accordingly. Irradiation tests were performed at representative working conditions using gamma rays and protons of different energies, fluxes and exposure geometry.

RADFET specifications and readout

The RADFET (Radiation Field Effect Transistor) is a Metal-Oxide Semiconductor with a thick oxide layer between FET Gate and Si-bulk optimised for radiation sensitivity. Radiation induced holes trapped in the oxide affect the Gate-Source threshold voltage for switching the transistor on. PSI tested packaged RADFETs consisting of two P-MOS transistors with 4000 Å implanted gate oxide thickness. During the mission, the RADFET dosimeters are connected to the SREM read-out circuit for permanent monitoring of the threshold voltage signal (read mode operation) and temperature. The circuit used during irradiation in PSI for the device powering and read-out is equivalent to SREM readout circuit on STRV1-c.

Experimental Procedures

Irradiation tests were performed at PSI using the PIF OPTIS facilities and Gamma Irradiation Station. All RADFET exposures to radiation were carried out in air. Dose rates varied between 2 and 80 rad/sec and the minimum deposited dose was equal to 5 krad(Si). The dose was applied in steps between 0.2 and 1 krad, until the total dose was reached. Proton energies covered the range from 9 to 300 MeV. Gamma irradiation were done using ^{60}Co source. For consistency purposes two RADFETs were irradiated and measured simultaneously.

Results summary and conclusions

The RADFET response towards both proton and gamma radiation can be described with a power function between deposited dose D and threshold voltage shift ΔV_{th}:

Equation 1 $$\Delta V_{th} = a D^{\gamma}$$

a, γ - fit coefficients.

Proton response functions were found independent of particle exposure angle and flux but to have a slight energy dependence. This has to be verified in further experiments.

The response sensitivity threshold as a function of the proton energy was consistent with the stopping power (respectively thickness) of the RADFET housing. However, the devices revealed large response variability among themselves as shown in Figure 1.

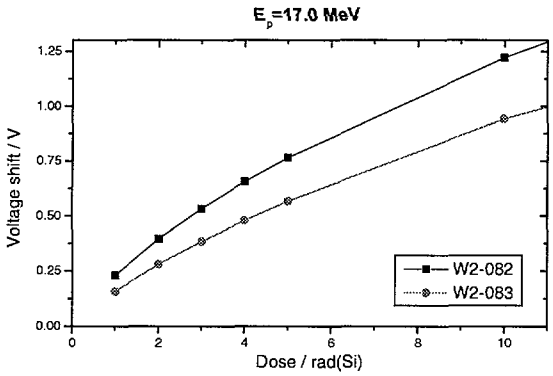

Figure 1 Response variations as a function of selected RADFET device for 17 MeV protons at 0°.

Studies of response difference between proton and gamma rays were done with the same device exposed to both types of radiation. As shown in Figure 2, response for protons and gammas (electrons) is slightly different. Further tests with heavy ions are foreseen in near future. With present results, one concludes that RADFETs must be pre-calibrated before using (see Equation 1). For operation with relatively low total doses of less than 2 krad, the distinction between proton and gamma response is small – below 5%. Other applications that require much better precision or higher total doses should be constrained to single type radiation fields.

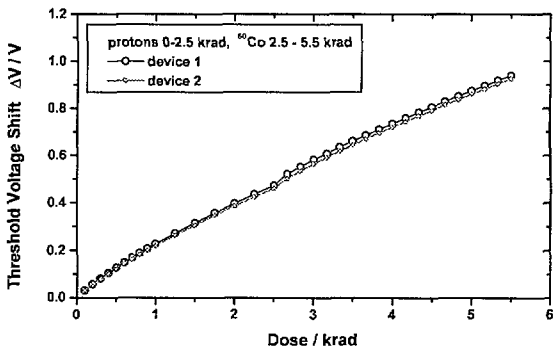

Figure 2 Threshold shift as a function of deposited dose for devices irradiated with protons and gamma rays.

NEXT PAGE(S) left BLANK

Laboratory for Muon Spin Spectroscopy

LABORATORY FOR MUON-SPIN SPECTROSCOPY

D. Herlach

Research at the Laboratory for Muon-Spin Spectroscopy (LMU) uses positive (and occasionally negative) muons (μ^+, μ^-) as local magnetic probes in matter. The experimental techniques used are referred to as "μSR" – *M*uon-*S*pin *R*otation, *R*elaxation, *R*esonance or *R*esearch. Unlike other local probes such as nuclear magnetic resonance (NMR), Mössbauer spectroscopy or $\gamma\gamma$ perturbed angular correlation (PAC), which require specific target nuclei, μSR is universally applicable since muons can be implanted in *any material.*

The muon is a versatile, very sensitive probe of both static and dynamic microscopic magnetic fields: due to its mean lifetime $\tau_\mu = 2.2\,\mu$s and gyromagnetic ratio $\gamma_\mu = 2\pi \cdot 135.5$ MHz/T, the accessible magnetic fields and widths of field distributions range from $\sim 10\,\mu$T to several Tesla, and the characteristic times from nano- to milliseconds. Moreover, due to parity violation in the pion decay, muons are emitted with perfect spin polarisation, providing μSR with a great advantage: whereas NMR and ESR rely upon a thermal equilibrium spin polarisation, μSR begins with a perfectly polarised probe regardless of the conditions of the sample. As "light isotopes" of the proton ($m_\mu = 0.11 m_p$) positive muons can also form a hydrogen-like quasi atom (Muonium, $\mu^+ e^-$) which substitutes for hydrogen in insulators and organic materials, providing a very sensitive spin label. All this would be of little use did not the muon decay into an energetic positron (or electron) which, again due to parity non-conservation, is emitted preferentially in the direction of the muon spin, thus carrying information on the μ-spin polarisation out of the investigated material.

At LMU, solid-state physicists, chemists and materials scientists from PSI and abroad use muons to investigate fundamental and technologically relevant aspects of structural, magnetic and electronic phenomena in magnets, superconductors, semiconductors and insulators. Samples range from pure elements to inorganic and organic compounds and molecular systems. LMU maintains and actively develops a μSR User Facility, presently consisting of five different spectrometers covering a wide range of techniques and applications. In 1999, the Facility was used for 74 research proposals, involving over 250 scientists from 15 countries.

Two unique extensions to μSR have been developed at PSI. First, *Low Energy muons,* which can be implanted at very small and controllable depths below the surface of a sample (a few to a few hundred nm), allow all the advantages of μSR to be applied to thin samples and multilayered structures, near surfaces and as a function of implantation depth. Striking demonstrations of the power of the LE-μSR technique are the first direct measurement of the functional form of the penetration depth of a magnetic field beneath the surface of a superconductor in the Meissner state and the measurement of the evolution of the flux line lattice as it emerges through the surface. The wealth of new applications becoming possible with LE-μSR has been highlighted in the first workshop on "Applications of low energy muons to solid state phenomena", organized by our laboratory at PSI in February 1999. Over 80 scientists from 15 countries attended.

The second important development is a fast-switching electrostatic deflector, able to extract single muons from a continuous beam upon request (*"MORE"*) from a spectrometer. Routinely available since 1998, this provides unique frequency resolution and increases measurable relaxation times to milliseconds at the full time resolution (1ns) of our spectrometers.

MUON SPIN RELAXATION AND DISORDER-DRIVEN NON-FERMI LIQUID BEHAVIOR IN $UCu_{5-x}Pd_x$

D. E. MacLaughlin,[1] *R. H. Heffner,*[2] *J. E. Sonier,*[2] *G. J. Nieuwenhuys,*[3] *B. Andraka,*[4] *R. Chau,*[5] *M. B. Maple*[5]

RA-90-05, RIVERSIDE[1] – LOS ALAMOS[2] – LEIDEN[3] – GAINESVILLE[4] – SAN DIEGO[5]

Theories of non-Fermi liquid (NFL) behavior in heavy-fermion alloys based on disorder-driven mechanisms have failed to agree on whether the disorder affects single f-ion properties (e.g., the "Kondo disorder" model [1]), or results in a form of inhomogeneous phase transition due to f-moment clustering and Griffiths-phase behavior [2]. It has been speculated [3] that muon or nuclear spin relaxation measurements at low temperatures could decide between these possibilities. In the Kondo disorder picture the fluctuation rates of most f moments are near the relatively high average Kondo energy scale and hence give rise to weak muon or nuclear relaxation, whereas clusters in the Griffiths-phase scenario might fluctuate at much slower rates and thus relax muons or nuclei more rapidly.

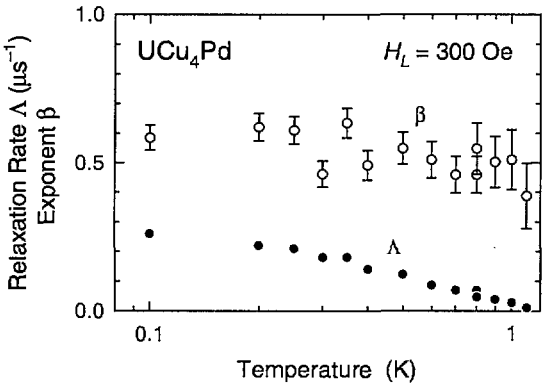

Figure 1: Temperature dependence of relaxation rate Λ and power β in UCu_4Pd, longitudinal field $H_L = 300$ Oe.

Our μ^+ relaxation measurements in the LTF on the NFL alloys $UCu_{5-x}Pd_x$, $x = 1.0$ and 1.5, bear out the above speculation. The data exhibit the sub-exponential decay characteristic of an inhomogeneous distribution of relaxation rates, and in a preliminary analysis have been fit to the power-exponential relaxation function $G(t) = \exp[-(\Lambda t)^\beta]$. The relaxation rate $\Lambda(H,T)$ at low temperatures T and applied magnetic fields H is found to be two orders of magnitude too rapid to be described by the simple Kondo disorder model, and seem to rule out this picture for these alloys. The temperature and field dependence of Λ and β, shown for UCu_4Pd in Figs. 1 and 2, respectively, suggest soft fluctuations and weak divergences associated with a critical point at $T = H = 0$. There is no sign of spin-glass or other magnetic ordering in the 0.1–0.2 K temperature range, contrary to other experimental results [4]. For fields of a few hundred Oe $\Lambda(T)$ varies approximately as $\ln T$ above ~0.2 K but appears to saturate below this temperature. The dependence of Λ on

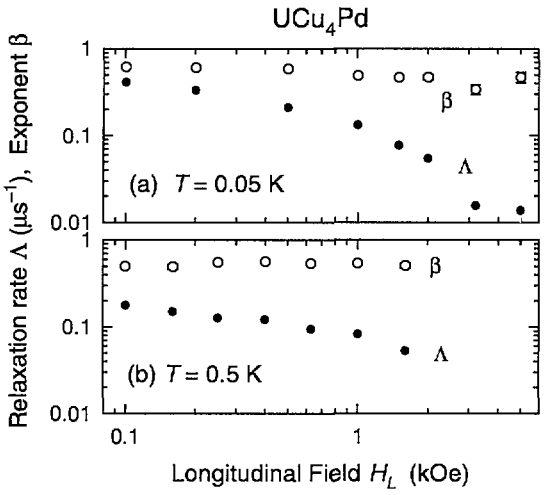

Figure 2: Dependence of relaxation rate Λ and power β on longitudinal field H_L in UCu_4Pd. (a) Temperature $T = 0.05$ K. (b) $T = 0.5$ K.

low longitudinal field H_L (Fig. 2) is reminiscent of the weak power-law divergence of the dynamic susceptibility $\chi''(\omega)$ in the Griffiths-phase model of Castro Neto and co-workers [2], if the field dependence is taken to reflect variation of the muon Larmor frequency at which $\chi''(\omega)$ is evaluated. It can also be seen from Fig. 2(a) that the relaxation at 0.05 K is strongly suppressed by fields greater than ~1 kOe.

The Griffiths-phase model in its simplest form predicts no temperature dependence of $\Lambda(H,T)$ [2], contrary to our results. We conclude that the data suggest a cooperative NFL mechanism in $UCu_{5-x}Pd_x$, but that current theory does not give a full description of the spin-fluctuation behavior at low temperatures.

REFERENCES

[1] O. O. Bernal, D. E. MacLaughlin, H. G. Lukefahr, and B. Andraka, Phys. Rev. Lett. **75**, 2023(1995).

[2] A. H. Castro Neto, G. Castilla and B. A. Jones, Phys. Rev. Lett. **81**, 3531(1998).

[3] C.-Y. Liu *et al.*, Phys. Rev. **B 61**, 432(2000).

[4] R. Volmer *et al.*, Physica **B 230-232**, 603(1997); E. W. Scheidt *et al.*, Phys. Rev. **B 58**, R10104(1998).

μSR STUDY OF THE MAGNETIC INSTABILITY IN HEAVY-FERMION U(Pt, Pd)$_3$

A. de Visser[1], M.J. Graf[2], P. Estrela[1], A. Amato[3], C. Baines[3], F.N. Gygax[4], D. Andreica[4], A. Schenck[4]

RA-95-18, AMSTERDAM[1] – BOSTON[2] – PSI[3] – ETH ZÜRICH[4]

The pseudobinaries U(Pt$_{1-x}$Pd$_x$)$_3$ present an exemplary system to study incipient magnetism and its interplay with unconventional superconductivity in heavy-electron materials. Pure UPt$_3$ is a small-moment antiferromagnet (SMAF). Neutron-diffraction experiments [1] have shown that SMAF state is robust to alloying with Pd. The ordered moment grows, while the Néel temperature T_N remains $\sim$ 6 K. The size of the ordered moment correlates to the splitting of the superconducting phase transition as measured in specific heat experiments [2]. This provides further evidence for the Ginzburg-Landau scenario with SMAF acting as symmetry breaking field, which causes the splitting of the superconducting transition. A second antiferromagnetic state appears upon doping with Pd in the concentration range 0.5-1 at.and is stable up to $\sim$ 10 at.%Pd. This large-moment antiferromagnetic phase (LMAF) is of the spin-density wave type and has been observed by a number of techniques, among which neutron-diffraction [1] and zero-field μSR [3]. For 5 at.% Pd (optimal doping) T$_N$= 6 K and the ordered moment $m = 0.6\ \mu_B$/U-atom.

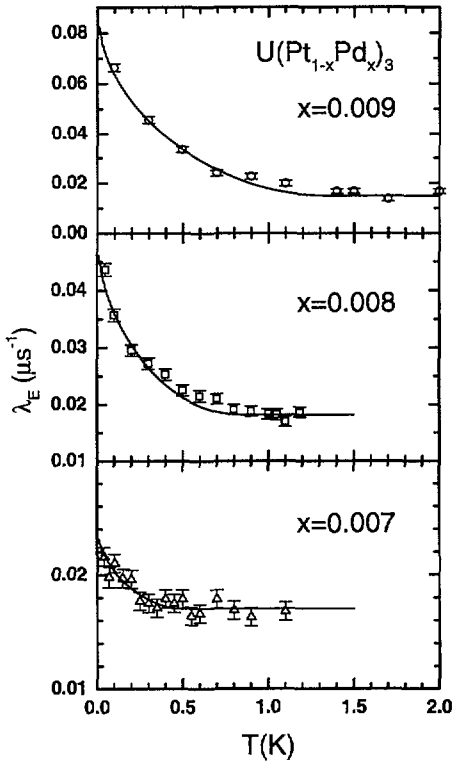

Figure 1: Exponential damping rate (TF 100 G) as function of temperature for polycrystalline U(Pt$_{1-x}$Pd$_x$)$_3$. The solid lines are to guide the eye.

The aim of the present μSR experiments is to determine in detail the critical Pd concentration $x_{afm,c}$ for the emergence of LMAF. To that purpose polycrystalline U(Pt$_{1-x}$Pd$_x$)$_3$ samples were prepared with $x = 0.007, 0.008$ and 0.009. Transverse field (TF= 100 G) experiments were carried out using the LTF (low-temperature facility). In order to reduce the background contribution the data for samples with $x = 0.007$ and 0.008 have been taken using MORE. The TF muon depolarization curves are best fitted using an exponential damping factor. Fig. 1 shows the temperature dependence of the exponential relaxation rate λ_E. Below a certain threshold temperature λ_E starts to rise above its background value. We identify this threshold temperature with T_N for the LMAF phase. Plotting the resulting values of $T_N = 0.45 \pm 0.10$ K, 0.85 ± 0.10 K and 1.4 ± 0.10 K for $x = 0.007$, 0.008 and 0.009, respectively, in the magnetic and superconducting phase diagram we find $x_{afm,c} \sim 0.006$ (see Fig. 2).

Interestingly, Fig. 2 shows that $x_{afm,c} = x_{s,c}$, where $x_{s,c}$ is the critical concentration for the suppression of superconductivity. We conclude that stabilization of LMAF order suppresses superconductivity. This provides further evidence for spin-fluctuation mediated superconductivity. The discovery of a double (i.e. magnetic and superconducting) quantum critical point in the U(Pt$_{1-x}$Pd$_x$)$_3$ phase diagram undoubtedly presents a challenge for future theoretical and experimental work.

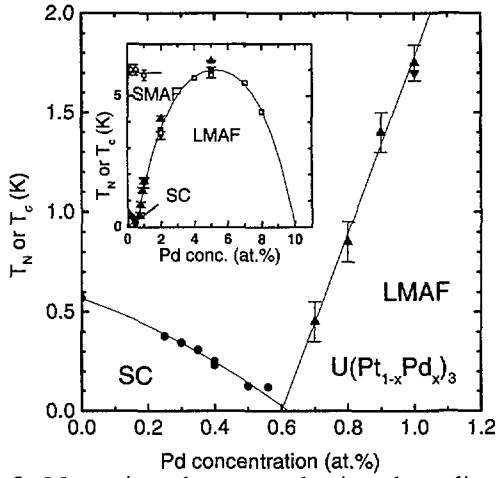

Figure 2: Magnetic and superconducting phase diagram for U(Pt$_{1-x}$Pd$_x$)$_3$ compounds [1, 2, 3]. SC denotes superconductivity. SMAF and LMAF denote small and large moment antiferromagnetic order. Data for x = 0.007-0.009 are from the present work.

REFERENCES

[1] R.J. Keizer et al., Phys. Rev **B 60**, 6668(1999).

[2] R.J. Keizer et al., Phys. Rev. **B 60**,10527(1999).

[3] R.J. Keizer et al.,
J. Phys: Condens. Matter **11**, 8591(1999).

MICROSCOPIC STUDIES OF THE NONMAGNETIC-MAGNETIC TRANSITION IN HIGHLY CORRELATED ELECTRON SYSTEMS

D. Andreica[1], A. Schenck[1], F.N. Gygax[1], M. Pinkpank[1], A. Amato [2], J. Sierro[3], D. Jaccard[3], G. Wiesinger[4], C. Reichl[4], E. Bauer[4], Ch. Geibel[5], G.J. Nieuwenhuys[6]

RA-98-07, ETH ZÜRICH[1] – PSI[2] – GENEVA[3] – VIENNA[4] – DRESDEN[5] – LEIDEN[6]

We have used chemical and external pressure to investigate the phase diagram of the following rare-earth systems: $Yb(Cu_{1-x}Ni_x)_2Si_2$, $Yb(Cu_{5-x}Al_x)$ and $CeRh_2Si_2$. Since the most exciting results were obtained for the $CeRh_2Si_2$ samples (first low temperature and high pressure μSR experiments), only a brief presentation of the results on the two other compounds will be given here.

$\mathbf{Yb(Cu_{1-x}Ni_x)_2Si_2}$ is nonmagnetic for x=0 and magnetic ([1] and ref. therein) for $x > 0$. The spin dynamics of the Yb ions were investigated using the μSR technique in longitudinal field (LF) configuration. A decrease of the relaxation rates with the increase of the magnetic field, followed by a plateau at high fields was observed in all samples with $x > 0$. This behaviour can be ascribed either to: a) a magnetic field induced suppression of the Yb spin-spin correlations, the plateau reflecting the fast uncorrelated fluctuations of the Yb spins or to: b) a two channel dynamic relaxation mechanism, one with slow and the other with fast dynamics. The slow dynamics could arise from induced fluctuations of the Cu nuclear magnetic moments by the (fast) fluctuating Yb electronic moments. No change of the relaxation rates under pressures up to 7 kbar were observed for the $YbNi_2Si_2$ sample. This result was indeed expected in view of the 80 kbar needed to induce a magnetic signature for $YbCu_2Si_2$ (ref. 4 in [1]).

$\mathbf{Yb(Cu_{5-x}Al_x)}$ is nonmagnetic for x=0..1.5 and magnetic for $x > 1.5$ [2]. A Kubo-Gauss function fits the μSR spectra at temperatures $T > 60$ K for all the investigated samples (x=1, 1.5, 2). In this temperature range, the field distribution at the muon site is Gaussian and static, given by the random distribution of the Cu and Al nuclear magnetic moments. Below 60 K the muon depolarization function is a damped Kubo-Gaussian, the exponential (λ) part reflecting the dynamics of the Yb magnetic moments. The relaxation rate λ is observed to increase with the Al concentration x. A slight increase of the relaxation rate λ was observed under pressures 0 kbar< p <7 kbar fo the x=1.5 compound but no sign of magnetic ordering was detected.

$\mathbf{CeRh_2Si_2}$ has two antiferromagnetic transitions at low temperatures and p=0 ([3] and ref. therein) which are suppressed by an external pressure of about 10 kbar. Below T_{N1} the magnetic structure is described by a **q**=(1/2,1/2,0) propagation vector. The muons are depolarised by a static Lorentzian field distribution with zero average. Figure 1 exhibits the Brillouin-like behaviour of the temperature dependence of the relaxation rate λ for $T_{N2} < T < T_{N1}$ suggesting a scaling between the relaxation rate and the static Ce magnetic moment.The Lorentzian field distribution could originate from slight disorder at a μ site where the internal fields cancel. Below T_{N2} the magnetic structure changes, and additional reflections (1/2,1/2,1/2) appear in the neutron diffraction spectra. A wiggling component is seen in the μSR spectra indicating a μ^+ site with a field distribution around a non-zero value. Some puzzling results appeard under pressures up to 7 kbar. The most striking result is that the muon frequency ν does not change under pressure and shows a very weak temperature dependence. This suggests that the low temperature magnetic transition is first order.

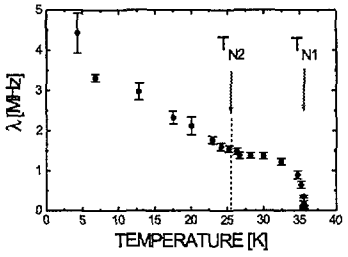

Figure 1: Temperature dependence of the depolarization rate of the non-wiggling component in $CeRh_2Si_2$.

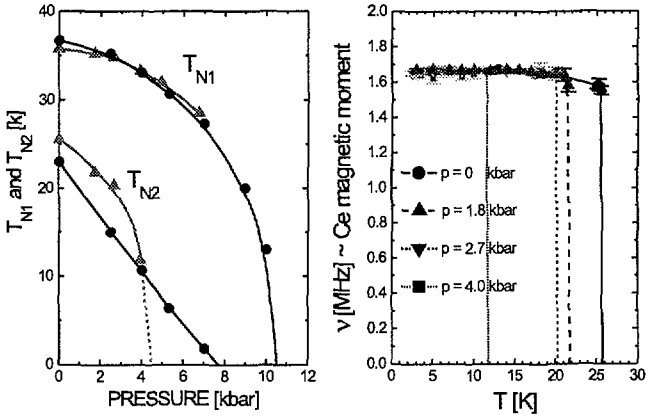

Figure 2: Left: Pressure dependence of T_{N1} and T_{N2} as determined by μSR (triangles) and resistivity (circles) [4]. Note the discrepancy for T_{N2}. Right: Temperature dependence of the spontaneous muon frequency for different pressures.

REFERENCES

[1] D. Andreica et al., to be published in Physica **B**.

[2] E. Bauer et al., Phys. Rev. **B 52**, 4327 (1995).

[3] Y. Yamamoto et al., to be published in Physica **B**.

[4] F.M. Grosche et al., Physica **B 237-238**, 197 (1997).

HEAVY-FERMION BEHAVIOUR AND STRIPE ORDER IN ELECTRON DOPED CUPRATES

D. Baabe[1], H. H. Klauß[1], W. Kopmann[1], D. Mienert[1], M. Birke[1], F. J. Litterst[1], P. Adelmann[2]

RA-94-12, BRAUNSCHWEIG[1] – KARLSRUHE[2]

$Nd_{2-y}Ce_yCuO_4$ (NCCO) is the prototype of electron doped superconducting cuprates. In these compounds Ce doping influences the Cu-3d magnetism by introducing charge carriers with mainly Cu-3d character and also changes the Nd-4f spin system by diluting it. The origin of heavy fermion behaviour – e.g. indicated by macroscopic measurements of the specific heat and the magnetic susceptibility [1] – is still under discussion. In this work we want to differentiate between the proposed theoretical models e.g. [2] from the viewpoint of μ^+SR. Another topic we want to report is the examination of supposed charge and stripe order in $(Eu, Pr, Nd)_{2-y}Ce_yCuO_4$ with y = 1/8. At this charge carrier concentration charge and spin stripes have been observed by Tranquada et al. [3] in hole doped $La_{1.6-y}Nd_{0.4}Sr_yCuO_4$.

Single Ion Model vs. Cooperative Models

In 1999, we performed zero field (ZF) and longitudinal field (LF) μ^+SR experiments on polycrystalline samples NCCO with y = 0.165 and on compounds with diluted Nd-Nd bonds (e.g. due to substitution of Nd by nonmagnetic RE = Pr, Eu) like $(RE_{1-x}Nd_x)_{2-y}Ce_yCuO_4$ with x = 0.1 and y = 0.16. The temperature dependend *normalized transversal relaxation rate* $\Lambda_T(T) = \lambda_T(T)/\lambda_T(100\text{ mK})$ – obtained by χ^2 minimization to $A(t) = A_L \exp(-\lambda_L t) + A_T \exp(-\lambda_T t)$ – of NCCO and the diluted compounds exhibit nearly the same behaviour (Fig.1, top). Hence, we support the *individual Nd-Cu coupling scenario* proposed by e.g. Fulde et al.

Spin Dynamics in $Nd_{2-y}Ce_yCuO_4$ (NCCO)

We performed ZF and LF μ^+SR experiments on polycrystalline samples NCCO with y = 0.165 and 0.18. For both compounds we found an increasing transversal relaxation rate λ_T below 10 K and a saturation value at 100 mK $\lambda_T(100\text{ mK}) = (8 \pm 2)$ MHz and (12 ± 2) MHz, respectively. At 100 mK these compounds show a strong field fluctuation rate ν of about 420 MHz calculated by means of Redfield analysis. For $Nd_{1.85}Ce_{0.15}CuO_4$ (single crystal) we observed in 1998 an increasing λ_T with decreasing temperature as well, however a calculated ν in the MHz range and a $\lambda_T(100\text{ mK}) = (4 \pm 1)$ MHz. Roughly speaking, a small increase of the charge carrier concentration from y = 0.15 to 0.165 changes the spin dynamics (ν) drastically. This mirrors the insulator-metall transition with no magnetic long range order. For y = 0.15 there are short range correlations resulting in a moderately fluctuating Cu spin system. μ^+SR investigations on $Nd_{1.80}Ce_{0.20}CuO_4$ have shown an increasing relaxation rate below 3 K and $\lambda_T(100\text{ mK}) = 1$ MHz. The reduction of the saturation value $\lambda_T(100\text{ mK})$ between y = 0.18 and 0.20 is associated with the disappearence of superconductivity at this Ce doping level.

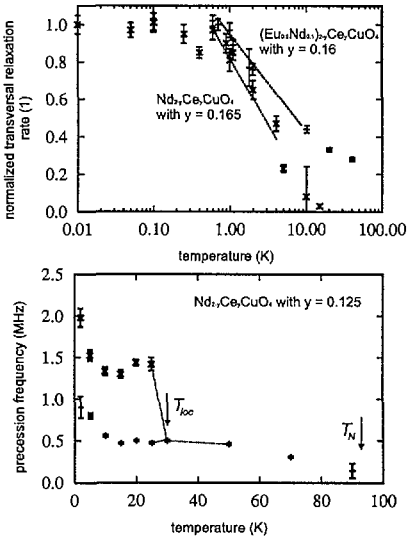

Figure 1: **Top:** Temperature dependend normalized transversal relaxation rate Λ_T for NCCO with y = 0.165 and $(Eu_{0.9}Nd_{0.1})_{1.84}Ce_{0.16}CuO_4$. **Bottom:** Temperature dependend muon presession frequency ν_μ for e.g. $Nd_{1.875}Ce_{0.125}CuO_4$. – The dotted lines are a guide to the eye only.

Charge Carrier Localization and Spin Stripes

We performed ZF and LF μ^+SR experiments on polycrystalline specimens of $(Eu, Pr, Nd)_{2-y}Ce_yCuO_4$ with y = 1/8. These compounds show long range antiferromagnetic order below $T_N \approx 90$ K, which leads to one finite muon precession frequency ν_μ (Fig.1, bottom). Below ≈ 30 K (denoted with T_{loc}), a second frequency – obtained by χ^2 minimization to $A(t) = A_L \exp(-\lambda_L t) + A_{T1} \cos(\omega_1 t) \exp(-\lambda_{T1} t) + A_{T2} \cos(\omega_2 t) \exp(-\lambda_{T2} t)$ – with nearly 1/2 of the total signal amplitude appears in the ZF spectra. Akimitsu et al. [4] observed **single frequency** μ^+SR time-spectra and explain a sharp frequency change at ≈ 50 K in $Pr_{2-y}Ce_yCuO_4$ by *Cu spin reorientations*. Contrarily, we associate the observed **two frequency spectra** with the *localization of electrons* in the μSR time window. These results may indicate the supposed appearance of stripe order in these componds with y = 1/8.

REFERENCES

[1] T. Brugger et al., Phys. Rev. Lett. **71**, 248(1993).

[2] P. Thalmeier et al., Physica **C 266**, 89(1996).
S. Tornow et al., Ann. Physik **5**, 501(1996).
J. Igarashi et al., Phys. Rev. **B 52**, 15966(1995).

[3] J.M. Tranquada et al., Phys. Rev. Lett. **78**, 338(1997).

[4] J. Akimitsu et al., Hyp. Int. **85**, 187(1994).

STUDY OF THE MAGNETIC PROPERTIES OF $Ce_3Pd_{20}Si_6$ AND $Ce_3Pd_{20}Ge_6$ COMPOUNDS

A. Amato[1], Ch. Baines[1], V. N. Duginov[2], A. V. Gribanov[3], K. I. Gritsaj[1], D. Herlach[1], A. A. Nezhivoy[4] V. N. Nikiforov[3], V. Yu. Pomjakushin[2], A. N. Ponomarev[4], Yu. D. Seropegin[3], U. Zimmermann[1]

RA-97-04, PSI[1] – DUBNA[2] – MOSCOW[3] – KURCHATOV INSTITUTE[4]

The systems $Ce_3Pd_{20}X_6$ (X = Ge, Si) manifest unusual physical properties which categorize them as a Kondo magnetic. The competition between magnetic and Kondo interactions was traditionally considered to result in either the magnetic ground state with significant full suppression of Kondo features, or in a nonmagnetic Kondo ground state. However, in last decade it has been found that there are many f-electron compounds in which magnetic ordering coexists with Kondo behaviour. The $Ce_3Pd_{20}X_6$ (X = Ge, Si) systems belong to them.

Last year we concentrated our efforts on the experiments with $Ce_3Pd_{20}Si_6$. It is known, there are two relatively separated cerium subsystems in this compound[1]. One of the subsystems involves Ce^{3+} ions in Ce2 positions which form 'small' cubes inside of the unit cell. Ions of each cube make up magnetic 'molecules' with a magnetic moment that increases with decreasing temperature and undergo antiferromagnetic-like ordering at T_{magn}.

The second cerium subsystem consists of Ce1 ions. These ions are less magnetically active because they have Si(Ge) as nearest neighbors. The Ce1 atoms may mostly play role of Kondo scattering centers for the conduction electrons. In $Ce_3Pd_{20}Si_6$ near $T_{magn} \approx 65$ K the Ce1 ions become free of strong magnetic interactions with the 'magnetic molecules' which are competitive with Kondo ones and would be responsible for the Kondo scattering of the conducting electrons in $Ce_3Pd_{20}Si_6$.

It is interesting, that a similar situation occurs in HTSC, in which the AF ordering of the rare earth sublattice coexists with the superconductivity in copper-oxygen planes.

The polycrystalline samples of $Ce_3Pd_{20}Si_6$ were prepared by using a melting technique in an arc furnace in argon atmosphere. The samples were annealed under argon atmosphere (about 24 days).

Zero-field μSR measurements were undertaken to gain information about the magnetic ordering at low temperatures. The experiments were performed on the surface-μ^+ beamline πM3 using the LTF-setup. The depolarization function was represented by a Gaussian function. We observe a partial recover of the polarization in longitudinal-field measurements, with fields up to 25 kOe. This proves the dynamic nature of part of the muon spin depolarization. More detailed experiments are planed at low longitudinal magnetic field. Below 0.4 K the increase of the depolarization rate represents the development of quasi-static ordering of magnetic moments of electronic origin most probably randomly oriented[2].

We performed transverse-field μSR measurements on the muon decay channel μE1 with the GPD-setup. The precession time spectra $A(t)$ are described by the sum of two signals , where the background signal $A_b(t)$ corresponds to the muon stopping in the sample holder and cryostat walls. The value of the external magnetic field during these measurements was controlled by the muon spin precession frequency of the background signal. The measurements were performed in external fields from 1 to 5 kOe. A clear frequency shift was seen at temperature below 60 K. The temperature dependence of the magnetic field seen by the muons (at 3 kOe) is shown in Fig. 1. The dashed line on this corresponds to the external magnetic field $B = \omega_b/\gamma_\mu$. For other field values a similar behaviour was observed. These measurements were performed in two runs with two samples and in two cryostats(CCR and Janis). The reproducible results were obtained.

Test measurements with the nonmagnetic related compound $La_3Pd_{20}Si_6$ were performed also. The absence of muon-spin frequency shift in this sample stresses the Ce contribution in the origin of the frequency shift.

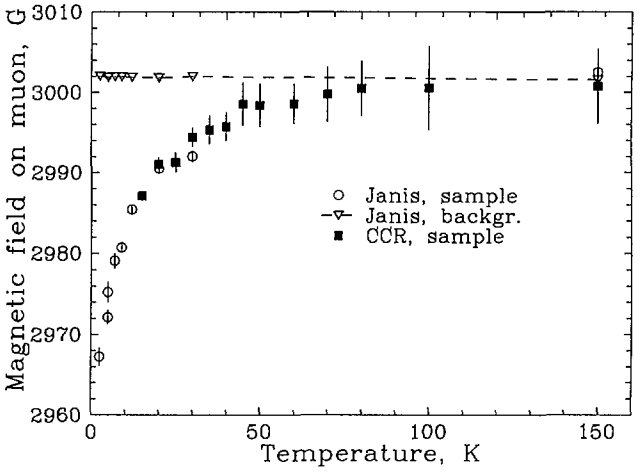

Figure 1: Temperature dependence of the internal magnetic field acting on the muon in $Ce_3Pd_{20}Si_6$

The μ Knight-shift on Pd is too small to explain our results. Further experiments at low magnetic fields are required for the direct evidence of the superparamagnetic cubes. It seems that all magnetic anomalies can be observed only at sufficiently low magnetic field.

REFERENCES

[1] V.N. Nikiforov *et al.*, J. Magn. Magn. Mat. **163**, 184(1996).

[2] V.N. Duginov *et al.*, submitted to Physica **B**.

μSR STUDY OF THE SPIN DYNAMICS IN AXIAL MAGNETS

C. T. Kaiser[1], *P. C. M. Gubbens*[1], *P. Dalmas de Réotier*[2], *A. Yaouanc*[2], *A. A. Menovsky*[3]

RA-95-14, TU DELFT[1] – CEA GRENOBLE[2] – AMSTERDAM[3]

Using the zero-field muon spin relaxation technique we have previously studied at ISIS and PSI the spin dynamics of the uniaxial ferromagnet $PrCo_2Si_2$. This compound crystallizes in a tetragonal structure. In order to reach a quantitative understanding of our data we need to know the muon site and the hyperfine coupling constant. To get these informations, in 1999 we have performed Knight shift measurements on a single crystal of spherical shape.

In Fig. 1 we present the angular dependence of the muon frequencies measured in a field of 0.6 T. The sample was rotated around its c axis. Our previous data are consistent with two possible muon sites: the center of the square of the basal plane and the site between the Pr atoms located at the corner of the square. The symmetry of the results of the angular scan shows clearly that the muon occupies the site between the Pr atoms.

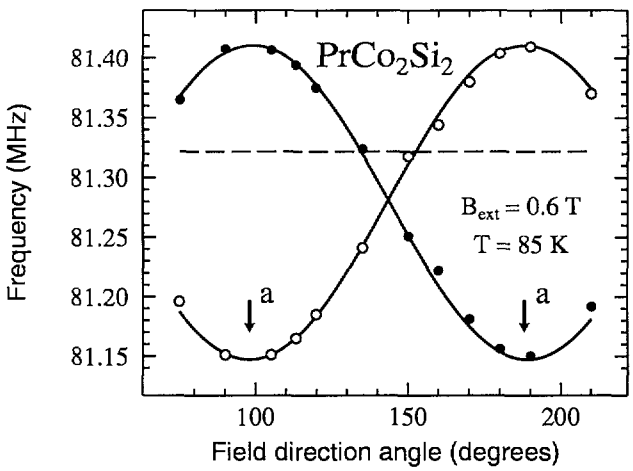

Figure 1: Angular dependence of the muon frequencies measured on a crystal of $PrCo_2Si_2$ at 85 K in a field of 0.6 T. The sample was rotated around its c axis. The solid line is a fit to a Legendre polynomial of order 2. The dashed line indicates the frequency corresponding to the applied magnetic field.

As shown by many examples presented by the ETH muon research group, an efficient way to detect the possible influence of the muon charge on the studied compound is to compare the muon Knight shift K_μ with the bulk susceptibility χ_B. In Fig. 2 this is done for the field applied along the c and a axes in the form of Clogston-Jaccarino plots. The observed linear relation between K_μ and χ_B for $\mathbf{B}_{\rm ext} \parallel c$ suggests that the possible influence of the muon charge on the uniaxial magnetic properties of $PrCo_2Si_2$ is negligible. On the other hand, the plot for $\mathbf{B}_{\rm ext} \parallel a$ clearly indicates that the muon electric charge modifies the crystal field energy level scheme. A detailed investigation is under way.

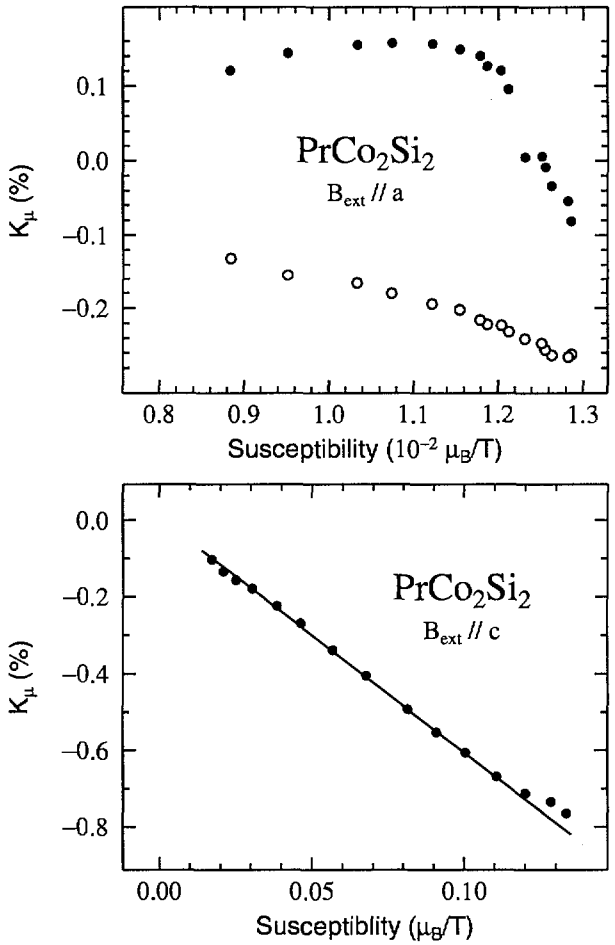

Figure 2: So called Clogston-Jaccarino plot for $PrCo_2Si_2$ measured for a field applied either along the a or c axis. The field intensity is 0.6 T.

STUDY OF THE DYNAMIC MAGNETIC PROPERTIES IN RNi_5

C. T. Kaiser[1], *P. C. M. Gubbens*[1], *A. M. Mulders*[1], *A. Amato*[2], *F. N. Gygax*[2], *A. Schenck*[2], *P. Dalmas de Réotier*[3], *A. Yaouanc*[3], *F. Kayzel*[4], *A. A. Menovsky*[4]

RA-90-03, TU DELFT[1] – PSI[2] – CEA GRENOBLE[3] – AMSTERDAM[4]

This year we have continued our muon Knight shift study on RNi_5 compounds. Previous Knight shift measurements, both angular and temperature dependent, have shown a change of preferential muon site in $GdNi_5$ starting below T $\sim$ 80 K [1]. Here the muon hops from a $6m$ to the preferred $3f$ site. This hopping process effectively increases the relaxation rate λ over this temperature range [2].

$DyNi_5$ crystallizes in the hexagonal $CaCu_5$ structure and has an easy plane anisotropy below T_C = 12.2 K. Prior zero field measurements on $DyNi_5$ showed a broad maximum for λ around $\sim$ 85 K. Since no other transitions around 85 K are known from literature, we have performed Knight shift measurements to see, whether this increase of λ is due to a change in muon site.

The measurements were done on a spherical single crystal with GPS in "fly past" mode. Fig. 1 presents the Knight shift of the muon frequencies as function of temperature with the applied field parallel to the a-axis. Below T = 80 K the data are fitted with a single exponential contribution, whereas above 80 K a fit with two exponential and an asymmetry ratio of 1:2 was needed. This latter analysis suggests the muon is located at a $3f$-site for high temperature.

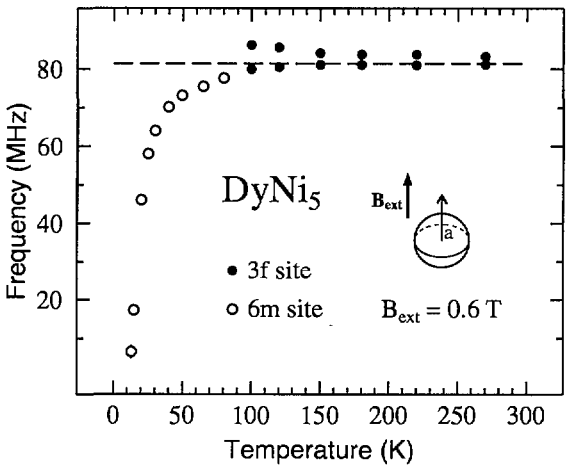

Figure 1: Temperature dependence of the muon frequencies measured in a field of 0.6 T applied along the a-axis of a spherical crystal of $DyNi_5$. The dashed line indicates the frequency corresponding to the applied magnetic field

In Fig. 2 we present the angular dependence of the muon frequencies in the $a\bar{a}$-plane at 120 K. The data have been fitted with three exponential contributions with equal asymmetry. The solid lines are Legendre polynomials shifted by 60 degrees, which corresponds to the symmetry at the $3f$ site. The fact that the data points around 80 MHz appear to be more scattered is probably due to the large damping rate of $\sim$ 10 MHz and an overlap with a background contribution corresponding to the applied field. A similar angular scan in the $a\bar{a}$ plane at 25 K was analysed with a single exponential contribution and shows no angular dependence. This latter result might indicate that just like in $GdNi_5$ the $6m$ is populated at lower temperatures. A contribution of the $3f$ site below 80 K is not observed. A reduction of the asymmetry by about a third with decreasing temperature suggests that this site is still populated but detection is hindered by a continuing increase of the damping rate. A detailed analysis including the site hopping process, as performed for $GdNi_5$ [2], is in progress.

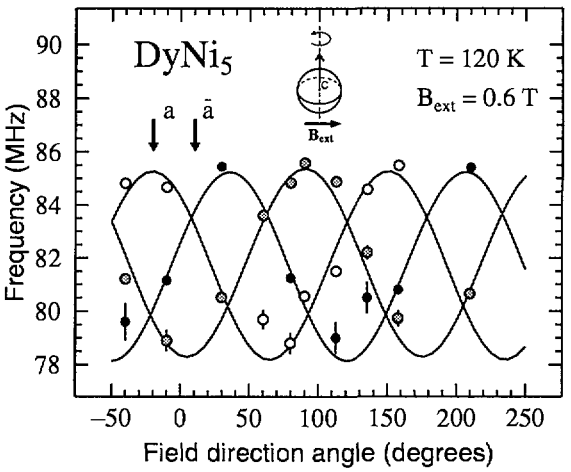

Figure 2: Angular dependence of the muon frequencies measured on a crystal of $DyNi_5$. The sample is rotated around its c-axis. The solid lines are fits to 60 degrees shifted Legendre polynomials of order 2.

REFERENCES

[1] A.M. Mulders *et al.*, PSI Ann. Rep. **1997.**

[2] A.M. Mulders *et al.*, Physica **B**, in press.

SPIN BEHAVIOUR IN NOVEL TRANSITION MAGNETS

R. H. Heffner,[1] *J. E. Sonier,*[1] *J. S. Sarrao,*[1] *D. E. MacLaughlin,*[2] *G. J. Nieuwenhuys*[3]

RA-98-04, LOS ALAMOS[1] – RIVERSIDE[2] – LEIDEN[3]

$La_2Cu_{1-z}Li_zO_4$ and related systems [1] are based upon the parent material La_2CuO_4 (214) which gives rise to high temperature superconductivity, and thus comprise a very interesting class of spin-charge-lattice coupled compounds. When 214 is doped with Sr, antiferromagnetism (AFM) is destroyed at about 3% Sr content; beyond 3% a so-called 'spin-glass' phase exists, which coexists with superconductivity between about $6 - 10\%$ Sr doping [2]. Both Li doping on the Cu site (Li^{1+} replaces Cu^{2+}) and Sr doping on the La site destroy long-range AFM order at about the same rate; e.g., $T_N \rightarrow 0$ at about 3% Li doping [3, 4]. Beyond 3%, Li doping also leads to short-range, quasi-static magnetic order, as found previously by us in polycrystals with $z < 0.10$ [3].

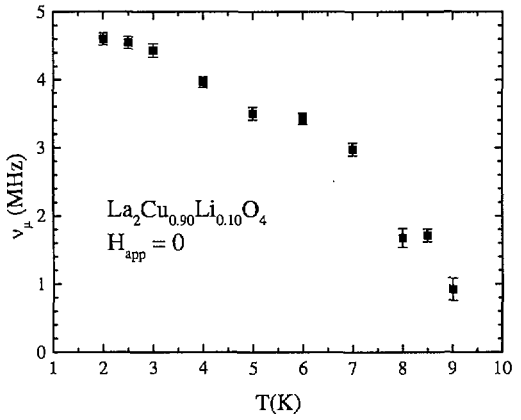

Figure 1: Temperature dependence of muon precession frequency ν_μ below the freezing temperature ≈ 9.5 K.

There are significant differences in the Li- and Sr-doped 214 materials, however. Although Sr doping leads to superconductivity, Li-doped 214 remains an insulator out to at least $z = 0.50$ [1]. Thus, the similar depression of T_N is remar

Last April we conducted μSR measurements on the same $z = 0.10$ crystal as used in the inelastic neutron scattering measurements [5] mentioned above. We find clear evidence for some sort of magnetic ordering below 9.5 in this material, as shown by the temperature dependence of the muon precession frequency ν_μ (Fig. 1) and spin lattice relaxation rate $1/T_1$ (Fig. 2). For temperatures between the freezing temperature ≈ 9.5 K and about 14 K a two-exponential relaxation function is observed; above 14 K only a single exponential is found. The nature of this phase is so far undetermined, but it looks somewhat similar to the 'spin-glass' phase found for Sr doping between $0.03 < x < 0.10$.

We will conduct a systematic investigation of the magnetic and superconducting phases in single crystals of $La_{2-x}Sr_xCu_{1-z}Li_zO_4$ to compare these phases with similar

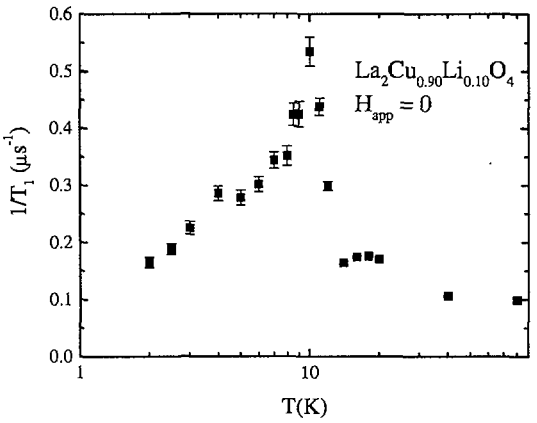

Figure 2: Temperature dependence of the zero-field spin lattice relaxation rate, showing critical slowing down near the freezing temperature ≈ 9.5 K.

similar studies of the Sr-doped 214 materials.

REFERENCES

[1] J. L. Sarrao *et al.*, Phys. Rev. **B 54**, 12014 (1996).

[2] Ch. Niedermayer *et al.*, Phys. Rev. Lett. **80**, 3834(1998).

[3] L. P. Le *et al.*, Phys. Rev. **B 54**, 9538(1996).

[4] B. J. Suh *et al.*, Phys. Rev. Lett. **81**, 2791(1998).

[5] W. Bao *et al.*, submitted to Phys. Rev. Lett. (1999).

STUDY OF U- AND RE-INTERMETALLIC COMPOUNDS EXHIBITING QUADRUPOLAR ORDERING: CeAg

A. Schenck[1], *D. Andreica*[1], *F.N. Gygax*[1], *M. Pinkpank*[1], *Y. Ōnuki*2, *A. Amato*[4]

RA-98-06, ETHZ[1] – OSAKA[2] – LONDON[3] – PSI[4]

Among others, we have started to look at the system CeAg which is known to show a martensitic transition from the cubic CsCl- to a tetragonal structure at $T_Q = 15$ K, driven by quadrupolar ordering [1]. It is followed at 5 K by a second order phase transition into a ferromagnetically ordered state. A polycrystalline sample of CeAg was investigated before by Hyomi et al. [2] at KEK, but due to the limited time resolution at this pulsed facility only an incomplete picture could be obtained. In particular a loss of asymmetry starting already below 30 K suggested the presence of magnetic effects already far above T_c and T_Q. Our motivation to study this system was triggered by the possibility that the structural and magnetic properties are strongly coupled. Using two tiny single crystals we performed transverse field measurements with $B = 0.05$ T oriented parallel to a (100)-axis. Below 5 K the μSR signal turned out to be completely wiped out. Above 5 K a two component structure was seen consisting of a fast and a slowly, exponentially damped signal. The temperature dependence of the asymmetries and the relaxation rates λ are displayed in Figs. 1 and 2. The fast damped signal showed also a pronounced frequency shift as can be seen in Fig. 3. The slowly damped component appeared to vanish on approaching T_c. It seems that the ratio of the fast and slow components is affected by the quadrupolar transition. Also the temperature dependence of ν_{slow} is affected by T_Q (not shown). The λ's seem to follow grosso modo a power law temperature dependence ($\propto T^{-\beta}$) with exponents near 3 for the fast component and near 2 for the slow component. No critical slowing down near T_c is observed. A few LF-measurements prove the relaxation rates to be dynamically induced. Small anomalies near T_Q may imply that the underlying Ce 4f-spin dynamics is affected by the structural transition. To get a complete picture additional measurements, also as a function of crystal orientation, in TF, ZF and LF-geometry will have to be performed.

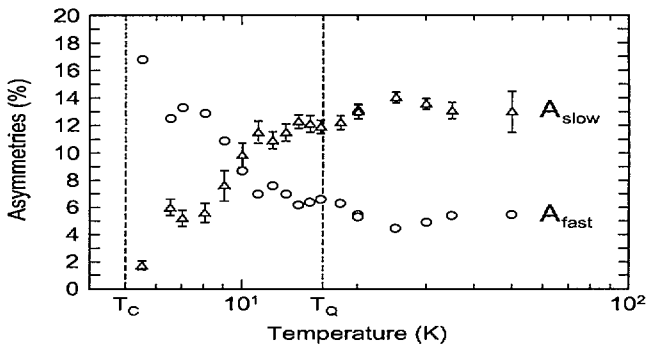

Figure 1: Temperature dependence of the amplitudes of the two components in the TF-μSR signal.

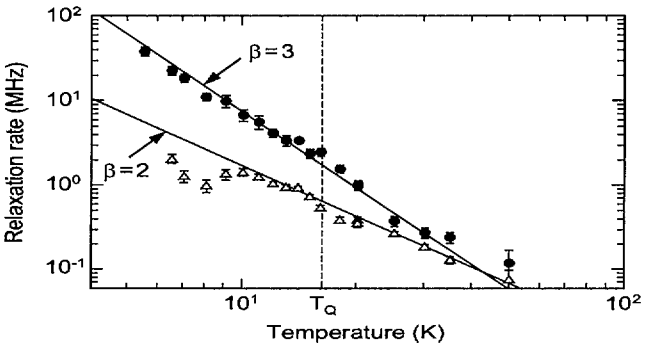

Figure 2: Log-Log plot of the temperature dependence of λ_{slow} and λ_{fast}.

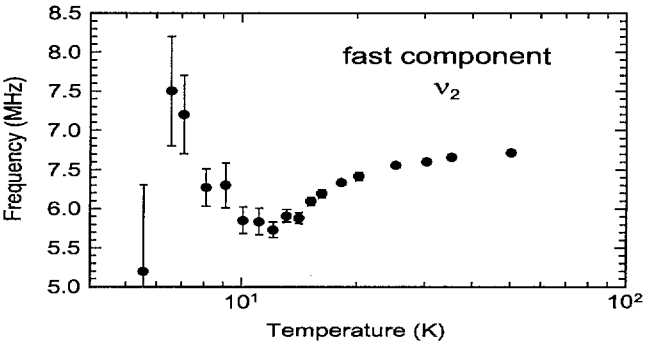

Figure 3: Temperature dependence of the precession frequency ν_{fast} of the fast component. Note the unusual change in slope.

REFERENCES

[1] P. Morin, J. Magn. Magn. Mater. **71**, 151(1988).

[2] K. Hyomi et al.,
J. Magn. Magn. Mater. **76-77**, 462(1988).

SPIN DYNAMICS IN SUBSTITUTED MANGANATES AND IRON OXIDES

S. J. Blundell[1], *I. M. Marshall*[1], *A. Husmann*[1], *F. L. Pratt*[1,2], *B. W. Lovett*[1], *W. Hayes*[1], *P. D. Battle*[1], *M. J. Rosseinsky*[1]

RA-97-19, OXFORD[1] – RIKEN[2]

There has been much recent interest in colossal magnetoresistance (CMR) effects which have been discovered in various conducting manganese oxides, usually with the perovskite structure. However similar effects have recently been seen in some conducting oxides of cobalt and iron [1].

We report a study of measurements of the temperature dependent muon-spin relaxation in powder samples of five compounds in the family $SrFe_{1-x}Co_xO_3$ where Co substution varies from $x = 0$ to 0.2. $SrFeO_3$ is an itinerant helical antiferromagnet while $SrCoO_3$ is a ferromagnetic metal. Between $x = 0.0$ and $x = 0.1$ the Néel temperature of the screw phase decreases with increasing x from 134 K down to around 90 K. Between $x = 0.1$ and $x = 0.2$ a ferromagnetic state begins to develop with an increasing critical temperature, but there is a divergence between field-cooled and zero-field-cooled susceptibility data below the transition, suggestive of glassy ground states. For higher Co substitution level, the critical temperature decreases (from 268 K to 212 K as x increases from 0.3 to 1). These compounds all have an undistorted cubic perovskite structure but have low electrical resistivity. High spin Fe^{4+} is isoelectronic with Mn^{3+} and therefore $SrFeO_3$ was originally expected to be an A-type antiferromagnet like $LaMnO_3$. The magnetic moment in the helical antiferromagnetic state has been measured by neutron scattering to be 3.1 μ_B suggesting that $SrFeO_3$ is high spin with three electrons which fill the t_{2g} band while the remaining e_g electron is itinerant. The 3d electrons of the Fe and the Co hybridize with the band-like oxygen 2p orbitals and this gives rise to a conduction band. X-ray and ultraviolet photoemission experiments largely confirm this picture [2].

Our undoped sample has a measured transition temperature equal to 136 K, almost identical to the ideal value for $SrFeO_3$. For each sample the magnetic susceptibility approximately follows a Curie-Weiss law above the transition temperature. The temperature dependence of the magnetisation for our $x = 0, 0.05, 0.1$ samples are similar: there is a relatively sharp peak at T_N and a slight divergence at low temperature between the zero-field cooled and the field cooled data. For $x = 0.15, 0.2$ we observe a peak at the ferromagnetic transition which is much broader and the divergence between the zero-field cooled and field cooled data starts almost immediately below T_c. This suggests the ground states of all the samples have a glassy nature.

We have used μSR at ISIS and PSI in a previous study to the CMR family, $Sr_2LnMn_2O_7$ where Ln=lanthanide [3]. In this experiment for the $x = 0$ sample, we were unable to distinguish μSR oscillations in the raw data; instead there was a very fast initial relaxation in the asymmetry which developed below T_N suggesting a large spread in internal fields at the muon-site. However in the two Co rich samples, a damped but clearly resolvable spin-precession signal was observed, indicating a quasi-static local field at the muon site. Raw data with fits for the $x = 0.2$ sample are shown in Figure 1.

The temperature dependence of the frequency of the precession signal for both the $x = 0.15$ and $x = 0.2$ doped samples shows an unusual temperature dependence, with an almost linear decrease of internal field over a large range in temperature and a sudden drop close to the transition temperature. Our measured Curie temperature in the $x = 0.2$ sample is the larger of the two, consistent with our susceptibility measurements. The muon-site in these systems is not precisely known, but by analogy with the orthoferrites, which have an orthorhombically distorted perovskite structure, we expect the formation of an $(O\mu)^-$ bond, with the muon-site determined by the approximately 1 Å bond-length and by Coulomb interactions with neighbouring atoms [4].

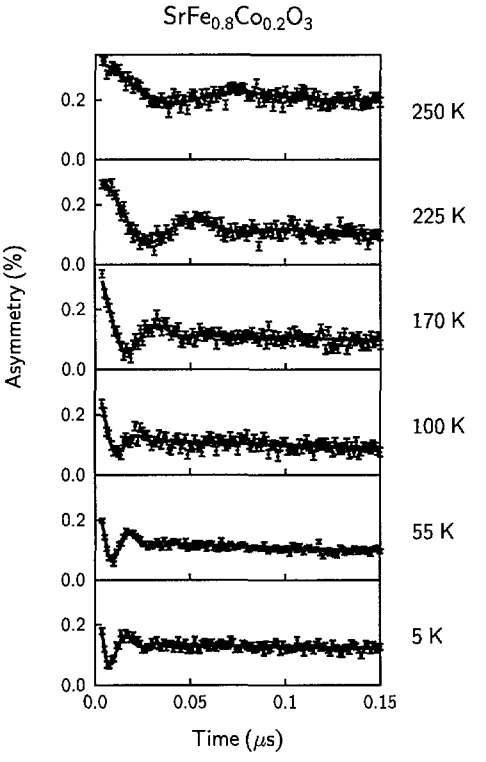

Figure 1: Time dependent asymmetry for several temperatures for $SrFe_{0.8}Co_{0.2}O_3$. These data are fitted to an exponentially damped oscillation addded to a very slowly relaxing exponential function.

REFERENCES

[1] G. Briceno et al, Science **270**, 273(1995);
P. D. Battle et al., Chem. Comm., 987 (1998).

[2] A. E. Bocquet et al, Phys. Rev. **B 45**, 1561(1992).

[3] R. Bewley et al., Phys. Rev. **B 60**, 12286(1999).

[4] E. Holzschuh et al., Phys. Rev. **B 27**, 5294(1983).

ZERO AND LONGITUDINAL FIELD RELAXATION IN LOW DOPING MANGANITES: SEARCH FOR STATIC AND DYNAMIC FERROMAGNETIC CLUSTERS

R. De Renzi[1], *G. Allodi*[1], *M. Cestelli*[1], *G. Guidi*[1], *M. Hennion*[2], *L. Pinsard*[3], *A. Caneiro*[4], *S. Oseroff*[5], *A. Amato*[6]

RA-99-06, PARMA[1] – LBL[2] – PARIS SUD[3] – BARILOCHE[4] – S. DIEGO[5] – PSI[6]

Hole doping induced by substitution in orthomanganites leads to a rich phase diagram where transport and magnetic properties are strictly related: the pure La antiferromagnetic insulator evolve with doping towards a metallic ferromagnetic state exhibiting colossal magnetoresistance. In the present experiment we have explored the low doping side of the phase diagram, starting from a single crystal of pure $LaMnO_3$, a layer antiferromagnet, including two insulating compositions of $La_{1-x}Ca_xMnO_3$ ($x = 0.08$ and 0.15) and complementing the survey with pellets of vacancy doped $(LaMn)_{1-y/6}O_3$ ($0 < y < 0.1$; $x, y = [Mn^{4+}]$).

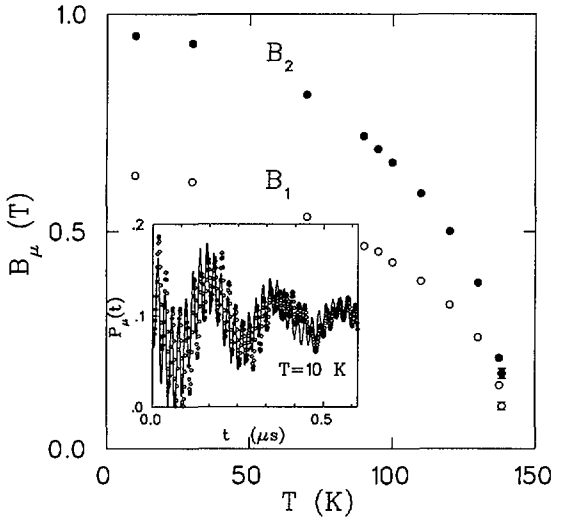

Figure 1: left: Temperature dependence of the two internal fields in $LaMnO_3$; inset: Precessions at 10K in the rotating frame

In $LaMnO_3$ two spontaneous frequencies are observed in zero field below $T_N = 139.5$ K. The temperature dependence of the local fields, B_1 and B_2, is shown in Fig. 1, together with a best fit of the muon polarization at 10K (shown in a rotating reference frame). Comparison with neutron data indicates that the internal field is proportional to the spontaneous sublattice magnetization, $M_s(T)$. The static properties probed by $\mu\mathcal{SR}$ agree with the expectations for a normal antiferromagnet.

We have identified the low field site, (0.623, 0.934, 0.25) in the orthorhombic $Pnmb$ cell; it lies within a crystalline mirror plane, 1.05 Å from an O ion, in the largest available interstitial, where dipolar sums at $T = 0$ K yield a local field of 0.65 T, aligned along the c axis (*vs.* $B_1(0) = 0.6290(2)$ T). The assignment is based on the work of Holzschuh *et al.*, Phys. Rev. B 27 (1983) 5294, on a family of orthoferrites isostructural to $LaMnO_3$. The local field orientation, common to all sites in the mirror $z = 1/4$ plane, is demonstrated by applying a field of 1 KOe ($H \gg H_s$), since in these, and only in these conditions one always has $\boldsymbol{B_1} \cdot \boldsymbol{H} > 0$, and obtains a single frequency peak with $\nu > \gamma_\mu B_1$.

In the $x = 0.08$ sample inelastic and small angle neutron scattering demonstrated the appearance of static small polarons below T_N, characterized by nanoscopic dimensions and an enhanced ferromagnetic moment. In this static inhomogeneous condition the $\mu\mathcal{SR}$ Fourier spectra at low temperatures consist of extremely broad peaks, close to the frequencies observed in the pure material. Both our doped crystals show a transition to the low temperature fully ordered phase ($T_N = 107$ K for $x = 0.08$, $T_C < 100$K for $x = 0.15$) preceded by a second higher transition temperature, $T_c = 123.5(5)$ K for $x = 0.08$, and $T_c = 165(5)$ K for $x = 0.15$, which marks the *nucleation* of an ordered phase. This second transition is revealed by the development of two distinct muon signals for $T < T_c$. In a zero field experiment the first signal appears as a fast Kubo-Toyabe relaxation function, with a large internal frequency width Δ indicating dipolar fields roughly as large as in the low temperature ordered phase. Hence we attribute this signal to ordered clusters. The second signal exhibits only a moderate relaxation and it is attributed to clusters where the majority of the Mn spins fluctuate. An easy separation of the two signals in the fitting procedure is thus granted by the very different timescale of the two relaxation times - much less then 10^{-7} s and much more than 10^{-6} s, respectively.

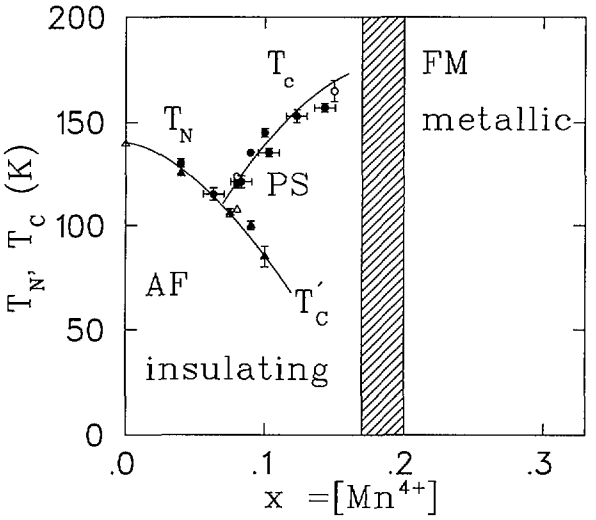

Figure 2: The low doping phase diagram (PS=phase separation)

This behaviour, observed also in the vacancy doped materials, is attributed to a first order magnetic transition, with coexistence of fluctuating and ordered clusters. The temperature interval for the coexistence increases with x, as it is shown in the phase diagram of Fig. 2.

μSR INVESTIGATION OF THE SPIN DYNAMICS IN DOUBLE LAYERED MANGANITES

D. Andreica[1], A. Schenck[1], F.N. Gygax[1], T. Chatterji[2], R. Suryanarayanan[3], R. van de Kamp[4]

RA-99-05, ETH ZURICH[1] – ILL GRENOBLE[2] – PARIS XI [3] – BERLIN[4]

We have studied the static and dynamic spin behaviour in the double layered manganite $La_{2-2x}Sr_{1+2x}Mn_2O_7$.The magnetic properties of these compounds are under intense investigations due to the colossal magnetoresistence observed close to the insulator-to-metal transition temperature at x = 0.4 as well as due to their two-dimensional behaviour. Ordering of the $d_{3x^2-r^2}/d_{3y^2-r^2}$ orbitals of the Mn^{3+} ions accompanied by a real space ordering in the Mn^{3+} /Mn^{4+} distribution was indeed observed in $LaSr_2Mn_2O_7$ below around 225 K ([2] and references therein). The charge/orbital ordering is "melted" by the in-plane ferromagnetic ordering. **$LaSr_2Mn_2O_7$** [1]: The zero-field (ZF) μSR spectra show near-exponential relaxation behaviour over the entire investigated temperature range 3-300 K. The results shown in Fig. 1 were obtained by fitting the spectra to an exponential depolarisation function with free asymmetries. Although a simple exponential fit was not optimal the trend in the spectra was clearly brought out in this way. It is clearly seen from

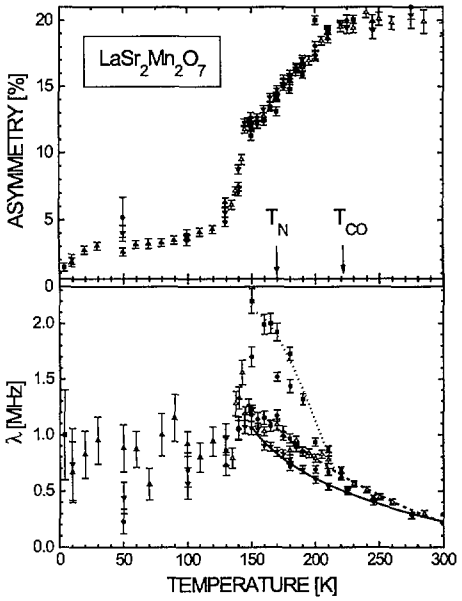

Figure 1: Temperature dependence of the signal amplitude (upper part) and the relaxation rates (lower part). (see text)

the temperature dependence of the asymmetry that below ~220 K, the temperature of the CO transition, a fast component sets in and below ~150 K the depolarisation of the μSR signal is even stronger. The data shown in the lower part of Fig. 1 are from ZF temperature scans recorded on cooling (solid line) or heating (dashed line) and for different field histories of the sample (dotted line). One can clearly see that the asymmetry is neither dependent on the type of the ZF measurements (on cooling or heating) nor on the magnetic history of the sample. Totally different is the behaviour of the relaxation rates in the paramagnetic phase, where a clear increase is observed on crossing T_N with increasing temperature compared to the measurements performed on cooling the sample (temperature hysteresis). A huge field history dependence was observed when the magnetic field was switched on and off in the charge ordered regime. The fact that the asymmetry is independent of the temperature cycle and of the field history of the sample implies that the volume fraction associated with the observable muons is not affected by the experimental procedure. The extremely fast depolarisation of the muons in the rest of the sample volume, rendering them invisible also above T_N, is puzzling and not understood at present. We interpret the increase of the relaxation rates after the field on/off treatment as arising from a field-induced correlation (via magnetic-polaron formation) between the Mn spins which survives even after switching off the magnetic field. **$(La_{0.9}Pr_{0.1})_{1.2}Sr_{1.8}Mn_2O_7$**: a μSR test measurement was performed on a single crystalline sample in ZF and longitudinal-field (LF) configurations. The signature of a magnetic transition below 110 K was seen in both the ZF and LF measurements (Fig. 2). In ZF and LF measurements we observed the slowing down of the Mn spin fluctuations when the transition temperature is approached from above. We should point out here that no slowing down effect was observed in the $LaSr_2Mn_2O_7$ sample. There, the increase of the relaxation close to the transition temperature is associated with the increase of the correlation length. Clear wiggles in the μSR spectra were observed below the transition temperature (insert of Fig. 2) indicating a non-zero field at the muon site and an excellent quality of the sample. A more complete analysis of the data is under way.

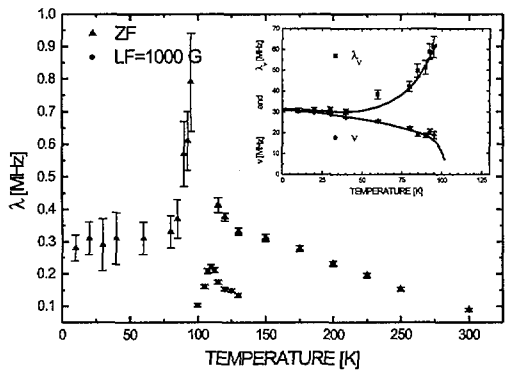

Figure 2: Temperature dependence of the spin lattice relaxation rates in $(La_{0.9}Pr_{0.1})_{1.2}Sr_{1.8}Mn_2O_7$ in zero and longitudinal field. The insert shows the spontaneous frequency appearing below 110 K.

REFERENCES

[1] D. Andreica et al., to be published in Physica **B**.

[2] T. Chatterji et al., Phys. Rev. **B 61**, 570 (2000).

STUDY OF THE DYNAMIC AND STRUCTURE FEATURES OF MAGNETISM IN HOLMIUM

V.N. Duginov[1], *K.I. Gritsaj*[1], *D. Herlach*[2], *A.A. Nezhivoy*[3], *B.A. Nikolsky*[3], *V.G. Olshevsky*[1], *V.Yu. Pomjakushin*[1,2], *A.N. Ponomarev*[3], *U. Zimmermann*[2]

RA-98-01, DUBNA[1] – PSI[2] – MOSCOW[3]

It is known that two magnetically ordered states occur in holmium below room temperature. For 20 K $< T <$ 132 K the magnetic structure of holmium is an antiferromagnetic helicoid, which restructures into a ferromagnetic helicoid at $T_C = 20$ K. In both cases the axis of the helicoid is directed along the hexagonal *c*–axis of the crystal perpendicular to the basal plane of the crystal lattice. The atomic magnetic moments in the antiferromagnetic state of holmium lie in the basal planes. Their directions in each separate plane are parallel to each other and make an angle α with the neighboring plane. α increases continuously from $\alpha \sim 30°$ at $T = 20$ K up to $\alpha \sim 50°$ at $T = 130$ K.

The spiral structure wavelength along the c–axis and the distance between the basal planes of the crystal lattice are, generally speaking, incommensurate. A phenomenological description of such an incommensurate helicoid is the model of a magnetic spin–slip structure, according to which only six equivalent directions of magnetic moments in the basal planes are possible, corresponding to the hexagonal symmetry. According to the spin–slip model, an individual angle α_{ind} between the directions of magnetization of two neighboring basal planes can assume only two values, 0 (doublets planes) or 60° (singlets planes). For $\alpha_{ind} = 0$ pairs (doublets) of two identically polarized basal planes form and for $\alpha_{ind} = 60°$ two neighboring doublets are rotated with respect to each other by an angle of 60°. The sequence of doublets alternates with single planes. The formation of such a singlet plane is termed spin–slip.

The μSR method was used to measure the internal magnetic fields B_μ at interstitial sites of the crystal lattice. In a simple helicoid structure ($\alpha_{ind} = \alpha$) all interstitial sites are magnetically equivalent, and in a μSR experiment only one muon precession frequency should be observed at a given temperature. In the spin–slip structure, the interstitial fields in different sections of the helicoid are different and the frequency spectrum of the muon signal should be more complicated.

ZF measurements were performed on GPD setup with holmium single crystal which was cut off from the textured sample used earlier[1]. High statistic spectra were measured below the Néel temperature point. At every temperature two time spectra were measured - with the c-axes oriented perpendicular and parallel to the polarization of the muon beam.

The temperature dependence of the muon spin precession frequency in the magnetic field in holmium is shown in Fig. 1[2], which also displays the calculated temperature dependencies of the μSR frequency in the dipole magnetic field B_{tet}(solid line) and B_{oct}(dashed line) at the tetrahedral and octahedral interstitial sites, respectively, of the crystal lattice of holmium for the case of a simple magnetic spiral, i.e., for $\alpha_{ind} = \alpha$ in the antiferromagnetic state.

The calculations of the dipole magnetic fields took account of the temperature dependencies of the wavelength of the helicoid, the crystal lattice parameters, and the magnetic moment of the holmium ions in the crystal. One can see from Fig. 1 that the experimentally measured fields differ from the calculated dipole magnetic fields. This difference is due to the Fermi contact magnetic field of polarized conduction electrons at the muon site $B_c = 8/3\pi\mu_B\rho(0)P_e$. Here μ_B is the Bohr magneton, $\rho(0)$ is the density of the electronic wave function at the muon and P_e is the polarization of the conduction electrons.

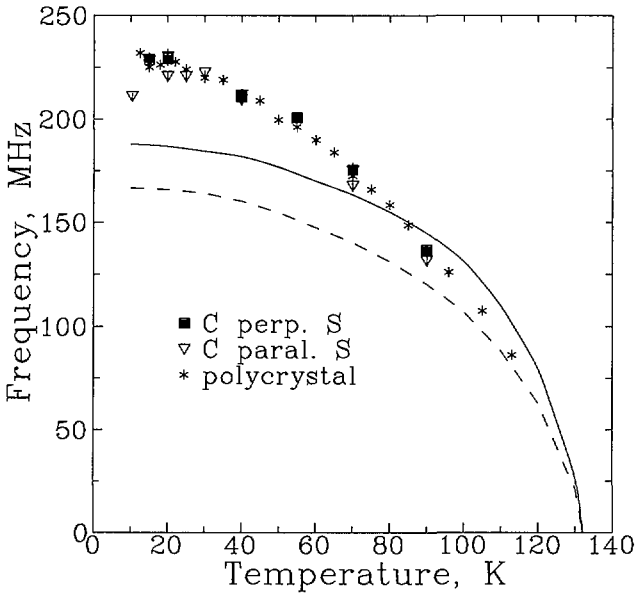

Figure 1: Temperature dependence of the muon spin precession frequency in holmium and results of dipolar field calculations for tetrahedral (solid line) and octahedral (dashed line) interstitial sites. The difference to the measured B_μ is due to the Fermi contact field.

The experimental spectrum was described by a single muon spin precession frequency. At the same time, the high values of the relaxation rate, could be due to overlapping of several frequencies for the spin–slip structure.

REFERENCES

[1] I.A.Krivosheev et al., JETP Letters. **65**, 81(1997).

[2] A.N. Ponomarev *et al.*, submitted to Physica **B**.

MAGNETIC ORDERING IN Li_2CuO_2

A. Amato, B. Roessli and U. Staub

RA-98-20, PSI

Recently, much attention has been drawn to the compound Li_2CuO_2 with a chain-like arrangement of the copper ions [1] and superexchange pathways bridged by Cu-O-Cu bonds. As the high temperature specific heat could be reproduced with a ferromagnetic intrachain exchange interaction, Li_2CuO_2 was first considered as an ideal 1D-ferromagnetic $S = 1/2$ system. However, antiferromagnetic resonance experiments have shown that the largest exchange interaction couples the spins along the body diagonal. Therefore, Li_2CuO_2 should be described as a 3D-antiferromagnet in agreement with magnetic susceptibility results and bandstructure calculations. The magnetic structure has been determined by neutron diffraction and consists of ferromagnetic sheets of Cu^{2+} ions in the orthorhombic plane with spins aligned perpendicular to the chain axis and layered antiferromagnetically along the c-axis. The magnetic moment at saturation is close to the value of 1 μ_B of the free Cu^{2+} ion.

We present here μSR measurements on single crystals performed at the μSR Facility. Figure 1 shows a μSR spectrum recorded at $T = 4$ K with the c-axis of the crystal parallel to the muon polarization. The modulation of the signal is due to the spontaneous precession of the muon spin in the internal fields originating from the ordered magnetic moments. A Fourier transform reveals three well defined frequencies and suggests the presence of magnetically inequivalent μ^+-sites. Additional measurements performed with the initial muon polarization along the a-axis, where no oscillation of the muon signal was observed, indicate that the internal fields at the μ^+-sites are parallel the a-axis.

Upon cooling the sample below $T' = 2.4$ K, the lowest frequency splits. In addition, the highest frequency slighty shifts below T', while the middle frequency remains practically unchanged (see Fig.2). This indicates that an additional phase transition occurs in Li_2CuO_2 at T'. Magnetization measurements have reported a field-induced weak ferromagnetic moment in Li_2CuO_2 below about 2.8 K. The behaviour of the low temperature magnetization has been interpreted in terms of competition between magnetocrystalline anisotropy and exchange couplings leading to a spin canting of the Cu magnetic moments. We note that unlike the situation above T', μSR spectra with the initial polarization parallel to the a-axis performed below 2.4 K show a weak oscillatory signal, in agreement with the occurence of a slight spin canting.

In addition to the splitting observed below T', a remarkable observation is the quite different temperature evolution of the component #2. This frequency, which is unaffected by the phase transition at T', shows a much steeper increase for decreasing temperatures below T_N than the two other components. Therefore, in addition to the copper ions ordering, the μSR signal seems to reveal the presence of a second intrinsic magnetic sublattice in Li_2CuO_2 which suggests that approximately 40% of the effective magnetic moment is located at the bridging oxygens. The different components of

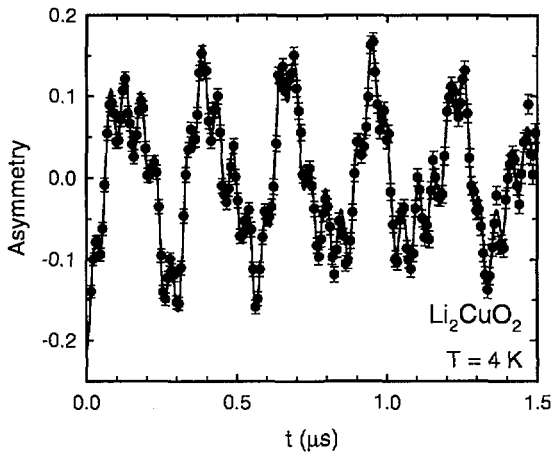

Figure 1: Zero-field μSR spectrum of Li_2CuO_2 at $T = 4$ K with the initial muon polarization along the c-axis.

the μSR signal would reflect stopping sites located at different crystallographic positions respective to the copper and oxygen ions and probing therefore differently the two sublattices.

A complete report of the present results will be published elsewhere [2].

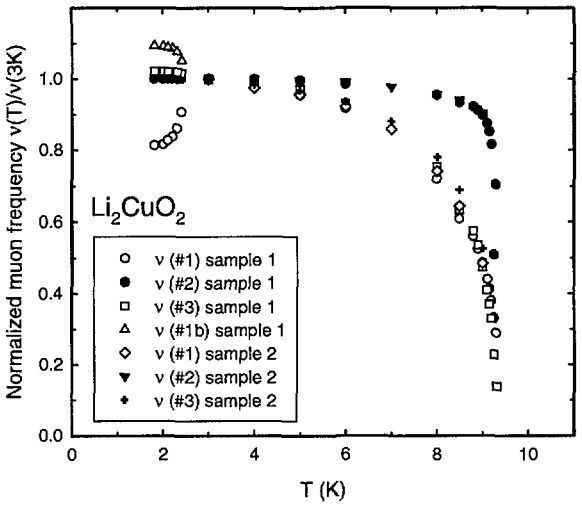

Figure 2: Temperature dependence of the normalized spontaneous muon frequencies in Li_2CuO_2 measured on two sincle crystals.

REFERENCES

[1] See for example: M. Boehm *et al.*, Europhys. Lett **43**, 77 (1998) and references therein.

[2] U. Staub, B. Roessli and A. Amato, Physica **B**, in press.

MAGNETIC CORRELATIONS IN ONE DIMENSIONAL SPIN SYSTEMS

D. Mienert[1], H. H. Klauss[1], D. Baabe[1], W. Kopmann[1], H. Walf[1], M. Birke[1], H. Luetkens[1], F. J. Litterst[1], U. Ammerahl[2], B. Büchner[2], Chr. Geibel[3].

RA-99-01, BRAUNSCHWEIG[1] – KÖLN[2] – DRESDEN[3]

In this work we study the magnetic phases of quasi one dimensional spin-1/2-systems as a function of impurity and charge carrier doping.

1999 RESULTS ON $(Sr, Ca, La)_{14}Cu_{24}O_{41}$

The System $(Sr, Ca, La)_{14}Cu_{24}O_{41}$ contains CuO_2 chain and Cu_2O_3 2-leg ladder structures [1] which can be doped with charge carriers. $Sr_{14}Cu_{24}O_{41}$ exhibits a doping of 0.6 holes per Cu-atom on the chain sites and nearly undoped ladder sites. Ca doping leads to a considerable charge transfer from the chains to the ladder structures. The conductivity becomes more metallic and around $Ca_{11}Sr_3$ superconductivity was found under external pressure of 4 GPa [2]. Doping whith La reduces the number of holes and for La_6Ca_8 the chain and ladder structures are nominally undoped. In this compound neutron scattering experiments revealed an antiferromagnetic order of moments at the chain copper and oxygen sites with an incommensurate helical modulation below $\approx$ 10 K [3]. Our first aim is to determine the muon site. In-

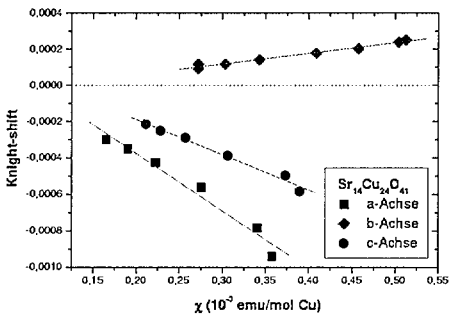

Figure 1: Knight-shift vs. susceptibility in all three crystal directions of $Sr_{14}Cu_{24}O_{41}$ (above 50 K).

elestic neutron scattering results showed that the spin gap energy of the ladders in all compounds is close to 330 K. Therefore we assume that below 200 K the Knight shift is dominantly caused by local moments on the chain copper ions. We performed 6 kG TF measurements on Sr_{14}, $Ca_{11.5}Sr_{2.5}$ and La_5Ca_9 along the three crystal axes. In all three compounds a single frequency signal with a strong temperature dependent Knightshift is observed. Above $\approx$20 K the Knightshift scales well with the corresponding susceptibilities (see e.g. Figure 1). From the data a single muon site can be deduced. Dipole calculations favor a muon site close to the ladder structures at (0, 0.2, 0).

We also performed ZF and LF experiments on these compounds and La_4Ca_{10} with $\vec{P}_\mu(t = 0)$ parallel to the c-axis. Surprisingly all systems show strong magnetic relaxation in the spin gap state (see e.g. Figure 2). The Sr_{14} compound shows a slowing down of the magnetic fluctuations but no static order whereas the other systems show static order be-

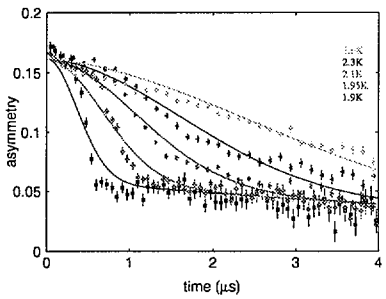

Figure 2: Low temperature ZF asymmetry spectra of $Sr_{2.5}Ca_{11.5}Cu_{24}O_{41}$ (1.9 K - 2.6 K).

low 2.4 K ($Sr_{2.5}Ca_{11.5}$), 6 K (La_4Ca_{10}) and 9.5 K (La_5Ca_9). The observation of spin freezing with μSR in systems with a high spin gap energy is also reported for the Na-Vanadate (see below and [4]) and is not understood so far.

1999 RESULTS ON $\alpha' - NaV_2O_5$

In ZF and LF experiments on a single crystal of $\alpha' - NaV_2O_5$ we have also found magnetic correlations developing gradually below 20 K and a saturation below 10 K (see Figure3).

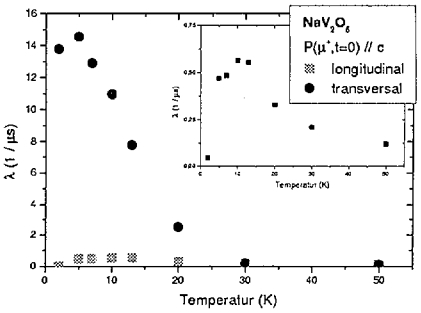

Figure 3: Longitudinal and transversal relaxation rates vs. Temperature for $\alpha' - NaV_2O_5$ (below 50 K).

The plot of the average fluctuation rate ν presents an Arrhenius like behavior with a resulting activation energy of $\approx$70 K. This is of the same order of magnitude as the spin gap formation temperature and in good agreement with E_g=72.2 K obtained by [4] using the same method.

REFERENCES

[1] M.Matsuda et al., Phys. Rev. **B 54**, R15626 (1996).

[2] T.Nagata et al., Phys. Rev. Lett. **81**, 1090 (1998).

[3] M.Matsuda et al., Phys. Rev. **B 57**, 11467 (1998).

[4] Y.Fudamoto al., Phys. Rev. Lett. **83**, 3301 (1999).

μSR ON MONODISPERSE NANOSCALE Pd CLUSTERS AT LOW TEMPERATURES

C. T. Kaiser[1], P. C. M. Gubbens[1], F. M. Mulder[1], P. Dalmas de Réotier[2], A. Yaouanc[2], P. M. Paulus[3], L. J. de Jongh[3], G. Schmid[4]

RA-99-07, TU DELFT[1] – CEA GRENOBLE[2] – LEIDEN[3] – ESSEN[4]

The properties of nanometre-scale metallic particles differ from those of the same material in bulk. Since conduction electrons have a wave-like nature, they can have only certain discrete values of kinetic energy or wavelength, leading to 'quantum size effects'. This leads to a separation of discrete electronic energy levels, of which the distances increase with a decreasing size of the metallic particle. Coulomb charging effects are also present. They are purely classical in origin and occur when the energy to add one electron to a conducting sphere exceeds the mean thermal energy $k_B T$. In theory the combination of quantum size effects and Coulomb charging effects should cause the properties of small metallic particles to depend sensitively on whether they have an odd or even number of electrons [1].

The materials we study belong to a class of giant molecular clusters, in which the metal cores are members of a series of 'magic number' clusters obtained by surrounding an atom by successive shells of atoms of its kind. The magic numbers that are obtained are 1, 13, 55, 147, 309, 561 and so on. Organic ligands are necessary to stabilize the particles, and for obtaining a mono-disperse material. Studies of the magnetic susceptibility and electronic specific heat, which are sensitive to the electrons in the highest occupied levels (at the Fermi level), were performed and they showed a clear size dependence for the 5, 7 and 8 shell Pd clusters [2].

Our purpose with the μSR technique is to study the delocalized magnetic moment of the uncompensated electronic spin of a nano-scale metallic particle with an odd number of electrons. Because of the random packing of the clusters there is a varying dipolar coupling between their magnetic moments.

In this report we present μSR results obtained on the 1.2 nm Pd cluster with formula $Pd_{55}[PPh_3]_{12}O_{30}$. The weight of the sample is $\sim$ 50 mg. The measurements have been performed at GPS using the so-called 'fly-past' method. Thus only positrons decaying from muons catched by the sample are detected. The measurements have been performed from 1.65 K up to 290 K.

An appreciable fraction of the available asymmetry is lost, reflecting probably the muons implanted in the ligands. They probably form muonium and therefore do not contribute to the asymmetry. The measured asymmetry displays an exponential relaxation. As seen in Fig. 1 the exponential relaxation rate λ_Z exhibits an increase below $\sim$ 10 K. The study of the field dependence of the spectra indicates that the cluster magnetic moments are quasi-static: at 1.85 K a characteristic fluctuation time of the magnetic correlations of $\sim$ 1.8 μs is measured. Therefore quasi-static electronic magnetism has been found for nano-particles. The width of the field distribution probed by the muons is relatively narrow for a field of electronic origin because the distance between the muons and the mainly delocalized magnetic moments is about an order of magnitude larger than in crystalline solids. From $\sim$ 10 K up to $\sim$ 115 K λ_Z is constant. This behaviour has been observed at high temperature for a number of magnets. It is the signature of the loss of correlations between the cluster magnetic moments.

Unfortunately because of the small amount of material available, it was not possible to perform measurements at LTF.

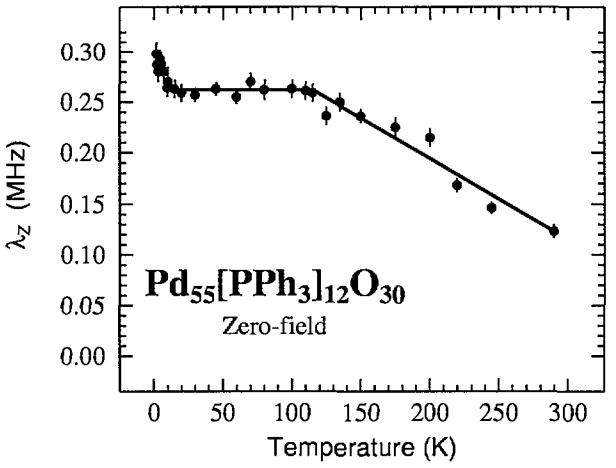

Figure 1: Temperature dependence of the zero-field relaxation rate λ_Z of the 1.2 nm Pd cluster $Pd_{55}[PPh_3]_{12}O_{30}$. The line is a guide to the eyes.

REFERENCES

[1] R. Kubo, J. Phys. Soc. Japan **17**, 975 (1962).

[2] Y. Volokitin, *et al.* Nature **384**, 621 (1996); see also N&V *ib* 612.

QUANTUM FLUCTUATIONS OF THE MAGNETIZATION IN HIGH SPIN MOLECULES A – μSR STUDY

A. Keren[1], *Z. Salman*[1], *Ph. Mendels*[2], *A. Scuiller*[3], *M. Verdaguer*[3], *C. Baines*[4]

RA-97-06, TECHNION[1] – ORSAY[2] – JUSSIEU[3] – PSI[4]

High spin molecules (HSM) consist of magnetic ions coupled by ferromagnetic or antiferromagnetic interactions. These molecules crystallize in a lattice where neighboring molecules are magnetically separated, yielding, at low temperatures, noninteracting giant spins S. When the temperature is much lower than some coupling constant the only possible relaxation mechanism is of quantum mechanical origins.

Here we report a study of $[Cr(CN)Ni(tetren)_6](ClO_4)_9$ denoted as $CrNi_6$ and $[Cr(CN)Mn(trispicmeen)_6](ClO_4)_9$ denoted as $CrMn_6$.

The Hamiltonian of these systems at high temperatures was found to agree with the form $\mathcal{H} = \sum_M J_{Cr-M} S_{Cr} S_M$ (where M is either Ni or Mn). In $CrNi_6$ [1], the Cr^{3+} ion ($S = \frac{3}{2}$) interacts ferromagnetically with 6 Ni^{2+} ions ($S = 1$) and creates a ground state of total spin $S = \frac{15}{2}$ [1]. Susceptibility measurements show that $J_{Cr-Ni} = -24$ K, and the blocking temperature is $T_B = 4.1$ K [1]. In $CrMn_6$ the interaction between the Cr^{3+} ion ($S = \frac{3}{2}$) and 6 Mn^{2+} ions ($S = \frac{5}{2}$) is antiferromagnetic [2], and the total spin of the ground state is $S = \frac{27}{2}$. Similar susceptibility measurements [2] show $J_{Cr-Mn} = 11.5$ K and a blocking temperature of $T_B = 5.3$ K. The different spin values of the samples allow us to investigate the effect of S on the fluctuation rate which we determined by μSR. The magnetic field and temperature

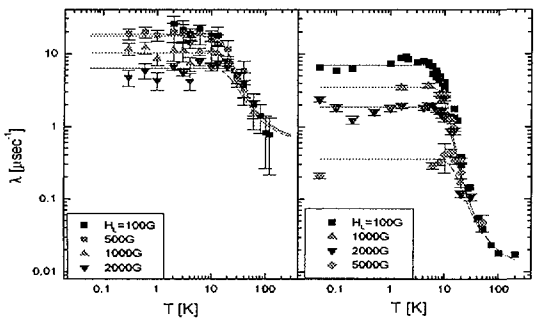

Figure 1: The relaxation rate on the asymmetry as a function of temperature for different magnetic fields. The relaxation rate saturates at low temperatures.

dependence of the muon spin depolarization rate λ in $CrNi_6$ and $CrMn_6$ is presented in Figs. 1. The field is applied parallel to the initial muon spin direction.

As the temperature is decreased towards $T_c \sim 6$ K for $CrNi_6$ and ~ 10 K for $CrMn_6$ the relaxation rate increases.

However, below T_c the relaxation rate reaches saturation. Such a saturation of the relaxation rate suggests that the fluctuations below T_c is of quantum nature. The solid lines in Fig. 1 are fits of the relaxation rate λ to a function of the form $\lambda(T,H) = 1/[Q(H_L) + C\exp(-U/T)]$ where C and

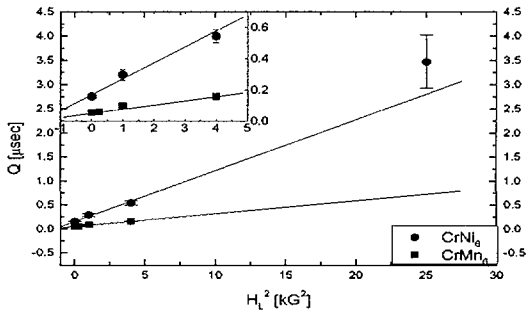

Figure 2: The saturated relaxation time Q as a function of H_L^2 for both $CrMn_6$ and $CrNi_6$. The solid lines are linear fits of Q vs. H_L^2. The inset shows the low fields range.

U are global parameters for all fields. The saturation value of the relaxation time $Q(H_L)$ is found to be proportional to the LF squared, H_L^2, as shown in Fig. 2. This fact could be explained by a single field-field correlation function [3], $\langle B_\perp(0) B_\perp(t) \rangle = \langle B_\perp^2 \rangle e^{-\nu t}$ where ν is the field-field correlation rate, and $\langle B_\perp^2 \rangle$ is the mean squared field (at a given muon site), combined with multiple muon occupation sites. The multiple sites introduce a distribution of $\langle B_\perp^2 \rangle$. For long times $\nu t \gg 1$ (which is satisfied in our case) the relaxation rate λ^{-1} reduces to [3]

$$\frac{1}{\lambda} = \frac{1}{2\nu a^2} H_L^2 + \frac{\nu}{2\gamma_\mu^2 a^2} \qquad (1)$$

where a represents the range of possible $\langle B_\perp^2 \rangle$. From Fig. 2 and Eq. (1), we obtained the fluctuations rates $\tau^{-1} = \frac{\nu}{2} = 50 \pm 5$ MHz and 60 ± 15 MHz for $CrNi_6$ and $CrMn_6$ respectively. We found that the ratio of the fluctuation rates in both samples ν_{Ni}/ν_{Mn} is equal to the coupling energy between the ions $\frac{J_{Cr-Ni} S_{Cr} S_{Ni}}{J_{Cr-Mn} S_{Cr} S_{Mn}}$. This suggestes that internal degrees of fredome are responsible for the fluctuation in our molecules.

REFERENCES

[1] T. Mallah et al., J. Chem Soc., Chem. Commun. **1**, 61 (1995).

[2] A. Scuiller, T. Mallah, A. Nivorozkhin, M. Verdaguer, P. Veillet, New J. Chem. **20**, 1 (1996).

[3] Y. Uemura, T. Yamazaki, D. R. Harshman, M. Senba and E. J. Ansaldo, Phys. Rev. **B 31**, 546 (1985); A. Keren, Phys. Rev. **B 50**, 10039 (1994).

STRIPE ORDER AND SPIN DYNAMICS IN NICKELATES

H.-H. Klauß[1], *D. Baabe*[1], *W. Kopmann*[1], *D. Mienert*[1], *M. Birke*[1], *H. Luetkens*[1], *F. J. Litterst*[1], *O. Friedt*[2], *M. Hücker*[2], *B. Büchner*[2], *S. W. Cheong*[3]

RA-98-11, BRAUNSCHWEIG[1] – KÖLN[2] – MURRAY HILL[3]

In this project we examine the formation of charge and spin stripes in the lanthanum nickelates $La_{2-x}Sr_xNiO_{4+\delta}$. Since in these compounds the hyperfine coupling to the muon is much stronger (saturated spontaneous muon precesssion $\approx$ 40 MHz) than in the cuprates ($\approx$ 5 MHz) the sensitivity to anisotropy effects is enhanced and a typical signature of stripe correlations easier detected. In former μSR experiments on polycrystals the authors mainly focused on the doping dependence of the transition temperature and the mean local field at the muon site [1].

Results of 1999 experiments

In 1999 we performed ZF/LF experiments on a $La_{2-x}Sr_xNiO_4$ single crystal with x= 0.33 and 5 polycrystalline samples with x=.2, .25,.3, .4 and .5 to determine the concentration range with stripe order in the nickelates.

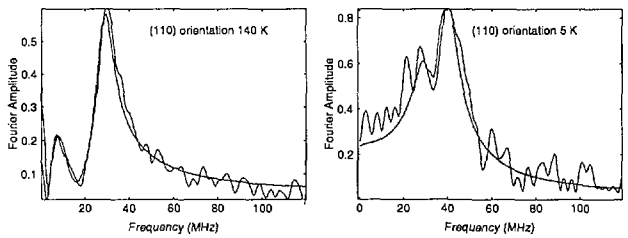

Figure 1: Typical ZF frequency spectra for $La_{2-x}Sr_xNiO_4$ with x= 0.33. The smooth lines correspond to time domain fit functions.

The x= 0.33 doped single crystal showed a spontaneous muon spin precession below 190 K with a very strong relaxation ($\lambda \approx 30\ \mu s^{-1}$). Typical frequency spectra in the orientation with the (110)-axis parallel to the initial muon spin are shown in Figure 1. Between 100 K and 185 K we were able to trace a second precession frequency of about 10 MHz in the full temperature range below 190 K down to 5 K (Figure 2). These two frequency distribution can be identified as the signature of the inhomogeneous ordered stripe phase known from the neutron scattering experiments. Below 100 K the lower frequency line is broadend considerably and exhibits an additional increase which is not observed in the temperature dependence of the high freuqency. This behavior can be associated with the formation of a spin glass like phase as proposed from neutron scatterring below 40 K caused by a freezing of the spin1/2-holes. This affects dominantly the muon signal from the hole rich domain walls. This picture is also supported by the temperature dependence of the longitudinal relaxation rate shown in Figure 3 which shows a considerable spin dynamics only above 40 K.

The signal intensities of the precession signals with the initial muon polarization along (110) and (001) are in both cases $\approx 3/5$ of the total sample signal. The spatial field distribution is nearly isotropic. We conclude a broad distribution of internal field orientations due to the strong inhomogeneous magnetic structure.

To identify a second low frequency component in the polycrystalline samples proved to be difficult since the transverse relaxation rates are larger than in the x=0.33 single crystal. Only in the x=0.25 and 0.3 samples with magnetic ordering temperatures above 100 K two distinct signals have been observed. At higher Sr doping a broad low frequency shoulder like in the x=0.33 crystal at 5K exists since the magnetic ordering temperatures are below 100 K.

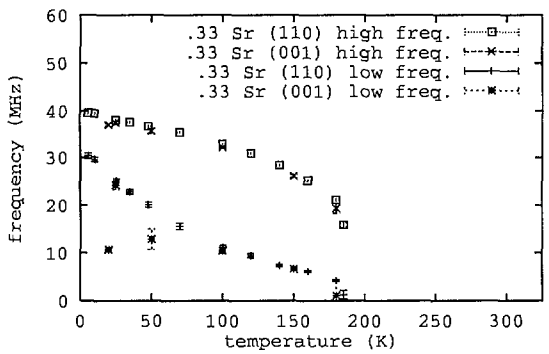

Figure 2: Spontaneous muon precession frequencies in ZF for the $La_{2-x}Sr_xNiO_4$ single crystal with x= 0.33

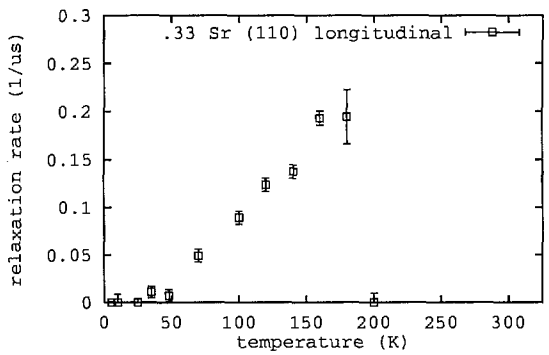

Figure 3: Longitudinal relaxation rate in ZF for the $La_{2-x}Sr_xNiO_4$ single crystal with x= 0.33

REFERENCES

[1] Th. Jestädt et al.: Phys. Rev. **B 59**, 3775 (1999).

[2] S.-H. Lee and S.-W. Cheong et al., Phys. Rev. Lett. **79**, 2514 (1997).

POSITIVE MUONS IN RARE-EARTH DIDEUTERIDES

F. N. Gygax[1], *P. Vajda*[2], *D. Andreica*[1], *M. Pinkpank*[1] *and A. Schenck*[1]

RA-97-17, ETH-ZÜRICH[1] – PALAISEAU[2]

The β-phase rare-earth (R) dihydrides (or dideuterides), $RH(D)_2$, crystallize in the fcc fluorite-type structure, where the H-atoms occupy ideally all tetrahedral sites. Additional H-atoms can be inserted on octahedral interstices, giving the superstoichiometric compounds β-RH_{2+x}. Adding H or D to the compounds one induces modifications of the electronic band structure leading to profound changes in the physical properties, such as metal-insulator transitions and strong interactions with eventually present magnetic configurations.

μSR measurements have been performed in the β-phase rare-earth dideuterides $HoD_{2.0}$, $HoD_{2.12}$, $DyD_{2.0}$, $DyD_{2.13}$. For the two Ho compounds and for $DyD_{2.0}$ the temperature dependences of the zero-field (ZF), longitudinal-field (LF), and transverse-field (TF) relaxation rates λ_i are similar [1]. One can define a "critical" temperature at which a rate λ_i peaks. This temperature T_{ci} roughly corresponds to the magnetic transition temperature found in bulk magnetic measurements [2, 3]. Above T_{ci}, where practically the full μSR-signal asymmetry is observed, the rates λ_i are described by $\alpha_i|T - T_{ci}|^{-\beta_i} + \lambda_{0i}$. Below T_{ci} only a reduced fraction of the muons is visible in the signal.

For $DyD_{2.13}$ zero-field and low transverse field measurements show that already below $\sim$ 300 K only a reduced and variable fraction of the muons contribute to the observable signal. At temperatures below $\sim$ 10 K a weak and rapidly damped spontaneous oscillation at a frequency of $\approx$ 90 MHz is found in the ZF data, e.g., Fig. 1. The frequency is practically temperature independent, whereas the large relaxation rate increases for $T > 6$ K and the signal is lost above 10 K, Fig. 2. The asymmetry (obtained tentatively from a simple exponential fit) is more or less constant and amounts to 4–6%, corresponding to a fraction of about 1/3 of the muons (powder average, ZF signal).

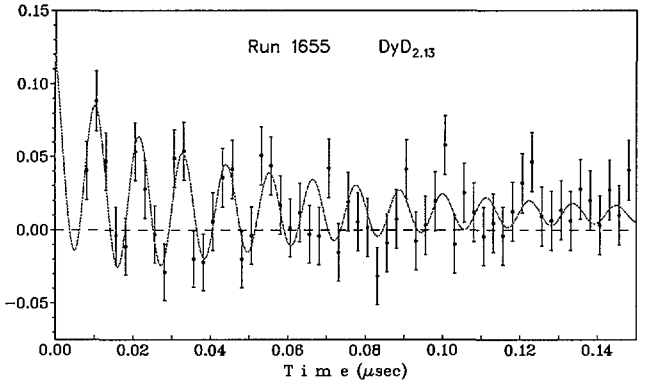

Figure 1: $DyD_{2.13}$, ZF data at 5 K. A spontaneous 89.2(7) MHz oscillation is visible at the beginning of the spectrum.

In the $DyD_{2.13}$ sample, neutron diffraction studies show no magnetic long-range order but indicate short-range ordered domains of unknown magnetic structure for T below 4–6 K [3]. In $DyD_{2.0}$, a nearly commensurate magnetic modulation, close to the commensurate structure with a period $4a_0/\sqrt{11}$ along [113], with the magnetic moment on the Dy ion oriented along [001], is determined for $T \leq 3.5$ K [3].

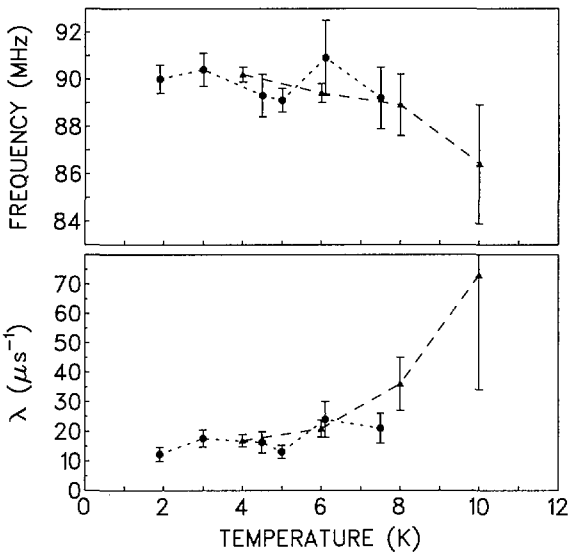

Figure 2: Temperature dependence of the oscillating signal in the ZF $DyD_{2.13}$ data.

Tentatively one postulates, for a simple model calculation, the commensurate structure mentioned above, close to the effective incommensurate modulation seen in $DyD_{2.0}$, around the μ^+. This structure has to be short-range ordered to stay compatible with the bulk measurements in $DyD_{2.13}$. With the model one calculates for one half of the octahedral μ^+ sites a single non-zero field value, and a field zero for the other half of the octahedral μ^+ positions. The magnetic moment on the Dy ion would have to be $|\mu| = 1.6\ \mu_B$ to yield the observed μ^+-precession frequency of 90 MHz. This is even more reduced (because of magnetic short-range order alone) with regard to the estimated $|\mu| = 3.5(5)\ \mu_B$ from neutron diffraction measurements in $DyD_{2.0}$ [3], which was already strongly quenched from the free-ion value of 10 μ_B by the cubic crystal field.

In a transverse field of 0.2 T the Knight shift K_μ of the μSR signal in $DyD_{2.13}$ has been measured as a function of T in the range 100–300 K. This dependence can be discussed in terms of the magnetic susceptibility of the compound.

REFERENCES

[1] For the previous measurements see F. N. Gygax *et al.*, PSI Scientific Report **1998**, Vol. I, 84.

[2] P. Vajda *et al.*, Phys. Rev. **B 57**, 5830 (1998).

[3] P. Vajda *et al.*, Phys. Rev. **B 55**, 3028 (1997).

MAGNETISM IN TETRAGONAL $La_{2-x-y}RE_xSr_yCuO_4$

H.-H. Klauß[1], *W. Kopmann*[1], *D. Baabe*[1], *D. Mienert*[1], *M. Birke*[1], *H. Luetkens*[1], *F. J. Litterst*[1], *M. Hücker*[2], *B. Büchner*[2]

RA-93-05, BRAUNSCHWEIG[1] – KÖLN[2]

In this project we study the physics of the LTT phase of doped La_2CuO_4 which turns out to be very different from the LTO phase. This might lead to a better understanding of superconductivity in the cuprates. Surprising effects like static stripe order and suppressed superconductivity have been found. These observations could become helpful for a better understanding of superconductivity in the cuprates. μ^+SR as a method to observe local magnetic order has played an important role in these investigations, e.g. the existence of magnetic order in $La_{2-x-y}RE_xSr_yCuO_4$ with $y \approx 0.15$ has been proven by this project and the magnetic phase diagram of the LTT phase has been established.

In 1998 we have investigated single crystals of $La_{1.8-y}Eu_{0.2}Sr_yCuO_4$ with $y = 0.08$, $y = 0.125$ and $y = 0.15$. Except of $y = 0.125$, the saturations frequencies and magnetic ordering temperatures are in good agreement with previously measured polycrystalline samples.

When rotating the sample relative to the initial direction of the muon spin, the intensity ratio between the precessing and non-precessing signals changes. For $y = 0.15$ the local magnetic field at the muon site is mainly oriented perpendicular to the c axis (Figure 1). As expected for the magnetic structure of the stripe order, no difference between (100) || beam and (110) || beam is visible.

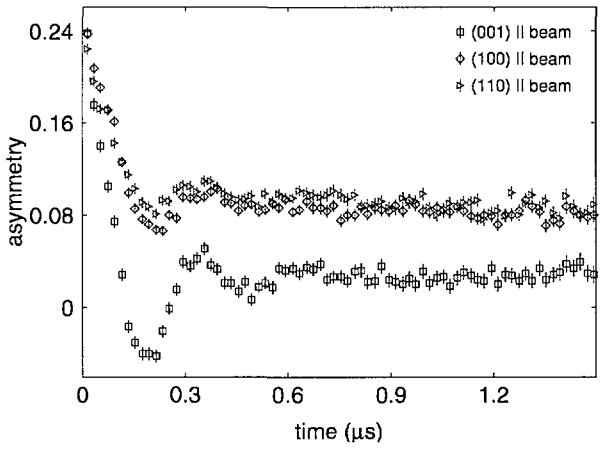

Figure 1: Asymmetry plot of single crystalline $La_{1.65}Eu_{0.2}Sr_{0.15}CuO_4$ at $T = 8$K in different orientations

Results in 1999

We performed ZF-measurements along different crystal axes on a new single crystal with $y = 0.0$ at 2 K. The aim was to compare the anisotropy of the internal field between the antiferromagnetic long range ordered and the stripe ordered phases. Figure 2 shows some obtained spectra. In this case the local magnetic field at the muon site is mainly oriented perpendicular to the a-b-diagonal with a larger component along the c-axis. Surprisingly, a second and third precession signal with much smaller amplitudes and frequencies of 1.4 and 3.5 MHz are found in addition to the usual 4.8MHz signal known from undoped LSCO (Figure 3). These lines arise either from structural inhomogenities (small changes of the muon site in the direct vicinity of an Eu-dopand) or from spin modulations already present in the AFM regime.

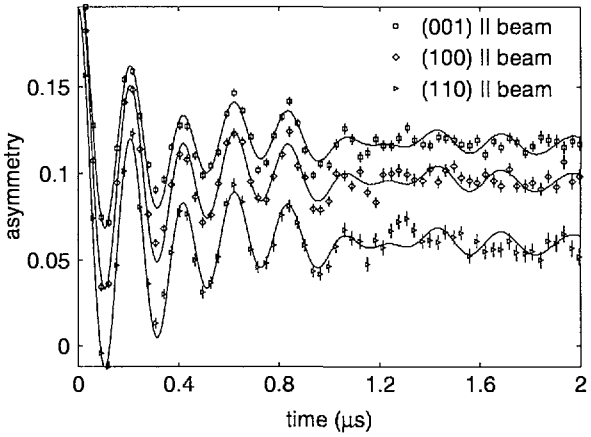

Figure 2: Asymmetry plot of single crystalline $La_{1.65}Eu_{0.2}CuO_4$ at $T = 2$K in different orientations

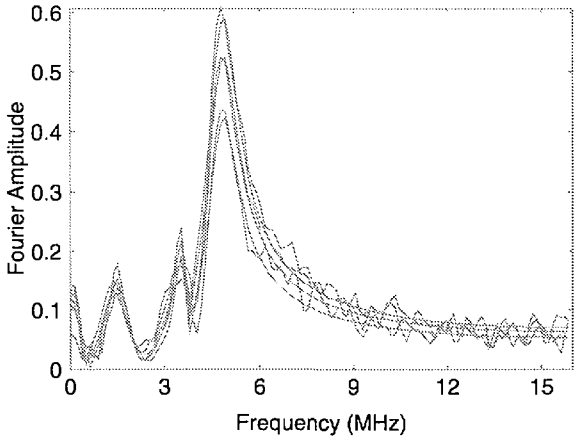

Figure 3: ZF Frequency spectrum of single crystalline $La_{1.65}Eu_{0.2}CuO_4$ at $T = 2$K in (001), (100) and (110) orientation

GIANT OXYGEN ISOTOPE EFFECT ON THE SPIN GLASS TRANSITION IN $La_{2-x}Sr_xCu_{1-z}Mn_zO_4$ AS REVEALED BY MUON SPIN ROTATION

A. Shengelaya[1], *Guo-meng Zhao*[1], *C. M. Aegerter*[1], *K. Conder*[2], *I. M. Savić*[1], *H. Keller*[1]

RA-90-07, ZÜRICH[1] – ETH ZÜRICH[2]

There is increasing evidence that a strong electron-phonon coupling is present in cuprates [1], which may lead to the formation of polarons (bare charge carriers accompanied by local lattice distortions) [2]. Several independent experiments have demonstrated that superconductivity and the underlying lattice vibrations are intimately linked. On the other hand, little is known about the influence of the electron-phonon interaction on magnetism in cuprates. Conventional theories of magnetism neglect atomic vibrations; the atoms are generally considered as infinitely heavy and static in theoretical descriptions of magnetic phenomena, so there should be no isotope effect on magnetism. However, if charge carriers are polaronic, i.e., nuclear and electronic motions are no longer decoupled, one might expect isotope effects on magnetic properties. The question is whether such an isotope effect exists in the cuprates.

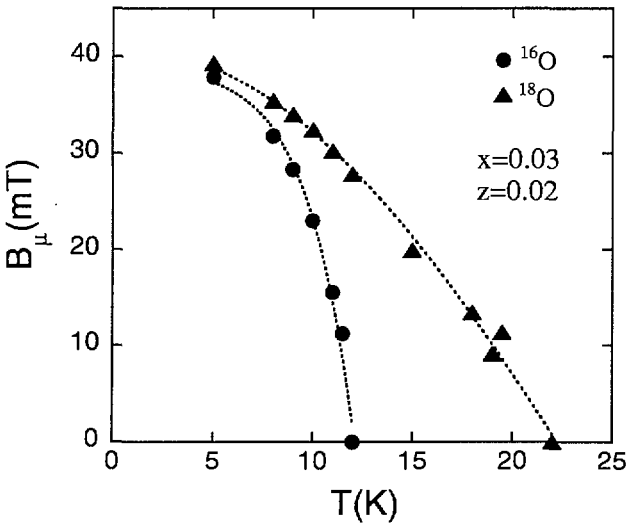

Figure 1: Temperature dependence of the internal magnetic field at the muon site B_μ for the ^{16}O and ^{18}O samples of $La_{1.97}Sr_{0.03}Cu_{0.98}Mn_{0.02}O_4$. Dotted lines are guides to the eye.

In order to answer this question we performed studies of the oxygen-isotope effect on the low temperature magnetism in $La_{2-x}Sr_xCu_{1-z}Mn_zO_4$ (x = 0.03,0.05; z = 0, 0.02) using the zero-field μSR technique. These samples are in the so-called cluster spin glass regime. The pair of samples with different oxygen isotopes ^{16}O and ^{18}O were mounted on the two sides of the sample holder. This allows one to switch between the two isotope samples by rotating the sample holder without removing it from the cryostat, so the two isotope samples can be measured at the same experimental conditions.

At low temperatures in all studied samples we observed damped oscillations due to muon-spin precession in local magnetic fields. A clear oscillation observed in ZF-μSR spectra implies that the muons sense a well defined internal magnetic field, in agreement with previous μSR measurements [3]. Fig.1 shows the internal magnetic fields B_μ for the two oxygen isotope (^{16}O and ^{18}O) samples (x = 0.03, z = 0.02) as a function of temperature. One can see that the spin glass freezing temperature T_g is strongly isotope dependent. The T_g of the ^{18}O sample is 10 K higher than that of the ^{16}O sample. This results in a huge value of the oxygen isotope exponent for the spin glass freezing temperature: $\alpha_{T_g} = -d\ln T_g/d\ln M$ = - 6.0(7), which is the largest *negative* oxygen isotope exponent ever measured for any phase transition temperature. These novel isotope effects clearly demonstrate a strong effect of lattice vibrations on magnetism in cuprates which can be explained taking into account the polaronic nature of the charge carriers [4].

REFERENCES

[1] Proc. Int. Workshop on *Anharmonic Properties of High-T_c Cuprates*, edited by D. Mihailovic, G. Ruani, E. Kaldis, and K. A. Müller), 118-146 (World Scientific, Singapore, 1994).

[2] A. S. Alexandrov and N. F. Mott, Int. J. Mod. Phys. **8**, 2075 (1994).

[3] A. Weidinger, Ch. Niedermayer, A. Golnik, R. Simon, E. Recknagel, J. I. Budnick, B. Chamberland, and C. Baines, Phys. Rev. Lett. **62**, 102 (1989); Ch. Niedermayer, C. Bernhard, T. Blasius, A. Golnik, A. Moodenbaugh, and J. I. Budnick, Phys. Rev. Lett. **80**, 3843 (1998).

[4] A. Shengelaya, Guo-meng Zhao, C. M. Aegerter, K. Conder, I. M. Savić, and H. Keller, Phys. Rev. Lett. **83**, 5142 (1999).

MUON-SPIN ROTATION STUDY OF THE MAGNETIC CORRELATIONS IN $La_{2-x}Ca_{1+x}Cu_2O_{6+d}$ SUPERCONDUCTORS

P. W. Klamut[1], *B. Dabrowski*[1], *R. Dybzinski*[1], *Z. Bukowski*[1], *A. Shengelaya*[2], *R. Khasanov*[2], *S. Dottinger*[2], *H. Keller*[2],

RA-97-12, NORTHERN ILLINOIS[1] – ZURICH[2]

The interplay between superconductivity and magnetic order in the high temperature superconductors (HTSC) has been widely studied by the variety of experimental techniques. The muon spin rotation (mSR) technique is a unique tool that can probe short and weak magnetic correlations existing on the time scale longer than about 1 ns. In addition, by investigating of the magnetic field distribution in superconducting mixed state, one can probe supercoducting properties such as the penetration depth.

We have investigated the series of $La_{2-x}Ca_{1+x}Cu_2O_6$ (x=0.12, 0.16, 0.22; T_c=44, 46, 55 K, respectively) superconductors. What makes $La_{2-x}Ca_{1+x}Cu_2O_6$ system unique and attractive among other HTSC is the simplicity of its crystal structure with only one Cu site with a five-fold pyramidal coordination of oxygen. The double- CuO_2 planes are separated by a simple atomic layer similar to the intermediate region characteristic of $La_{2-x}M_xCuO_4$ (M=Sr, Ca, Ba). Therefore, the compound can be expected to provide important information on the intrinsic properties of the superconductivity of CuO_2 planes. Ansaldo et al. in [1] reported ZF-mSR oscillations for nonsuperconducting $La_2SrCu_2O_{6+d}$ but also for a $La_2CaCu_2O_{6+d}$ system in which the superconducting minority phase was simultaneously detected.

In order to ensure better homogeneity of the material we have synthesized samples via citrate pyrolysis technique. Solid state synthesized x=0.16 sample was also measured in order to investigate the effect of material's homogeneity on its properties. The results of our transverse-field (TF) and zero=field (ZF) mSR measurements performed in the temperature range 1.3-80 K (beam line ϖM3) can be summarized as follows [2] :

High damping rate of the asymmetry observed below 5 K in ZF experiment for solid-state synthesized superconductor suggests the presence of an inhomogeneous magnetic state with a broad distribution of local fields or can be attributed to critical spin fluctuations, presumably freezing into static order at the temperature lower than accessible in this experiment. From the observed asymmetry at t=0 we deduce that almost all muons stopping in the sample participate in the process, implying that the observed behaviour can not be attributed to minority phases and represents an intrinsic property of the material. For wet-chemistry prepared samples we do not observe oscillations or fast damping of ZF asymmetry at low temperatures. The temperature dependencies of the depolarization rate ς(T) (measured at $H_{ext} = 200mT$), diverge up for temperatures lower than 6 K. The differences in magnetic behaviour observed in mSR experiments for differently synthesized samples occur despite of similar superconducting properties measured by resistivity and magnetization measurements. The SQUID measurements confirmed the presence of bulk superconductivity (about 30% of volume) for all investigated samples. We conclude that the anticipated increase in La/Ca inhomogeneity for solid state synthesis made material has a profound effect in producing magnetic correlations, which are presumable dynamic in character.

For wet chemistry prepared samples we extrapolated to 0 K the plateau observed in ς(T) dependencies between 20 and 10 K. Extrapolated values of the superconducting contribution to the depolarization rate ς(T=0 K) are presented in Fig. 1 and compared to the generic behaviour expected for underdoped superconductors [3]. The values match well with the universal Uemura line shown in Fig. 1, which scales T_c with the density of superconducting quasiparticles (ς is proportional to $n_s/^*m$, where $^*m$ is the effective mass) [3].

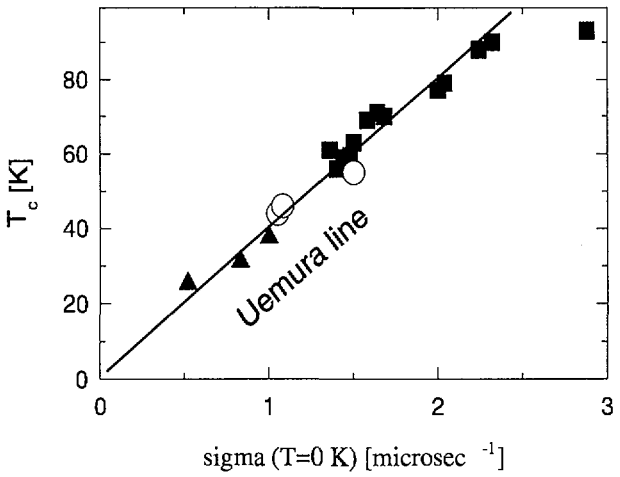

Figure 1: T_c vs. ς(0) for $La_{2-x}Ca_{1+x}Cu_2O_6$ (open circles). Squares represent literature data for $YBa_2Cu_3O_{7-x}$, triangles for $La_{2-x}Sr_xCuO_4$.

This work was supported by the US NSF Science and Technology Center for Superconductivity under grant No. DMR-91-20000 and Swiss National Science Foundation.

REFERENCES

[1] E.J. Ansaldo et al., Phys. Rev. **B 46**, 3084 (1992).

[2] P.W. Klamut et al., J. Appl. Phys., in press.

[3] Y.J. Uemura et al., Phys. Rev. Lett. **62**, 19 (1989);
Y.J. Uemura et al., Phys. Rev. Lett. **66**, 2665 (1991).

μSR STUDY OF CATION DISORDER EFFECTS IN A_2CuO_4 SUPERCONDUCTORS

J.P. Attfield[1], *A. Lappas*[2], *J.A. McAllister*[1], *K. Prassides*[2], *S. Rouzière*[2]

RA-99-12, CAMBRIDGE[1] – SUSSEX[2]

Recent studies on $Ln^{3+}_{2-x}M^{2+}_xCuO_4$ (Ln= La, Nd; M= Ca, Sr, Ba) in which x is fixed at the optimum x= 0.15 doping level have shown that variations in superconducting and other physical properties can be described by a simple statistical description of the A (=Ln/M) cation distribution [1]. Both the mean A cation radius, $< r_A >$ and the variance in the A cation size, $\sigma^2 = < r_A^2 > - < r_A >^2$ are found to have significant effects. The superconducting critical temperature, T_c decreases linearly with increasing σ^2 at a constant value of $< r_A >$. Susceptibility and transport measurements show that the carrier densities in both the normal and superconducting states decrease with increasing σ^2, suggesting that cation size disorder leads to trapping of holes although the total concentration remains constant at 0.15 per Cu atom. In addition, the structural transition between the high temperature tetragonal (HTT) and low temperature orthorhombic 1 (LTO1) shows a strong linear increase with σ^2. High σ^2 samples were found to show further transitions to the low temperature orthorhombic 2 (LTO2) and low temperature tetragonal (LTT) superstructures at low temperatures.

In the present series of ZF-μSR experiments, we studied five copper oxide compositions with fixed $< r_A >$ at 1.223 Å and fixed doping level at 0.15: $La_{1.85}Sr_{0.15}CuO_4$ (**1**), $La_{1.85}Sr_{0.09}Ca_{0.034}Ba_{0.026}CuO_4$ (**2**), $La_{1.85}Sr_{0.016}Ca_{0.074}Ba_{0.06}CuO_4$ (**3**), $La_{1.75}Nd_{0.1}Ca_{0.064}Ba_{0.086}CuO_4$ (**4**), and $La_{1.75}Nd_{0.15}Ca_{0.056}Ba_{0.094}CuO_4$ (**5**). The A-site cation radius variance, σ^2 increases monotonically from 0.0006 Å^2 for (**1**) to 0.0033 Å^2 for (**5**) across the series.

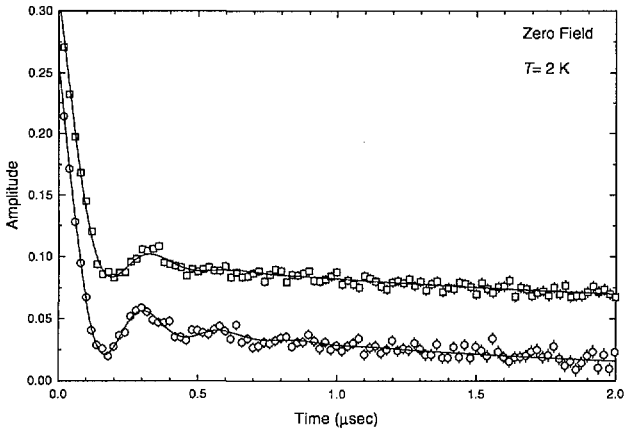

Figure 1: Time evolution of the zero-field μ^+SR spin polarisation at 2 K for samples (**4**) (squares) and (**5**) (○).

The ZF-μSR measurements reveal the development of long range magnetic order in part of the sample at low temperatures for compositions (**3**), (**4**), and (**5**) through the appearance of a rapidly-relaxing oscillating signal (Fig. 1). The oscillating component is best modeled by a Bessel function implying a modulated magnetic structure. The volume fraction of the LRO part of the sample grows across the series with increasing values of σ^2, while at the same time the freezing temperature, T_f also increases (Fig. 2). We note that for all three samples the magnitude of the local static field at the muon site appears to saturate towards the same value ($B_\mu \approx$ 265 G for (**5**) at 2 K). Multicomponent nature of the sample was also revealed for (**2**) but this time, no evidence for LRO was found. Instead a rapidly-relaxing non-oscillating component (λ= 2.5 μs^{-1} at 1.7 K) appears, implying a disordered form of magnetism for this low σ^2 sample. Composition (**1**) was the only one remaining single phase at low temperatures.

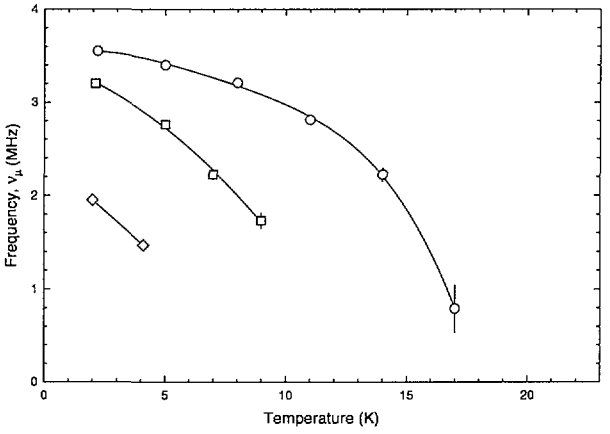

Figure 2: Temperature dependence of ZF precession frequency, $\nu_\mu(T)$ for samples (**3**) (◇), (**4**) (squares) and (**5**) (○).

In conclusion, the results provide a clear picture of microscopic phase separation becoming more pronounced with increasing A-site cation disorder, σ^2. For very small σ^2, no evidence of phase separation is found. As σ^2 increases, a rapidly fluctuating magnetic component appears in part of the sample volume. This further grows and slows down, until it evenually gives rise to magnetic LRO of modulated nature. Thus as local moment magnetism develops in part or the whole of the sample, T_c and the superconducting fraction go gradually towards zero. The results are strongly reminiscent of the development of charge stripes, as it has been observed before for the x= 1/8 composition of the 214 family [2].

REFERENCES

[1] J.P. Attfield, A.L. Kharlanov, J.A. McAllister, Nature **394**, 157 (1998); J.A. McAllister, J.P. Attfield, Phys. Rev. Lett. **83**, 3289 (1999).

[2] A. Lappas *et al.*, Hyperfine Interactions **105**, 101 (1997); B. Nachumi *et al.*, Phys. Rev. **B 58**, 8760 (1998).

STUDY OF PHASE SEPARATION IN La_2CuO_{4+x}

V. Yu. Pomjakushin[1,2], A. A. Zakharov[3], A. M. Balagurov[2], F. N. Gygax[4], A. Schenck[4], A. Amato[5], D. Herlach[5], V. N. Duginov[3], A. N. Ponomarev[2]

RA-95-10, LNS/ETHZ[1] – JINR DUBNA[2] – KI MOSCOW[3] – IPP/ETHZ[4] – PSI[5]

The problem of the coexistence of superconductivity and static antiferromagnetism in La_2CuO_{4+x}-based cuprates is now understood by finding more and more evidences of microscopically phase separated (PS) state. However, it is not clear whether the formation of spatial inhomogeneity is essentual or harmfull for the superconductivity [1]. In Ref.[2] the authors argue that the formation of antiferromagnetic (AFM) stripes separated by charged metallic regions in $La_{1.6-x}Nd_{0.4}Sr_xCuO_4$ competes with the appearance of the superconductivity. In Refs. [3, 4] in the oxygen doped La_2CuO_{4+x} the authors found a surprising coincidence of the superconducting and magnetic transition temperatures.

A specific feature of the La_2CuO_{4+x} series of crystals which we study [3] is the low oxygen mobility (LOM) which results in the absence of a macroscopic phase separation by oxygen diffusion for the crystals with $x \leq 0.03$ as distinct from the $x < 0.01$ for "canonical" samples, possessing high oxygen mobility. When $x > 0.03$ the LOM-crystals are also macroscopically phase separated, however the stoichiometries of the oxygen rich and poor phases, determined from the orthorhombic strains, are different from "canonical" ones. One "canonical" crystal, which possess high oxygen mobility with x=0.02 (labeled N1) was also studied for comparison. Table 1 shows the summary of the La_2CuO_{4+x} crystals studied. Decreasing the temperature the LOM-crystals with $x > 0.03$ first undergo the AFM-transition and then the transition to LTMS. The LTMS does not give the magnetic Bragg peaks at the commensurate positions of the (100) type, as distinct from the high temperature AFM state [3]. The transition to the LTMS was observed by μSR as the increasing (or appearance in non-PS crystals) of the AFM-fraction of the crystal and by the divergence of the Cu-spin correlation time τ_c (Fig. 1). Neither the muon spin precession frequency nor the relaxation rate are changed at T_{LTMS}, implying that AFM structure of LTMS is similar to one of La_2CuO_4.

Table 1: La_2CuO_{4+x} crystals studied. The M4 and L2 crystals are denoted as A and B in Ref. [3].

Crystal	x	T_c	T_N	T_{LTMS}
m4	0.02	15	-	15 AFM
L1	0.03	10	-	8 spin glass
L2	0.04	25	250	25 AFM
N52	0.033	25	100	$\leq$ 25 AFM
L5	$\sim$ 0.04	25	140	20 AFM
high oxygen mobility "canonical" crystal				
N2	0.02	35	250	no

In conclusion, the magnetic ordering in superconducting La_2CuO_{4+x} single crystals with low oxygen mobility was studied via μSR spectroscopy and neutron diffraction. Regardless of the presence or absence of the macroscopic phase separation, an antiferromagnetically or spin-glass ordered state appears at low temperature concomitantly with the onset of superconductivity with the transition temperatures from 8K to 25K. We suggest that a microscopic spatial phase separation, which occur in the vicinity of T_c, is responsible for this effect.

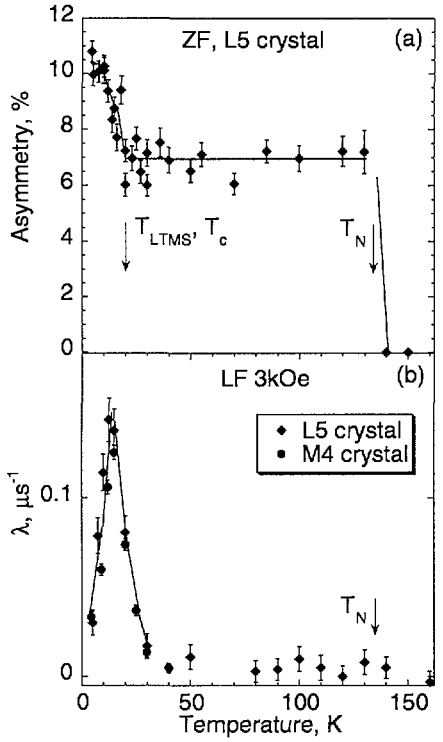

Figure 1: **(a):** Asymmetry of the spontaneous muon spin precession as a function of temperature in La_2CuO_{4+x} (L5 crystal) in zero external field. The spontaneous muon spin precession frequency $f(T \to 0) = 5.4$ MHz. **(b)** Longitudinal muon spin relaxation rate $\lambda \propto \tau_c$ measured in a longitudinal field $H_L = 3$ kOe.

REFERENCES

[1] Arthur P.Ramirez, Nature **399**, 527 (1999).

[2] J. M. Tranquada, J. D. Axe, N. Ichikawa, et al., Phys. Rev.Lett. **78**, 338 (1997).

[3] V. Yu. Pomjakushin, A. A. Zakharov, A. M. Balagurov et al., Phys. Rev. **B 58**, 12350 (1998).

[4] Y. S. Lee, R. J. Birgeneau, M. A. Kastner, et al., Phys. Rev. **B 60**, 3643 (1999).

HOLE DYNAMICS AND LOCALIZATION IN HIGH-TEMPERATURE SUPERCONDUCTORS

H.-H. Klauß[1], *W. Kopmann*[1], *D. Baabe*[1], *D. Mienert*[1], *M. Birke*[1], *H. Luetkens*[1], *F. J. Litterst*[1], *M. Hücker*[2], *B. Büchner*[2]

RA-98-10, BRAUNSCHWEIG[1] – KÖLN[2]

Susceptibility and resistivity measurements have shown that Zn-doping of high T_C superconductors strongly localizes the charge holes introduced by Sr doping. This influences in the magnetic regime the Néel temperature T_N and the sublattice magnetization curve and at higher hole doping superconductivity is strongly suppressed. The advantage of μ^+SR in comparison to macroscopic methods in the examination of magnetic order is the easy accessibility of the static sublattice magnetization via the spontaneous muon spin precession frequency. In addition in the antiferromagnetic compounds the spin fluctuations below the magnetic ordering temperature measured via the longitudinal relaxation rate can be used to study the charge carrier dynamics.

In 1999 we have continued our μSRexperiments on two series of samples with fixed Sr-doping and variable Zn-doping and established a phase diagram for a stongly localized series with fixed Zn-doping and a variable Sr-doping.

$La_{1.983}Sr_{0.017}Cu_{1-z}Zn_zO_4$

We have investigated three additional Zn concentrations z = 0.02, 0.04, 0.075 since already in this low doping regime strong localization effects occur. For these low Zn concentrations, the hole localization caused by Zn doping leads to an increase of T_N, for higher dopings, however, this effect is overcompensated by the decrease of T_N due to spin dilution.

The hole localization effect is clearly visible as a suppression of the low temperature increase of the sublattice magnetization at 20 K and as a peak in the longitudinal relaxation rate. This T_1 relaxation rate maximum between 6 and 15 K is gradually suppressed by the Zn doping (Fig. 1) and disappears for z=0.075.

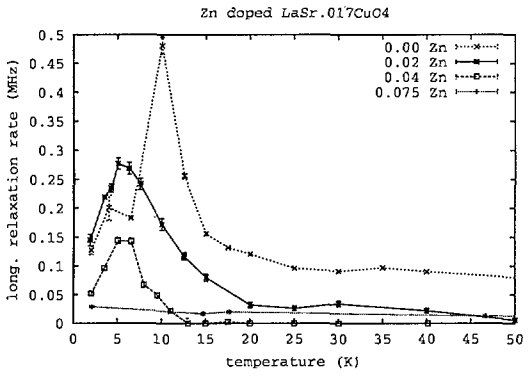

Figure 1: Temperature dependence of the longitudinal relaxation rate in $La_{1.983}Sr_{0.017}Cu_{1-z}Zn_zO_4$ with $0 \leq z \leq 0.075$

$La_{1.979}Sr_{0.021}Cu_{1-z}Zn_zO_4$

The Sr concentration $x = 0.021$ is at the crossover from the AFM region to the cluster spin glass region. The 1998 experiments on low Zn dopings of z= 0.005, 0.02 and 0.04 have shown the strong increase of T_N from 18 to 100 K but no complete suppression of the charge localization effect. This year we extended the measurements to higher Zn doping z= 0.006, 0.10, 015 and 0.20. The evolution of $\nu(T)$ and $\lambda l(T)$ showed that a Zn concentration of $z = 0.10$ is neccessary to fully suppress any charge mobility effects in $\nu(T)$ and in the longitudinal relaxation rate.

$La_{2-x}Sr_xCu_{0.85}Zn_{.15}O_4$

To determine the electronic phase diagram of a strongly localized Cuprate system as a function of the charge carrier concentration we examined Sr concentrations between x=0.017 and 0.15 with a fixed Zn doping of z= 0.15 in ZF μSR .

Only up to x=0.06 we found long range magnetic order with spontaneous spin precession. At higher hole doping only a weak but quasistatic relaxation has been found below $\approx$ 6 K This may be caused by small magnetic clusters distributed very diluted in the Cu-O_2-planes, similar to the cluster spin glass (CSG) known from $La_{2-x}Sr_xCuO_4$.

The antiferromagnetic regime is extended to a higher Sr doping of x=0.06 by the charge localization effect of the 15 % Zn doping. At higher Sr concentrations a very diluted cluster spin glass phase is present and supercondictivity is completely suppressed.

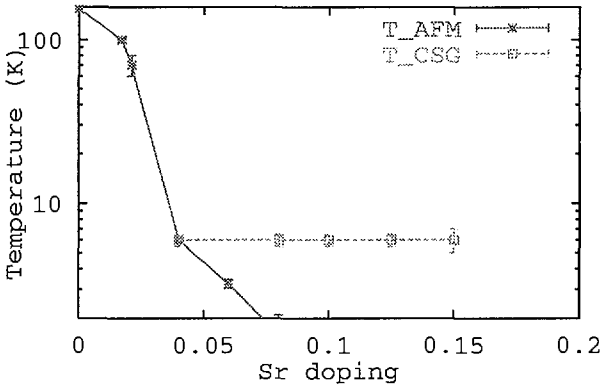

Figure 2: Phasediagram of $La_{2-x}Sr_xCu_{0.85}Zn_{.15}O_4$: long range AFM T_{AFM}, cluster spin glass T_{CSG}

μSR INVESTIGATION OF THE MAGNETIC PHASE DIAGRAM OF $Bi_{2.15}Sr_{1.85}CaCu_2O_{8+\delta}$

S. L. Lee[1], *F. Y. Ogrin*[1], *C. M. Ager*[1], *H. Keller*[2], *T. Riseman*[3], *E. M. Forgan*[3], *F. L. Pratt*[4]

RA-94-04, ST-ANDREWS[1]-ZÜRICH[2]-BIRMINGHAM[3]-RIKEN-RAL[4]

One method to dramatically enhance the pinning in high-T_c materials is to irradiate them with high energy heavy ions. The ions are caused to penetrate the sample where they cause amorphous tracks of damage which act as extended anisotropic pinning defects. These columnar defects (CD) can act as particularly effective pins, particularly if their density is greater than that of the vortices. It is convenient to introduce the concept of the matching field B_Φ, which is the field at which the density of the vortices equals that of the CD. The influence of CD on vortex behaviour was investigated theoretically by Nelson and Vinokur [1, 2], who mapped the system onto one of boson localisation in two dimensions. At low temperature and at fields $B < B_\Phi$, a 'Bose-glass' (BG) phase is predicted, with flux lines localised on the columnar pins, with a sharp phase transition at higher temperature to an entangled liquid of vortex lines.

A great deal of experimental data has been interpreted within the Bose glass theory, yet one can question whether the existence of a true Bose-glass phase is realistic in a CD sample. In reality several of the assumptions in the BG model are difficult to realise experimentally. In particular, even below B_Φ the positions of the vortices may not be random, but there may exist spatial correlations in a plane perpendicular to the field, which is demonstrated in numerical simulations by Täuber and Nelson [3]. These correlations are believed to originate from two sources: firstly, a random distribution of defects will naturally contain some areas where they are closely spaced, such that vortex-vortex interactions will make it energetically unfavourable for all of them to be occupied, even at the matching field. Secondly, for a sample cooled in an applied field at which vortex-vortex interactions are significant (strongly overlapping vortices) at the depinning temperature, the vortices will already be correlated as they enter the irreversible region. As they become localised onto tracks, significant vortex-vortex correlations are thus frozen in [4]. This year we have carried out some muon experiments which throw light on these issues.

For a conventional vortex-line lattice $p(B)$ the shape of the μSR lineshape is highly asymmetric (Fig. 1a), with a second moment given by $\langle \Delta B^2 \rangle = \frac{0.00371\Phi_o^2}{\lambda^4}$, where λ is the superconducting penetration depth [5]. For the case of an ideal Bose-glass system with perfect pinning and a field equal to the matching field, such that each vortex is trapped by a defect, the positions of the vortices would be random in a plane perpendicular to the applied field. In this case the width of the distribution is given by $\langle \Delta B^2 \rangle = \frac{B_{app}\Phi_o}{4\pi\lambda^2}$ [5]. These two extremes are illustrated in Fig. 1a, where we compare the numerically simulated lineshape for an ideal vortex lattice with that for a random distribution of rigid vortex lines. We also include an intermediate case, where we have taken the spatial distribution of vortices found in Monte Carlo simulations of an irradiated system [3], where vortex correlations have been allowed to develop for reasons discussed above.

In Fig. 1b we present a measured lineshape from a BSCCO sample which has been irradiated parallel to the c-direction to produce a matching field $B_\Phi = 100$ mT. The lineshape is compared with that from the simulations of Täuber and Nelson [3] in which vortex-vortex spatial correlations exist. There is clearly a fair correspondence between the two curves, indicating that the latter is a reasonable representation of the positional correlations in this system at low temperature, which are clearly not random. This indicates that caution must be exercised when trying to relate the predictions of Bose-glass theory to the behaviour of vortices in irradiated samples.

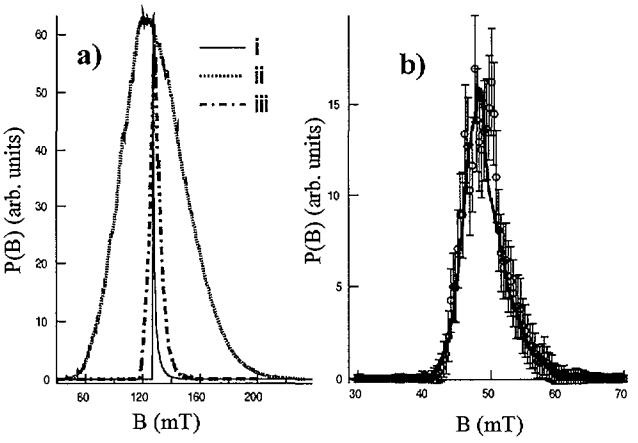

Figure 1: (a)Numerical simulations of the μSR lineshape for (i) an ideal triangular vortex lattice of lattice parameter $a = 0.67\lambda$, (ii) a random arrangement of vortices of with the same average density as in 1), and (iii) a vortex arrangement for a Monte Carlo simulation of rigid vortices in a CD matrix with $B \sim B_\Phi/2$. (b)A measure μSR lineshape for an irradiated BSCCO sample a matching field of 100 mT, after cooling in a field of 50 mT to a temperature of 5 K. The solid line is the result of a numerical simulation of the lineshape using the results of Monte Carlo simulations for similar conditions taken from ref. [3], using a penetration depth of 2000 Å.

REFERENCES

[1] V. M. Vinokur and D. R. Nelson, Phys. Rev. Lett. **68**, 12398 (1992).

[2] V. M. Vinokur and D. R. Nelson, Phys. Rev. **B 48**, 13060 (1993).

[3] U. C. Täuber and D. R. Nelson, Phys. Rev. **B 52**, 16106 (1995).

[4] A. E. Koshelev *et al.* Phys. Rev. **B 53**, R8855 (1996) .

[5] C. M. Aegerter and S. L. Lee, Appl. Mag. Res. **13**, 75 (1997).

μSR STUDY OF THE EFFECTS OF Li SUBSTITUTION IN $YBa_2Cu_3O_{6+x}$

P. Mendels[1], *A. McFarlane*[1], *J. Bobroff*[1], *H. Alloul*[1], *N. Blanchard*[1], *A. Keren*[2], *G. Collin*[3], *J. Marucco*[4] *V. Guillen*[4]

RA-99-13, ORSAY[1] - TECHNION[2] - LLB[3] - LEMHE[4]

Substitution of impurities in the key CuO_2 planes of high T_c superconductors has proven to be an exceptionally powerful tool to study the novel electronic properties of these systems. On one hand, the case of Zn^{2+} and Ni^{2+} in $YBa_2(Cu_{1-y}M_y)_3O_{6+x}$, as in other cuprates, have been carefully studied as they both substitute Cu^{2+} within these planes without noticeably changing hole-doping[1]. On the other hand Ca^{2+}/Y^{3+} substitution in $YBa_2Cu_3O_6$ induces hole doping and progressively destroys the magnetic state, leading to superconductivity for concentrations of the order of 20% Ca[2]. The Li^+/Cu^{2+} substitution in $YBa_2Cu_3O_{6+x}$ combines both interesting problems: possible doping in the AF state ($x = 0.0$) and scattering in the normal state. NMR and T_c measurements indeed proved that 50 to 70% Li substitutes into the CuO_2 planes with a similar depression of T_c as for Zn as well as local moments induced on the Cu surrounding an impurity.

- *Superconducting state*: The penetration depths at $T = 0$ were determined by field cooled TF measurements. Our results are gathered with the Zn case in Fig. 1 on the well-celebrated Uemura plot. The variation of sigma versus T_c with impurity concentration is the same as in the Zn case. Combining this observation with the striking similarity in the induced moments on Cu around the impurity[3], we conclude that magnetic moments induced around an impurity and unitary scattering leading to pair-breaking are 2 facets of the physics of spinless impurities substituted in the CuO_2 planes.

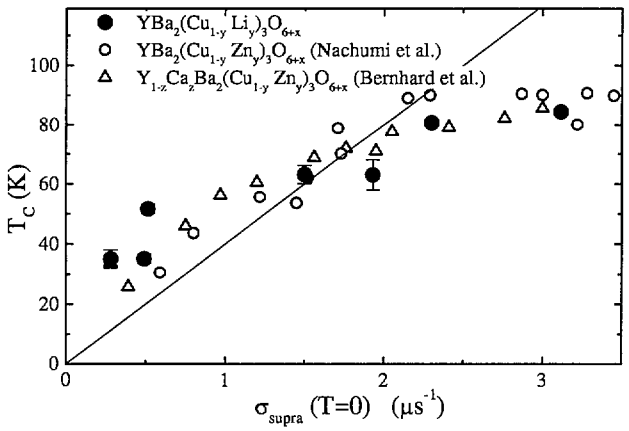

Figure 1: T_c versus the depolarization rate σ extrapolated at $T = 0$ (Uemura Plot) with our data (solid symbol) compared to existing ones [4][5]. The straight line is a fit to the data in pure underdoped samples.

- *Intermediate oxygen contents*: in the non-superconducting state which extends to higher x than in pure compounds, we have found a magnetic state below 10 K in the Li8% and 4% samples respectively. The Li4% concentration was studied in more detail between $x = 0.4$ and 0.6. At the base temperature of the GPS cryostat, ZF runs show a fast depolarization of the muon signal, due to static magnetism as proven by LF scans. The average internal field was found to be of the order of a few 100G, a value typical of the YBaCuO antiferromagnetic compound. No definitive conclusion regarding the degree of disorder of the magnetic state (antiferromagnetism versus dilute glass) could be drawn as 1.5 K is still too high as compared to the broad transition in most of our samples.

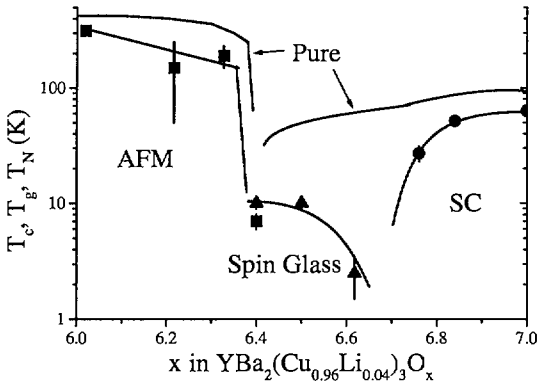

Figure 2: Sketch of the phase diagram for Li4% substitution

- *Antiferromagnetic phase*: $Li4\%O_6$, $Li2\%O_6$ and $Li4\%O_{6.2}$ samples were investigated using ZF measurements. This allows us to map up a sketch of the phase diagram for 4% Li substitution (Fig. 2). Furthermore, we investigated carefully the possibility of hole doping and therefore of hole localization by the trapping potential expected for Li^+ in a CuO_2 plane as in the case of Y^{3+}/Ca^{2+} substitution[2]. Unexpectedly, we did not find any sign of an associated $1/T_1$ divergence. Nor did we find a sizeable depression of T_N by Li substitution. This demonstrates that Li substitution in YBaCuO substantially differs from the case of La_2CuO_4 where Cu^{2+}/Li^+ substitution is similar to the La^{3+}/Sr^{2+} heterovalent substitution[6] and indicates that a hole might be strongly localized in the vicinity of an impurity in the AF state.

REFERENCES

[1] H. Alloul *et al.*, Phys. Rev. Lett. **67**, 3140 (1991).

[2] C. Niedermayer, Phys. Rev. Lett. **80**, 3843 (1998).

[3] J. Bobroff *et al.*, Phys. Rev. Lett. **83**, 4381 (1999).

[4] B. Nachumi *et al.*, Phys. Rev. Lett. **77**, 5421 (1996).

[5] C. Bernhard *et al.*, Phys. Rev. Lett. **77**, 2304 (1996); Phys. Rev. Lett. **80**, 205 (1998).

[6] J.L. Sarrao *et al.*, Phys. Rev. **B 54**, 12014 (1996).

LOCAL ORDER IN UNDERDOPED $YBa_2(Cu_{0.96}M_{0.04})_3O_7$, M = Al, Co

J. A. Hodges[1], *P. C. M. Gubbens*[2], *C. T. Kaiser*[2], *P. Dalmas de Réotier*[3], *A. Yaouanc*[3]

RA-98-15, CEA SACLAY[1] - TU DELFT[2] - CEA GRENOBLE[3]

We have compared the behaviour of $YBa_2Cu_3O_7$ when substituted, in turn, with equal amounts of Al or Co. Each ion substitutes at the Cu(1) or chain sites where each has the same valency. Each substitution decreases the doping level and lowers the superconducting transition temperature (T_{SC}) relative to the optimum value by essentially the same amount. One difference between the two substitutions is that Co^{3+} carries an intrinsic magnetic moment whereas Al^{3+} is diamagnetic. The aim of this study was to obtain further information concerning the observation that specific substitutions at the Cu(1) site introduce correlated magnetic moments at the Cu(2) sites within fully superconducting samples [1, 2].

The zero field μSR measurements for the sample with $Al_{0.04}$ (T_{SC} = 78 K) at 100 and 2.5 K are shown in Fig. 1. These were obtained using the MORE mode. The depolarisation is essentially the same at the two temperatures. It has the characteristic Kubo-Toyabe dependence showing it is controlled by the nuclear moments. The same dependence is also seen in unsubstituted $YBa_2Cu_3O_7$ [3]. The substitution of Al thus lowers T_{SC} without introducing any detectable (electronic based) magnetic moments into the sample.

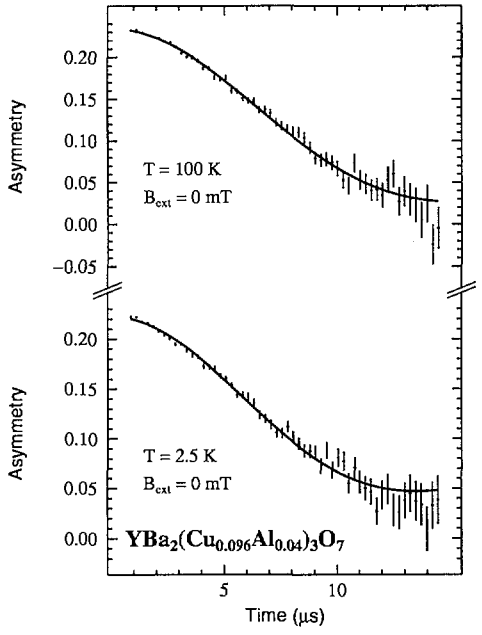

Figure 1: Muon depolarisation in superconducting $YBa_2(Cu_{0.96}Al_{0.04})_3O_7$. The solid lines are fits to a Kubo-Toyabe (nuclear origin) function.

The zero field data for the sample with $Co_{0.04}$ (T_{SC} = 73 K) at 200 and 30 K are shown in Fig. 2. For these, the MORE mode was not used. The depolarisation has the Kubo-Toyabe dependence (nuclear) at high temperatures whereas at low temperatures, additional depolarisation attributed to fluctuating correlated electronic based moments is visible. This contribution to the depolarisation becomes more pronounced as the temperature is further lowered and there is no evidence of any spin freezing transition down to 2.5 K. At 30 K, a small longitudinal field has a notable influence on depolarisation function as shown in Fig. 2.

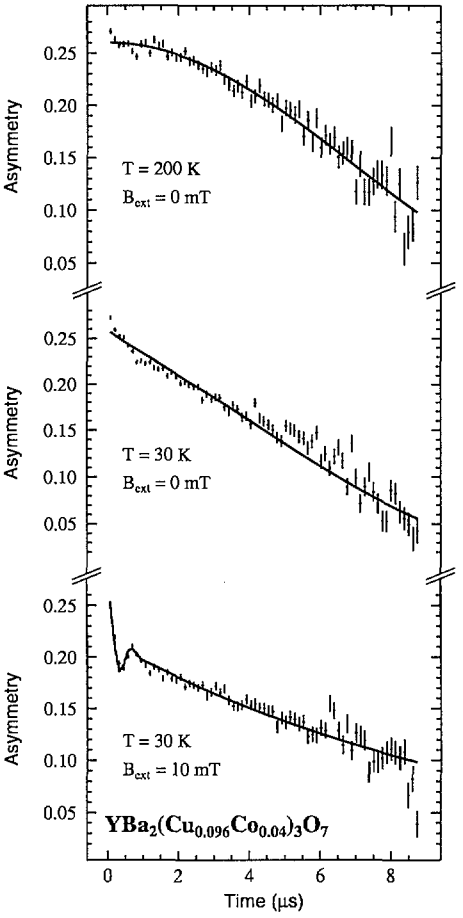

Figure 2: Muon depolarisation in superconducting $YBa_2(Cu_{0.96}Co_{0.04})_3O_7$. At 200K, the line is a fit to a Kubo-Toyabe (nuclear) function. At 30 K in zero field the line is a fit to a product of Kubo-Toyabe (nuclear origin) and stretched exponential (electronic) function. At 30 K in 10 mT (longitudinal), the line is a fit to a Kubo-Toyabe (electronic origin) function.

REFERENCES

[1] C. Vaast, J.A. Hodges, P. Bonville, A. Forget, Phys. Rev. **B 56**, 7886 (1997).

[2] M. Matsumura, Y. Takayanagi, H. Yamagata, Y. Oda. J. Phys. Soc. Jap. **63**, 2382 (1994).

[3] R. Kiefl et al., Phys. Rev. Lett. **64**, 2084 (1990).

EFFECT OF AN APPLIED CURRENT ON THE FLUX LINE LATTICE OF $NbSe_2$

A. Yaouanc[1], *P. Dalmas de Réotier*[1], *P. C. M. Gubbens*[2], *C. T. Kaiser*[2], *F. Lefloch*[1], *P. L. Gammel*[3], *A. Amato*[4]

RA-99-10, CEA GRENOBLE[1] – TU DELFT[2] – BELL LAB[3] – PSI[4]

A type II superconductor in a magnetic field is penetrated by a lattice (usually hexagonal) of quantized flux lines. An applied current imposes a Lorentz force on these lines, but motion of the lattice will always be inhibited by pinning to material defects. Beyond a certain critical current density, the lattice can break free of its pins and flow, dissipating energy and destroying superconductivity in the sample. The microscopic nature of this process is still poorly understood. Recent small angle neutron scattering (SANS) measurements on $NbSe_2$ have shown the existence of three regimes as a function of increasing current [1]: first, no motion; then plastic motion; and finally, at high velocities, a coherently moving flux crystal. These results verify theoretical predictions [2]. They have been obtained through the analysis of the longitudinal disorder (parallel to the applied magnetic field) of the flux line lattice (FLL) which is reflected in the width of the rocking curves [3].

Recently, muon spin rotation (μSR) experiments have been reported on $NbSe_2$ [4]. These experiments measured the magnetic field distribution induced by the FLL. They were performed without applying a current. Their purpose was to determine the two fundamental length scales of a superconductor in its mixed state: the magnetic penetration length and the radius of the vortex core. The work of Sonier *et al.* [4] has shown that the FLL field distribution in $NbSe_2$ is easily measured by μSR.

Since the SANS technique has shown that the magnetic disorder in the FLL can be manipulated by an applied current, the shape of the field distribution induced by the FLL should be influenced as well by a current.

We probed by the transverse field μSR technique the $NbSe_2$ sample previously used by the Bell Laboratories - Risø collaboration [1]. It is a crystal of 9 $\times$ 5 mm^2 fixed on a plate. Because we had to mask the electrical contacts, the effective area for exposure to the muon beam was only 4 $\times$ 3 mm^2. The mask was a plate covered by hematite powder. The field distribution in the hematite was supposed to be large enough to suppress the contribution from the sample holder to the measured spectra.

Two Fourier transforms of μSR spectra recorded at 1.9 K after cooling the sample in a field of 50 mT are presented in Fig. 1. The top panel is the spectrum obtained at zero current and the lower panel for a current of 2 A. The spectra reflect the field distribution from the flux line lattice and the hematite. The latter contribution is unfortunately relatively large. A study of our hematite mask showed that the peak centered around 6.8 MHz originates from the hematite. It has also an additional contribution at $\sim$ 5.95 MHz. A comparison of the two spectra shows that the peak due to the flux line lattice centered at $\sim$ 6.35 MHz is narrower for the spectrum recorded with 2 A. Therefore the current suppresses at least part of the magnetic disorder. According to the neutron work, 2 A is sufficient to anneal the flux line lattice. Therefore the muon and neutron results are consistent.

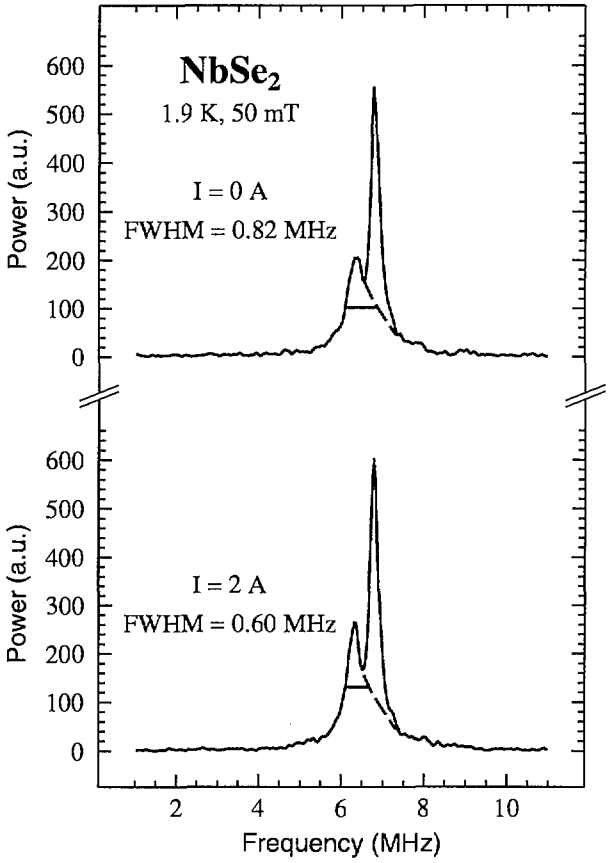

Figure 1: Fourier transforms of μSR spectra recorded at 1.9 K in a magnetic field of 50 mT applied along the c axis of $NbSe_2$. Notice that the peak at $\sim$ 6.35 MHz arising from the flux line lattice has an estimated full width at half maximum (indicated on the figure) which is smaller for the spectrum recorded with the current. This strongly suggests that the lattice is more ordered when a current is applied.

REFERENCES

[1] U. Yaron *et al*, Nature **376**, 753 (1995).

[2] A. E. Koshelev and V. M. Vinokur, Phys. Rev. Lett. **73**, 3580 (1994).

[3] U. Yaron *et al*, Phys. Rev. Lett. **73**, 2748 (1994).

[4] J. E. Sonier *et al*, Phys. Rev. Lett. **79**, 1742 (1997).

STRUCTURE OF THE SUPERCONDUCTING INTERMEDIATE STATE NEAR H = H_C

C. Baines[1], *V. S. Egorov*[2], *D. Herlach*[1], *G. Solt*[1], *U. Zimmermann*[1]

RA-99-09, PSI[1] – KURCHATOV[2]

Present knowledge on the intermediate (I) state of type 1 superconductors [1] has been based on magnetization and resistivity data, optical observations *at the sample surface* and measurements in small cavities of the sample. In the I state superconducting (S) and normal (N) domains with interfaces parallel to the external field $\boldsymbol{H}$ coexist for $(1-n)H_c < H < H_c$ (n = demagnetization factor). By taking into account also the energy of the interfaces for a sample thickness d, a field $H = H_{cI} < H_c$ lower than the critical is obtained for the $N-I$ transition,

$$H_{cI} \approx H_c[1 - 2\theta(\delta/d)^{1/2}]; \qquad \theta = \sqrt{\ln 2/\pi} \qquad (1)$$

($\delta \approx \xi - \lambda_L$, with the correlation and penetration lengths ξ and λ_L). The field B in the N domains is also predicted to be below H_c, with a lowest value $B = H_{cI}$ at the $N-I$ transition, and increasing towards H_c as H decreases [1]. Since at the transition, where the superconducting fraction ρ_S goes to zero, B cannot be homogeneous (at the domain interfaces $B = H_c$), a 'dip' is predicted for the average $\overline{B}$. For $\rho_S \to 0$, however, Eq.(1) is no longer valid, since the period of the assumed laminar structure, $D \approx (d\delta)^{1/2}/\rho_S$, becomes comparable or larger than the thickness d, making demagnetization in the N laminae non-uniform. In this limit thread-like 'antivortices' of S regions, instead of laminae, become energetically more favourable [2].

Experimentally, $H_{cI} < H_c$ was indeed observed in earlier magnetization data, but hysteresis made an accurate evaluation difficult. As to spectroscopic measurements of B *inside* the specimen (done exclusively by μSR [3, 4]), the $N-I$ transition was seen [4] only in an elongated sample set parallel to $\boldsymbol{H}$, thus not in a thin plate suited to test Eq.(1). Already the first μSR results [5] for a plane geometry showed interesting new features of the $N-I$ transition. The present data for the induction $\overline{B}$ in the N domains are seen in Fig.1.

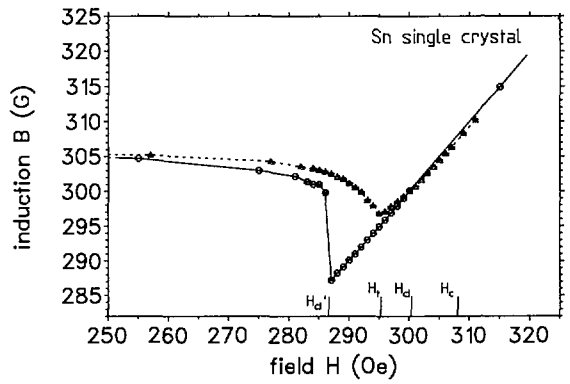

Figure 1: The $N-I$ transition at $T = 0.08$ K, $\boldsymbol{H}||[100]$, in decreasing (solid line) and increasing (dashed line) fields. For decreasing H the N state is 'undercooled' down to $H_{cI}' \approx 287$ G, while for increasing field the S-laminae transform into tubes at $H_t \approx 295$ G and the $I \to N$ transition occurs at $H_{cI} \approx 300$ G.

The plateau of B at $\approx 305.5 \pm 0.5$ G gives the 'spectroscopical' value of H_c (standard values are 308-309 G). The transition is not reversible: the N phase is undercooled and transforms by a jump of $\overline{B}$ to the I state, whereas on varying H upwards the transition is continuous, both routes being reproducible in repeated field runs. The predicted depression of H_c by Eq.(1) for $\delta \approx 10^{-4}$ cm and $d = 0.56$ mm is 4%, in reasonable agreement with H_{cI}/H_c in Fig.1. The dip in $\overline{B}$ as $\rho_S \to 0$ is due to the increase of the period of the laminar structure $D \approx (d\delta)^{1/2}/\rho_S$: with D comparable to the thickness d, the field in the broad N domains becomes inhomogeneous (H_c near the interfaces and $\approx H$ in the middle). This field inhomogeneity appears as a large peak in λ, seen

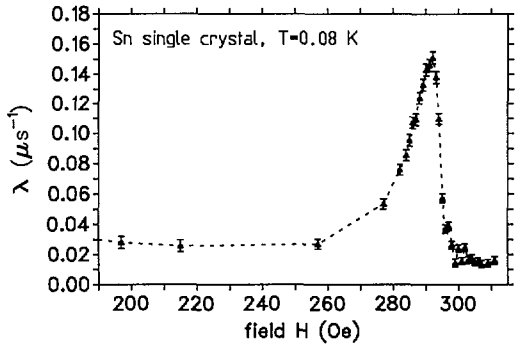

Figure 2: Damping rate λ vs H, upwards field scan. The peak coincides with the dip in $\overline{B}$ in Fig.1. The plateau value of λ in the I state is twice that in the N state, reflecting the inhomogeneity contribution from within the interfaces.

in Fig.2.

The cusp-like minimum in Fig.1 at $H = H_t \approx 295$ G marks the transition to the tubular S phase at $\rho_S \approx 0.04$ and, by comparing the energies of a thread-like S region and of a lamina, an estimate of the radius R_t of the 'antivortices' at the transition becomes possible.

REFERENCES

[1] M. Tinkham, Introduction to Supercoductivity, Mc-Graw, New York 1996.

[2] L. D. Landau, J. Phys. U.S.S.R. **7**, 99 (1943).

[3] M. Gladisch et al., Hyperf. Int. **6**, 109 (1979).

[4] V. G. Grebinnik, et al., Soviet Phys. JETP **52**, 261 (1980).

[5] V.S. Egorov, G. Solt, C. Baines, D. Herlach, U. Zimmermann, Physica **B**, to appear.

μSR STUDIES OF SUPERCONDUCTIVITY AND MAGNETISM IN ORGANIC MOLECULAR CRYSTAL SYSTEMS

S. J. Blundell[1], *F. L. Pratt*[1,2], *A. Husmann*[1], *I. M. Marshall*[1], *Th. Jestädt*[1], *B. W. Lovett*[1], *W. Hayes*[1], *R. M. Macrae*[2]

RA-93-06, OXFORD[1] – RIKEN[2]

Organic charge transfer (CT) compounds, formed by combining electron donor elements, such as TTF, with electron acceptor elements, such as TCNQ , provide an interesting variety of materials, with properties ranging from superconductivity and magnetism to spin and charge density waves and the quantum Hall effect. μSR has been used in studies of many of these materials, often revealing new insight into the delicate balance of interactions governing their electronic properties. When a muon is implanted as a magnetic probe in a charge transfer salt, it is usually in a diamagnetic state. Often it is not strictly necessary to know the exact location and nature of the muon state, e.g. when studying superconducting vortex lattice phenomena [1]. However any information that can be obtained about the muon binding sites in these materials and the parameters of the hyperfine interaction between the muon and the electronic states would significantly enhance the effectiveness of the muon as a quantitative probe of the electronic states. Crystals of the raw donor or acceptor molecules are insulators. This means that when muonium reacts with one of the molecules, the muonium electron remains localised on the molecule forming a muonium radical species, which can be studied by the methods of muonium radical spectroscopy.

TTF contains one central and two outer carbon double bonds, which might be expected to form radical states on muonium addition to a carbon. The main feature of the ALC spectrum is a Δ_1 resonance seen around 1.2 T at lower temperatures, corresponding to an isotropic hyperfine constant of around 300 MHz and a dipolar width of around 13 MHz. As temperature increases this resonance shifts to lower field and an additional weak resonance appears around 0.95 T at temperatures above 300 K. The TF measurements measured on TTF using the GPS instrumnet show a striking beat structure in the rotation signal, indicating the presence of signals close to the diamagnetic frequency. The hyperfine correlation spectrum shows a state with a very low hyperfine coupling in the region of 5 MHz. The fit to the time dependent asymmetry includes terms from a strongly coupled (A$\sim$300 MHz) radical and a weakly coupled (A$\sim$5 MHz) radical and the sum of these signals plus the diamagnetic fraction accounts for almost all of the expected asymmetry.

The temperature dependence of the muon hyperfine constant and the electron relaxation rate are shown in Fig.1. The muon hyperfine constant and the electron relaxation rate are found to follow a similar activation behaviour with activation energies of 25(5) and 31(9) meV respectively. This suggests that the hyperfine shift and the electron relaxation may both result from the excitation of a molecular vibrational mode in the 200 cm^{-1} region. The weak resonance at 0.95 T could be interpreted as a proton Δ_0 resonance with coupling A_p ranging from 130 MHz at 275 K to 116 MHz at 375 K. However, these proton couplings are significantly higher than the muon coupling scaled by γ_k/γ_μ. Since the muon coupling is usually higher than the proton coupling by 20-30% and in view of the temperature dependence of the weak resonance, it seems more likely that this resonance corresponds to the Δ_1 resonance of a separate radical with $A_\mu \sim 255$ MHz and probably corresponds to a central carbon adduct. We have also performed experiments on TCNQ and on BEDT-TTF [2]. Radical states with very low hyperfine coupling are seen in both TTF and BEDT-TTF, and we believe that the most likely mechanism for these states is addition to the sulphur sites. This detailed information about the muon states and muon hyperfine coupling parameters will allow μSR to be used to study the electronic properties of CT salts in a more quantitative manner than was previously possible.

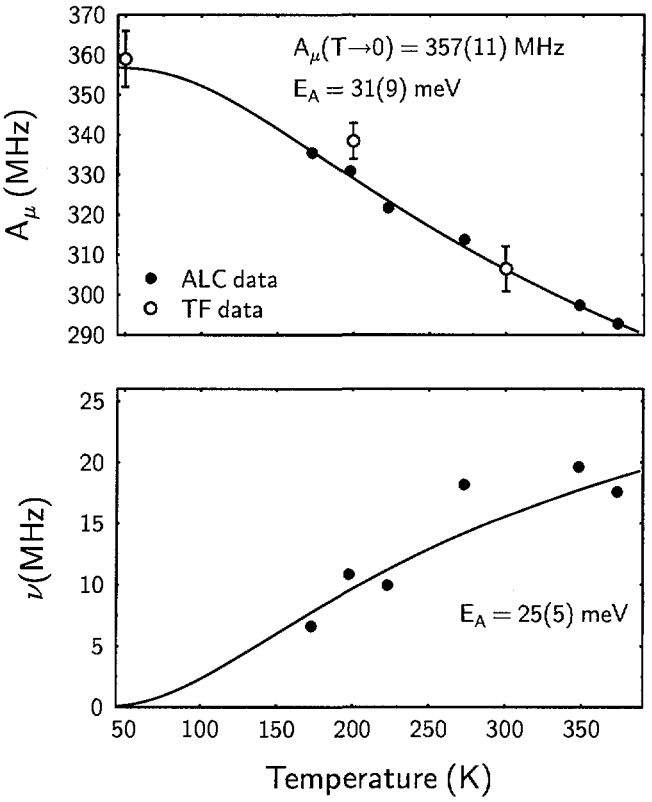

Figure 1: The upper plot shows the muon isotropic hyperfine constants A_μ in TTF as a function of temperature; the solid line is a fit to $A_\mu(T) = A_\mu^0 + (A_\mu^\infty - A_\mu^0)e^{-E_A/kT}$. The lower plot shows the temperature dependence of the electron relaxation rate; the solid line is fit to $\nu(T) = \nu_0 e^{-E_A/kT}$.

REFERENCES

[1] S. L. Lee et al, *Phys. Rev. Lett.* **79**, 1563 (1997).

[2] F. L. Pratt et al, *Mag. Res. Chem.* in press.

QUANTUM DIFFUSION OF TETRAHEDRAL INTERSTITIAL MUONIUM IN DIAMOND

I. Z. Machi[1], *S. H. Connell*[1], *J. P. F. Sellschop*[1], *K. Bharuth-Ram*[2], *J. Major*[3], *R. Scheuermann*[4], *A. Seeger*[3]

RA-97-24, JOHANNESBURG[1] – DURBAN[2] – MPI STUTTGART[3] – STUTTGART[4]

Introduction: In very pure diamond, Mu_T does not show appreciable spin relaxation, while impure or micro-crystalline samples exhibit substantial spin relaxation. In this work, samples exhibited essentially one defect type. The aim was to study the dynamics of Mu_T and its interaction with defects. The results are interpreted in the framework of coherent tunneling of light interstitials, followed by deep trapping.

Experimental: TF-μSR measurements were conducted at PSI (Switzerland), at 7.5 and 10 mT, and 3-300 K. The three diamond samples contained respectively 1 ppm of e^--irradiation induced vacancies (V^0), 0.04 ppm of γ-irradiation induced vacancies V^0 and a semi-conducting sample con$_T$tained 0.28 ppm of boron acceptors.

Results and Discussion: The spin relaxation rate (λ) for the Mu_T state was determined [1], and is shown in Fig. 1 for the insulating and semi-conducting diamonds. The results clearly indicate that Mu_T interacts with defects relating to the presence of V^0 and boron dopants in the samples, as no temperature dependent λ have ever been observed in pure diamonds. This temperature dependent λ must be related to some diffusion mechanism followed by a Mu_T-defect interaction mechanism, such as

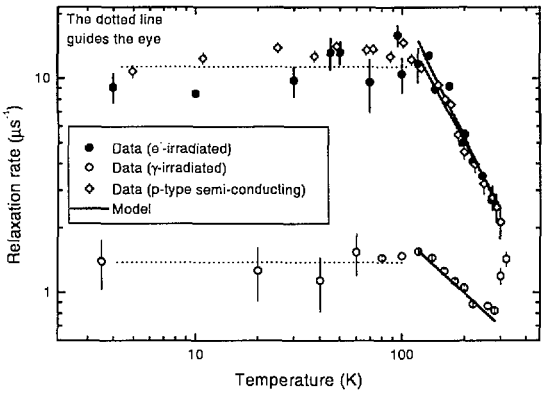

Figure 1: Plot of relaxation rate, against the temperature, of Mu_T in two insulating diamonds with e^-- and γ-induced vacancies and in semi-conducting diamond with boron.

(1) a diffusion, trapping, detrapping model where the depolarization mechanism depends on the dynamical effects related to the interaction with local moments. This model fits the data but cannot explain why the immobile Mu_{BC} species did not experience broadening from the static distribution of the local moments.

(2) a diffusion, trapping, detrapping model where the depolarization mechanism depends on the different muonium residence times in the traps. Quantum diffusion must be introduced to explain the faster arrival times at the traps for the lower temperatures. This model fits the data, however, trap depths are unphysically small.

(3) an alternative possibility [2] considers deep trapping (where the depolarisation occurs) following diffusion, where coherent quantum tunneling dominates over a large region below 300K. Further details on this model are explored below.

The expression relating the spin relaxation rate (λ) to the diffusion coefficient is discussed elsewhere (see, e.g., [1]). In the coherent quantum diffusion regime $\lambda \propto DT^{\beta} \propto T^{-\alpha}T^{\beta}$ Here α accounts the temperature dependence of D in much of this regime and $\beta > 0$ accounts the temperature dependence of the trapping process (eg the capture radius of the traps [4]). The proportionality 'constant' would contain terms incorporating details such as dressed tunneling matrix element, the phonon density of states, trap concentration, and the coupling strength of the Mu_T to the lattice. α is expected to lie between 1 and 7 in insulators [3]. In the presence of trapping, the power law dependence of λ (but not D) will be slightly weaker. The specific value and the range of validity of the simple power law depends also on β the detailed description of the phonon spectrum. In the case of Mu_T propagation through diamond (below 300 K), we note that the polaron effect and the coupling to the electron bath are both small, (the Debye temperature is large, and the lattice is homogeneous). Therefore the tunneling transition amplitude is expected to be comparatively large and coherence will persist to relatively high temperatures. The λ should exhibit a minimum as the coherent tunneling expires and is replaced by incoherent tunneling where it increases again. The data in Fig. 1 clearly exhibit the typical form of quantum diffusion (a low temperature plateau followed by a power law decrease) Incoherent tunneling is not yet evident for any of the samples except the photon-irradiated type IIa, where data points extend to slightly higher than 300 K. It is therefore reasonable to identify the low temperature increase in λ (with decrease in temperature), with the two-phonon dominated coherent tunneling mechanism. The power law curves, fitted in Fig. 1 predict values of $\alpha - \beta = 2.0(7)$, 1.8(3) and 0.9(1), for the e^--irradiated, γ-irradiated IIa and the p-type semiconducting diamonds, respectively.

REFERENCES

[1] B.D. Patterson, Rev. Mod. Phys. **60**, 70 (1988).

[2] R.F. Kiefl, Phys. Dept., UBC, Private communications.

[3] V.G. Storchak, Rev. Mod. Phys. **70**, 929 (1998).

[4] Yu Kagan and NV Prokof'ev *Quantum Tunneling in Condensed Media*, Elsevier (1992) 37-143.

MUON PARAMAGNETIC AND KNIGHT SHIFTS IN SEMICONDUCTORS AND SEMIMETALS

S. F. J. Cox[1], *M. Charlton*[2], *P. A. Donnelly*[2], *A. Amato*[3] *A. Schenck*[4].

RA-98-17, ISIS-RAL[1] – SWANSEA[2] – PSI[3] – IPP-ETHZ[4]

This experiment concerns the interplay of crystallographic site and charge state for muonium in semiconductors at high temperatures and the related question of incipient muonium formation in semimetals. In Si and Ge, we have re-examined the régime of rapid capture and loss of conduction electrons which gives rise to strong depolarization of the interstitial muons above room temperature [1, 2]– a behaviour which has important implications for the electrical activity of hydrogen impurity [3]. This charge–exchange implies that the muons spend some fraction of the time in the paramagnetic states, Mu_T^0 or Mu_{BC}^0, even though the cycles are so rapid that the μSR signals appear to be from an electronically diamagnetic state. The intermittent contact interaction should then, by its time average, give rise to a small effective field acting on the muon spin which is proportional to the electronic polarization of the paramagnetic state and to the fraction p_0 of time spent in this state. Assuming that occupancy of the isotropic state Mu_T^0 with hyperfine constant A gives the dominant contribution, the expected proportional shift of the muon Larmor frequency is given by

$$\frac{\delta f}{f} \approx \frac{hA}{4kT}\frac{\gamma_e}{\gamma_\mu}p_0.$$

In measurements made at the GPS instrument in a field of 0.6 T, we have demonstrated the existence of such a shift in nearly intrinsic Si. The shift sets in as expected with the onset of charge exchange just below 500 K but then rises rapidly to the unexpectedly large value of 0.6% around 600 K. The inferred neutral fraction p_0 reaches values close to unity above 600 K, implying that the rate of electron capture greatly exceeds that of ionization at these temperatures [4]. Existing models of muonium dynamics [1, 3, 5] account well for the onset of the charge–exchange régime but do not predict such a high neutral fraction at the higher temperatures. Our results raise the question of whether the dynamics change in character at high temperature, for instance whether ionization is suppressed if the thermally energetic muonium atom can no longer access the bond–centre site.

In Ge, on the other hand, although a variation of the Larmor frequency was discernable in these furnace experiments it did not exceed 60 ppm in the temperature range 300–800 K. The behaviour around the onset of charge exchange (which occurs below room temperature in Ge [2]) remains to be investigated, however.

In the semimetal Bi, where the muon Knight shift has previously been measured below room temperature [6], but not above, we find that the Larmor frequency varies approximately linearly with temperature, increasing by about 130 ppm in the range 300–500K. Screening of the muon charge will be ineffective in a material of such low conduction-electron density and our data could imply that the nominally diamagnetic muon state in fact includes a temperature dependent admixture of muonium–like states, i.e. a neutral fraction p_0 up to about 0.5%. This interpretation remains to be distinguished from a band–structure effect in which the density of states at the Fermi energy varies with temperature, as in Cd [6].

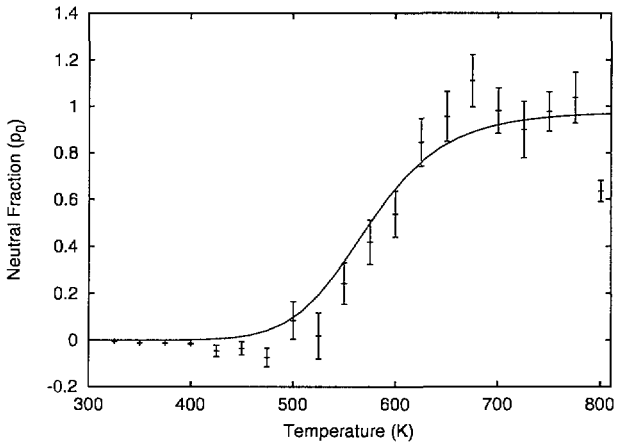

Figure 1: Temperature dependence of the neutral muonium fraction in Si.

REFERENCES

[1] K. H. Chow *et al*, Phys. Rev. **B 47**, 16004 (1993).

[2] R. L. Lichti *et al*, Phys. Rev. **B 60**, 1734 (1999).

[3] S. F. J. Cox, Phil. Trans. R. Soc. Lond.**A 350**, 171 (1995).

[4] S. F. J. Cox *et al*, contribution to μSR'99 (Les Diablerets, 1999), to be published.

[5] B. Hitti *et al*, Phys. Rev. **B 59**, 4918 (1999).

[6] A. Schenck, *Muon Spin Rotation Spectroscopy* (Adam Hilger, Bristol, 1985) plus refs therein.

OXYGEN-RELATED MUON SPECIES IN CRYSTALLINE SILICON

M. Schefzik[1], *A. Seeger*[1,2], *D. Herlach*[3], *O. Kormann*[1], *J. Major*[1,2], *A. Röck*[1], *L. Schimmele*[2]

RA-93-10, STUTTGART[1] – MPI STUTTGART[2] – PSI[3]

Systematic investigations on differently doped floatzone- and Czochralski-grown silicon samples have been carried out by means of transverse-field μSR (TFμSR). In some of the investigated samples a new precession frequency at applied magnetic fields between 2 mT and 6 mT was observed at T = 5 K, see Figure 1. This frequency cannot be attributed to any of the known muon species, i.e. the normal (tetrahedral location, Mu_T) or the anomalous (bond-centre location, Mu_{BC}, analogous to the AA9 or E3′ hydrogen centre) muonium nor any diamagnetic muon species [1]. It does not correspond to the recently observed vacancy-related muonium centre Mu_V [2, 3, 4] either.

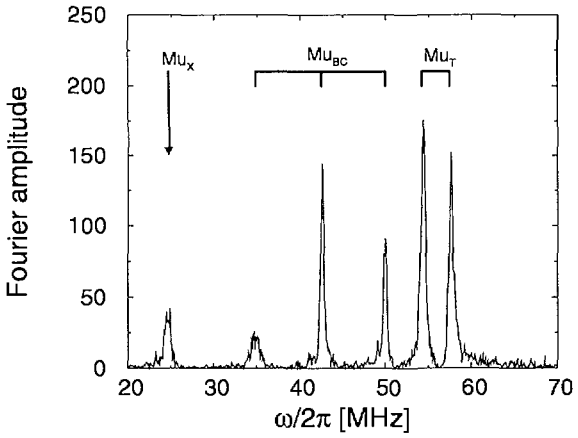

Figure 1: Precession frequencies obtained in TFμSR experiments in an applied magnetic field of 4 mT with $\boldsymbol{B}\|\langle 110\rangle$ on an intrinsic silicon sample ($8.15 \cdot 10^{11}\mathrm{cm}^{-3}$ phosphorus, $1.4 \cdot 10^{15}\mathrm{cm}^{-3}$ oxygen) at T = 5 K.

Since this additional frequency was only observed when the magnetic field was applied parallel to the $\langle 110\rangle$ crystallographic axis, it must belong to an anisotropic muon species [5, 6], which we denote by Mu_X. We determined the hyperfine tensor of this species from the magnetic-field dependence of the observed frequency. The hyperfine tensor is axially symmetric around the $\langle 111\rangle$ crystallographic axis with the components $A_x = A_y = (-82.6 \pm 3)$ MHz and $A_z = (+5.3 \pm 3)$ MHz. The hyperfine tensors of Mu_X and Mu_{BC} ($A_x = A_y = -92.6$ MHz, $A_z = -16.8$ MHz, z-axis parallel to $\langle 111\rangle$) are very similar, the differences, however, are significantly larger than the experimental uncertainties.

The Mu_X species was observable in all samples in which the oxygen concentration was much larger than the dopant concentration, independently of how the crystal was grown. Therefore, Mu_X is interpreted as a muonium–oxygen complex, the formation of which may be efficiently suppressed by the presence of other dopants. Since the hyperfine parameters of Mu_X and Mu_{BC} are very similar, it is assumed that the muon is also located at a bond-centered site in the species Mu_X. The interaction with a nearby presumably interstitial oxygen, which is also located at a bond-centered site, may account for the deviation of the Mu_X hyperfine parameters from those of Mu_{BC}.

A further distinction between Mu_X and Mu_{BC} comes from TFμSR experiments with electrostatic fields applied parallel to the initial muon-spin direction. The precession signal of Mu_X was influenced by the electrostatic fields. By contrast, no such influence was found for Mu_{BC} or any other species. In the case of Mu_X, an increase of the relaxation rate was observed, whereas the muon-decay asymmetry remained unchanged.

The temperature dependence of the Mu_X precession signal was also investigated. The precession signal vanishes between 160 K and 170 K, like that of Mu_{BC}. This also supports the picture that Mu_X is a 'weakly perturbed' Mu_{BC}.

The samples are kindly supplied by Dr. W. Zulehner, Wacker Siltronic AG, Burghausen, Germany. The work was funded by the Bundesministerium für Bildung und Forschung, Bonn, Germany under contract nos. 03–MA5ST1 and 03–MA5ST2.

REFERENCES

[1] B. Patterson, Rev. Mod. Phys. **60**, 69 (1988).

[2] M. Schefzik, J. Schmidl, R. Scheuermann, L. Schimmele, A. Seeger, D. Herlach, O. Kormann, J. Major, and A. Röck, Solid State Comm. **107**, 395 (1998).

[3] M. Schefzik, A. Seeger, D. Herlach, O. Kormann, J. Major, R. Scheuermann, A. Röck, and L. Schimmele, PSI Annual Report **1999**, 80.

[4] M. Schefzik, R. Scheuermann, L. Schimmele, A. Seeger, D. Herlach, O. Kormann, J. Major, and A. Röck, submitted to Physica **B**.

[5] M. Schefzik, R. Scheuermann, L. Schimmele, A. Seeger, D. Herlach, O. Kormann, J. Major, and A. Röck, Phil. Mag.**B 79**, 1561 (1999).

[6] M. Schefzik, L. Schimmele, A. Seeger, D. Herlach, Kormann, J. Major, and A. Röck, submitted to Physica **B**.

MEASUREMENT OF RELAXATION RATE AND PARAMAGNETIC FREQUENCY SHIFT OF NEGATIVE MUON SPIN PRECESSION IN SILICON

T.N. Mamedov[1], *D. G. Andrianov*[2], *V.N. Gorelkin*[3], *K. I. Gritsaj*[1], *D. Herlach*[4], *O. Kormann*[5], *J. Major*[5,6], *M. Schefzik*[6], *A. V. Stoykov*[1], *U. Zimmermann*[4]

RA-97-25, DUBNA[1] – MOSCOW[2,3] – PSI[4] – STUTTGART[5,6]

Investigation of negative muon polarization in silicon is of interest from the point of view of understanding the behaviour of acceptor impurities in the semiconductors with a diamond crystal structure. Earlier [1, 2, 3] it was shown that the μ^-SR experiment makes it possible to find the relaxation rate of the magnetic moment of a shallow acceptor centre in silicon in the temperature region below 50 K and preliminary data on the relaxation rate dependence on the impurity concentration were obtained.

The measurements carried out in 1999 were aimed at investigating the effect of impurities on the relaxation rate of the magnetic moment of the shallow acceptor centre. TF measurements were carried out on four silicon samples with boron impurity ($7.4{\cdot}10^{13}$ cm^{-3}, $5.5{\cdot}10^{16}$ cm^{-3}, $1.4{\cdot}10^{18}$ cm^{-3}, $4.1{\cdot}10^{18}$ cm^{-3}), two samples with gallium impurity ($1.1\cdot 10^{15}$ cm^{-3}, $1.1{\cdot}10^{18}$ cm^{-3}) and two samples with arsenic impurity ($8.0{\cdot}10^{15}$ cm^{-3}, $2.0{\cdot}10^{17}$ cm^{-3}) in the temperature range $4 - 300$ K. For all the samples investigated the relaxation and the shift of the muon spin precession frequency in the external magnetic field were observed. Depending on the impurity concentration the relaxation rate of the muon spin measured at the same temperature differs up to 10 times for different samples.

Found from the experimental data were

1) the value of the constant of the hyperfine interaction of the muon magnetic moment and the electron shell in the acceptor centre (muonic atom $_\mu$Al);

2) the analytical function for the temperature dependence of the relaxation rate of the magnetic moment of the Al acceptor centre in silicon.

The values of $A_{\rm hf}/2\pi$, the hyperfine interaction constant, are close to 30 MHz for different samples with an exception of two samples with a high concentration of boron impurity ([B]=$1.4\cdot 10^{18}$ cm^{-3} and [B]=$4.1\cdot 10^{18}$ cm^{-3}). For these samples the temperature dependencies of the muon spin precession frequency shift are studied incompletely for unambiguous determination of $A_{\rm hf}$. The temperature dependencies of the relaxation rate of the magnetic moment of the acceptor centre (muonic atom) for the samples investigated are well approximated by the power function $\nu(T) = C \cdot T^q$.

Figure 1 shows the dependencies of the parameter q on the decimal logarithm of the concentration of impurity for n- and p-type silicon. As is seen, in the impurity concentration range from $3.2\cdot 10^{12}$ cm^{-3} to $5\cdot 10^{17}$ cm^{-3} q is practically constant and close to 3. But in the concentration range $5\cdot 10^{17}$ cm^{-3} – $5\cdot 10^{18}$ cm^{-3} q decreases by several-fold. It is worth mentioning that in this range of concentrations the relaxation rate of the acceptor centre magnetic moment is observed to increase by more than order of magnitude in absolute value with increasing impurity concentration at the same temperature.

To prove the suggestion [4] that the relaxation rate of the muon spin depends on the strength of the external magnetic field H, we carried out measurements for an intrinsic silicon sample at $H = 200$ Oe, 400 Oe, 800 Oe, 1600 Oe and 2000 Oe at 13.5 K. The values of λ obtained for different external magnetic fields do not differ within the experimental errors.

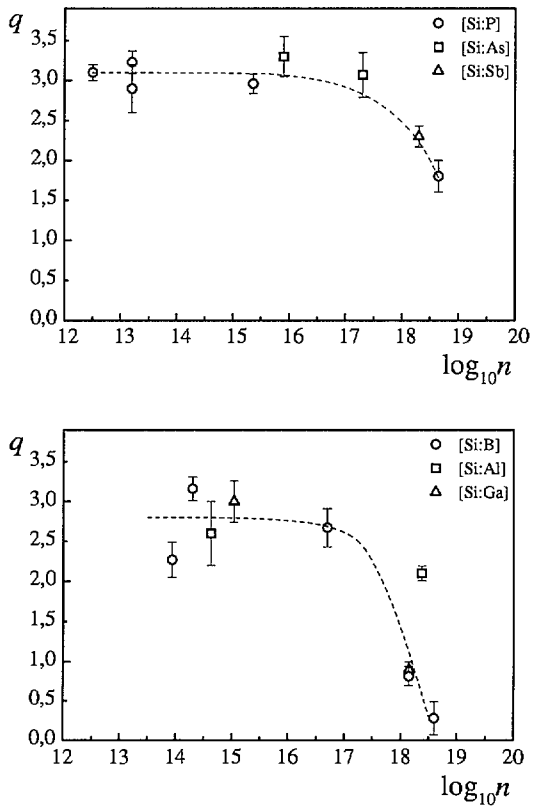

Figure 1: The dependence of the power index q in the function ($\nu = C \cdot T^q$) on the impurity concentration (n) in n-type (up) and p-type (down) silicon samples. (The dashed curves serve as eye guides.)

REFERENCES

[1] T. N. Mamedov et al., Hyp. Int. **86**, 717 (1994).

[2] T. N. Mamedov et al., Sov. Phys. JETP Lett. **63**, 566 (1996).

[3] T. N. Mamedov et al., J.Phys.: Condens.Matter **11**, 2849 (1999).

[4] R. Kadono et al., RIKEN-RAL Muon Facility Report **1**, 41 (1997).

MUON-SPIN SPECTROSCOPY IN SULPHUR AND SELENIUM

S. F. J. Cox[1,S], *I. D. Reid*[2]

RA-97-28, RAL[1] – PSI[2]

We have reported in recent years [1, 2, 3, 4, 5] our observations on positive muon charge states in sulphur and selenium, and the interesting and sometimes contradictory results. To summarise:

- LF repolarization measurements at RAL showed the existence of two paramagnetic states in sulphur at 300 K, attributed to a muoniated radical and to interstitial Mu.
- TF-μSR experiments in sulphur at 300 K showed no evidence for either a radical or muonium. They did, however, reveal two apparently diamagnetic signals, one with an extremely fast relaxation.
- ALC experiments in sulphur did, however, detect a very weak signal at low temperatures (<100 K) which was consistent with a ΔM=1 resonance from a radical with a similar hyperfine coupling as detected at RAL.
- TF-μSR experiments at 3 kG, in the temperature range 20–420 K showed that the fast component appeared above 150 K, its amplitude reaching a maximum around 300 K where essentially the full precession amplitude was recovered in the two diamagnetic signals.
- The relaxation rate of the fast component increased up to 300 K, but then decreased again. However, above the melting-point (392 K) the fast relaxation disappeared and the full asymmetry appeared in a slowly-relaxing signal.
- Observations in selenium gave weak ALC resonances at similar positions to the sulphur resonances.
- High-field TF-μSR experiments in Se from 77–320 K also showed two apparently diamagnetic signals, but in this case the fast component had significantly slower relaxation than in S and there was still a significant missing-fraction at 320 K.

While technically this collaboration is no longer active, it was possible in 1999 to obtain a short period in the GPS spectrometer to investigate a region not yet studied – low temperature and low fields. Experiments were carried out at 8 G at several temperatures between 5 and 133 K. Data were analysed by fitting the four 10 μs histograms to a non-relaxing diamagnetic component plus muonium presession at the same field. A very rapidly damped Mu signal was seen in all cases (Fig. 1), with relaxations around 60 μs^{-1}. Thus it seems likely that there is prompt Mu formation, which very quickly reacts into another species, but the results should be treated with caution as it is sometimes difficult to distinguish between Mu and radicals at low fields. Unfortunately, a major power-outage interrupted the already short amount of beam-time available to us, so we were not able to do follow-up experiments at, say, 100 G, which could help discriminate between Mu and radical signals.

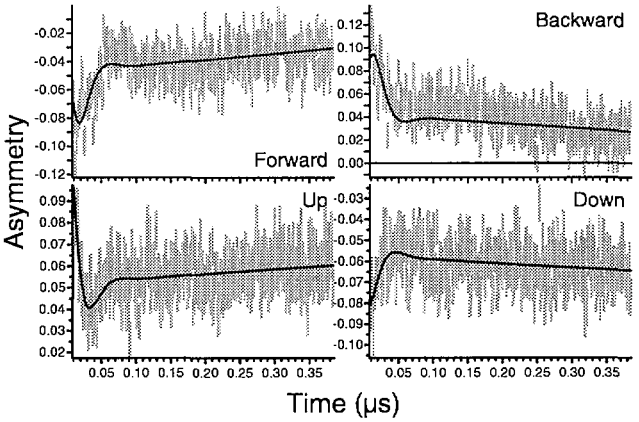

Figure 1: TF-μSR asymmetry in sulphur at 8 G and 50 K. The solid lines are a simultaneous fit to all four 10 μs histograms of a model representing a non-relaxing μ^+ signal and a relaxing Mu signal. λ_{Mu}=60±6 μs^{-1}.

Another interesting development in 1999 was the re-examination of the TF-μSR data from Se which found tantalising evidence of a radical with a hyperfine coupling of 230 MHz in the 77 K experiment. This value agrees closely with that extrapolated from the ALC Se data, but it must be verified in future experiments taken to higher counting statistics.

In light of the body of data now accumulated on μ^+ in S and Se, a further collaboration has been formed to, *inter alia*: more closely examine the prompt paramagnetic state in S; extend Se data to higher temperatures and better statistics; and, if possible, to study metastable "red" selenium, consisting of Se_8 rings similar to S_8, to probe the influence of structure on relaxation rates.

REFERENCES

[1] S. F. J. Cox, S. P. Cottrell, G. A. Hopkins, M. Kay and F. L. Pratt, Hyp. Int. **106**, 85 (1997).

[2] S. F. J. Cox and I. D. Reid, Appl. Mag. Res. **12**, 227 (1997).

[3] S. F. J. Cox, I. D. Reid, K. L. McCormack and B. C. Webster, Chem. Phys. Lett. **273**, 179 (1997).

[4] I. D. Reid and S. F. J. Cox, Physica **B** (in press).

[5] S. F. J. Cox, I. D. Reid, U. A. Jayasooriya and G. A. Hopkins, submitted to Magm. Reson. Chem.

μSR IN II-VI SOLAR CELL MATERIALS

N. Ayres de Campos[1], J. M. Gil[1], H. V. Alberto[1], R. C. Vilão[1], J. Piroto Duarte[1], A. Weidinger[2], Ch. Niedermayer[3], S. F. J. Cox[4]

RA-97-23, COIMBRA[1] – HMI BERLIN[2] – KONSTANZ[3] – ISIS[4]

1. CdS

The recently discovered shallow level muonium centre in CdS [1, 2, 3] was further studied. The main results are:

i) The temperature behaviour at low temperatures, below the ionisation temperature of around 20 K, is slightly sample dependent. The ionisation temperature in a high resisitivity (10^3 Ωcm at room temperature) sample is slightly higher than in the previously studied ones (1 Ωcm at room temperature), and the behaviour below the ionisation temperature seems also to be somewhat different. The higher degree of compensation in the new sample is thought to be responsible for the observed differences (shift of the Fermi level).

ii) The shallow level being ionised above around 20 K, it is supposed to give way to a diamagnetic state that stays in the same crystallographic site until it has enough energy to start diffusing. By a careful measurement of the dipolar-interaction relaxation in transverse field at temperatures above the ionisation, we could confirm the existence of motional narrowing at around 250 K, indicating that the site change occurs at this temperature (as in other semiconductor systems).

2. CdTe

CdTe exhibits a low-hyperfine interaction muonium state at low temperatures, similarly to CdS, as can be seen in the time spectrum of Fig. 1, obtained in a transverse field of 100 G and at 2.1 K, on a CdTe sample with cubic structure, oriented with the $< 100 >$ axis parallel to the external field, i.e. with all Cd-Te bonds at 54.7° to the field. The splitting

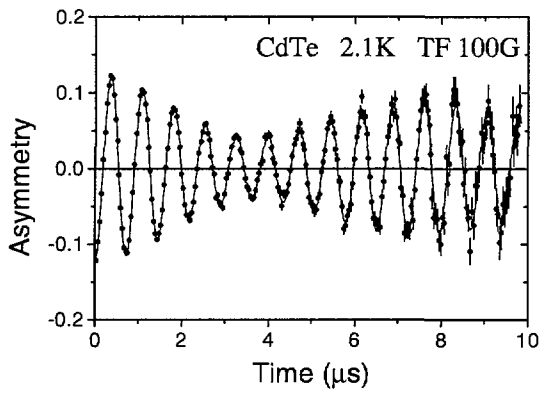

Figure 1: Muon-spin precession in a transverse field of 100 G, on CdTe at 2.1 K.

is of the same order of magnitude of that in CdS, although we notice here a much larger intensity of the middle diamagnetic line, and a reasonably large missing fraction. No signs of high frequencies, which could be associated to isotropic muonium, were observed with a time resolution of 1.25 ns.

A temperature dependent study was performed in the same field and orientation conditions. The diamagnetic fraction amplitude is depicted as a function of temperature in Fig. 2. The sudden increase at around 15 K corresponds to the ionisation of the low-temperature shallow level muonium state.

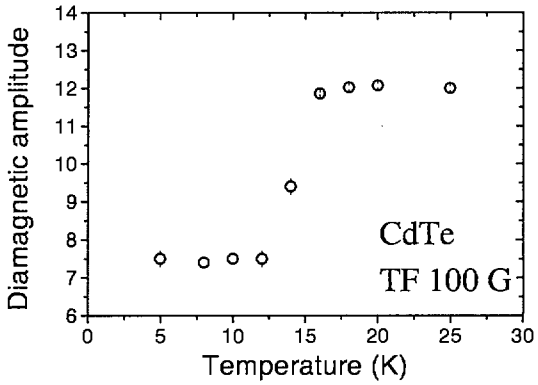

Figure 2: Diamagnetic fraction amplitude in CdTe as a function of temperature.

REFERENCES

[1] RA-97-23, PSI Scientific Report **1998**, Vol. 1, 83.

[2] J. M. Gil, H. V. Alberto, R. C. Vilão, J. Piroto Duarte, P. J. Mendes, L. P. Ferreira, N. Ayres de Campos, A. Weidinger, J. Krauser, Ch. Niedermayer, S. F. J Cox, Phys. Rev. Lett. **83**, 5294 (1999).

[3] JM Gil, HV Alberto, RC Vilão, J Piroto Duarte, PJ Mendes, N Ayres de Campos, A Weidinger, J Krauser, Ch Niedermayer, SFJ Cox,
Proc. μSR **1999**, O-6, Les Diablerets, Switzerland.

REORIENTATIONAL DYNAMICS OF AZA-CYCLOHEXADIENYL RADICALS IN PYRIDINIUM TETRAFLUOROBORATE

E. Roduner [1], *H. Dilger* [1], *B. Beck* [1], *P. Czarnecki* [2], *D. G. Fleming* [3], *I. D. Reid* [4], *Ch. J. Rhodes* [5]

RA-86-07, STUTTGART[1] – POZNAŃ[2] – TRIUMF[3] – PSI[4] – LIVERPOOL[5]

Pyridinium tetrafluoroborate (denoted $PyBF_4$) is a ferroelectric with a continuous paraelectric-ferroelectric phase transition which is exceptional for multidirectional ferroelectrics. It shows a sequence of two solid-solid phase transitions of order-disorder character taking place at T_1=238.7 K and T_2=204 K. In the high temperature phase the cations are disordered and reorient around their pseudo-hexagonal axis. Below T_2 the cations are nearly static. The phases below T_1 are ferroelectric. The ferroelectricity reflects the onset of ordering of the cation [1]. Avoided-Level-Crossing Muon-Spin-Resonance (ALC-μSR) [2] has been applied to investigate the reorientational dynamics of Mu substituted aza-cyclohexadienyl radicals in a powder sample of $PyBF_4$ in the temperature range between 194 K and 302 K and the field range between 1.3 T and 3.0 T. ALC-μSR is a special variant of magnetic resonance which interprets the relaxation of a polarized muon spin-label in the radical as a function of a longitudinally applied magnetic field which is scanned through avoided crossings of magnetic energy levels. The resonance fields are related to the hyperfine coupling constants in the adduct of muonium (Mu≡ μ^+e^-, chemically a light hydrogen isotope with a polarized muon as a nucleus). In the present case the adduct is the cationic aza-cyclohexadienyl radical, $C_5H_6NMu^+$. If the radical undergoes changes in reorientational dynamics, in the present case a rotation around the axis perpendicular to the molecular plane is expected, the line shapes of the resonances will change. A typical spectrum of $PyBF_4$ (see Fig. 1) shows six strong resonances between 1.8 T and 2.8 T which are assigned to the Δ_1 and methylene Δ_0 resonances of the three different radicals formed by Mu addition to the ortho, meta and para position of the pyridinium cation with respect to the nitrogen atom [3]. From the resonance positions we deduce coupling constants of 163.7 MHz (ortho), 175.8 MHz (meta) and 208.9 MHz (para) for A'_μ and 133.0 MHz (ortho), 131.1 MHz (meta) and 157.5 MHz (para) for A_p of the methylene protons with the value of the para radical being extremely high. Line width analysis of the Δ_1 resonances (see Fig. 2) revealed a dramatic change of reorientational dynamics of the aza-cyclohexadienyl radical between 233 K and 240 K reminiscent of the first phase transition at T_1=238.7 K, found by Czarnecki [1]. The data give clear evidence that the cations perform fast uniaxial rotation around the axis perpendicular to the molecular plane confirming the results of Czarnecki. In addition they show that superimposed on the rotational motion there is a wobbling motion of the rotational axis which freezes in around the first phase transition temperature, perhaps due to the change of the crystal structure at this point.

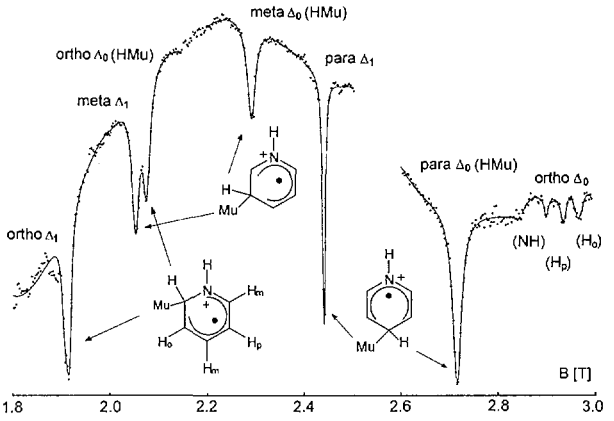

Figure 1: ALC-μSR spectrum of $PyBF_4$ at 302 K; structure of ortho, meta and para radical.

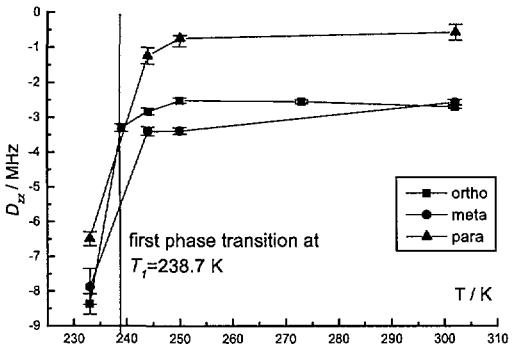

Figure 2: Axial hyperfine anisotropy of Δ_1 resonances.

REFERENCES

[1] (a) P. Czarnecki, I. Szafraniak, Phys. Stat. Sol. (b) **209**, 211 (1998).
(b) P. Czarnecki, A. Katrusiak, I. Szafraniak, J. Wasicki, Phys. Rev. **B 57**, 3326 (1998).

[2] (a) E. Roduner, Chem. Soc. Rev. **22**, 337 (1993).
(b) E. Roduner, Appl. Magn. Res. **13**, 1 (1997).

[3] B. Beck, E. Roduner, H. Dilger, D.G. Fleming, P. Czarnecki, I.D. Reid, Ch.J. Rhodes, Physica **B**, (2000), accepted.

APPARENT DIFFERENTIAL REACTIVITY IN HYDROGEN/MUONIUM ATOM ADDITION TO PYRIDINE AND TO THE PYRIDINIUM CATION

Ch. J. Rhodes[1,S], *H. Morris*[1] *and I. D. Reid*[2]

RA-96-09, LIVERPOOL[1] – PSI[2]

The formation of free radicals which are hydrogen-atom adducts of molecules that have been exposed to ionizing radiation has often been viewed as being an actual addition of initially formed hydrogen atoms. This need not be so, since proton and electron migration, even in cold solid materials, can also lead to these species without free hydrogen atoms ever being formed. Telling which mechanism is dominant is usually impossible.

In contrast, by irradiating materials with positive muons, "hydrogen adducts" are formed in which the muon provides a radioactive and magnetic atomic "hydrogen" nucleus. Since the majority of these radicals really do form by addition of initially formed such ("muonium") hydrogen atoms, their detection reveals the regioselectivity pattern for true hydrogen atoms, ionic routes largely being absent.

In this study, we have used the transverse-field muon spin rotation (TF-μSR) technique to detect muonium adducts of pyridine and the pyridinium cation, produced in samples of liquid pyridine and of solid pyridinium tetrafluoroborate (PyH^+ BF_4^-), for which coupling constants and relative radical yields are listed in the Table. In pyridine, 2 radical species are formed having relatively large coupling constants, and so are (aza)cyclohexadienyl radicals; however, there is also a radical with a very small muon coupling (6 MHz) which must be the N-Mu adduct – the muonated pyridinyl radical. According to semi-empirical calculations, the aza-cyclohexadienyl radicals should be ascribed to the ortho and meta adducts and so the para carbon site appears relatively unreactive to muonium atoms, since we could not detect a third isomer.

The pyridinium cation exhibits notable differences in its behaviour, particularly that the para position now shows significant reactivity (Table). The formation of a radical by "hydrogen" (Mu) atom addition to the $N(H^+)$ atom is unexpected; indeed, it has been proposed [1] that protonation of the pyridine N-atom serves to "block" it against addition of an H-atom. However, the evidence is compelling, and we consider that the most probable mechanism involves addition of muonium to the $N(H^+)$ atom, followed by deprotonation.

Previous workers have used ESR spectroscopy to identify the free radical species formed as products from pyridine by the action of ionizing radiation, as isolated in neutral alcohol glasses [1, 2] and in acidic media [1, 3] as solid matrices at 77 K. In alcohol glasses, overall H-atom addition to the N-atom was found, whereas in acidic matrices, addition predominantly to the para carbon atom was confirmed by deuterium labelling [3]. A similar order of reactivity was deduced for both monomeric and polymeric (2/4)-vinylpyridines [1], N-H radicals being formed in neutral media, but C-H adducts ($PyCH.CH_3$ or polymer azacyclohexadienyl radicals, respectively) when the N-atoms were protonated. Muonium addition to (2/4)-vinylpyridines was reported previously [4].

Why then, are all these results so different from those we obtain with genuine H-atoms (in the form of muonium)? The answer must be that entirely different mechanisms are operative, and since the radicals generated by ionizing radiation are all formed in entirely different selectivity, their origin must be ascribed to subsequent charge-neutralization of initially formed ionic species, true hydrogen-atom addition playing, at most, a minor role.

These results demonstrate the unique utility of the positive muon as a radioactive, magnetic "hydrogen" nuclear probe in exploring reaction mechanisms in the context of hydrogen atom reactivity.

Substrate	Site of Addition			
	ortho	meta	para	N
Pyridine	503.9[a]	526.8[a]	n.d.	5.8[a]
	(28%)[b]	(30%)[b]	n.d.	(42%)[b]
Pyridinium ion	521.4[a]	559.6[a]	664.7[a]	0.9[a]
	(23%)[b]	(16%)[b]	(19%)[b]	(42%)[b]

Table 1: Results for Muonium Atom Addition to Pyridine and the Pyridinium Cation. [a]muon hyperfine coupling (MHz); [b] yield of each radical expressed as a fraction of the total observed radical yield.

REFERENCES

[1] J. C. Ronfard Haret, A. Lablache Combier and C. Chachaty, J. Phys. Chem. **78**, 899 (1974).

[2] C. Chachaty, Comp. rend. **264**, 1421 (1967).

[3] H. J. Bower, J. A. McRae and M. C. R. Symons, J. Chem. Soc. **A**, 1918 (1968).

[4] C. J. Rhodes and E. Roduner, J. Chem. Soc., Chem. Comm., 1227 (1988).

HETEROGENEOUS PROCESSES INVOLVING ENVIRONMENTAL FREE RADICALS

Ch. J. Rhodes[1,S], *T. C. Dintinger*[1], *H. Morris*[1], *I. D. Reid*[2]

RA-99-15, LIVERPOOL[1] – PSI[2]

Organo-halogen compounds are widely used as industrial solvents and refrigerants (e.g. CFCs), but when released into the environment they are very harmful. They are degraded to free radicals by atmospheric sunlight, and until recently it was thought that such processes occurred entirely in the gas-phase; however, it has emerged that a significant part is played by aerosols, which include solid particulate matter. Since the processes of degradation of these materials involve free radicals, we have chosen substrates intended to reflect typical substitution patterns in chlorine- and fluorine-containing radicals and to study their interaction with a silica surface; silica is used to model typically siliceous atmospheric dust, arising from wind-blown desert regions [1].

This work utilises a special "thin-cryostat" which enables variable temperature measurements to be made in a longitudinal external magnetic field (LF), using the GPD spectrometer. We have measured the LF relaxation rates over the temperature range 85-300 K, from which motional correlation times could be extracted: the data in Table 1 is obtained from Arrhenius plots of *ln*(correlation time) vs 1/T.

Radical	Pre-factor/(s^{-1})	E_a/(kJ/mol)
$MuCH(Cl)CCl_2$	$3.7x10^{-11}$	6.3
MuCH(Cl)CHCl (from trans-1,2-dichoroethene)	$4.6x10^{-11}$	6.6
MuCH(Cl)CHCl (from cis-1,2-dichloroethene)	$2.9x10^{-11}$	7.1
$CF_3C(Mu)(Cl)C(Cl)CF_3$	$3.4x10^{-10}$	2.4

Table 1: Activation parameters determined for reorientational motion of halocarbon free radicals on silica.

This follows our previous work [2] on $MuCH_2CCl_2$ radicals sorbed in silica and in kaolin, which yielded activation energies E_a of ca. 9 kJ/mol for the major sorbed fraction identified; though there was an additional weakly sorbed component ($E_a < 2$ kJ/mol) present in both media. The current measurements identified only one sorbed fraction for each substrate, and it is noteworthy how close is the agreement among all these chlorine-substituted radicals regarding their binding-strength with the silica surface. (Muonium addition to either cis- or trans-1,2-dichloroethene, of course, yields the same radical species). Not so for the latter entry in Table 1, which is for a radical with 2 weakly polarisable CF3 groups attached. This is very weakly bound to the silica surface, according to the activation energy of only 2.4 kJ/mol. Escape, therefore, of this radical into the gas-phase should pose little difficulty. (Such behaviour is reminiscent of a "non-stick frying pan", whose surface of carbon-bound F atoms only weakly attach to the contents of the pan).

REFERENCES

[1] R. van Dingenen, N.R. Jensen, J. Hjorth and F. Raes, *J. Atmospheric Chemistry* **18**, 211 (1994).

[2] C.J. Rhodes, T.C. Dintinger, C.A. Scott and I.D. Reid, *Magnetic Resonance in Chemistry*, (2000), in press.

MUON STUDIES ON WEAK CHARGE TRANSFER SYSTEMS

R. M. Macrae[1], *I. D. Reid*[2], *J. U. von Schütz*[3], *K. Nagamine*[1]

RA-97-15, RIKEN[1] – PSI[2] – STUTTGART[3]

ALC-μSR studies have been carried out on a series of weak organic charge transfer compounds with tetracyanobenzene (TCNB) as the acceptor moiety, and anthracene (A), naphthalene (N), and hexamethylbenzene (HMB) as the donors. These systems all have charge-neutral ground states but exhibit differing degrees of charge transfer in their triplet excited states. (The approximate degrees of CT are A/TCNB: 5-10 %; N/TCNB: 30 %; HMB/TCNB: 90 % [1]. See Figure 1 for the relevant molecular structures.)

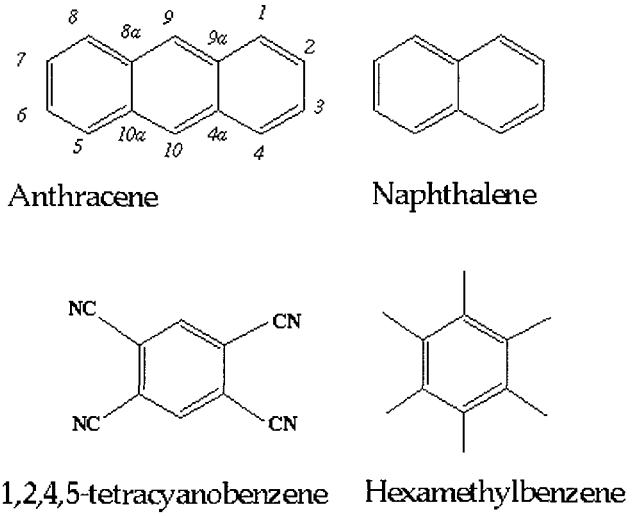

Figure 1: Structures of donors and acceptors.

As a result of the rather complex structural nature of these binary crystalline systems, the behaviour in the ground state as a function of temperature is dominated by molecular reorientation dynamics, order-disorder transitions, and crystallographic phase transitions. In particular, A/TCNB exhibits a transition at 207 K associated with reorientation of the anthracene molecules in a potential well which changes from single-minimum to double-minimum [2]. ALC-μSR measurements on this system showed several radical Mu adducts to anthracene (the three chemically-distinct adducts produced by Mu addition at the non-bridging carbons, with additional multiplicity due to crystallographic site inequivalences), and lineshape changes as a function of temperature indicated that in this system the μSR methods function mostly as a probe of order-disorder behaviour, *via* differences in the hyperfine tensors exhibited by radicals associated with different crystallographic sites and dependent upon averaging behaviour [3]. It is particularly noteworthy that these studies revealed *inter*molecular effects on hyperfine interactions to be quite large in these systems. Studies on N/TCNB and HMB/TCNB showed similarly complex behaviour [4], but in none of the three cases were adducts to TCNB observed. The reactivities of the components of these charge transfer systems were explored separately in liquid phase TFμSR measurements on solutions of these materials in appropriate solvents.

Three radicals were observed in a saturated anthracene/dioxan solution at 300 K, with reduced couplings $A'_\mu = 58.7$ MHz, 87.0 MHz, and 105.6 MHz respectively. These compare with 112.1 MHz and 137.1 MHz in naphthalene/acetone [5], and 161.6 MHz in benzene [6]. The general diminution in A'_μ with increasing radical size is due to increased potential for delocalisation of the unpaired electron. By analogy with naphthalene and with the aid of density functional calculations [3], these are assigned to the 9, 1, and 2 adducts respectively.

In TCNB/dioxan and HMB/THF, however, high statistics runs yielded no radical signals above the noise background. In the case of HMB, ALC data on the pure material and on HMB/TCNB show that radicals are indeed formed at room temperature. The non-observation of these radicals under TF conditions implies that the formation process is slow with respect to the inverse muonium hyperfine frequency, assuming Mu to be the precursor state. This in turn is largely a result of the hindering effect of the six methyl groups. By extension, radical-forming addition at CH in TCNB must be a still-slower process, since TCNB adducts are not seen in ALC measurements even where the strongly-hindered HMB is the donor molecule.

Work is presently underway towards completion of the analysis of TFμSR and ALC-μSR data with a view to understanding the reorientational dynamics and order-disorder behaviour in these interesting systems.

REFERENCES

[1] J. Krzysztek, J.-U. von Schütz, *adv. Chem. Phys.* **LXXXVI**, 167 (1993) and references within.

[2] J. J. Stezowski, *J. Chem. Phys.* **73**, 538 (1980).

[3] R. M. Macrae, I. D. Reid, J. U. von Schütz, K. Nagamine, Physica **B**, accepted for publication.

[4] R. M. Macrae, I. D. Reid, J. U. von Schütz, K. Nagamine, PSI Newsletter **1998**.

[5] I. D. Reid and E. Roduner, Struct. Chem. **2**, 419 (1991).

[6] E. Roduner, *The Positive Muon as a Probe in Free Radical Chemistry*, Springer, Heidelberg, 1988.

μSR STUDIES OF SPIN EXCITATIONS IN CONDUCTING POLYMERS

F. L. Pratt[1,2], *S. J. Blundell*[1], *Th. Jestädt*[1], *B. W. Lovett*[1], *A. Husmann*[1], *I. M. Marshall*[1], *W. Hayes*[1], *A. Monkman*[3], *R. Martin*[4]

RA-93-12, OXFORD[1] – RIKEN[2] – DURHAM[3] – CAMBRIDGE[4]

Conducting polymers such as those in Fig.1 are becoming increasingly important technological materials as applications are developed which make use of their unique electronic and optoelectronic properties. A good understanding of the charge transport mechanisms in such systems is of fundamental importance and we have been particularly interested in using μSR to study how the structural and dynamical properties of the polymer affect the anisotropic motion of the polaron in these systems.

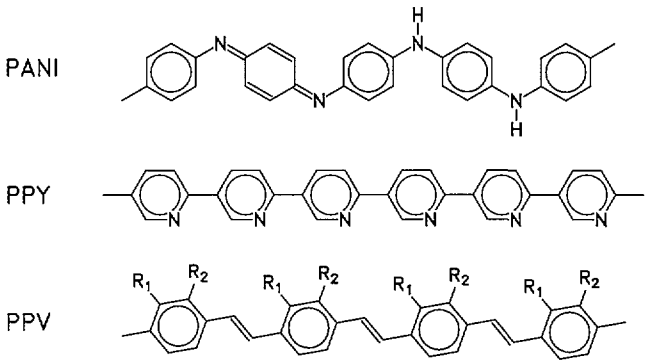

Figure 1: The conducting polymers polyaniline (PANI), polypyridine (PPY) and polyphenylenevinylene (PPV).

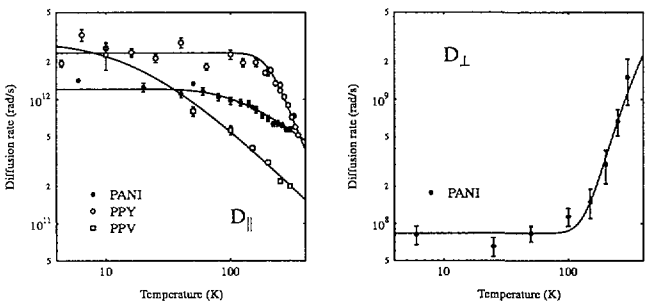

Figure 2: Polaron diffusion rates derived from muon measurements: (a) on-chain $D_{||}$ and (b) inter-chain $D_\perp$.

A comparison of polaron diffusion rates derived from muon relaxation data are shown in Fig.2. Marked differences are seen between the temperature dependent behaviours of the various materials. In PANI and PPY the parallel diffusion rate shows a very weak negative temperature coefficient at temperatures below ~100 K, which becomes much stronger at higher temperatures where the diffusion rate becomes inversely proportional to temperature. This is suggestive of phonon-limited metallic-style transport. Fitting the data to a model involving thermal activation of phonons gives phonon energies of 11.7(0.6) meV for PANI and 93(8) meV for polypyridine (the fits are shown as solid lines in Fig.2). The higher value seen for PPY is believed to reflect the stiffer structure involving direct linkage of the rings. The perpendicular motion in PANI also shows a thermally activated behaviour, but in this case the transport is assisted by the motion rather than hindered by it. The solid line for $D_\perp$ in Fig. 2 shows a fit to a phonon energy of 69(8) meV. In the case of PPV, $D_{||}$ follows 1/T down to much lower temperatures, suggesting that the diffusion is controlled by a much lower energy excitation (E~2meV).

In order to focus more closely on the relation between muon relaxation and polymer dynamics, we have studied some simple non-conducting polymers such as polybutadiene (PBD), where the double bonds are separated by polyethylene segments, so that the muonium radical formed on reaction with the PBD double bond is highly localised. In this case modulation of the hyperfine coupling tensor by polymer motion rather than modulation of the spin density by polaron motion becomes the dominant relaxation mechanism. As the simplest glass-forming polymer, PBD is also an important model system for studying the glass transition. Using a variety of μSR techniques we have been able to study the dynamical nature of the glass transition in PBD and related polymers. Fig.3 shows the temperature dependence of the radical signal in PBD measured by TF Spin Rotation Spectroscopy (Fig.3a) and by Avoided Level Crossing Spectroscopy (Fig.3b). At high temperatures a strong narrow signal is observed in the TF data (Fig.3a), due to efficient dynamical orientational averaging of the hyperfine anisotropy. On cooling towards the glass transition (T_g ~165K) the line becomes broader as the polymer dynamics slows down. Similar behaviour is seen for the $\Delta M=0$ transition in the ALC spectrum (Fig.3b), but the $\Delta M=1$ transition shows the opposite behaviour, since it requires residual anisotropy for oscillator strength. Below about 230K all the radical signals become too broad to extract reliably from the background. However longitudinal field relaxation can be used at lower temperatures to complete the dynamical picture obtained by μSR.

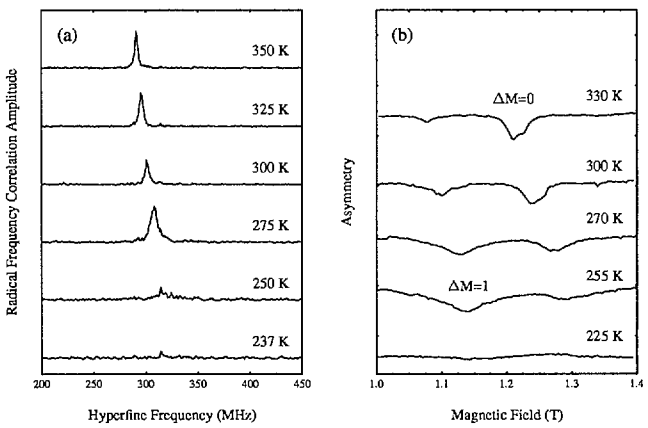

Figure 3: Temperature dependence of the μSR radical signal in cis-PBD. (a) Radical correlation spectrum for muon spin rotation in 3kG TF. (b) ALC spectrum.

μ^+SR ON CHARGE DENSITY ORDERING 5-4-10 INTERMETALLIC COMPOUNDS

F. Galli[1], *G. J. Nieuwenhuys*[1], *R. H. Heffner*[2], *D. E. MacLaughlin*[3], *S. Ramakrishnan*[4], *J. A. Mydosh*[1]

RA-94-03, LEIDEN[1] – LOS ALAMOS[2] – RIVERSIDE[3] – BOMBAY[4]

The 5-4-10 series of tetragonal compounds, e.g. $RE_5Ir_4Si_{10}$, have received attention over the last decade due due to their rich variety of ordered states: magnetic, superconducting, and charge density wave (CDW) [1]. These compounds form rather easily and, via pressure and variation of the f- or d-element (including pseudo binaries), we have a handle on the various energy scales associated with magnetic order, superconductivity, valence fluctuation and charge density wave ordering. The 5-4-10 series thereby opens a new source for novel magnetic and electronic ground states. Recently, the Leiden group has grown single crystals of three of these compounds, $Lu_5Ir_4Si_{10}$, $Er_5Ir_4Si_{10}$ and $Tm_5Ir_4Si_{10}$. The first one exhibits CDW order at 83 K and becomes superconducting at 3.9 K [2]. Experiments under moderate pressure show the strong correlation between these phenomena. $Er_5Ir_4Si_{10}$ shows two CDW transitions at 55 K and 155 K and two magnetic transitions at 2.9 K and 1.4 K, as established by investigations on single crystals in Leiden via bulk techniques, in Berlin, at the Hahn-Meitner Institute, via neutron diffraction [3], and in Hamburg, at DESY, via high intensity x-ray diffraction [4].

To study the influence of the CDW transition on the magnetic properties and to further reveal the magnetic structure in the ordered state, we have investigated $Lu_5Ir_4Si_{10}$, $Er_5Ir_4Si_{10}$, $Ho_5Ir_4Si_{10}$ (poly-crystal), $Tm_5Ir_4Si_{10}$ by μ^+SR using GPS and Dolly. The relaxation rate in zero applied field of the μ^+ in the magnetic compounds (Er, Ho and Tm) is quite large and surprisingly strongly temperature dependent. However, most remarkably, the CDW transitions as found via x-ray and electrical resistivity experiments, are clearly shown in the relaxation rate as function of temperature. In Fig. 1, we display the results for $Er_5Ir_4Si_{10}$ and $Tm_5Ir_4Si_{10}$. The arrows in this figure indicate the temperatures of the CDW transitions as observed via resistivity on the same samples [4, 1]. $Ho_5Ir_4Si_{10}$ showed a similar temperature dependence (not plotted) but the CDW ordering is not found with μ^+SR; we think this is due to the smaller gapping of the Fermi surface at the CDW transition in this compound as seen in the resistivity [1]. A similar measurement on $Lu_5Ir_4Si_{10}$ showed, as expected, a small and temperature independent relaxation rate. Longitudinal fields up to 0.6 T have only a minor influence on the relaxation rate, indicating it to be of dynamic origin. Due to difficulties in reaching the lowest temperature on GPS, we have only investigated $Er_5Ir_4Si_{10}$ in its antiferromagnetic state (2 K $< T <$ 3 K); no spontaneous precession was observed. The rather complicated magnetic structure that we have determined in the meantime at the Hahn Meitner Institute could explain this absence. Preliminary analysis of the neutron diffraction data of $Tm_5Ir_4Si_{10}$ shows a much simpler magnetic structure, so that an investigation of the magnetic transitions of this compound is on our list.

We speculate that the dynamics of the RE-magnetic moments is modified as a consequence of the band-structure changes, leading to a gapping of the Fermi surface caused by the inset of the CDWs. Magnetic measurements did not show a change in the magnetic moment at the CDW; also the displacements of the RE-ions are rather small, as observed from x-ray diffraction.

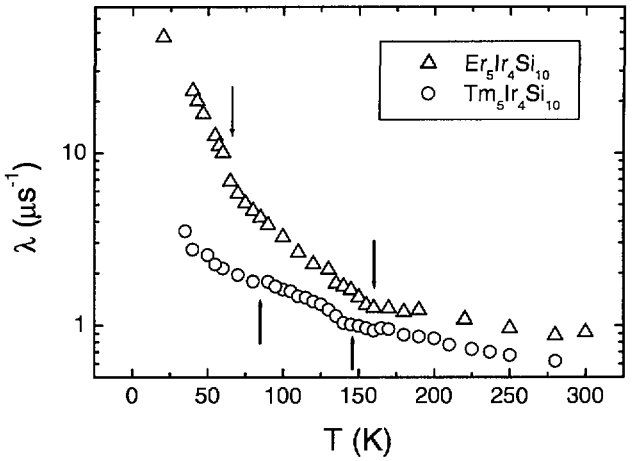

Figure 1: Relaxation rate versus temperature for $Er_5Ir_4Si_{10}$ and $Tm_5Ir_4Si_{10}$. The arrows indicate the CDW transition temperatures as found in resistivity , specific heat and x-ray diffraction [1, 4].

REFERENCES

[1] H.D. Yang, P. Klavius and R.N. Shelton, Phys. Rev. **B 43**, 7688 (1991).

[2] B. Becker, thesis Leidenuniversity, 1998, and B. Becker *et al.*, Phys.Rev. **B 59**, 7266 (1999).

[3] F. Galli *et al.*, to be published.

[4] F. Galli *et al.*, submitted to PRL.

NOVEL ELECTRONIC GROUND STATE OF QUENCHED CUBIC Cs_1C_{60}

W. A. MacFarlane[1], *V. Brouet*[1], *A. Lappas*[2], *T. N. Le*[3], *S. Garaj*[3], *L. Forro*[3], *K. Prassides*[4]

RA-99-14, ORSAY[1] – HERAKLION[2] – LAUSANNE[3] – SUSSEX[4]

In July, 1999, we made our initial attempt to study the quenched cubic (QC) phase of Cs_1C_{60} with μSR. This material possesses four crystallographic phases each with distinct electronic properties: a high T cubic phase above 450K, a polymerized phase, and two metastable quenched phases, the QC and the dimerized phases. Our sample was quenched from 180C to liquid nitrogen at PSI, and mounted cold into the GPS spectrometer. This quenching procedure reliably produced the QC phase in NMR samples, which are generally lower mass and vacuum–sealed in quartz tubes[1]. We planned to study the unusual nonsuperconducting nonmagnetic non-simple-metallic electronic ground state of this QC phase, which exists only below about 130K. NMR experiments[1] indicate that the ground state is somehow microscopically electronically phase separated, and we planned to elucidate this behaviour using μSR. The results may also prove relevant to recent NMR evidence for competing ground states in the polymeric Cs_1C_{60}[2].

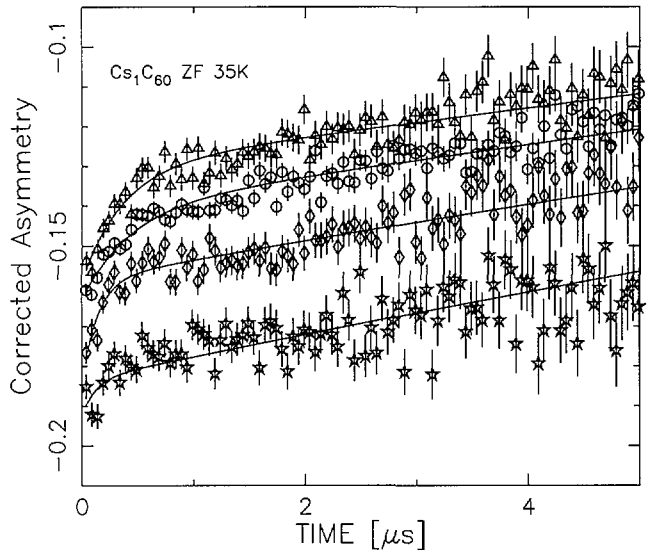

Figure 1: ZF μSR spectra at 35K for the dimer phase (triangles), Quench 1 (circles), Quench 2 (diamonds), and the annealed polymer phase (stars). The full asymmetry is about -0.25.

The quenching procedure did not yield pure QC phase, but rather a mix of QC and dimer phases. We were thus not able to accomplish the proposed study; however, we have general indications of the behaviour of QC, which will guide future studies once a more effective quenching method is developed. The ZF-μSR spectra (Fig. 1) show the different behaviour of the annealed dimer and polymer phases in comparison with the two trial quenches. Quench 2 was more effective, i.e. produced less dimer. The large missing fraction in the dimer is likely due to an exohedral muonium radical, but radical precession was not observed likely due to an extremely fast relaxation. This is confirmed by LF repolarization measurements on the quenched phase which indicate an isotropic hyperfine parameter about 10% of the vacuum value. Further indication of the distinct behaviour of the QC phase is found in the dependence of the longitudinal field relaxation rates ($1/T_1$) of the two quenched samples (Fig. 2). In the quenched phases, we also found an extremely small vacuum–like Mu precession signal, but it is not clear if this signal originates in the dimer or QC fraction.

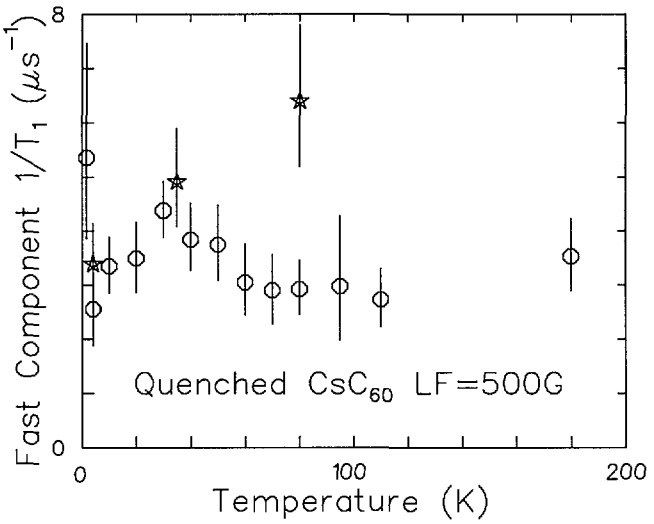

Figure 2: LF relaxation rates in 500 G for the fast relaxing signal for the first quench (circles) and the second (stars). The T dependence for the first quench is remarkably similar to the NMR T_1 of the dimer, but scaled up by about 10^7.

In conclusion we have qualitatively mapped the behaviour of the dimerized phase of Cs_1C_{60}, and we have exhibited the feasiblity of this kind of experiment with μSR. However, the primary goal of our study, the QC phase, remains elusive and awaits subsequent studies.

REFERENCES

[1] V. Brouet *et al.*, Phys. Rev. Lett. **82**, 2131 (1999).

[2] B. Simovic *et al.*, Phys. Rev. Lett. **82**, 2298 (1999).

RANGE OF LOW ENERGY MUONS IN Cu FILMS

H. Glückler[1], M. Birke[1,2], E. M. Forgan[3], R. Khasanow[1,4], H. Luetkens[1,2], E. Morenzoni[1,S], Ch. Niedermayer[5], M. Pleines[1,5], T. Prokscha[1], H. P. Weber[1]

PSI[1] – BRAUNSCHWEIG[2] – BIRMINGHAM[3] – ZÜRICH[4] – KONSTANZ[5]

In 1999 we have extended our investigation of low energy muon ranges in thin metallic films on quartz glass substrates [1]. In this report we present preliminary results obtained for Cu films.

Two Cu films with a thickness of 68 nm and of 500 nm were prepared by sputtering pure Cu onto a 50 mm in diameter quartz glass disc. After the preparation the thickness of the thin film was measured by a RBS analysis [2].

TF–μSR measurements were performed in a 5 mT magnetic field at 20 K by using low energy μ^+ with adjustable implantation energies E_μ between 0 keV and 29.4 keV. In nonmagnetic metals like Cu, the μ^+ precess in an applied magnetic field with a frequency of 136 kHz/mT whereas in quartz glass muonium formation is favored. In the latter case the precession frequency is 13.9 MHz/mT. The amplitudes of these two signals are a direct measure of the fractions of μ^+ stopped in the metal film or in the quartz glass backing.

In Fig. 1 the observed μ^+–asymmetries A_μ for the thin Cu film (solid symbols) and the thick Cu film (open symbols) are shown as a function of E_μ. In the thin Cu sample A_μ decreases from 26 % for E_μ = 10 keV to 5 % for E_μ above 25 keV. This reflects the increasing fraction of μ^+ thermalized in the quartz glass with increasing energy. A diamagnetic asymmetry $A_{\mu,quartzglass}$ of 5 % is also observed in 5 mT TF–μSR measurements on uncovered quartz glass. This signal corresponds to the fraction of μ^+ which do not form Mu in quartz glass. In the thick Cu sample no energy dependence of A_μ is found for E_μ above 10 keV. In both samples an almost constant A_μ for energies between 3 keV and 10 keV is found. At these energies all μ^+ are thermalized in the Cu film. The strong decrease of A_μ for energies below 3 keV can be explained in part by the increasing fraction of μ^+ which are backscattered from the sample. From measurements about the backscattering behavior of protons from metals it is known that a large fraction of backscattered particles are neutralized.

To compare the measured energy dependence of A_μ with predictions from range calculations, Monte Carlo simulations using the computer code TRIM.SP [3] were performed. Due to the lack of energy loss data for μ^+, velocity scaled energy loss data for protons were used. In the simulation, the fractions of μ^+ stopped in the metal and in the quartz glass for a given energy are calculated. Taking into account that all μ^+ stopped in the metal contribute to A_μ whereas μ^+ stopped in the quartz glass have an $A_{\mu,quartzglass}$ of 5 % we obtain the curves shown in Fig. 1. The solid and the dotted lines represent the predictions for the energy dependence of the μ^+–asymmetry for the thin and the thick Cu sample, respectively. As one can see in Fig. 1 the agreement between measured and calculated A_μ as a function of E_μ in the thick Cu sample is excellent whereas for the thin Cu sample a small deviation between measured and calculated A_μ is visible for energies between 10 and 15 keV. The measured asymmetries are smaller then the calculated possibly reflecting a slightly larger projected range in Cu than predicted. Further measurements are planned to clearify this effect.

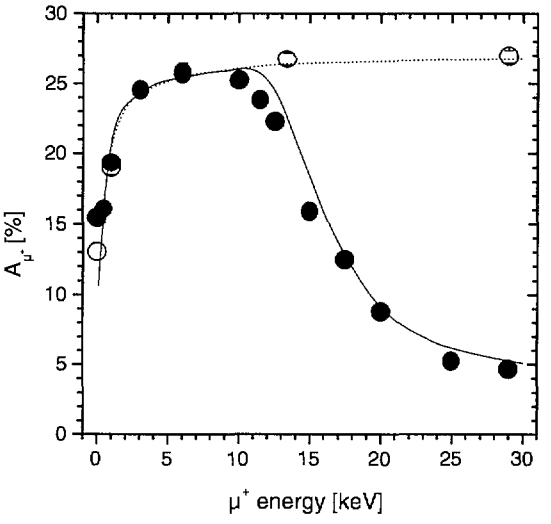

Figure 1: Energy dependence of A_μ in Cu films sputtered on quartz glass. Solid symbols: thin (d = 68 nm) Cu, open symbols : thick (d = 500 nm) Cu. Solid line: simulated energy dependency of A_μ for 68 nm Cu; dotted line: 500 nm Cu.

REFERENCES

[1] H. Glückler et al., Physica **B**, in press.

[2] The samples were prepared by M. Horisberger, PSI; the RBS analysis was done by M. Döbeli, PSI.

[3] W. Eckstein, Computer Simulation of Ion–Solid Interactions, Springer Verlag Berlin Heidelberg New York (1991).

DIRECT MEASUREMENTS OF THE PENETRATION OF A MAGNETIC FIELD INTO A SUPERCONDUCTOR IN THE MEISSNER STATE

E. M. Forgan[1], *H. Glückler*[2], *T. J. Jackson*[1], *J. Litterst*[4], *H. Luetkens*[2,4], *E. Morenzoni*[2], *Ch. Niedermayer*[3], *M. Pleines*[1,3], *T. Prokscha*[2], *T. M. Riseman*[1], *G. Schatz*[3], *H. P. Weber*[2]

BIRMINGHAM[1] – PSI[2] – KONSTANZ[3] – BRAUNSCHWEIG[4]

Low energy muons extend the utility of μSR to thin films and multilayers, and to studies of near surface properties distinct from bulk behaviour [1]. In this report we describe the use of low energy muons to measure directly the in plane penetration depth λ_{ab} of an YBCO ($YBa_2Cu_3O_{7-\delta}$) superconducting film in the Meissner state. The depth of muon implantation was controlled between 20 and 150 nm by tuning the incoming muon energy from 3 to 30 keV.

The YBCO film was a 700 nm thick film grown epitaxially on a 50 mm diameter $LaAlO_3$ substrate by H. Kinder's group at TU München. The magnetic field B_0 of approximately 10 mT was applied using a permanent magnet assembly as shown in [2].

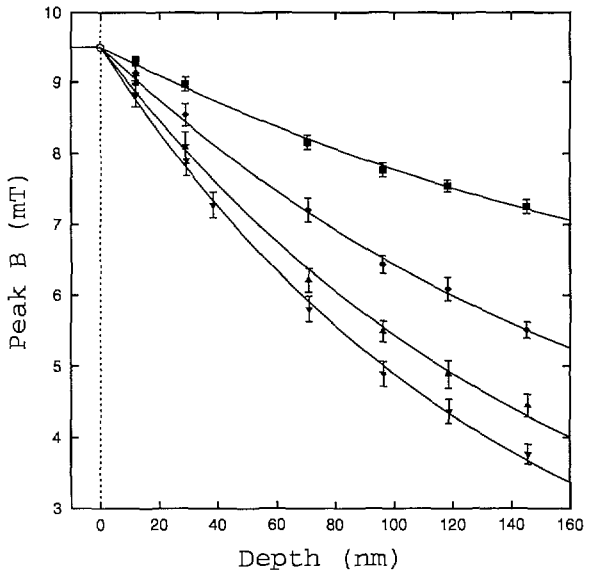

Figure 1: Field profile inside the YBCO film in the Meissner state at different temperatures. Inverse triangles: 20 K, triangles: 50 K, diamonds: 70 K, and squares: 80 K.

The field was applied perpendicular to the YBCO c-axis after zero field cooling the sample through the superconducting transition, so that the field was screened by supercurrents flowing within the ab-planes. Twinning within the ab planes precluded experiments with the field applied along a unique in-plane axis. The depth dependent field profile B(z) within such a semi-infinite superconducting slab follows from the well-known London exponential decay law, and is described by

$$B(z) = B_0 \frac{\cosh[(d - z)/\lambda_{ab}]}{\cosh(d/\lambda_{ab})}, \qquad (1)$$

where d is the half thickness of the film [3]. The results of our measurements are shown in Fig. 1, in which the solid lines represent fits of equation 1 to the experimental data, shown by the points. The muon implantation profile was determined from simulations [4] and the field at the most probable depth determined from Maximum Entropy analysis [5] of the decay histograms.

Equation 1 describes the data well, yielding a value of λ_{ab} at 20 K of 146(3) nm, with which other less direct determinations agree [6]. This method offers unique possibilities for measurements of the field penetration in other geometries and materials where the London law is not expected to be apply.

REFERENCES

[1] E. Morenzoni et al., Physica **B**, in press.

[2] H. Glückler et al., *Progress on the low energy μ^+ apparatus*, PSI Scientific Report, **1999**, Vol. I.

[3] D. Schoenberg, Superconductivity, Cambridge University Press, Cambridge (1952).

[4] H. Glückler et al., Physica **B**, in press.

[5] T.M. Riseman and E.M. Forgan, Physica **B**, in press.

[6] Ch. Niedermayer et al., Physical Review Letters **83**, 3932 (1999).

TEMPERATURE DEPENDENCE OF THE MAGNETIC PENETRATION DEPTH IN AN $YBa_2Cu_3O_{7-\delta}$ FILM

M. Pleines[1,2], M. Birke[4], E. M. Forgan[3], H. Glückler[2], T. J. Jackson[3], F. J. Litterst[4], H. Luetkens[2,4], E. Morenzoni[2], Ch. Niedermayer[1], T. Prokscha[2], T. M. Riseman[3], G. Schatz[1], H. P. Weber[2]

KONSTANZ[1] – PSI[2] – BIRMINGHAM[3] – BRAUNSCHWEIG[4]

In many of the potential applications of high temperature superconductors thin films will play an important role. A proper characterization of the superconducting parameters of these films is therefore of great interest. One of the fundamental parameters is the magnetic penetration depth λ_{ab}. We have used the low energy muon source [1] to study the temperature dependence of λ_{ab} of an $YBa_2Cu_3O_{7-\delta}$ (YBCO) film.

The measurements were performed on a 700 nm thick, c-axis orientated YBCO film (T_c = 87.5 K), grown epitaxially by thermal coevaporation on a $LaAlO_3$ substrate. The film was characterized by a spatially resolved J_c - measurement using an inductive technique [2]. The J_c (77 K) map of the investigated film, displayed in Fig.1, shows that the critical current density is very homogeneous over the whole sample area of the 2 inch wafer.

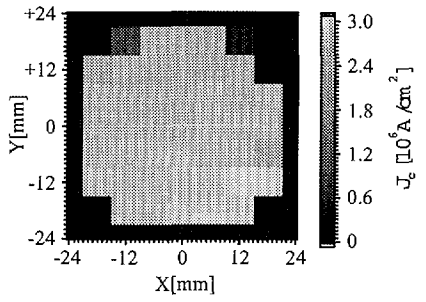

Figure 1: Map of the critical current density J_c. In the area of the film (2 inches diameter) the critical current density varies between $2.5 \cdot 10^6$ A/cm^2 and $3 \cdot 10^6$ A/cm^2.

An external field of 10.4 mT was applied parallel to the c-axis of the film. The sample was then field-cooled into the superconducting state. The energy of the incoming muon beam was fixed at 29 keV.

YBCO is an extreme type II superconductor. When a magnetic field $H_{ext} > H_{c1}$ is applied, a vortex lattice of the magnetic flux is formed. The field variation $\mathbf{B}(\mathbf{r})$ within the vortex lattice produces an asymmetric field distribution p(B) with a cusp which corresponds to the most probable field B_{sad}.

The measured field distribution was obtained from the time evolution of the muon spin polarization P(t) via Maximum Entropy Technique. As it was shown earlier [3] there is a good agreement between measured and theoretical field distribution.

The penetration depth can be derived from the shift between the mean field B_{ext}, and the cusp field B_{sad}:

$$B_{ext} - B_{sad} = c(H)\frac{\Phi_0}{\lambda_{ab}^2}, \qquad (1)$$

where c(H) is a field-dependent prefactor.

Figure 2 shows the temperature dependence of the magnetic penetration depth λ_{ab}. The solid curve represents a fit to a power law of the form

$$\lambda_{ab}(T) = \lambda_{ab}(0)\,[1 - (T/T_c)^n]^{-1/2}, \qquad (2)$$

with $\lambda_{ab}(0)$= 137(10) nm and n = 1.7(3).

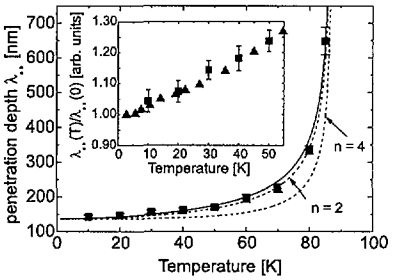

Figure 2: Temperature dependence of the magnetic penetration depth λ_{ab} of a 700 nm thick YBCO film. For comparison the dashed lines with n = 2 and n = 4 are shown, where n = 4 is obtained from the two fluid model and observed for classical superconductors.

Our value of the penetration depth $\lambda_{ab}(0)$ is in good agreement with results from conventional μSR measurements [4] on bulk samples. The inset shows $\lambda_{ab}(T)/\lambda_{ab}(0)$ below 55 K in more detail together with data points from conventional μSR measurements on $YBa_2Cu_3O_{6.95}$ single crystals [4]. There is a very good agreement between both sets of data. The observed linear temperature dependence was taken as evidence for an unconventional symmetry (*d*-wave) of the superconducting order parameter.

REFERENCES

[1] E. Morenzoni, Appl. Magn. Reson. **13**, 219 (1997).

[2] H. Kinder et al., Physica **C 107**, 282 (1997).

[3] C. Niedermayer et al., Phys. Rev. Lett. **83**, 3932 (1999).

[4] J.E. Sonier et al., to be published.

DIMENSIONAL CROSS-OVER IN *Au*Fe SPIN-GLASS STUDIED BY LOW ENERGY MUONS

G. J. Nieuwenhuys[1], *E. Morenzoni*[2], *Ch. Niedermayer*[4], *H. Glückler*[2], *Th. Prokscha*[2], *H. Luetkens*[2,3], *R. Khasanov*[2,5], *H. P. Weber*[2], *M. Pleines*[2,4], *A. Schenck*[5], *F. N. Gygax*[5], *A. Amato*[2], *M. B. S. Hesselberth*[1], *F. Galli*[1], *J. A. Mydosh*[1]

RA-94-15, LEIDEN[1] – PSI[2] – BRAUNSCHWEIG[3] – KONSTANZ[4] – ETH ZÜRICH[5]

Since its discovery in 1972 [1], the spin freezing in e.g. diluted *Au*Fe alloys has been the subject of many discussions in literature [2]. The question whether the spin-glass freezing is a phase transition, with all its consequences, is still not fully answered. One of the important ingredients for such a discussion is the existence and the size of a characteristic length scales associated with the freezing and its dynamics. In 'normal'3D phase transitions' the transition temperature is a function of the shortest length of the sample as this length comes in the vicinity of the correlation length ξ. The finite size scaling of the dc-properties of spin glasses has been studied by Cowen et al, [3], and in particular for *Au*Fe by Hoines et al. [4]. They found that the freezing temperature, T_f, essentially approaches zero as the thickness of the films goes to zero. These experiments were measurements of the static magnetic susceptibility carried out with a SQUID magnetometer on *multilayered* samples. An investigation of the -slow- dynamics as function of sample thickness has been performed by Sandlund et al. [5].

The slowing down of the spin system as the freezing temperature is reached from above has been the subject of a number of μSR experiments [6, 7, 8, 9]. In general it has been found that the decay of the muon polarization for $T > T_f$ can be described by a so-called stretched exponential, $\exp[-(\lambda t)^{\beta}]$. The value of λ increases rapidly near T_f, while the value for β becomes $\frac{1}{3}$.

We have investigated the muon relaxation in thin samples of *Au*Fe 3 at.% using the low energy muon facility at the Paul Scherrer Institute [10]. The films have been sputter deposited on a silicon waver from the same composite target in one run and the concentration and thickness were verified using Rutherford BackScattering and Elecron MicroProbe Analysis. Positive muons with energies of 1, 2.5 and 6 keV were implanted in the films of 10, 20 and 50 nm thickness, respectively. The stopping range was calculated using the program TRIM.SP [11], from which it was clear that in all cases more than 75 % of the muons stop in the the *Au*Fe thin film. A transverse field of 100 Gauss was used, and the runs were taken with a total of 600,000 events in the four counters (at a rate of more than 80 events per second).

In Fig. 1 the results for the relaxation rate as a function of temperature is shown. The relaxation rate was obtained form fits of the asymmetry with a stretched exponentional function. The result for the thickest sample (50 nm) is very similar to that obtained on bulk samples, as already reported by Schenck et al. [12]. Most surprisingly, the results for the thinner samples do show not only the expected decrease of the freezing temperature, but also the relaxation rate *does not* become as large as for the bulk samples. Also, the stretched exponentional power, β, does not reach $\frac{1}{3}$ anymore in the thinner spin glasses. These low energy μSR results indicate that the character of the spin-glass freezing changes dramatically when one of the dimensions of the sample becomes smaller than about 20 nm.

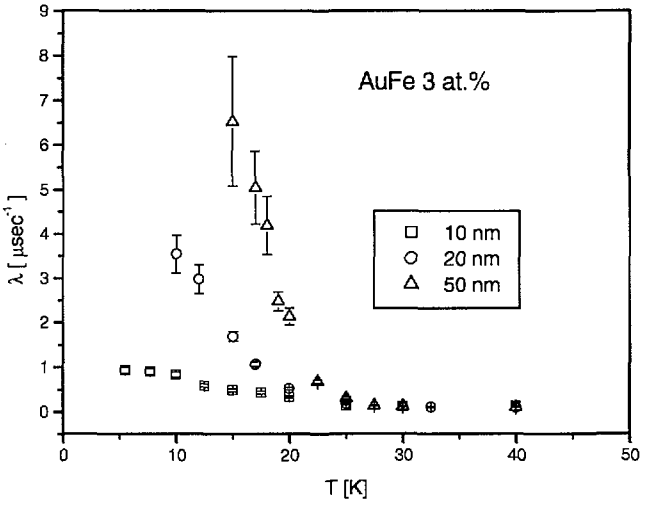

Figure 1: Relaxation rate versus temperature for *Au*Fe 3 at.% films of 50, 20 and 10 nm thickness.

REFERENCES

[1] V. Canella and J. A. Mydosh, Phys. Rev. **B 6**, 4220 (1972).

[2] J. A. Mydosh, *Spin Glasses: an experimental introduction,* Taylor & Francis, London, 1993.

[3] J. A. Cowen, G. G. Kelling and J. Bass, J. Appl. Phys. **64**, 5781 (1988).

[4] L. Hoines, J. A. Cowen and J. Bass, Physica **B 194-196**, 309 (1994).

[5] L. Sandlund *et al.*, Phys. Rev. **B 40**, 869 (1989).

[6] Y. Uemura *et al.*, Phys. Rev. **B 31**, 546 (1985).

[7] D. E. MacLaughlin *et al.*, Phys. Rev. Letters **51**, 927 (1983).

[8] A. Keren *et al.*, Phys. Rev. Letters **77**, 1386 (1996).

[9] I. Campbell *et al.*, Phys. Rev. Letters **72**, 1291 (1994).

[10] E. Morenzoni *et al.*, J. Appl. Phys. **81**, 3340 (1997); E. Morenzoni *et al.*, to be published in Physica **B**, 2000.

[11] W. Eckstein, Radiation Effects and Defects in Solids, **130-131**, 239 (1994); H. Glückler *et al.*, to be published in Physica **B**, 2000.

[12] A. Schenck *et al.*, PSI News **1998**; muSR1999, Switzerland, 1999; to be published in Physica **B**, 2000.

A LOW ENERGY MUON STUDY OF THE DIPOLAR FIELDS PRODUCED BY AN ASSEMBLY OF IRON NANOCLUSTERS IN SILVER

E. M. Forgan[1], H. Glückler[2], T. J. Jackson[1], R. Khasanov[2,5], H. Keller[5], J. Litterst[4], H. Luetkens[2,4], E. Morenzoni[2], Ch. Niedermayer[3], M. Pleines[1,3], T. Prokscha[2], T. M. Riseman[1], G. Schatz[3], H. P. Weber[2]

BIRMINGHAM[1] – PSI[2] – KONSTANZ[3] – BRAUNSCHWEIG[4] – ZÜRICH[5]

Low energy muons [1] were used to measure the spatial and temporal properties of the random dipolar fields produced by an assembly of iron nanoclusters, supported in a silver thin film matrix. The samples were prepared by C. Binns, at Leicester University. Unsupported clusters have been observed to follow a log normal diameter distribution, with a mean diameter of 2.8 nm and a width of 0.5 nm. We used an assembly of such iron nanoclusters supported in a non-magnetic thin film matrix. Most of the implanted muons stop at random sites in the matrix, in the regions between the clusters.

The results of our measurements on a sample containing clusters with an estimated median diameter of 2.8 nm are shown in Fig. 1. For transverse μSR measurements, shown by the circles in Fig. 1, a magnetic field of 10 mT was applied perpendicular to the surface of the sample [1]. The results of zero field measurements are shown by the diamonds in Fig. 1.

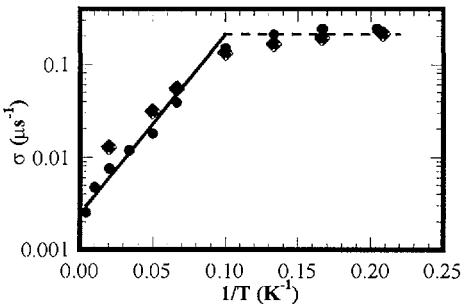

Figure 1: Muon polarisation relaxation rate from transverse and zero field low energy μSR measurements.

At low temperatures thermal energy is insufficient to cause significant activation of the cluster moments and a static Lorentzian field distribution is obtained within the sample. In transverse μSR measurements, this causes a pure exponential damping of the muon decay spectra. At high temperatures (for this sample above 10 K, see [2]), thermal activation of the clusters' moments has a motional narrowing effect and a "stretched" exponential damping, with an exponent of 0.5, was fitted to the data. In Fig. 1, the broken line shows the average low temperature muon relaxation rate of $\sigma = 0.22\ \mu s^{-1}$. The full line shows the results of a linear fit to the high temperature relaxation rates. The slope of this linear fit gives an activation energy of 37(4) K. From the intercept the attempt frequency for thermal activation of the cluster moments $\nu_0 = 67(15) \times 10^6$ Hz is calculated [2]. The diamonds in Fig. 1 show the results of zero field μSR measurements. The muon decay spectra were fitted with a Lorentzian Kubo function [3] and is seen to be consistent with the transverse field data.

Figure 2 shows the results of simulations of the low temperature distribution of static dipolar fields. The simulations show the field distribution as revealed by the front and back detectors in the low energy muon spectrometer. The solid line is a Lorentzian fit to the data, with HWHM of 2.2 mT. This width corresponds to a muon relaxation rate of $\sigma = 1.8\ \mu s^{-1}$, from which the volume concentration of iron in the sample can be determined [2].

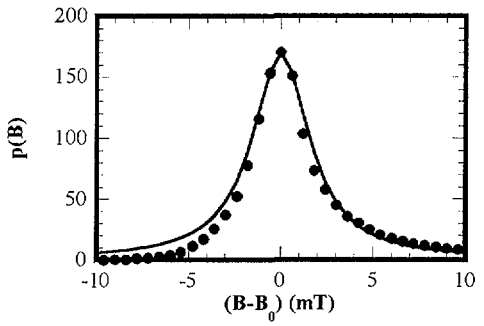

Figure 2: Simulation of the static dipole field due to iron nanoclusters at a concentration of 0.3% by volume in an applied field of 10 mT. The saturation magnetisation of the clusters is assumed to be 2 T in the simulations.

REFERENCES

[1] E. Morenzoni et al., Physica **B**, in press.

[2] T. J. Jackson et al., J. Phys: Cond. Matt, in press.

[3] Y. J. Uemura, in *Muon Science*, eds. S. L. Lee, S. H. Kilcoyne and R. Cwyinski, Institute of Physics, Bristol 1999.

DIFFUSION OF MUONS IN METALLIC MULTILAYERS

H. Luetkens[1,2], E. M. Forgan[3], H. Glückler[2], B. Handke[5], R. Khasanov[2,6], H. Keller[6], J. Korecki[5], F.J. Litterst[1], E. Morenzoni[2], Ch. Niedermayer[4], M. Pleines[2,4], T. Prokscha[2], G. Schatz[4], T. Slezak[5]

BRAUNSCHWEIG[1] – PSI[2] – BIRMINGHAM[3] – KONSTANZ[4] – KRAKOW[5] – ZÜRICH[6]

The development of a low energy muon source with tunable energy between eV and several keV opens the possibility to extend the bulk μSR technique to the study of thin films and multilayers (LE-μSR [1]). Here we report on muon diffusion in the 40 nm Au layer of an epitaxial Cr/Au/Cr trilayer. This is a basic experiment to understand the role of muon diffusion in low dimensional metallic systems including sticking at interfaces and the influence of small hexagonal distortion of the lattice due to epitaxial growth.

Below $T_N \approx 285$ K the 10 nm Cr films are in a magnetic state resulting in a very fast depolarisation of muon spins in their direct environment [2] while in pure Au practically no depolarisation is observable. Therefore LE-μSR can yield information about muons diffusing from the Au layer to one of the Cr layers giving rise to depolarisation of the muon spin ensemble. Additionally, with this method it is for the first time possible to study muon diffusion in non-magnetic elements without introducing magnetic impurities into the sample. The principle of the experiment is shown in Fig. 1.

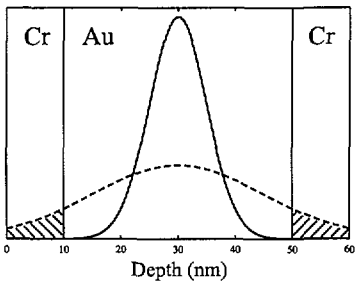

Figure 1: Initial muon implantation profile (solid line) and time dependent muon distribution due to thermally activated diffusion (dashed line). The fraction of muons reaching a Cr interface leads to a depolarisation of the LE-μSR signal.

By tuning the muon implantation energy to $E_{impl} = 6.5$ keV most of the muons stop in the Au layer giving a maximum of the observed initial asymmetry, see Fig. 2. This observation

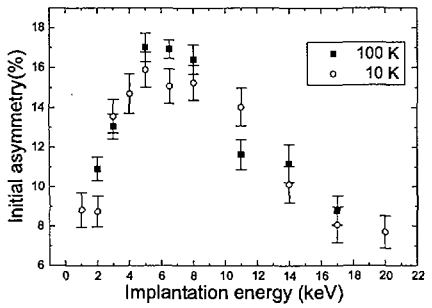

Figure 2: The measured asymmetry as a function of the muon implantation energy directly provides the fraction of muons which come to stop within the sandwiched gold film.

is well reproduced by the Monte Carlo code TRIM.SP [3], which is used to calculate the muon implantation profiles [4].

While the initial asymmetry is independent of temperature for the same implantation energy the depolarisation rate λ clearly shows the onset of muon diffusion around 125 K, Fig. 3. The increase of λ reflects the faster broadening of

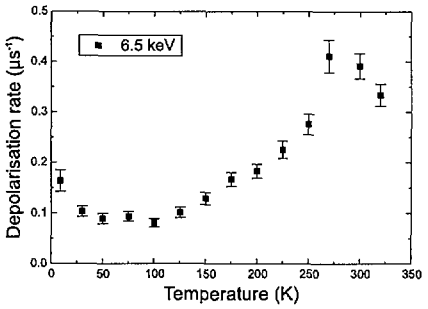

Figure 3: Temperature dependence of the depolarisation rate for 6.5 keV muons.

the initial stopping distribution with increasing temperature. Above $T_N = 285$ K the reduction of λ indicates the magnetic phase transition of the 10 nm Cr layers [2] which occurs ≈ 25 K below the Néel temperature of bulk Cr due to the size effect.

Monte Carlo simulations of the muon diffusion process taking into account the calculated initial muon stopping distribution as well as sticking at interfaces are in progress. From this, quantities such as diffusion constant and activation energy can be obtained.

REFERENCES

[1] E. Morenzoni, Appl. Magn. Reson. **13**, 219 (1997).

[2] H. Luetkens et al., Physica **B**, in press.

[3] W. Eckstein, Computer Simulation of Ion-Solid Interactions, Springer, Berlin, 1991.

[4] H. Glückler et al., Physica **B**, in press.

ENERGY DEPENDENCE OF MUONIUM FORMATION IN SOLID Ar, N_2, Xe, AND SiO_2

T. Prokscha[1], H. Glückler[1], R. Khasanov[1,4], H. Luetkens[1,2], E. Morenzoni[1], Ch. Niedermayer[3], M. Pleines[1,3], M. Birke[2]

PSI[1] – BRAUNSCHWEIG[2] – KONSTANZ[3] – ZÜRICH[4]

Charge differentiation in μ^+ or muonium (Mu) as a consequence of the slowing down of μ^+ in matter is of fundamental interest in the μSR method. It is also of relevance for the understanding of the moderation process of μ^+ in van der Waals solids like s-Ar or s-N_2 [1, 2], which are currently most suitable to generate epithermal μ^+ with a mean energy of $\sim$ 15 eV. These moderators are used as the source for the low-energy μ^+ (LE-μ^+) beam at PSI.

There is a lack of knowledge regarding the cross sections for electron capture and electron loss at energies below 1 keV, as well as for the interaction of epithermal μ^+ with the spur electrons of their own ionisation track. Muonium and μ^+ fractions have been studied only after implantation of energetic μ^+ [3, 4]. We started LE-μSR investigations on thin s-Ar, s-N_2, s-Xe films, and a quartz glass disk (SUPRASIL, SiO_2), to determine the μ^+ and Mu fraction in these samples in dependence on the implantation energy. The layers were prepared by condensing research purity gas for 1/2 h onto the cold head of a cryostat at partial pressures of 2×10^{-5} mbar (s-N_2), 1×10^{-5} mbar (s-Ar), and 3×10^{-6} mbar (s-Xe). This corresponds to thicknesses of 2200 nm (s-N_2), 800 nm (s-Ar), and 230 nm (s-Xe), which are sufficient to stop the LE-μ^+ beam in the layers. The thicknesses were measured offline by mounting a microbalance at the sample position and repeating the deposition procedure under same conditions. The temperatures were set to 10 K (s-Ar), 13.5 K (s-N_2), 30 K (s-Xe), and 20 K (SiO_2).

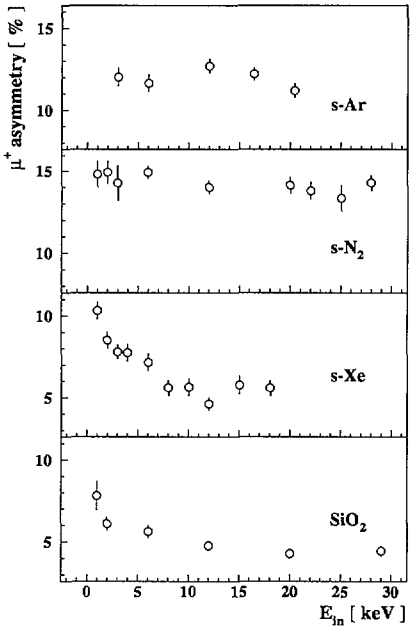

Figure 1: Dependence of the μ^+ asymmetry on the μ^+ implantation energy E_{in}.

At implantation energies between 1 and 30 keV we measured the μ^+ asymmetry A_μ by applying an external transverse magnetic field of 10 mT, and measured simultaneously the muonium signal A_{Mu} and A_μ at 0.8 mT. The results for A_μ are shown in Fig. 1. The preliminary analysis shows an energy independent asymmetry for s-Ar of $\sim$ 12%, and $\sim$ 14% for s-N_2. This corresponds to μ^+ fractions of $\sim$ 40% and $\sim$ 50%, respectively, by taking into account the maximum asymmetry of 27% which includes a background asymmetry of $\sim$ 2% due to μ^+ missing the sample. The missing fraction is due to Mu formation in the layer which is confirmed by the A_{Mu} measurement at low field. The s-Xe and SiO_2 data show an energy dependence of A_μ: at energies below 10 keV, A_μ starts to increase corresponding to a decreasing muonium signal. At energies larger than 10 keV, A_μ is constant and the μ^+ fraction in the sample amounts to about 10%.

The 10% μ^+ fraction in SiO_2 is consistent with data we obtained by implanting surface μ^+ into quartz glass at the GPS spectrometer. Investigations with surface μ^+ on thick solid gas samples show a small ($<$ 10%) μ^+ fraction in s-Xe [3], and only a 10–20% μ^+ fraction in s-Ar [3] and s-N_2 [4]. This is very distinct from our data yielding larger μ^+ fractions.

Qualitatively, the s-Xe and SiO_2 data are very similar as well as the s-Ar and s-N_2 data. This is reflected also in the moderation properties: whereas Ar and N_2 are efficient moderators, Xe and SiO_2, where a higher Mu formation is observed, yield only about hundred times smaller moderation efficiencies. This indicates the crucial role played by the suppression of Mu formation for the moderation process.

Further systematic studies of the dependence on B- and E-field, implantation energy, and different growing conditions during layer preparation are necessary to understand the difference observed between the results obtained with surface μ^+ in van der Waals bulk, and the results in thin layers.

REFERENCES

[1] T. Prokscha et al., Phys.Rev. **A 58**, 3739 (1998).

[2] E. Morenzoni, in *Muon Science*, IOP Publishing (1999).

[3] R. Kiefl et al., J.Chem.Phys. **74**, 309 (1981).

[4] V. Storchak et al., Phys.Lett. **193**, 199 (1994).

PROGRESS ON THE LOW ENERGY μ^+ APPARATUS

H. Glückler[1], *H. Luetkens*[1,3], *E. Morenzoni*[1,S], *T. Prokscha*[1], *H. P. Weber*[1], *E. M. Forgan*[2], *T. J. Jackson*[2], *M. Pleines*[1,4]

PSI[1] – BIRMINGHAM[2] – BRAUNSCHWEIG[3] – KONSTANZ[4]

In the constant effort to improve the LE-μSR method, several developments of the experimental setup have been pursued in 1999. A study was performed to find the optimum choice for geometry and materials of the sample environment, to achieve maximum detection efficiency of the decay positrons, maximum asymmetry of the μSR signal, while guaranteeing low sample temperatures. The absorption and scattering of the positrons interacting in their way from the sample to the scintillator telescopes, as well as their detection have been investigated with the GEANT program. As a consequence of this study, various components of the sample environment, such as sample holder, cold head of the cryostat, and the cooling shield have been modified. To reduce the amount of interacting material and improve thermal contact critical elements have precisely machined in very pure Aluminum instead of OFHC copper. Tests have shown that with the new setup essentially the same base temperature as with OFHC copper can be achieved. For instance with sample insulated by a sapphire crystal 6.7 K can be obtained. It must be taken into account that the very low energy of the muons impinging on the sample does not allow the use of a cooling shield in front of it. The reduced absorption and scattering of the decay positrons in the low density material translates into an increased detection efficiency by about 30 % and a relative increase of 5-10 % of the signal asymmetry.

In close collaboration with the University of Birmingham and the PSI magnet group a special magnet was designed and built for the application of magnetic fields parallel to the surface of the sample. The field of this magnet has to be uniform as possible over the surface of the sample, while decreasing rapidly with distance away from the sample to minimize the sideways deflection of the incoming low energy muon beam. These specifications have been fulfilled with a very compact design making use of permanent magnets and a soft iron return yoke, which is partially mounted very near to the sample in the UHV region (Fig. 1). Ferrite or NdFeB permanent magnets provide magnetic field strength of up to 20 mT with an homogeneity over the sample surface better than 1.5 %. At the same time a guiding system allows switching on/off of the field under controlled conditions as it may be necessary during zero field cooling experiments. With this setup the first direct measurement of the magnetic field profile near the surface of a HT_c superconductor in the Meissner phase and absolute determination of the magnetic penetration depth have been performed [1].

Improvements of the sample experimental chamber included the design and construction of a new shielding for the scintillator telescopes, which has reduced the positron background by more than 30 %. Furthermore the gate valve chamber used for sample load has been modified to reduce the sample changing time.

In view of a smooth transition to a more facility like operation, where also users external to the present low energy muon collaboration may be able to perform experiments, we started to implement computer control of relevant components such as the high voltage supplies of the electrostatic transport system and of the liquid nitrogen cooling of electrostatic lenses and traps.

During the beam time at the πE3 beamline we performed a comparison under the same experimental conditions of low energy muon intensity and polarization with thick (60 mm) and thin (42 mm) production target E. Whereas the polarization is unaffected by the target change, indicating that the accepted fraction of cloud muons is independent of the target length, we experienced a 30 % reduction of the surface muon flux accepted by the low energy muon apparatus.

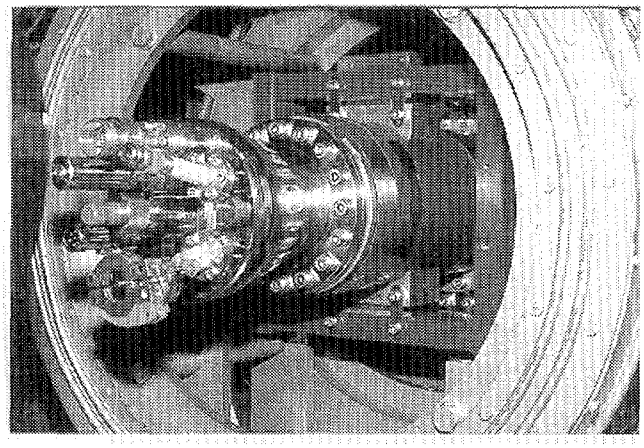

Figure 1: View of the sample chamber, with the magnet generating a field parallel to the sample surface. The flange of the sample cryostat is also visible.

REFERENCES

[1] T. J. Jackson, T. M. Riseman, E. M. Forgan, H. Glückler, T. Prokscha, E. Morenzoni, M. Pleines, Ch. Niedermayer, G. Schatz, H. Luetkens and J. Litterst, *Measurement of magnetic field as a function of depth with a precision of a few nm below the surface of a High T_c superconductor*, to be published, 2000.

A NOVEL SET-UP FOR FAST MUON-SPIN-ROTATION EXPERIMENTS

H. Dilger,[1] *E. Roduner,*[1] *R. Scheuermann,*[2] *J. Major,*[3] *M. Schefzik,*[3] *R. Stößer,*[4] *M. Päch,*[4] *D. Herlach,*[5] *A. Raselli,*[5] *I. D. Reid,*[5]

RA-98-18, STUTTGART[1] – RIKEN[2] – MPI STUTTGART[3] – BERLIN[4] – PSI[5]

The scientific aim of the experiment is to obtain information on isotope and temperature effects on the hyperfine interaction of atomic hydrogen in cages. This will contribute, for example, to a better understanding of solvent and cage effects in chemical reactions. For this purpose the hyperfine coupling constant of muonium (A_μ) in different liquids and solids (H_2O, D_2O, and siloxanes) was determined.

For muonium in vacuum the hyperfine coupling constant is $A_\mu^{vac} = 4463.3$ MHz. In order to detect small changes in A_μ, which may originate from the dynamics of Mu in a cage or cage-like surrounding, a novel zero-field spectrometer for measurements with very high time resolution (150 ± 10) ps) was developed [2] and installed in area μE4 at PSI, based on the pioneer work of HOLZSCHUH *et al.* [1]. An accuracy for the hyperfine coupling constant of < 1 MHz was required.

The data-acquisition system is based on the ORTEC picosecond time analyzer (pTA) mod. 9308, the scheme of the detection system is shown in Fig. 1. Since the data-acquisition software GUSTAV [3] is limited to 16000 histogram bins, the histogram length is reduced to 320 ns at a time-resolution of 19.53 ps/bin required in the present experiment. Therefore, a new data-acquisition software which allows the utilization of the full 262144 channel capability of the pTA has been developed [4]. For a clean (not folded) histogram, a so-called 'muon echo' signal is generated after each muon ('start') event with a delay Δ which is slightly shorter than the pTA time range. The corresponding part of the electronics is marked by dash-dotted lines in Fig. 1.

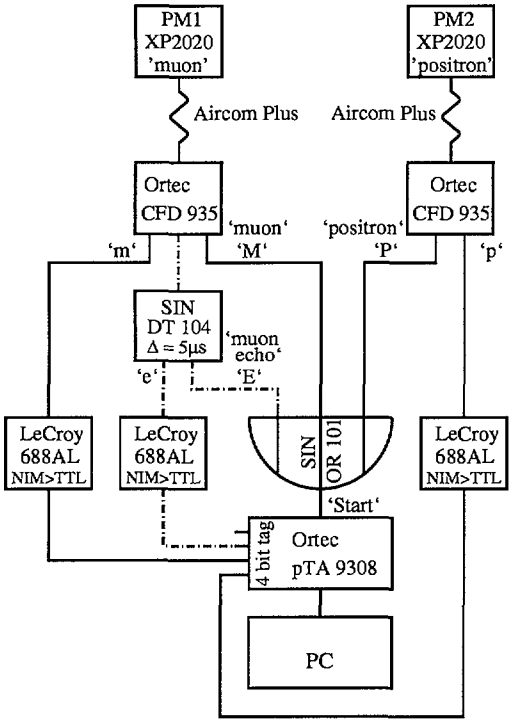

Figure 1: Complete scheme of the electronic detection system. It consists of two detectors (PM1 and PM2), four NIM modules (constant fraction discriminator CFD, level adapter LeCroy 688AL, logic unit SIN OR 101, and delayed-trigger module SIN DT 104), and an Ortec pTA connected to a PC. The dash-dotted line marks the 'muon echo' branch used to generate a pile-up gate within the full time-span of the pTA.

The novel set-up was used to determine room-temperature values of A_μ for muonium in molecules containing different cube-shaped Si_8O_{12} units (octasilsesquioxanes), in H_2O, D_2O, Optipur and Suprasil (tab. 1). In the case of MeT_8 and EtT_8 this is the first determination of A_μ. The coupling constant is higher for MeT_8 than for EtT_8, which is probably due to a stronger compression of the electron wave function in the cage. For Mu in H_2O and D_2O the two values are almost identical, which at first glance seems to be at variance with the solvent isotope effect discovered by RODUNER *et al.* [5]. An explanation might be, that, compared to H, the threefold higher vibration frequency of Mu in a cage formed by water molecules leads to a loss of the coupling to the librational motion of the surrounding water molecules, and thus Mu can no longer discriminate well between the two environments.

The result for Optipur is comparable to the TF results of Cab-O-Sil [6]. A_μ of Mu in fused quartz (Suprasil) is about 1.4% lower than for a quartz single crystal [1]. A more detailed discussion of the data can be found in [7].

Table 1: Hyperfine coupling constant A_μ (in MHz) and $f = A_\mu/A_\mu^{vac}$ for muonium in different materials at room temperature.

	Optipur	Suprasil	MeT_8	EtT_8	H_2O	D_2O
A	4457.6	4436.2	4431	4405.9	4431	4428
f	0.9987	0.9939	0.9928	0.9871	0.9928	0.9921

The work was partially funded by the Ministerium für Bildung und Forschung, Bonn, Germany under contract nos. 03–MA5ST1 and 03–MA5ST2.

REFERENCES

[1] E. Holzschuh *et al.*, Helv. Phys. Acta **54**, 552 (1981).

[2] R. Scheuermann *et al.*, Physica **B** (2000), accepted.

[3] J. Major *et al.*, Physica **B** (2000), accepted.

[4] A. Raselli *et al.*, **B** (2000), accepted.

[5] E. Roduner *et al.*, J. Chem. Phys. **102**, 5989 (1995).

[6] D. R. Harshman, *Hyperfine Int.* **23**, 847 (1986).

[7] H. Dilger *et al.*, Physica **B** (2000), accepted.

Laboratory for Micro and Nano Technology

Foreword

Silicon based nanomaterials

Molecular Nanotechnology

Nano Factory

LABORATORY FOR MICRO- AND NANOTECHNOLOGY

J. Gobrecht

1999 for LMN was dominated on the one hand by remarkable scientific activities and results, and on the other by some strategic and organisational changes.

Highlights in the *silicon-based nanomaterials* research included the achievement of a full understanding of the growth mechanisms and the morphology of C-induced Ge nano-aggregates on Si-surfaces and demonstration of the „size-effect" on the wavelength of the photons emitted from the nanodots. In the field of *molecular nanotechnology* we invented and developed a new enzyme immuno-assay for the detection of antibiotic residues in food with ppb-sensitivity. This achievement has high application potential and is a major step towards the long term goal of a fast-response amperometric immunosensor. From the area of *micro- and nanostructuring* technology, first results were transferred into commercial products: the master for a high-precision angular encoder disk (Baumer-Electric) and a moulded plastic chip with nano surface-reliefs for the calibration of low-cost SPM microscopes (Nanosurf). In addition to serving a growing community of external customers with special structuring process technologies, we realised binary and stepped Bragg-Fresnel zone plates as optical elements for X-rays which demonstrate excellent performance in microscopy with synchrotron-light. There is no doubt that the SLS project will profit from this capability in future.

In order to focus the research activities into fewer but larger strategic projects, it was decided to concentrate the internally funded research work on two scientific topics:

- *Light emission from silicon-based nanomaterials*
- *Molecular nanotechnology for biomolecule recognition and detection.*

The activities in the micro- and nanostructuring area should serve the needs in the these two research areas and the external user-community in form of a „base-laboratory". Also of considerable importance is the contribution to the extension and improvement of PSI's large facilities such as the SLS.

In order to achieve this concentration of effort, we are in the process of phasing out solar cell research (except for the IR-photocell work for TPV-systems which has a high synergy with the light-emission from Si topic) and transfer our know-how to industry wherever possible. We are also phasing out cantilever-based sensor work with the finalisation of the MINAST projects.

Two new activities were started in '99 which will further strengthen our position within the defined strategy: we finally were able to start with the build-up of the „Nanojunction-lab", an experimental facility in the molecular nanotechnology group which will allow the simultaneous investigation of single molecules by both X-ray photoelectron-spectroscopic as well as scanning-probe microscopic methods. The second new challenge is the definition and planning of projects in the area of nanostructuring using the advantages of synchrotron X-rays. Experiences in this field shall be gathered in order to become able to build up this competence at the SLS.

Looking out into the year(s) ahead we can conclude that LMN should be well positioned and also fits well with the new "Leistungsauftrag"-regime for PSI. The portfolio of our research activities focuses on highly relevant, interdisciplinary projects in the area of materials research. There are well established, continuing and increasing cooperations with universities, technical high-schools and industry and we intensively contribute to academic education by a comparably high number of PhD and diploma students in LMN.

I would like to take the opportunity to thank the PSI management for continuous support, the various funding agencies for sponsoring a significant part of our research work and of course the numerous partners from industry and academia in many of our projects for a very fruitful cooperation. Most important, I thank all the members of the LMN for their engaged work, the output of which you find summarised on the following pages.

NUCLEATION OF Ge DOTS ON THE C-ALLOYED Si(001) SURFACE

O. Leifeld, A. Beyer, D. Grützmacher(PSI), K. Kern (EPFL)

Carbon predeposition onto the bare Si(001) surface has been shown to alter the (2×1) surface structure by formation of c(4×4) reconstructed domains containing a high C-concentration. Here we study by scanning tunneling microscopy the effect of this restructured surface on the nucleation of Ge dots deposited by molecular beam epitaxy. Ge is found to form three-dimensional islands already at sub-monolayer coverage, resulting in a Volmer-Weber growth mode. This is opposed to the Stranski-Krastanov growth mode of Ge on bare Si(001). It can be explained by surface strain effects that repel Ge ad-atoms from the C-rich domains, leading to enhanced Ge island formation on the C-free surface regions. The very small islands define the positions of the larger islands at higher Ge coverage, that exhibit enhanced photoluminescence (PL) properties.

The self-assembly of three-dimensional (3D) dots in the group-VI-semiconductor system Si/Ge/C is a promising concept towards the ambitious goal of Si based optoelectronics in this indirect band gap material. It has been found recently that dot densities can be drastically increased and the size substantially decreased at deposition temperatures around 500°C by depositing Ge onto a C-alloyed Si surface. In this case dot formation occurs clearly below the critical thickness of 4-5 ML for Ge dot formation on clean Si(001) surfaces. These C-induced Ge islands have significantly enhanced photoluminescence properties. However, from the relatively thick Ge layers, where at a coverage of 2.5 ML islands are readily developed, no definitive conclusions can be drawn about the actual nucleation process. At which coverage the 3D island nucleation exactly sets in, remained rather speculative until now. With this work details of the initial Ge dot nucleation on the C-alloyed Si(001) surface can be explained.

We analysed the structural details of the C-alloyed Si surface in a previous work. The deposition of 0.1-0.2 ML C onto the Si(001) surface leads to distinct C-rich areas exhibiting a c(4×4) reconstruction, while the areas in between remain (2×1) reconstructed and, hence, free of carbon. Deposition of 0.1 to 1 ML Ge onto this pre-structured surface at 350°C has been investigated. Already at 0.1 ML Ge several small Ge islands of single layer height nucleate on terraces. These islands are always surrounded by a certain number of buckled dimer rows in the terrace layer, i.e. they nucleate on the (2×1) areas. Ge ad-layer islands are not found directly on top of a carbon rich c(4×4) region. This is in perfect agreement with the finding of a repulsive interaction of Ge and C in the SiGeC material system. It can be understood as follows: In the c(4×4) areas the Si surface is under compressive strain due to the high carbon content. Consequently, the average lattice constant here is smaller than that of Si, which discourages the larger Ge atoms to nucleate in these areas. Furthermore, as C is also present directly at the surface here, the formation of Ge–C bonds would be very costly in energy, involving severe amounts of strain due to the bond length difference of -37%. Instead, the Ge tends to wet the Si(2×1) regions first, since they are unstrained or are even subject to tensile strain in between the carbon-containing areas. The resulting lattice mismatch of less than 4% favours Ge nucleation on the Si(2×1) areas.

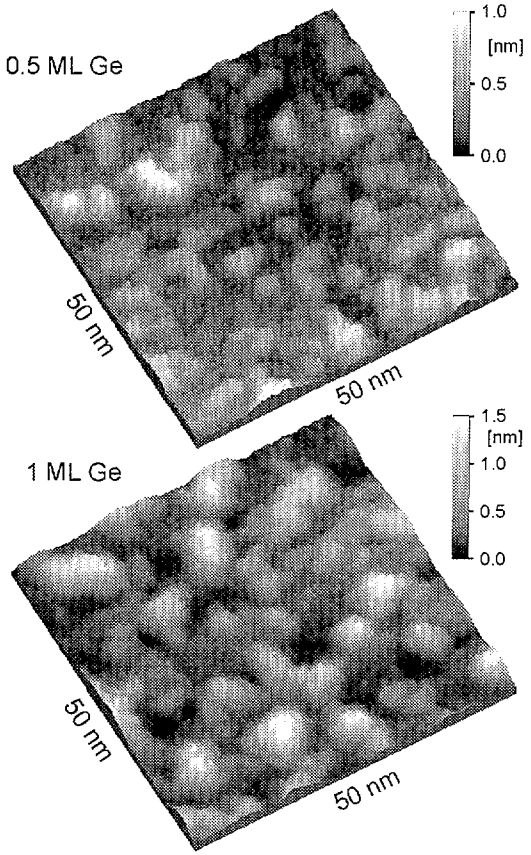

Increasing the Ge coverage to 0.5 and 1 ML (upper and lower figure, respectively), the islands grow in size and height. But their lateral extension is restricted by the c(4×4) areas. Still, the Ge atoms avoid the formation of Ge-C bonds and therefore start nucleating on top of the existing islands, resulting in 3D island growth. The restructuring of the Si surface due to the C pre-deposition obviously forces Ge to grow in Volmer-Weber mode rather than in Stranski-Krastanov mode. So the C-predeposition permits the fabrication of extremely small islands at the given temperature of 350°C, having sizes about 3-5 nm at 0.5 ML Ge. The 3D growth is clearly demonstrated in the above figures, where the 3D dots are all surrounded by c(4×4) areas. The small dots are the starting point for further Ge agglomeration and thus define the positions for the PL-active dots at higher coverage. The latter then have a gradual composition change from SiGe at the bottom towards pure Ge at the apex and are surrounded at the bottom by a SiC alloy. This gives a spatially separated confinement for electrons and holes and defines the spatially indirect luminescent recombination path.

FUNDING: PSI, EPFL

OPTICAL AND STRUCTURAL PROPERTIES OF C-INDUCED GE QUANTUM DOTS

A. Beyer, E. Müller, S. Stutz, H. Sigg, D. Grützmacher (PSI), K. Ensslin (ETHZ)

Pronounced low temperature photoluminescence (PL) was observed from carbon-induced Ge quantum dots grown by molecular beam epitaxy (MBE). Reducing the amount of Ge deposited from 2.9 to 1.4 monolayer results in a 200meV blue shift of the PL signal. The phonon assisted PL is negligible in comparison to the no phonon PL of the Ge dots. The lineshape of this PL signal is characteristic for systems with a high carrier localisation and so the PL originates from 0-dimensional Ge quantum dots. The effect of growth parameters, amount of C and Ge deposited, Si barrier width, growth temperature and post-epitaxial treatments on the PL properties have been studied in detail.

One way to improve the optical properties in an indirect bandgap material is the spatial localisation of the carriers, which increases the uncertainty in momentum and thereby enhances optical transitions without the use of phonons. Recently a new approach to improve the localisation in silicon was presented [1]: Predeposition of carbon reduces the size of self assembled germanium islands from 50nm to 10nm in diameter at a growth temperature of around 500°C.

We have grown such islands by MBE using e-beam evaporation of silicon and germanium. The carbon was evaporated from a pyrolythic graphite filament. All samples grown at 460°C contain 10 sheets of C induced Ge islands separated from each other by a silicon spacer layer.

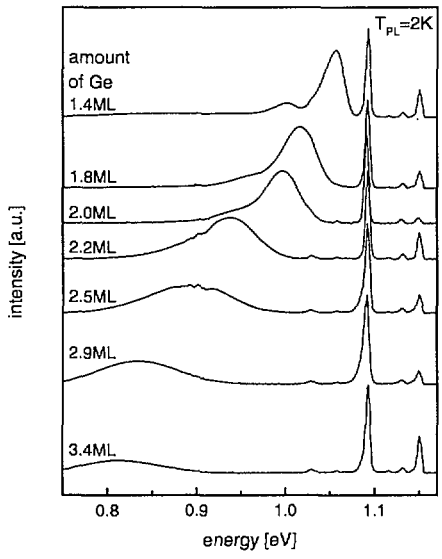

The first figure shows a series of PL spectra taken from samples, grown with different amounts of Ge. The carbon coverage is kept constant at 0.2 monolayer (ML) and the silicon spacer thickness at 8nm. After growth the samples were subject to a rapid thermal annealing (RTA) step for 10 minutes at 650°C. The RTA step is used to anneal point defects present in low temperature MBE grown samples and as a consequence an increase in the PL intensity by a factor of up to four is detected. In all spectra the typical PL features from the silicon bulk material are visible. These are the NP signal at 1.15eV, the TA phonon line at 1.132eV and the TO phonon assisted PL at 1.093eV. The PL signal assigned to the Ge dot luminescence is shifted from around 1.06eV to 0.81eV when in the amount of Ge from 1.4ML to 3.4ML is increased. This redshift is due to the increase in Ge island size (quantum confinement shift). The shift to lower energies is linked to a broadening of the PL signal, which indicates a broader size distribution of larger islands as compared to the smaller islands. This effect might be due to the coalescence of islands at higher Ge coverages. The upper spectra shows two clear resolved PL lines from the Ge dots. The more intense line at 1.06eV is assigned to the NP line from the quantum dot. The corresponding TO phonon line at 1.00eV is significantly weaker. The optical transitions without the use of phonons dominate the PL spectra due to the carrier localisation in the quantum dots. The broadening of the two lines at higher Ge coverages prevents the observation of phonon resolved spectra.

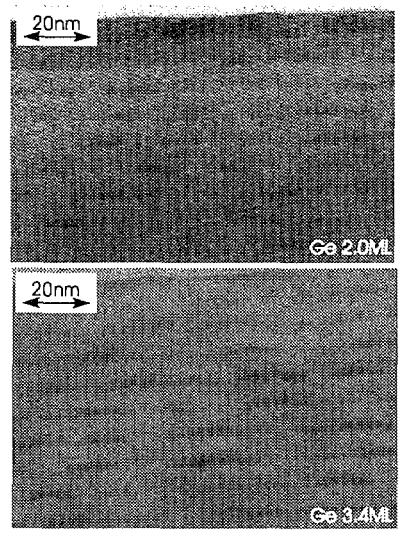

The second figure compares two TEM images of samples whose PL spectra are presented in the first picture. The amount of Ge is given in the bottom right corner of the TEM images. The increase in island size at higher Ge depositions is clearly visible. The island size differs in the two samples by an factor of approx two.

In further investigations the silicon spacer layer thickness was increased from 8nm to 16nm. This causes a significant increase in NP-luminescence intensity accompanied by a blueshift. This is attributed to the loss of the weak coupling of neighbouring dots by increasing the spacer. Further enhancement of the silicon spacer results in a less intense redshifted PL-peak and larger islands.

FUNDING: SNF, PSI.

REFERENCE

[1] O.G. Schmidt, C. Lange, K. Eberl, O. Kienzle, and F. Ernst, Appl. Phys. Lett. **71**, 2340 (1997).

ELS/SPA-RHEED: A NEW TOOL FOR IN-SITU ANALYSIS OF MBE GROWN NANO STRUCTURES

O. Kirfel, D. Grützmacher, J. Gobrecht (PSI), K. Kern (EPFL), B. Müller (ETHZ), M. Escher, M. Merkel (Focus)

The luminescence of Ge nanostructures on Si can be increased by a factor of 100 when the growth of these structures is influenced by carbon. This influence on the growth of the Ge nanostructures and on the crystalline quality can be analysed with the SPA-RHEED system. The increase of the luminescence can be examined with the ELS system. The new feature of this system is the combination of surface observation and electron loss spectroscopy for in-situ analysis. Up to now we have made the first characterisation of the new ELS/SPA-RHEED.

1 INTRODUCTION

With the new ELS/SPA-RHEED (Electron Loss Spectroscopy / Spot Profile Analysis - Reflection High Energy Electron Diffraction), it is possible to carry out in-situ measurements of high resolution electron reflection and electron loss spectroscopy. Energy filtered RHEED is used for the characterisation of surfaces. Inelastic scattered electrons are cut off by RHEED, although they have important information about the electronic structure of the sample. These inelastic scattered electrons can be measured at different angles by the ELS. With the new tool the surface and the electronic structure can be measured in-situ.

2 SCOPE OF APPLICATION

Ge-dots produced by self-organized growth have typical lateral dimensions of 50-100 nm and therefore are still close to 2-dimensional confinement limit of carriers. The luminescence of these dots is quite weak, even though it is stronger than that of Si. To obtain the expected strong increase in the luminescence intensity the size of the dots has to be further reduced to diameters of less than 10 nm while maintaining high crystalline quality. The surface, and therefore the crystalline quality of the MBE grown structures, can be analysed in-situ with the SPA-RHEED.

First luminescence results of 10 nm C-induced Ge islands on Si indeed show a strong increase in luminescence. The origin of this increase may either due to localisation of carriers or due to a spatial indirect recombination of electrons confined in the C-rich regions and the holes confined in the Ge dots [1]. The electronic structure will be examined by the ELS.

In addition to the ELS/SPA-RHEED measurements we can compare our results with the STM measurements of the same samples.

3 CHARACTERIZATION

The first characterisation has been done by measuring Si(100) using a primary electron energy up to 15 keV. The SPA-RHEED pattern for such a sample is shown on the left side. The reflections directly correspond to the 2x1-dimer surface reconstruction for Si(100), shown in the picture on the right side. Line-scans along the (00)-reflection exhibit an angular resolution of 2.5% of the Brillouin-zone for these Si(100) samples.

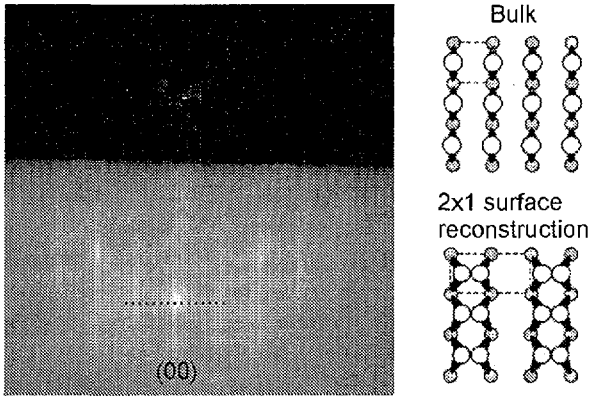

Fig. 1: RHEED pattern of a (2x1) reconstructed Si (100) surface

Measurements of the direct beam of the electron gun indicates that the angular resolution can be improved.

The energy loss can be measured for different angles and at each position of the SPA-RHEED pattern. The energy loss spectrum was measured for the (00)-reflection of the SPA-RHEED pattern.

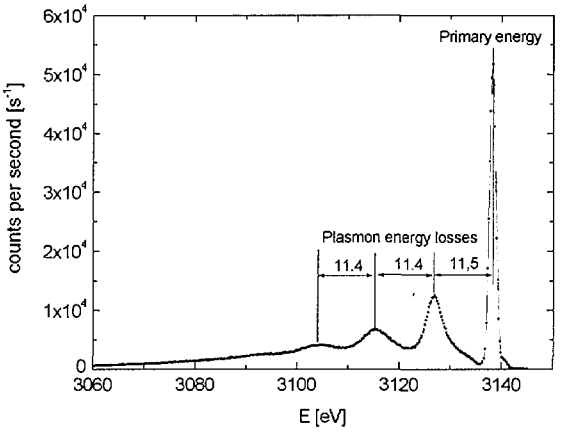

Fig. 1: Electron loss spectrum of the (00) reflection of a Si (100) surface

It shows typical equidistant plasmon losses of 11.4 eV. The energy resolution for the ELS is smaller than 0.8 eV

FUNDING: NF, PSI

REFERENCE

[1] O. G. Schmidt, C. Lange, and K. Eberl, O. Kienzle and F. Ernst, *Formation of carbon-induced germanium dots*, Appl. Phys. Lett. **71,** 2340 (1997).

ATOMIC SCALE ANALYSIS OF Si_nGe_m SUPERLATTICES

C. Guedj, E. Müller, H. Sigg, U. Gennser, S. Stutz (PSI), E. Presting (Daimler-Chrysler, Ulm), T. Pearsall (Corning Glas, Paris)

Si_nGe_m superlattices have been studied at the atomic scale using a combination of HRTEM image analysis, Raman spectroscopy and anharmonic Keating modeling. For such low dimensional heterostructures, the control of the structural properties at the atomic scale should contribute to improve their light emission efficiency.

For Si-based devices, nanostructural properties are closely linked to light emission. Several strategies are being considered to overcome the fundamental indirect bandgap of silicon and to produce light-emitting devices suitable for industrial applications. For example, it was proposed that a Si_mGe_n superlattice with m+n=10 would possess a quasidirect energy band as a result of the Brillouin-zone folding. However, in practice, an intense light emission from such structures has not been obtained yet. One major difficulty in the experiment might be due to the severe atomic intermixing at the interfaces that smears out the potential and causes an invalidation of the zone folding. To investigate the possible mechanisms limiting light emission in such systems, a Si_5Ge_5 superlattice has been studied at the atomic scale using an original image analysis of high resolution transmission electron microscopy (HRTEM) images [2] in conjunction with Raman spectroscopy and theoretical modeling [3].

A direct insight into the local lattice distortions is obtained by filtering [4] HRTEM images. This process is depicted in Figure 1. The positions of the black spots of the filtered image are statistically analysed and the results can be correlated to the actual positions of the atoms in the crystal.

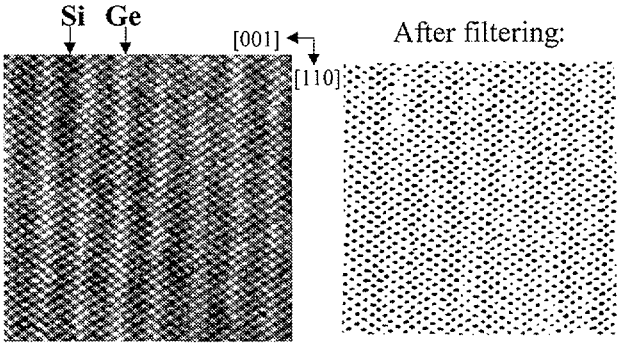

Fig 1: Filtering of the HRTEM image of a Si_5Ge_5 superlattice.

An example of statistical analysis is displayed in Figure 2. The lattice parameters of germanium (~0.565795 nm) is superior to the one of Si (~0.543095 nm), therefore the interspot distance is correlated to the local strain and composition. An anharmonic Keating model is used to compute the theoretical atomic positions in the case of a perfect superlattice. To have an intuitive picture of this theoretical modeling, the reader may go to the PSI forum to see the experiment where solid spheres are interconnected with springs. From comparison between theory and experiment, physical effects such as interdiffusion or local ordering at the interface can be interpreted and associated with the optical properties.

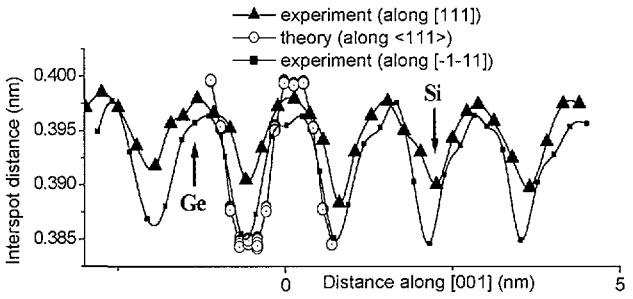

Fig. 2: Statistical analysis of filtered HRTEM images

In such solids, atoms tend to vibrate, and the lattice dynamics is fundamental to understand the interaction between light and matter. Phonon properties may be assessed by Raman spectroscopy, and Figure 3 shows an example of such measurement for our Si_5Ge_5 supperlattice. The signature of the phonon zone folding is observed at 136.4 cm^{-1}. From the comparison with our modeling, the statistical atomic arrangements are inferred.

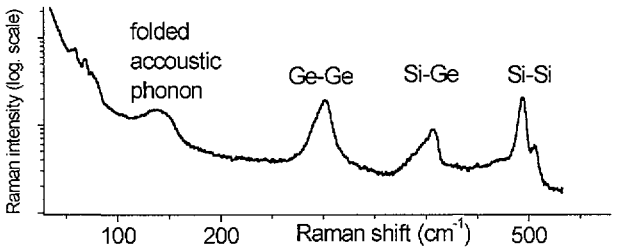

Fig. 3: Raman spectrum of the Si_5Ge_5 superlattice

In conclusion, an original analysis of TEM pictures has been used in conjunction with Raman spectroscopy and anharmonic Keating modeling to study the nanoscopic properties of Si_nGe_m superlattices epitaxially grown on silicon. Nanostructural peculiarities were measured and interpreted. The control of this local distribution of atoms is necessary to improve the light emission efficiency in this family of heterostructures.

REFERENCES

[1] S. Salpathy, R. Matin, and C. G. Van de Walle, Phys. Rev. **B 38**, 13 237 (1988).

[2] C. Guedj, M. Vasiliu, Proc. of the 13th International Conference on Digital Signal Processing, Santorini, Greece, July (1997), Vol.**2**, p. 547.

[3] C. Guedj, J. Kolodzey, A.Hairie, Phys. Rev. **B 60**, 22 (1999).

[4] C. Guedj, french patent n° 9709416 (FR2766598), european patent n°98401751.7-2201 (EP0893783), US patent pending.

RESONANT TUNNELING DIODES WITH HIGH PEAK TO VALLEY RATIOS GROWN BY LOW TEMPERATURE MBE

G. Dehlinger, U. Gennser, H. Sigg, L. Diehl, D. Grützmacher, D. Bächle (PSI), K. Ensslin (ETHZ)

Light emission from silicon based devices is restricted due to the indirect bandgap. The new approach of using intersubband transitions is a possible way to circumvent this. One elemental part of a light emitting quantum cascade structure is the resonant tunnelling structure (RTS), which we have realised in the Si/SiGe material system. We have studied such kind of devices in terms of structural properties, the influence of the emitter, as well as in terms of processing parameters. By using low growth temperatures to handle the strain between the Si and SiGe layers and to reduce the Ge segregation we have obtained excellent diodes with record peak to valley current ratio.

The discontinuity in the valence band offset between Si and SiGe-alloy permits to confine 2D hole states in a SiGe quantum well (QW) using Si barriers. In this study, this double barrier structure is sandwiched in SiGe cladding layers. By applying a voltage the quasi confined energy levels in the well can be aligned with the level of the carriers in the emitter, this enhances the transmission probability and leads to a resonant current peak in the I-V curve. Thus, this structure can be used to map out the subband levels of holes in the SiGe QW.

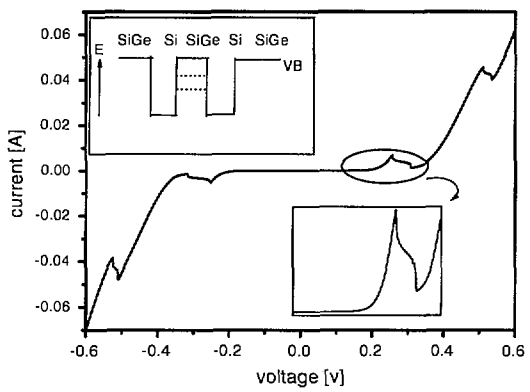

Fig. 1: I-V curve of a resonant tunnelling diode

By varying the well width, the position of the energy levels can be changed. This has been done for a set of samples; comparing the positions of the resonaces, a clear confinement shift is seen. This shift was compared with a simple model calculation of a particle in a box times a lever arm factor. The agreement between measured and calculated peak positions indicate, that the peaks are due to tunneling through the quasi-confined levels and that defect related tunneling can be excluded.

The design of a quantum cascade structure in the valence band of Si/SiGe structure requires careful band gap engineering. Thus the exact knowledge of the valence band states (heavy holes, light holes) is necessary. Temperature dependent and measurements in magnetic fields have been used to unravel some details of the valence band structure.

When the temperature is increased a second peak appears on the low voltage side of the first one. To explain this peak one has to take a careful view to the emitter structure. A shallow quantum well forms before the first barrier with different sublevels, due to the Ge onset and the applied bias. If one of this sublevel is slightly above the fermi edge, the level can be populated with thermal carriers, which are then tunnelling through the quantum well from this higher lying level. There are samples which show also at low temperature a double peak structure, this may be due to sublevels in the emitter below the fermi edge.

A magnetic field applied perpendicular to the current can give additionally helpful information about the tunnelling path. The measurements are done in a cryostat at low temperature and in magnetic fields up to 8 tesla. In several samples a new peak appears on the high voltage side of the lowest resonance. This extra peak seems to be related to the emitter structure and so, samples with different spacer lengths on both sides of the heterostructure were grown. The new resonance is only visible on the side with the shorter emitter. Further experiments and also enhanced model calculations will be necessary to find the origin of this peak.

In recent experiments with samples grown at low temperature (350°C) we have tried to determine the limits of thermal treatment during the processing. Even the unannealed samples show good characteristics, an indication of the cleanness of the growth chamber. Other samples were post growth annealed for a short time (1min) up to 900°C. The resonances show a shift to higher bias voltages with increasing annealing temperature. This can be explained with interdiffusion at the interfaces between the Si and the SiGe layers, leading to a smoother shape of the potential. Fascinating is the increase in the peak to valley current ratio (PVR) with temperature. After 1 min at 800°C, the PVR of the lowest resonance is raised to 4.7 and thus as large as the highest values reported in the literature.

The obtained knowledge about the physics of tunneling in the valence band of SiGe and the improved processing makes it possible to go for more complicated devices, like triple barrier structures and finally for intersubband emitters.

FUNDING: NF, PSI

COEXISTENCE OF WEAK LOCALIZATION AND A METALLIC PHASE IN Si/SiGe QUANTUM WELLS

V. Senz, G. Dehlinger, U. Gennser, D. Grützmacher (PSI), K. Ensslin, T. Heinzel and T. Ihn (ETHZ)

Magnetoresistivity measurements on p-type Si/SiGe quantum wells reveal the coexistence of a metallic phase and weak localization. Deep in the metallic regime, pronounced weak localization reduces the metallic behavior around zero magnetic field without destroying it. As the hole density is decreased, both the weak localization as well as the metallic behavior are reduced.

The recently discovered metal-insulator transition (MIT) in Si-MOSFETs [1] challenges the scaling theory of localization for non-interacting electrons in two dimensions (2D) in a weakly disordered regime ($k_F l >> 1$, where l is the elastic mean free path). In spite of considerable theoretical and experimental research the origin of the metallic phase is still not known.

The samples employed in this study were grown by molecular beam epitaxy, and consist of a p-modulation doped 200Å wide $Si_{0.85}Ge_{0.15}$ quantum well. The hole density can be tuned between 1.1×10^{11} cm^{-2} $\leq p \leq 2.6 \times 10^{11}$ cm^{-2}. Fig. 1 shows a series of magnetoresistance measurements for several carrier densities and temperatures. At high hole densities (a, b), the resistivity at B=0 clearly decreases with decreasing temperature, indicating a metallic phase in the framework of the MIT in 2D. The metallic behavior becomes insulating as the carrier density is further reduced. (d, e). At intermediate hole densities (c), the temperature dependence of ρ behaves insulating at low temperatures, and switches to metallic at higher temperatures. Magnetoresistivity measurements allow for a distinction between different contributions to the total resistivity. While the magnetoresistivity experiences a negative correction due to the weak localization effect, spin-orbit coupling results in a positive magnetoresistivity. Interactions produce a complex magnetoresistivity, which depends on the sample parameters.

From the magnetic field dependence of the resistivity one can clearly discern a negative magnetoresistance in the metallic phase (a-b). Theoretical curves for the weak localization (WL) correction of ρ(B) are fitted to the data with the phase coherence time $\tau_\phi(T)$ as a parameter. We find $\tau_\phi \propto T^{-\gamma}$, with γ = 0.9-1.4. For dephasing by quasi-elastic electron-electron collisions (i.e. Nyquist noise), γ = 1 is expected. Hence, from the T dependence of τ_ϕ, there is no indication of a novel dephasing mechanism due to the presence of the metallic phase. Furthermore, γ does not depend significantly on p in the metallic phase. Assuming that Nyquist noise causes the dephasing, we find that τ_ϕ is a factor ≈3.2 below the value expected from theory. Similar discrepancies between experiment and theory are found for insulating 2D carrier systems. These results indicate that even in the metallic regime, a significant amount of carriers still contribute to WL.

In order to distinguish the temperature dependence of WL from the background resistance, we compare the resistivity at B = 0 with the one at B = 0.3 T, where the WL is quenched. Especially at low temperatures the metallic behavior becomes more pronounced as one moves out of the weak localization peak. This suggests that two different conductivity mechanisms (or two conducting systems, respectively) exist, one with a metallic temperature behavior and another one with a standard, insulating weak localization behavior. A possible theoretical description could be the two-phase model proposed recently by He and Xie.

As one enters the insulating phase at B=0, (Fig. 1d), a very broad negative magnetoresistivity develops that determines the overall temperature dependence. In this situation, (i.e. $k_F l \leq 1$) τ_ϕ cannot be extracted from the data. In this regime, the sample looks rather like a conventional 2D carrier gas with low mobility.

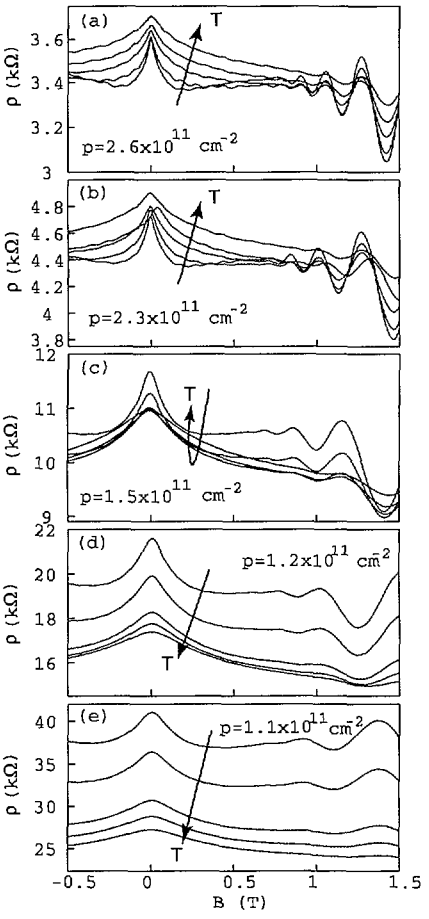

Fig. 1: Magnetoresistivity for different carrier densities

FUNDING: SNF

REFERENCE

[1] S.V. Kravchenko, *et al.*, Phys. Rev. B **50**, 8039 (1994).

DIRECT OBSERVATION OF THE DEPOLARIZATION SHIFT OF THE INTERSUBBAND RESONANCE

S. Graf, H.C. Sigg, H. Siegwart (PSI), W. Bächtold (ETHZ), K. Köhler (IAF Freiburg i. Br.)

We have studied the intersubband resonance of GaAs/AlGaAs multi quantum well systems by comparing photon drag and absorption spectra obtained by in-plane photo current and -conduction measurements. The peak absorption at room temperature is found to be blue-shifted from the photon drag resonance by as much as 33 cm^{-1}. We argue that this difference gives directly the depolarization shift.

A single electron in a semiconductor quantum well (QW) would obey the single-particle, linear Schrödinger equation, and resonantly absorb light at a frequency equal to the difference between quantized subband energies. Since many electrons are present in real QWs, oscillating fields inside the well are dynamically screened. In simple systems like GaAs QWs, collective effects lead to a blue shift of the resonance - the so called *depolarization shifted* intersubband resonance (ISR).

The photon drag (PD) effect is a current, which is excited in the plane of the two dimensional electron gas by the absorbed photons. We could show that this effect yields a new method to directly observe the depolarization shift even at room temperature [1]. The basic idea is the following: While the absorption process is basically a zero wave vector collective excitation and thus blueshifted from the ISR, the PD effect, in particular the resonant part of the PD, can only be understood as a consequence of single particle excitations, with k extending from zero up to the Fermi wave vector. Because of the subband level dependent momentum relaxation rate this current is different for excitation at opposite sides of the single particle dispersion. Since the transition energy for these excitations differ by the Doppler effect, an antisymmetric current response is obtained, and the transition energy at the electron propagation vector k = 0 (which is by definition the single particle transition energy in a system with parallel subbands) is apparent from the zero crossing of the resonant photon drag current [2].

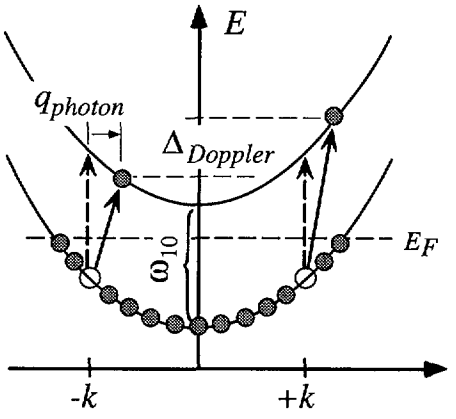

In order to enable an accurate comparison between the PD and the ISR absorption, pulsed photocurrent and photo conduction (PC) measurements have been performed under positive and negative bias, cf. inset of figure. The corresponding spectral response of the PC and the PD are analytically obtained by, respectively, the difference and the sum of the signals of each polarity. The PC spectrum, which is proportional to the IS absorption (open circles), has a Lorentzian lineshape with the peak position at 866 cm^{-1}.

In order to determine the PD resonance position, the PD spectrum (diamonds) must be decomposed into its so called direct and resonant parts, shown in (b). The ω-dependence of the direct part coincides with the spectral dependence of the IS absorption. The resonant component has its zero crossing at 833 cm^{-1}. The single particle excitation energy is thus blue-shifted by 33 cm^{-1}, illustrating the importance of screening even at RT.

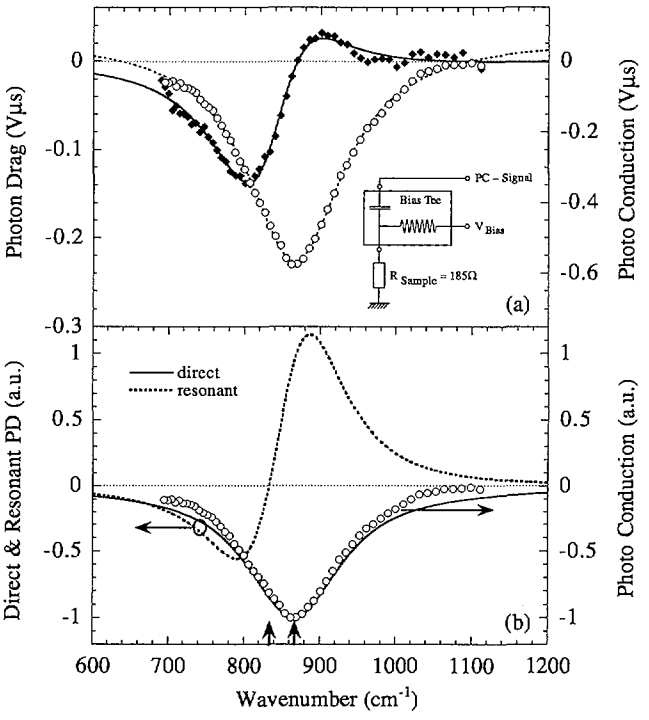

Fig. 1: Intersubband spectra

This technique has also been applied to study the depolarization shift dependence on excitation intensity. An unexpectedly strong screening effect has been found at room temperature, up to intensities close to saturation.

FUNDING: PSI, SNF.

REFERENCES

[1] S. Graf, H. Sigg, K. Köhler, and W. Bächtold, accepted for publication in Phys. Rev. Lett.

[2] M. Zaluzny, Solid State Comm. **103**, 435 (1997).

BUILDING BLOCKS FOR MICRO-CRYSTALLINE THIN FILM SI SOLAR CELLS ON GLASS SUBSTRATE

J. A. Anna Selvan, D. Grützmacher, H. Sigg, S. Stutz, E. Müller, C. Musil, R. Kirchhofer, T. Neiger, A. Wokaun, D. Bächle, E. Ortelli, J. Panitz , J. Gobrecht (PSI)

Thin film Si solar cells possess the potential of low cost fabrication, reduced material requirements, large area deposition, roll-to-roll production and low cost substrates. For the development of such a process the following tasks were studied:1) the evaluation of deposition techniques for the formation of micro crystalline silicon (μc-Si:H) thin films with reduced defects during growth and high growth rate, simultaneously. 2) the growth of microcrystalline silicon (μc-Si:H) thin films on low temperature substrates such as glass by DC remote Plasma Enhanced Chemical Vapour Deposition (PECVD) and Molecular Beam Epitaxy (MBE). 3) the development of efficient light trapping structures for thin film solar cells using TCOs, glass substrates or thin film silicon. 4) the development of Transparent Conducting Oxides (TCOs) for contact layers, efficient NIR reflectors, AR coatings or diffusion barriers for thin film solar cells, and 5) the deposition of metal thin films for efficient back reflector systems.

The scope of the present work is the evaluation of deposition techniques for the formation of microcrystalline silicon thin films on low temperature substrates, such as, glass. High quality (μc-Si:H) films with a growth rate of 0.8nm/sec have been achieved by the DC remote PECVD method. Using a new configuration, the DC remote PECVD, it is possible to control the crystallinity, the amorphous content in the material, the incorporation of hydrogen, the orientation, the columnar nature and the surface texture.

Further, the effects of the system geometry of the DC-PECVD system on the growth mechanism have been analysed. Regimes which permit a simultaneous increase in crystallinity as well as growth rate have been identified. By MBE, highly columnar (μc-Si:H) films with an average grain size of 750nm have been obtained.

Light trapping techniques are mandatory for thin film solar cells. The Surface texture growth of Si has been obtained by MBE and DC remote PECVD methods. Different light trapping schemes for thin film solar cells were developed. Efficient light trapping structure with an haze factor of 63% at 1000nm were obtained.

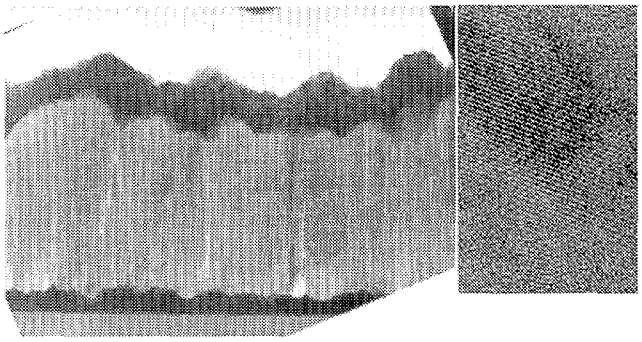

Another important requirement for thin film Si Solar cells are Transparent Conducting Oxides (TCOs). Highly conducting Sn doped InO_3 and Al doped ZnO films with a resistivity of $4x10^{-4}$ohm.cm and a high optical transmittance of above 80% were grown using reactive sputtering. The effect of process parameter on the elecrical properties, optical transmittance, color centres, surface texture and the chemical stability of these TCO films were studied. These films can be used as contact layers, efficient NIR reflectors, AR coating and diffusion barriers for thin film Si solar cells.

The first figure shows the cross sectional HRTEM of a thin film Si solar cell. The μc-Si is grown by MBE on a Pd coated glass substrate. The film exhibits a columnar structure and a pronounced facetting of the surface that provides light trapping. Figure at the right hand side show HRTEM picture of microcrystalline grains of Si grown on glass substrate by DC remote PECVD.

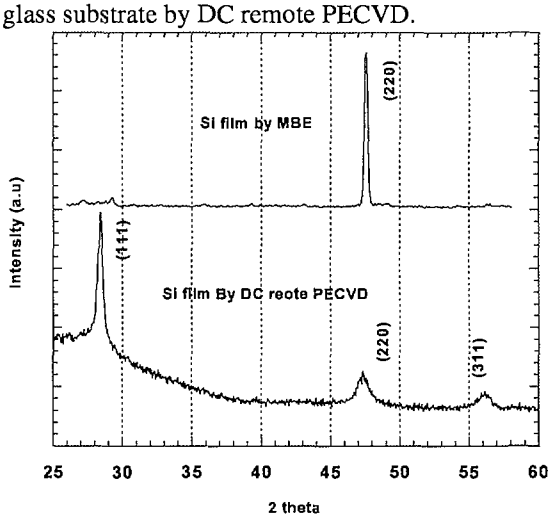

The second figure shows typical x-ray diffraction patterns of Si thin films grown by MBE and DC remote PECVD. Orientation along <220> direction in Si films grown by MBE correspond to highly columnar grains with a lateral grain size of about 750nm.

The established development of an efficient Si thin film growth system, the study of μc-Si:H film deposition on low temperature substrates and the development of TCOs and back reflectors are essential requirements, since they form the building blocks for thin film Si solar cells on low temperature compatible substrates.

FUNDING: European Commission and BBW.

REFERENCES

[1] J. A. Anna Selvan, D. Grützmacher, et al, proceedings of 16th European PV Conference, 2000, Glasgow.

[2] J. A. Anna Selvan, D. Grützmacher, et al. Materials Research Society Proceedings, Spring 2000.

CRITICAL COMPONENTS FOR TPV APPLICATIONS

B. Bitnar, D. Bächle, W. Durisch, D. Grützmacher, B. Haas, B. Ketterer, R. Kirchhofer, J.C. Mayor, D. Seiler, J. A. Anna Selvan, H. Sigg, F. von Roth, J. Gobrecht (PSI)

Thermophotovoltaics (TPV) generate electrical power by using photovoltaic cells illuminated by the radiation of a flame-heated emitter. The critical components for a highly efficient TPV system are: an emitter with a selective high emissivity, a selective filter reflecting far IR-radiation back to the emitter and photocells with a high efficiency in the emitted spectral range. We report on the first results using an Yb_2O_3 selective emitter and silicon photocells.

A key application of TPV is the integration in residential heating systems. Electrically self-powered gas heaters can be realised which will be independent on power failures of the grid. The power of such a TPV generator is an electrical output of 150 W with a typical thermal input power of 20 kW. In addition a TPV system with at least 1 kW electrical power can be used as an electrical power generator of a grid independent house. Even the production of electricity at high peak periods with a large number of peripheral gas heating systems is a promising application of the TPV, leading to a more efficient use of fossil fuels.

At PSI, TPV prototype systems with Yb_2O_3 selective emitters and silicon photocell generators are developed by the group 'Angewandte Photovoltaik'[1]. Up to now an efficiency of 1.3% could be reached in a system with 1.35 kW thermal power. An enlarged 20 kW burner has reached an electrical output power of 80 W with commercially available silicon solar cells.

We aim for the long term 1 kW electrical power with such a system. The three critical parts of the TPV system are the selective emitter, the filter which keeps the IR radiation away from the photocells and the photocell generator itself.

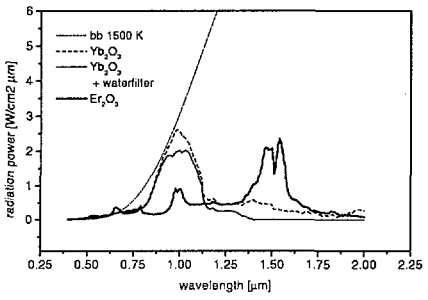

The Fig. above shows measured spectra of the selective emitter radiation of selected rare earth emitters. The Yb_2O_3-spectra were measured in the 1.35 kW TPV system. A 5 mm thick waterfilter absorbs radiation with longer wavelength than 1100 nm to protect the photocells from heating by IR-radiation not converted to current. The spectra were measured with and without the waterfilter. The waterfilter absorbs 34% of the emitter radiation.

With these measured spectral distributions the maximum emitter radiation power can be calculated by using a combustion model [2]. The next Fig. shows as a result the emitter radiation power P_{em} as a function of the thermal input power P_{th} for Yb_2O_3 and Er_2O_3 emitters.

An Yb_2O_3 emitter with an area of 500 cm^2, which is used in the 20 kW system, can produce a radiation power of 3.3 kW. A slightly higher radiation power is given by an Er_2O_3 emitter of the same size. A stronger increase in P_{em} is reached by an enlarging of the Yb_2O_3 emitter area to $10^3 cm^2$

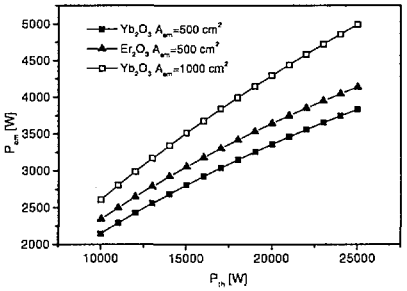

To avoid the radiation absorption in the waterfilter, TCO bandedge filters are in development, which reflect the long wavelength radiation back to the emitter.

Silicon photocells for a high efficiency cell generator have been produced. The following table gives the IV-characteristic of such cells:

	I_{SC} [mA/cm²]	V_{OC} [mV]	η [%]	spectrum
M	37.5	647	18.9	AM1.5
C1	45.3	640	23.6	Yb_2O_3, WF
C2	53.7	651	28	Yb_2O_3, 1100nm

M is a measurement under AM1.5 illumination with the solar simulator. C1 and C2 are calculations using the simulation program PC1D and the Yb_2O_3 emitter radiation through the water filter (WF) and a bandedge filter with 1100 nm cutoff wavelength respectively.

In conclusion, theoretical calculations show that an Yb_2O_3 emitter/silicon photocell-TPV system with an electrical power of 1 kW can be realised: An emitter with an area of 1000 cm^2 produces at P_{th} = 25 kW about 5 kW radiation power. With a cutoff filter at 1100 nm, a filter absorption of 5% and an efficiency of the photocells of 28% the electrical power is 1040 W. The emitter temperature in this example is 1900 K. A comparable electrical power at lower emitter temperatures is possible with an Er_2O_3 emitter and low bandgap photocells. For the near future we plan to practically realise a high power TPV system with an Yb_2O_3 emitter and silicon cells. For the long term goal we will study the possibility of producing lower gap germanium photocells with a comparable efficiency to the silicon cells.

FUNDING: BFE, PSI

REFERENCES

[1] W. Durisch, B. Grob, J.C. Mayor, J.C. Panitz, A. Rosselet, *4th NREL Conf. on TPV* 403 (1999).

[2] M. Schubnell, P. Benz, J.C. Mayor, *Solar Energy Mat. and Solar Cells* **52**, 1-9 (1998).

HIGHLY SENSITIVE ENZYME IMMUNOASSAY (EIA) FOR DETECTION OF PENICILLIN IN MILK

A. Grubelnik, C. Padeste, J.-J. Hefti, L. Tiefenauer (PSI)

A new type of enzyme immunoassay for detection of benzylpenicillin has been developed. With a combination of highly sensitive antibodies against the hydrolysed form of the benzylpenicillin and transformation of the analyte into this form, benzylpenicillin could be detected in milk in concentrations down to 0.1 ppb. The high sensitivity achieved may allow application in food quality control and assurance.

The β-lactam antibiotics, in particular the penicillins, are most frequently used for the prophylaxis and therapy of infectious diseases in veterinary medicine. Unauthorised drug use, prolonged drug excretion and neglect of the withdrawal times may result in residues of penicillins in milk and animal tissues. Because traces of antibiotics can inhibit bacterial starter cultures used in diary food production, we are developing an amperometric immunosensor device for monitoring β-lactam antibiotics in milk. A sensitive antiserum is crucial for an immunosensor. Since no suitable antiserum was commercially available, we decided to raise own antisera.

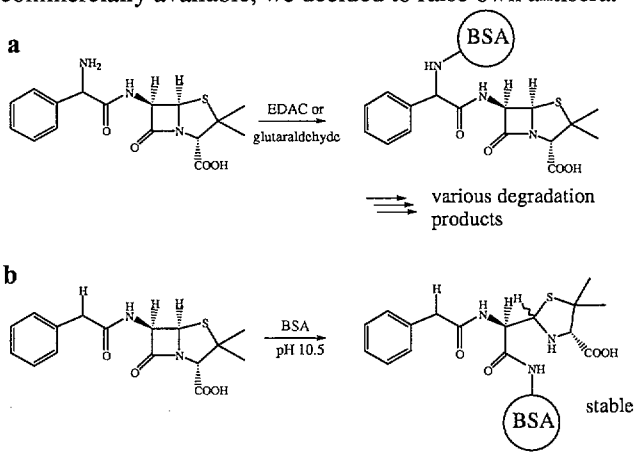

The production of a sensitive antiserum against penicillin turned out to be difficult due to the low immunogenity of benzylpenicillin conjugates. We suppose that this problem originates from degradation of the immunogen during immunisation (a). Therefore, we synthesised a stable protein conjugate of the hydrolysed form of benzylpenicillin for immunisation (b).

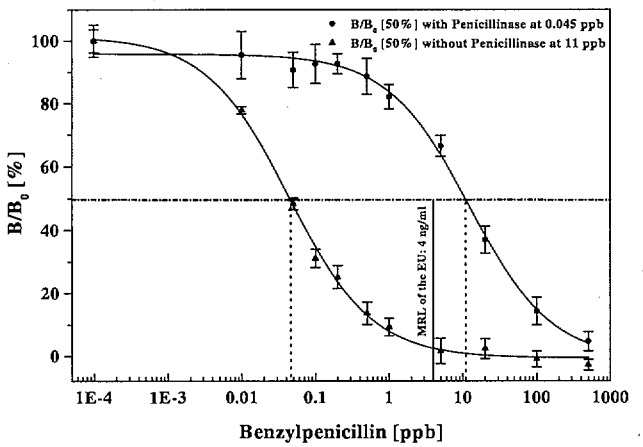

Fig. 1: Calibration curve for benzylpenicillin

Addition of penicillinase to the sample during the assay leads to controlled hydrolysis of penicillin to the corresponding hydrolysed penicilloyl compound which is recognised specifically by the antibody. It was observed that the 50% inhibition was shifted from 11 ppb to 0.05 ppb upon addition of penicillinase [1]. In other words, the sensitivity of the assay increased by a factor of 220 (Fig. 1).

The usefulness of the assay to determine benzylpenicillin in real samples was tested using milk as the matrix. Recovery experiments in spiked milk samples in the concentration range from 0 to 10 ppb have been carried out. The results show that detection of benzylpenicillin in milk in concentrations down to 0.1 ppb i. e. more than one order of magnitude below the MRL of the EU can be achieved easily. Furthermore, the crossreactivity of all other relevant β-lactam antibiotics is negligible.

Benzylpenicillin added (ppb)	Benzylpenicillin found (ppb)	Recovery (%)
10	>5	-
3.2	3.28 ± 0.73	104
1.0	0.99 ± 0.14	99
0.32	0.37 ± 0.05	117
0.10	0.11 ± 0.01	110
0.03	0.04 ± 0.01	130
0	<0.02	-

Table 1: Recovery experiment

The new method developed for benzylpenicillin may also be applicable to other β-lactam antibiotics of interest, as far as they can be hydrolysed by β-lactamases. A set of specific and sensitive antisera against the most common β-lactam antibiotics could be raised by immunisation with the corresponding protein conjugates. These antisera could be used to specifically determine antibiotic residues or, when combined, to determine the sum of β-lactam antibiotics in a sample of interest. This invention may further promote the analysis of antibiotics by immunological methods and provide a powerful tool for monitoring food quality.

REFERENCE

[1] A. Grubelnik, C. Padeste and L. Tiefenauer, (1999) Swiss Patent Application No. 1764/99.

CHARACTERISATION OF ANTIBODY-ANTIGEN INTERACTIONS BY SINGLE MOLECULE FORCE SPECTROSCOPY

R. Ros, D. Bächle, L. Tiefenauer (PSI), F. Schwesinger, A. Plückthun (Univ. Zürich), D. Anselmetti (Solvias AG), T. Strunz, H.-J. Güntherodt (Univ. Basel)

The characterisation of ligand–receptor interactions is fundamental for drug design and diagnostics. We measured binding forces of a series of antibody-antigen complexes using atomic force microscopy (AFM) techniques. Their thermodynamic and kinetic values were also determined and we found a correlation between forces and k_{off}-values.

Single molecule force spectroscopy is potentially useful to characterise antibody molecules. First, thermodynamic and kinetic properties of a series of single-chain Fv antibody molecules (scFv) were determined which all bind specifically the antigen fluorescein. From three scFv-variants recombinant mutant proteins have been produced. Their rates of the unbinding reaction (k_{off})varied over 3 orders of magnitudes and dominate the value of the dissociation constants.

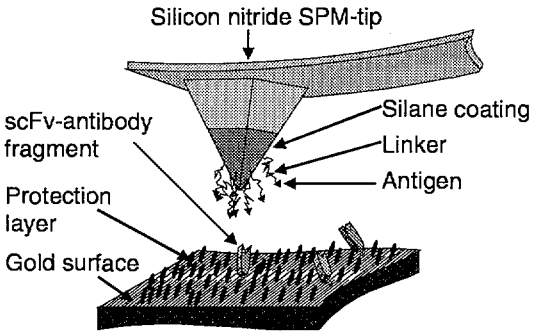

For the force spectroscopy experiments the antigen is attached covalently via a 40 nm polymer-linker to the AFM-tip while the scFv-fragments are immobilised directly via their terminal cysteine onto a flat gold surface. For recording the force distance curves the bending of the cantilever is measured which changes when the AFM-tip is approached to and subsequently retracted from the surface.

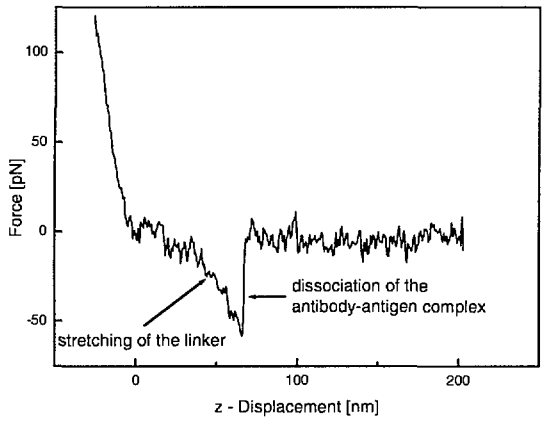

Fig. 1: Force distance curve

In the retracting part of the curve the stretching of the polymer-linker is observed, followed by the rupture of a single antigen-antibody complex. In order to minimise noise and to clearly reveal this sharp jump we used high data sampling rates (10 kHz) and averaged the data points.

Based on about 100 curves the rupture force F for one specific scFv-antigen complex can be determined. From all nine different scFv unbinding force values were measured and by comparison with an original scFv (wild type) statistically significant differences in rupture forces (ΔF) were obtained. When these ΔF were put in relation to thermodynamic and kinetic values, a strong logarithmic correlation (r=-0.96) to k_{off}-values was found.

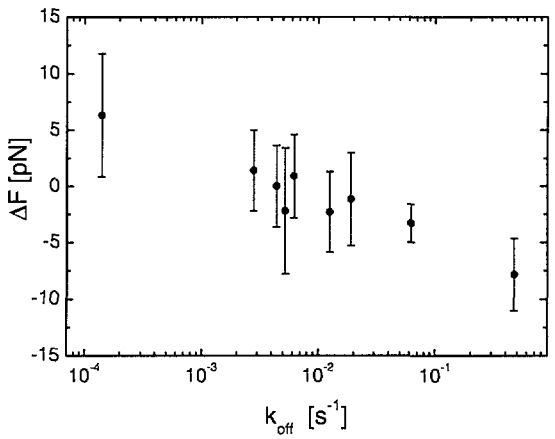

Fig. 2: Force differences vs. off-rates

This result can be explained with a model in which an applied force accelerate thermal dissociation of the complex. Because k_{off} is closely related to K_D, force spectroscopy will also be helpful to screen antibodies for low dissociation constants.

The results demonstrate the potential of AFM-techniques for a direct and label-free antibody characterisation. The power of this method is the minimal required quantity of antibody: in principle a single molecule will be sufficient.

FUNDING: NFP 36 Nanoscience, PSI.

REFERENCE

[1] R. Ros, F. Schwesinger, C. Padeste, A. Plückthun, D. Anselmetti, H.-J. Güntherodt, and L. Tiefenauer; *Proceedings of SPIE* **3607,** 84-89 (1999).

MODIFICATION OF NANOSTRUCTURES AND FORCE MEASUREMENTS AT THE SOLID-LIQUID INTERFACE

B. Baumeister, R. Ros, L. Tiefenauer, T. Jung, L. Scandella (PSI), B. Bucher (FH Rapperswil), A. Fechtenkötter and K. Muellen (MPIP Mainz)

The assembly of individual nanometerscale objects into well defined arrangements is one of the important technologies for the engineering of nanoscale structures. Molecules as nanoscale objects require novel methods for positioning which are optimised using Si-nanodots. Force experiments with single molecules deliver technologically relevant information in the context of molecular life sciences, sensor systems, miniaturisation of technological functions like data storage and for the science of new nano-composite materials.

Molecular positioning of individual units into larger suprastructures is one of the key techniques to construct well defined nanoscale structures and explore their properties. Mechanical experiments with single individual molecules require a special software and hardware interface to perform movements with the force sensor in all three directions. These systems have been successfully established at PSI to measure the unbinding of an antigen-antibody complex. A newly built liquid cell enables us to perform these experiments in a liquid flow. Recently software algorithms have been designed and implemented to automatically recognize and identify individual molecular units. The top image shows an atomic force micrograph of nanotowers as they were built from a Si wafer using lithographic techniques. By applying an increased and modulated force around 10^{-7} N individual nanotowers can be detached from the 2-dimensional array and repositioned across the interface (bottom image).

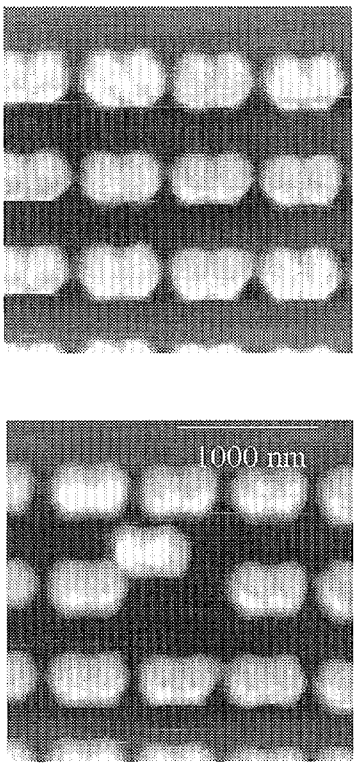

Fig. 1: Nanotower positioning by using AFM

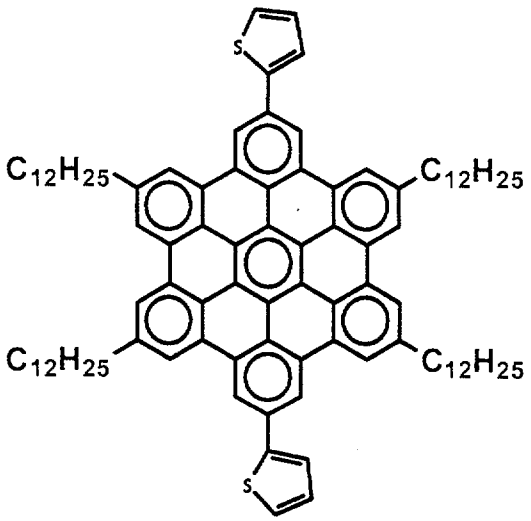

Fig. 2: Structure of HPB

Planar polyaromatic molecules, like the hexaphenylbenzol (HPB) derivative shown above, are strong adsorbates to solid substrates and will be used as objects for positioning. At the solid-vacuum interface the formation of supramolecular structures has been demonstrated [1]. The selectivity of molecular adsorption on nanopatterned substrates has been shown in reference [2]. At the solid-liquid interface, the intermolecular and surface forces are modified by the interactions between the substrate, the solvate and the solvent. In our experiments we apply atomic force microscopy to study these forces for nanosize objects and single molecules. The properties of the HPB derivatives with different substituents will be compared for specific molecules selected in collaboration with sythetic chemists. Using synchrotron light and diffraction methods we expect to further understand molecular adsorption and diffusive and induced motion at the single molecule level.

FUNDING: SNF, PSI

REFERENCES

[1] T.A. Jung, R.R. Schlittler, J.K. Gimzewski, H. Tang, C. Joachim, Science **271**, 181 (1996).

[2] H. Rauscher, T.A. Jung, J.-L. Lin, A. Kirakosian, F.J. Himpsel, U. Rohr, K. Müllen, Chemical Physics Letters **303**, 363 (1999).

MOLECULAR WIRING FOR ELECTROCHEMICAL BIOSENSORS

C. Padeste, A. Grubelnik, J.-J. Hefti, L. Tiefenauer (PSI)

Avidin-ferrocene conjugates have been synthesised which combine the unique binding properties of avidin for biotinylated compounds and the reversible redox chemistry of ferrocenes. When immobilised on electrodes, the new conjugates provide a multifunctional base for electrochemical biosensors. As a demonstrator example biotin-micro-peroxidase conjugates were bound and used to electrochemically detect hydrogen peroxide.

Avidin immobilised on surfaces is widely used to generate platforms for various analytical applications. By binding biochemically active molecules via biotin, the specificity of the surface is adapted to analytical problems of interest. For use in electrochemical detection schemes, the insulating barrier of avidin mono- and multilayers has to be overcome.

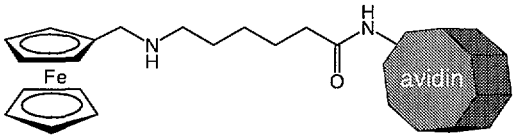

A ferrocene derivative with a flexible spacer was synthesised and covalently linked to avidin. The synthesis was optimised to yield 10-30 redox centres per protein molecule. Binding tests using radiolabeled biotin revealed intact binding sites of the conjugates.

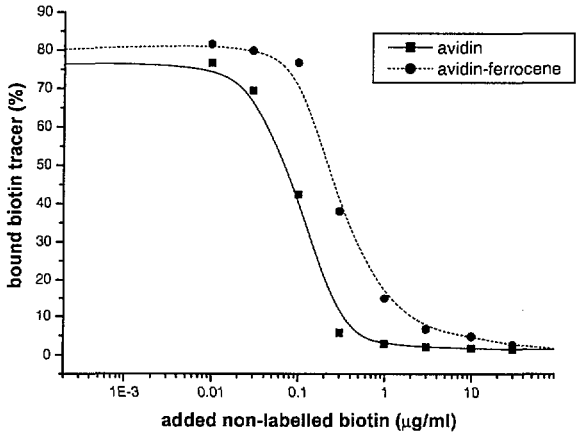

Fig. 1: Binding capacity for biotin

For electrochemical characterisation, the conjugates were then covalently bound to gold electrodes using a bifunctional linker. Cyclic and square wave voltammograms recorded in phosphate buffer solutions showed signals of the immobilised ferrocene. When multilayers of the conjugates were immobilised, the intensity of the corresponding signal was increased.

Of main interest is the compatibility of the conjugate with electrocatalytic processes, which are fundamental for electrochemical enzyme- or immunosensors. As a model system mircoperoxidase MP11 was used, which catalyses the electrochemical reduction of hydrogen peroxide (H_2O_2)

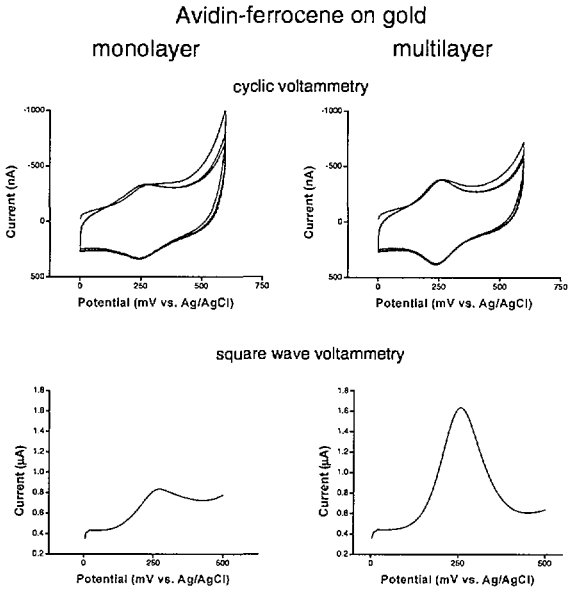

Fig. 2: Cyclic voltammograms of avidin-ferrocene

at moderate potential. MP11 was coupled to biotin and the conjugate was bound to gold electrodes with immobilised avidin or avidin-ferrocene, respectively. The electrodes were then placed in an electrochemical flow cell. Small quantities of H_2O_2 injected at a potential of 175 mV (vs. Ag/AgCl) resulted in reducing currents. The measured peak intensities were significantly higher when ferrocene was coupled to avidin (right). These results indicate an efficient electron transport through the avidin-ferrocene monolayers.

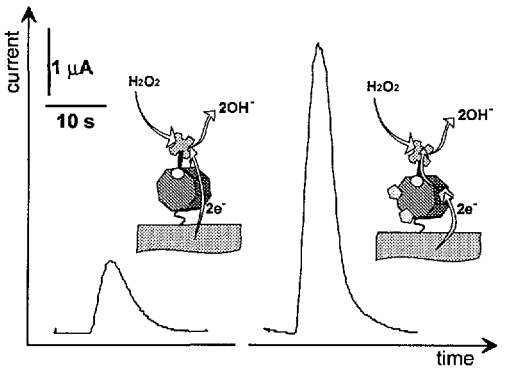

Fig. 3: Electrocatalytic current from peroxidase

In a next step, the conjugates will be used for an electrochemical immunosensor set-up. Biotin-antigen conjugates are bound to avidin-ferrocene immobilised on a gold electrode and the binding of the corresponding micro-peroxidase labelled antibody is detected electrochemically.

PATTERNING OF ADHESION PROTEINS FOR NEURITE GUIDANCE ON GLASS

H. Sorribas, C. Padeste, K. Ballmer, L. Tiefenauer (PSI), L. Leder, P. Sonderegger (Univ. Zürich), R. Douglas (ETH/Uni Zürich)

Using photolithographic techniques patterns of a neural cell adesion protein were created. These protein patterns can guide growing neurites of dissociated neurons to form networks of defined connectivities. Application of this technique on the neurochip developed in this project will facilitate neuron cell positioning into the areas designed for extracellular recording.

The capacity to generate guided neurite outgrowth by chemical modification of surfaces is essential for the generation of neuronal networks on glass chips. Here we report on the lithographic patterning of the adhesion protein axonin-1, a member of the Ig-superfamily involved in neurite outgrowth, axonal pathfinding, and neurite fasciculation.

A recombinant axonin-1 molecule with a C-terminal cysteine (Cys-axonin-1) was constructed and expressed in an eucaryotic cell line. The C-terminal cysteine allows a stable, covalent and oriented immobilisation of functional molecules directly on gold surfaces. On glass, a covalent immobilisation of Cys-axonin-1 was achieved using a reactive aminosilane and a heterobifunctional crosslinker. After immobilisation the protein was protected with a sucrose film to stand the harsh conditions during photolithographic processes. A positive photoresist was then spun on the chips and structured using a photolithographic mask with grid and line patterns. After development of the resist the chips were exposed to oxygen plasma to remove the protein from surface regions that were not protected by the photoresist. Finally, the resist was stripped by ultrasonic treatment in acetone. The protein functionality was assessed using a fluorescent-label antibody.

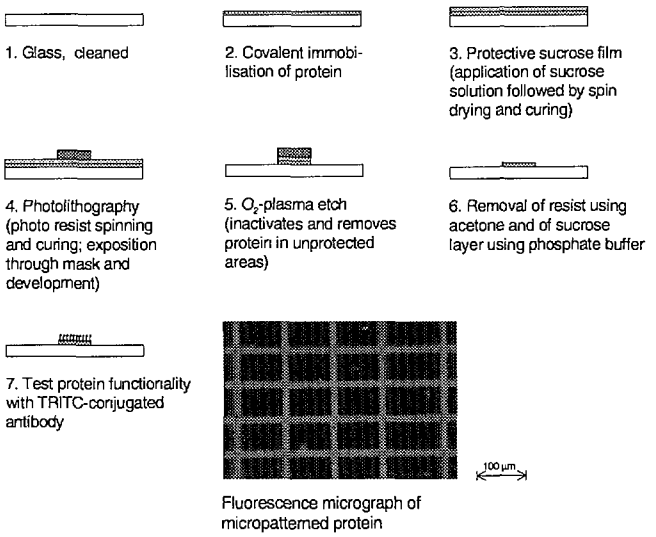

Fig. 1: Preparation of protein patterns

Dorsal root ganglion neurons isolated from 10-day-old chicken embryos were plated in serum-free medium at low surface density on the protein-patterned chips. After 24 h in culture neurites were growing along the adhesion protein lanes forming regular two dimensional networks on glass.

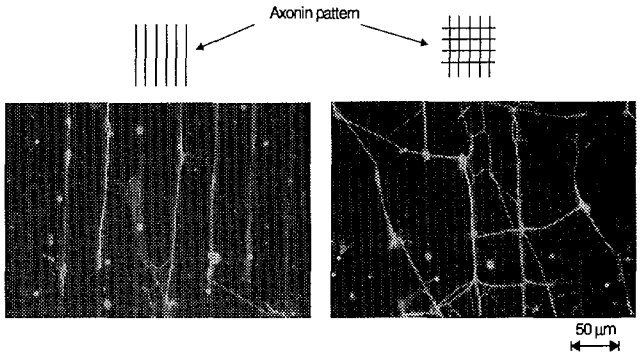

Fig. 2: Axon outgrowth along lines

As a next step towards the generation of defined neural networks on extracellular electrode arrays this technique will now be applied on a previously produced neurochip. Local immobilisation of the adhesion protein in the microgrooves (20 x 100 µm) is planned. These microgrooves are designed to host one neuron and have extracellular gold electrodes at each end that can be used for stimulation and recording of single neuronal activity.

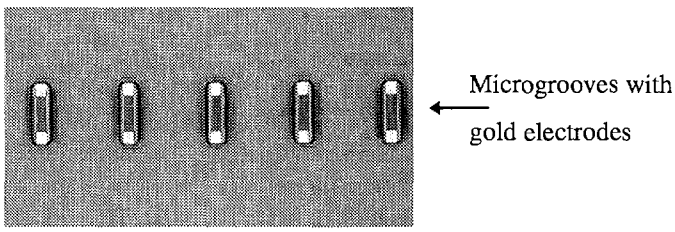

Fig. 3: Microgrooves in polyimide

FUNDING: SPP Biotech, PSI

REFERENCE

[1] H. Sorribas, C. Padeste, T. Mezzacasa, L. Leder, D. Fitzli, P. Sonderegger and L. Tiefenauer, J. Mat. Sci.: Mat. Med. **10**, 787-791 (1999).

POLYMER CHIPS FOR SCANNING PROBE MICROSCOPE CALIBRATION

H. Schift, D. Bächle, C. David, F. Glaus, J. Gobrecht, L.J. Heyderman, B. Ketterer (PSI), A. D'Amore, D. Simoneta and W. Kaiser (FH Aargau, Windisch), O. Fischer, M. Gabriel and M. Wey (AWM Werkzeugbau AG, Muri), L. Scandella (NanoSurf AG, Liestal)

Low-cost nanostructured calibration standards for Scanning Probe Microscopes have been fabricated using an advanced Compact Disc fabrication process. Regular grids with periods of 160 nm have been generated on a silicon wafer using e-beam lithography and etching techniques. The quality of the injection molded plastic replicas of these masters was found to be well suited for the lateral calibration of AFM and STM piezo scan mechanisms.

Scanning Probe Microscopes (SPM) are now widely used for the nanoscopic characterization of surface structures and properties. Because of the nonlinear behavior and drift of the the piezo scan mechanism used for the lateral displacement of the tip versus the sample, it has to be calibrated before quantitative measurements can be performed. For this purpose calibration samples are needed having a surface relief with defined lateral and vertical dimensions, which can serve as a rapid reference scale.

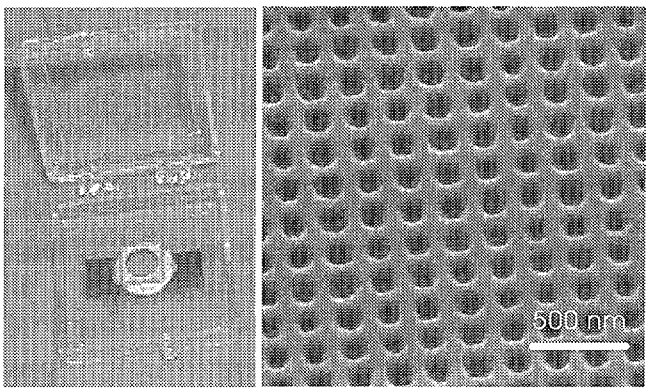

Crossed gratings with sub-µm periods are ideal when the lateral calibration has to be done for small scanning distances, but are usually expensive or difficult to obtain. Molding has demonstrated its potential for the mass fabrication of nanostructured surfaces. Structure sizes down to 25 nm and aspect ratios up to 3:1 have been replicated in polymers using hot embossing and thermal injection molding of thermoplastic materials [1]. For this purpose a single master grating structure has to be produced with a precise period, from which many identical structures can be replicated.

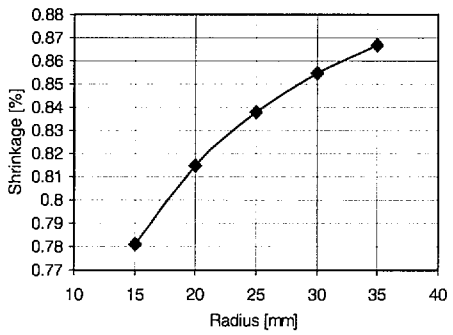

Master structures were fabricated on silicon wafers by electron beam exposure of thin PMMA films and subsequent dry etching. Gratings with periods ranging from 120 nm to 400 nm were fabricated. The master was inserted into a Compact Disc molding tool from AWM and several hundred discs with a diameter of 80 mm were produced with cycle times down to 10 sec. The polymer used was a polycarbonate, „Makrolon CD 2005" from BAYER. The precision of the distance between neighboring grating lines is considered to have the 2.5 nm accuracy of the interferometrically controlled stage of our LION LV1 e-beam writer. Its high positioning accuracy can also be used to determine local deviations of structure positions on a molded disc from the master with sub-µm precision. Using this we measured the radial dependence of the process shrinkage of the polymer on a disc (see diagram).

For the miniaturized low-cost Scanning Tunneling Microscope (STM) „easyscan" of NanoSurf, a 2x2 mm^2 area grating with a period of 160 nm was considered most suitable for the calibration of its maximum scanning distance of 500 nm. Small pieces of 7 x 7 mm^2 containing the surface grating were cut out of the disc and glued onto a round metal holder (see picture). Sufficient electrical surface conductivity was achieved by sputtering of a thin layer of AuPd onto the surface.

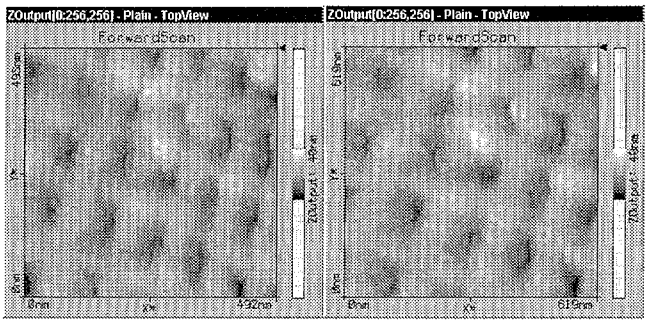

The plastic replicas were investigated by SEM, AFM and STM techniques and show a high fidelity reproduction of the nanogratings of the silicon master. The micrograph above displays structures imaged with an easyscan STM before (left) and after (right) calibration of the instrument. We estimate an absolute accuracy of the STM measurement of +/-5nm over a measuring field of 500x500 nm^2.

NanoSurf is now able to offer this precision calibration chip for its SPMs. Apart from this application, a large potential of the injection molding technique for the mass fabrication of nanostructured devices such as optical encoders can be seen.

FUNDING: SNF (NFP36), PSI, FHA, AWM.

REFERENCES

[1] S. Köppel, H. Schift, M. Gabriel and W. Kaiser, Kunststoffe-Synthetics **2/99,** 11-14 (1999).

RHEOLOGY OF THIN POLYMER FILMS USED IN HOT EMBOSSING

L.J. Heyderman, D. Bächle, C. David, J. Gobrecht, B. Ketterer, J. Mahler, T. Neiger, H. Schift (PSI), T. Schweizer (ETHZ)

The viscous flow of thin PMMA films into microcavities during hot embossing has been investigated in order to optimise the moulding of nanostructured surfaces. A key fill mechanism was determined to be the flow of PMMA from the borders of a cavity. The fastest embossing times were obtained at temperatures greater than 100°C above T_g and with these conditions, a good filling of both microstructures and nanostructure arrays was obtained.

The hot embossing process is a low cost, fast method for the parallel replication of structures at the micro- and nanoscale. With a single master or stamp, identical structures can be reproduced as required over large surfaces. In Hot Embossing Lithography (HEL, see diagram below), a thin layer of thermopastic material is used as a resist for subsequent pattern transfer. Previous work has shown that structures down to 10 nm can be moulded and at the present time, it seems that any structure size provided by the stamp can be replicated. It is often the case that both microstructures and nanostructures have to be moulded at the same time. In order to optimise the embossing process for the more complex stamp geometries, an insight into the way in which the mould fills during embossing is of fundamental importance. In particular, as the structures become smaller, understanding of the polymer flow at the nanoscale will be essential.

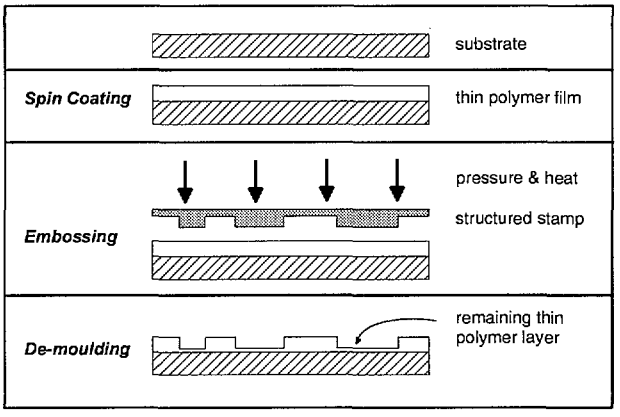

Hot embossing makes use of the difference in the thermomechanical properties of a hard stamp and a thermoplastic film as they come into temporary intimate physical contact. First, the polymer is heated above the glass transition temperature so that it assumes a viscous state. It can then be shaped under pressure by imprinting with a hard master. During the embossing, the viscous polymer flows into the cavities of the mold. Once the polymer has exactly conformed to the shape of the stamp, it is hardened by cooling and then the master is demoulded. To ensure good pattern transfer, the remaining thin polymer layer (see diagram) should be as thin as possible.

The process parameters required to give a minimum embossing time have been determined. For this, embossing temperatures greater than 100°C above Tg with PMMA viscosities in the range 300 to 3000 Pas are required for polymer films of thicknesses below 200 nm. Higher molecular weights give higher PMMA viscosities and therefore require higher embossing temperatures.

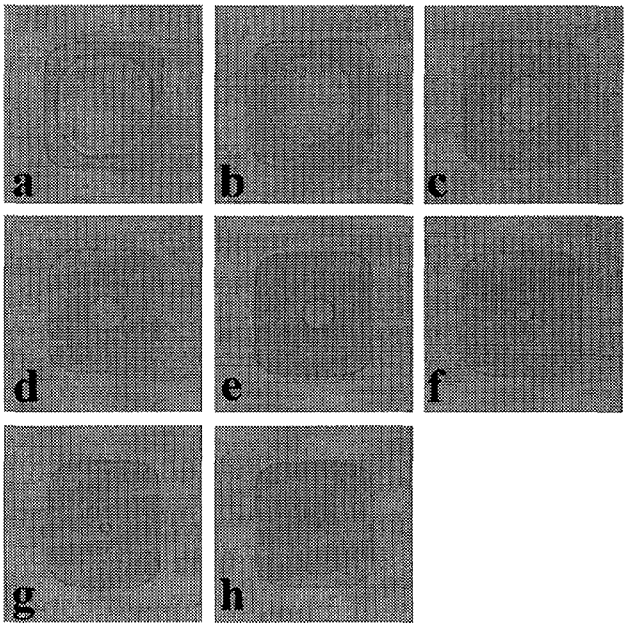

The way in which the polymer flows into various microstructure arrays has been observed by hardening the polymer and demoulding before the stamp cavities are completely filled. For the filling of the 20 μm square cavity shown above (height 175 nm), the process starts with the polymer flowing into the cavity from the borders. As the filling continues, the surface tension becomes important and the hole becomes circular. The final filling occurs by decrease of the size of the hole.

The same embossing conditions are required for both microstructures up to 20 μm and nanostructured areas with periods down to 120 nm, and it seems likely that the basic fill process, as described above, is the same. With the knowledge gained, the best conditions for the embossing step in the Hot Embossing Lithography (HEL) process can be chosen.

FUNDING: SNF (NFP36), PSI

REFERENCES

[1] H. Schift, R.W. Jaszewski, C. David and J. Gobrecht, MNE'98, Bruxelles, Belgium, Sept. 22-24, 1998, Microelectronic Engineering **46,** 121-124 (1999).

FABRICATION OF MICROMECHANICAL CANTILEVER SENSORS FOR NANOSCALE THERMAL DETECTION

J.-H. Fabian, L. Scandella, T. Mezzacasa, D. Bächle, J. Gobrecht, Ph. Lerch (PSI), E. Meyer (University of Basel)

Arrays of cantilever sensors have been designed and fabricated. These sensors are used as thermogravimetric devices for the analysis of nanogram weight samples and achieve picogram mass accuracy. When used as calorimeters these devices can detect heat changes of about a Pico-Joule. The device design was optimised with the use of numeric finite element simulations. The simulated structures were micro-machined into bulk silicon through a process involving 3 mask levels. The beams of the cantilevers have a spring constant of about $2 \cdot 10^{-2}$ N/m.

The resonance frequency of a (cantilever + sample) system is a function of its mass (see figure 1). A variation in the mass of the system induces a shift in the resonance frequency. The temperature of silicon cantilevers fabricated with an integrated electrical conductive layer is accurately controlled by the electrical power dissipated within the device. A sensitive thermobalance is realised when the dissipated Joule heat is varied while changes in the resonance frequencies are measured.

If a thin Al layer is evaporated onto the backside of the device, a bimetallic actuator is formed. This bimetallic strip forms a very sensitive thermometer able to sense temperature variations resulting from endothermic or exothermic reactions in the material of a sample deposited at the end of cantilever beam.

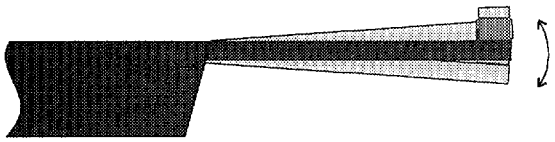

Fig. 1: In the thermogravimetric application the cantilever is excited to vibrate at its resonance frequency, which governed by the mass of an attached specimen.

In order to optimise the design of Joule heated U-shaped cantilevers for thermogravimetric applications, finite element simulations were performed. The current density and the temperature distributions resulting from the current flow through a doped silicon layer were calculated. A very uniform temperature distribution near the apex region can be realised by slitting the U-shaped cantilever. In such devices, the power can be minimised by minute changes in their geometry. For the operation as calorimeter, the slit is placed close to the cantilever support. The regions near the slit define the heater (higher current density) whereas the cantilever's upper part is forms the bimetallic strip (figure 3, left side).

Arrays of cantilever sensors were microfabricated out of silicon wafers with a 1 µm thick highly p-doped zone on one side. An etch mask of 1 µm thick wet oxide layer was then grown on both sides. Backside windows were patterned and etched in 20% KOH down to the p-doped layer which forms a membrane. After removal of the oxide mask, the cantilever structures were etched by SF_6 reactive

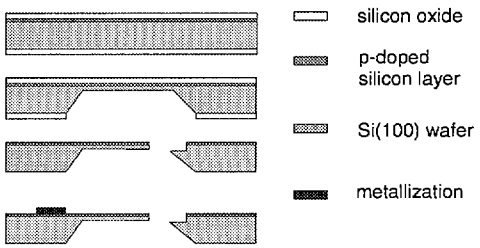

Fig. 2: Schematic of the cantilever array fabrication process.

ion etching. Electrical contacts were deposited on the p-doped side with a 200 nm thick film of gold evaporated through a mechanical shadow mask.

Several designs were tailored to the operation mode of the device (see figure 3). On a single chip 20 cantilevers work in parallel. The cantilevers vary in length and width ranging from 150 µm to 500 µm and from 50 µm to 100 µm, respectively. We achieved thicknesses down to 1 µm, resulting in a spring constant as low as $\approx 2 \cdot 10^{-2}$ N/m.

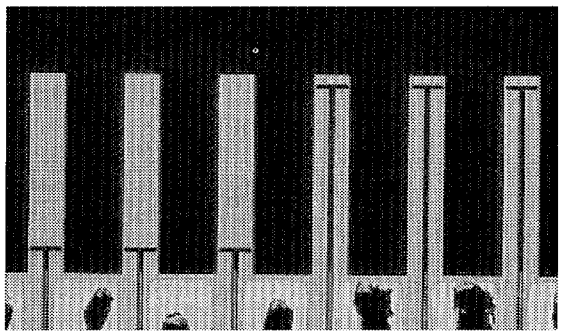

Fig. 3: Cantilevers optimised for calorimetric (left) and for thermogravimetric (right) operation.

The thermal relaxation time was measured to be in the ms range. Thus, the devices can be cycled up to 1000 K at a rate of about a kHz. The desorption behaviour of a single zeolite crystal with its dimension of 20×40×80 μm^3 was determined in a thermogravimetric experiment. Bimetallic cantilevers enable thermogravimetric and calorimetric analysis with nanogram sample quantities.

FUNDING: SPP MINAST, PSI.

REFERENCE

[1] J.-H. Fabian et al., *Ultramicroscopy* **82**, 69-77 (2000).

FABRICATION OF CUSTOM X-RAY OPTICAL COMPONENTS

C. David, P. Häberling, B. Ketterer, F. Glaus, B. Haas (PSI), A. Souvorov, B. Kaulich, J. Susini, P. Elleaume (ESRF)

A variety of diffractive x-ray optical components have been fabricated using electron beam lithography and reactive ion etching. The devices are tailored to the specific requirements of beam line set-ups at the ESRF. Moreover, a novel method to generate high aspect ratio structures with asymmetric stair-case profiles opens up new possibilities for the fabrication of extremely efficient diffraction optics.

Many experiments at synchrotron beam lines require an optical element to select the photons with the right energy and to focus them onto the sample region of interest. The demands of such an optical element e.g. with respect to their energy range, spatial and spectral resolution, tune-ability, or alignment properties are very specific for a given set-up. Therefore, a tailored optical element can improve the performance significantly.

An example of such devices devices are Bragg-Fresnel Lenses (BFLs), which can be used to collimate hard x-rays. They combine the Bragg reflection of a crystal or multi-layer with the focusing properties of a Fresnel zone plate. The most common devices are linear zone plates etched into silicon <111> crystals. For maximum diffraction

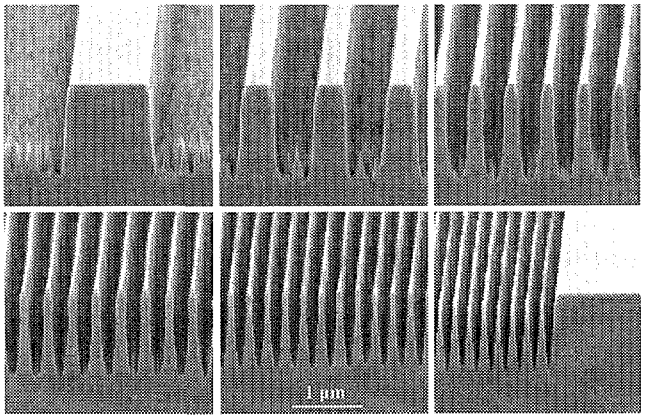

efficiency, binary structures should be etched to a depth of 1.24µm irrespective of the photon energy. Our BFLs have 100nm wide outermost zones, and the efficiency was measured to be 26% at 13keV photon energy. Through the very small structure size, our BFLs are capable of collimating three times more flux than any previously reported device of this kind [1]. The SEM images above show the Si structures in different regions of a BFL.

For other set-ups it is advantageous to use transmission elements. For a beam monitoring experiment at 25 keV photon energy we fabricated Fresnel zone plates with 5µm high phase shifting structures etched into germanium. The smallest structure width was 500nm.

The scanning x-ray microscope at ESRF requires high resolution zone plates for element mapping and x-ray fluorescence detection of sulphur at 2.4keV photon energy. For this purpose we generated germanium zone plates on 250nm thick Si_3N_4 membranes with 300 - 500µm diameter

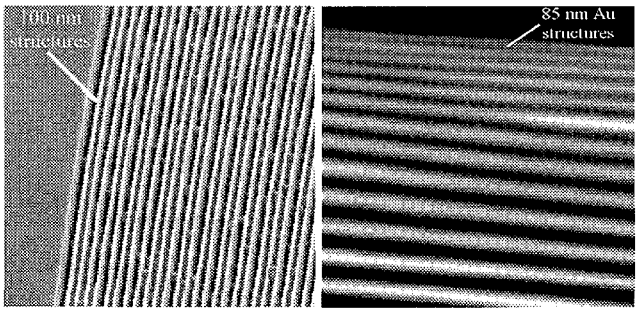

and 800nm high structures with an outermost zone width of 100nm (see left picture above). A diffraction efficiency of up to 9% was measured. The excellent imaging properties of the lenses were demonstrated by imaging a gold test object. The smallest 85nm wide structures could clearly be resolved (right picture above). This resolution has not been achieved before at this photon energy.

In comparison to binary diffraction structures, stair-case like profiles can provide twice as much diffraction efficiency. The SEM picture below shows a silicon zone plate with four height levels generated by two aligned e-beam exposures and stepwise reactive ion etching [2]. The 1.5µm high structures have an outermost pitch of 480nm. This new technique will be of great interest for microfocus applications in the intermediate (1-8keV) x-ray range.

REFERENCES

[1] C. David, A. Souvorov: Rev. Sci. Instr. **70,** 11 (1999).

[2] C. David: Accepted for publication in Microelectronic Engineering 1999.

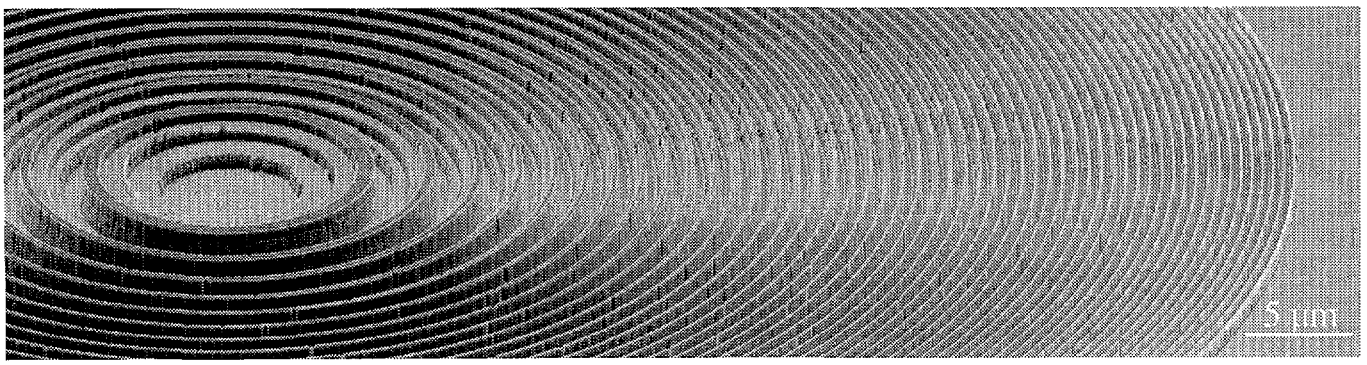

APODISED BRAGG GRATINGS IN SiON PLANAR WAVEGUIDES

C. David (PSI), D. Wiesmann, D. Erni (ETHZ), B.J. Offrein, F. Horst, R. Germann, G.L. Bona (IBM Rüschlikon)

We present the first realisation of a Bragg grating apodisation based on a variation of the duty cycles. The gratings were fabricated by electron beam lithography and reactive ion etching in SiON planar waveguides. The reflected signal exhibits a sidelobe suppression better than -20 dB outside a bandwidth of 1.36 nm. The gratings are perfectly suited to serve as the wavelength-selective element of a Mach-Zehnder add/drop filter.

The growing deployment of wavelength division multiplexing for telecommunication purposes requires wavelength-selective filters for adding and dropping a single wavelength channel. These functions can be well performed with Bragg gratings etched into waveguide structures, which can be combined to Mach-Zehnder add/drop filters (see figure below). It is desirable to have a sharp resonance of the filters in order to separate a single

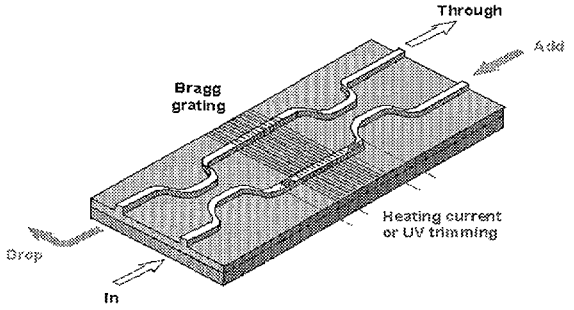

channel even for a small channel distance. The grating resonance has to be strong enough to ensure that the transmission loss for the dropped channel is more than 30 dB so minimising the crosstalk between the dropped and the added signal of the same wavelength channel. This requirement results in a grating length in the order of 10 mm which corresponds to about 20.000 lines. However, the spectral response of a uniform coupler grating shows undesired sidelobes. This can be overcome by apodising the grating, i.e. by gradually decreasing the coupling strength near the ends of the grating according to a bell-shaped taper function. This can either be accomplished by varying the etching depth of the grating structures, which is hard to do with sufficient accuracy, or by varying the structure widths and thus the duty cycle.

To define the apodised Bragg gratings we used a LION-LV1 electron-beam lithography system (Leica Microsystems Jena). Two unique features of this system make it particularly suited for our application: first, its continuous path control exposure mode avoids all field stitching errors. Second, every grating line can be exposed with an individual focus setting of the electron beam, which allows a continuous variation of the line width and thus the duty cycle [1]. Grating patterns with a pitch of 522 nm and up to 10 mm length were exposed using this method. The line width was varied from 260 nm down to 50 nm according to numerically optimised taper functions. The pattern was transferred by lift-off and reactive ion etching to a depth of 70 nm into the SiON waveguide layer and finally overgrown by a SiO_2 upper cladding. The SEM pictures show the SiON structures from different regions of the same grating before overgrowth.

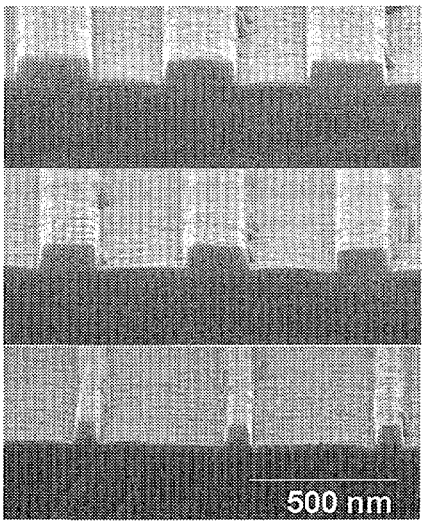

The spectral response of uniform and apodized gratings was measured. The data (solid lines) match well with the numerical simulations (dashed lines) [2]. The apodised grating (a) has an excellent supression of better than 20 dB outside a bandwidth of 1.36 nm while a uniform grating with the same dimensions (b) has only 10 dB suppression outside the same bandwidth.

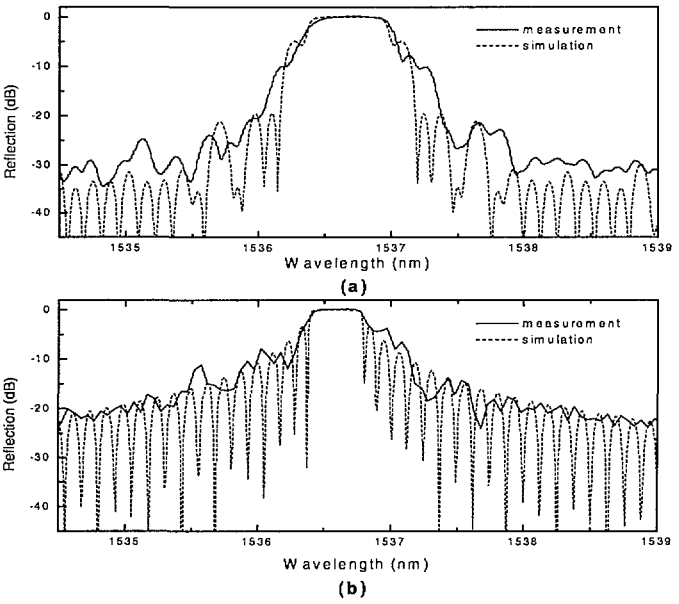

Fig. 1: Simulated and measured reflection spectra

REFERENCES

[1] C. David and D. Hambach, Microelectr. Engineering **46,** 219-222 (1999).

[2] D. Wiesmann, C. David, R. Germann, D. Erni, G.L. Bona, submitted to IEEE Photon. Technol. Lett.

EFFICIENT E-BEAM EXPOSURE FOR LARGE ARRAYS OF NANOSTRUCTURES

C.R. Musil, D. Bächle (PSI), M. Stamou, C. Duschl (EPFL)

The flexibility of e-beam lithography is often compromised by low throughput, which can limit both the total exposed area (~1 mm^2) and number of pattern elements (~10^5). Diffractive optical components, however, typically require densely packed, sub-micron sized, features over much larger areas. One of the challenges of e-beam nanostructuring lies in the efficient exposure of such patterns. In this regard, large area, two-dimensional arrays of circular openings in PMMA with a precise diameter were fabricated and transferred into a pattern of mixed self-assembled monolayers for use as an index grating in the optical recognition of biomolecular processes.

In e-beam writing, the maximum attainable writing speed (exposed area per unit time) is equal to the beam current I divided by the sensitivity D_0 which characterises the resist/development system. Usually, D_0 is constrained by the pattern transfer process, while I is limited by the minimum desired feature size and, for non-shaped systems, by the maximum scanning speed of the beam. Furthermore, system overhead, e.g. the time required to position the beam or stage and to transfer pattern data, can greatly impair throughput, particularly for patterns consisting of a very large number of sub-μm features. As an extension to the work done on linear gratings, the patterning capabilities of the LION-LVI have been exploited in the efficient exposure of large area, two-dimensional arrays of dots [1].

In order to minimise the number of pattern elements, each deflection field was uniformly rastered with a pixel spacing sufficiently large to prevent the overlap between individual pixels. The diameter of the exposed and developed dots was controlled by the pixel dwell time and by a precise defocus of the beam, which results in a relatively uniform distribution of the beam current over a circular area. In the graph below, the measured dot diameter $2r$ is plotted against the charge delivered per pixel Q with the amount of defocus Δh as a parameter for the exposure by 2.5 keV electrons of 100 nm thick PMMA resist developed for 60 sec in solution of 1:3 MiBK:IPA. A fit to the envelope of the curves gives $Q = D\,\pi\,r^2 + Q_0$ with $r = ½\,\alpha\,\Delta h$, $D = 23$ μ C cm^{-2}, $Q_0 = 1$ fC, and $\alpha = 11$ mrad, from which the pixel charge and defocus setting required for a dot radius within the range from 25 to 250 nm can be obtained. Using these results, an array of dots 200 nm in diameter with a spacing of 1 μm was exposed over an area of 1 cm × 1 cm (10^8 features) in about 6 hours, which is very close to the minimum time required for a beam current of 40 pA.

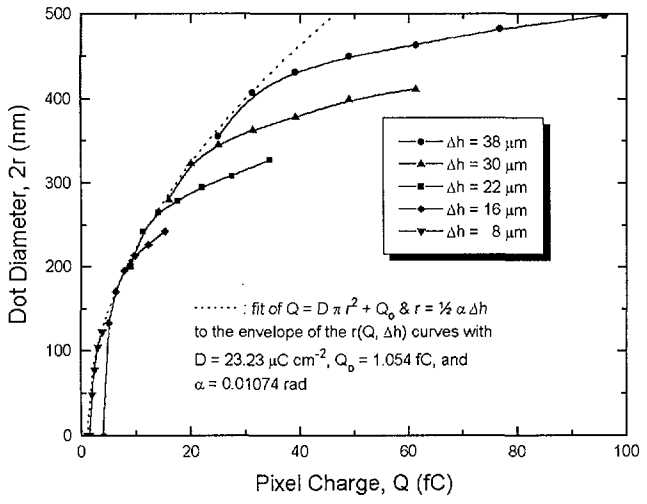

In a subsequent pattern transfer step, the nanostructured PMMA film served as a mask for the selective formation of a self-assembled monolayer (SAM) of Octadecane thiol (ODT) on the underlying gold surface. After the removal of the PMMA, the remaining gold surface was then covered by a second SAM of Mercaptoundecanoic acid (MUA). The mixed monolayer pattern was investigated by lateral force microscopy, in which the spots covered by hydrophobic ODT SAM clearly exhibited a lower friction compared to the surrounding area covered by the hydrophilic MUA SAM (see the lateral force micrograph below). The edge resolution and minimum feature size which are achievable by this method exceed those readily attained by micro-contact printing methods, while covering a comparable area.

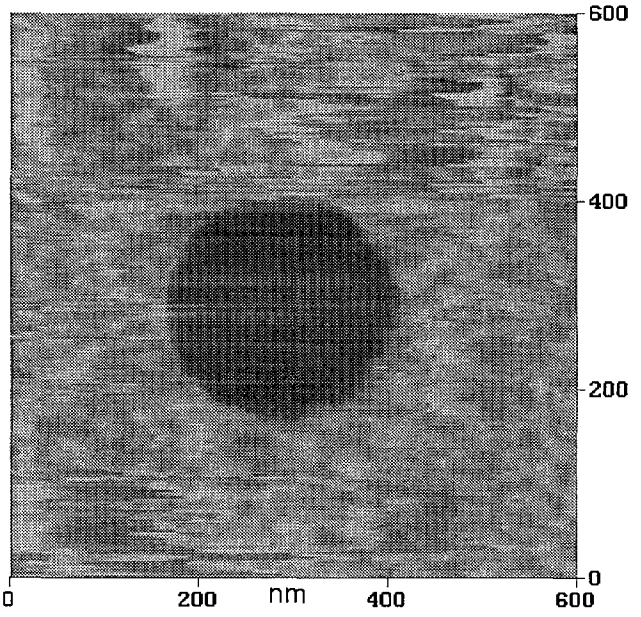

The variation in SAM endgroup properties and the precise control over the dot size permit the spatially periodic immobilisation of individual vesicles, whose trans-membrane properties can then be optically investigated by employing the ensemble as a nanometer thick, refractive index grating in a Kretschmann-type configuration. The ability to fabricate flat, large area surfaces with spatially well-defined, sub-micron sized areas of tailored surface chemistry has great potential in the development of new bioanalytic methods.

FUNDING: SPP MINAST, PSI

REFERENCES

[1] C. David *et al.*, Microelec. Eng. **46**, 219-222 (1999).

NANOSTRUCTURED MODEL CATALYSTS BUILT WITH INTERFERENCE LITHOGRAPHY AND WET ETCHING

Y.C. Bonetti, J. Gobrecht (PSI), M. Schildenberger, R. Prins (ETHZ)

With the use of interference lithography and wet etching techniques, we have been able to build model systems for heterogeneous catalysis, consisting of pitted oxidized silicon wafers with deposited metal particles. They exhibit high stability in oxidation and reduction treatments comparable to those used for industrial catalysts. As a model reaction, the oxidation of Carbon monoxide on Palladium particles has been investigated, clearly showing activity of the catalyst.

INTRODUCTION

The detailed investigation of heterogeneous catalysis still suffers from gaps between model systems and "real-world" catalysts. The latter ones are used under high pressure and temperature conditions, whilst the former most often cannot withstand these without modification of the particle size. A main problem in systems built by deposition of metal particles onto flat substrates like silica or alumina, is sintering of mobile particles.
To circumvent this, structured substrates can be used, which fix the particles in a purely physical way, not interfering with chemical processes during catalytical reactions.

LASER INTERFERENCE LITHOGRAPHY

In a laser setup with two interfering beams from a HeCd laser, an entire 4-inch wafer (oxidized to 120nm and coated with photoresist) can be exposed with a linear grating pattern. By applying a second exposure with the same parameters, but after rotation of the wafer by 90°, a latent grid pattern is present in the photoresist. After developing, a dot- or hole-pattern is created, depending on the exposure time: short exposure times result in a resist layer with holes. Using this as a mask, the oxide layer is etched in buffered hydrofluoric acid, creating pits of 60nm depth. Then 20nm of Palladium are deposited by e-beam-evaporation. Finally, the photoresist is removed together with the metal laying on top of it in a lift-off-process by use of solvents and ultrasonics. The following figure is a sideview of the edge of a cleaved wafer after processing (white bar corresponds to 200nm).

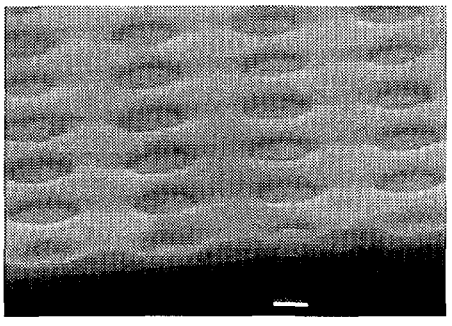

CATALYTICAL MODEL REACTION

In a specially designed reactor, the processed wafer has been investigated for its usability as a catalyst. First, the Palladium was reduced by exposure to Hydrogen atmosphere and heating to 350°C.
Then the wafer was put in a stream of 6ml/min Argon and 2ml/min Carbon monoxide at 1bar and 300°C. After stabilization, 2ml/min Oxygen was added. At the exhaust, a quadrupole mass spectrometer was continuously monitoring the amount of ions at a mass/charge ratio of 44amu/e, which corresponds to Carbon dioxide.
The temperature was slowly increased. At about 350°C, a strong raise of the Carbon dioxide signal was detected, which levelled off at about 360°C.

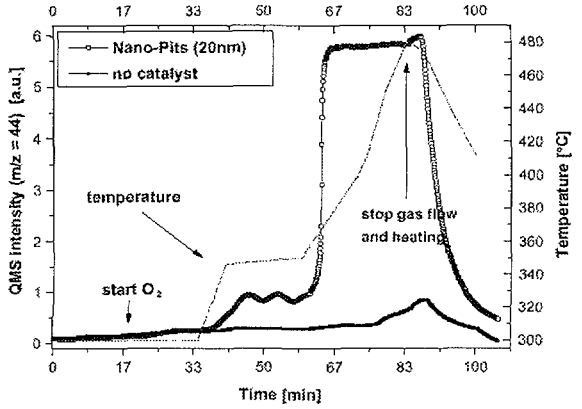

For estimation of the background activity due to the reactor and tubing material, the experiment was repeated without the structured wafer, resulting in the signal shown in the lower part of the figure.
These experiments show that the lithographically produced model system is catalytically active. The particles are stable and do not sinter. For test purposes, the samples have been heated up to 700°C, and even under such harsh conditions, only reshaping, but no sintering has been observed, as can be seen from the following scanning force micrograph.

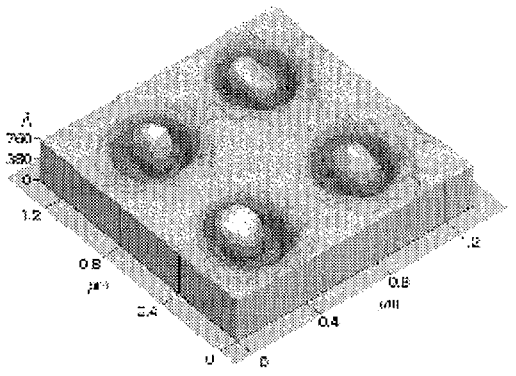

FUNDING: NFP36, PSI

NEXT PAGE(S) left BLANK

Laboratory for Radio- and Environmental Chemistry

LABORATORY FOR RADIO- AND ENVIRONMENTAL CHEMISTRY

H.W. Gäggeler (Univ. Bern & PSI)

GENERAL

Four groups of our laboratory perform basic research in close collaboration with the University of Bern and the ETH Zürich. Most of the research is pursued in form of doctoral thesis projects. In addition, two groups are working in applied radiochemistry and are mostly supported by external sources. The highlights of each research group are summarized below.

HEAVY ELEMENTS

For the first time in Switzerland, a new element of the Periodic Table was chemically investigated. This element is bohrium (atomic number 107). First, a new long-lived isotope of bohrium was discovered (^{267}Bh; $T_{1/2}$ = 17s) in an experiment performed at the 88-inch cyclotron of the Lawrence Berkeley National Laboratory. This new isotope was produced in the fusion reaction between ^{22}Ne projectiles and a ^{249}Bk target. During a second experiment, conducted at the PSI-PHILPS cyclotron, this new isotope was used to perform a first ever chemical study of this very heavy element. The experiment used the so-called OLGA technique, an on-line isothermal gas chromatography device, jointly developed by PSI and the University of Bern. During a 90 shift (1 shift = 8 hours) beam time six atoms of bohrium could be identified unequivocally after chemical separation. It was possible to show that bohrium forms oxychloride molecules which were less volatile compared to the same species formed with its lighter homologous elements Re and Tc, both members of group 7 of the Periodic Table.

SURFACE CHEMICAL STUDIES

The surface chemistry group investigates heterogeneous reactions of relevance to atmospheric chemistry in the laboratory. These include reactions of oxides of nitrogen and bromine with aerosol particles typically present in the atmosphere, i.e., soot, inorganic salts, mineral dust, and ice. These reactions are studied by using short-lived radioactive tracers prepared using the gas-jet facilities at the Philips Cyclotron and SINQ. We have investigated the reaction of NO_2 on soot which yields HONO, an important atmospheric trace constituent. For the first time, these experiments were performed not on artificial soot but on soot directly sampled from a diesel engine. In parallel, the formation of HONO from diesel soot has also been studied within an international collaboration at EUPHORE, a 200m^3 outdoor smog chamber facility in Valencia, Spain.

The main removal pathway of nitrogen oxides in the atmosphere is the reaction of HNO_3, their final oxidation product, with aerosol particles. First reaction studies were performed with ^{13}N labeled HNO_3 and aerosol particles prepared from synthetic sea-salt solutions.

In the polar troposphere, bromine compounds are able to affect the ozone budget significantly by complex heterogeneous reaction routes. With the aim to perform tracer studies similar to those using ^{13}N, a source of bromine nuclides as a product from thermal neutron inuced fission of ^{235}U has been established at the SINQ gasjet facility. Several bromine nuclides (^{86}Br ($T_{1/2}$=55s), ^{84}Br ($T_{1/2}$=30min)) are now available for experiments. With this source, first attempts to synthesize labeled HOBr, one of the key molecules in ozone depletion, have been made.

ANALYTICAL CHEMISTRY

The analytical services performed by this group included roughly 30'000 elemental and ionic determinations for nearly all divisions of the PSI. Besides this routine work research concentrated mainly on palaeo atmospheric studies using glacier ice archives. The highlights were clearly the two bedrock ice core drills at Cerro Tapado (5500 m asl) in Chile and Illimani (6300 m asl) in Bolivia. Both field campaigns required enormous logistical efforts and could only be successfully performed thanks to an excellent collaboration with the French organization IRD. It is worth mentioning that during the campaign the Swiss ambassador in Santiago de Chile visited the ongoing drill campaign. Presently, the Cerro Tapado ice core is analyzed. Isotopic as well as glaciochemical data indicate that El Nino events are well preserved at this site.

The project regarding Alpine glaciers was continued, first by finalizing the analysis of the cores from the Grenzgletscher (4200 m asl), and second by extending the high-resolution glaciochemical record at Colle Gnifetti back to the 9th century.

AEROSOL CHEMISTRY

This group is responsible for the aerosol measurements at the Jungfraujoch in the framework of the Global Atmosphere Watch Programme of the World Meteorological Organization. In this context, our research was included in the evaluation of the experiments in environmental sciences at the Jungfraujoch that took place in June. The report of the international group of experts noted that the Jungfraujoch is ideally suited to the study of tropospheric processes as modified by human activities, and mentioned the work on the life cycle of aerosol particles by the Paul Scherrer Institute as particularly important.

Furthermore, a major instrumental development was achieved with the construction of an instrument that is capable of measuring the hygroscopic properties of aerosol particles at temperatures below 0°C. This instrument, which is the first of its kind worldwide, will be deployed in future field campaigns at the Jungfraujoch and is expected to contribute significantly to the advancement of knowledge on the impact of aerosol particles on climate.

CHEMICAL INVESTIGATION OF BOHRIUM (Bh, ELEMENT 107)

R. Eichler, Ch. Düllmann, H.W. Gäggeler (Univ. Bern & PSI), B. Eichler, D.T. Jost, D. Piquet, L. Tobler, A. Türler, P. Zimmermann (PSI);T. Häfeli, V.M. Lavanchy (Univ. Bern);K.E. Gregorich, D.C. Hoffman, U. Kirbach, C.A. Laue, H. Nitsche, J. Patin, D. Strellis, P. Wilk (UCB&LBNL); R. Dressler (TU Dresden), S. Hübener, S. Taut, A. Vahle (FZR;) W. Brüchle, M. Schädel (GSI); Y. Tsyganov, A.B. Yakushev (JINR)

Neutron-rich nuclides of bohrium were produced in the reaction $^{249}Bk(^{22}Ne,4n\text{-}5n)^{266,267}Bh$ at the PSI Philips cyclotron. Bh was separated from other reaction products in a remotely controlled low temperature OLGA III set-up in the form of volatile oxychloride. The detection of genetically linked α-decay chains of ^{267}Bh was accomplished using the ROMA detection system.

The neutron-rich $^{266,267}Bh$ have been discovered in spring of 1999 in a joint experiment performed at the Lawrence Berkeley National Laboratory [1]. These Bh nuclides were formed in the heavy ion induced "hot" fusion reaction $^{249}Bk(^{22}Ne;4,5n)^{267,266}Bh$. The half-life of ~17 s for ^{267}Bh and the production cross section of about 50 pb make ^{267}Bh an ideal candidate to be used for gas phase chemical studies.

Assuming Bh to be a member of group 7 in the Periodic Table, a suitable chemical isolation procedure was developed in several model experiments using various nuclides of Tc and Re [2,3,4]. In thermochromatography experiments with trace amounts of $^{101,104}Tc$ and $^{183,184}Re$ in the reactive gas mixture HCl/O_2 in quartz columns the formation of only one single volatile compound was observed, which was interpreted as the formation of MO_3Cl (M = Tc, Re) molecules. Volatile oxychlorides were formed also on-line with short-lived nuclides $^{108}Tc(t_{½}=5.2$ s) and $^{169}Re(t_{½}=16$ s) (Fig.1).

Between August 20th and September 26th a 670 μg/cm² ^{249}Bk target, prepared by LBNL, was irradiated with a total beam dose of $3.02*10^{18}$ $^{22}Ne^{6+}$ particles at a beam energy of 118 MeV and an average intensity of about 250 pnA. The recoiling reaction products were thermalised and transported with a 1 l/min He/C-aerosol gas-jet to the reaction oven of the 3 m distant remotely controlled [5] low temperature OLGA III set-up. A reactive gas mixture of 50 ml/min HCl and 50 ml/min O_2 was added in order to oxidise the C-aerosols and to form oxychloride compounds. Volatile compounds were separated from less volatile compounds in the adjoining isothermal section (1.5 m legth, 1.5 mm i.d.) of the quartz chromatography column depending on their adsorption behaviour and half-life of the nuclide. This section was kept at three different isothermal temperatures (Tab.1, T_{iso}). After passing the column the isolated products were reattached to a 1 l/min He/CsCl gas-jet in the recluster chamber and transported to the ROtating wheel Multidetector Analyser (ROMA). The aerosol particles were impacted in vacuum (~5 mbar) on thin (30-40 μg/cm²) polyethylene foils, which were mounted on the circumference of the wheel. The stepping time was 10 s. Each of the collected samples was then measured between 12 pairs of PIPS-detectors for α- and sf-decays. Since the target contained 100 μg/cm² ^{159}Tb, ^{176}Re was also produced, serving as a yield monitor for the chemical separation. The overall yield of the whole separation process - from thermalisation of the recoiling ^{176}Re to the collection of the CsCl aerosols in the ROMA set-up was determined to be about 16%.

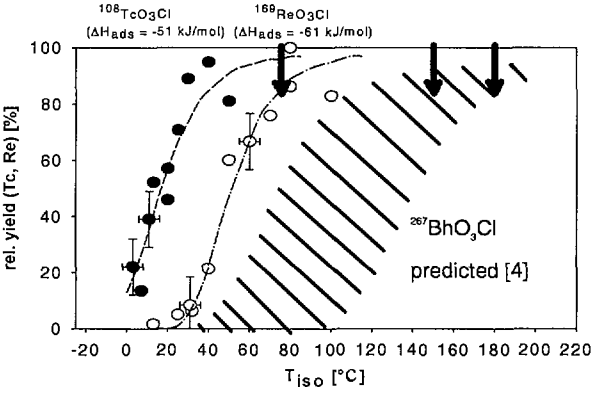

Fig. 1: Rel. yield vs T_{iso} for $^{108}TcO_3Cl$, $^{169}ReO_3Cl$. The arrows (➡) indicate isothermal temperatures, at which the retention behaviour of Bh-oxychloride was studied.

The detection efficiency for an a- or sf-decay was about 70%. Six correlated decay chains, which are directly linked to the decay of ^{267}Bh [6], were detected.

Table 1: Experimental conditions.

T_{iso} [°C]	Beam dose: $*10^{18}$ $^{22}Ne^{6+}$	Samples (measured foils)
180°C	1.02	62285
150°C	1.00	57652
75°C	1.00	57740

ACKNOWLEDGMENTS

We are indebted to the US DOE for making the ^{249}Bk target material available through the transplutonium element program at Oak Ridge National Laboratory. We thank the staff of the PSI Philips cyclotron for providing intense beams of ^{22}Ne.

REFERENCES

[1] P. Wilk et al., this annual report.

[2] R. Eichler et al., PSI-Scient. Rep. **1998**, I, p.123.

[3] R. Eichler et al., submitted to Radiochimica acta.

[4] R. Eichler et al., this annual report, p.135.

[5] D.T. Jost et al., this annual report, p.140.

[6] R. Eichler et al., this annual report, p.128.

RESULTS OF A PRELIMINARY ANALYSIS OF THE BOHRIUM EXPERIMENT

R. Eichler, Ch. Düllmann, H.W. Gäggeler (Univ. Bern & PSI), B. Eichler, D.T. Jost, D. Piguet, L. Tobler, A. Türler, P. Zimmermann, (PSI),T. Häfeli, V.M. Lavanchy (Univ.Bern), K.E. Gregorich, D.C. Hoffman, C.A. Laue. U. Kirbach, H. Nitsche, J. Patin, D. Strellis, P. Wilk (UCB&LBNL), R. Dressler (TU Dresden), S. Hübener, S. Taut, A. Vahle (FZR), W. Brüchle, M. Schädel (GSI), Y. Tsyganov, A.B. Yakushev (JINR)

With the observation of 6 decay chains, starting with the decay of ^{267}Bh after chemical separation, we conclude that Bh forms a volatile oxychloride, presumably BhO_3Cl. Bh behaves therefore like a typical member of group 7 of the Periodic Table. From the yield observed at tree different isothermal temperatures BhO_3Cl appears to be less volatile than its lighter homologues TcO_3Cl and ReO_3Cl. A standard adsorption enthalpy on quartz surface $\Delta H_{ads}(BhO_3Cl) = -77^{+10}_{-8}$ kJ/mol was evaluated from the experimental data.

The nuclide ^{267}Bh was produced at the PSI Philips cyclotron in the reaction ^{249}Bk(^{22}Ne;4n)^{267}Bh and chemically isolated as volatile oxychloride using the On-line Gas Chromatography Apparatus OLGA [1].

A total of 6 correlated decay chains attributed to the decay of ^{267}Bh were observed and listed in Tab.1 together with the evaluated number of expected random events (N_R).

At 180°C and 150°C isothermal temperature (T_{iso}) 4 respectively 2 events were detected. At 75°C no event was registered. The unambiguous identification of Bh after chemical separation allows to conclude that Bh like its lighter homologues forms a volatile oxychloride compound, presumably BhO_3Cl and behaves like a typical member of group 7 of the Periodic Table.

The relative yields of Bh are shown in Fig. 1 together with the yield vs. isothermal temperature curves of the corresponding compounds of Tc and Re. Assuming the Bh compound to be BhO_3Cl and applying a microscopic model of the adsorption process developed by Zvara [2], we evaluated the standard adsorption enthalpy of BhO_3Cl on the quartz surface, $\Delta H_{ads}(BhO_3Cl) = -77^{+10}_{-8}$ kJ/mol (68%c.i.).

The series of the adsorption enthalpies of group 7 oxychlorides MO_3Cl (M=Tc, Re, Bh) on quartz yields the sequence Tc>Re>Bh. This sequence can also be expected from stability trends in the Periodic Table.

In our experiment BhO_3Cl was reclustered with CsCl. This is an additional indication that BhO_3Cl is more similar to ReO_3Cl than to TcO_3Cl, since TcO_3Cl could only be reclustered with $FeCl_2$-aerosol particles [3].

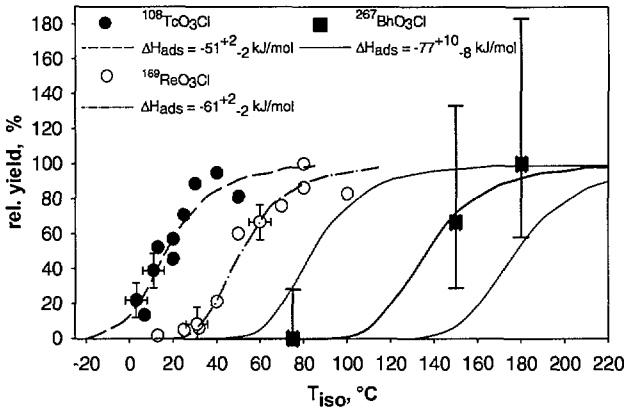

Fig. 1: Yield vs. isothermal temperature curves for the oxychlorides of ^{108}Tc ($t_{½}$=5.2 s), ^{169}Re ($t_{½}$=16 s), and ^{267}Bh ($t_{½}$=17 s). Symbols: experimental data with 1s-error bars. Lines: Monte Carlo model [2] with 1s-error range (thin lines).

ACKNOWLEDGMENTS

We are indebted to the US DOE for making the ^{249}Bk target material available through the transplutonium element program at Oak Ridge National Laboratory. We thank the staff of the PSI Philips cyclotron for providing intense beams of ^{22}Ne. This work was supported by the Swiss National Science Foundation.

T_{iso} [°C]	beam dose: ^{22}Ne^{6+}	Decay chain	E_{a1} [MeV]	t_1 [s]	E_{a2} [MeV]	Dt_2 [s]	E_{a3} [MeV]	Dt_3 [s]	Decay assignment	N_R
180°C	1.02*10^{18}	1	8.84	26.7	8.35	73.4			^{267}Bh → ^{263}Db or ^{259}Lr	
		2	8.72	2.9	8.40	29.9			^{267}Bh → ^{263}Db or ^{259}Lr	1.2
		3	8.81	18.4	101	16.3			^{267}Bh → ^{263}Db or ^{259}Lr	
					86					0.1
		4	8.91	10.5	8.37	0.8	8.41	14.6	^{267}Bh → ^{263}Db → ^{259}Lr	0.001
150°C	1.00*10^{18}	5	8.81	24.5	82	21.1			^{267}Bh → ^{263}Db or ^{259}Lr	
		6	8.85	34.4	46	98.9			^{267}Bh → ^{263}Db or ^{259}Lr	0.1
75°C	1.00*10^{18}	-	-	-	-	-	-	-	-	

Table 1: Correlated decay chains related directly to the decay of ^{267}Bh detected after the chemical separation.

REFERENCES

[1] R. Eichler et al., this report, p.127.

[2] I. Zvara, Radiochimica Acta **38**, 95 (1982).

[3] R. Eichler et al., this report, p.135.

TWO NEW ISOTOPES OF ELEMENT 107: ^{266}Bh AND ^{267}Bh

P.A. Wilk, K.E. Gregorich, V. Ninov, J.L. Adams, U.W. Kirbach, M.R. Lane, C.A. Laue, D.M. Lee, J.B. Patin, D.A. Shaughnessy, D.A. Strellis, H. Nitsche, D.C. Hoffman (LBNL), R. Eichler, H.W. Gäggeler (Univ. Bern & PSI), A. Türler (PSI)

Two new, long-lived isotopes of element 107 were produced in the reaction ^{249}Bk(^{22}Ne; 4,5n)^{267,266}Bh at the Lawerence Berkeley National Laboratory 88-Inch cyclotron and identified by observing correlated a-decay chains.

1 INTRODUCTION

The longest-lived known isotope of element 107, ^{264}Bh, has a half-life of only 440 ms [1], too short for investigations with the currently available chemical separator systems. Due to the expected influence of the closed shells at Z=108 and N=162 [2], the more neutron-rich Bh-isotopes ^{266}Bh and ^{267}Bh were expected to have considerably longer half-lives. These nuclides could be produced in the complete fusion reaction ^{249}Bk(^{22}Ne; 4,5n)^{267,266}Bh, with an expected production cross section of about 50 pb [3]. Based on the predicted Q-values for electron capture and α-particle decay, ^{266}Bh and ^{267}Bh should decay predominantly by α-particle emission and possibly by spontaneous fission, with half-lives of the order of a few seconds and tens of seconds, respectively [4,5].

2 EXPERIMENTAL

A 810 μg/cm^2 thick target of ^{249}Bk in the form of BkO_2, deposited on a 2.73 mg/cm^2 beryllium foil by a molecular plating technique, was irradiated with ^{22}Ne ions at the Lawrence Berkeley National Laboratory 88-Inch cyclotron. The 148 MeV ^{22}Ne beam passed through a 2.73 mg/cm^2 Be vacuum window, 0.5 mg/cm^2 nitrogen cooling gas, and the Be target backing before interacting with the Bk target material, resulting in a beam energy of 116 to 118 MeV in the target. A second experiment performed at 153 MeV, resulted in an energy range of 122 to 124 MeV in the target. The average ^{22}Ne^{6+} beam intensity amounted to 1 eμA at 148 MeV and to 2 eμA at 153 MeV beam energy. The ^{249}Bk target was covered with a 50 μg/cm^2 Al foil in order to suppress sputtering of the highly radioactive target material into the recoil chamber. Nuclear reaction products, recoiling from the thin ^{249}Bk target, were stopped in He gas loaded with KCl aerosols, and – adsorbed to their surface – continuously transported within about 0.6 s through a Teflon capillary (1.4 mm i.d., 7 m long) to the MG (merry go-round) detection system.

The MG detection system consists of a rotating wheel, which is stepped between six pairs of passivated, ion-implanted planar silicon (PIPS) detectors. The reaction products are deposited on polypropylene films (~40 μg/cm^2) located around the periphery of the wheel. The energy resolution of the detectors facing the wheel from the collection side was FWHM 40 keV, while the energy resolution of the detectors registering α-decays from the back side was FWHM 100 keV due to the energy degradation in the polypropylene foil. For this experiment, a parent-daughter stepping mode was used to provide detection of α-α correlations in a background free environment. Polypropylene foils were placed in every other hole in the 80-position collection wheel. Every ten seconds, the wheel is double-stepped between the six pairs of α-particle detectors until a possible parent decay is detected in a bottom detector (between 8.5 and 10.5 MeV). It is assumed that the daughter dubnium nucleus, ^{263}Db, recoiled out of the sample into the top detector. Then, daughter-search mode is initiated by single stepping the wheel, positioning a hole between the detectors. At the end of the preset daughter mode interval of 60 s, the wheel is single stepped again and parent-search mode is resumed.

3 RESULTS

Five atoms of ^{267}Bh and one atom of ^{266}Bh were identified during the experiment (Table 1). The half-life of ^{267}Bh was evaluated as 17^{+14}_{-6} s. At the lower bombarding energy of 117 MeV the ^{249}Bk(^{22}Ne, 4n)^{267}Bh production cross section is 48^{+27}_{-12} pb, whereas at the higher energy of 123 MeV a production cross section of 67^{+39}_{-17} pb was determined. The characteristics of the only 3 member decay chain, observed at the higher bombarding energy, were consistent with those expected from the α-decay of ^{266}Bh, produced in the 5n evaporation channel.

Table 1: α-decay chains observed in the reaction ^{22}Ne+^{249}Bk.

Beam energy (MeV)	E_{α_1} (MeV)	t_1 (s)	E_{α_2} (MeV)	Δt_1 (s)	E_{α_3} (MeV)	Δt_2 (s)	decay chain assignment
117	8.83	5.26	8.47	59.04			^{267}Bh→^{263}Db/^{259}Lr
117	8.87	24.67	8.39	35.02			^{267}Bh→^{263}Db
117	8.87	45.15	8.39	24.49			^{267}Bh→^{263}Db
123	8.73	2.71	8.46	51.90			^{267}Bh→^{263}Db/^{259}Lr
123	8.84	21.83	8.36	26.49			^{267}Bh→^{263}Db
123	9.29	0.87	8.54	27.83	8.74	0.03	^{266}Bh→^{262}Db→^{258}Lr

ACKNOWLEDGMENTS

We are indebted to the US DOE for making the ^{249}Bk target material available through the transplutonium element production program at Oak Ridge National Laboratory.

REFERENCES

[1] S. Hofmann et al., Z. Phys. **A 350**, 281 (1995).
[2] R. Smolanczuk et al., Phys. Rev. **C 52**, 1871 (1995).
[3] J.V. Kratz, Proc. R.A. Welch Foundation 41st Conf. on Chemical Research, 65 (1997)
[4] Y. Hatsukawa et al., Phys. Rev. **C 42**, 674 (1990).
[5] S. Cwiok et al., Nucl. Phys. **A 573**, 356 (1994).

EXCITATION FUNCTION OF THE REACTION $^{248}Cm(^{22}Ne, 4n)^{266}Sg$

R. Dressler (TU Dresden), B. Eichler, D.T. Jost, A. Türler (PSI), R. Eichler, H.W. Gäggeler (Univ. Bern & PSI)

The production of ^{266}Sg in the reaction $^{248}Cm(^{22}Ne, 4n)$ was investigated at bombarding energies of 112±1 and 116±1 MeV. At the lower bombarding energy no ^{266}Sg was detected resulting in a cross section limit of 62 pb (68% upper limit), whereas at the higher bombarding energy one decay of ^{266}Sg was identified resulting in a production cross section of cross-section of 54^{+96}_{-29} pb. A comparison with the HIVAP code shows a discrepancy of 4 MeV of the determination of the maximum of the excitation function in comparison with the experimental data.

The nuclide ^{266}Sg was first produced in experiments by Lazarev et al. [1] using the reaction $^{22}Ne + ^{248}Cm$ at beam energies of 116 and 121 MeV with production cross sections of 80 pb and 60 pb, respectively. In independent experiments the production of ^{266}Sg was confirmed for a small range of ^{22}Ne beam energies (118-123 MeV; see [2]). In order to test the predictive power of the HIVAP model [3,4], which predicts the maximum of the excitation function at 112 MeV, two measurements of the production cross sections of the reaction $^{248}Cm(^{22}Ne, 4n)^{266}Sg$ at 112 MeV and 116 MeV were made. A ^{248}Cm target on a Be-backing (2.34 mg/cm^2) with a thickness of 0.73 mg/cm^2 was bombarded with $^{22}Ne^{6+}$ ions delivered by the PSI Phillips cyclotron with a primary energy of 156.93 MeV. In the first experiment two set-ups to degrade the beam to about 112±1 MeV were used. In the first set-up, the beam passed a Nb degrader foil with a thickness of 5μm and an inclination of 42 degree to the beam axes, a 10μm Be vacuum window, the nitrogen cooling gas, and the target backing. In the second set-up the beam passed through a 5μm Havar foil with an inclination of 27 degree to the beam axis, a 4μm Havar vacuum window, the nitrogen cooling gas, and the target backing. In the second experiment the beam energy of 116±1 MeV was adjusted using two 4μm thick Havar foils one serving as degrader and the other one as vacuum window. Here the degrader foil was mounted rectangular to the beam direction. The reaction products were transported from the recoil chamber to the PSI tape system using a graphite aerosol gas-jet. Using a 5 m long steel capillary (2 s transport time) a transport efficiency of about 70 % was reached. To detect α-particles and SF-fragments 6 PIPS detectors were mounted in the tape system and the TANDEM software was used to register all events in an event-by-event mode. The efficiency of the PIPS detectors was measured for α-particles to be 30 % and for SF-fragments to be 60 %. The a-resolution was experimentally determined to be 50 keV. The experiments at 112±1 MeV were performed with two different stepping times. During the first period (6.9×10^{16} ^{22}Ne particles) steps of 30 s and in the second (3.8×10^{16} ^{22}Ne particles) steps of 15 s were performed. In these experiments no correlated events attributable to the decay of ^{266}Sg were found. An upper limit for the cross-section of 62 pb (68% upper limit) was deduced. In the second experiment (1.92×10^{17} ^{22}Ne particles) a stepping time of 15 s was used. The sum of all α-spectra of all 6 detectors are plotted in Fig. 1. One correlated α-SF-event was observed. The α-decay of ^{266}Sg occurred 13.62 s after the end of the collection period (E_α=8.72 MeV) and 4.68 s later the SF of its daughter ^{262}Rf was observed. A production cross-section of 54^{+96}_{-29} pb was deduced, in agreement with the value given by Lazarev et al. [1]. A total of 118 SF-fragments and 43 α-particles in the region 8.625-8.775 MeV (see [2]) were detected. A mean number of expected random correlations of 0.18 was calculated. In Fig. 2 the production cross-sections of ^{266}Sg in the reaction $^{22}Ne+^{248}Cm$ taken from [1,5] are compared with predictions of the HIVAP code [3,4]. While the maximum production cross section is predicted in reasonable agreement with the experimental data, the maximum of the excitation function is shifted by about 4 MeV to higher bombarding energies.

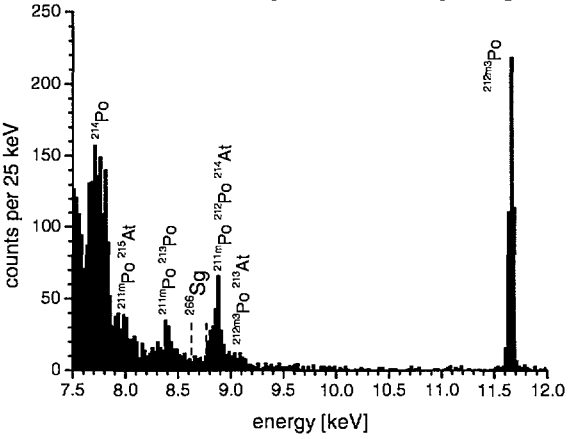

Fig. 1: Sum of all α-spectra of all 6 detectors at a beam energy of 116±1 MeV.

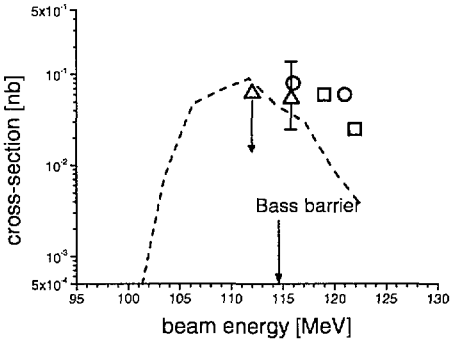

Fig. 2: Comparison of measured production cross-sections of ^{266}Sg (Δ: this work, O [1], □ [5]) with HIVAP.

ACKNOWLEDGMENTS

This work was supported by BMBF, Germany. We are indebted to GSI for making the ^{248}Cm target available as a loan for this experiment.

REFERENCES

[1] Yu. A. Lazarev et.al., Phys. Rev. Lett. **73**, 624 (1994).
[2] R. Dressler et al., this annual report.
[3] W. Reisdorf, M. Schädel, Z. Phys. **A 343**, 46, (1992).
[4] R. Dressler, PSI Scientific Report **1998**, I, p.131.
[5] A. Türler, et. al., Phys. Rev. **C 57**, 1648 (1998).

DECAY PROPERTIES OF ^{266}Sg AND ^{262}Rf

R. Dressler (TU Dresden), A. Türler (PSI), H.W. Gäggeler (Univ. Bern & PSI), S. Taut (FZR)

The decay properties of ^{266}Sg and ^{262}Rf were deduced from all until now observed correlated decay chains. The summed up data seems to suggest two α-lines for ^{266}Sg, 8.585±0.038 MeV and 8.724±0.028 MeV, however, most of the low energy alphas are contributed by just one single experiment. The half-lives of ^{266}Sg and of ^{262}Rf were determined as $21.1^{+19}_{-8.2}$ s and $1.88^{+0.64}_{-0.50}$ s, respectively.

After the discovery of the long-lived Sg nuclides ^{265,266}Sg by Lazarev et al. [1] these isotopes were used to investigate the chemical properties of Sg. The decay properties of these isotopes are important for their unambiguous identification after chemical isolation as well as for the determination of chemical parameters, e.g. the adsorption enthalpy in gas-chromatography. Due to its long half-life, ^{266}Sg is preferred for such experiments. However, the production cross-section in the used reaction ^{22}Ne + ^{248}Cm is only about 80 pb [1] and, therefore, only few events correlated with the decay of the α-decay daughter ^{262}Rf have been detected up to now. In Tab. 1 all correlated events assigned to the decay of ^{266}Sg and ^{262}Rf taken from [1-5] are shown. For the events from [1] a maximum correlation time window of 60 s was assumed. Two groups of α-events can be distinguished, as already reported in [3]. The superposition of the probability densities to detect an event (assumed to be Gaussians with FWHM quoted in the original work) for the first group of events (1-4, 8, 11) and for the second (5-7, 9, 10, 12, 13), as well as of all events are plotted in Fig. 1. Alpha decay energies of 8.585±0.038 MeV (95 % error limit) and an abundance of 46±32 % (68 % error limit), and 8.724±0.028 MeV and 54±35 % were obtained for the first and the second peak, respectively. However, most of the low energy events have been observed in the work of Lazarev et al. [1].

Table 1: correlated events of the decay of ^{266}Sg and ^{262}Rf

No	^{266}Sg				^{262}Rf		Lit.
	E_α [MeV]	fwhm [MeV]	t_{decay} [s]	t_{meas} [s]	Δt [s]	t_{corr} [s]	
1	8.54	0.10			0.215	(60.0)	[1]
2	8.59	0.10			0.748	(60.0)	[1]
3	8.60	0.10			0.191	(60.0)	[1]
4	8.60	0.10			2.011	(60.0)	[1]
5	8.69	0.10			0.360	(60.0)	[1]
6	8.74	0.10			6.453	(60.0)	[1]
7	8.69	0.10	3.8	120.0	0.875	120.0	[2]
8	8.52	0.10	48.9	70.0	2.8	6.3	[3]
9	8.74	0.05	3.5	70.0	2.4	6.3	[3]
10	8.79	0.05	15.1	70.0	1.7	6.3	[3]
11	8.66	0.03	84.9	100.0	7.0	15.0	[4]
12	8.70	0.03	4.8	100.0	3.7	15.0	[4]
13	8.72	0.05	13.62	90.0	4.68	90.0	[5]

Due to the lack of implantation signals in [1] for the events 1-6 only the life times of ^{262}Rf were measured in the discovery experiments. These events can only be used to determine the half-live of ^{262}Rf. Using the method of total ignorance [6], we can take into consideration the different lengths of measuring intervals (t_{meas}) and correlation time windows (t_{corr}) in the experiments [1-5]. The probability distribution p for the decay constant λ is than given by:

$$p\left(\lambda \mid M,\langle t\rangle,\left\{t_{mi}\right\}_{i=1}^{M}\right)=\frac{\prod_{i=1}^{M}\left(\frac{\lambda\cdot e^{-\lambda\langle t\rangle}}{1-e^{-\lambda\cdot t_{mi}}}\right)}{\int_0^\infty\prod_{i=1}^{M}\left(\frac{x\cdot e^{-x\langle t\rangle}}{1-e^{-x\cdot t_{mi}}}\right)\cdot dx}$$

M is the number of events, <t> the mean value of the decay (t_{decay}) or life times (Δt) and t_{mi} the length of the measuring intervals. In Tab. 2 the half-lives and their 68 % error limits are listed for different event groups. The calculated half-life of ^{262}Rf from the data of experiment [1] differs by more than 1 s in comparison to that using only the data from experiments [2-5]. However, both values are within the confidence belt of the mean value, if all events are included in the calculation. This value is in good agreement with the half-life of 2.1±0.2 s given by Lane et al. [7].

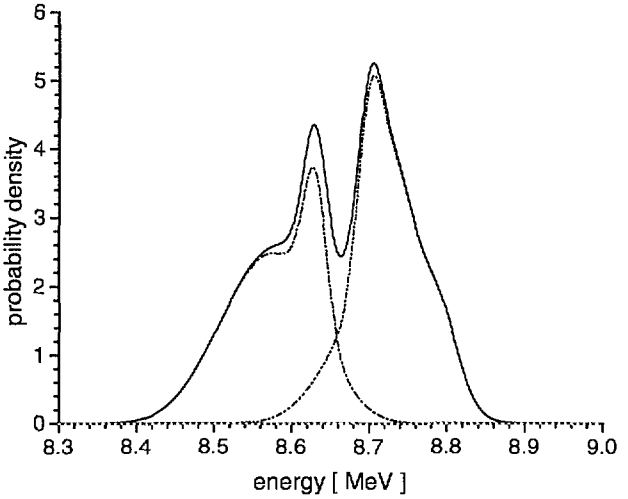

Fig. 1: superposition of the probability densities of all known correlated events

Table 2: Calculated half-lives of ^{266}Sg and ^{262}Rf

events	^{266}Sg $T_{1/2}$ [s]	^{262}Rf $T_{1/2}$ [s]
all		$1.88^{+0.64}_{-0.50}$
1-6		$1.15^{+0.52}_{-0.40}$
7-13	$21.1^{+19}_{-8.2}$	$2.9^{+1.9}_{-1.1}$

REFERENCES

[1] Yu. A. Lazarev et.al., Phys. Rev. Lett. **73**, 624 (1994).
[2] K. E. Gregorich et. al., NSD Ann. Rep. LBNL-39764.
[3] A. Türler et. al., Phys. Rev. **C 57**, 1648 (1998).
[4] S. Hübener et. al., PSI Scientific Report **1998**, I, p.124.
[5] R. Dressler, et. al., this annual report.
[6] R. Dressler, A. Türler, unpublished.
[7] M. R. Lane et al., Phys. Rev. **C 53**, 2893 (1996).

SEARCH FOR ^{263}Rf IN AQUEOUS SOLUTION

D. Schumann, R. Dressler (TU Dresden), F. Bruchertseifer (TU München), H. Bruchertseifer, A. Eichler, B. Eichler, D.T. Jost, A. Türler, P. Zimmermann (PSI), R. Eichler, H.W. Gäggeler (Univ. Bern & PSI)

The reaction ^{248}Cm(^{22}Ne, α3n) was used to produce the nuclide ^{263}Rf. A Rf fraction was isolated using cation exchange chromatography. Two events were found which could probably be attributed to the α-particle decay of ^{263}Rf.

1 INTRODUCTION

The development of heavy element research within the last years clearly shows evidence for the existence of relatively long-lived neutron-rich nuclei in the region Z=108 and N=162, but also for the newly discovered most neutron-rich isotopes of superheavy elements with Z=108-114 [1]. Isotopes of heavy elements with half-lives longer than one hour are very interesting, especially for studies of their chemical behaviour in aqueous solution. Unfortunately, these long-lived nuclei are not accessible by hot fusion neutron evaporation reactions. One alternative to produce such very neutron-rich isotopes is the use of (HI,αxn) reactions [2]. Several studies of the nuclear reaction ^{22}Ne + ^{248}Cm showed evidence for the formation of ^{263}Rf in the α3n reaction channel, see e.g. [2]. Predictions of the decay properties of ^{263}Rf indicate that this nuclide may decay by α-particle emission with a half-life of the order of one hour [3]. Preliminary studies with model nuclides as well as with short-lived Hf isotopes [4,5] showed that ion exchange on strongly acidic cation exchangers with 0.5 M HF solution as eluent is suitable for the separation of Rf both from all unwanted contaminants like Bi, At and Pb isotopes as well as from its α-decay product No.

2 EXPERIMENTAL

A Cm target (0.73 mg/cm^2 ^{248}Cm electrodeposited on 2.34 mg/cm^2 Be, 95.7 % ^{248}Cm, 4.2 % ^{246}Cm, 0.1 % other Cm-isotopes) was bombarded with an integral beam dose of 1.03×10^{17} ^{22}Ne particles. The beam energy in the middle of the target was 122±1 MeV. The reaction products were transported from the target chamber to the laboratory with a KCl aerosol gas-jet system with an average yield of 55 % and collected on a Nucleopore filter for one hour. Then, the activity was washed from the filter with 0.8-1.0 ml 0.5 M HF solution and passed through a cation exchange column (DOWEX 50Wx8, 200-400 mesh, 300 mg) with a flow rate of about 75 ml per minute. The eluate, containing the Rf fraction, was evaporated to dryness in a quartz vessel and diluted in about 150 ml of a solution containing 40 % ethanol, 1 M HCl, 0.5 M HF and 5 Bq/ml ^{241}Am tracer as inner standard. The chemical procedure, from washing the filter till the beginning of measurement, lasted about 25 min. Samples suitable for 4π α-measurements were prepared by evaporating the final solution on thin polypropylene foils (40 μg/cm^2). These foils were measured in 6 α-counting chambers. With a collection time of one hour a measuring time of about 6 hours for each sample was obtained. 36 samples were prepared and measured within an experiment time of 1929 min.

3 RESULTS

In Fig. 1 the sum of all α-particle spectra from all detectors is shown. Although the separation from Bi and Fm/Md is better than in earlier experiments using gas-phase chemistry [2], there is still ^{214}Po at 7.68 MeV, which interferes with the detection of both the expected α-decay of ^{263}Rf (7.8-8.0 MeV) and, especially, its α-decay daughter ^{259}No.

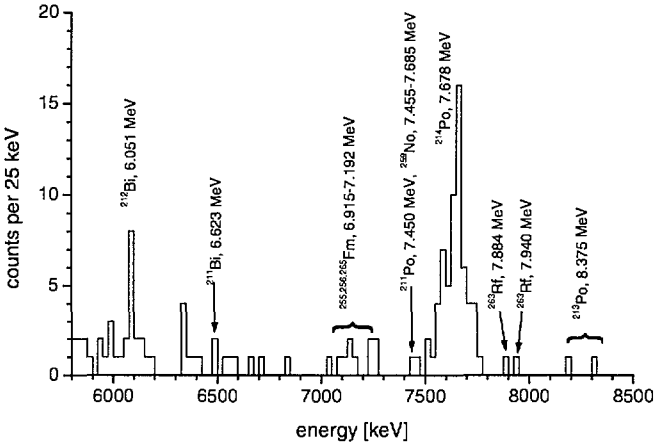

Fig. 1: Sum of all α-particle spectra from all detectors.

Table 1 shows the measured decay data of the two events which can possibly by attributed to ^{263}Rf along with the data of an earlier gas-phase chemistry search experiment.

Table 1: Possible α-decay events of ^{263}Rf.

	α-energy [MeV]	life-time [s]	
1	7.883	25'868	this work
2	7.939	5'749	this work
3	7.791	5	Ref. [2]
4	7.873	1'058	Ref. [2]

The measured life-times lead to a half-life of 1.6 h for ^{263}Rf. Further experiments including improvements of the purification from Po are necessary to confirm this result.

ACKNOWLEDGMENTS

This work was supported by BMBF, Germany. We are indebted to GSI for making the ^{248}Cm target available as a loan for this experiment.

REFERENCES

[1] Yu. T. Oganessian et.al., Nature **400**, 242 (1999).
[2] R. Dressler, PhD thesis, Universität Bern (1998).
[3] S. Cwiok et al., Nucl. Phys. **A 573**, 356 (1994).
[4] D. Schumann et.al., PSI Scientific Rep. **1998**, I, p.128.
[5] D. Schumann et.al., PSI Scientific Rep. **1998**, I, p.129.

FLUORIDE COMPLEXATION OF RUTHERFORDIUM (Rf, ELEMENT 104)

E. Strub, J.V. Kratz, A. Kronenberg, A. Nähler, P. Thörle, S. Zauner (Universität Mainz), W. Brüchle, E. Jäger, Z. Li, M. Schädel, B. Schausten, E. Schimpf (GSI Darmstadt), D. Schumann, U. Kirbach (TU Dresden), D. Jost, A. Türler (PSI), H.W. Gäggeler (Univ. Bern & PSI), M. Asai, Y. Nagame, M.Sakara, K. Tsukada (JAERI, Tokai), J.P. Glatz (ITU Karlsruhe)

Previous had been shown that Rf behaves differently from Zr/Hf and resembles Th on ion exchangers in HF/HNO_3 solutions. These studies have been extended to higher HF concentrations. It has been demonstrated that Rf forms anionic complexes but is not adsorbed effectively on the AIX in the presence of nitrate ions.

It had been shown experimentally [1,2] that ^{261}Rf is not eluted from the cation exchange (CIX) column under the condition of previously performed seaborgium (Sg, element 106) experiments [3,4] and can only appear in the Sg sample as a result of the decay of ^{265}Sg.

The distribution coefficient (K_d) of ^{261}Rf on cation and anion exchange resins at a various HF concentration had been studied [1,2]. Rf was eluted at higher HF concentrations from CIX than Zr and Hf and rather resembled Th. Up to 0.05 M HF, Rf was not retained on the AIX.

Now, the K_d values of Rf at HF concentrations > 0.05 M (in 0.1 M HNO_3) have been determined to establish at which concentration the K_d value on AIX is increasing indicating that anionic complexes of Rf are being formed.

^{261}Rf was produced in the ^{248}Cm(^{18}O,5n) reaction at the PSI Philips Cyclotron. A 730 μg/cm^2 ^{248}Cm target was bombarded with a 0.5 μA_{part} $^{18}O^{5+}$ beam. The target contained 10% Gd thus producing simultaneously short-lived Hf isotopes. Rf and Hf were transported by a He(KCl) gas jet and collected for 90 s by impaction on a slider in the Automatic Rapid Chemistry Apparatus ARCA II. The residue was dissolved in 200 μl 0.1 M HNO_3/x M HF (x variable) and fed onto the AIX. The effluent was evaporated to dryness as sample 1. In order to elute remaining Rf from the column, a second fraction (200 μl) was collected which is known to elute group 4 elements from the column (5 M HNO_3/0.01 M HF). This fraction was prepared as sample 2. 78-s ^{261}Rf was detected by α-spectroscopy. The counting time was 12 min. Every 8th pair of samples was monitored by additional γ-spectroscopy to determine the distribution of Hf.

The data (see figures) show that Rf behaves differently from Zr and Hf and seems to resemble Th on both AIX and CIX (dotted lines). It is remarkable, that the Hf on-line data is in agreement with the Hf offline data while the Rf behaviour is clearly different.

On the CIX, the four elements are strongly retained as cations below 10^{-3} HF. For Zr and Hf, the fall of the K_d values due to the formation of fluoride complexes occurs between 10^{-3} M HF and 10^{-2} M HF. For Rf and Th, this fall is observed at one order of magnitude higher HF concentrations. On the AIX, for Zr and Hf, a rise of the K_d values due to the formation of anionic fluoride complexes is observed in the same range of HF concentrations where the fall on the CIX is observed, yielding a consistent picture. For Rf and Th, on the AIX, no rise of the K_d values is observed even if the HF concentration is increased up to 1 M.

By varying the concentration of the counter ion NO_3^- which is competing for the binding sites on the AIX resin, it could be shown, nevertheless, that Rf does form anionic fluoride complexes (i.e. the K_d value varies with the nitrate concentration). This is in agreement with reported results [5,6,7].

We conclude that the observerved behaviour of Rf is a result of a specific competition with NO_3^- on the AIX.

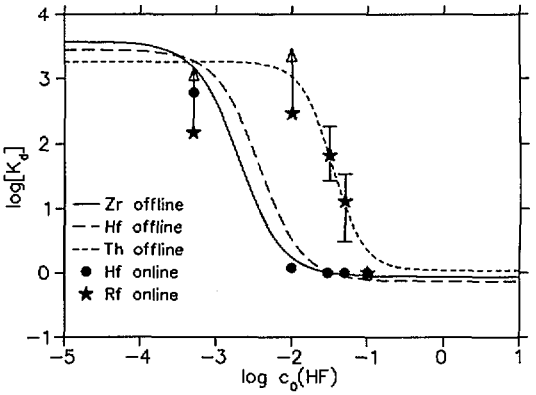

Fig.1: Sorption of Zr, Hf, Th and Rf in 0.1 M HNO_3 on aCIX resin (Aminex A6) at various HF concentrations.

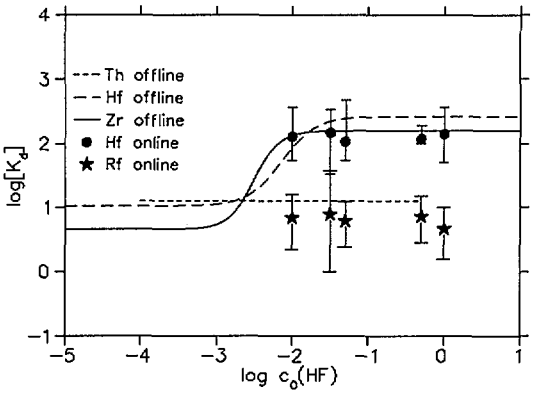

Fig.2: Sorption of Zr, Hf, Th and Rf in 0.1 M HNO_3 on a AIX resin (Riedel de Haen) at various HF concentrations.

REFERENCES

[1] E. Strub et al., PSI Annual Report **1997**, p.6.
[2] E. Strub et al., PSI Annual Report **1998**, p.9.
[3] M. Schädel et al., Nature **388**, 55 (1997).
[4] M. Schädel et al., Radiochim. Acta **77**, 149 (1997).
[5] Szeglowski et al., Radiochim. Acta **51**, 71 (1990).
[6] C.D. Kacher et al., Radiochim. Acta **75**, 135 (1996).
[7] G. Pfrepper et al., Radiochim. Acta **80**, 7 (1998).

SEARCH FOR UNUSUAL α-γ COINCIDENCES IN THE DECAY OF ^{210}Fr

M. Rupp, G. Langrock, N. Wiehl, H.O. Kling, M. Mendel, U. Tharun, J.V. Kratz (Univ. Mainz), A. Türler (PSI)

We have searched for an α-decaying superdeformed state in ^{210}Fr populating a superdeformed rotational band in the daughter nucleus ^{206}At by performing α-γ coincidences. We seem to be unable to confirm previous evidence for this state.

A. Marinov et al. reported in [1] the discovery of a strongly enhanced low energy α decay from a superdeformed isomeric state of ^{210}Fr produced in the reaction of 80 MeV ^{16}O with ^{197}Au. In this experiment, 5.20 MeV α-particles were observed in coincidence with γ-transitions which were attributed to a superdeformed rotational band in the daughter nucleus ^{206}At.

To confirm this unexpected observation, ^{210}Fr was produced in the ^{197}Au(^{18}O,5n)-reaction at 100 MeV in April 1999 at the PSI Philips cyclotron. The reaction products recoiling out of the 445 μg/cm^2 Au-target were stopped in two 60 μg/cm^2 C catcher foils after passing a 270 μg/cm^2 C degrader foil.

Four 180 min irradiations have been performed with an average beam intensity of 50 pnA. The two catcher foils were measured alternately between a Si α-detector and a 7600 mm^2 Ge-detector with 39.6 mm thickness. α- and γ-singles as well as α-γ coincidences were recorded.

γ spectra were evaluated using DECAN, a collection of macros for analysis of γ-decay data [2]. α spectra and α-γ correlation spectra were analyzed using GOOSY. $^{205-209}$At, ^{205}Po, ^{199}Tl, ^{199m}Hg, ^{27}Mg and ^{211}Rn/^{207}Po (long-lived growth, uncertain) were identified in the γ spectra. ^{212}Fr, $^{208-211}$Rn and $^{205-211}$At were found in the α spectra, but resolution of ^{209}Rn/^{210}Rn, ^{211}Rn/^{211}At and ^{208}At/^{209}At was not possible because of the small differences in their α-decay energies.

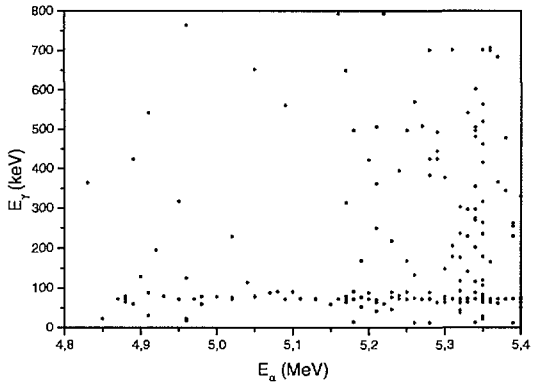

Fig. 1: α-γ correlations.

The distribution of reaction products indicates that the 5n- and 6n-channel were the most populated. Identification of ^{199}Tl and ^{199m}Hg gave evidence for the occurence of transfer reactions. This interpretation is supported by many signals in the range of 60-95 keV, which can be assigned to X-rays of the elements Hg, Tl, Pb, Bi, Po, At, Rn. Therefore, a lot of random correlations in the α-γ correlation plot are to be expected in this energy range. In [1], the assignment of the α-particles (E_α=5.20 MeV, $T_{1/2}$=90 m) to ^{205}Po is denied because there are no α-γ coincidences in the ^{205}Po decay scheme.

23 correlations were found in an a-energy window 4.8...5.4 MeV. 19 of these α-γ correlations were considered to be random, because their γ-energies are characteristic for the above listed other nuclides. There remain 4 correlations:

Table 1: Possible α-γ correlations in the decay of ^{210}Fr

E_α [MeV]	E_α (corr.) [MeV]	ΔE_α [MeV]	E_γ [keV]	ΔE_γ [keV]
5.30	5.33	+ 0.04	43.37	- 0.60
5.17	5.20	- 0.09	52.15	- 0.61
5.26	5.29	0	88.79	+ 0.86
5.31	5.34	+ 0.05	141.01	+ 0.32

The 6.04 MeV α-signal of ^{209,210}Rn was detected at 6.01 MeV. Thus, the correction of α-energies for the energy loss in the 60 μg/cm^2 C-Folie was set to 0.030 MeV. The average α-energy, 5.29±0.055 MeV, differs from the energy given in [1] ($5.20^{+0.05}_{-0.25}$ MeV) and the scatter of the deviations ΔE_α is larger than what is expected according to the FWHM of the 6.01 MeV α line of 0.060 MeV. The discrepancies between experimental and theoretical γ-energies, ΔE_γ, are rather large so that the attribution to rotational levels is to be doubted. The complete α-γ correlation plot of the investigated energy range is shown in Fig. 1. Random correlations are clearly to be seen at E_γ = 60...95 keV and also at $E_\alpha \approx 5.35$ MeV (^{210}Po).

In the 5.17...5.31 MeV α-energy window defined by the above listed α-γ coincidences additional correlations with γ-energies of 100...800 keV are observed. Thus, the question is raised whether the four α-γ coincidences in Table 1 really present sufficient evidence for the α decay of a superdeformed isomeric state in ^{210}Fr into rotational states in the superdeformed second minimum of ^{206}At. In order to definitely exclude the evidence presented by Marinov et al [1], it would be necessary to perform an additional experiment, using the reaction ^{16}O + ^{197}Au at E_{lab} = 80 MeV.

REFERENCES

[1] A. Marinov, S. Gelberg, D. Kolb, Mod. Phys. Lett. **A 11**, 861 (1996).

[2] M. Rupp, diploma thesis, 1999, Institut für Kernchemie, Universität Main.

THE BEHAVIOUR OF TRACE AMOUNTS ^{101,104,108}Tc IN THE REACTIVE GAS SYSTEM He/O_2/HCl AND EVALUATION OF CHEMICAL TRENDS IN GROUP 7

R. Eichler, H. W. Gäggeler (Univ. Bern & PSI), B. Eichler, A. Türler (PSI)

In thermochromatography experiments with ^{101,104}Tc in the reactive gas system He/O_2/HCl the formation of a single, very volatile Tc compound was observed. This compound was most probably TcO_3Cl. The behaviour of short-lived ^{108}Tc in the same reactive gas mixture was studied using the low temperature OLGA III. The adsorption data of TcO_3Cl were evaluated. The behaviour of the corresponding Bohrium (Bh, element 107) compound was predicted from the trends established for the ad-sorption behaviour of the compounds MO_3Cl (M = Tc, Re).

Trace amounts of ^{101,104,108}Tc are available at the ^{252}Cf-fission source "Miss Piggy" at Bern University.

Thermochromatography studies of ^{101,104}Tc in the reactive gas mixture He/O_2/HCl showed the formation of a single very volatile compound. We assigned this compound to TcO_3Cl. It was not possible to distinguish the deposition peak of this compound from the deposition of water ice in the column. Thus, we evaluated only an upper limit of the adsorption enthalpy from the experiments: $-\Delta H_{ads}(TcO_3Cl) < 53$ kJ/mol.

An on-line gas phase separation technique of volatile oxychloride compounds of trace amounts of group 7 element Re based on the OLGA III technique was developed [1,2]. We studied Tc under the same chemical conditions as Re using the same set-up.

The OLGA technique requires a so-called "reclustering" step. The separated volatile compounds pass the isothermal part of the set-up and are then reattached to new aerosol particles in order to transport them with a gas-jet to the detection system. In experiments with Re a CsCl/Ar gas-jet was used. Surprisingly, the very volatile TcO_3Cl did not attach to the CsCl surface. Therefore, we used $FeCl_2$ as reclustering material to reduce the highly oxidised Tc compounds to less volatile oxidation states.

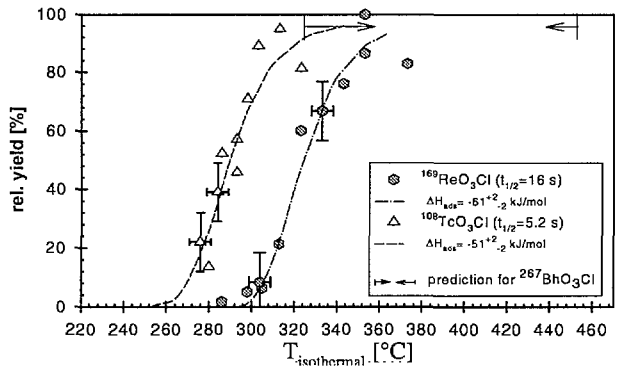

Fig. 1: Gas chromatographic retention curves of Re and Tc in the reactive gas system O_2/HCl

Gas chromatographic retention curves were measured for TcO_3Cl with short-lived ^{108}Tc (Fig.1). The adsorption enthalpy $\Delta H_{ads}(TcO_3Cl)$=-51 kJ/mol was evaluated using a microscopic model of the chromatographic process (dashed line)[3]. With respect to $\Delta H_{ads}(ReO_3Cl)$=-61 kJ/mol [1,2] Tc forms a more volatile oxychloride compound than Re in the reactive gas mixture O_2/HCl/He.

Since only very scarce thermochemical data are available for oxychloride compounds of group 7 [2], an empirical correlation method was used to predict the adsorption behaviour of BhO_3Cl on quartz. A linear correlation of the evaluated adsorption enthalpies of MO_3Cl (M = Tc, Re) on quartz with the sublimation enthalpies of the metals was employed to predict empirically an interval of possible (arrows in Fig. 2) $\Delta H_{ads}(BhO_3Cl)$ values. The sublimation enthalpies of the transactinides were predicted by extrapolative [4], semi-empirical [5], and relativistic [6] methods. A similar empirical correlation holds also for the oxychlorides of group 6 metals. The experimentally determined $\Delta H_{ads}(SgO_2Cl_2)$ [7] lies within the predicted range of values from Mo and W.

From the empirical evaluation we would expect an adsorption enthalpy of $BhOCl_3$ on the quartz surface between -57 and -74 kJ/mol. The corresponding isothermal temperatures where close to 100% relative yield are expected after the chemical separation >325 K and <470 K (Fig. 1 arrow). From relativistic calculations the volatility order of Tc>Re>Bh was predicted for MO_3Cl (M = Tc, Re, Bh) [8].

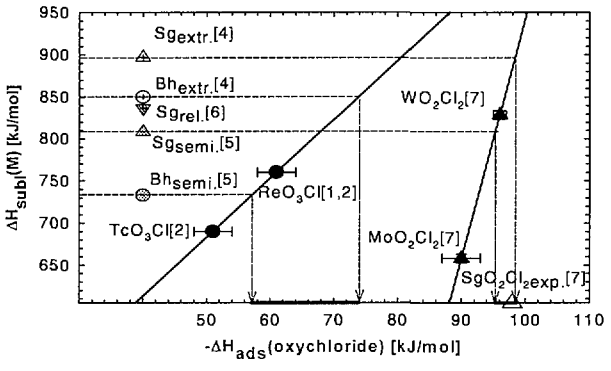

Fig. 2: Prediction interval for $\Delta H_{ads}(BhO_3Cl)$.

REFERENCES

[1] R. Eichler et al., PSI Scient. Rep. **1997**, IIIA, p.128.
[2] R. Eichler et al., submitted to Radiochim. acta.
[3] I. Zvara, Radiochimica Acta **38**, 95 (1982).
[4] B. Eichler, Kernenergie **19**, 307 (1976).
[5] G.V. Ionova, Radiokhimiya **37**, 307 (1995).
[6] V.G. Pershina et al., J. Phys. Chem. **98**, 6468 (1994).
[7] A. Türler et al., Angew. Chem. **38**, (15), 2212 (1999).
[8] V.G. Pershina, private communication.

THERMOCHROMATOGRAPHIC INVESTIGATION OF Tc IN THE GAS SYSTEM O_2/H_2O

T. Häfeli (Univ. Bern), H. W. Gäggeler, R. Eichler, Ch. Düllmann (Univ. Bern & PSI)

The behaviour of Tc isotopes in the gas system O_2/H_2O on SiO_2 surface was investigated using the methods of thermochromatography and OLGA III. Using a Monte Carlo approach and the quasi third law method, the adsorption enthalpy and adsorption entropy of TcO_3 and $HTcO_4$ were determined. Based on an empirical correlation, the sublimation enthalpy of these species was estimated.

1. INTRODUCTION

Technetium is an element of group 7 of the Periodic Table. It is important to know the chemical behaviour of this element to model the chemical behaviour of the heaviest known element of this group, bohrium (element 107). Several compounds of group 7 elements might be suited for gas chemical investigation. In this contribution the volatility of Tc compounds formed with oxygen and water vapour as reactive gas were studied.

2. EXPERIMENTAL

For the thermochromatographic experiments ^{101}Tc and ^{104}Tc from the ^{252}Cf fission fragment source Miss Piggy [1] and ^{99m}Tc from a ^{99}Mo/^{99m}Tc-generator was used. Empty SiO_2-columns in a negative temperature gradient from 1150 down to –60 °C were used. Thirty-nine experiments were carried out at gas flow rates between 5 ml/min and 250 ml/min and duration between 5 min and 4 h. The gas was a mixture of He and O_2. The amount of O_2 varied between 0 % and 100 %.

In a second series of experiments the retention of short lived technetium isotopes (^{106,107,108}Tc) was investigated with OLGA III [2]. Using the Monte Carlo model [3] and the quasi third law method [4], the adsorption enthalpy and adsorption entropy of TcO_3 and $HTcO_4$ were determined.

3. RESULTS AND DISCUSSION

In Fig. 1 one of the measured thermochromatogram is shown. We assign the first deposition peak at the higher temperature to TcO_3 and the second one to $HTcO_4$. Without addition of O_2 the $HTcO_4$-peak disappears. The following average adsorption enthalpies and adsorption entropies were calculated from all experiments:

$\Delta H_{ads}(TcO_3)$=-155±7 kJ/mol, $\Delta H_{ads}(HTcO_4)$=-75±5 kJ/mol, $\Delta S_{ads}(TcO_3)$=-163.95±0.3 J/molK and $\Delta S_{ads}(HTcO_4)$= -167.40±0.3 J/molK. Using these results the sublimation enthalpies were estimated with an empirical correlation between adsorption enthalpy and sublimation enthalpie [5]: $\Delta H_{subl}(TcO_3)$=218±20kJ/mol, $\Delta H_{subl}(HTcO_4)$=103±15 kJ/mol. Technetium oxides and hydroxides are more volatile than oxides and hydroxides of manganese but less volatile than the same compounds of rhenium. Technetium is more similar to rhenium than to manganese.

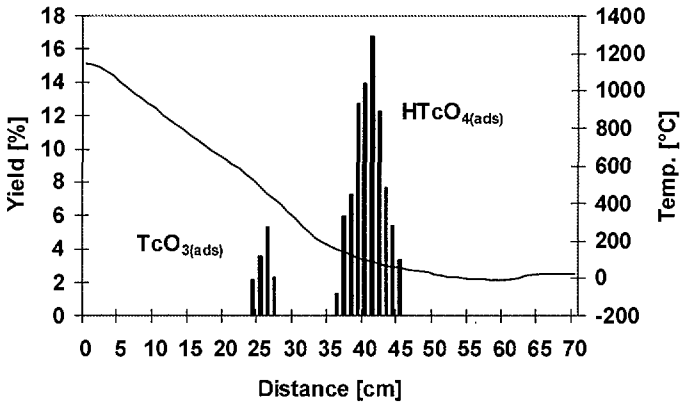

Fig. 1: Thermochromatogram of Tc after an experiment lasting 10 min with a gas flow rate of 25 ml/min, 20 % O_2.

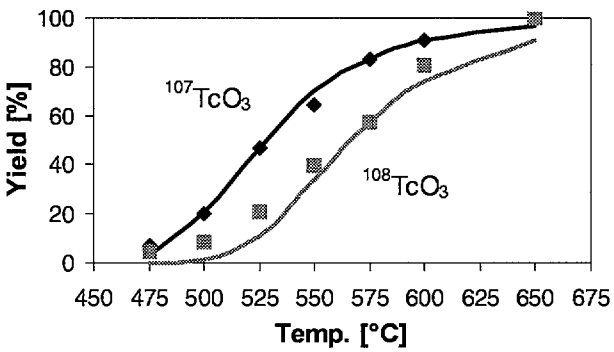

Fig. 2: OLGA III experiment with ^{107}Tc and ^{108}Tc. Carrier gas: N_2 1000 ml/min, He 20 ml/min and O_2 200 ml/min.

REFERENCES

[1] D. T. Jost et al., PSI-Ann. Rep. **1998**, p.2.

[2] H. W. Gäggeler, Nucl. Instr. Meth. **A309**, 201 (1991).

[3] I. Zvára, Radiochim. Acta. **38**, 95 (1985).

[4] B. Eichler, Radiochim. Acta. **30**, 333 (1982).

[5] B. Eichler, Journ. Rad. Chem. **28**, 143 (1975).

HITGAS EFFICIENCY IN THE SEABORGIUM OXIDE HYDROXIDE EXPERIMENT

S. Taut, R. Dressler, A. Vahle, S. Hübener (FZ Rossendorf), D. Jost, A. Türler (PSI)

The chemistry efficiency of the high temperature gas chromatography apparatus HITGAS in the seaborgium oxide hydroxide experiment is calculated with the spectra from tungsten isotopes which are produced as monitor nuclides during the seaborgium experiment.

INTRODUCTION

A first determination of the chemistry efficiency of the high temperature gas chromatography apparatus HITGAS [1] for the group 6 oxide hydroxide system was carried out in [2]. For 1350 K isothermal temperature we obtained 53 % efficiency for ^{166}W and 63 % for ^{168}W.

Unfortunately, this approach requires similar pressures in the target chamber in both experiment parts because the aerosol attachment of the nuclear reaction products is pressure dependent. This was not possible in our seaborgium experiment at GSI [1].

ALGORITHM

With the following quantities and equations we estimated the HITGAS efficiency from on-line gamma spectra.

$fh;r$	indices indicating filter holder and ROMA
$\dot{n}$	nuclide production rate
n_0	number of atoms collected during $t_{coll,r}$
λ	nuclide decay constant
$t_{coll,x}$	sample collection period; x = fh, r
t_{jet}	gas jet transport time
t_{step}	duration of ROMA step movement
t_{int}	ROMA step interval length; $t_{int} = t_{coll,r} + t_{step}$
$\varepsilon_{det,x}$	detection efficiency; x = fh, r
ε_{jet}	gas jet efficiency
ε_{hitgas}	chemistry efficiency of HITGAS
J	number of ROMA detection places
$J+1$	number of ROMA deposition places
K	actual ROMA detector place
L	number of ROMA wheel rotations during $t_{coll,r}$
N	number of ROMA deposition places which were counted N times
$J+1-N$	number of ROMA deposition places which were counted $(N-1)$ times
D_x	number of detections during $t_{coll,x}$; x = fh, r

In a first step, the production rate of the nuclide under study is determined with a catcher foil experiment.
In a following direct catch experiment, the gas jet is directed to a glass fiber filter holder which is counted during the nuclide collection. Eq. 1 expresses the measured number of nuclide detections. A simple rearrangement gives the gas jet efficiency.

$$D_{fh} = \dot{n} \cdot e^{-\lambda \cdot t_{jet}} \cdot \left(t_{coll,fh} - \frac{1 - e^{-\lambda \cdot t_{coll,fh}}}{\lambda} \right) \cdot \varepsilon_{det,fh} \cdot \varepsilon_{jet} \tag{1}$$

Finally, the nuclide accumulation onto the ROMA wheel is detected on-line during a HITGAS experiment. Eq. 2 describes the number of collected atoms in one ROMA deposition place during one sample collection period:

$$n_0 = \dot{n} \cdot \frac{1 - e^{-\lambda \cdot t_{coll,r}}}{\lambda} \cdot e^{-\lambda \cdot t_{jet}} \cdot \varepsilon_{jet} \cdot \varepsilon_{hitgas} \tag{2}$$

This unknown number can be calculated from the number of detections which are measured in the ROMA over a longer period (L wheel rotations) with eq. 3 and the abbreviations a, b, and c:

$$D_r = n_0 \cdot a \cdot [N \cdot b + (J + 1 - N) \cdot c] \tag{3}$$

$$a = \frac{e^{-\lambda \cdot t_{step}} \cdot e^{-(K-1) \cdot \lambda \cdot t_{int}} \cdot (1 - e^{-\lambda \cdot t_{coll,r}}) \cdot \varepsilon_{det,r}}{1 - e^{-(J+1) \cdot \lambda \cdot t_{int}}} \tag{4}$$

$$b = L - \frac{1 - e^{-L \cdot (J+1) \cdot \lambda \cdot t_{int}}}{e^{+(J+1) \cdot \lambda \cdot t_{int}} - 1} \tag{5}$$

$$c = L - 1 - \frac{1 - e^{-(L-1) \cdot (J+1) \cdot \lambda \cdot t_{int}}}{e^{+(J+1) \cdot \lambda \cdot t_{int}} - 1} \tag{6}$$

The HITGAS chemistry efficiency remains as the only unknown in eq. 2 and can be calculated easily.

RESULTS

The results are shown in the table. The efficiency for ^{168}W agrees very well with that determined in [2]. The low efficiency for ^{166}W indicates a HITGAS dwell time between 10 and 20 seconds. This was already obtained with a yield curve Monte Carlo simulation in [2]. However, all tungsten peaks in the on-line gamma spectra of the seaborgium experiment [1] had a poor signal to noise ratio. Therefore, we consider our results from [2] to be more precise.

Nuclide	Half Life [s]	HITGAS Efficiency
^{166}W	18.8	30 %
^{168}W	51	60 %
^{169}W	76	40 %
^{171B}W	642	50 %

ACKNOWLEDGMENTS

We gratefully acknowledge the support by both the BMBF, contract 06 DR 824, and GSI, contract DRNITK.

REFERENCES

[1] S. Hübener, et. al., PSI Annual Report **1998**, p.9.

[2] A. Vahle, et. al., Radiochimica Acta **84**, 43 (1999).

IVO, A NEW APPARATUS FOR IN-SITU VOLATILIZATION AND ON-LINE DETECTION OF TRANSACTINIDE ELEMENTS

Ch.E. Düllmann, R. Eichler, H.W. Gäggeler (Univ. Bern & PSI), A. Türler, D. Piguet, H. Blumer, B. Eichler, D.T. Jost (PSI)

An new gas chromatography system was developed to isolate highly volatile species of transactinide elements. In contrast to the OLGA technique, volatile species are formed in-situ behind the target in the recoil chamber and swept by the carrier gas directly to a chromatography column. Volatile species leaving the chromatography column are chemically adsorbed to the surface of aerosol particles in a cluster chamber and transported to a on-line detection system. The system was tested using short-lived osmium (Os) and mercury (Hg) nuclides produced in heavy ion reactions at the PHILIPS Cyclotron.

INTRODUCTION

The newly discovered isotopes of the heaviest elements hassium (Hs, Z=108)[1], 112 and 114 [2] have sufficiently long half-lives to be suitable for chemical studies. Theoretical predictions of the chemical behavior of these elements [3,4] suggest that they are homologuous to osmium (Os), mercury (Hg) and lead (Pb). Microamounts of all three elements can be volatilized already at low temperatures. Os in the form of the tetroxide, Hg and Pb in the elemental state.

EXPERIMENTAL

Because of the very low production cross sections of heaviest elements - of the order of a few pb or even less - a very efficient chemistry device with high overall yield is required. A new set-up was built that can be attached to the beam tube of the PHILIPS cyclotron. It consists of a recoil chamber, flushed with a gas where the reaction products are thermalized. A small admixture of reactive gas provides the in-situ formation of volatile compounds. Volatile molecules (or elements) are swept through a quartz chromatography column, which reaches into the recoil chamber.

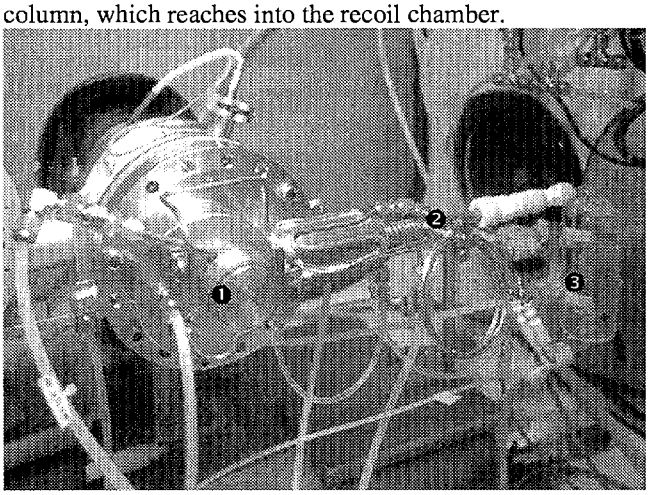

Fig. 1: The IVO setup: On the left side, the target chamber with the water-cooled beam stop ❶ is visible. On the right side, the heated quartz chromatography column ❷ with the vertically mounted cluster chamber ❸ is visible.

The first few cm of the 30 cm long quartz column are heated to 600-800 °C to increase the diffusion of less volatile, unwanted byproducts to the wall, where they are adsorbed irreversibly and thus retained. The elevated temperature also favors the formation of volatile compounds. At the end of the column, a cluster chamber is attached. Specially tailored aerosol particles that chemisorb the molecules that passed through the column are used to transport the separated products to a detection system. For short-lived nuclides, the Rotating Wheel Multidetector Analyzer ROMA [5] or the PSI Tape System [6] are used.

RESULTS

The setup was tested with two different chemical species, OsO_4 and elemental Hg. Short lived Os nuclides were produced in the reaction $^{156}Dy(^{22}Ne,5\text{-}6\ n)^{172,173}Os$. As carrier gas He with 10% O_2 was used. The chemical yield of the system was about 50%. The decontamination with respect to Po, an element that is often produced in heavy element experiments from impurities in the target and the target assembly and strongly interferes with the α-spectroscopic detection of transactinides, was about $2 \cdot 10^4$. Fig. 2 shows two α-spectra obtained in experiments with Os. The spectrum on the left side was obtained by collecting all nuclear reaction products with a graphite aerosol directly behind the target and transporting them to the detection system. On the right side, a spectrum is shown where Os was chemically isolated as OsO_4 using IVO. Po was not volatile under the conditions of the experiment and retained quantitatively.

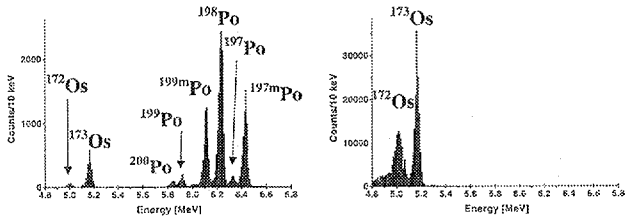

Fig. 2: Left side: α-particle spectrum of a direct catch experiment. Several Os and Po isotopes are visible. Right side: α-particle spectrum of chemically isolated Os using IVO.

In the reaction $^{168}Yb(^{22}Ne,6n)^{184}Hg$, short-lived Hg was produced and transported in He as carrier gas. Pd aerosol particles were used as cluster material. The results of our experiments seem very promising for future experiments with Hs and even heavier transactinide elements.

REFERENCES

[1] S. Hofmann et al., Z. Phys. **A 354**, 229 (1996).
[2] Yu. Ts. Oganessian et al., Nature **400**, 242 (1999).
[3] B. Eichler, Kernenergie **19**, 307 (1976).
[4] G.V. Ionova et al., Radiokhimiya **37**, 307 (1995).
[5] K. Sümmerer et al., GSI Ann. Rep. **1983**, 246 (1984).
[6] D.T. Jost et al., IEEE Trans. Nucl. Sci. **39**, 186(1992).

PRODUCTION AND CHARACTERIZATION OF LEAD AEROSOLS

Ch.E. Düllmann, H.W. Gäggeler (Univ. Bern & PSI), A. Türler, B. Eichler (PSI)

Small lead particles are especially well suited to irreversibly adsorb OsO_4. Two different methods were used to generate lead aerosols with various number concentrations and size distributions. Production by spark discharge yielded smaller particles and lower concentrations than production from a Pb melt. In addition, the influence of different residence times in a large volume was investigated. It was shown that particles produced by spark discharge did not coagulate as much as the ones produced from a melt, probably due to an electrical charging of the primary aerosol particles.

1 INTRODUCTION

The heaviest element whose chemistry has been investigated so far is bohrium (Bh, element 107) [1]. The next heavier element hassium (Hs, element 108) is expected to form a very volatile tetroxide, similar to ruthenium and osmium, which are believed to be its lighter homologues. Therefore, HsO_4 is ideally suited for on-line gas chromatographic investigations. In order to detect the α-decay of Hs, the very volatile HsO_4 must be chemically adsorbed onto a solid surface. Earlier experiments at Dubna [2] and also at PSI showed that lead aerosol particles are especially well suited to strongly adsorb OsO_4.

2 EXPERIMENTAL

One method to produce lead aerosol particles is to heat molten lead to a temperature of 650-900 °C in a flow of argon gas. The evaporating material rapidly condenses to small particles with an average diameter of the order of about 10 nm. Another method to produce Pb aerosol particles is by spark discharge. Two Pb electrodes were placed at a distance of a few millimetres in flowing Ar gas. A high voltage of up to 2.5 kilovolts was applied to these electrodes resulting in spark discharges with a frequency of about 2 Hz. Electrode material was evaporated, carried out of the region of the plasma by the carrier gas flow and rapidly condensed to small particles. After the aerosol generator, a ^{85}Kr source was installed to reach charge equilibration. Primary particles produced with either method were fed into a container with a adjustable volume of 1-7 l. Depending on the volume of the container and the gas flow rate, different residence times of up to several minutes permitted coagulation to larger agglomerates. By varying the temperature of the oven and the volume of the coagulation vessel, the desired particle concentration and average particle diameter of about 100 nm could be achieved. As particle analyser, a differential mobility analyser DMA (TSI 3071 A) connected to a condensation particle counter CNC (TSI 3022 A) was used.

3 RESULTS

The spark discharge method yielded much lower Pb aerosol number concentrations than the production from a melt. Typical values were of the order of $1 \cdot 10^6$ to $4 \cdot 10^6$ cm^{-3}, depending on the volume of the container. The use of a ^{85}Kr source yielded larger particles when applying a large coagulation volume compared to the experiments without this source. Production from a melt resulted in number concentrations as high as $3 \cdot 10^7$ cm^{-3}. Fig. 1 shows the data of experiments for oven temperatures between 650 and 900 °C and coagulation volumes between 1 and 7 l.

REFERENCES

[1] R. Eichler et al., this annual report.

[2] B. L. Zhuikov et al., Report JINR P7-86-322, Dubna, 1986, p. 15 (unpublished).

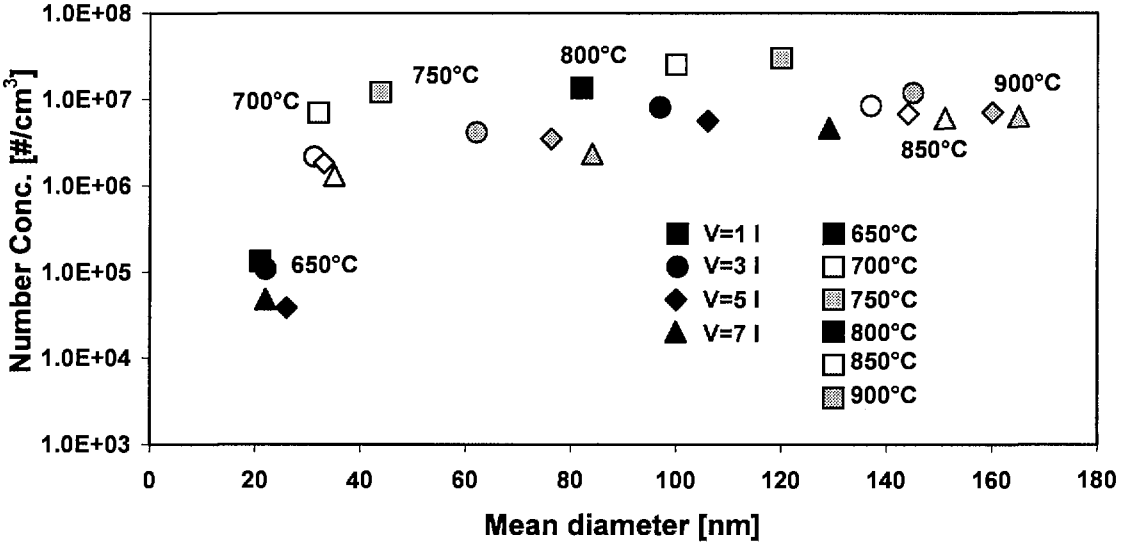

Fig. 1: Production of lead aerosols from a melt with 0.5 l/min Ar as carrier gas as a function of temperature of the melt and volume of the coagulation container.

ON-LINE ^{267}Bh CHEMISTRY IN THE TARGET AREA NE-C AT PSI

D.T. Jost, D. Piguet, R. Eichler, A. Türler (PSI)

Studies of the chemical properties of element 107, Bh with the short half-lives of the available nuclides make it necessary to operate the chemical separation and the detection system close to the production site in the experimental area.

Due to the short half-lives of the nuclides of the heaviest elements, the investigation of their chemical properties demand very fast chemical methods and short transfer times from the production to the chemistry and detection system. The decay-losses with the approach used so far, production in the target area NE-C and other components in the chemistry laboratory (WGBA/C41) 50m away, were too high. The installation of all components in the target area posed some interesting problems in terms of safety, radiation shielding and remote control.

A gas cooled double window target system was used to irradiate a 670 µg ^{249}Bk target. A very fast slammer valve 6m up streams of the target with a separate trigger detector was installed in order to protect the accelerator in case of a failure of the vacuum window from the gas inrush and the radioactive target material.

The gaschemistry apparatus OLGA III [1] was installed in a stainless steel bio hazard fume hood. Since the ventilation system of the target area was not designed to accept corrosive gases, a separate exhaust line from the fume hood to the ventilation system of the laboratory WBGA/C41 was built. A color video camera was used to observe the installations in the fume hood. Since the waste gas form the exhaust of the pump still contained HCl it was neutralized in a gas scrubber and fed into the exhaust line of the hood.

While beam was on target the experiment was run remotly. The operation of chemistry apparatus (oven temperatures, pH of gas scrubber) and the pressure in the detection system were monitored from the laboratory via RS232 device and Labview applications. The stepping of the ROMA sample wheel was controlled by a Windows95 PC in the target area which in turn was connected via ethernet and a remote control program (Norton PC-anywhere) to the monitor station in the laboratory. The spectroscopic data acquisition systems were already designed for network operation and could easily be operated from the laboratory.

First Experiments were conducted with a wall of 50cm concrete and 20cm borated paraffin between the target and the Roma detection system. In this configuration a γ-dose of 35 µSv/h was measured at the position of the detection system. The alpha spectrum showed a continuous background of about 0.66 counts per hour in the 8.45-8.55MeV region. This background rate was too high to identify unambiguously the ^{267}Bh decay chains. The background was caused by fast neutrons from beam/target interaction and the capture thereof in the detectors and preamplifiers. An additional 50 cm concrete shielding around and above the detection system reduced the γ-dose rate to 5.3 µSv/h and the background in the 8.5 MeV range to 0.25 counts per hour. This background rate was acceptable for the identification of the decay chains.

The handling of highly radioactive target materials and corrosive gases necessitated elaborate procedures for the operation and an automatic save shutdown of the experiment in case of a malfunction. The procedures included check lists for starting and shutting down the experiments, change of the sample wheel in the detection system and manipulations at the target box with dose limits set by the radiation protection rules. The corrosive gas tank and the mass flow control were installed in the chemistry laboratory. A 3 mm o.d. teflon tube was used to transport the gas to the chemistry apparatus. A shutoff valve in the laboratory and the target area reduced the amount of HCl that could escape to a minimum. The valves could only be opened if all other operating parameters were within normal conditions. An alarm from the HCl sensor could only be reset at the sensor in the fume hood itself, forcing the operator to inspect the chemistry apparatus

Table 1: Operating conditions of the ^{267}Bh experiment

Beam line pressure	< 10-3 bar
Slammer valve	open, trigger active
Cooling gas pressure	0.9 - 1.5 bar
Target pressur	0.9-1.8 bar
Target cooling water flow	4-6 lpm
He Carriergas flow	0.5-2 lpm
O_2 flow	< 0.1 lpm
HCl flow	< 0.1 lpm
HCl sensor	< 10 ppm
Fume hood fan	running

Future experiments with the chemical separation attached directly to the target chamber and smaller detection systems that will be easier to shield and less susceptible to background neutrons will open the path to even shorter lived nuclides and lower production rates.

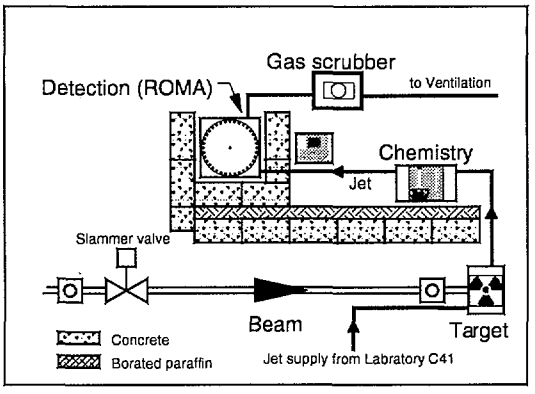

Fig. 1: Schematic set up of the ^{267}Bh experiment in the target area NE-C.

REFERENCES

[1] R. Eichler et al., PSI Annual Report **1997**, IIIA, p.61.

THERMOCHROMATOGRAPHIC ADSORPTION STUDIES OF BERKELIUM

S. Hübener, S. Taut, A. Vahle (FZ Rossendorf), B. Eichler (PSI), N.Trautmann (Univ. Mainz), J.R. Peterson (Univ. Tennessee, Knoxville)

The adsorption of ^{250}Bk atoms on Nb was studied thermochromatographically at temperatures as high as 1850 K at the starting position of the column. The trivalency in the adsorbed state is concluded from the adsorption behavior.

In continuation of thermochromatographic adsorption studies of the heavy actinides [1,2] and envisaging experiments with the heaviest actinide element lawrencium the goal of the present studies was to measure adsorption enthalpies for berkelium on niobium and to test the experimental setup at temperatures as necessary for studying lawrencium.

The experimental setup used in the present studies resembles to that one described in [1]. We chose a temperature of 1850 K at the starting position in the column and a sapphire support tube for the thermochromatographic columns made of niobium foils. ^{254}Es electroplated on tantalum was used as the ^{250}Bk source. The ^{250}Bk source was placed at the starting position into the column. After that the column was flushed with helium used as the carrier gas at a flow rate of 50 cm^3 per minute. To start chromatography the hot oven was moved into the working position. In this work we used a mobile oven whereas the sapphire tube was stationary. After 30 min thermochromatography time the thermochromatogram of berkelium was measured with a resolution of 1 cm by gamma ray spectrometry of the ^{250}Bk 989 keV and 1022 keV lines.

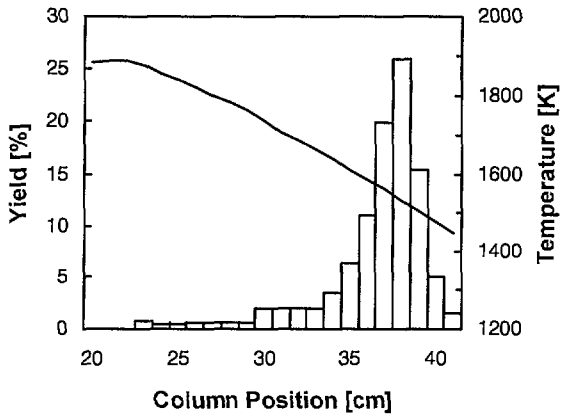

Fig. 1: Thermochromatogram of ^{250}Bk on niobium.

Fig. 1 shows a decay corrected thermochromatogram of ^{250}Bk ($t_{1/2}$ = 3.217 h). The position with maximum berkelium concentration determines the deposition temperature which was found to be 1535 K in two identical experiments.

The standard enthalpy of adsorption, ΔH^0_{ads}, was calculated from the deposition temperature and the experimental parameters as described in [1]. To calculate the standard entropy of adsorption, ΔS^0_{ads}, the period of oscillation of the adatom, τ_0, was taken to be $0.81 \cdot 10^{-12}$ s as determined for the adsorption of Es on niobium [3]. We obtained ΔH^0_{ads} = -332 kJ/mol and ΔS^0_{ads} = -152 J/(K mol).

As seen from Fig. 2 there is a regular trend in the adsorption enthalpies from berkelium over californium to the divalent actinides einsteinium, fermium, and nobelium. In analogy to the electronic properties of the actinide metals we interpret the value of the adsorption enthalpy of berkelium having the [Rn]5f^{9}7s^2 ground state with an adsorption on niobium in the trivalent 5f^{8}6d^{1}7s^2 state.

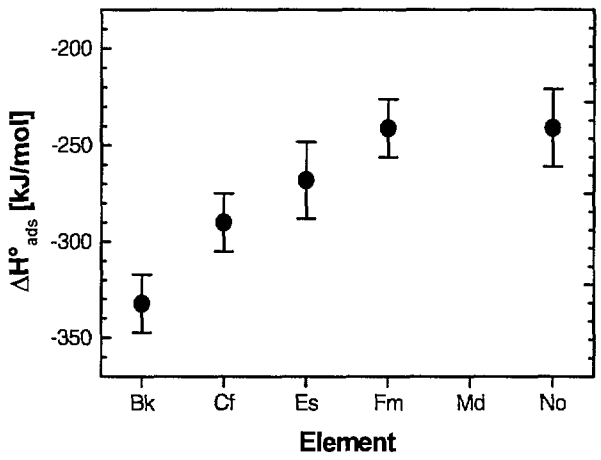

Fig. 2: Adsorption enthalpies on niobium. Values for Cf, Es, Fm, and No from [2].

ACKNOWLEDGMENTS

The authors are indebted for the use of ^{254}Es to the Office of Basic Energy Sciences, U.S. Department of Energy, through the transplutonium element production facilities at the Oak Ridge National Laboratory, managed by Lockheed Martin Energy Research corporation. The support by the DFG under contract Hu 642/1-2 is gratefully acknowledged.

REFERENCES

[1] S. Taut et al., Radiochim. Acta **78**, 33 (1997).

[2] S. Taut et al., J. Alloys Comp. **271-273**, 316 (1998).

[3] S. Taut et al., Report FZR-**218**, 84 (1998).

THERMOCHROMATOGRAPHY OF CURIUM AND BERKELIUM ON NIOBIUM COLUMNS

S. Taut, A. Vahle, S. Hübener, (FZ Rossendorf) B. Eichler, D. Jost, A. Türler (PSI)

The adsorption of elemental curium and berkelium onto metallic niobium was measured by thermochromatography. Adsorption enthalpies of –392±15 kJ/mol (curium) and –349±15 kJ/mol (berkelium) were determined.

INTRODUCTION

In the last years we have studied the adsorption of the metallic divalent actinides einsteinium, fermium, and nobelium in their elemental states on several metals. [1, 2, 3]
Recently, we extended our research to berkelium [4] and curium. This in preparation of the planned adsorption study of lawrencium, the last member of the actinide series. The adsorption behavior of lawrencium is expected to be very similar to that of Cm.

EXPERIMENTAL

We used a similar experimental setup as described in [2] with a sapphire support tube instead of the tantalum tube.
The chromatographic samples were obtained in the following way: A ^{248}Cm target (0.7 mg/cm^2) was irradiated with an ^{18}O beam (about $2 \cdot 10^{12}$ s^{-1}) at the PSI Philips cyclotron. The reaction products and curium which was sputtered from the target during the bombardment was caught in zirconium catcher foils behind the target. These foils were used as samples without further preparation.
The samples were transferred into the cold chromatographic column. After flushing the column with purified helium we adjusted the helium flow rate to 50 cm^3/min and moved the hot gradient furnace over the column. The temperature in the starting position was 1890 K. After 10 or 20 minutes the heating was switched off. The immediate cooling stopped the chromatography process. Finally, the column was cut in 1 cm sections. These pieces were counted off-line in an alpha spectrometer.

RESULTS

Fig. 1 shows the distribution of curium and berkelium along a niobium column.

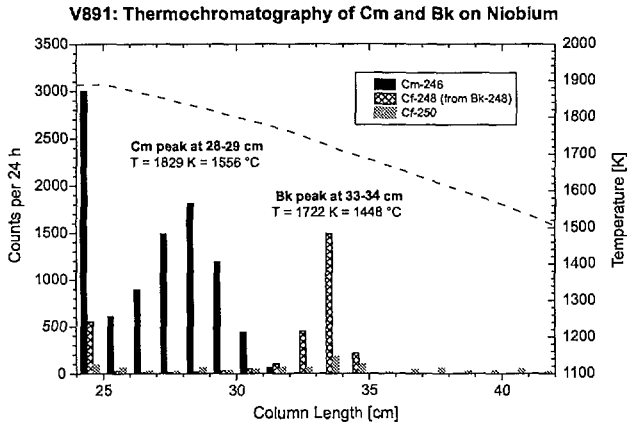

Fig. 1: Thermochromatogram of curium and berkelium on a niobium column.

We assign the ^{248}Cf as the daughter activity of ^{248}Bk for two reasons:
From previous experiments [2] it is known that the Cf deposition temperature under similar conditions is about 1200 K, far below the range covered in this experiment.
^{252}Cf, as the main californium transfer product of the used nuclear reaction [5], is not present. The ^{248}Cf is therefore the decay product of the shortlived ^{248}Bk and represents the Bk chromatographic peak.
Fig. 2 shows the experimentally determined adsorption enthalpies [6] of berkelium and curium on niobium in comparison to earlier experimental data [1, 2, 3, 4] and EICHLER-MIEDEMA model calculations.

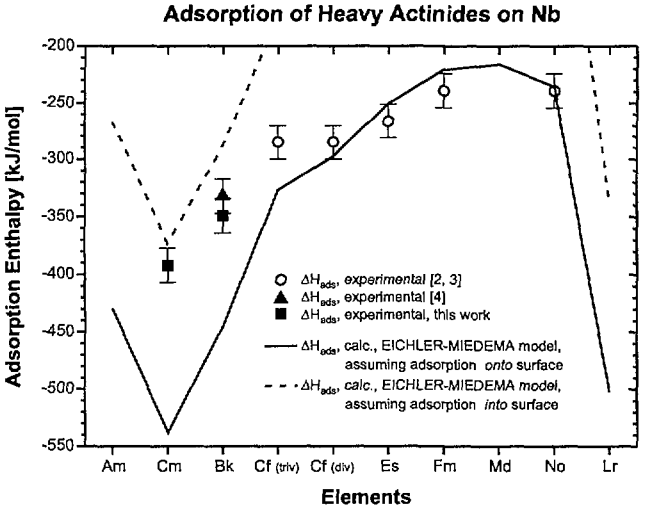

Fig. 2: Adsorption enthalpies of actinides on niobium and EICHLER-MIEDEMA model calculations [7].

ACKNOWLEDGMENTS

The support of Deutsche Forschungsgemeinschaft, contract Hu 642/1-2 is gratefully acknowledged. We are indepted to the Gesellschaft für Schwerionenforschung for making the ^{248}Cm target available as a loan for this experiment.

REFERENCES

[1] S. Taut, et. al., Radiochimica Acta **78**, 33 (1997).
[2] S. Taut, et. al., J. Alloys. Comp. **271**, 316 (1998).
[3] S. Taut, et. al., report FZR, FZR-**218**, 84 (1998).
[4] S. Hübener, et. al., this Annual Report.
[5] D. Lee, et. al., Phys. Rev. **C 27**, 2656 (1983).
[6] B. Eichler, et. al., Radiochimica Acta **30**, 233 (1982).
[7] B. Eichler, report ZfK, ZfK-**396**, (1979).

IN-SITU CHEMISTRY OF ^{218}Po IN THE GAS PHASE

M. Gärtner (Univ. Bern), R. Dressler, B. Eichler, A. Türler (PSI), H.W. Gäggler (Univ. Bern & PSI

A new approach was chosen to investigate the chemical reactivity and behaviour of ^{218}Po in gas phase directly after the decay of ^{222}Rn: A decay chamber which is used as in-situ reaction device was connected with an On-line Gas Chromatography Apparatus.

1 INTRODUCTION

The successful use of the **O**n-Line **G**as chromatography **A**pparatus (OLGA III) in seaborgium experiments [1] showed that there will be a limitation in half life for the isotopes under investigation of about 3 s. Therefore, it is necessary to investigate modified on-line gas chromatography systems in preparation of future heavy element experiments.

2 EXPERIMENTAL SET-UP

A source containing 255 kBq ^{226}Ra fixed on a column was flushed with 100 ml/min Ar/H_2 (98:2) to transport ^{222}Rn into a 0.9 l decay chamber where decay to ^{218}Po and the in-situ reaction with e.g. HCl took place (see Fig. 1). The reaction products were directly introduced into a isothermal quartz column followed by a recluster chamber where the products were attached onto CsCl aerosol particles. Afterwards, the aerosol particles were transported via a capillary to the PSI tape device to measure the α-activity. These parts of the set-up were analogous to OLGA III[2].

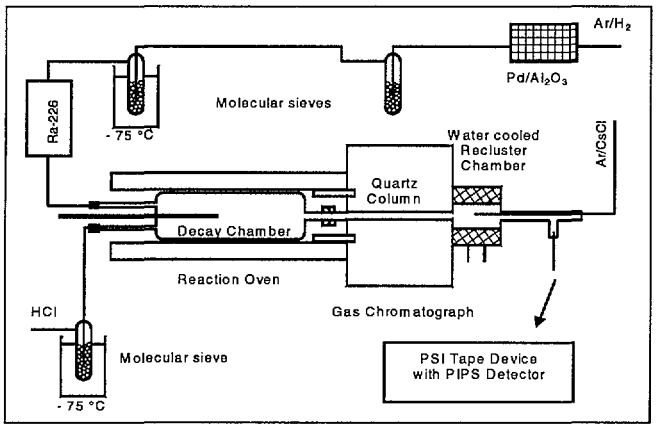

Fig. 1: Schema of the set up.

3 EXPERIMENTS AND RESULTS

The selected gas flow rates were:

Po production:	100 ml/min Ar/H_2 (98:2)
Reactive gas:	112 ml/min HCl
Recluster gas:	500 ml/min Ar
Total gas flow:	712 ml/min

The results are shown in Fig. 2. The difference between the two measured curves might be explained as follows:

A slight condensation was visible in some experiments in front of the molecular sieve from the HCl supply (see Fig. 1). In these cases the reaction products needed a higher isothermal temperature to pass the quartz column. It seems that this observation indicates a higher trace amount of water passing the molecular sieve which influences the chemical reaction of ^{218}Po, presumably to form PoO_2Cl_2. We anticipate that a pure polonium chloride was produced in those experiments where no condensation was visible. The shown adsorption enthalpies which were deduced by a Monte Carlo simulation were slightly lower than previous results obtained with OLGA III [3]. Nevertheless, the difference between the adsorption enthalpies of the two Po species in both series of experiments are in good agreement which might show a systematic difference of the set-ups.

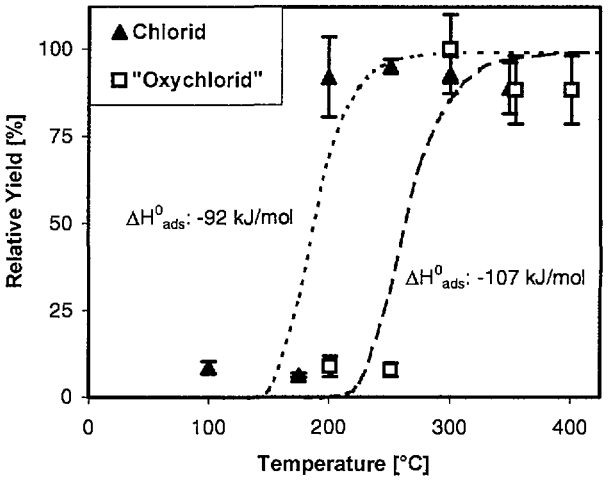

Fig. 2: Relative yield curves in HCl systems: symbols represent measurement, lines simulations.

4 CONCLUSION

The chosen approach opens a opportunity for future heavy element experiments. A next step in development could be a similar set-up at the ^{252}Cf fission source which allows model investigations with many elements of the Periodic Table.

REFERENCES

[1] H.W. Gäggeler, J.All.Comp. **271-274**, 277 (1998).

[2] A. Türler, Radiochim. Acta **72**, 7 (1996).

[3] M. Gärtner et al., PSI Annual Report **1995**, IIIA, p.69.

ENTROPIES OF TRANSACTINIDES

B. Eichler (PSI), H.W. Gäggeler (Univ.Bern & PSI)

The standard entropies of transactinides were predicted by extrapolation. The extrapolations are based on linear correlations of the entropies on ln A for elements within the groups of the Periodic Table. The entropies of the gaseous elements Sg,112 and 114 were estimated with the known correlation of entropies for elements with closed shells and subshells on ln A

The entropy of elements in solid state plays a key role in the physical and chemical properties of the elements. The solid state entropies have connections with e.g. atomic mass A, atomic volume, density , bulk modulus, metallic radius /1/ , density of electrons at the Wigner-Seitz cell boundery /2/ , volatility /3,4/ . These quantities are connected to each other by well know relations.

For the entropies of gaseous elements there exist in the groups a lineare correlation on ln A. For the entropies of gaseous elements with closed electron shells and subshells, there exists a common linear dependence with lnA independent of the groups. The regression line through the experimental literature data yields

$$S\ (g) = 108.837 + 12.475\ \ln A \qquad (1)$$

wich is in excellent agreement with the *Sackur-Tetrode* equation.

This means that the standard entropies for the gaseous elements Sg, 112 and 114 can be predicted with eq.(1). For elements in the solid state basically four different contributions add to the standard entropy S_s:

$$S\ (s) = S_{struct} + S_A + S_{magn} + S_{el} \qquad (2)$$

where S_{struct} is depending on the structure and atomic radius, S_A and S_{el} are depending on the atomic mass and the number of free itinerant electrons and S_{magn} is the magnetic entropy, deduced from the electronic structure after relaxation of the residual atom (without those electrons which contributed to the metallic bonding). As a result, especially for transactinides the accurate values of the 4 contributions can not be calculated reliably . We therefore decided to test an empirical correlation with the atomic mass only:

$$S\ (s) = a + b \ln A \qquad (3).$$

The reasons for this approach are , (i) the sum of two first terms of eq.(2) resemble the vibrational entropy, which itself is direct proportional to the mass, (ii) S_{el} is generally small and (iii) S_{magn} is expected to add to a constant value for elements of a given group of the Periodic Table .

It can be demonstrated that the entropies of solid elements, in a first approximation, yield a linear correlation on ln A. All results of the predictions are compiled in Table 1.

Table 1: Extrapolated standard entropies of the transactinides in gaseous and solid state

Z	A	S (g) ($J\ mol^{-1}K^{-1}$)	S(s) ($J\ mol^{-1}K^{-1}$)
103	262	188.4	56.35
104	263	188.1	47.96
105	263	188.5	45.69
106	264	178.4	35.43
107	265	193.3	37.61
108	265	196.1	33.66
109	268	197.5	36.69
110	269	195.1	45.47
111	272	184.5	52.29
112	277	179.0	72.49
113	280	182.6	72.00
114	282	179.2	68.05
115	284	190.8	60.90
116	286	191.7	65.17
117	288	190.4	61.94

In the periods with increased numbers of valence electrons, entropies decrease, if all valence electrons participate in metallic bonds. When the number of non bonding electrons increases, the solid state entropy increases up to the s^2d^{10} elements. For the group VII elements (Mn,Tc,Re,Bh) the strong paramagnetism indicates that not all valence electrons participate in metallic bonds, causing higher than expected entropy values. This effect decreases in the group with increasing Z .The extrapolated values of solid state entropies permit the calculation of volatilities of the elements, the adsorption enthalpies on metallic surfaces, and the potentials for the electrodeposition on the surface of metallic electrodes. These quantities are essential for designing an experiment to study the radiochemical behavior of transactinides.

REFERENCES

[1] J.W. Ward, H.H. Hill, in "Heavy Element Properties " Eds. W.Müller and H. Blanck, North-Holland Publishing Company , Amsterdam 1976 , p.65.

[2] B. Eichler, Rossbach, H. Radiochimica Acta **33**, 121 (1983).

[3] A.R. Miedema, J. Less-Common Met. **41**, 272 (1976).

[4] A.R. Miedema, Z. Metallkde. **69**, 287 (1978).

SEPARATION OF BROMINE FROM MOTHER NUCLIDE SELENIUM AND DEVELOPMENT OF AN ON-LINE BROMINE-NUCLIDE-SOURCE

M. Wachsmuth, L. Tobler, M. Ammann (PSI), H.W. Gäggeler (Univ. Bern & PSI)

The separation of bromine and its precursor selenium was realised by a controlled decomposition and was used to operate an on-line labelled bromine-source (Br-^{84}Br), which can be applied in tracer studies in atmospheric chemistry.

Short-lived bromine and selenium nuclides are generated in the thermal neutron induced nuclear fission of ^{235}U, which had been placed in the three target chambers of the SINQ gas-jet facility [1]. For the experiments described in the following, the target with the 6 µm Ni degrader foil, which suppresses the heavy mass peak, was used. The fission products can be either transported on aerosols or in a particle free carrier gas. Aerosol transport requires a difficult separation procedure in the lab and its efficiency is low for volatile elements. Instead, adding a reactive species to the inert carrier gas (He) could lead to a more selective transport. The addition of carbon monoxide (600 ppm) resulted not, as expected, in stable bromine compounds, which would act as transport molecules for bromine nuclides to the laboratory, but the precursor of bromine, selenium, reacted with carbon monoxide and was transported as carbonyl selenide (COSe) [2]. Fig. 1 shows that all Br activity in the laboratory comes exclusively from the decay of the transported Se nuclides. If the separation of bromine from selenium is possible, the system can be used to generate bromine nuclides.

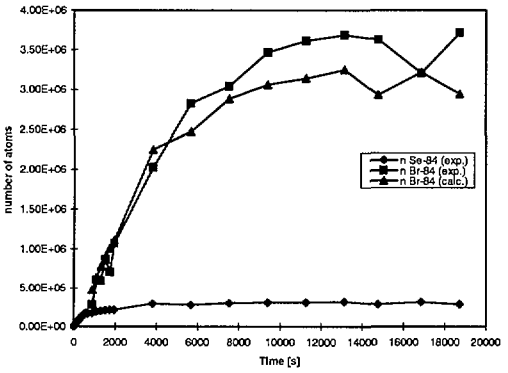

Fig. 1: Number of Br and Se atoms measured in an activated carbon trap at the end of the gas-jet, compared to the number of Br atoms calculated from the decay of the measured Se atoms.

COSe can easily be transported to the lab, where it is cracked in a tube furnace at 800 °C to elemental selenium (Se^0) in the gas phase. In a second tube furnace, the selenium atom is deposited on quartz wool at 120 °C. The reaction of the added carrier bromine (914 ppb Br_2) [3] with the resulting daughter bromine atom leads to an isotope exchange and results in labelled diatomic bromine (Br-^{84}Br). At 120 °C, this molecule is volatile enough to be transported out of the second tube furnace. The use of silver as trapping material in the form of for example silver granules (+60 mesh) or silver coated quartz-wool showed to be very effective. In this way, the labelled bromine is deposited on silver, where it can be detected by γ-spectroscopy. All other fission products, especially short-lived krypton isotopes and their decay products, are collected on activated carbon.

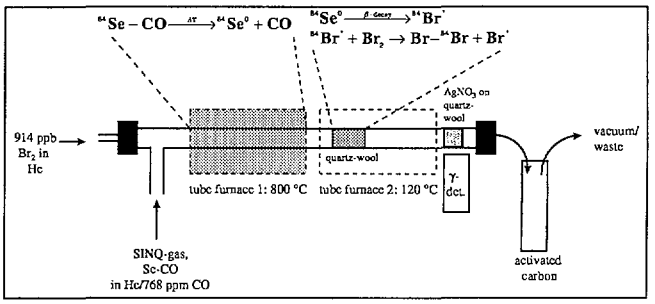

Fig. 2: Set-up of the online Br-^{84}Br source. By using ion-chromatography, it could be shown, that the maximum concentration of H^{84}Br, the second possible volatile product, is 5 %.

The described system is very stable in view of continuous separation of bromine from selenium. During several hours no selenium breakthrough could be observed. Only the position of the quartz-wool in the second tube furnace can be a limiting factor: If it is placed too close to the hot area of the first tube furnace (T>300 °C), the back-reaction to carbonyl selenide occurs.

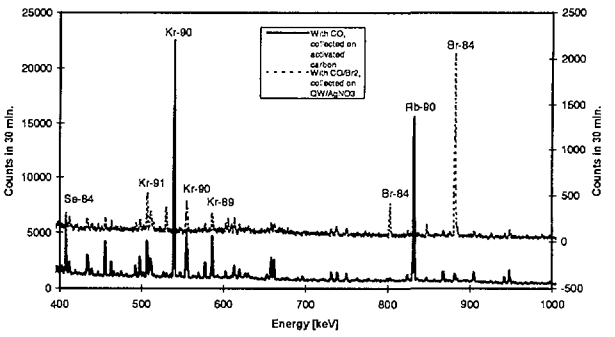

Fig. 3: The influence of the added carrier bromine results in a mobilisation of the bromine nuclides, the decay product of selenium. For comparison, the total yield of selenium, collected on activated carbon, is shown.

REFERENCES

[1] D.T. Jost et al., PSI Annual Report **1997**, IIIA, p.20.

[2] R.S. Baldwin et al., Radiochim. Acta **16**, 94 (1971).

[3] K. Rengan, J. Radioanal. Nucl. Chem. **142**, 173(1990).

FORMATION OF HONO FROM THE REACTION OF NO_2 WITH DIESEL SOOT

F. Arens, M. Ammann, L. Gutzwiller, U. Baltensperger (PSI), H.W. Gäggeler (Univ. Bern & PSI)

In the polluted troposphere gaseous nitrous acid (HONO) may be formed via a reaction between nitrogen dioxide (NO_2) and soot particles. We investigated HONO formation on with diesel soot covered exhaust tube walls and on diesel soot samples which were extracted from diesel exhaust under atmospheric dilution conditions after removal of all combustion gas phase species.

Nitrous acid (HONO) may play an important role in initiating daytime photochemistry by its rapid photolysis yielding OH radicals. The source of HONO in the atmosphere has not yet been conclusively identified. From field measurements it was concluded that NO_2 is converted to HONO by heterogeneous reactions on surfaces in the atmosphere. Several studies have recently identified soot as possible reactive surface for reaction with NO_2 leading to HONO.

In all experiments a diesel engine with 4,5kW nominal power without exhaust treatment devices was used. In a first part of the experiment diesel soot was sampled on glass fiber filters as follows: A part of the hot exhaust gas was passing a heated dilution device (dilution ratio 1:20 at 75°C) where a small volume of exhaust gas was extracted into synthetic N_2. To avoid uncontrolled losses of charged particles and in order to get a representative soot sample the diluted particles passed a ^{85}Kr neutraliser and an electrostatic precipitator. Subsequently, a series of diffusion denuders removed all gas-phase H_20, VOC and NO_x. This ensured that no undesirable reactions occurred on the filter during sampling. Parallel to sampling, the soot surfaces were measured by using a differential mobility analyser (DMA). In a second part of the experiment, the soot containing filters were analysed by exposing them to ^{13}N labelled NO_2 at varying concentrations and humidities, respectively. The amount of surface bound species and the amount of HONO, NO_2 and NO downstream of the filter were measured by using γ-detectors combined with compound specific gas traps.

Figure 1 and 2 show the dependence of HONO formation as a function of NO_2 concentration and relative humidity, respectively. The reaction rate increases almost linearly with the NO_2 concentration. The corresponding reaction probabilities of about 10^{-6} are small. In relation to relative humidity HONO formation seems to be almost independent, but weakly raised under dry and wet conditions.

In another experiment a part of the hot exhaust passed a passively cooled tube (condensation tube). When diesel exhaust passes this tube it can be expected that organic matter condenses on the wall and on particles in dependence of temperature. In a turbulent flow also part of the particles are deposited on the wall. A piecewise analysis (as described above) of the corresponding tube segments by exposing them to about 100 ppb NO_2 showed that HONO formation increases when the temperature is below about 60°C (Figure 3). This is a hint that semivolatile organic compounds are involved in the conversion of NO_2 to HONO.

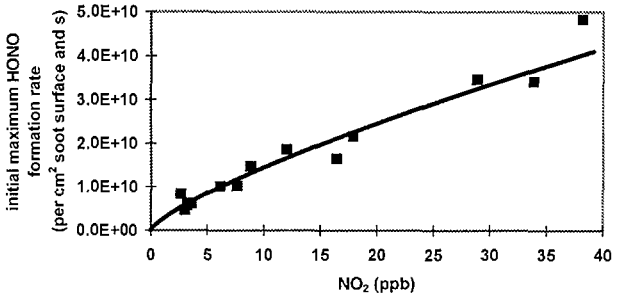

Fig. 1: HONO formation on diesel soot filter samples as a function of the NO_2 concentration (r.h. = 30%).

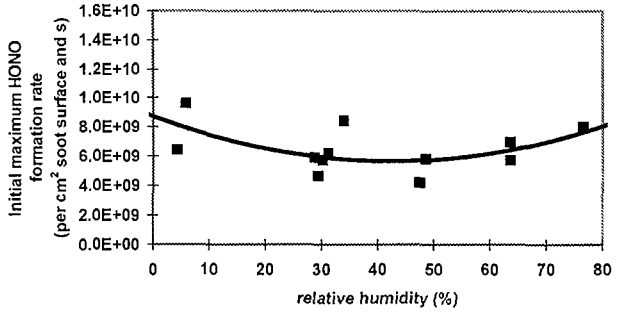

Fig. 2: HONO formation on diesel soot filter samples as a function of the relative humidity (NO_2 = 3 ppb).

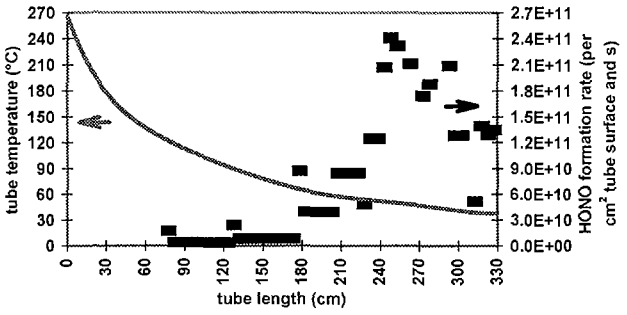

Fig. 3: HONO formation on tube walls in dependence of the exhaust tube temperature. The tube walls are covered with soot and the corresponding organic matter.

ACKNOWLEDGEMENT

This work was supported by the Komission für Technologie und Innovation (KTI).

REFERENCES

[1] M. Ammann et al., Nature **395**, 157 (1998).

[2] M. Kalberer et al., JGR **104**, 13.825 (1999).

ASSESSING HONO FORMATION BY REAL DIESEL EXHAUST IN A SMOG CHAMBER EXPERIMENT

L. Gutzwiller, M. Ammann, U. Baltensperger (PSI), J. Kleffmann, M. Lackhoff, P. Wiesen (Univ. Wuppertal), K. Wirtz (Centro de Estudios Ambientales del Mediterraneo (CEAM)), V. Scheer, R. Vogt, H. Hass (Ford Aachen)

The influence of diesel exhaust on photochemistry, in particular HONO formation, is studied in the European Photoreactor under natural sunlight conditions. An innovative measurement technique is described.

The influence of diesel exhaust on photochemistry needs to be assessed for various diesel fuel compositions in order to define photosmog abatement strategies. Nitrous acid (HONO) may play an important role in initiating daytime photochemistry by its rapid photolysis yielding OH radicals. The source of HONO in the atmosphere has not yet been conclusively identified, but several studies have recently identified soot as a possible reactive surface for reaction with NO_2 [1].

For the Diesel Fuel and Soot project DIFUSO an engine test rig was installed in the machine room of the European Photoreactor (EUPHORE) chamber B in March 1999. The EUPHORE is an outdoor photoreactor of almost 200 m^3 volume in which photochemistry can be simulated under natural sunlight condition [2]. The engine test rig consists of a 1.8 l commercial Diesel engine and an air-cooled eddy current brake and the control unit for the brake. The exhaust gas is guided in heatable tubes to a three way valve under the simulation chamber. This valve allows for dosing the exhaust gas into the smog chamber.

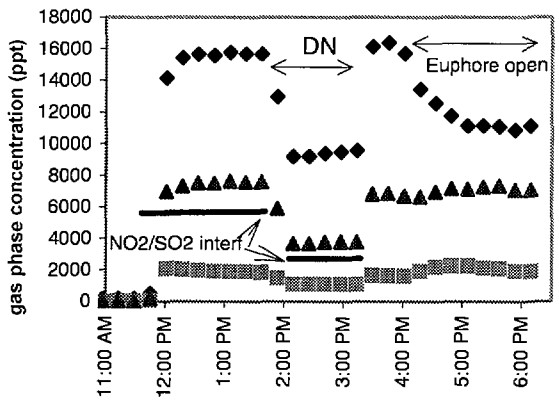

Fig.1: Raw signals of nitrite (diamonds), nitrate (squares) and sulfate (triangles) as detected by the wet effluent diffusion denuder. During two minutes the exhaust of the idling diesel engine was injected at 11:40 am. The subsequent gas phase concentration of NO, NO_2 and SO_2 were 450ppb, 230pbb and 20ppb, respectively. From 2 to 3 pm the carbonate denuder was placed in front of the WEDD in order to determine the nitrite interference, and at 3:50 pm the chamber hood was opened to allow for photolysis. The horizontal bars show the nitrite interference from NO_2 in the presence of SO_2 (with and without carbonate denuder = DN) determined in separate laboratory experiments. The relative humidity was 50%.

The principle of the wet effluent diffusion denuder (WEDD) is decribed in [4]. A constant air flow of typically 1 l min^{-1} is drawn through a wet parallel plate diffusion denuder. The denuder effluent is preconcentrated on ion exchange columns and afterwards automatically analyzed by ion chromatography. Nitrite, nitrate and sulfate are monitored. Possible interferences in the nitrite signal are discussed in another report.

The instant increase of the nitrite signal of the WEDD to a steady state level after injection of the exhaust (Fig.1.) indicates large interferences on the WEDD by NO_2/SO_2 and NO_2/organics rather than HONO formation within the chamber. Using a carbonate denuder as well as separate laboratory experiments we account for the nitrite interference on the WEDD due to the presence of SO_2 and polar organics. This method yields a steady state level of HONO of 3.5ppb (at dark) which is established instantaneously. Part of it may be due to HONO formation on the surfaces of the soot particles and the tube walls in the exhaust transfer line (6m length) from the engine to the smog chamber or might be directly contained in the engine exhaust [3]. From the instantly established steady state level we conclude that either the particle surface rapidly passivates or that HONO might even be slowly destroyed by the particles since there is no additional formation as compared to the pure NO_x experiment which shows HONO formation in the chamber.

As observed in laboratory experiments, beside SO_2, polar organics from the exhaust gas may dissolve into adsorbed water (on WEDD and chamber walls) and reduce gaseous NO_2 to nitrite. Depending on the acidity of this adsorbed water, nitrite may form gaseous HONO which might further complicate the interpretation of the experiments studying the oxidation capacity of the diesel exhaust in the EUPHORE chamber.

REFERENCES

[1] M. Ammann, M. Kalberer, D.T. Jost, L. Tobler, E. Rössler, D. Piguet, H.W. Gäggeler and U. Baltensperger, Nature **395**, 157 (1998).

[2] K.H. Becker (ed.); Final report ot the EC Project EV5V-CT92-0059, Wuppertal, Germany, (1996).

[3] T.W. Kirchstetter, R.A. Harley and D. Littlejohn, Environ. Sci. Technol. **30**, 2843 (1996).

[4] C. Zellweger, M. Ammann, P. Hofer, U. Baltensperger, Atmos. Environ. **33**, 1131 (1999).

HETEROGENEOUS REACTION OF NO_2 ON MINERAL DUST

L. Gutzwiller, S. Olivier, M. Ammann (PSI)

The irreversible upake of NO_2 on Arizona Test Dust (ATD) was measured using the radioactive tracer ^{13}N. Subsequent formation of nitrite and nitrate was assessed using ion chromatography.

The ratio of NO_x to NO_y in the troposhpere directly influences O_3 concentrations and can be strongly influenced by reactions of nitrogen compounds on mineral dust [1]. Recent estimates suggest that up to 5000 Tg of mineral aerosol are uplifted annually into the mid troposphere by surface winds from dry soils in arid regions especially in East Asia (i.e. Gobi desert), and North Africa (Sahara) [2]. Miller et al. [3] determined spectroscopically nitrite and nitrate as surface bound products of the heterogeneous reaction of NO_2 on oxides of aluminum and titanium, and distinguished between two types of nitrate as a function of relative humidity. Although NO_2 may change the surface properties of mineral dust particles, its uptake coefficient is known only for pure alumina and at very low relative humidities [4]. For this reason we applied the very sensitive radioactive tracer method using the short-lived isotope ^{13}N (half-life 9.96min.). The experimental setup consisted of a PFA tube filled at the top with ATD and downstream with the trapping material (NaCl, Na_2CO_3, NDA, Co_2O_3) each one separated by a plug of quarz wool. Different concentrations of NO_2 in N_2 were drawn through this sample column which allows to discriminate between ATD bound ^{13}N and gas phase HNO_3, HONO, NO_2, NO corresponding to the above trapping materials.

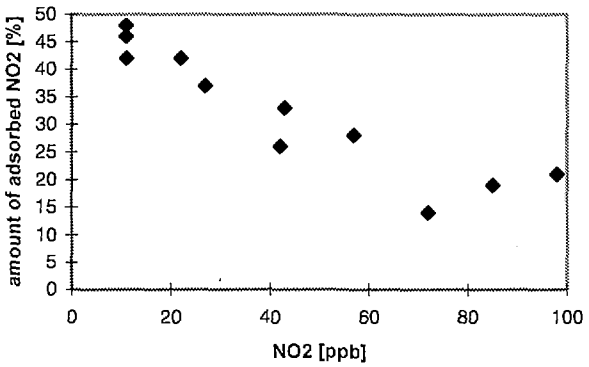

Fig. 1: Fraction of adsorbed NO_2 on the mineral dust as a function of NO_2 mixing ratio at 16% relative humidity.

Fig.1. shows that the fraction of adsorbed NO_2 on the ATD decreases as a function of NO_2 partial pressure. This feature can be interpreted by a limited amount of available surface sites and thus increasing competition for adsorption towards higher NO_2 concentrations. The relative humidity was 16%. Upon shuting off the NO_2 flow through the column the activity on the ATD must decay. In the present case this decay was of the same order as the half life of ^{13}N. Thus the molecules stay considerably longer than 10 min. in the dust sample, eventually indicating that all measured NO_2 molecules have been taken up by the sample. Beside the possibility of dissociative or non-dissociative chemisorption of NO_2, its disproportionation to nitrite and nitrate in the adsorbed water layer is also a possible fate. The basic character of clean mineral dust would prevent these acids from desorbing.

Fig.2. shows the preliminary result for the NO_2 uptake on ATD as a function of relative humidity. It seems that the uptake decreases as a function of relative humidity suggesting competitive adsorption of NO_2 and water. The calculated uptake coefficients at 13±3ppb NO_2 were $7 \cdot 10^{-7}$ and $3.5 \cdot 10^{-6}$ at 70 and 17% relative humidity, respectively.

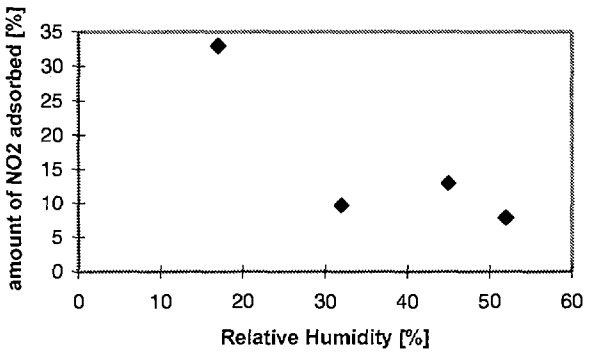

Fig. 2: Fraction of adsorbed NO_2 on the mineral dust as a function of relative humidity at a mixing ratio of 40ppb NO_2.

In order to assess the ATD bound products the following procedure was chosen: Previously washed ATD samples were exposed to unlabeled NO_2 during several hours, suspended in milliQ water during one hour, filtered and analyzed by ion chromatography. Preliminary results clearly show that both nitrite and nitrate are formed on the ATD surface due to the interaction with NO_2. Further investigation is needed, however, to assess the exact reaction pathway.

REFERENCES

[1] F.J. Dentener, G.R. Carmichael, Y. Zhang, J. Lelieveld, P.J. Crutzen, J. Geophys. Res. **101**, 22869 (1996).

[2] I. Tegen, I. Fung, J. Geophys. Res. **99**, 22897 (1994).

[3] T.M. Miller, V.H. Grassian, Geophysical Research Letters **25**, 3835 (1998).

[4] C. Börensen, U. Kirchner, V. Scheer,R. Vogt, Eurotrac-2 Subproject Chemical Mechanism Development (CMD), HEP 4 (1998).

NO_2 REACTION WITH SOLID ANTHRACENETRIOL AS MODEL PROCESS FOR HONO FORMATION ON DIESEL SOOT

F. Arens, M. Ammann, L. Gutzwiller (PSI), H.W. Gäggeler (Univ. Bern & PSI)

Soot aerosol particles containing hydrocarbons have been shown to be a substrate for the conversion of NO_2 to HONO, an important trace constituent of the atmosphere. We investigated HONO formation on solid anthracenetriol surfaces as a possible model process for HONO formation on soot aerosol particles.

NO_2 reacts with soot surfaces to form nitrous acid (HONO) which may accelerate ozone formation in polluted air masses. Several studies have recently identified soot as possible reactive surface for reaction with NO_2 leading to HONO, but the corresponding reaction mechanisms are still unknown. Soot surfaces are rich in polycyclic aromatic hydrocarbons. Spectroscopic studies also show the presence of OH and other functionalities on soot samples. Because of the idea that HONO formation could be caused by OH containing surface bound PAH's, we investigated the HONO formation potential of some aromatic compounds (Figure 1). It could be shown that these compounds react in the condensed phase with gaseous NO_2 to form HONO.

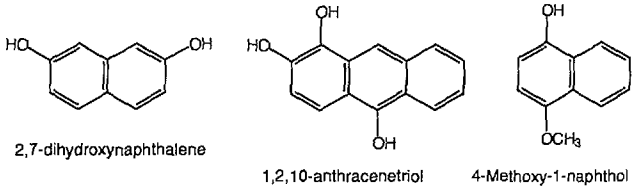

Fig. 1: Typical solid aromatic compounds which react in the condensed phase with gaseous NO_2 to form HONO.

More detailed experiments have been done with 1,2,10-anthracenetriol which has a sufficiently low vapour pressure. NO_2 adsorbed on solid anthracenetriol and possible gaseous reaction products (HONO, NO_2, NO) were measured using the ^{13}N tracer technique: ^{13}N-labelled NO_2 in humidified air passes a plain duct formed by two parallel sandblasted glass plates with 1 mm distance in between. The first part is coated with anthracenetriol, immediately followed by the coatings trapping the gaseous product species (Figure 2). The surface area of the anthracenetriol coating is estimated from microscopic inspection of the coating after the experiments.

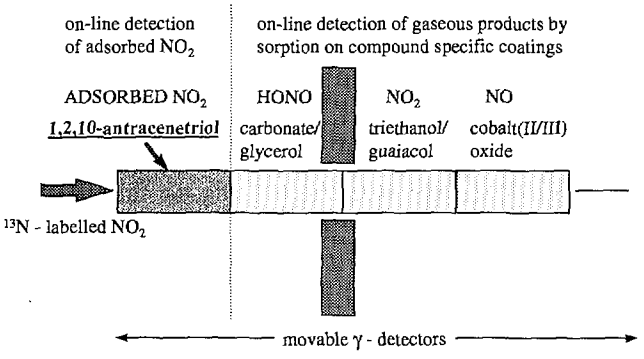

Fig. 2: Experimental approach

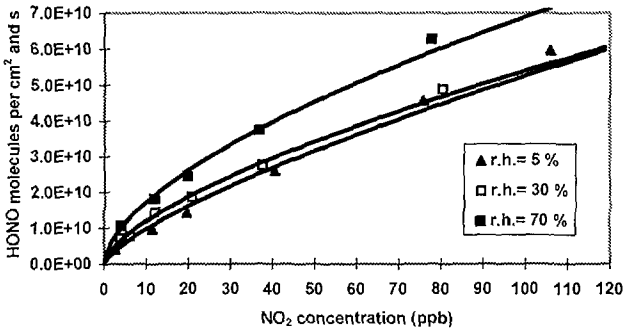

Fig. 3: HONO formation from the reaction of NO_2 with condensed anthracenetriol as a function of NO_2 concentration for different relative humidities.

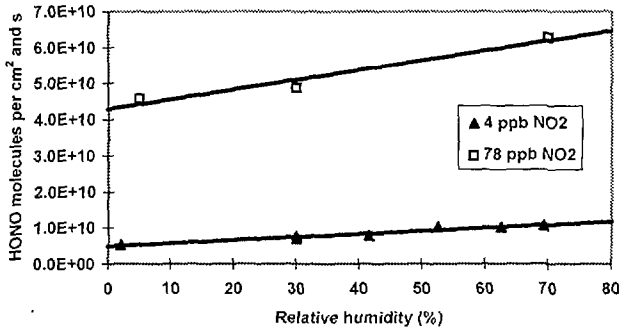

Fig. 4: HONO formation from the reaction of NO_2 with condensed anthracenetriol as a function of relative humidity for different NO_2 concentrations.

Figure 3 and 4 show the dependence of HONO formation as a function of NO_2 concentration and relative humidity, respectively. The reaction rate increases almost linearly with the NO_2 concentration. The corresponding reaction probabilities of about 10^{-6} are small and similar to reaction probabilities of HONO formation on real diesel soot. Because of the almost linear behaviour in respect to relative humidity, water seems to be important for reaction.

As reaction mechanism we propose an electron transfer process according to: *(Ar = aromatic system)*

$$ArOH + H_2O \leftrightarrow ArO^- + H_3O^+$$

$$ArO^- + {}^{\bullet}NO_2 + H_3O^+ \rightarrow ArO^{\bullet} + NO_2^- + H_3O^+ \xrightarrow{air} HONO + products$$

ACKNOWLEDGEMENT

This work was supported by the Komission für Technologie und Innovation (KTI).

REFERENCES

[1] M. Ammann et al., Nature **395**, 157 (1998).

UPTAKE OF NO_2 INTO AQUEOUS NAPHTHALENEDIOL SOLUTION

M. Ammann, E. Rössler, L. Gutzwiller (PSI)

Uptake of NO_2 into aqueous solution containing naphthalenediol was studied using the wetted wall flow tube technique at atmospheric pressure. The main product was nitrite ion for NO_2 concentrations below 300ppb and pH's between 3 and 9.

The oxidation of aromatic compounds in the atmosphere leads to phenolic species as intermediates. It has been shown that in aqueous solution dissolved NO_2 reacts with phenolate ion [1]. Although this reaction is not a significant degradation pathway for phenols under atmospheric conditions, it may be a significant source of nitrite in the atmospheric aqueous phase which in turn may be a source of HONO in the gas-phase. Therefore, the uptake of NO_2 into aqueous naphthalenediol solutions was studied under atmospheric conditions. Naphthalenediol, rather than phenol, was chosen because of its higher stability and lower vapour pressure making corrections for the transfer into the gas-phase unnecessary.

The 10^{-5} to 10^{-3} M aqueous naphthalenediol solutions were fed into a vertically mounted sand-blasted glass-tube (12mm i.d.), and care was taken that the solution was covering the whole tube wall during the experiment. The liquid was pumped away at the tube exit and sampled for nitrite analysis by ion chromatography. The gas-flow passing the flow tube ($5cm^3s^{-1}$) contained 50 to 300 ppb NO_2 in synthetic air. From the lower tube end, a teflon tube ('extractor') was pushed into the flow tube. The position of this extractor determined the contact time of the gas with the aqueous phase. The gas flow was sampled by a chemiluminescence NO_x detector (CLD) with internal molybdenum converter for quasi-continuous measurement of NO and NO_y. An additional carbonate denuder was regularly switched into the sampling line to discriminate HONO against NO_2.

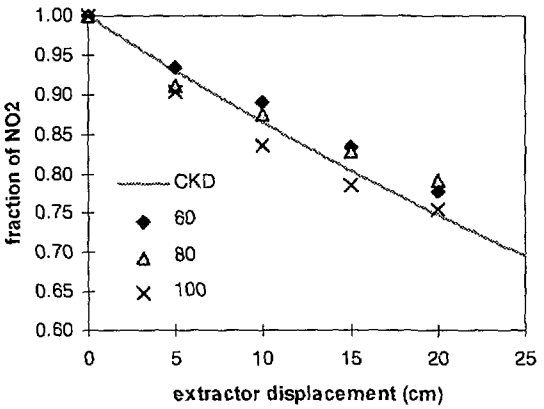

Fig. 1: Relative NO_2 loss in the wetted wall flow tube as a function of the extractor position at 60, 80, and 100ppb NO_2. The solid line gives the calculated loss using an uptake coefficient of $1.5 \cdot 10^{-6}$.

The uptake coefficient, i.e. the probability that an NO_2 molecule hitting the aqueous surface is actually lost to the aqueous phase, is determined from the difference of the NO_2 concentration upstream and downstream of the flow tube using a numeric model treating radial diffusion [2]. For the present geometry and gas flow rates uptake coefficients below about 10^{-5} could be determined.

Figure 1 shows the typical results of an experiment displaying the NO_2 loss as a function of the extractor position. The uptake coefficients derived were ranging from 10^{-7} to 10^{-6} for concentrations up to $5 \cdot 10^{-4}$ M. They increased with increasing pH consistent with the idea that the deprotonated form, the phenolate ion, is the species reacting with NO_2.

Figure 2 shows for one case that all NO_2 lost to the aqueous phase as quantified from the uptake measurements using the CLD is converted to nitrite which has been found in the aqueous phase exiting the flow tube. Thus, the main fate of NO_2 in these solutions is nitrite ion suggesting that the electron transfer from phenolate ion to NO_2 is the main reaction pathway under these conditions.

The kinetics of this reaction system will be derived from a detailed analysis of the results obtained as in Figure 1 as a function of the naphthalenediol and NO_2 concentrations, and pH. An assessment of the implications for the atmosphere should include model calculations adequately treating source and sink reactions for phenolic species in the gas and aqueous phases.

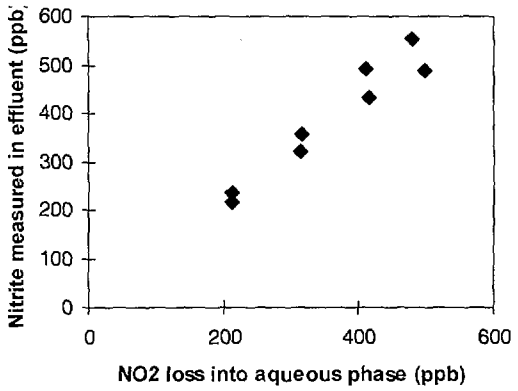

Fig. 2: Comparison of NO_2 loss in the flow tube with nitrite measured in the effluent aqueous. The NO_2 loss is converted to concentration in aqueous solution assuming that all NO_2 taken up is reacting to nitrite. The naphthalenediol concentration was $5 \cdot 10^{-4}$ M at a pH of 9. Only experiments using the full length of the flow tube are included (extractor removed).

REFERENCES

[1] Z.B. Alfassi et al., J. Phys. Chem. **94**, 8800 (1990).

[2] D.M. Murphy, D.W. Fahey, Anal. Chem. **59**, 2753 (1987).

POSSIBLE INTERFERENTS IN THE HONO DETERMINATION BY WET EFFLUENT DIFFUSION DENUDERS

L. Gutzwiller, N. Streit, U. Baltensperger, M. Ammann (PSI)

The aqueous reduction of NO_2 by different species is investigated not only in view of correcting an instrumental artefact but also to shed new light on sources of nitrite, a potential precursor of atmospheric HONO.

Field data of nitrous acid (HONO) have often shown differences between Differential Optical Absorption Spectroscopy and the wet effluent diffusion denuder (WEDD) technique, with the WEDD results usually being 100-200 ppt higher. However, the reason for this has not been elucidated so far. Numerous investigations of possible artefacts by uptake of gaseous NO_2 in WEDDs have been made, and have shown to produce negligible artefacts (e.g., Zellweger *et al.* [1] reported that gaseous NO_2 resulted in an artefact of less than 0.1%). On the other hand, Lee and Schwartz [2] reported an enhanced NO_2 uptake in S(IV) containing water, with a first order reaction both in NO_2 and SO_2. Therefore, it has to be expected that the NO_2 interference in WEDDs might be enhanced by the presence of SO_2.

The interfering reactions are:

$$2\,NO_2\,(aq) \Rightarrow 2\,H^+ + NO_2^- + NO_2 \qquad (1)$$

$$2\,NO_2\,(aq) + HSO_3^-\,(aq) \Rightarrow 2\,NO_2^- + 3\,H^+ + SO_4^{2-} \qquad (2)$$

In this paper we present first the above reaction system without SO_2 but with a unknown interferent acting analogously. Secondly, we have investigated the above system at SO_2 concentrations above 1ppb and NO_2 concentrations below 1ppm. As we shall see, reaction (1) including the unknown interferent is negligeable under these conditions.

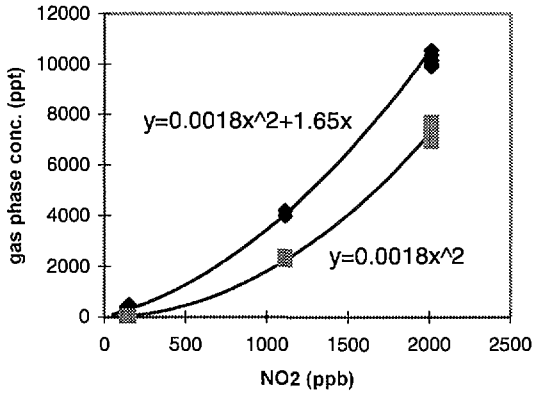

Fig. 1: Gas phase HONO (diamonds) and HNO_3 (squares) as measured by the WEDD and plotted against the NO_2 concentration. The HONO term is corrected for a potential interferent X in the effluent leading to a NO_2 interference: 1.65 = k *X.

Fig.1. presents the amount of disolved nitrite and nitrate expressed as gas phase HONO and HNO_3, respectively, as a function of NO_2 partial pressure. The measured HONO concentration is larger than the HNO_3 concentration thus contradicting the disproportionation reaction (1). We interpret the increased HONO signal as due to an unknown interferent X analogous to sulfite in reaction (2): $HONO^{interf}$ (g, ppt) = k * X * NO_2 (g, ppb), where k * X = 1.65.

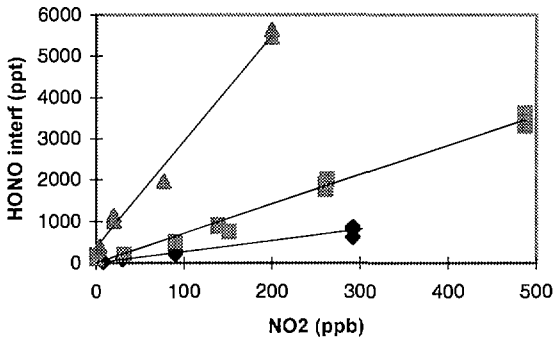

Fig. 2: Nitrite formation in the WEDD caused by the above reactions and plotted as gas phase HONO vs. NO_2 . The triangles, squares and diamonds correspond to 15.8, 4.8 and 1.5 ppb SO_2, respectively. The corresponding linear regressions yield slopes of 25.5, 7.1 and 2.7.

Plotting the slopes displayed in Fig.2. as a function of sulfate concentration yields the interference correction factor f^{interf} =1.6 for the overall reaction:

$HONO^{interf}$ (g, ppt) = f^{interf} * NO_2 (g, ppb) * SO_2 (g, ppb)

This scheme allows for a simple correction of HONO field measurements for the interference caused by NO_2 and SO_2. Further investigations are needed to check to what extent these laboratory results are applicable to field experiments and if other interferents such as organics may cause additional HONO artefacts. The study of species reducing NO_2 to nitrite not only elucidates the interference in HONO measurements but sheds also new light on possible sources of nitrite, a potential precursor of atmospheric HONO.

REFERENCES

[1] C. Zellweger, M. Ammann, P. Hofer, U. Baltensperger, Atmos. Environ. **33**, 1131 (1999).

[2] Y.N. Lee, S.E. Schwartz, in Precipitation Scavenging, Dry Deposition and Resuspension, Vol. 1, ed. by H.R. Pruppacher, R.G. Semonin, and W.G.N. Slinn, Elsevier, New York, (1983).

REACTIVE NITROGEN (NO_y) AT THE HIGH ALPINE SITE JUNGFRAUJOCH

C. Zellweger (PSI & EMPA), U. Baltensperger, M. Lugauer, S. Nyeki, N. Streit, E. Weingartner, (PSI), P. Hofer B. Buchmann, R. Rüttimann, J. Forrer (EMPA)

Measurements of total NO_y along with seasonal field campaigns of speciated NO_y determination were performed over a two-year period at the Jungfraujoch. Station specific meteorological filters were used to discriminate between undisturbed free tropospheric conditions and periods which were influenced by planetary boundary layer air.

Measurement of total reactive nitrogen (NO_y) along with seasonal field campaigns of speciated NO_y determination (NO, NO_2, peroxyacetyl nitrate (PAN), HNO_3 and particulate nitrate) were performed over a two-year period at the high-alpine research station Jungfraujoch (JFJ), 3580 m asl. One of the main topic of this work was to investigate the influence of different meteorological processes on the NO_y mixing ratio and speciation over the Alpine region in order to distinguish between the undisturbed free troposphere (FT) and periods which are influenced by planetary boundary layer (PBL) air. Several meteorological processes (föhn events, synoptical lifting, thermally induced vertical transport) were identified to have a strong influence on the NO_y mixing ratio at the JFJ [1]. Figure 1 shows the levels and speciation of NO_y during selected periods.

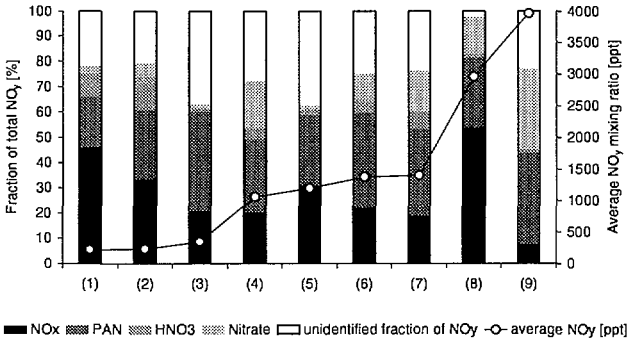

Fig. 1: NO_y level and speciation at the Jungfraujoch:

(1) winter, undisturbed FT, 12 - 13 Feb 1998
(2) summer, undisturbed FT, 27 - 30 Jul 1997, 0300–0900
(3) spring, undisturbed FT, 27 - 30 Mar 1998
(4) summer, influenced by thermally induced transport, 27-30 Jul 1997, 1500-2100
(5) winter, influenced by synoptical lifting, 22 - 24 Feb 98
(6) summer, syn. lifting, 25 Aug 1900 - 26 Aug 0700, 1997
(7) summer 16-22 Aug 1997, convective days with low wind speed at the 500 hPa level [2]
(8) spring, south foehn, 14 Apr 1400 - 16 Apr 1600, 1998
(9) spring, influenced by thermally induced transport, 30 Mar - 2 Apr 1998, 1500-2100

The NO_y mixing ratio remained relatively constant during undisturbed FT periods. Highest NO_y mixing ratios were observed during spring, but the seasonal difference between summer and winter was small. However, differences can be seen in the NO_y speciation. The NO_x/NO_y ratio was highest during winter (0.46) and lowest during spring (0.21). This reflects the lower photochemical activity during the winter months. By similar reasons, PAN/NO_y was highest during spring (0.39) and lowest during winter (0.20). Meteorological processes also have a strong influence on the level and speciation of NO_y. The NO_y speciation for selected periods (thermally induced vertical transport, föhn, frontal systems) is also shown in Figure 1. The NO_y mixing ratio reached an average level of 1 to 4 ppb, a factor 4 to 10 higher compared to undisturbed FT conditions. The NO_x/NO_y ratio was lowest during episodes with thermally induced vertical transport, accompanied by high NO_3/NO_y and PAN/NO_y ratios. This reflects the photochemical transformation of NO_x during thermally induced upward transport.

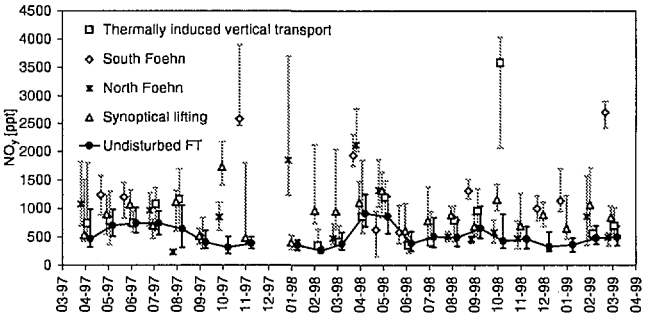

Fig. 2: Seasonal variation in monthly median values of NO_y for the filtered data as well as for different meteorological situations. The first and third quartiles are indicated by bars.

The knowledge of the above meteorological transport processes allowed the discrimination between the undisturbed FT and periods with an influence of PBL air at the JFJ, which is illustrated in Figure 2 for NO_y. It can be seen that the above meteorological processes generally caused an increase of the mixing ratios as well as of the variability for NO_y. The knowledge of the station specific meteorological processes which influence the composition of the air is of great importance for the interpretation of a given data set, e.g. for trend analysis of the undisturbed FT or for establishing a link between source regions and pollution episodes at the Jungfraujoch.

REFERENCES

[1] J. Forrer et al., Variability of trace gases at the high Alpine site Jungfraujoch caused by meteorological transport processes. J. Geophys. Res., in press, 1999.

[2] C. Zellweger et al., Summertime NO_y speciation at the Jungfraujoch, 3580 m asl, Switzerland. J. Geophys. Res., in press, 1999.

SIZE DEPENDENT ACTIVATION OF AEROSOL PARTICLES TO CLOUD DROPLETS AT THE HIGH ALPINE SITE JUNGFRAUJOCH (3580 M ASL)

S. Henning, E. Weingartner, S. Nyeki, M. Schwikowski, U. Baltensperger (PSI), H. W. Gäggeler (Univ. Bern & PSI)

Measurements of the interstitial and total aerosol were conducted at the high-alpine research station Jungfraujoch during a summer campaign. Additionally cloud droplet size distributions were recorded.

Atmospheric aerosol particles influence the climate directly and indirectly. The aerosol direct effect causes a change of the global radiation budget by absorption and reflection of solar radiation. The indirect aerosol effect is due to the modification of number concentration, composition and size of cloud droplets. Atmospheric aerosols may act as cloud condensation nuclei (CCN) if their diameter is above the Kelvin diameter, which is dependent on the particle chemical composition (soluble fraction of the particle) and the supersaturation S_c of the cloud. For a constant liquid water content (LWC), clouds with higher CCN concentrations have higher droplet concentrations and smaller droplets, thus lead to higher cloud reflectivity.

The aim of this project at the high-alpine research site Jungfraujoch is to study the relation between aerosol size distribution, droplet size distribution and their influence on the activation diameter.

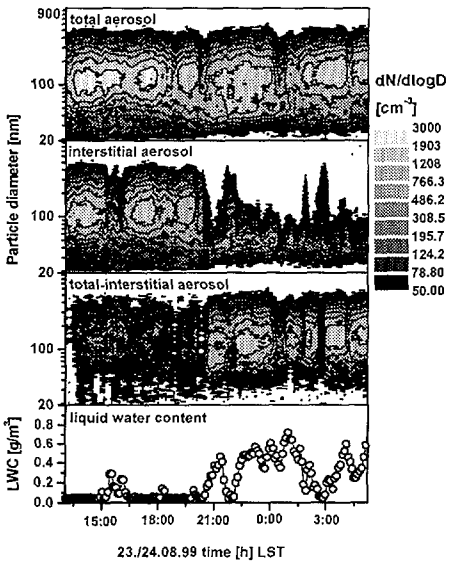

Fig. 1: LWC, total & interstitial aerosol number size distribution and difference of both during the cloud event from 23./24.08.99

A first measuring campaign was conducted during this summer at the Sphinx building of the high-alpine research station Jungfraujoch (3580 m asl, 46.548°N, 7.984°E). Cloudy conditions occur about 40% of the time at this site and LWC measurements are performed routinely. Thus the site is ideal for obtaining information on cloud formation.

During the campaign the size distributions of the total and interstitial aerosol were measured with a Scanning Mobility Particle Sizer (SMPS, D = 0.01 to 0.8 μm). For measuring the total aerosol a heated inlet was used which is designed to evaporate cloud droplets [1]. A cold aerosol inlet with a cut-off diameter at D = 5 μm was used for the interstitial aerosol (particles which are not activated and remain between droplets). In the absence of clouds, spectra from the heated and cold inlet should be identical.

Fig. 1 shows the LWC, the total and interstitial aerosol number size distribution as well the difference of both for a cloud event. It can be seen that the number concentration is strongly influenced by clouds. With increasing LWC activation of particles occurs, which is clearly dependent on particle size.

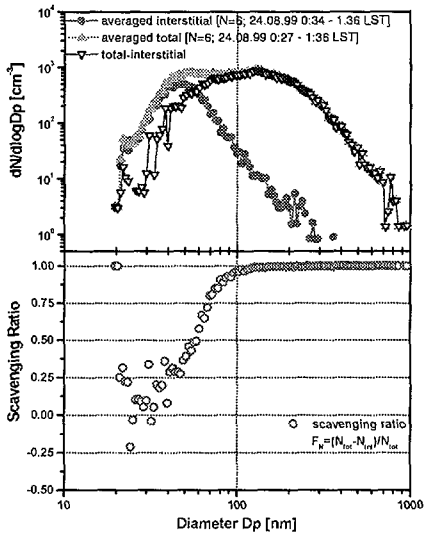

Fig. 2: Interstitial & total aerosol number size distribution and scavenging ratio, mean LWC = 0.66 g/m3

Fig. 2 shows total and interstitial size spectra and the scavenging ratio (i. e., the fraction of activated particles) as a function of particle diameter. For the presented case with high LWC values all particles greater than 100 nm are activated. A diameter for 50% scavenging D_{P50} of 50 nm was observed. With the assumption of pure ammonia sulphate particles a supersaturation S_c = 0.4% is needed to activate particles of this size. This is a value which occurs in nature [2].

The analysis of all cloud events from the summer campaign and further investigation of the aerosol-cloud interaction during a winter campaign will follow.

REFERENCES

[1] E. Weingartner et al., J. Geophys. Res. **104**, 26809 (1999).

[2] H.R. Pruppacher, J.D. Klett; D. Reidel Publ. Comp., Dordrecht, Boston, London (1978).

HYGROSCOPIC PROPERTIES OF AEROSOL PARTICLES AT LOW TEMPERATURES (T < 0°C)

E. Weingartner, M. Gysel, U. Baltensperger (PSI)

The ability of hygroscopic atmospheric aerosols to absorb water is of great importance for our climate. To avoid artefacts it is important that these hygroscopic properties are measured at ambient conditions, i.e. at low temperature for the middle and upper troposphere. Therefore, a new instrument was developed to measure the water uptake of submicrometer aerosol particles in the temperature range -20°C < T < 20°C.

In the field, hygroscopicity measurements are commonly performed using a Hygroscopicity Tandem Differential Mobility Analyzer (H-TDMA). So far, most of these measurements were performed at temperatures between 20 and 30°C. The aim of this study is to measure aerosol hygroscopic properties at remote locations such as the high-alpine site Jungfraujoch at 3580 m asl in Switzerland. Average ambient temperatures at the station are low (-1°C in summer and -14°C in winter). At these temperatures, semi-volatile compounds (such as nitrate or lower-molecular-weight organics) may be adsorbed and considerably alter aerosol hygroscopic properties. To minimize artefacts due to volatilization, aerosol hygroscopic behavior should be measured at ambient conditions.

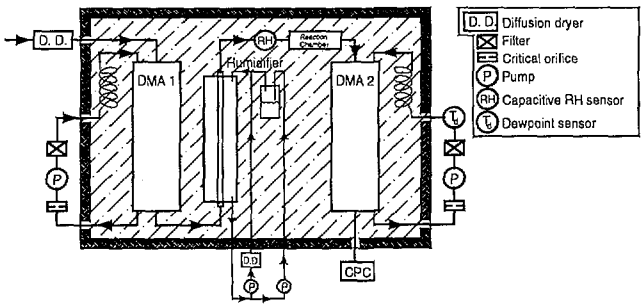

Fig. 1: Sketch of the experimental setup.

Figure 1 shows the experimental setup of the low temperature H-TDMA. The aerosol is dried and fed into the first DMA where particles of a certain "dry" size are selected ($D=D_o$). After exposure to higher RH, the new particle diameter is determined with a second DMA combined with a condensation particle counter (CPC). To ensure a constant temperature within the entire H-TDMA system, both DMAs, as well as the humidifier, are submersed in a water/ethylene glycol bath which can be cooled down.

The H-TDMA was tested with several salt aerosols which were generated by atomization of aqueous solutions. Measurements were performed at 20°C, 0.5°C and -9°C, and RH was calculated with respect to water. Figure 2 shows that NaCl particles are characterized by an abrupt increase in diameter at the deliquescence humidity (DH), which is due to the phase transition of particles from "dry" crystals to saturated solution droplets. The diameter of the droplet is described by the Köhler theory (solid lines in the Figures) which applies only to sufficiently diluted droplets. For 20°C and 0.5°C, DH is about 75% and agrees well with measurements reported by other investigators (see [1] and references therein). For all presented temperatures a good agreement with Köhler theory is found. The agreement at T = -9°C supports the idea that NaCl particles remain liquid at this temperature.

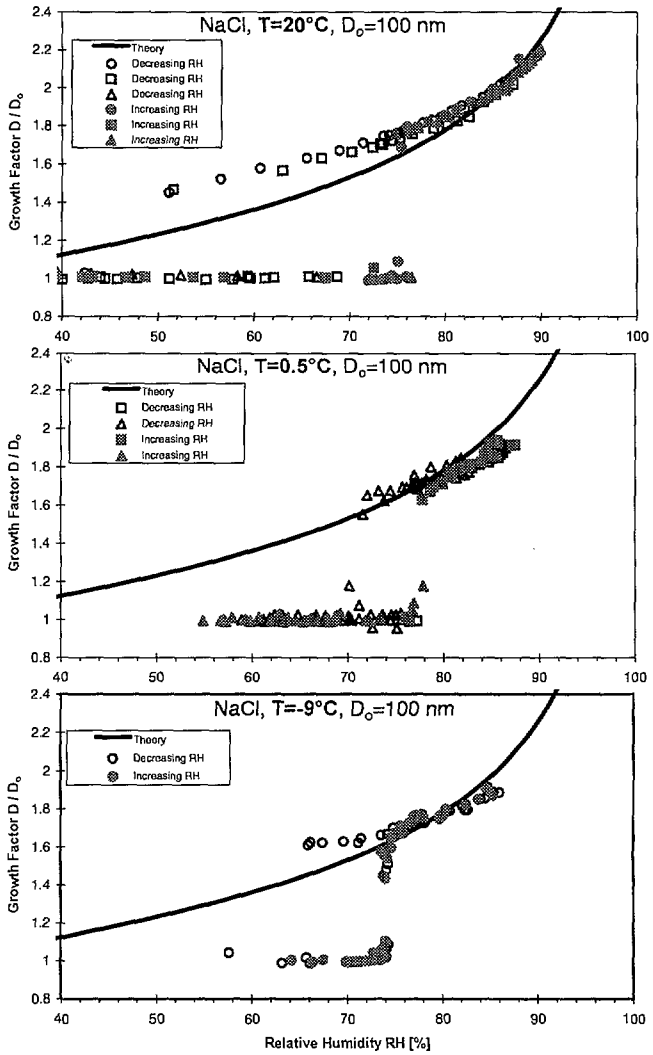

Fig. 2: Humidograms of NaCl test aerosol at different temperatures. Since a fraction of the aerosol particles is temporarily subjected to higher RH in the humidifier, more than one diameter is often found for a fixed RH. Solid lines are theoretical curves calculated with a simplified Köhler theory.

REFERENCE

[1] J.H. Seinfeld and S.N. Pandis, Atmospheric Chemistry and Physics, Wiley New York, 1998.

AEROSOL VOLATILITY MEASUREMENTS AT THE GAW STATIONS JUNGFRAUJOCH AND NY ÅLESUND

S. Nyeki, U. Baltensperger, S. Henning, N. Streit, E. Weingartner (PSI), K. Eleftheriadis (NCSR), I. Colbeck (Essex Uni.)

Aerosol volatility/size spectra measurements were conducted at two remote European GAW stations during summer field-campaigns in order to measure representative aerosol chemical and physical parameters.

The complexity of the atmospheric aerosol lifecycle ideally requires physico-chemical measurements to be conducted in real-time if mechanisms relevant to climate change are to be elucidated. While such instruments are still under development, the aerosol volatility/size spectra technique is a simple method that fulfils the above requirements in part. The method is based on the different volatilization characteristics of aerosols at ambient and higher specific temperatures T (e.g. [1]). Sulphuric acid is evaporated at $T < 110$°C, while $(NH_4)_2SO_4$ / NH_4HSO_4 decompose at $T < 300$°C. The remaining fraction at $T > 300$°C, known as the refractory aerosol, is composed of sea-salt, black carbon (BC), and mineral dust. When combined with an aerosol size spectrometer (e.g. TSI SMPS system), qualitative chemical composition of the size-resolved atmospheric aerosol may be determined in real-time.

A number of studies have measured the volatility of background aerosols [1], however, such measurements are still lacking. The present work reports physico-chemical and volatility measurements conducted at two European Global Atmosphere Watch (GAW) sites: i) the arctic baseline station Ny Ålesund (NYA; 474 m asl, 78.90°N 11.88°E, Svalbard) and, ii) the high-alpine clean continental station Jungfraujoch (JFJ; 3573 m asl, 46.55°N 7.98°E, Switzerland).

Measurements were conducted during the 1998 summer season (NYA, Aug.-Sept; JFJ, July) with a well-characterised volatility-desorber system [2]. A new feature of this particular design is the desorber section, which ensures better removal of evaporated gases using activated charcoal. Preliminary measurements for NYA (Figure 1) illustrate a comparison of the aerosol volume at 300°C ($d \leq$ 200 nm; TSI SMPS) and BC concentration (aethalometer; Magee AE-10). The good correlation ($R^2 = 0.88$) illustrates that the refractory aerosol was mainly composed of BC, although certain periods are seen to have been influenced by mineral dust and/or sea-salt. As Svalbard is predominantly covered in glaciers, and lies in the Greenland Sea, sea-salt is most probably enhanced during these periods. A site-specific aethalometer calibration is yet to be conducted on BC samples using a thermal method [3]. This is likely to result in a lower instrumental absorption efficiency α_{API} and hence in systematically higher BC concentrations than shown in Figure 1.

The NYA data set, taken during the arctic annual minimum in aerosol concentration, extends previous measurements during the annual maximum in March-April 1989 [1]. A comparison of fractional aerosol volume concentrations (V_{CONC}; d = 14-750 nm) for NYA and the JFJ according to wind direction is shown in Figure 2. The relative fraction of refractory aerosols are similar at both sites but the JFJ aerosol is seen to be more neutralised than at NYA. The JFJ experiences a summer maximum in the aerosol concentration cycle and hence accounts for a larger V_{CONC} value, as indicated by the numbers in Figure 2. An implicit assumption in similar volatility studies is the presence of a small volatile organic carbon fraction, which is reasonable for remote sites. This will be further assessed by organic and inorganic speciation from impactor and filter measurements taken during the campaigns.

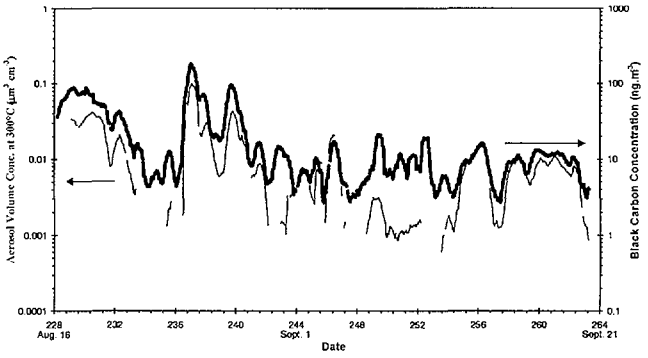

Fig. 1: Aerosol volatility results at NYA, late Summer 1998.

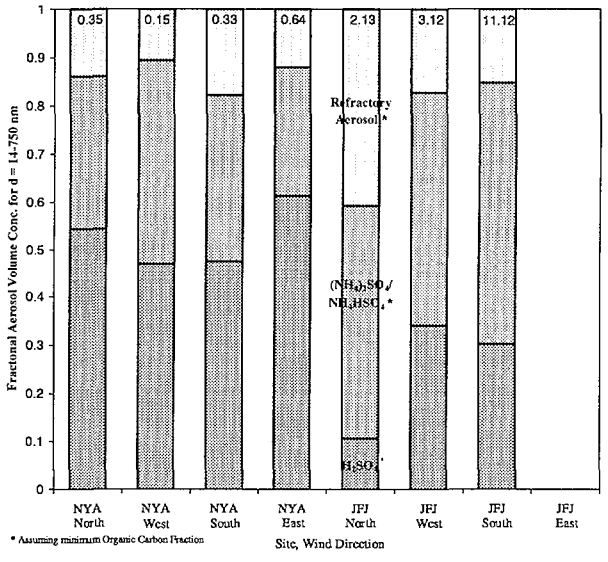

Fig. 2: Fractional V_{CONC} at NYA and the JFJ. Numbers indicate the total SMPS aerosol V_{CONC} ($\mu m^3.cm^{-3}$) at 30°C.

REFERENCES

[1] D.S. Covert and J. Heintzenberg, Atmos. Environ. **27A**, 2989 (1993).

[2] H. Burtscher et al., in preparation.

[3] V. Lavanchy et al., Atmos. Environ. **33**, 2759 (1999).

DETERMINATION OF THE AMOUNT OF AEROSOL VOLATILIZED IN THE THERMODESORBER AT 280°C BY FITTING ITS SURFACE SIZE DISTRIBUTION

N. Streit, E. Weingartner, U. Baltensperger (PSI), H.W. Gäggeler (Univ. Bern & PSI)

The thermodesorber is an instrument to measure the volatility of the aerosol. In the highest temperature range above 280°C, the volume size distributions are difficult to determine because of interfering coarse mode particles. Fitting the surface size distribution with a log-normal curve proves to be a method to resolve problem.

The thermodesorber is one of the numerous instruments operated during the 1998 PIPAPO field campaign [1]. It measures the volatility of the aerosol. In the highest temperature range above 280°C, the accumulation mode volume size distributions are difficult to determine because of interfering coarse mode particles. To avoid these problems, the aerosol surface concentrations determined by the thermodesorber were fitted with a log-normal size distribution (Figure 1). The log-normal curve can be used to reduce the amount of data and allow for the interconversion between number, surface and volume mean geometric diameters [2], according to a long-known analytical relationship [3]. The surface distribution was preferred for the fit over the other moments for two reasons:

- The number size distribution on the one hand is dominated by the very small channels, where losses in the thermodesorber can lead to uncertainty, and the volume size distribution on the other hand is hampered by the poor counting statistics of the measurement of particles with large diameters (> 500 nm).
- The error propagation is kept at a minimum by re4duction of the number of calculation steps from the fitted moment to the other ones, choosing the so to speak intermediate surface as a starting point.

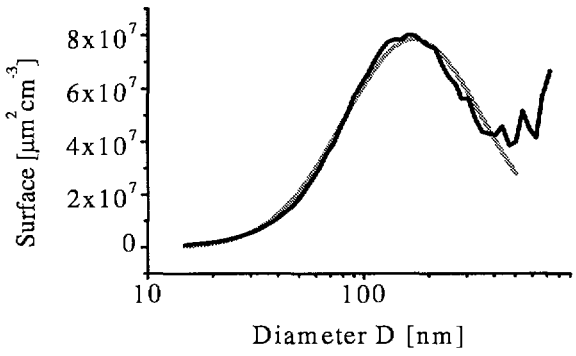

Fig. 1: An example of a surface size distribution of the fraction of the aerosol surviving thermal treatment at 280 °C (black) and the respective log normal fit (gray).

The starting values for the fit were $1 \cdot 10^{11}$ nm^2cm^{-3} for the aerosol surface (S), 200 nm for the surface mean diameter (d_{gS}) and a geometric standard deviation (σ_g) of 2. The exceedingly large aerosol surface was chosen as a starting value since the algorithm used performed better when decreasing the surface value during the fit. Only the diameters below 500 nm were used in the fitting procedure, as the counting statistics are bad for channels with higher diameters, especially in the case of 280°C, where the number concentration generally is lower and thus the influence of geogenic particles reaching into the size range larger. Even though at lower temperatures the results of the fitting procedure did not vary with an upper limitation of the diameter, the same limit of 500 nm was applied to all size distributions for better intercomparability. The fitted values of d_{gS} and σ_g were then used to calculate the number and volume mean diameters (d_{gN}, d_{gV}) according to the following equations [after 2]:

$$d_{gN} = \frac{d_{gS}}{e^{2(\ln \sigma_g)^2}} \qquad d_{gV} = \frac{d_{gS}}{e^{3(\ln \sigma_g)^3}}$$

Using these calculated mean diameters and the fitted parameters including S, the number and volume concentrations (N, V) were calculated:

$$N = \frac{S\left(e^{(\ln \sigma_g)^2}\right)^2}{{d_{gS}}^2}$$

$$V = \frac{4}{3}\pi\left(\frac{d_{gV}}{2}\right)^3 \cdot N \cdot e\left(-\frac{\left(\ln d_{gV} - \ln d_{gN}\right)^2}{2(\ln \sigma_g)^2}\right)$$

As the algorithm was not able to fit all of the size distributions satisfactorily, only those with a geometric standard deviation σ_g below 2 were used. The values of N and V obtained through fitting S and the calculations indicated above were then compared to the values obtained when directly adding up the counts measured in each SMPS channel. The good agreement between the values of number, surface and volume concentrations (slope 1-1.1, R^2 > 0.9) obtained by fitting and addition leads to the conclusion that during most of the time the aerosol indeed did follow a log-normal distribution. The parameters as determined by the fitting can thus be used for further study. On average the volume remaining at 280°C represented 32% of the initial volume at 30 °C.

REFERENCES

[1] N. Streit et al., PSI Annual Report **1998**, I, p.143.

[2] J. Heintzenberg, Properties of the log-normal size distribution, Aerosol Sci. Technol. **21**, 46 (1994).

[3] T. Hatch, S. P. Choate, Statistical description of the size properties of non-uniform particulate substances, J. Franklin Inst. **307**, 369 (1929).

CHARACTERIZATION OF FRESH AND AGED SOOT PARTICLES

E. Weingartner, N. Streit, U. Baltensperger (PSI), H. Saathoff, M. Schnaiter, U. Schurath (FZK, Karlsruhe), U. Kirchner (Ford Reseach Center, Germany), V. Lavanchy (Univ. Bern)

In October 1999, physical and chemical properties of soot particles were studied as a function of aging time in the aerosol chamber facility AIDA.. The aim of this project is to investigate important physical and chemical characteristics of artificially generated soot, of Diesel engine soot, of ammonium sulfate aerosol particles, and of mixtures of them as a function of aging time. Additionally some of these aerosols were coated with organic material from the ozonolysis of α-pinene.

The AIDA facility of the Institute for Meteorology and Climate Research (IMK) at the Research Center Karlsruhe is a thermostated chamber (volume = 84.3 m^3) surrounded by 3 levels of working platforms supporting the instruments for trace gas and aerosol analysis. During the intensive soot campaign the following aerosol parameters were measured: Hygroscopic properties, number concentration, size distribution, carbon and ion mass concentration, morphology, single particle composition, surface functionalities, optical properties (extinction and scattering in the ultraviolet, visible and infrared), photoelectric yield and active surface area. For the experiments the chamber could be filled (within a few minutes) with the aerosol particles and the modification of the aerosol properties was observed for several hours.

In the following, first results of an experiment are presented, where the chamber was filled with diesel soot (total carbon concentration = 103 μg/m^3) and $(NH_4)_2SO_4$ particles (dry mass concentration = 1688 μg/m^3). Figure 1 shows the temporal evolution of the hygroscopic properties of this mixed aerosol measured with the HTDMA at 19°C. In this instrument, dry particles with a diameter of D_{dry} = 190 nm are exposed to high relative humidity (typically 90%) and the new size distribution is measured. In these distributions, the particles can be distinguished according to their hygroscopic behavior: $(NH_4)_2SO_4$ particles are hygroscopic and grow to solution droplets with D ≈ 300 nm. With increasing aging time, the $(NH_4)_2SO_4$ particles become slightly less hygroscopic which can be explained with the incorporation of soot particles. In contrast, soot particles are hydrophobic and "shrink" to D ≈ 185 nm. This is due to capillary condensation which leads to a more compact structure of the aggregates. It can be clearly seen that particles with D_{dry} = 190 nm remain externally mixed even after an aging time ΔT=37 h.

Additional information about the mixing state of the particles can also be gained by measurement of optical properties. With another instrument (DMA-OPC setup), monodisperse particles (D = 400 nm) are selected and fed into an optical particle counter. This instrument classifies individual particles are according to their light scattering behavior which depends on the particle size, morphology and refractive index (depending on chemical composition). Figure 2 shows such optical size spectra of monodisperse aerosol particles. The small optical diameters found for soot particles (D_{opt} ≈ 130 nm) are mainly due to their aggregated structure. $(NH_4)_2SO_4$ particles are characterized by larger optical diameters which is due to their compact structure and refractive index. With this instrument the transformation towards a totally internally mixed aerosol is not observed after an aging time of ΔT = 41 h either.

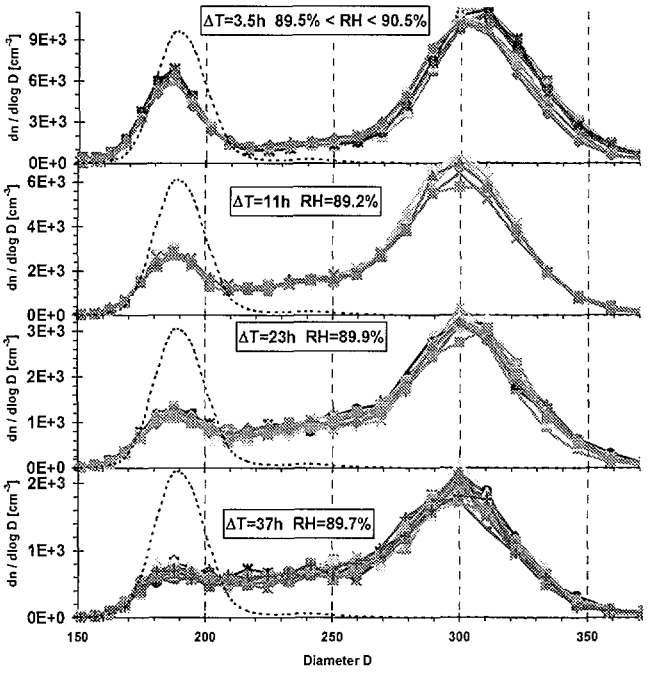

Fig. 1: Temporal evolution of HTDMA size spectra. Dry monodisperse particles (D_{dry} = 190 nm, dashed line, arbitrary concentration units) are exposed to high relative humidity RH (lines with points). Coagulation leads to a decrease of total number concentration with aging time ΔT.

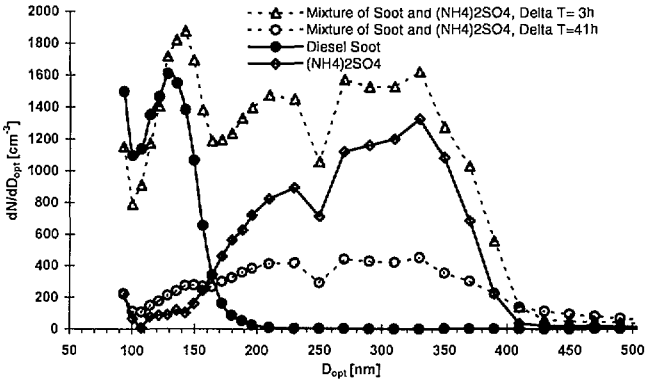

Fig. 2: Optical size distribution of monodisperse (D = 400 nm) particles for different aerosols and aging times. The optical diameter D_{opt} is an equivalent diameter, i.e. the diameter of spherical Latex particles with the same light scattering intensity.

DIESEL AEROSOL SAMPLING METHODOLOGY AND THE MOBILE EMISSION LABORATORY

N. Bukowiecki, U. Baltensperger (PSI), W.F. Watts, D.B. Kittelson (Univ. of Minnesota)

From August to November 1999 exhaust plumes from selected diesel trucks were sampled and analyzed by a mobile emission laboratory under typical traffic conditions on highways in Minnesota (USA). These roadway studies were part of a research project led by the University of Minnesota Center for Diesel Research. The project aims to develop methods allowing aerosol size distributions under road conditions to be properly simulated in laboratory dynamometer tests.

A mobile emission laboratory (MEL) was constructed to compare laboratory diesel emission data obtained during dynamometer tests to data from corresponding roadway situations. The MEL was used during on-highway, truck chase experiments [1]. The diesel exhaust plume of the followed truck was captured and analyzed several seconds after it was emitted from the exhaust stack. In an additional experiment, chase conditions were simulated in a full-scale wind tunnel (Langley, VA). The laboratory was installed in a cargo container that was mounted on a platform hauled by a tractor. During the chase experiments, exhaust plumes were collected with a 3.6 m aluminum boom mounted over the cab of the tractor. The boom brought the sample aerosol to a distribution manifold in the interior of the MEL. A flow-regulating vane pump and a large bypass flow for the instruments maintained constant suction at the inlet of the boom.

1. Bag sampler

A portion of the sampled aerosol could be used to fill a large plastic bag in about 5s to obtain a snapshot of the collected plume for analysis by a Scanning Mobility Particle Sizer (SMPS). One or more size distribution scans were run on each bag sample, each taking about 90 s. Repeated scans showed that the bag sample procedure did not significantly change the size distribution of the collected aerosol.

2. Real-time instruments

The following aerosol and gas instruments sampled from a distribution manifold:

- An Epiphaniometer determined the Fuchs surface of the aerosol [2]. The well characterized measuring method made the Epiphaniometer a standard for the other surface measuring instruments, despite the lower time resolution in comparison to other instruments.
- The Photoelectric Aerosol Sensor (PAS) responds to photoemitting substances on the surface of aerosol particles. Diesel soot has been found to show a large response.
- A Diffusion Charger (DC), consisting of a diffusion charging section combined with a current sensor, measured the surface area concentration of the aerosol. The fast response time (0.5 s) made the instrument useful as fast plume indicator. The combination DC/PAS has been described as a powerful tool for the identification of diesel soot [3].
- The aerosol number concentration was monitored using a Condensation Particle Counter (CPC).
- An Electrostatic Low Pressure Impactor (ELPI) was used to determine particle size distributions based on the aerodynamic aerosol diameter.
- Four gas analyzers measured the CO_2 and NO concentrations in the plume and in the exhaust stack of the chased truck. Concentrations in background air were also measured. These measurements allowed the dilution ratio of the exhaust plume to be determined.

In addition to the instruments listed above, a MOUDI impactor was used during the wind tunnel experiments. The chase experiments covered 3 different speed conditions, 2 different engine types, 2 different load conditions and 2 fuel types. Additionally, frequent background measurements were performed. An example for a roadway chase particle size distribution is depicted in Fig. 1. It is hereby emphasized that no interpretation with respect to engine and fuel type is possible in this context.

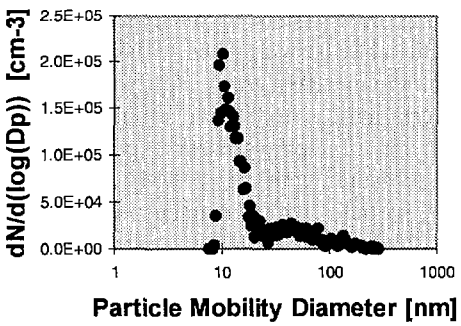

Fig.1: Example of a roadway chase SMPS size distribution.

ACKNOWLEDGEMENTS

Funding support for the project is sponsored by the following U.S. Institutions: Coordinating Research Council (CRC), Department of Energy/National Renewable Energy Laboratory (DOE/NREL). Co-Sponsors are the Engine Manufacturers Association, Southcoast Air Quality Management District, California Air Resources Board, Cummins Inc., Caterpillar Inc. and Volvo Inc. The project will continue in 2000 with additional experiments and publication of results.

REFERENCES

[1] http://www.me.umn.edu/centers/cdr/Proj_CRC.html

[2] H. W. Gäggeler et al., The Epiphaniometer, a new device for continuous aerosol monitoring, J. Aerosol Sci. **20**, 557 (1989).

[3] U. Matter et al., Dynamic field measurements of submicron particles from diesel engines, Environ. Sci. Technol. **33**, 1946 (1999).

ATMOSPHERIC CONCENTRATION OF ^{7}Be AT THE JUNGFRAUJOCH

S. Hübener (Univ. Bern), L. Tobler (PSI), H.W. Gäggeler (Univ. Bern & PSI)

The atmospheric concentration of ^{7}Be at Jungfraujoch has been measured routinely since April 1996. The data are presented and compared with ^{7}Be data from other stations.

The cosmogenic radionuclide ^{7}Be ($T_{1/2}$ = 53d) is frequently used as a tracer for studying atmospheric processes. Within the EU projects VOTALP I and II, ^{7}Be has been measured routinely at Jungfraujoch (3580 m a.s.l.) since April 1996 with a time resolution of 48 h. Particle bound ^{7}Be was collected on glass fibre filters using a HIVOL air sampler and determined via its γ-line at 478 keV. Fig. 1 shows averaged monthly arithmetic mean values of the atmospheric concentration of ^{7}Be at Jungfraujoch (JFJ) from April 1996 to August 1999. Obviously, only a weak seasonal variation is observed with slightly enhanced values in summer and lower values in early winter. A similar weak seasonal dependence is also found for the nearby low altitude site Mühleberg at the Swiss Plateau (KKM data in Fig. 1, taken from [1]). The annual variation of the atmospheric concentration of ^{7}Be at the Jungfraujoch is much less pronounced compared to those of ^{210}Pb, ^{212}Pb, ^{214}Pb, or the Epiphaniometer (aerosol surface) signal [2] due to different source areas and transport processes.

At the Jungfraujoch station the atmospheric concentration of ^{7}Be is higher than at the mountain stations Zugspitze (2960 m a.s.l.) and Sonnblick (3106 m a.s.l.). The mean activity concentrations for the time period July 1996 to June 1997 for Jungfraujoch (JFJ), Zugspitze (ZUG), Sonnblick (SBK), and Mühleberg (KKM) are 7.40, 4.60, 5.03, and 2.02 mBqm^{-3}, respectively (Fig. 2).

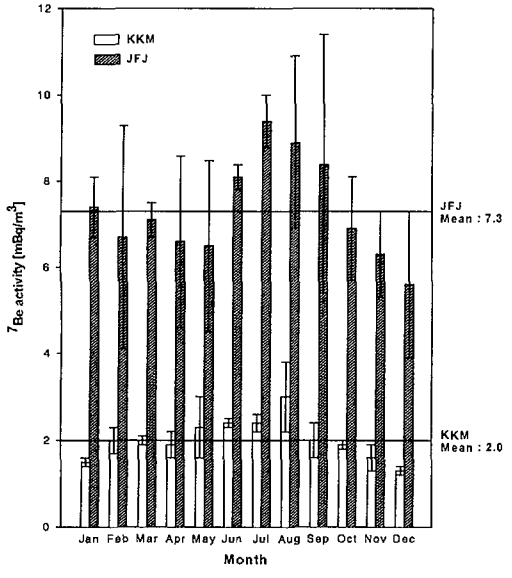

Fig. 1: Average monthly mean activity concentrations for ^{7}Be at Jungfraujoch for the time period April 1996 to August 1999 (JFJ) and at the nuclear power station Mühleberg for the time period January 1996 to December 1998 (KKM) [1].

^{7}Be concentrations at higher altitudes over Switzerland have been measured in 24 air filter samples collected in 1973 by aircraft in the range of ± 2000 m relative to the height of the tropopause (11200 ± 950 m a.s.l.) [3]. Across the tropopause a steep ^{7}Be concentration gradient was observed. The ^{7}Be concentration varied in the region of ± 500 m relative to the height of the tropopause by one order of magnitude. As seen from Fig. 2, the absolute ^{7}Be concentrations AC1 and AC2 measured in two samples collected at altitudes of 8100 and 9200 m a.s.l. fit quite well to the linear dependency of the activity concentration as a function of altitude.

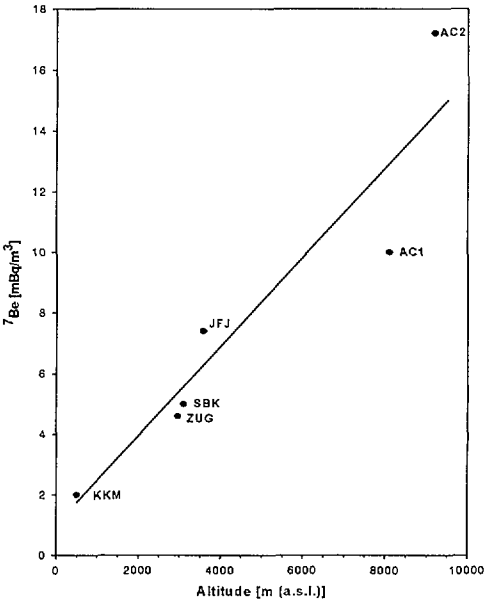

Fig. 2: Average annual ^{7}Be activity concentrations for Mühleberg (KKM), Zugspitze (ZUG), Sonnblick (SBK), and Jungfraujoch (JFJ) as well as single data from air craft measurements (AC1 and AC2) as a function of altitude. The linear fit is from the ground-based data KKM, ZUG, SBK, and JFJ.

ACKNOWLEDGMENT

This study was part of the EU research projects VOTALP I and II and was funded by the Bundesamt für Bildung und Wissenschaft (BBW) of Switzerland

REFERENCES

[1] H. Surbeck, G. Ferreri, Annual Reports Environmental Radioactivity and Radiation Exposure in Switzerland 1996, 1997, and 1998, Fribourg 1997, 1998, and 1999, B4.1.

[2] H.W. Gäggeler et al., Atmospheric Environment **29**, 607 (1995).

[3] P. Winiger et al., Tellus **28**, 434 (1976).

AEROSOL CONCENTRATIONS AT THE CERRO TAPADO, CHILE

M. Schwikowski, D.T. Jost (PSI), H.W. Gäggeler (Univ. Bern & PSI), P. Ginot (Univ. Bern)

Aerosol concentrations were measured near the base camp of the Cerro Tapado ice core drilling project. The concentrations showed pronounced diurnal fluctuations due to vertical transport. Aerosol concentrations are an important factor in the interpretation of the climatic records contained in the ice of the glacier.

In 1998 a ice core drilling project on Cerro Tapado (Chile) was started in order to study the climatic records stored in the ice of the glacier. For the interpretation of ice core records it is important to understand how the aerosol particles, which are found in the ice, reach the glacier site. For this purpose, an epiphaniometer [1] was installed in March 1998 at about 4000 m asl close to the base camp of the drilling project within sight of the glacier. In February 1999 [2] an ice core was drilled at this glacier down to the bedrock.

The epiphaniometer monitors continuously the aerosol surface concentration and is most sensitive for particles in the accumulation mode (diameter d: $0.1 < d < 1$ μm). Assuming a constant size distribution, the epiphaniometer signal is proportional to the bulk aerosol concentration for particles with diameters smaller than 1 μm. The instrument operates remotely, powered by solar energy and data are stored as hourly averages.

The first data set could be retrieved from the epiphaniometer in the February 1999 drilling campaign. Unfortunately, due to an instrument failure, measurements stopped in June 1998, and therefore the data set is restricted to the time period of 28 March to 7 June 1998. The aerosol concentrations during this period are illustrated in Fig. 1. They show distinct diurnal variations with a concentration peak in the late afternoon. This is a typical feature of high-mountain sites, where thermally driven convective valley wind system causes vertical transport of aerosol particle rich air from the valley floor up to the mountain. This has been studied in great detail at different high-altitude sites in the European Alps [3]. The effects of the valley wind system are also obvious in the fluctuation of the wind speed and direction measured by an automatic climate station installed at Tapado base camp immediately besides the epiphaniometer (Ch. Kull, private communication). The pronounced diurnal variation is even more evident when looking at monthly averages of the aerosol concentration for each 1-hour interval of the day (Fig. 2). The concentration peak occurred between 16:00 and 24:00 which is consistent with the observations in the Alps [3]. However, one has to keep in mind that the data sets of the months March and June are incomplete (3 and 7 days).

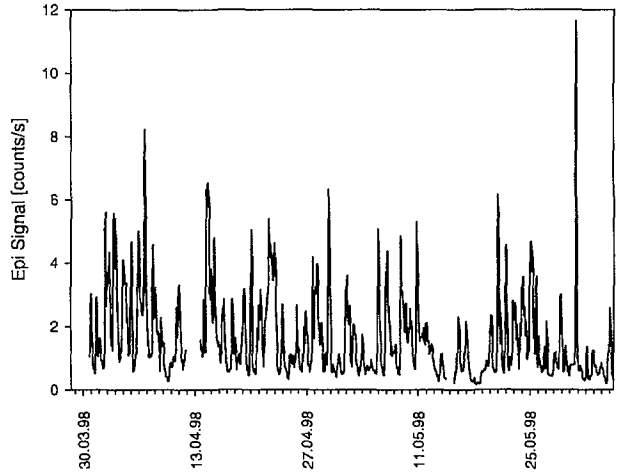

Fig. 1: Hourly values of the aerosol concentration at Tapado base camp (4000 m asl).

During the investigated time period monthly median values decreased steadily (March: 1.6, April: 1.3, May: 0.9, June: 0.8 counts s^{-1}), reflecting the transition from austral autumn to winter. In winter the frequent cloud cover hinders the full development of the valley wind system. The monthly medians are comparable to those observed during autumn and winter at a high-mountain site in the Alps (Colle Gnifetti, 4450 m asl) [4]. The Epiphaniometer has been repaired and the next data set should provide a measuring period of about one year covering a full winter/summer cycle.

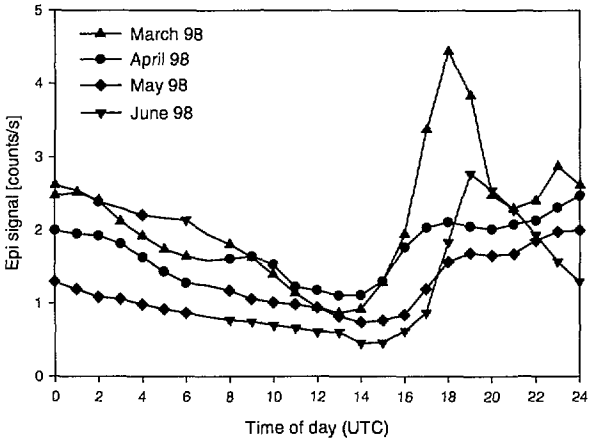

Fig. 2: Monthly averages of the aerosol concentration for each 1-hour interval of the day.

ACKNOWLEDGEMENT

This work was supported by the Swiss National Science Foundation, Project # 21-050854.97.

REFERENCES

[1] H.W. Gäggeler et al., J. Aerosol Sci. **20**, 557 (1989).
[2] P. Ginot et al., this Annual Report.
[3] U. Baltensperger et al., J. Geophys. Res. **102**, 19707 (1997).
[4] M. Lugauer et al., Tellus **50B**, 76 (1998).

ENVIRONMENTAL RECORDS FROM ANDEAN GLACIERS INFLUENCED BY THE TROPICAL AND THE EXTRA-TROPICAL CIRCULATION REGIMES

P. Ginot (Univ. Bern), H.W. Gäggeler (Univ. Bern & PSI), Ch. Kull (Univ. Bern), B. Pouyaud (IRD La Paz), U. Schotterer (Univ. Bern & PSI), M. Schwikowski (PSI), F. Stampfli (FS Inventor), B. Zweifel (VAW)

Ice cores were drilled on glaciers representing extra-tropical (Cerro Tapado, Chile) and tropical conditions (Illimani, Bolivia) in order to reconstruct past environmental conditions of the last centuries.

The cold ice caps of the highest peaks of the Andes represent natural archives of past environmental conditions [1]. The "South American Arid Diagonal" is the transition zone between the tropical circulation (continental/Atlantic moisture) and the extra-tropical (Pacific moisture) Westerly pattern. The glaciers located near this zone are most sensitive to climatic changes in the Southern American continent. A reconstruction of the last climatic variations should allow to better understand and predict future changes, particularly those dependent on the phenomenon El Niño which seem to have occurred more frequently and more strongly during the last years. Moreover, the locality of the glacier sites should allow to observe the effects of anthropogenic pollution in these areas.

The two precipitation regimes have different impacts in the two areas. They are opposite in wet and dry seasons (rain season in Bolivia during the southern summer, in Chile during the winter). In addition, the impact of the El Niño phenomenon is different, leading to more precipitation in the area influenced by the Westerlies where the Cerro Tapado is located and greater dryness in the tropical area of Illimani.

One year after our successful shallow core drilling [2] at the top of Cerro Tapado (5536m, 30°08'S, 69°55'W, Chile), we performed a deep drilling to bedrock in February 1999. For that purpose, we used a new portable 3-inch electro-mechanical drill. In four working days, we drilled a 36m long core to the rock and a 17m parallel core. This successful campaign enabled us to perform another major drilling campaign in June on Illimani (6432m, 16°39'S, 67°47'W, Bolivia), where we extracted a 138m long core covering the entire glacier thickness.

The ice core record of Cerro Tapado is characteristic of a rather dry area. It is not formed by a continuous annual precipitation, but only a short period of precipitation intersected by long dry periods. In order to understand the effects of such dry periods on the chemistry and stable isotopes records, process studies were performed parallel to the drilling. Additionally, a meteorological station recorded climatic data for the experimental period and "lysimeters" were operated to directly measure the sublimation.

The effects of sublimation and dry deposition on the chemistry records could be observed by analysis of a 30 cm snow pit. The topmost 4cm showed extremely high concentrations compared to deeper samples (Fig. 1). By collecting samples of 1cm surface snow twice a day from a prepared surface at 10 cm depth over a period of four days, we could study in more detail the alteration of the chemical and isotopic composition of the surface (Fig. 2).

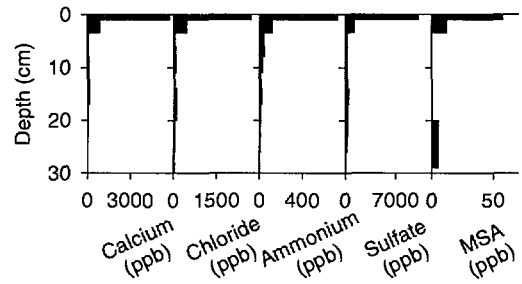

Fig. 1: Concentration profiles from a 30cm snow pit on Cerro Tapado.

The evolution of the concentrations in relation to the initial values (expressed as concentration ratios in Fig. 2) revealed three groups of chemical species. Group 1 (ammonium, acetate, formate and MSA) showed constant concentration and represents reversibly deposited species. Group 2 (chloride, nitrate, sulfate, sodium and potassium) is characterised by a medium increase due to sublimation (factor 2-3, proportional to sublimation of water). The species are assumed to be irreversibly deposited. Group 3 (calcium, fluoride and magnesium) showed a strong increase (factor 3-5) which is explained by the combined effects of H_2O sublimation and dry deposition of coarse particles originating from surrounding volcanic rocks. Since the signature of these processes is recorded in the ice core, the regional climate history can be reconstructed by identifying wet and dry periods.

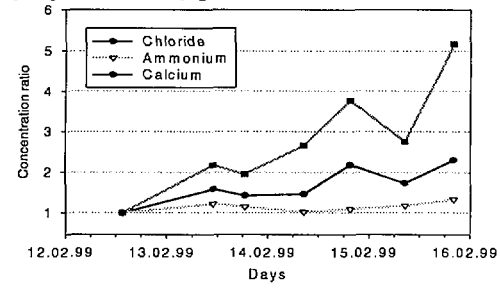

Fig. 2: Evolution of chemical concentrations expressed as ratios on the initial values.

ACKNOWLEDGMENT

The work was supported by the Swiss National Science Foundation, Project 2100-050854.9.

REFERENCES

[1] L.G. Thompson et al. Science **282**, 1858 (1998).

[2] P. Ginot et al., PSI Annual Report (1998) p.32.

PALAEO ATMOSPHERIC CHEMISTRY AND CLIMATE RECORD FROM CERRO TAPADO ICE CORE

P. Ginot (Univ. Bern), H.W. Gäggeler (Univ. Bern & PSI), V. Furrer (PSI), U. Schotterer (Univ. Bern & PSI), M. Schwikowski (PSI), W. Stichler (GSF Neuherberg), B. Pouyaud, R. Gallaire (IRD), A. Rivera (Univ. de Chile)

A 36m ice core from Cerro Tapado was analysed for concentrations of major ionic species and for stable isotope composition. ^{210}Pb dating revealed that the ice core covers a period of about one century. Minimum values of ^{210}Pb initial activity and δ^2H were identified as fingerprint signature of El Niño events.

In February 1999, we performed a deep drilling (36m to bedrock) on top of Cerro Tapado (5536m, 30°08'S, 69°55'W, Chile) [1]. The recovered ice cores were transported to PSI in frozen condition.

The ice core segments were photographed, measured and weighed before cutting in a cold room. Ice segments were cut with various resolutions for the different analyses. Samples of 70cm length were used to determine activities of tritium and ^{210}Pb. 1.5cm sections of the inner, uncontaminated part of the ice core were used for chemical analysis of major ions (Na^+, K^+, NH_4^+, Ca^+, Mg^{2+}, NO_3^-, Cl^-, SO_4^{2-}) by ionic chromatography. In 1.5cm samples from the outer part stable isotopes ratios ($\delta^{18}O$, δ^2H, Deuterium-Excess) were determined by mass spectrometry.

The dating of the ice core was performed using the measured activity of the naturally produced radioactive isotope ^{210}Pb which decays with a half life of 22.3 years [2]. A linear regression fit of the ^{210}Pb activities reveals an age of the deepest ice of about 100 years (Fig. 1). However, with this fit the thinning of the ice is not taken into account. By using a simple 1D ice flow model a more realistic depth-age relationship was obtained (Fig. 1). This agrees well with the tritium maximum from thermonuclear weapon tests (Fig. 2) in the southern hemisphere. With this dating, the annual accumulation on the glacier could be reconstructed. The variations in annual accumulation are in agreement with precipitation recorded at a near-by weather station (La Laguna) and correlate well with Sea Surface Temperature Anomalies (SST) associated with the phenomenon El Niño.

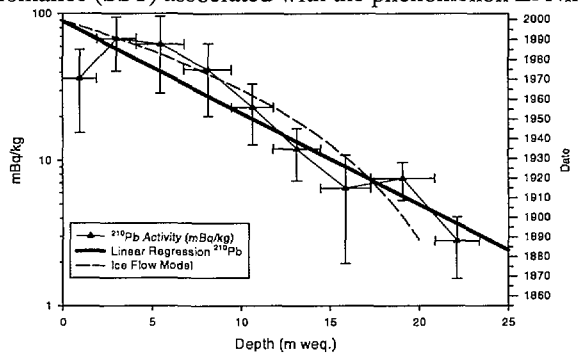

Fig. 1: ^{210}Pb activities versus depth of the ice core.

The ^{210}Pb activities normalized to t=0 show distinct fluctuations which correlate well with the variations of δ^2H (Fig. 2). The minimum values of ^{210}Pb and δ^2H were observed in years with major El Niño events: 1997/98, 1992, 1982/83, 1972/73, 1940/41, 1932, 1925/26, 1917, 1891. It is assumed that El Niño events, characterised in this area by higher precipitation rates, lead to a dilution of the ^{210}Pb activity. In addition, the low ^{210}Pb activity might reflect the Pacific ocean as the source region of the air masses. Over oceans, the atmospheric ^{210}Pb concentrations are lower than over continents. The more negative δ^2H and $\delta^{18}O$ values may be due to a significant rainout of the atmospheric moisture along the source-glacier trajectory. Hence, the low ^{210}Pb activity and the more negative δ^2H seem to be useful indicators to identify El Niño periods.

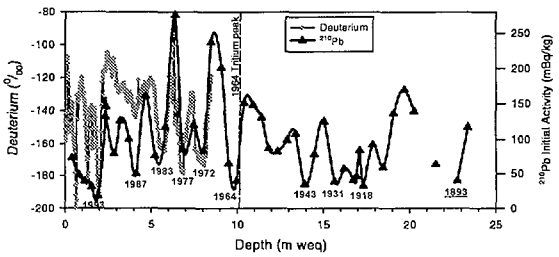

Fig. 2: δ^2H and initial ^{210}Pb activity profiles along the ice core. Dates calculated from ^{210}Pb decay fitted by ice flow model or linear regression (underlined).

In agreement with results from our field experiments [1], we observed distinct effects from sublimation and dry deposition in the chemical and isotope records. Strong sublimation is marked by an enrichment of the heavy water isotopes (^{18}O and ^2H) and a peak in the concentration of chemical species (NH_4^+, NO_3^-, Na^+, Cl^-). Dry deposition resulted in horizons located just above the levels marked by sublimation, characterised by high concentrations in ionic species contained in the surrounding volcanic rocks (Ca^+, Mg^{2+}, SO_4^{2-}, K^+). The variation of the concentrations of chemical species in the core therefore allows to identify dry and wet periods during the last century.

ACKNOWLEDGMENT

This work was supported by the Swiss National Science Foundation. The help in the field of the Chilean Army and the storing of the ice by the AZM is highly acknowledged.

REFERENCES

[1] P. Ginot et al., this Annual Report.

[2] H.W. Gäggeler et al., J. of Glaciology **29**, 165 (1983).

ICE THICKNESS MEASUREMENTS ON THE GLACIER OF CERRO TAPADO, NORTE CHICO, CHILE

A. Rivera, A. Giannini, J. Quinteros (Universidad de Chile, Santiago), M. Schwikowski (PSI)

Detailed measurements of the ice thickness on the ice cap of Cerro Tapado, Chile, were performed indicating a maximum ice thickness of 33 m at the drilling site of the bedrock core.

In February 1999, during the ice core drilling campaign on top of Cerro Tapado (5536m, 30°08'S, 69°55'W, Chile) [1], detailed ice thickness measurements were carried out with a portable radio-echo sounding system. Three radar profiles were measured (Figure 1) with a maximum ice thickness of 42 m around to stake 4. Near the ice core drilling site the ice thickness reaches 33 m. This corroborates earlier results from the first radar survey conducted during the exploratory drilling of shallow firn cores in 1998 [2].

With the aim of obtaining subglacial topography profiles, a ground-based digital impulse radar system was used. This radar system consisted of a transmitter developed by the University of Bristol, UK, with a maximum output voltage of 670 V_{pp}. Furthermore, the antennas consisted of resistively-loaded dipoles, with a 5 m antennas length, which result in a central frequency of 10 MHz. The receiver is composed by a digital FLUKE oscilloscope connected to the receiving antennas, transferring the data through a serial port to a portable PC, were they were stored in the hard disk.

The complete system was mounted on fibreglass fishing rods, with a separation of 10 m between the receiver and the transmitter. The whole system was carried by two persons who walked on the surface of the glacier measuring one point each 5 seconds.

In order to obtain a geographic position for each thickness measurements, a topographic quality GPS receiver was used to fix the positions of the stakes. By means of a differential correction methods, GPS data was obtained simultaneously at base camp, the horizontal precision attained was 5 m.

The ice thickness data was georeferenced to the regular cartography of the IGM (Figure 1), which was compiled and digitised in our laboratory, in order to produce the final chart of the study area.

ACKNOWLEDGEMENTS

Appreciation is expressed to Dirección General de Aguas and to the Chilean Army, for the support of the field work. Project Fondecyt 1980293 supported the Chilean authors. The field campaign was supported by the Swiss National Science Foundation.

REFERENCES

[1] P. Ginot et al., this Annual Report.

[2] P. Ginot et al., PSI Annual Report 1998, p. 33.

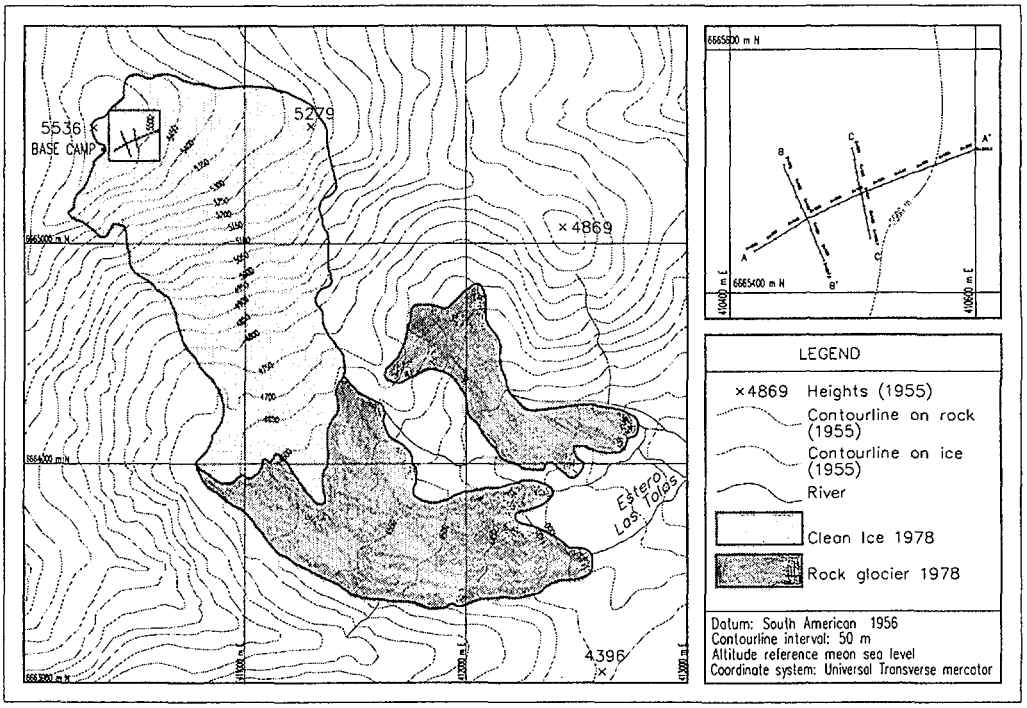

Fig. 1: Topography of the glacier on Cerro Tapado along with the location of the radar profiles.

ENGLACIAL ICE TEMPERATURES AT ILLIMANI

B. Zweifel, M. Funk (VAW), H.W. Gäggeler (Univ. Bern & PSI), P. Ribstein (IRD), M. Schwikowski (PSI)

In the frame of a drilling campaign to recover an ice core from Illimani (Bolivia) for palaeo atmospheric and climate studies, englacial temperatures were measured as part of the glaciological studies to characterise the glacier.

Firn temperature measurements on Illimani were performed in the 138m deep borehole drilled in June 1999 by a joint expedition PSI/IRD. We used thermistors of negative temperature coefficient (NTC) type Fenwal 135-103FAG-J01, which were solded to individual two conductor cables. All thermistors were calibrated at 13 reference temperatures in the range -20 to 0 °C. The calibration was performed with connected cables in exactly the same configuration and with the digital multimeter used in the field. The accuracy of measured temperatures variies between 70 and 118 mK over the temperature range -10 to -5 °C. Thermistors were installed in the first borehole immediately after completion of the drilling on June 4th 1999. It is not clear if the borehole temperatures reached an undisturbed state at that time. However, the three readings taken during the following 12 hours didn't vary more than 0.1 kW indicating more or less stable thermal conditions in the borehole.

A striking bend of the temperature profile to warmer temperatures is clearly visible in the upper 70m of the temperature profile (Fig.). Such a feature has recently also been observed on Colle Gnifetti [1-3] (Haeberli and Funk, 1991 ; Luthi, 1999 ; Luthi and Funk, 1999) and some decades ago on White Glacier (Axel Heiberg, Canadian Arctic) [4] (Blatter, 1987).

The heat flux at the glacier bed can be calculated from the measured temperature gradient using a density dependent thermal conductivity. For the Illimani glacier bed we obtain a heat flux of 25 mW m^{-2}, which is rather a low value if compared with the results obtained at Colle Gnifetti where it ranges between 35-40 mW m^{-2}.

The englacial temperatures are interpreted by using the heat diffusion-advection equation [5]

$$\rho C (\delta T/\delta t + v \nabla T) = \nabla (k \nabla T) \qquad (1)$$

with ρ being the density, C the specific heat capacity, v the velocity field, k the density dependent thermal conductivity and T the temperature. The dissipative heat production is not considered here. Because the density profile at Illimani is not yet available, we have used for the model calculations the measured profile at Colle Gnifetti [2]. At the borehole location, the horizontal velocity is expected to be very low and is therefore neglected. For this reason we can solve equation (1) only for the case of vertical diffusion and advection. The basal boundary condition is the measured temperature gradient with a value of -0.012 Km^{-1}. The vertical velocity field is assumed to vary linearly with depth. At the glacier surface the vertical velocity corresponds to the measured mean accumulation rate (a steady state geometry is assumed) of 0.5 ma^{-1} (0.43-0.52 ma^{-1}) and at the bed it is set to zero. The steady state temperature distribution is then calculated with a prescribed surface temperature in order to match the measured temperature profile in the lower part (Fig. 1). The corresponding surface temperature is -9.8 °C. The difference between the measured and calculated steady state temperature profile clearly indicates a transient situation. Therefore we did run a transient model by increasing linearly the surface temperature by 2.9 K over a time period of 50 years (Fig. 1). Although the agreement between model results and measurements is not perfect, it seems that the temperature profile exhibits a strong warming trend of almost 3 K over the last five decades. This warming trend, if real, is much more pronounced than recently observed at Colle Gnifetti [2], where an increase of surface temperature by 1.2 K over the last two decades was found. This observed warming trend at Illimani must be scrutinised more in detail. It can first be compared with air temperature records at a nearby climate station.

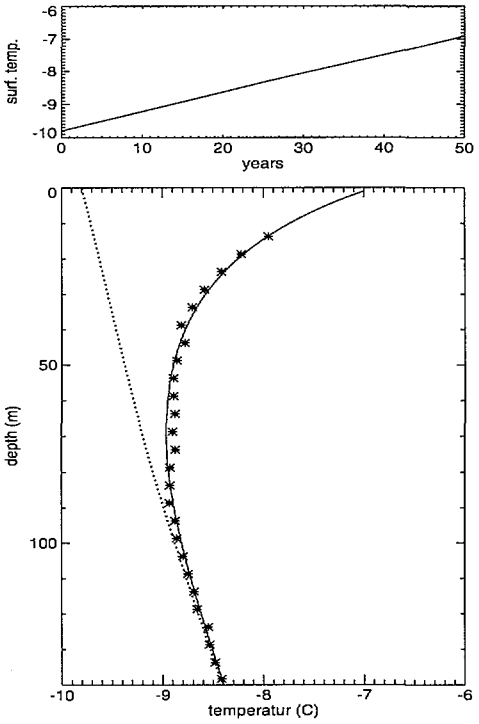

Fig. 1: Measured and modelled firn temperatures at Illimani (dashed line: steady state; full line: transient state after 50 years warming according to the upper figure).

REFERENCES

[1] W. Haeberli, M. Funk, J. Glaciol. **37**, 37 (1991).
[2] M. Lüthi, Ph.D. Thesis, ETH Zürich (1999).
[3] M. Lüthi, M. Funk, Annals of Glaciol., in press.
[4] H. Blatter, J. Glaciol. **33**, 200 (1987).
[5] K. Hutter, Theoretical glaciology (1983).

GAS MEASUREMENTS OF ENTRAPPED AIR IN ICE CORES FROM COLLE GNIFETTI, SWITZERLAND

A. Dällenbach, C. Lang (Univ. Bern), U. Schotterer, (Univ. Bern & PSI), Th. Stocker (Univ. Bern)

Gas measurements from polar ice cores have reconstructed past atmospheric composition. Since they offer also unique dating possibilities, measurements of gas content, methane, and isotopic and elemental ratios were applied to ice cores from Colle Gnifetti. A 1500-year time scale could be established and preliminary results indicate that the lowermost part might be 6000 – 8000 years old.

Several ice cores were drilled on Colle Gnifetti (4450m) at the Swiss-Italian border during the last 24 years. In 1982, the core RC reached bedrock at 124m, BC stopped at 109m. In 1995, both cores KCS and KCH reached bedrock at 100 and 65 m respectively. Since seasonal layering is disturbed, the upper part was dated by other methods like ^{3}H, ^{210}Pb, known volcanic eruptions, and Saharan dust falls. For deriving an age/depth relation over the whole core length, ice flow modelling was applied too. To support the models by direct dating we finally started the gas measurements.

Since CH_4 shows significant global variations during the last centuries, the Holocene, and the ice age, in principal any suitable CH_4-record from cold glaciers like Colle Gnifetti can be dated relative to the well-dated methane record from polar sites [1]. We measured CH_4 on 33 depth levels between 39 and 100 m at the BC-core, on 15 depth levels between 39 and 100 m at the KCS-core and on 7 depth levels between 39 and 60 m at the KCH-core. For isotopic and elemental ratios additional measurements were performed in the lowermost part of the BC and RC cores. In all samples the total gas content was measured too. Several considerations had to be taken into account to determine the age of the individual data points:

The CH_4 concentration in the Alps is about 1% lower than in Greenland [2] and the difference between gas-age and ice-age is only about 44 years in all cores (close-off depth of the air bubbles was derived from the total gas content). Furthermore, our knowledge about the occlusion process is limited [3]. In all the cores the CH_4 concentrations vary from 1350 to 680 ppbv. Therefore, the gas age in the ice is about 1500 years in a depth of about 5m (KCH, KCS) and 20m respectively (BC) above bedrock.

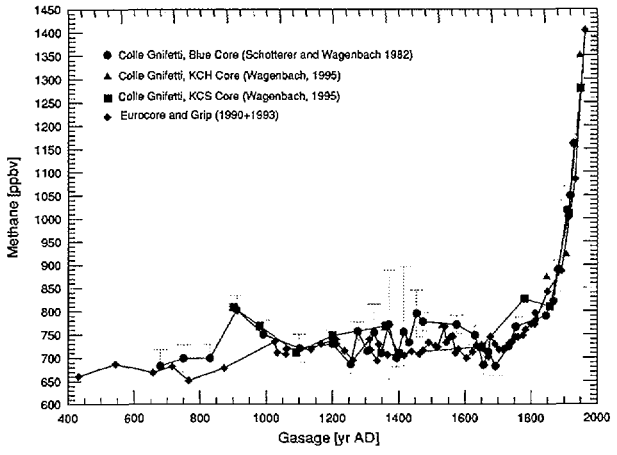

In the deepest five meters we measured very high CH_4 values in KCH, KCS, and RC together with a decrease in total gas content. This may be probably due to a disturbing influence from the bedrock [3]. Also the sample quality (micro-fissures) may play a role as well as a smaller pore volume at close off due to lower temperatures and reduced accumulation at certain times during build-up of the glacier.

More information can be expected from the isotopic and elemental ratios ($\delta^{15}N$, $\delta^{18}O$, $\delta Ar/N_2$ and $\delta O_2/N_2$). Two samples from BC and 12 samples from RC in the lowermost part were analysed. Beside the mentioned tendency of gas content depletion, the ^{18}O-record in the occluded air bubbles shows also a tendency to lower values towards the bedrock. By comparing with other $\delta^{18}O$ records [3,4] this may be assigned to an age of 6000 to 8000 years because this was the only time when negative values of about -0.3 ‰ where reached. Since the measured values are far lower than the ice age values of about 1.2 ‰, an origin of the samples from the last ice age can be excluded. However, single extreme values in the $\delta^{18}O$ record (115.2m, 116.8m, 118.2m) are difficult to explain: unexpected high $\delta Ar/N_2$ values and lower $\delta O_2/N_2$ values cast some doubts whether these excursions are of atmospheric origin or due to changes in the ice. Especially oxygen consuming bio-chemical processes could shift $\delta^{18}O$ towards higher values [5]. For final clarification, further investigations are necessary.

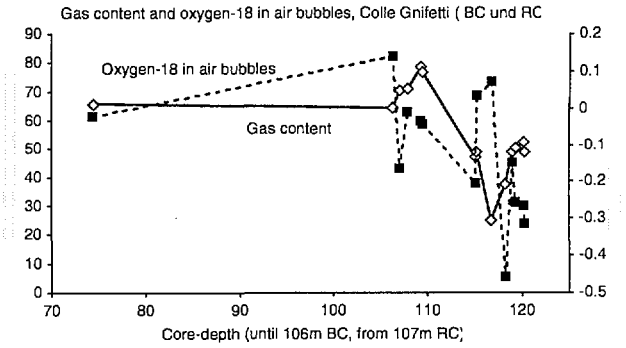

REFERENCES

[1] J. Chappellaz,et al., Journal of Geophysical Research **102**, 15987 (1997).

[2] L.P. Steele et al., Journal of Atmospheric Chemistry **5**, 125 (1987).

[3] T. Blunier, Proc. Glaciers from the Alps, PSI, 57 (1996).

[4] A. Fuchs and M. Leuenberger, Geophys. Res. Lett., **23**, 1049 (1996).

[5] T. Sowers and M. Bender, Science **269**, 210 (1995).

1000 YEAR PALAEO RECORD OF THE EUROPEAN ATMOSPHERE FROM AN ALPINE ICE CORE (COLLE GNIFETTI, SWISS ALPS)

M. Schwikowski, S. Brütsch (PSI), H.W. Gäggeler, U. Schotterer (Univ. Bern & PSI), A. Dällenbach (Univ. Bern)

106 m ice core from Colle Gnifetti representing a time period of more than 1000 years were analysed and dated. The calcium record indicates so far unexplained enhanced concentrations of atmospheric mineral dust before 1400A.D.

In order to understand the atmospheric cycling of species with short atmospheric life-times such as aerosol particles, palaeo atmospheric data from mid-latitudes regions are highly desired. In Europe such data can be reconstructed from Alpine ice cores which has already been shown on a century time scale by various studies [1, 2]. In this study we analysed 106 m of an ice core drilled on the Colle Gnifetti (4450 m asl, Swiss Alps) where the total glacier thickness is about 124 m. This glacier site is characterised by a low net snow accumulation of about 30 cm water equivalent per year [1]. With the given glacier thickness, this allows to reconstruct glaciochemical records covering more than 1000 years.

The dating of the ice core was performed by using stratigraphic horizons as described in [1]. For ice older than 230 years (depth > 70 m) the identification of such horizons becomes increasingly difficult. In addition, the historical records are less complete and reliable. Therefore other dating methods have to be used instead. One possibility is the determination of the methane concentration by analysing air entrapped in bubbles in the ice [3]. The obtained record can then be related to the methane concentrations reconstructed from well dated polar ice cores showing significant variations in the Holocene. The resulting dating points are in good agreement with the age-depth relationship predicted by a three dimensional ice flow model [4] revealing that the analysed 106 m cover a time period of about 1300 years (Fig 1).

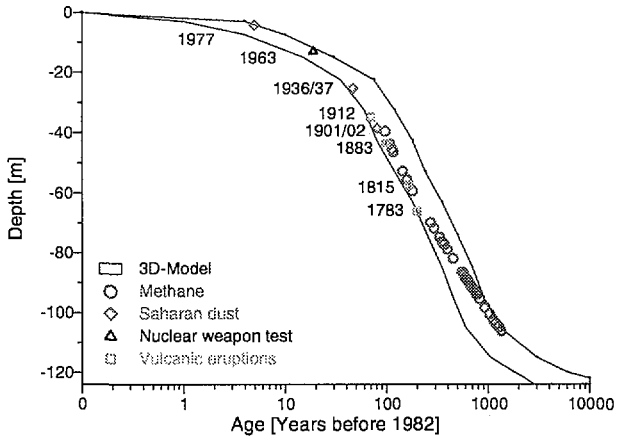

Fig. 1: Age-depth relationship for the Colle Gnifetti ice core established by stratigraphic markers, methane concentrations and 3D ice flow modelling.

From the dated core 100 m were analysed by ion chromatography with 2 to 5 cm resolution in order to determine concentrations of main ionic species. In Fig. 2 the resulting calcium record is presented which indicates enhanced concentrations of mineral dust in the atmosphere before the onset of the little ice age, i.e. before about 1450. In addition, the record of ex-sulphate is given. Ex-sulphate was calculated by applying the following formula: $[ex\text{-}SO_4^{2-}] = [SO_4^{2-}] - 0.12 \cdot [Na^+] - 0.175 \cdot [nssCa^{2+}]$ (concentrations in $\mu eq\ l^{-1}$) which corrects the sulphate concentration for the sea-salt and the mineral dust contribution [5]. This correction is based on a correlation between $nssSO_4^{2-}$ and $nssCa^{2+}$ observed for the period 1756-1870 [5]. Ex-sulphate is assumed to originate from SO_2 oxidation in the atmosphere and increased steadily from 940 to 1975. However, in the period 940 to 1430 many negative values are observed, indicating that the $nssSO_4^{2-}$ to $nssCa^{2+}$ concentration ratio applied for correction does overestimate the mineral dust contribution to the sulphate concentration. This suggests that heterogeneous reactions of SO_2 on atmospheric mineral dust particles might have increased the $nssSO_4^{2-}$ to $nssCa^{2+}$ ratio.

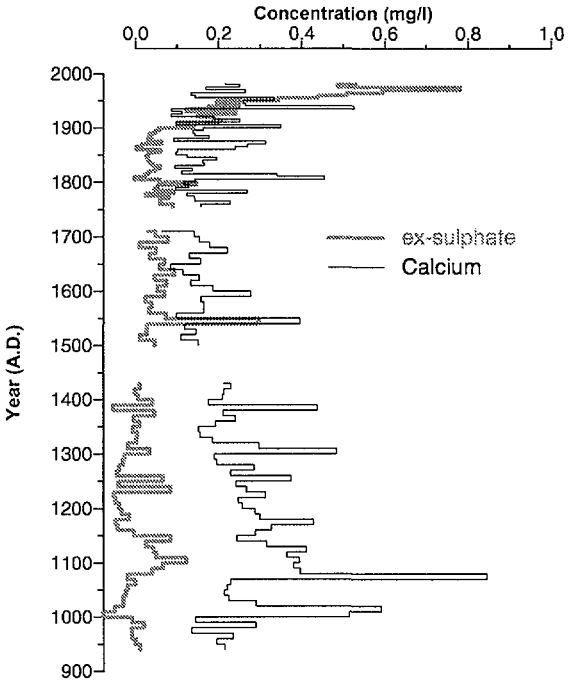

Fig. 2: Records of 5-year (1755-1980) and 10-year (940-1710) averages of calcium and ex-sulphate concentrations

REFERENCES

[1] A. Döscher et al., Water, Air and Soil Pollution **85**, 603 (1995).

[2] V.M.H. Lavanchy et al., J. Geophys. Res. **104**, 21227 (1999).

[3] T. Blunier, Proc. Glaciers from the Alps, PSI, 57 (1996).

[4] S. Wagner, Ph.D. thesis, ETH Zurich, 1996.

[5] M. Schwikowski et al., Tellus **51B**, 938 (1999).

HISTORY OF LEAD CONCENTRATIONS AND LEAD ISOTOPE RATIOS RECONSTRUCTED FROM AN ALPINE ICE CORE

L. Tobler, M. Schwikowski (PSI), T. Döring, H.W. Gäggeler, U. Schotterer (Univ. Bern & PSI)

Analysis of lead concentrations and isotopic ratios by inductively coupled plasma mass spectrometry (ICP-MS) were continued on the 109 m long ice core drilled at Colle Gnifetti (Monte Rosa) in 1982. Historical evolution of lead concentrations and ratios in this palaeorecord are shown.

High-altitude cold alpine glaciers can be used as archives for air-borne species emitted over Europe. They provide deep insight into historical changes in atmospheric heavy metal concentrations. A 109 m long ice core, drilled at the high-altitude glacier saddle Colle Gniffeti (4450 m asl., Monte Rosa massif) in 1982, was analysed for metal concentrations and lead isotopic ratios by ICP-MS [1,2].

Ice core sections of varying lengths from 15 to 35 cm were manually decontaminated in a class 100 clean bench located in a cold-storage chamber (-20°C). The outer layers of the core sections were removed by chiselling, in order to eliminate contaminations from the contact with the drill and the storage polyethylene bags. Only the central parts of the core sections were then used for chemical analyses. Lead concentrations and lead isotopic ratios were determined by a double focusing ICP-MS (ELEMENT, Finnigan MAT). The high sensitivity and accuracy of this instrument is a prerequisite for analysing such low concentrated ice samples.

Pb concentrations determined in the 387 ice samples as well as annual averages show a large variation due to changing meteorological conditions. Beside the emission source strength, the concentrations of trace species in an annual layer of snow are influenced by the seasonality of precipitation and of atmospheric transport as well as in the case of Colle Gnifetti by the effect of wind erosion after deposition. In order to relate changes in concentrations in the ice to changes in the emissions, longer periods have to be averaged to result in values with comparable meteorological conditions. 5-year averages were calculated for the period 1900-1982, because these values seem to be independent of meteorological variability. Since data density is lower for the time range 1756-1900 (lowest 30 m) an averaging period of 10 years was chosen. Dating of the ice core was established by using a combination of different dating methods [3, 4].

Fig. 1 shows the lead concentrations and isotope ratio $^{206}Pb/^{207}Pb$ consisting of 5 to 10 year averages for the time period 1760 - 1982. Pb concentrations increase by a factor of 36 between the 1760-1800 average (0.087 µg l^{-1}) and the maximum of 3.15 µg l^{-1} in 1970 (Fig. 1). From the mid-19th century until 1940 an increase in lead concentrations is observed, which is discontinued in 1930 by the economic recession. This increase might be mainly attributed to emissions from coal burning.

The temporal trend of the isotopic composition $^{206}Pb/^{207}Pb$ is characterised by an overall decrease from about 1760 to 1975 (Fig. 1). The oldest 10-year average ratio is just approaching the natural background range, indicating the anthropogenic influence even as early as 1760, consistent with already increasing Pb concentrations. After a weak decrease between 1760 and 1800, a rather constant ratio is reached until about 1880. This ratios might represent a mixture of anthropogenic Pb emitted from coal combustion and mining and the natural background. From 1880 to 1975 $^{206}Pb/^{207}Pb$ ratios declined further with a strong enhancement after 1955, which points to additional anthropogenic sources, i.e. waste incineration and the use of leaded gasoline. The steep decrease after 1955 reflects the exponentially increasing amounts of leaded gasoline consumed. After 1975 a recovery to more radiogenic values seems to occur.

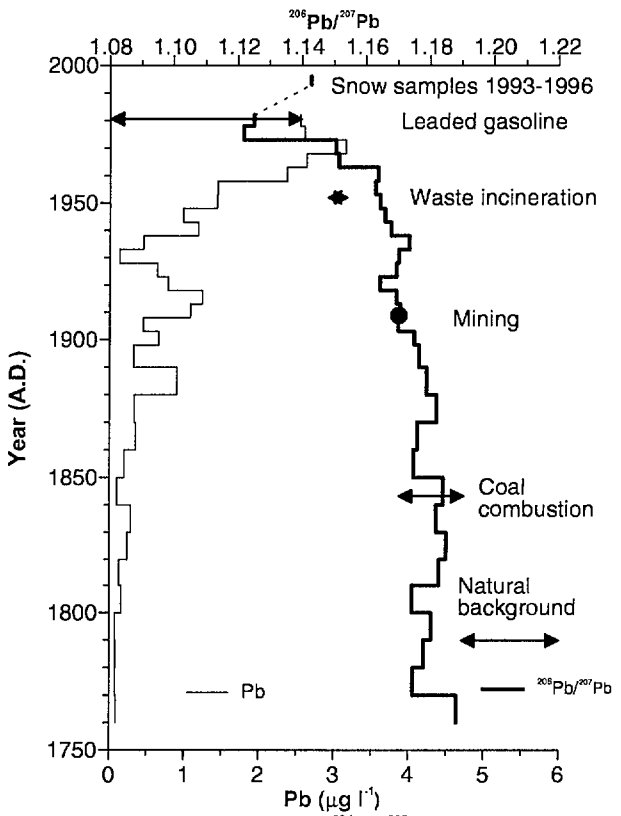

Fig. 1: Lead concentration and $^{206}Pb/^{207}Pb$ ratio record with five-year (period 1900-1982) and ten-year averages (1760-1900). Typical ranges of $^{206}Pb/^{207}Pb$ ratios of different atmospheric Pb sources are indicated.

REFERENCES

[1] T. Döring, Ph.D. Thesis Universität Bern (1999).

[2] T. Döring et al., Fresenius J. Anal. Chem. **359**, 382 (1997).

[3] A. Döscher et al., Water, Air and Soil Pollution **85**, 603 (1996).

[4] M. Schwikowski et al., Tellus **51B**, 938 (1999).

RADIOACTIVE STRATIGRAPHIC MARKERS IN AN ALPINE ICE CORE

A. Eichler (Univ. Bern & PSI), M. Schwikowski (PSI), H.W. Gäggeler (Univ. Bern & PSI), J. Beer (EAWAG), H.-A. Synal (PSI & ETH Hönggerberg), U. Schotterer (Univ. Bern & PSI)

^{137}Cs and ^{3}H activities and ^{36}Cl concentrations were measured in an Alpine ice core. These records reflect the emissions by atmospheric nuclear weapon tests in the fifties and early sixties as well as by the reactor accident in Chernobyl in 1986. The integrated inventories agree well with model calculations and former measurements.

Atmospheric testing of nuclear weapons between 1952 and 1962 led to a huge injection of fission products into the stratosphere. Furthermore, large amounts of radioactive material were spread over a large area of the northern hemisphere during the reactor accident in Chernobyl on April 26, 1986. These events, leaving increased activities of several species, became time markers in many hydrological studies. We determined ^{137}Cs and ^{3}H activities and ^{36}Cl concentrations in an Alpine ice core from Grenzgletscher. This 125 m (104 m w.eq.) long core was drilled in 1994 [1]. The initial aim for the measurements was to find reference horizons in order to corroborate the dating of the core.

The activities of the isotopes ^{137}Cs and ^{3}H along the ice core are presented in Figure 1A and B. Both records reflect the atmospheric weapon tests in the fifties and sixties in a broad activity peak between 55 and 85 m w.eq. depth. The maxima at approximately 76 and 69 m w.eq. depth are related to the test maxima of the years 1958 and 1962. They appear in the ice core with a time delay of approximately one year because of the slow stratosphere-troposphere transfer (see e.g. [2]). For the same reason activities appear in a broad peak. The maximum of the ^{137}Cs activity in 20 m w.eq. depth can be attributed to the radioactive fallout from the nuclear reactor accident in Chernobyl. The transport of the aerosol-bound fission products in the troposphere and their fast removal by wet deposition yielded a sharp signal in the ^{137}Cs activity record. The integrated ^{137}Cs activity from nuclear weapons fallout (3500 ± 800 Bq m^{-2}) agrees well with estimated values (e.g. 5040 Bq m^{-2} between 40° and 50° N [3], or about 4500 Bq m^{-2} at the Jungfraujoch, Switzerland [4]). For the estimations an annual average precipitation rate of 2.7 m w.eq. year^{-1} was used. The calculated ^{137}Cs fallout from the Chernobyl accident (800 ± 200 Bq m^{-2}) is at the lower limit of the values determined at Alpine sites (between 400 and 15000 Bq m^{-2} [5]). These differences in the deposited activities reflect the known regional heterogeneity of the Chernobyl fallout, which was strongly dependent on the precipitation pattern in the first days of May 1986.

The ice core ^{36}Cl record is presented in Figure 1C. Since anthropogenic ^{36}Cl is formed by the neutron activation of ^{35}Cl of sea water, the broad peak between 60 and 82 m w.eq. depth reflects the production by atmospheric weapon tests on ships and islands in the fifties. ^{36}Cl concentrations show a strong increase between 82 and 78 m w.eq., reaching concentrations about two orders of magnitude higher at the maximum in the year 1958 compared to the natural pre-bomb level. After 1958 a rapid decline can be observed, indicating that the main atmospheric tests over land from 1962, which led to the maxima in the ^{3}H and ^{137}Cs activities, did not strongly influence the ^{36}Cl concentration in the atmosphere. In order to determine the overall input of bomb produced ^{36}Cl, we integrated the measured inventory between 60 and 82 m w.eq. and derived a value of $(4.5\pm0.8)\cdot10^{12}$ atoms m^{-2}. The fallout of bomb produced ^{36}Cl was estimated, using a box model for the atmospheric transport of radionuclides [6]. The maximum of approximately $4.6\cdot10^{12}$atoms m^{-2} of the ^{36}Cl inventory was obtained in the mid-latitudes, between 40° and 50° N. The determined ^{36}Cl inventory at Grenzgletscher (ca. 45° N) fits well with the model results.

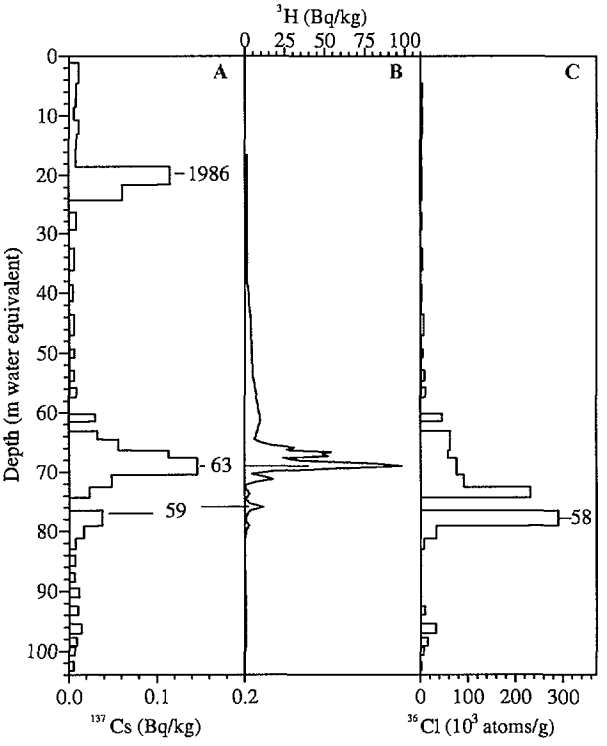

Fig. 1: Records of the ^{137}Cs (A) and ^{3}H (B) activities and ^{36}Cl concentrations (C) (calculated back to 10.94)

REFERENCES

[1] H.W. Gäggeler et al., Klimageschichte im Alpenraum, Vdf Hochschulverlag AG, ETH Zürich (1997).

[2] H.J. Emeleus et al., Advances in inorganic chemistry and radiochemistry **3**, Academic Press, New York (1961).

[3] H. Kiefer, KfK Nachr. **18**, 133 (1986).

[4] H.R. von Gunten and E. Rössler, Internal Report of the Paul Scherrer Institute, TM-CH-202 (1979).

[5] Haeberli et al., Ann. Glac. **10**, 48 (1988).

[6] Sachsenhauser et al., Proceedings of the Wengen Workshop, 21.-23.10.96, 103 (1997).

PREFERENTIAL ELUTION OF CHEMICAL SPECIES IN ALPINE FIRN

A. Eichler (Univ. Bern & PSI), M. Schwikowski (PSI), H.W. Gäggeler (Univ. Bern & PSI)

A depletion of the concentrations of certain ionic species was observed for a 13 m w.eq. part of the Grenzgletscher ice core. This effect is attributed to the inflow of meltwater leaching chemical species with different efficiencies. The preferential elution is explained by the fractionation of the species, occurring during snow metamorphic processes.

Ice core records of chemical impurities are not only determined by the atmospheric concentration of those species and depositional processes, but additionally by post-depositional processes taking place in firn or ice. In order to relate ice core records to past atmospheric composition, the understanding of such processes is crucial. A strong post-depositional effect, the leaching of chemical species probably caused by inflowing meltwater, was observed in an ice core from the upper Grenzgletscher in the Swiss Alps. This process aggravate the interpretation of the ice core records in depths between 11 and 24 m w.eq. of the 104 m w.eq. long ice core, drilled in 1994 [1]. However, it offers the unique possibility to study leaching processes occurring in firn layers under real conditions.

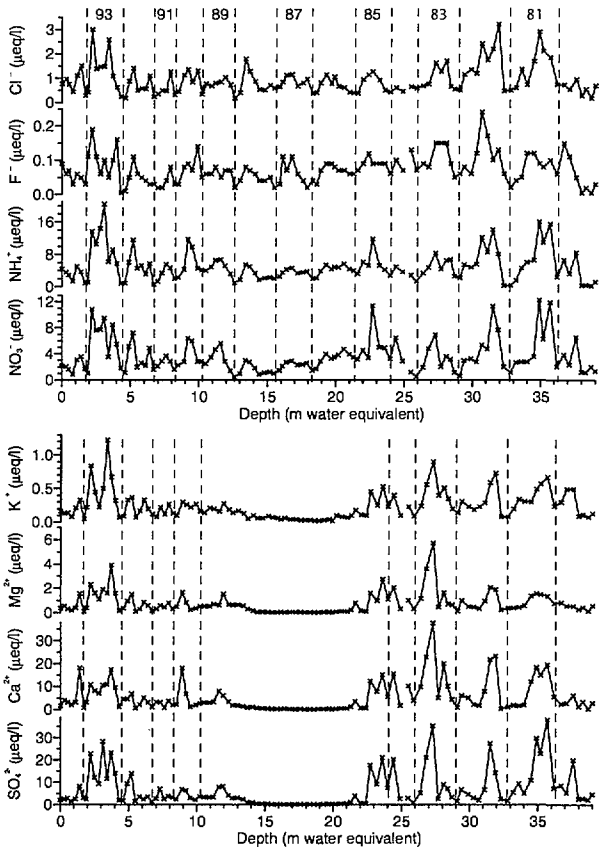

Fig. 1: Records of the Cl^-, F^-, NH_4^+, NO_3^-, K^+, Mg^{2+}, Ca^{2+}, and SO_4^{2-} concentrations. The dashed lines represent annual layers between 1980 and 1994.

The concentrations of the main inorganic ions from the upper 39 m w.eq. of the ice core are presented in Figure 1. This range covers the time period between 1980 and 1994. The concentrations of all species show a well pronounced seasonal pattern with summer maxima and winter minima, due to the seasonally dependent transport processes to the high-alpine sites [2]. All concentration profiles are in phase through the upper 12.5 m w.eq.. Below this depth the concentrations of K^+, Na^+ (not shown), Mg^{2+}, Ca^{2+}, and SO_4^{2-} decreased drastically, whereas the seasonal patterns of the Cl^-, F^-, NH_4^+, and NO_3^- concentrations seem to remained preserved. Deeper in the core (below depths of about 24 m w.eq.) all concentrations are in phase again.

The reason for the nearly complete removal of some species is assumed to be the elution by meltwater. We suppose an inflow of meltwater through a crevasse system in a depth of 10-12 m w. eq.. The meltwater then percolated through the underlying firn layers and mobilised a part of the impurities. Because there is no enrichment of the leached species below the influenced layers, we assume a draining of the meltwater in a depth of about 20-24 m w.eq., probably horizontally along the impermeable firn-ice border.

From the slope of the concentration ratios between the investigated ions we determined the following elution order:

$SO_4^{2-} > Ca^{2+} \sim Mg^{2+} > K^+ \sim Na^+ >> NO_3^- > NH_4^+ \sim F^- > Cl^-$.

SO_4^{2-} is most preferentially leached by the meltwater, whereas Cl^- seems to keep its initial concentration. The position of a species in the elution sequence can be attributed to its location in the snow grain. Initially individual snowflakes deposited on the glacier surface undergo different metamorphosis processes resulting in densely packed snow grains. During this metamorphosis, fractionation of chemical species occur, incorporating certain ions into the ice crystal interior and leaving others at the grain boundaries. F^- and NH_4^+ are most readily accepted by the ice lattice, becau-se of the similar ionic radii of F^- and N^{3-} with respect to O^{2-}. Cl^- and NO_3^- can enter the ice lattice too [3]. The complex anion SO_4^{2-} is most probably not incorporated into the ice lattice and the cations K^+, Na^+, Mg^{2+}, and Ca^{2+} are to large in comparison to H^+, which they would need to replace. Therefore these species are enriched at the grain boundaries and thus, are washed out firstly by rinsing meltwater. The hypothesis that SO_4^{2-} does not exist at the grain interior was verified for Antarctic ice [4]. It was estimated that 40-100% of the sulphate is present as liquid sulphuric acid at the triple junctions (junctions were three grains meet).

Because of the described post-depositional effects, for the interpretation of the concentration records from Grenzgletscher, the years 1985-1989 have to be excluded.

REFERENCES

[1] H.W. Gäggeler et al., Klimageschichte im Alpenraum, Vdf Hochschulverlag AG, ETH Zürich (1997).
[2] M. Lugauer et al., Tellus **50B**, 76 (1998).
[3] P. Hobbs, Ice physics, Oxford, Clarendon press (1974).
[4] R. Mulvaney et al., Nature **331**, 247 (1988).

CONTINUOUS ION CHROMATOGRAPHIC ANALYSES OF ICE CORES USING A GRADIENT SYSTEM

T. Huber (Univ. Bern & PSI), M. Schwikowski (PSI), H.W. Gäggeler (Univ. Bern & PSI)

The ion chromatography system used for anion analysis has been updated to a gradient system which allows the determination of inorganic as well as organic components in a shorter runtime. However, a simultaneous operation of the two different sample lines for anions and cations is still problematic due to mutual contamination by the respective eluent.

The system for continuous melting and ion chromatography analyses of ice cores described in [1] has been updated to a gradient system (IC20 and EG40, Dionex) and a new type of column (AS17, Dionex) has been used to analyse main watersoluble anions in ice. In Fig. 1 two chromatograms are compared: A shows a chromatrogram obtained with the new gradient system, B a chromatogram obtained by the previous isocratic system with an AS12A column (Dionex). It can be seen that the gradient system allows the reduction of the runtime to about nine minutes. In addition to the common anions fluoride (F), chloride (Cl), nitrate (NO_3) and sulphate (SO_4), also the organic components acetate (Ac), formate (Fo), methanesulfonate (MSA), and oxalate (Ox) can be determined.

With an isocratic carbonate eluent and a AS12A column it is not possible to separate the organic compounds Fo, Ac and MSA. Ox is eluated after SO_4 and therefore doubles the runtime.

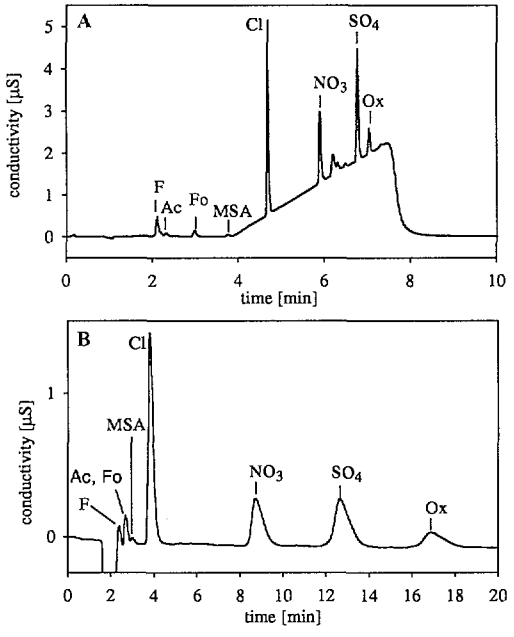

Fig. 1: Chromatograms of anion standards (20 ppb Ac, Fo, Ox; 50 ppb F, MSA; 500 ppb Cl, NO_3, SO_4) obtained by **A** column AS17 with hydroxide gradient (1–34 mM KOH, **B** column AS12A with isocratic carbonate eluent (2.7 mM Na_2CO_3, 0.3 mM $NaHCO_3$)

In Fig. 2 the schematic of the valve connections is shown. The sample stream is divided by a three-way-connection and distributed by a six-port-valve onto two different ten-port-valves. Parallel to one run of an ion chromatographic analysis the sample is collected on concentrator columns (TAC-LP1 (1), TCC-LP1 (1)). During this time, the eluents used for the analyses (KOH for anions, H_2SO_4 for cations) elute the pre-concentrated sample ions from the other concentration columns (TAC-LP1 (2), TCC-LP1 (2)) to the ion chromatographic systems (position 1). After the analysis, all three valves are switched and the sample is concentrated on columns (2), while the sample on columns (1) are analysed (position 2).

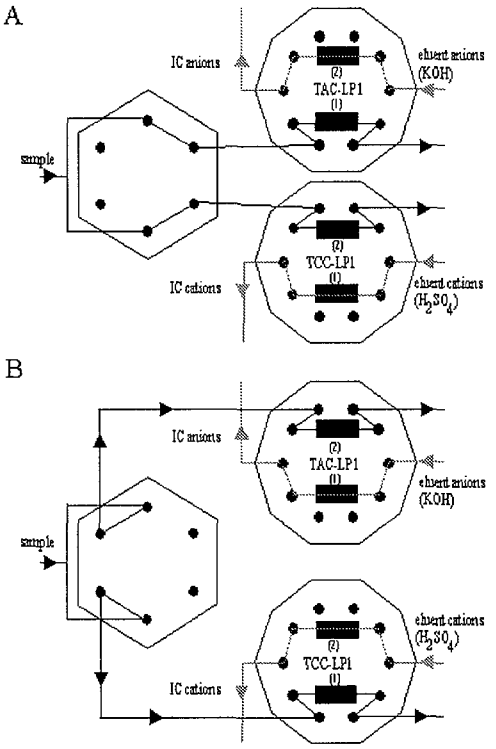

Fig. 2: Schematic of the valve connections. **A** corresponds to position 1, **B** to position 2.

However, it was observed that contaminations from the eluents occur. When concentrating high purity water onto the columns, potassium and sulphate could still be measured. It is therefore assumed that an exchange of eluent over the valves takes place. This could be proved by disconnecting one of the ten-port-valves. By disconnecting the anion-valve, e.g., the contamination of potassium could no longer be observed.

REFERENCE

[1] T. Huber et al., PSI Annual Report **1998**, p.40.

DATING ICE CORES BY ^{14}C MEASUREMENTS OF CARBONACEOUS PARTICLES

V.M.H Lavanchy (PSI & Univ. Bern), G. Bonani, I. Hajdas, M. Suter (PSI & ETHZ) M. Schwikowski (PSI), H.W. Gäggeler (Univ. Bern & PSI)

In this study we attempt to date ice cores by ^{14}C measurements on carbonaceous particles stored in ice. We report on first ^{14}C measurements of standard material containing less than 100 µg carbon.

Dating of glacier ice cores is a challenge, especially in the case of glaciers without regular snow accumulation throughout the year and when stratigraphic markers are missing. ^{14}C measurement is a widely used method for dating carbon-containing material for a time period between 500 to 50000 years before present. ^{14}C dating is performed by Accelerated Mass Spectrometry (AMS) measurement of the ratio $^{14}C/^{12}C$ of a sample as graphite. Normally, organic material, e.g. animal or plant remains, is used for the ^{14}C measurement. However, such material can usually not be found in glacier ice. Instead, we propose to use the organic carbon (OC) fraction of the carbonaceous particles stored in ice cores for dating by ^{14}C measurement. OC is the dominating carbon fraction in carbonaceous particles and is believed to originate from biogenic sources, at least for the time period before the use of fossil fuel. Thus, the ^{14}C age of the OC should correspond to the age of the ice section. For a conventional AMS measurement 70-150 µg of graphite ion source is required. Taking into account the organic carbon content of ice from pre-industrial times [1] this represents 1.5 – 3.5 kg ice.

Figure 1 shows the apparatus designed to capture CO_2 evolved during the determination of OC with a thermal method described elsewhere [2]. The CO_2 carried with N_2 is captured in a cryo trap, then vacuum-transferred and sealed in an ampoule. Recovery of CO_2 is only 20%. In a second step the CO_2 is reduced to graphite in a reaction with hydrogen using cobalt powder as a catalyst. The resulting graphite-cobalt mixture is pressed onto copper discs. $^{14}C/^{12}C$ isotopic ratios of the obtained graphite targets are measured at the ETH/PSI accelerator facility together with standards.

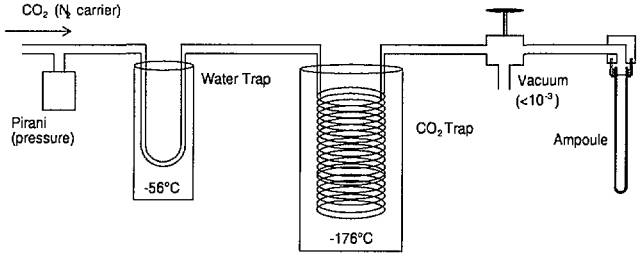

Fig.1. The CO_2 evolved during the determination of the carbonaceous particles sample is captured in a cryo trap (-176°C) and vacuum transferred into an ampoule.

First samples prepared from modern snow were measured together with oxalic acid standard material. The resulting amount of carbon obtained from the samples varied between 4 and 10 µg. The standards contained between 14 and 95 µg C. During the measurement of the $^{14}C/^{12}C$ isotopic ratio the measured ^{12}C current was between 0.6 to 0.9 µA for the samples and 0.9 to 10.5 µA for the standards.

The very low current of the snow samples resulted in a high experimental error and thus did not allow to determine the ^{14}C age of the samples.

Figure 2 shows the ^{14}C age of the standards derived from the ratio $^{14}C/^{12}C$ in dependence of the measured ^{12}C current. In addition, the certified age of the standard (-412 year) is plotted. The resulting ages of the standards that yielded a current higher than 6 µA correspond within the experimental error to the certified age. The ^{12}C current depends on the amount of graphite on the target and in this case of low amounts of graphite on the quality of the target preparation. The smallest samples yielding a current higher than 5 µA correspond to 34 µg carbon. This result is in good agreement with an earlier study [3].

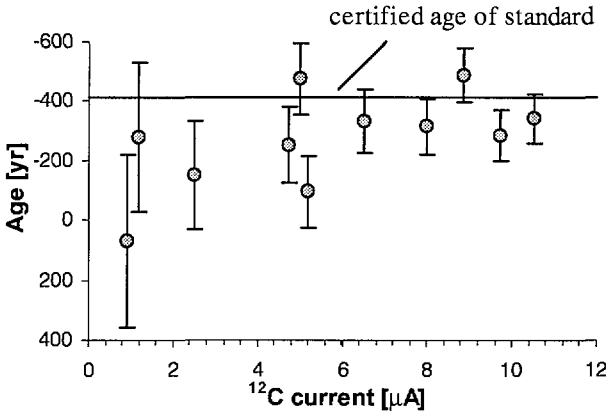

Fig. 2. The accuracy of the measured age depends on the yield of the ^{12}C current of the sample.

Further work is needed to achieve a more efficient capture of the CO_2 after thermal treatment of the OC. Measurements using the new AMS facility at the ETH/PSI are supposed to be less sensitive on target quality and therefore measurements of even lower amounts of carbon are assumed to be possible.

REFERENCES

[1] V.M.H. Lavanchy et al., J. Geophys. Res. **104**, 21227 (1999).

[2] V.M.H. Lavanchy et al., Atmos. Environ. **33**, 2759 (1999).

[3] J. Hauenstein (1994) Dissertation, Uni Bern (unpublished).

NUTRIENT RELEASE OF MELTING SNOW

P. Waldner, M. Schneebeli (WSL/SLF), M. Schwikowski (PSI)

The spatial and temporal variation of the nutrient release of a snow cover were measured in a not-forested field in the winter 1998/1999. Vertical profiles of the nutrient concentrations in the snow cover show peak displacements and diminution, due to snow pack settling and melt release.

1 INTRODUCTION

Chemical trace species in precipitation are a relevant source of rare nutrients for the vegetation. These nutrients are stored in the snow cover during winter. Their release from the snow cover during snow melt results in significant nutrient input into soil, vegetation and rivers. The effect of the release on plants, soil and rivers depends on the temporal and spatial distribution of the release. Nutrients considered in this study are the nitrogen containing ionic species ammonium and nitrate.

In the frame of a joint project of the WSL, the ETH Zurich, and the PSI the relations between melt water and nutrient release of a snow cover and the influence of the structure of the snow cover and of meteorological conditions on these processes are investigated.

2 METHODS

In winter 1998/1999 a field campaign was conducted in order to measure the spatial and temporal variations of the melt water release of a rather homogeneous snow cover. For this purpose a network of 32 melt water samplers each consisting of a basin of 0.4x0.7m was installed on top of the soil in a not-forested field in Alptal (1210 m a.s.l., Fig. 1). The Alptal area has a long tradition of field experiments concerning catchment hydrology and nutrient budgets [1, 2]. Melt water was periodically collected from the samplers and its amount was determined on-site by weighing. In addition, snow pit sampling was performed in order to gain information about vertical concentration profiles. Samples were analysed for concentrations of main ionic species by ion chromatography, inductively coupled plasma mass spectrometry and flow injection analyses. In the snow pit, density and grain structure were determined manually. Snow temperature was registered continuously 5 cm, 20 cm and 40 cm above ground.

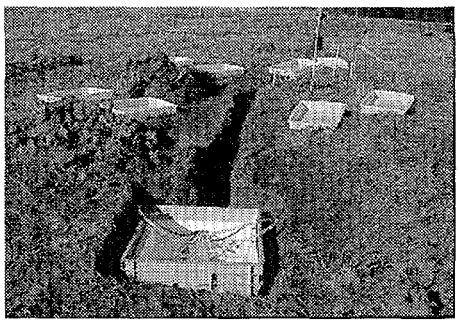

Fig. 1: Installation of the melt water samplers on a not-forested field in Alptal at 1210 m a.s.l.

3 RESULTS AND DISCUSSION

Extraordinary amounts of snow resulted in a highly layered and structured snow pack. This is indicated by the concentration profiles of nitrate which also reflect the snow pack settling (Fig. 2). While the downward displacement of the concentration peak between March 2 and April 27 can be explained by snow pack settling, the diminution of the concentration peak between April 27 and 29 is due release by melt water.

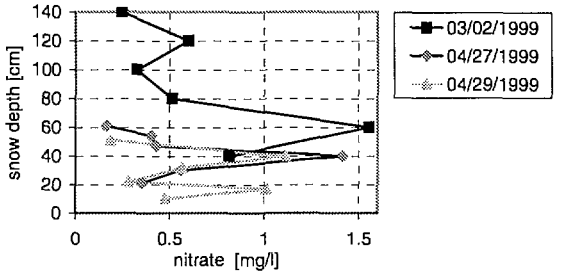

Fig. 2: Vertical concentration profiles of nitrate in the snow cover.

Three types of melt water fluxes were registered: A surface melt water percolation, a base melt flow (more or less constant over time) and some of the samplers received a large amount of water with an electrical conductivity above 50 µS/cm. The variability of the surface melt percolation (Fig. 3) is explained by the development of preferential flow paths in the snow cover.

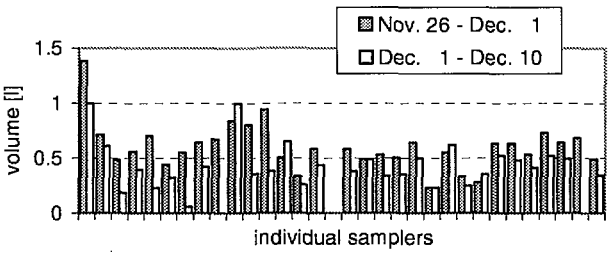

Fig. 3: Mean volume fluxes collected by the melt water samplers in the period 26 November – 1 December and 1– 10 December, respectively.

REFERENCES

[1] H. Burch, Beiträge zur Hydrologie der Schweiz, **35**, 18 (1994).

[2] P. Schleppi et al., Water, Air and Soil Pollution, **116,** 129 (1999).

ANALYSIS OF SIZE-CLASSIFIED ICE CRYSTALS BY CAPILLARY ELECTROPHORESIS

B. Tenberken-Pötzsch, M. Schwikowski (PSI)

Electrolyte systems were developed in order to analyse main inorganic cations, anions as well as carboxylic acids and dicarboxylic acids in ice crystal samples with sample volumes of less than 100 µL by capillary electrophoresis.

Precipitation in the moderate climate of Europe mostly develops in mixed phase clouds containing both supercooled cloud droplets and ice crystals and therefore separate sampling and analysis of these two cloud components is necessary to study precipitation processes. Due to the multiple scavenging processes of ice crystals, including nucleation, riming, gas and aerosol particle scavenging, the chemical content of ice crystals is of quite complex origin.

In order to investigate the chemical composition, techniques were developed to collect size-classified ice crystals [1,2] as well as to separate supercooled cloud droplets and ice crystals [3]. Since the developed sampling techniques result in small absolute sample volumes (< 100 µL) and the concentrations of the main solutes in ice crystals are in the low µmol L^{-1} range (1-10 µmol L^{-1}), a method of analysis using small injection volumes and having low absolute limits of detection (LOD) is required. Furthermore, for comprehensive interpretation of atmospheric processes the simultaneous determination of various components and a high sample throughput are necessary.

As the method for analysis we therefore chose capillary electrophoresis (CE), which is in particular well suited for this purpose and has already been used for similar problems of analysis, such as, for example, the investigation of raindroplets and fogdroplets [4-7].

In order to analyse the main inorganic cations (NH_4^+, K^+, Na^+, Ca^{2+}, Mg^{2+}) and anions (Cl^-, NO_3^-, SO_4^{2-}) as well as carboxylic and dicarboxylic acids in ice crystals by CE, electrolyte systems were developed and optimised with respect to limits of detection, resolution, reproducibility and analysis time [8]. We applied indirect UV detection, which enables the simultaneous detection of multiple components. Salicylic acid and 4-methylaminophenolsulfate were used as UV-active co-ions for analysis of anions and cations, respectively.

A special feature of these systems are the very low LODs of 0.3 - 0.9 µmol L^{-1} (i.e. absolute LODs are in the fmol range), which enable for the first time the analysis of various components in size-classified ice crystal samples. The reproducibilites of corrected peak areas and retention times are 2 - 11 % and 1 - 3 %, respectively. Additional properties of the systems are short analyses times of about 4 minutes, resulting in a high sample throughput.

Figures 1 and 2 show typical electropherograms of cations and anions in size classified ice samples.

The newly developed electrolyte systems were successfully applied during fied experimental studies performed at the high-Alpine research station Jungfraujoch. The results suggest a complex relationship between the size of an ice crystal and its chemical content and will be discussed in detail in [2].

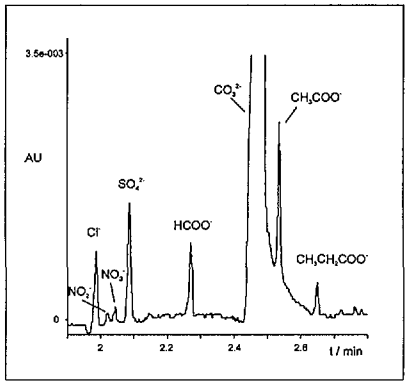

Fig. 1: Typical electropherogram of anions in a sample of size-classified ice crystals with diameters of 25 µm (Cl^-: 29 µM, NO_3^-: 2.3 µM, SO_4^{2-}: 24 µM, formate: 23 µM, acetate: 21 µM, propionate: 5.5 µM).

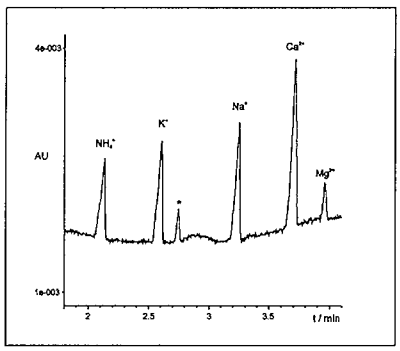

Fig. 2: Typical electropherogram of cations in a sample of size-classified ice crystals with diameters of 25 µm (NH_4^+: 58 µM, K^+: 59 µM, Na^+: 49 µM, Ca^{2+}: 35 µM, Mg^{2+}: 8 µM,).

ACKNOWLEDGEMENT

This work was supported by the Kommission für Technologie und Innovtion (KTI).

REFERENCES

[1] S.H. Ehrman et al., submitted to Atmos. Environ.
[2] B. Tenberken-Pötzsch et al., in preparation.
[3] B. Tenberken-Pötzsch et al., subm. to Atmos. Environ.
[4] B. Tenberken et al., J. Chromatogr. **A 745**, 209 (1996).
[5] B. Tenberken, K. Bächmann, J. Chromatogr. **A 755**, 121 (1996).
[6] B. Tenberken, K. Bächmann, J. Chromatogr. **A 775**, 372 (1997).
[7] B. Tenberken, K. Bächmann, Atmos. Environ. **32**, 1757 (1998).
[8] B. Tenberken-Pötzsch et al., J. Chromatogr., in press.

A METHOD TO SAMPLE AND SEPARATE ICE CRYSTALS AND SUPERCOOLED CLOUD DROPLETS IN MIXED PHASED CLOUDS

B. Tenberken-Pötzsch, M. Schwikowski (PSI)

A sampler to collect ice crystals and supercooled cloud droplets separately for subsequent chemical analysis was developed and for the first time used in a field experiment.

In the frame of the investigation of ice crystals and precipitation processes [1] a new sampling method was developed [2]. Since ice crystals and supercooled cloud droplets normally coexist in clouds, separate sampling of these two cloud components is required in order to study scavenging processes and the formation of precipitation. For the separation of ice crystals and cloud droplets we used an inertial impaction system. This approach is based on the assumption that the sticking properties of supercooled cloud droplets and ice crystals are different. Supercooled cloud droplets freeze immediately upon contact with the corresponding stage of an impactor whereas ice crystals should bounce off because they do not stick to the impaction surface. These ice crystals can then be sampled at a back-up filter as bulk sample.

To test this assumption laboratory studies were performed [2] and for the application in field experiments a prototype of a sampler was developed. For this purpose we used a modified version of a single-stage cloud water sampler (CWS) [3] which was especially developed for sampling of supercooled cloud droplets. A scheme of this device is given in Figure 1.

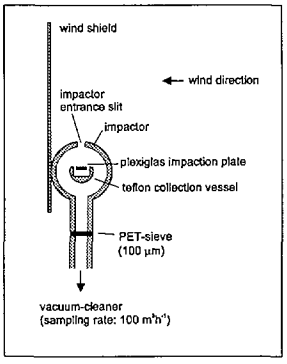

Fig. 1: Cross-sectional scheme of the modified single-stage cloud water sampler.

During sampling the supercooled cloud droplets froze onto the plexiglas impaction plate and built up an ice layer of maximum 1 mm thickness which was scraped off directly at the end of a sampling period and transferred into 0.5 - 1.9 mL polyethylene vials. Ice crystals bounced off the impaction plate and were sampled in a teflon collection vessel which was positioned behind the impaction plate. Furthermore, the device was modified by inserting a PET-sieve (100 µm mesh diameter) after the impactor in order to sample also small ice crystals which were not collected in the vessel. By visual examination it could be excluded that ice crystals froze on the plexiglas impaction plate. In addition, ice crystals could be visually observed in the collection vessel and on the PET-sieve. As the sampler was operated at temperatures between -13 and -26 °C no liquid film could be observed on the impaction surface which would had enhanced crystal retention.

The impaction plate, collection vessel and PET-sieve were cleaned by Milli-Q water prior to the experiment. After sampling, ice crystals were also transferred into 0.5 - 1.9 mL polyethylene vials. All samples were kept frozen until chemical analysis by CE was performed [1,4]. Blanks for all stages were below the limits of detection.

In Figure 2 first results for simultaneous sampling and separation of ice crystals and supercooled cloud droplets collected during a precipitation event at the high-Alpine research station Jungfraujoch are shown. The ambient temperature during sampling was -18.2 to -20.1 °C and average cloud droplet diameters determined by a PVM-100 were 44 µm (E. Weingartner, personal communication).

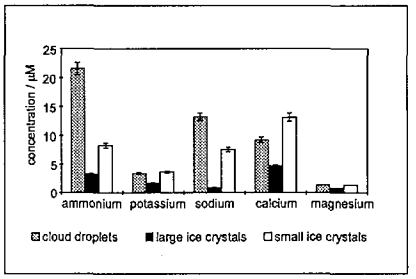

Fig. 2: Concentrations of water soluble cations in the different cloud compartments during the precipitation event 13/01/99, 7:10-8:30 am collected at the Jungfraujoch.

The concentrations of the cations NH_4^+, K^+, Na^+, Ca^{2+}, and Mg^{2+} were in the range of µM. Cloud droplets showed clearly higher concentrations of cations than large ice crystals. For the small ice crystals sampled on the PET-sieve the concentrations were usually higher than those of the large ice crystals. It can be seen that the concentrations of cations associated with coarse mode aerosol (K^+, Na^+, Ca^{2+}, and Mg^{2+}) in cloud droplets and small ice crystals are quite similar suggesting the preliminary assumption that coarse mode aerosol particles to the same extent contribute to both cloud droplet and ice crystal nucleation, or that these species are effective nuclei for supercooled droplets, and droplets containing these species freeze before droplets containing mainly soluble materials, such as ammonium.

This first experiment demonstrates the applicability of the new method and opens up interesting perspectives for future field experimental studies.

ACKNOWLEDGEMENT

This work was supported by the Kommission für Technologie und Innovtion (KTI).

REFERENCES

[1] B. Tenberken-Pötzsch et al., this Annual Report.
[2] B. Tenberken-Pötzsch et al., subm. to Atmos. Environ.
[3] C. Kruisz et al., Proc. of the EUROTRAC Symposium'92, 523 (1993).
[4] B. Tenberken-Pötzsch et al., J. Chromatogr., in press.

MULTIPLE FOIL ACTIVATION FOR NEUTRON SPECTRUM MEASUREMENTS AT SINQ

L. Tobler, H.U. Aebersold (PSI), F. Hegedüs (PSI, EPFL)

Neutron spectrum measurements have been performed by multiple foil activation method at the spallation neutron source SINQ. Different foils were irradiated with or without Cd-shielding at the pneumatic tube system of SINQ, in order to characterise the quality of data in a new cross section library (SPALLDOS) prepared for spallation neutron sources and to adjust the neutron spectrum at the irradiation position.

Neutron energies at the spallation source SINQ range from thermal energies (10^{-3} eV) up to 590 MeV. The determination of the neutron spectrum requires the use of a proper cross section library in this energy range. A new high energy neutron cross section library (SPALLDOS) was prepared for the use at spallation neutron sources [1]. Problem dependent sublibraries were created, one for the cold neutron beam and one for the thermal neutron tubes at SINQ. Multiple foil activation was performed in order to characterise the quality of the library data and to adjust the neutron spectrum at the irradiation position.

Different materials were irradiated with the pneumatic tube system (PNA). The foils were packed in an aluminium container and transported to the irradiation position. This is located in the thimble-shaped neutron tube (sector 60) inside the moderator tank (filled with D_2O), orthogonal to the direction of the bombarding proton beam, in a distance of 25 cm from the Zircalloy target. Foil material used for activation and the irradiation conditions are listed in Table 1.

Table 1: Foil material and irradiation conditions

No.	Foil material	1 mm Cd-shielding	Irradiation time [min]
1)	1% Au in Al, 2% Co in Al 4% Mn in Al 2% In in Al	no	5
2)	Al, Au, Ni, Ta, Ti	yes	15
3)	Bi, Mn, Lu_2O_3 (powder)	yes	25

After irradiation the foils were unpacked and γ-spectroscopy was done on a HPGe detector (rel. Efficiency 9 %, FWHM 1.95 keV at 1332 keV). Different measurement conditions (cooling time, counting time and counting geometry) had to be applied, due to the different decay times of the produced nuclides. The detector was calibrated for absolute detection efficiencies at the 2 geometries used for the measurements.

Measurements were performed on a OpenVMS-based data acquisition and analyses system (Genie, Canberra Industries, Inc.).

As an example the γ-ray spectrum of manganese is shown in Fig. 1. γ-lines from reactions induced by high energy neutrons, which were used for evaluation, are marked in the spectrum.

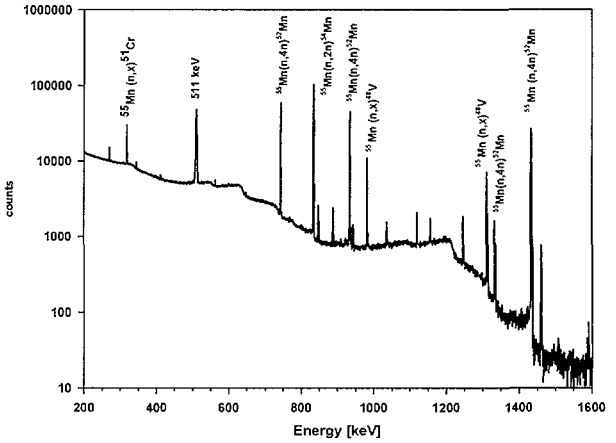

Fig. 1: γ-spectrum of manganese (0.99 g) after irradiation under Cd for 25 min, decay time 7 d, counting time 20 h.

These measurements were used for the neutron spectrum adjustment procedure. Due to the rather large uncertainty of the available input neutron spectrum [2], the deviation of the calculated reaction rates obtained with the solution neutron spectrum from the measured ones are in most cases acceptable [1].

However, the reaction rates of irradiation 2) are a factor of about 6 lower in comparison to the reaction rates of the other two irradiations. It is supposed that the transport container of this irradiation was not transported correctly to the irradiation position. This has to be confirmed by the repetition of the corresponding irradiation.

ACKNOWLEDGEMENTS

Special thanks are due to E. Bauer and E. Lehmann for supporting this work. The work of E. J. Szondy and E. Zsolnay is highly appreciated. Our thanks are extended to the staff of the SINQ and the radiation safety group .

REFERENCES

[1] E. J. Szondi et al., in Reactor Dosimetry, ASTM STP 1398, Eds. J. G. Williams et al, American Society for Testing and Materials, West Conshohoken,in press.

[2] F. Atchinson, PSI Report 98-03, 1998.

CEMENT CHEMISTRY: QUALITY CONTROL AND DEVELOPMENTS 1999

H.P. Zimmermann, M. Patorski, L. Döhring, M. Egloff (PSI)

This report gives a short summary of the developments in our group during 1999.

This year we received or produced 31 radioactive and 6 inactive sample-sets. The amount of samples to be tested depends strongly on the production schedules in the power plants and on modifications of recipes etc. Therefore, we had a somewhat lower number of compressive strength (about 290) and γ-spectrometric measurements (about 730 including glass and metal samples, see below).

In our endeavour to set up quality control procedures for the products of the ZWILAG plasma incinerator, we performed leaching tests of activated glass samples. We successfully used the pneumatic tube transport system of the SINQ (spallation induced neutron source) isotope production for neutron activation of some glass samples of known surface area. Since we only wanted to produce some longer lived activity in the sample, which could be used as tracers for leachability tests and as we had enough time for the decay of short-lived nuclides, few difficulties were encountered with the large number of fast neutrons produced by the SINQ. The leach-tests are finished but the γ-measurements are still running. Due to the very low level of leached activities, one measurement (of 132) requires 3-5 days at least, even with an acceptable detector efficiency. Still not solved is the problem of taking samples with a defined surface area (or at least the determination of that surface) from real active waste products since any cooling liquid during the sampling process had to be avoided.

The results of the preliminary leach-test of one activated metal sample are in good agreement with the results of the corrosion measurements on inactive samples of the same bulk, done by the LWR-group in the previous year [1]. Therefore, we decided to leave out the rest of the planned leach-tests of artificially activated simulated metallic waste and to perform those experiments with real active waste products from the incinerator.

The parallel plate squeezing-flow technique [1] was used for the product control of real bituminized waste products from KKG (Gösgen). In connection with the measurement of viscosities, we also performed a few simple theoretical calculations of sedimentation processes in a bituminized waste package under different conditions. Again this work was done in collaboration with EMPA.

The dismantling of the former research reactor DIORIT is still in progress. Our recipe tests for the efficient solidification of graphite have been successful and resulted in an application for a patent together with the section Radioactive Waste Treatment.

In order to be Y2k compliant, we have had to update the hard- and software of our most important computer systems, especially our PC-based γ-spectroscopy system.

REFERENCE

[1] H.P. Zimmermann et al., Annual Report **1998**, p.45.

SYNTHESIS AND CHARACTERIZATION OF BENZIMIDAZOLIC DTPA- AND DOTA-BASED ^{157}Gd CHELATES FOR GADOLINIUM NEUTRON CAPTURE THERAPY (GdNCT)

Ch. Salt, R. Weinreich (PSI), Th. A. Kaden (Universität Basel)

Three series of various charged and uncharged benzimidazolic ^{157}Gd chelates based on the bifunctional polyamino polycarboxylate chelating agents DTPA and DOTA have been synthesized. The combination of minor-groove-binding and fluorescence characteristics of the benzimidazolic system with the MRI properties of GdDTPA and GdDOTA of these novel conjugates are currently under investigation for potential use in GdNCT.

INTRODUCTION

^{157}Gd presents the highest thermal neutron capture cross section of all stable nuclides: 255'000 barn.The ^{157}Gd neutron capture reaction generates g radiation which is partly converted with the emission of conversion electrons. The vacancies left by these conversion electrons result in the emission of Auger electrons with a range of radiochemical damage limited to molecular dimensions.To exploit the Auger and Coster-Kronig effect and to a lesser extent the Gd nucleus recoil of the ^{157}Gd(n,g)*^{158}Gd reaction, it is necessary to deposit the Gd atoms in the immediate vicinity of the DNA helix[1, 2]. To achieve stable ^{157}Gd-labelled DNA minor groove binders, bifunctional polyamino polycarboxylate chelating agents such as DTPA and DOTA are used that possess a powerful metal chelating group and a carboxylate functionality for amide conjugation with a benzimidazolic chromophore targetting the DNA like the fluorescence stain Hoechst 33258 [2,3]. Three types of novel ^{157}Gd transport vectors that could function like 3-phase missiles (cf. Results and Discussion) for NCT have been designed (Fig.1):**Type 1:** ionic monomeric DTPA-based benzimidazolic ^{157}Gd ligands presenting one overall negative charge. **Type 2:** neutral dimeric DTPA-based benzimidazolic ^{157}Gd ligands possessing two benzimidazolic chromophore moieties. **Type 3:** neutral DOTA-based ^{157}Gd ligands.

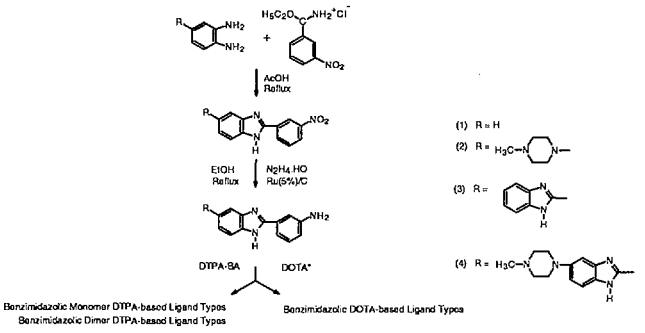

Fig. 1: General Reaction Scheme for the three Benzimidazolic Ligand Types

RESULTS AND DISCUSSION

The benzimidazolic DTPA- and DOTA-based ^{157}Gd chelates designed for GdNCT combine three essential properties of the separate ^{157}Gd conjugate components that together could hopefully function like a three-phase missile according to the following concept: **Phase 1:** DTPA-Gd and DOTA-Gd as known MRI contrast agents pass the blood-brain barrier. Is this property retained in the modified compounds e.g. MRI contrast agents coupled with the Hoechst moiety? **Phase 2:** The Hoechst moiety targets the DNA minor grooves [2] of the GBM cells in the brain. Are the minor groove binding properties of the fluorescence stain Hoechst retained when the conjugated with the ^{157}Gd chelates (i.e. the MRI contrast agents)? Hoechst is supposed to be taken up preferentially by tissue with high cell division rates (liver, bone marrow, tumours). What is the normal/tumour tissue uptake ratio of the new compounds? **Phase 3:** Neutron irradiation with radiotoxic effects due to Auger electron emission and ^{157}Gd nucleus recoil. Does the Auger effect take place? Do single and/or double strand breaks in the DNA occur? How many Gd atoms are necessary to kill one cell?

OUTLOOK

First biological tests comprise micro-inoculation trials consisting of compound injection into the cytoplasm of selected cell lines in order to assess the possible transport of the ^{157}Gd into the cell nucleoplasm. Also, the actual delivery of the ^{157}Gd atoms in the cell nucleus will have to be proved. In this context, there is the possibility of ^{153}Gd -labelling. Should the various ^{157}Gd -labelled compounds be traced to the cell nucleoplasm, fluorescence spectroscopy can provide information on the degree of DNA-binding of the altered fluorescence stains [3]. Cytotoxicity evaluations have to establish the possible compound concentrations importing ^{157}Gd atom concentrations high enough for the neutron capture reaction to take place and produce the Auger electron emission [1,2]. Here, the use of enriched gadolinium (>90% of ^{157}Gd vs. the natural isotope abundance of 15.7%) has the advantage of a six-fold increase in the neutron capturing isotope ^{157}Gd of the potential radiopharmaceutical.

REFERENCES

[1] J. C. Masiakowski, J.L. Horton, L.J. Peters, Med. Phys. **19**, 1277 (1992).

[2] A.D. Whittaker, D.P. Kelly, M. Pardee, A. Corder, H. Meriaty, B.J. Allen, R.F. Martin, Advances in Neutron Capture therapy, Ed. A.H. Soloway et al., Plenum Press, New York, 1993, p.383.

[3] K. Wiederholt, S.B. Rajur, J. Giuliano Jr., M.J. O'Donnell, L.W.McLaughlin, J. Am. Chem. Soc. **118**, 7055 (1996).

DETERMINATION OF THE RADIONUCLIDE INVENTORY IN ACCELERATOR WASTE

R. Weinreich, M. Argentini (PSI)

As an essential part of waste management the nuclide inventories of radioactive waste which has been generated in the PSI facilities must be determined. In dismantled parts of the "Beam dump" of Target E, 1.5x10^6-a ^{60}Fe could be determined for the first time by accelerator mass spectrometry. Further dismantled parts are the target BX 2 and the beam dump of the biomedical (π-meson) target.

Paul Scherrer Institute and CERN are Switzerland's (and perhaps Europe's) most important producers of radioactive accelerator waste which generally must be prepared for final disposal. This accelerator waste is located in machine and beam-lining elements and consists of long-lived activation products, originated by nuclear interactions of accelerated protons and secondary neutrons with (mostly metallic) target materials. Shielding materials, mostly concrete and as a minor content lead, are likewise activated.

Complementary to the mathematical determination of the radionuclide inventory, the activity of some principal radionuclides must be determined by measuring their radiation. The most interesting long-lived nuclides, however, emit β-particles or lower-energy electrons and request consequently a careful chemical separation before measurement.

To date, three main parts of the PSI cyclotrons have been disassembled: the beam dump of Target E (irradiation finished in 1990) which has been irradiated by 590 MeV protons, the target BX2 (finished in 1998) which has been irradiated by 72 MeV protons and the beam dump of the biomedical irradiation facility which was able to produce π-mesons (1994). Furthermore, some smaller aluminium and graphite parts have been dismantled. The radionuclide inventories of these elements should give a good survey of the activation relations in the PSI accelerator waste.

The main radionuclide in the inventory, also for the next years, is 5.27-a ^{60}Co. By a careful modeling, its yield implies that the beam dump should contain 3x10^{12} Bq ^{60}Co.

In cooperation with the Department of Ion Beam Physics, the yield of 1.5x10^6-a ^{60}Fe could be measured by accelerator mass spectrometry [1]. The data show that activities around 1x10^{-5} Bq/g could be measured by this sensitive method, even in the steel samples with iron as main component.

The measurement of the α-activities gave upper measuring limits only. The determination of the uranium content in the samples by ICP-MS gave no indication for the presence of α-emitters as well.

REFERENCE

[1] P. Gartenmann, Untersuchungen von anthropogenem ^{60}Fe und anderen mittelschweren Radionukliden mit Beschleunigermassenspektrometrie. Dissertation ETH Zürich 1999. Shaker Verlag. ISDN 3-8265-6409-X.

Table 1: Part of the radionuclide inventory of Beam dump of Target E (Bq/g), calibrated to June 30, 1998

Nuclide	Half-life	Measuring Method	Copper activated by protons	Copper activated by secondary particles	Shielding iron	Stainless steel 304L Construction material	Steel 37, Construction material
^{22}Na	2.6 a	Ge(Li)	6.21x10^3		4.08x10^1		
^{55}Fe	2.7 a	Low level	1.13x10^7	1.19x10^2	2.28x10^5	2.95x10^4	1.76x10^4
^{60}Fe	1.5x10^6 a	AMS	2.38	6.51x10^{-3}	5.47x10^{-5}	1.06x10^{-5}	1.91x10^{-5}
^{60}Co	5.27 a	Ge(Li)	1.09x10^7	1.26x10^3	5.61x10^4	5.71x10^4	1.12x10^5
^{108m}Ag	127 a	Ge(Li)	2.68x10^1	7.49x10^{-1}		3.78x10^{-1}	≤5.4x10^{-1}
^{125}Sb	2.77 a	Ge(Li)			3.81x10^1		
α emitters	sum	α-spectr.	≤2.4x10^{-2}	≤3.5x10^{-3}	≤8.7x10^{-3}	≤5.7x10^{-3}	≤8.6x10^{-3}

Laboratory for Ion Beam Physics

LABORATORY FOR ION BEAM PHYSICS

M. Suter (ETHZ), H.-A. Synal, M. Döbeli (PSI)

INTRODUCTION

Ion beam physics deals with the production and acceleration of electrically charged particles. Originally, most of the ion beam techniques have been developed for basic research to study fundamental properties of elementary particles, atoms and molecules. Today these methods have not only found applications in many technological fields but also in earth sciences, archeology and bio-medicine. The PSI/ETH Laboratory of Ion Beam Physics is located at ETH Hönggerberg. Presently, two particle accelerators are available: a tandem van-de-Graaff type accelerator with a maximum terminal voltage of 6 million volts and a new compact instrument providing ion beams with energies in the range of a few hundred keV to about 2 MeV.

ACCELERATOR MASS SPECTROMETRY

The laboratory's primary fields of research are related to new detection techniques including the development of novel instrumentation and equipment. Moreover, we are involved in a wide range of research programs within national and international collaborations. The main research activity is accelerator mass spectrometry (AMS). With an appropriate combination of mass spectrometric methods and accelerator technology this measurement technique allows do detect minute isotopic concentrations (10^{-10} to 10^{-15}) of ions with specific mass and nuclear charge. The sample size is typically in the range of about 1 mg. The method is especially suited for the measurement of long-lived radionuclides such as ^{10}Be, ^{14}C, ^{26}Al, ^{36}Cl, ^{41}Ca and ^{129}I. These nuclides are produced in the terrestrial environment by cosmic rays or by the decay of primordial radioactive nuclides. In addition, some of them have been produced and released in significant quantities as a consequence of military and civil use of nuclear fission. They can serve as tracers and can be used for dating purposes. Therefore, AMS has become an invaluable tool in climate studies ranging from the present to millions of years ago. The most important application is ^{14}C dating. With AMS, it has been possible to reduce the sample size by about 3 orders of magnitude compared to the conventional decay counting techniques. This opened many new applications in the earth sciences and allows for almost non-destructive dating of art objects.

MATERIALS SCIENCES

Nuclear scattering and reactions have been studied for many decades with extreme care and precision. Therefore, the cross sections and reaction products are so well characterized that some of the most reliable and sensitive methods of materials analysis could be developed. For analysis, the sample surface is bombarded by a MeV ion beam, and scattered particles or nuclear reaction products are detected. From their properties the composition of the surface can be deduced. The most commonly applied method is RBS (Rutherford Backscattering). A typical measurement takes only about ten minutes and yields the elemental concentration profile of approximately the uppermost micrometer of the sample surface. It has potential applications in most fields of science and technology. Services are also offered to industry. In addition, materials can be modified by irradiation with ion beams. Implantation of ions is used to produce structural damage, to dope materials, or even to synthesize layers of specific compounds. This allows to taylor electrical, optical or mechanical properties of surfaces.

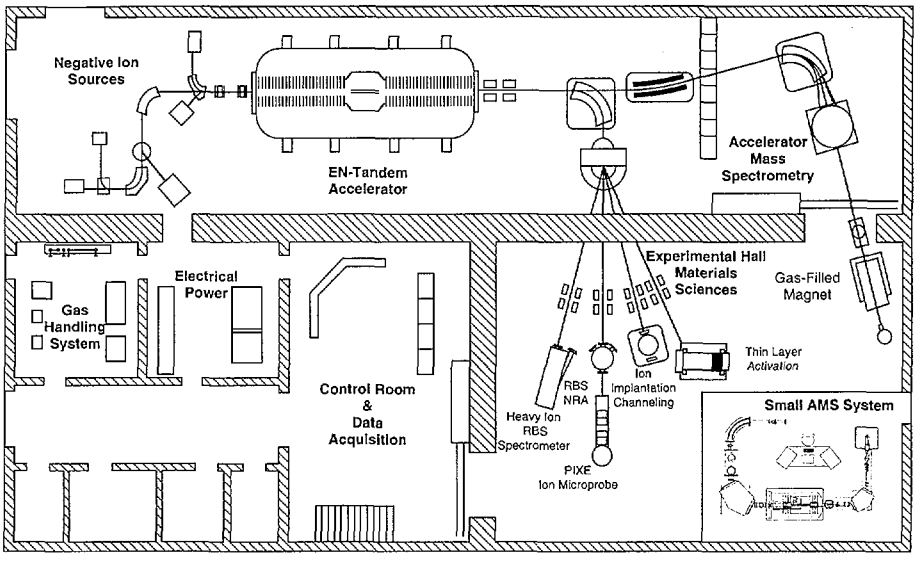

Layout of the experimental facilities of the Laboratory of Ion Beam Physics.

HE PSI/ETH TANDEM ACCELERATOR FACILITY

H.-A. Synal, M. Döbeli, H. Fuhrmann, P.W. Kubik (PSI),
G. Bonani, A. Duhr, P. Gartenmann, I. Hajdas, S. Ivy-Ochs, S. Jacob, C. Maden, R. Mühle,
J. Scheer, Ch. Schnabel, M. Suter, S. Tschudi (ETHZ)

The 1999 AMS operation of the PSI/ETH tandem accelerator facility at ETH Hönggerberg is summarised in a detailed compilation of beam time allocation and the number of measured samples, together with a breakdown according to major fields of research.

	Hours			%			Samples		
	1997	1998	1999	1997	1998	1999	1997	1998	1999
AMS Be-10	653	475	373	25.4	17.1	13.7	1193	1098	1187
C-14	718	881	842	27.9	31.7	30.9	1429	1755	1768
Al-26	71	103	48	2.8	3.7	1.8	129	231	83
Cl-36	227	161	313	8.8	5.8	11.5	534	401	623
I-129	121	111	103	4.7	4.0	3.8	310	291	327
Heavy Elements	106	81	99	4.1	2.9	3.6	5	2	12
Subtotal	1896	1812	1778	73.8	65.3	65.2			
Materials Sciences	295	416	357	11.5	15.0	13.1			
Accelerator SIMS	107	171	193	4.2	6.2	7.1			
Tests	82	119	57	3.2	4.3	2.1			
Conditioning	189	257	344	7.4	9.3	12.6			
Total	2569	2775	2729	100	100	100	3595	3778	4000

Beam time statistics 1997-1999

Research Field	Be-10	C-14	Al-26	Cl-36	I-129	Total	
Oceanography	194	227				421	11%
Polar ice	459			374		833	21%
Limnology	148				23	171	4%
Atmosphere	19	39		10	20	88	2%
Environmental Monitoring				10	128	138	3%
Exposure Age Dating, Others	79	137	58	113	28	415	10%
Earth Sciences (Total)	899	403	58	507	199	2066	52%
Meteorite/Cross Sections	16		6		6	28	1%
Archaeology		707				707	18%
Others, Tests	43	347	1	24	60	475	12%
Subtotal	59	1054	7	24	66	1210	30%
Standards	156	231	12	61	42	502	13%
Blanks	73	80	6	31	20	210	5%
Total	1187	1768	83	623	327	3988	100%

Compilation of measured AMS samples at the PSI/ETH AMS facility in 1999

With 2729 hours of operation, the PSI/ETH tandem accelerator was running approximately 2% less than in 1998 due to an unexpected shutdown in December. Insufficient voltage stability of the accelerator caused by the degrading performance of the charging belt prevented AMS measurements, which were planned for December 1999. However, the total number of analysed samples was still 6% more than in 1998. Of the total beam time 65% was devoted to accelerator mass spectrometry, 13% to materials sciences and 7% was used to measure stable trace elements in connection with the focused ion beam sputter source. About 13% of the total beam time were needed for conditioning the accelerator.

Again, the number of measured radiocarbon samples has increased. The trend toward measurements, which require high precision, is continuing in the research fields of oceanography and archaeology. In 1998, the average time of the measurement for a single ^{14}C, ^{36}Cl or ^{26}Al sample was about 30 min, whereas for ^{10}Be and ^{129}I samples less than 20 minutes of measurement time were needed. In particular in the case of ^{10}Be, the average beam time per sample could be reduced significantly due to the consequent use of the high current ion source. A very large number of measurements of ^{10}Be and ^{36}Cl samples have been made to analyse polar ice cores. The potential of ^{36}Cl measurement as a tool for surface exposure age dating has been evaluated.

Operation of the new small AMS system for radiocarbon dating has been started and first high precision measurements of standard samples were successfully conducted, which clearly demonstrate the potential of the new technique. Blank samples gave background values similar to those observed at the large AMS system.

MOLECULE DESTRUCTION BY COLLISION WITH STRIPPER GAS ATOMS THE KEY FOR AMS AT SUB MEV

S.A.W. Jacob, M. Suter (ETHZ), H.-A. Synal (PSI)

AMS using charge states $q \leq 2^+$ ions requires molecules to be suppressed in collisions with stripper gas atoms by as much as 10 orders of magnitude. Molecule destruction processes for carbon beams in several types of stripping gases have been investigated at energies between 200 keV and 600 keV at the new ETH/PSI small AMS facility.

Until recently it has been customary in AMS to eliminate molecular background by charge exchanging the negative ions into charge states $q>2^+$ where molecular bonds are no longer stable. But several experiments [1, 2, 3, 4, 5] have shown that molecules even in charge states $q=1^+$ and $q=2^+$ and at low energies can be destroyed solely in collisions with stripper gas atoms.
The intensity of molecules of atomic mass 14 in the charge states $q=1^+$ and $q=2^+$ has been studied as a function of stripper gas area density for various stripper gases and for energies between 200 keV and 600 keV.

EXPERIMENTS

All experiments have been performed using the internal gas stripper of the new ETH/PSI small AMS facility. At the focal point of the mass 14 beam between the magnet and the electrostatic analyzer (ESA) [5], a thin carbon foil can be inserted into the beam. Molecules surviving the stripping process in the accelerator will break up passing through this foil [6], and their fragments can be separated with the ESA. Energy spectra of the remaining particles (primary ions or molecular fragments) were measured with a silicon surface barrier detector.

RESULTS

A typical set of data for a stripping energy of 332 keV in Ar gas is shown in figure 1.

Figure 1

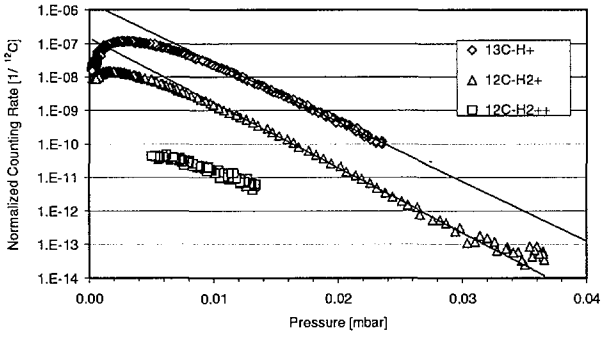

Fig. 1: Molecule intensity as measured after the stripper. The stripper gas area density can be calculated from the stripper pressure.

The negatively charged ions (atomic and molecular) entering the stripper change into positive charge states through electron loss processes. At stripper gas area densities below the density for charge state equilibrium, the population of the positive charge states increases, and information on the ionization cross sections and associated survival probabilities for molecules can be obtained. At higher stripper gas area densities an exponential decrease of the molecular component is found, which can be described with a destruction cross section σ.

$N(d) = N_0 \cdot e^{-\sigma \cdot d}$.

The dominant molecular component at mass 14 is $^{13}CH^+$. About one order of magnitude less intense is the $^{12}CH_2^+$ component. $^{13}CH^+$ is also the most intense molecular component of mass 14 extracted from the ion source. For charge state $q=2^+$ only the $^{12}CH_2^{++}$ component could be identified. $^{13}CH^{++}$ did not seem to be sufficiently stable to survive the stripping process with a detectable intensity.

All carbon molecules show a similar destruction behavior. Destruction cross sections are almost constant, around $8 \cdot 10^{-16}$ cm^2 for $^{13}CH^+$ in argon. This implies that a suppression factor of more than 10^{10} can be obtained with about 2 µg/cm^2 stripper gas area density. Destruction cross sections per target molecule have been compared for Ar, N_2 and CO_2. Also here, only slight variations have been found with CO_2 giving about 20% higher values compared to Ar and N_2.

CONCLUSIONS

The results clearly show the potential of radiocarbon AMS for terminal voltages down to only 200 kV. Molecules can be destroyed efficiently in collisions with stripper gas atoms in the entire energy range under investigation. In order to suppress the molecular background to levels sufficient for radiocarbon dating, stripper gas area densities of approximately 2 µg/cm^2 Ar equivalent are necessary.

REFERENCES

[1] H.W. Lee, A. Galindo-Uribarri, K.H. Chang, L.R. Kilius, A.E. Litherland, Nucl. Instr. and Meth. **B 5,** 208 (1984).

[2] H.W. Lee, Ph.D. Theses, Univ. of Toronto (1988).

[3] S.A.W. Jacob, Diploma Thesis at ETH Zürich (1996).

[4] M. Suter, S.A.W. Jacob, H.-A. Synal, Nucl. Instr. and Meth. **B 123,** 148 (1997).

[5] M. Suter, R. Huber, S.A.W. Jacob, H.-A. Synal, J.B. Schroeder, AIP Conference Proceedings **475**, „Application of Accelerators in Research & Industry 2", p. 665 (1999).

[6] B.J. Hughey, R.E. Shefer, R.E. Klinkowstein, X.L. Zhao, W.E. Kieser, A.E. Litherland, Nucl. Instr. and Meth. **B 123**, 186 (1997).

^{10}Be EXPOSURE DATING OF THE YOUNGER DRYAS SALPAUSSELKÄ I GLACIAL FORMATION IN SOUTHERN FINLAND

S. Tschudi, S. Ivy-Ochs, C. Schlüchter (University of Bern), P. Kubik(PSI), H. Rainio (Geological Survey of Finland)

Boulders of the Younger Dryas Salpausselkä I formation west of Lahti, southern Finland, were sampled for surface exposure dating. The ^{10}Be concentrations yield a minimum mean exposure age of 11'200 ± 270 years, using recently published production rates scaled for altitude and latitude and corrected for post-glacial isostatic rebound. If an erosion rate of 5 mm/ky is used as an estimated maximum value, our mean exposure age increases to a maximum exposure age of 11'780 ± 280 years. This is the first direct dating of the classical Younger Dryas formation Ss I, since previous dating was mainly based on varve counting supported by few radiocarbon dates.

INTRODUCTION

The Younger Dryas (YD) margin of the Scandinavian ice-sheet is one of the most impressive glacial formation on Earth. The Finnish Salpausselkä (Ss) ice marginal formations, two sub-parallel main ridges Ss I and Ss II, are part of this geomorphological feature, which can be mapped over a length of about 600 km. Studies on these formations have a long scientific tradition in Finland providing key information for the understanding of geologic processes during the last glaciation and its termination in northern Europe. The ages of the Ss formations were always among the most important questions to be answered. First estimates were given by Sauramo, using the technique of varve chronology [1] in southern Finland. The currently accepted time-frame for the deposition of Ss I in the area of Lahti, based on the varve chronology of Niemelä, Cato and Strömberg [2, 3, 4], ranges between 11'430 and 11'680 years BP. Donner [5] concluded that Ss I and also Ss II were formed during the YD Chronozone. This identification is, however, still based on indirect dating and correlation, and absolute dates are not available. This lack can be overcome by the technique of exposure age dating performed on rock surfaces using cosmogenic nuclides (e.g. ^{10}Be, ^{21}Ne, ^{26}Al and ^{36}Cl). The four samples were taken in the Vesala section of Ss I, west of Lahti (Fig. 1).

METHOD

To calculate exposure ages, we used the ^{10}Be production rate of Kubik et al. [6], which was scaled for altitude and latitude according to Lal [7]. The production rate was corrected for the sample thickness [8] and for a rapid and intensive uplift of the Fennoscandian lithosphere, which started just after the deglaciation [9]. The corrections lead to a production rate of 6.44 atoms per gram per year, which is 4 % lower than the value corresponding to the present elevation. No corrections for vegetation nor snow coverage were done, since both factors are rather unknown and not constant in time.

RESULTS AND CONCLUSIONS

The ^{10}Be exposure ages of the sampled boulders range from 10'820 to 11'680 calendar years [10]. The overall minimum exposure age of the Ss I formation west of Lahti, calculated as a non-weighted mean age of all four samples, is 11'200 ± 270 years. Exposure ages are calculated as minimum ages using a non-erosion condition. We also used a maximal erosion rate of 5 mm/ky for our four samples. This assumption increases our non-weighted mean exposure age of Ss I to 11'780 ± 280 years. Our results satisfy the Finnish varve chronology, which defines a deposition of Ss I between 11'430 and 11'680 calendar years and a correlation with the YD cold event, ranging from 11'550 to 12'700 calendar years, as defined by the GRIP ice core [11].

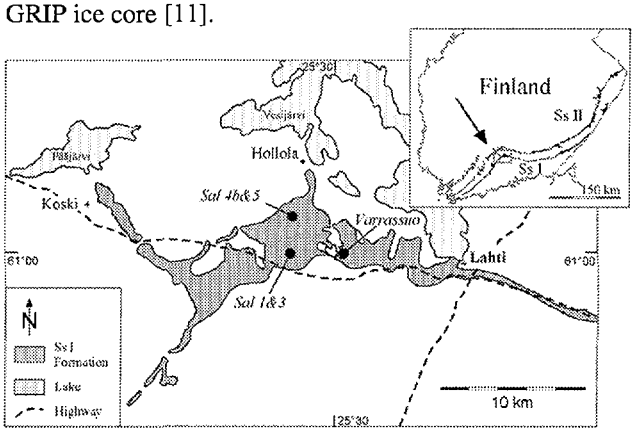

Fig. 1: Sketch map of the Salpausselkä I sample site.

REFERENCES

[1] M. Sauramo, Fennia **41 (1)**, 44 (1918).

[2] J. Niemelä, Geological Survey of Finland Bulletin **253**, 79 (1971).

[3] I. Cato, Sveriges Geologiska Undersökning Ser. **Ca 68**, 55 (1987).

[4] B. Strömberg, Ann. Acad. Scientarium Fennicae **A III 154**, 32 (1990).

[5] J.J. Donner, Com. Phys. Math. **48**, 11 (1978).

[6] P.W. Kubik et al., EPSL **161**, 231 (1998).

[7] D. Lal, EPSL **104**, 424 (1991).

[8] J. Masarik, R.C. Reedy, EPSL **136**, 381 (1995).

[9] N.A. Mörner, in Earth Rheology, Isostasy and Eustasy, John Wiley & Sons, Chichester, (1980) p. 251.

[10] S. Tschudi, S. Ivy-Ochs, C. Schlüchter, P. Kubik, H. Rainio, submitted to Boreas, (2000)

[11] S.J. Johnsen et al., Nature **359**, 311(1992).

THE DETERMINATION OF LARGE-SCALE EROSION RATES USING ^{10}Be, AND A COMPARISON TO CONVENTIONAL RIVER LOAD GAUGING TECHNIQUES

F. von Blanckenburg, M. Schaller (Universität Bern), N. Hovius (Cambridge), P.W. Kubik (PSI)

We have measured river catchment-wide erosion rates using cosmogenic ^{10}Be in the bedload-borne quartz of three European rivers. The comparison with conventional river load gauging shows that this is a feasible technique.

The most common method used for studies of large-scale continental erosion is to measure sediment and dissolved load discharged by rivers and then to convert this information to a rate of downwearing of the landscape [1, 2]. This requires long-term (decades), and daily measurements to account for variability in discharge and sediment load. Yet the results are mostly inaccurate, due to sediment released only during rare flood events, and the construction of dams that reduces sediment transport.

We are making use of a novel geochemical technique. Erosion rates can be measured by accelerator mass spectrometry (AMS), using the concentration of the rare cosmogenic nuclides ^{10}Be and ^{26}Al in quartz from the bedload of rivers. This techniques utilises the fact the earth's surface is continuously bombarded by cosmic rays which induce nuclear reactions in the upper decimeters of rocks. The concentration of nuclides thus produced is controlled by the erosion rate of the landscape. Initially this technique was developed for the determination of exposure ages and of bedrock erosion rates. Considering that an entire river catchment is the „sample" eroded, and assuming that this landscape is in steady state between erosion and nuclide production, then the catchments erosion rate can be determined from a handful of bedload-borne quartz [3, 4, 5].

We have tested this method on three rivers, and have compared the results with erosion rates that can be calculated from the suspended and dissolved loads measured in the past 30 years by the national river authorities. The three rivers are the Regen (Bayerischer Wald, SE Germany, crystalline bedrock), the Loire and Allier (Massiv Central, France, crystalline bedrock) and the Neckar (SW Germany, Mesozoic Sediments).

RESULTS

There is a good agreement between these entirely different techniques, and there is also a pattern of sedimentary bedrock areas (Neckar) that tend to erode more rapidly than crystalline basement areas. However, close comparison between the methods shows that in crystalline areas, conventional data is always 2-3x lower than cosmogenic rates (Table 1).

River	Conventional Rate	Cosmogenic Rate
Regen	8-10 mm/ka	22-27 mm/ka
Loire/Allier	5-20 mm/ka	25-55 mm/ka
Neckar	50-80 mm/ka	50-90 mm/ka

Tab. 1: Erosion rates (conventional and cosmogenic) for three European rivers systems

Possible reasons for this discrepancy are:

1. Monitoring of suspended loads is not performed on a daily basis, in cases of floods even on an hourly basis, and the correction of dissolved data for anthropogenic input is inaccurate.
2. The conventional rates miss out on rare high-magnitude low-frequency events, such as centennial or millennial floods. These events will carry the bulk of the sediment. By comparison, cosmogenic rates integrate over several thousand years (10ka Neckar; 20-30ka Regen, Loire).
3. The cosmogenic rates, given their long integration time, carry a „memory" of past, possibly higher erosion rates, such as prevailing possibly in the last cold period in Middle Europe.

We believe that the cosmogenic technique has considerable potential for the determination of time-integrated denudation rates. The erosion rates presented here for Middle Europe are low. However, the method is now maturing to a sufficient sophistication to become applicable to studies of active mountain belts. Further, this might become a tool to derive soil erosion taking place by action of nature (time-averaged cosmogenic erosion rates) vs soil erosion induced by man (short-term rates from river load gauging).

REFERENCES

[1] P. Pinet, M. Souriau, Tectonics **7**, 563 (1988).
[2] M. A. Summerfield, N. J. Hulton, J. Geophys. Res. **99**, 137871 (1994).
[3] D. E. Granger et al., J. of Geology **104**, 249 (1996).
[4] P. Bierman, E. J. Steig, Earth Surface Processes and Landforms **21**, 125 (1996).
[5] E. T. Brown, et al., Earth and Planet. Sci. Lett. **129**, 193 (1995).

EXPOSURE AGE AND PALEOCLIMATIC INTERPRETATION OF THE GSCHNITZ MORAINE AT TRINS, AUSTRIA

S. Ivy-Ochs (ETHZ & Univ. Bern), H. Kerschner (Univ. Innsbruck), P.W. Kubik (PSI), C. Schlüchter (Univ. Bern)

Preliminary ^{10}Be and ^{26}Al exposure ages indicate that the Gschnitz stadial moraine at Trins Austria formed around 16,000 years ago. Precipitation was one third of today's and summer temperature was 10 degrees lower, based on reconstruction of the former glacier topography.

The general downwasting of Alpine glaciers after the Last Glacial Maximum (LGM) around 20,000 years ago was interrupted by a number of successively smaller readvance periods ("stadials"). They are documented by numerous morainic systems in the alpine valleys and cirques, which have been mapped over wide areas of the Alps since the second half of the 19th century. With the exception of the Younger Dryas "Egesen Stadial" [1], the absolute age of the of the stadials remains unclear. Numerous minimum radiocarbon ages suggest that most of them, including the "Gschnitz Stadial" occurred before the onset of the Bølling Interstadial, that is during the Oldest Dryas. Geomorphological and geological field evidence shows that glaciers during the Gschnitz Stadial advanced over ice-free terrain for considerable distances. Consequently, large parts of the Central Alps were already ice-free and only covered by local glaciers some time before the beginning of the Bølling.

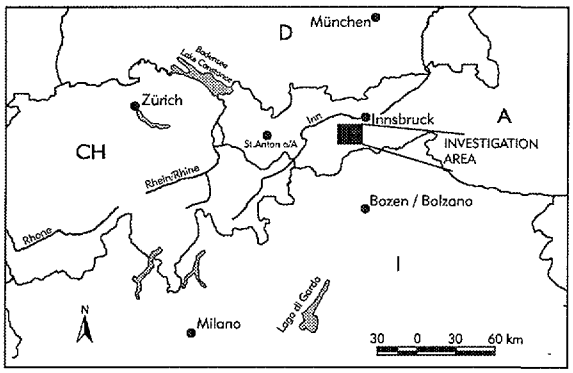

Fig. 1: The study area near Trins, Austria.

The moraine complex near Trins in the Gschnitz valley is situated ca. 30 km to the Southwest of Innsbruck and ca. 150 km from the LGM end moraines of the Inn Glacier system. The end moraine at Trins itself (at an altitude of 1200 m) is about 30 m high and shows no signs of post-depositional periglacial reworking. On the orographic left lateral moraine the glacier tongue was covered with crystalline rockfall debris. There, the end moraine complex is composed of several closely spaced walls. Kettleholes in the moraine complex show that the ice was thickly covered by debris. Samples were taken all along both sides of the lateral moraine system as well as the front of the end moraine. Most were of coarse-grained gneiss containing frequent stringers and blebs of quartz, which were sampled. Winter snow cover is typically in the order of a few tens of centimetres for 3 - 4 months. Five samples have been analyzed so far. Preliminary ^{10}Be and ^{26}Al exposure ages (production rates and scaling of [2]) range between 10,300 and 16,200 years, with no clear distribution related to location along the moraine complex. The reasons for the spread in ages are unclear. Some of the possible explanations are: exhumation of the boulders along the moraine crest [3], shattering of boulders (not apparent when sampling), thick drifts of snow due to the trees, or actual coverage by trees. Indeed, today several large boulders (not sampled) have trees (spruce, larch) growing directly on them. Perhaps a combination of all of these expresses what actually happened. When there is no distinct mode, the oldest age is generally taken to be closest to the age of moraine formation. Therefore, the moraine was finally stabilized after downwasting of the glacier about 16,000 years ago.

The lateral moraines are almost completely preserved for a distance of more than three kilometres up to an altitude of 1410 m. Above the village of Gschnitz, 6-6.5 km from the end moraine, remnants of moraines at an altitude of 1520 - 1540 m can be traced to the lateral moraines downvalley. Because of the simple shape of the valley, the former glacier topography can be easily reconstructed. The equilibrium line altitude (ELA) was at 1930 m, about 700 m lower than the Little Ice Age (1850) ELA in that area. With the ELA, ice flux through selected cross sections and mass-balance gradients are calculated from reconstructed glacier topography. They are used to determine net ablation and accumulation and precipitation under the assumption of steady-state. The former temperature at the ELA and temperature change is estimated using various glacier-climate models. During the Gschnitz stadial, precipitation was less than one-third of today's values and summer temperature was roughly 10 degrees lower or very similar to full glacial conditions [4]. In comparison, climate during the Younger Dryas (Egesen stadial) in the Alps was much warmer, only 2-3 degrees cooler than today [5].

REFERENCES

[1] S. Ivy-Ochs, C. Schlüchter, P.W. Kubik, G.H. Denton, Geografiska Annaler **81 A**, 313 (1999).

[2] D. Lal, Earth and Planet. Sci. Lett. **104,** 424 (1991).

[3] M.G Zreda, F.M. Phillips, D. Elmore, Water Resources Research **30,** 3127 (1994).

[4] H. Kerschner, S. Ivy-Ochs, C. Schlüchter, Annals of Glaciology **28,** 135 (1999).

[5] H. Kerschner, Z. Gletscherkunde Glazialgeologie **21,** 363 (1985).

COSMOGENIC ^{10}BE AND ^{26}AL EXPOSURE DATING OF ANTARCTIC GLACIATION

M. Bentley (University of Edinburgh), P.W. Kubik (PSI)

Preliminary cosmogenic Be-10 and Al-26 exposure dates on erratic boulders from the Weddell Sea region, Antarctica, reveal a complex glacial history for the area.

INTRODUCTION

The timing of glaciation in Antarctica is important for understanding mechanisms of global climate change and assessing the source of global sea level rise. The timing of ice retreat following the Last Glacial Maximum (LGM) in Antarctica relative to ice masses elsewhere in the world provides clues as to how the abrupt change from glacial to interglacial conditions occurred. It also allows us to determine the Antarctic contribution to the 120 m rise in global sea level following the LGM. The biggest unknown in the Antarctic contribution to global sea level is the former volume of ice in the Weddell Sea embayment during the LGM and the timing of its release into the global ocean.

For these reasons we have begun a programme of dating deglaciation from the Antarctic Peninsula flank of the Weddell Sea. We have sampled erratic boulders from nunataks. All boulders were sampled from level sites with minimal topographic shielding. Additionally, we have begun to map out the former horizontal and vertical limits of the ice sheet, and former flow directions in order to provide constraints for numerical ice sheet models.

ANALYTICAL PROCEDURES

Rock samples were crushed and the mineral sand selectively purified to pure quartz using heavy liquid separation and selective dissolution in weak hydrofluoric and nitric acids [1, 2]. The quartz was then dissolved and the cosmogenic Be-10 and Al-26 extracted and purified before measurement of isotopic ratios at the PSI/ETH AMS facility. Samples were spiked with a precisely known amount of a Be-9 1000 ppm standard solution. Total aluminium concentrations in the quartz were measured by Inductively Coupled Plasma Mass Spectrometry (ICPMS).

Preliminary exposure ages have been calculated using the production rates of Lal [3], scaled to sample latitude and altitude. Production rates have been corrected for local topographic shielding and sample thickness. The exposure ages are blank-corrected.

RESULTS

The exposure ages show a number of features. The dates for glaciation can be divided into three broad groups (Table 1). The youngest group lie between ca. 10 ka and 16 ka. Of particular interest is that three out of the four samples are from boulders of the same granitic lithology at the same nunatak site in the Behrendt Mountains, southern Antarctic Peninsula. For this reason these dates are interpreted as representing deglaciation of the Behrendt Mountains, with continuous exposure since that time. They imply that deglaciation of the southern Peninsula was underway by c. 14-16 ka. If these samples were reworked boulders with a complex exposure history, it is unlikely that they would give such similar exposure ages for different boulders from the same nunatak site.

Sample name	Be-10 age (ka)	Al-26 age (ka)
BEH 1	9.0 ± 0.9	10.7 ± 1.4
BEH 2	14.0 ± 1.1	14.4 ± 1.4
BEH 3	12.0 ± 3.4	16.2 ± 1.2
ABL 1	-	16.2 ± 1.4
BAT 1	37.5 ± 3.0	30.5 ± 3.5
BAT 3	-	30.8 ± 2.6
BAT 2	27.3 ± 3.2	33.5 ± 3.0
ABL 2	-	39.1 ± 3.8
SWE 1	-	45.7 ± 3.0
FER 1	55.4 ± 2.5	57.8 ± 4.5
DEW 2	52.6 ± 8.7	58.5 ± 3.9
DEW 1	104 ± 6	89.6 ± 7.0
SKY 1	140 ± 6	104 ± 7
SKY 2	134 ± 14	130 ± 9
FER 2	416 ± 9	344 ± 23

Tab.1: Exposure ages for erratic boulders

The second group of dates lie in the range ca. 30 -60 ka. There are at least two possible interpretations of these dates. First, they may represent one or more deglaciation events between ca. 30 ka and 60 ka, with continuous exposure since. This interpretation is supported by the consistent exposure ages of ca. 30 ka for the three samples from the Batterbee Mountains. The fourth date is from the nearby Ablation Valley. The three samples with slightly older exposure ages (SWE 1, FER 1, and DEW 2) all come from sites in the southern part of the study area. An alternative model for this group of dates is that they are reworked boulders and that they represent cumulative exposure over more than one interval. In this case, the samples are not old enough for this complex exposure history to be revealed by the differential decay of ^{10}Be and ^{26}Al. However, the concordance of dates from all three samples in the Batterbee Mountains suggest that the 30 ka dates may represent a 'real' event.

A third group of dates lie in the range ca. 90 to ca. 415 ka. For three out of four of these dates the Al and Be data do not agree within one standard deviation, with consistently higher Be exposure ages than for the Al. This is characteristic of samples with complex exposure histories.

REFERENCES

[1] C.P. Kohl, K. Nishiizumi, Geochim. Cosmochim. Acta **56**, 3583 (1992).

[2] H.A.P. Cockburn, Ph.D. Thesis, University of Edinburgh, (1998).

[3] D. Lal, EPSL **104,** 424 (1991).

EXPOSURE DATING USING IN SITU PRODUCED CHLORINE-36 AT ETH/PSI: INITIAL EXPERIMENTATION OF THE SPIKE TECHNIQUE

C. Roth (ETHZ), S. Ivy-Ochs (ETHZ & Univ. Bern), H.-A. Synal (PSI), C. Schlüchter (Univ. Bern)

To extend the methodology of exposure age dating at the Zurich accelerator mass spectrometry facility, improvements in the ^{36}Cl technique have been made. For the determination of the total Cl concentration of a rock, which needs to be accurately known, the so-called spike technique has been investigated in detail. ^{36}Cl exposure ages for samples of different total Cl concentrations have been compared to results obtained with other cosmogenic nuclide methods.

The main difficulty of the ^{36}Cl method is that both, the ^{36}Cl and the total Cl concentration of the investigated rock have to be known. The Cl concentration of the samples can be measured with the spike technique on the exact same samples by changing the natural $^{37}Cl/^{35}Cl$ ratio with a known amount of isotopically pure ^{35}Cl carrier. With this spike technique it is possible to measure Cl concentrations below 50 ppm, where commercial methods often fail.

Test measurements were made to investigate the suitability of this technique for the Zurich AMS facility. In a dilution series, samples corresponding to typical rock Cl concentrations of 5-200 ppm were produced and measured with Secondary Ion Mass Spectrometry (SIMS) at the ETH/PSI AMS system [1]. The ^{35}Cl spike solution was only certified to be better than 99%. By comparing the nominal and measured isotopic ratios of the dilution series samples the purity of the spike solution could be determined to 99.7%. This value was confirmed with a blank sample prepared from the spike solution during a rock sample measurement series.

Cl concentration measurements of rock samples can be made with an accuracy of 0.5% at the 1σ level (Fig. 1).

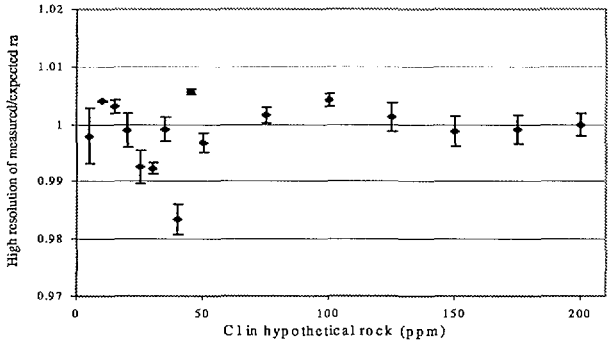

Fig. 1: The ratio of measured to calculated $^{37}Cl/^{35}Cl$ ratios for the dilution series. A ^{35}Cl purity of 99.7% for the spike results in a best fit to this ratio being equal to 1.

Four rock samples have been chosen for exposure age dating with ^{36}Cl and the Cl determination with the spike technique. Cl was extracted by dissolving the rock based on the method described by Ivy-Ochs [2] with significant modifications [3]. Cl was finally precipitated as AgCl for the SIMS and the AMS analyses. Two samples from Antarctica, involved in the palaeoclimate issue about the behavior of the East Antarctic Ice Sheet during the Pliocene, were chosen as representatives for old samples. From New Zealand, two samples of younger moraines were chosen, as they are involved in the issue about synchrony or asynchrony of Younger Dryas and Last Glacial Maximum (LGM) in the northern and nouthern hemispheres.

The Antarctic samples have Cl concentrations of 176 ± 2 ppm and 205 ± 3 ppm, which agree well with ion-selective electrode (ISE) data of the same samples. ISE was chosen as reference method, because it is generally used to determine Cl in rocks. The Cl concentrations of the New Zealand samples were 6.7 ± 0.1 ppm and 10.2 ± 0.1 ppm. ISE gave controversial results on one of these samples and could not determine the the concentration of the other one. The ages were calculated with production rates based on data from [4] and corrections for elevation, latitude and depth according to [5] and [6].

The spike technique performed well for high Cl concentrations, but it has to be studied further for the lower concentration ranges. The calculated ^{36}Cl exposure ages are in very good agreement with results of other cosmogenic isotope methods for the Antarctic samples [7]. The Antarctic sample ages fit into the theory of stable cold climate in Wright Valley during the last 3.8 Ma. The data of the younger New Zealand sample agrees well with results of boulders from the same moraine, measured with another cosmogenic isotope method [7]. It is slightly older than the YD event as recorded in the GRIP ice-core [8], but still lies in the range of error. The second New Zealand sample clearly can be assigned to the LGM moraine.

REFERENCES

[1] H.-A. Synal et al., Nucl. Instr. and Meth. **B 56/57**, 864 (1991).

[2] S. Ivy-Ochs, Ph.D. Dissertation, ETH Zürich (1996).

[3] C. Roth, Diploma Thesis, ETH Zürich (1999).

[4] F. Phillips et al., Geophys. Res. Lett. **23, No. 9**, 949 (1996).

[5] D. Lal, Earth and Planet. Sci. Lett. **104**, 424 (1991).

[6] M. Zreda, Ph.D. Dissertation. New Mexico Inst. of Mining and Technology, USA (1994).

[7] S. Ivy-Ochs, (unpublished).

[8] J.S. Johnson et al., Nature **359**, 311 (1992).

THE HYPOTHESIS OF A DIRECT INFLUENCE OF COSMIC RAYS ON THE EARTH'S CLIMATE

G. Wagner, J. Beer (EAWAG), P.W. Kubik, H-A. Synal (PSI)

Based on the observational period 1980-96 it was claimed recently that fluctuations in the flux of cosmic rays influence climate via global cloud cover. Cosmogenic nuclide data from a polar ice core call this hypothesis into question. The smoothed combined flux of ^{10}Be and ^{36}Cl at Summit, Greenland, from 20-60 kyr BP (which is proportional to the incoming cosmic ray flux) is unrelated to the corresponding climate proxies $\delta^{18}O$ and CH_4.

There is increasing evidence that changes in climate may be closely related to changes in solar activity. Observed changes in total solar irradiance, measured by satellite since 1978, are only about 1.5 ‰ and are therefore considered to be too small to contribute significantly to climate changes observed since 1850 [1]. Recently, Svensmark and Friis-Christensen [2] suggested that changing solar activity may be triggering changes in the earth's climate by modulating the galactic cosmic ray (GCR) flux penetrating into the atmosphere. This hypothesis is based on changes in global cloud cover, which occurred in phase with changes in the GCR flux during the 1980s and 1990s.

Since clouds are important for the earth's radiation budget, variations in cloud cover caused by changes in the GCR flux will affect the climate. When cosmic ray particles enter the Earth's atmosphere, reactions take place causing ionization in the atmosphere at the same altitudes at which cloud formation occurs.

If the proposed causal relationship between GCR flux, cloud cover and mean global temperature is correct, then long-term variations in the GCR flux can be expected to cause variations in the mean global temperature. A very significant change in the GCR flux occurred about 40 kyr ago, when the geomagnetic field intensity was only about 10 % of its present value (the so-called Laschamp event) [3, 4].

Measurements of the radionuclides ^{10}Be and ^{36}Cl in the GRIP ice core, which are proxies for the GCR flux, are available for the last ice age [5, 6]. It has been shown that, after low-pass filtering, the combined flux of ^{10}Be and ^{36}Cl reflects the GCR flux, which is modulated by the changing geomagnetic field [4]. $\delta^{18}O$ and CH_4 can be used as proxies for the climate of the North Atlantic region. Both records are available as functions of time [7].

In figure 1, the combined, low-pass filtered flux of ^{10}Be and ^{36}Cl (reflecting the GCR flux) is compared with the $\delta^{18}O$ and CH_4 data (reflecting the climate). If the Svensmark hypothesis is valid, the maximum of the combined flux of ^{10}Be and ^{36}Cl should be correlated with the $\delta^{18}O$ data (note the inverse scale) and with the CH_4 data. A high value of the combined flux of ^{10}Be and ^{36}Cl corresponds to a high GCR flux, which should result in an increase in global cloud cover and a lower mean global temperature. This is, however, clearly not the case. During the Laschamp event (36 - 41.5 kyr BP), marked by a peak in the radionuclide data, the combined flux of ^{10}Be and ^{36}Cl is not correlated significantly with either $\delta^{18}O$ or CH_4. The same applies over the whole time interval shown in figure 1. From this we conclude that the relationship between cosmic rays and climate proposed by Svensmark and Friis-Christensen [2] and Svensmark [1] is not valid for the period investigated here.

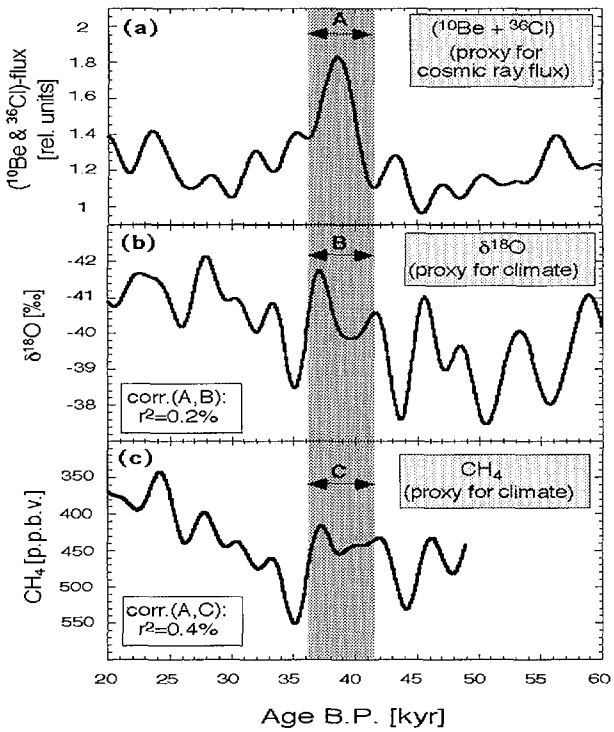

Fig. 1: (a) Normalized, combined flux of ^{10}Be and ^{36}Cl after low-pass filtering. (b, c) Corresponding $\delta^{18}O$ and CH_4 data from the GRIP ice core. These data can be interpreted as a climate proxy for the North Atlantic region. The $\delta^{18}O$ and CH_4 data are well correlated (r^2=0.61).

REFERENCES

[1] H. Svensmark, Phys. Rev. Lett. **81**, 5027 (1998).

[2] H. Svensmark and E. Friis-Christensen, J. Atm. Sol. Terr. Phys. **59**, 1225 (1997).

[3] Y. Guyodo and J.-P. Valet, Earth Planet. Sci. Lett. **143**, 23 (1996).

[4] G. Wagner, Dissertation ETH. No 12864.

[5] S. Baumgartner et al., J. Geophys. Res. **102 no. C12**, 26659 (1997).

[6] F. Yiou et al., J. Geophys. Res. **102 no. C12**, 26783 (1997).

[7] T. Blunier et al., Nature **394**, 739 (1998).

SPATIAL PREBOMB ^{36}Cl DISTRIBUTION IN CENTRAL GREENLAND ICE CORES

A. Stanzick, D. Wagenbach (Univ. Heidelberg), H.-A. Synal (PSI), S. Kipfstuhl (AWI, Bremerhaven)

Prebomb ^{36}Cl levels in 7 Central Greenland ice cores along the North Greenland Traverse have been measured. It turns out that deposition fluxes as well as the firn concentration of ^{36}Cl are controlled by the mean snow accumulation in this area. Re-evaporation of gaseous H^{36}Cl seem to be comparatively unimportant.

Between 1993 and 1995 the Alfred-Wegener-Institute for Polar and Marine Research and the Institute of Environmental Research of the University of Heidelberg carried out a largescale traverse in North-Central Greenland, where 12 deeper and 34 shallow firn cores have been recovered. The material has been used to study temporal and spatial trends of snow accumulation rates, stable isotopes (δ^{18}O, δD), aerosol related chemical species [1, 2] and cosmogenic and terrigenic radioisotopes (^{10}Be, ^{210}Pb).

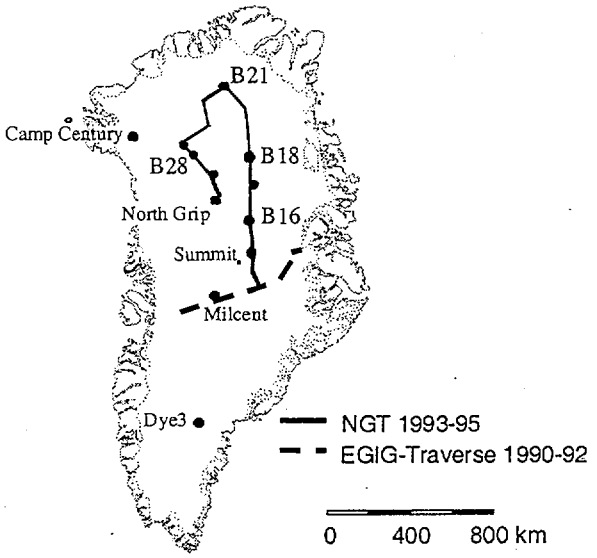

Fig. 1: Map of Greenland showing the sites where prebomb ^{36}Cl has been analysed along the North Greenland Traverse (NGT).

We have now analysed 7 deeper cores for prebomb ^{36}Cl. The annual accumulation rates of these locations vary between 0.1 m/yr and 0.18 m/yr. The new data are backed up by measurements of ^{10}Be covering the period 1861-1928 with a resolution of 22 years.

Supplemented by earlier measurements [3, 4] adjusted to the above period, a 300% spatial ^{36}Cl concentration variation for the Central Greenland ice sheet was found when the 36Cl concentration means of different sites were compared. A clear dependence of the ^{36}Cl concentration on the accumulation rate (Fig 2) suggests a relatively large dry deposition fraction. From the slope of the fitted line, a dry deposition rate of approximately 8 ^{36}Cl atoms / (m^2·sec) can be calculated, which corresponds to about 45% of the mean global ^{36}Cl production rate [5]. In contrast to nitrate [1], net loss of ^{36}Cl by re-evaporation of gaseous H^{36}Cl seems to play a minor role even at low accumulation sites taking into account the distribution pattern found.

Air/snow transfer studies and year round observations in Antarctica are expected to give new insights into the radioisotope's transport and deposition processes. In this context first analyses of atmospheric ^{36}Cl are going to be made at coastal Antarctica along with the two EPICA inland sites (DML & Dome C). Presently, also atmospheric sampling is performed at these sites during the summer campaign.

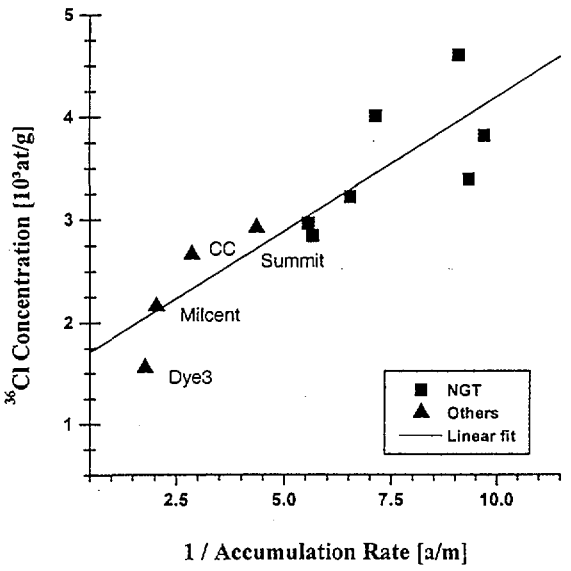

Fig. 2: Average prebomb ^{36}Cl concentrations versus inverse average snow accumulation rates for NGT and former measurements [3, 4] for Central Greenland.

REFERENCES

[1] H. Fischer, D. Wagenbach, J. Kipfstuhl, J. Geophys. Res. **103, (D17)**, 21927 (1997).

[2] H. Fischer et al., Geophys. Res. Lett. **25**, 1749 (1998).

[3] H.A. Synal et al., Nucl. Instr. Meth. **B 92**, 79 (1994).

[4] N.J. Conard et al., Radiocarbon **31 no. 3**, 585 (1989).

[5] J. Masarik, J. Beer, J. Geophys. Res. **104**, 12099 (1999).

PATHWAYS OF ^{10}Be IN HIGH NORTHERN LATITUDES

C. Strobl (Univerity of Heidelberg), P.W. Kubik (PSI), A. Mangini (Heidelberger Akademie d. Wissenschaften)

We investigated the sources and sinks of ^{10}Be in the Arctic Ocean. Our interest was focussed on the budget of „continental" ^{10}Be, especially in the shelf and continental slope area of the Laptev Sea (Siberia), which is characterized by an input of freshwater from the rivers Lena, Yana and Kathanga.

The cosmogenic radionuclide ^{10}Be ($t_{1/2}$ = 1.5 Ma) is a reliable stratigraphic tool for sediments from the Arctic Ocean with low or negligible content of biogenic carbonate. ^{10}Be records from sediment cores from the Norwegian and Greenland Sea exhibit high concentrations of ^{10}Be during the interglacials in contrast to lower values during glacial periods [1]. These distinct changes enable a glacial / interglacial stratigraphy of Arctic sediments.

The maxima of the ^{10}Be concentration could reflect an enhanced delivery of „continental" ^{10}Be with the Siberian rivers (e.g. Lena, Kathanga, Yenisei) during periods of deglaciation. As shown in Figure 1, the Arctic Ocean receives the influx of freshwater from several major river systems.

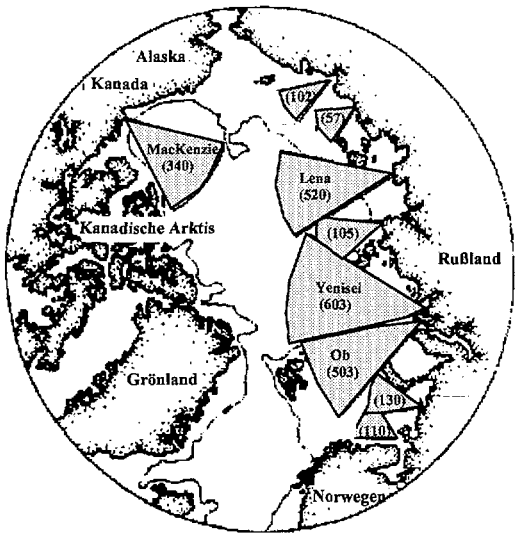

Fig. 1: River discharge to the Arctic Ocean (km^3 a^{-1}) [2].

As part of the Russian-German cooperative research project "System Laptev Sea" we focussed on the evaluation of the supply (e.g. rivers, atmosphere) and export fluxes (e.g. sea ice) of ^{10}Be in the shelf area and on the continental slope of the Laptev Sea.

RESULTS

In the Laptev Sea, near to the mouth of the river Lena, we determined depositional ^{10}Be fluxes of (140 ± 30) · 10^6 atoms a^{-1} cm^{-2}. The depositional ^{10}Be fluxes decrease clearly with increasing distance from the mouth of the River Lena (Fig. 2). 200 km away from the outflow area the values are about (20 ± 5) · 10^6 atoms a^{-1} cm^{-2}. These fluxes are 50 to 500 times higher than the atmospheric ^{10}Be input to the Arctic Ocean of (0.2 – 0.5) · 10^6 atoms a^{-1} cm^{-2} as determined in Greenland ice cores [3]. From this we conclude that the rivers are the main source of ^{10}Be in the shelf areas of the Arctic Ocean.

The depositional ^{10}Be fluxes on the continental slope of the Laptev Sea are in the range of (2 - 7) · 10^6 atoms a^{-1} cm^{-2}. These fluxes are still higher than the atmospheric input, whereas the depositional ^{10}Be fluxes of (0.2 - 0,.6) · 10^6 atoms a^{-1} cm^{-2} in the central Arctic Ocean reflect the atmospheric input of ^{10}Be. From these data we infer that the maxima of the ^{10}Be concentration observed in interglacial sediments of the central Arctic Ocean rather reflect the „normal situation", where the atmospheric flux is sedimented and the supply of „continental" ^{10}Be is negligible.

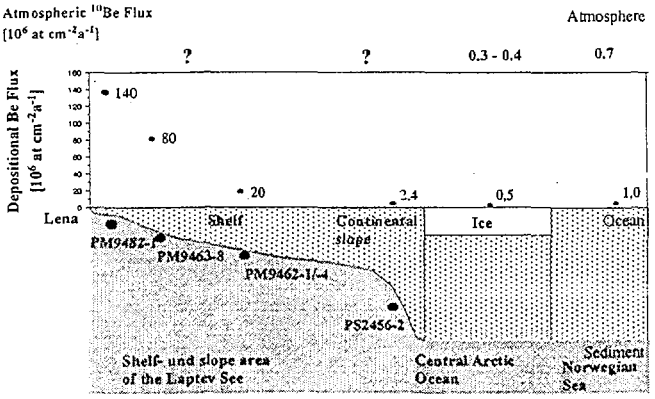

Fig. 2: Depositional ^{10}Be fluxes in the shelf and continental slope area of the Laptev Sea, the central Arctic Ocean and the Norwegian Sea.

CONCLUSION

From the comparison of the fluxes of ^{10}Be in the central Arctic Ocean, on the continental slope and in the shelf area of the Laptev Sea we conclude that most of the ^{10}Be delivered to the shelf area by the rivers Lena, Yana and Kathanga is deposited directly in the shelf area.

REFERENCES

[1] A. Eisenhauer et al., Earth Planet. Sci. Lett. **124**, 171 (1994).

[2] K. Aagard et al., J. Geophys. Res. **94 (C10)**, 14485 (1989).

[3] A. Stanzick, Diploma thesis, University of Heidelberg, (1996).

RADIOCARBON CHRONOLOGIES OF THE LATE GLACIAL COLD REVERSAL IN HUELEMO, CHILE AND MASCARDI, ARGENTINA

I. Hajdas, G. Bonani, D. Ariztegui (ETHZ), P. Moreno (Universidad de Chile)

Variability of atmospheric ^{14}C content complicates radiocarbon-based chronologies. However, specific features such as periods of constant ^{14}C age, so called plateaux (slow ^{14}C clock), or steep changes in radiocarbon ages (fast ^{14}C clock) can be helpful in correlation of climatic events. Here we report on the results of ^{14}C dating of two South American records of the Late Glacial climate: sedimentary records of the lake Huelmo in Chile and lake Mascardi, Argentina with well dated records in Northern Hemisphere.

The Younger Dryas (YD) cold event in the northern hemisphere belongs to the periods, which are most often discussed. Although this cold reversal observed in European records between 11 and 10 kyr BP was originally thought to be confined to the North Atlantic region, recently published studies of records around the world show similar events.

The question of inter-hemispheric climatic interactions remains open, however. Presence of the YD in the southern hemisphere, especially in South America, has been discussed for more than a decade. The debate cannot be settled with the help of models as long as there is not enough data to calibrate the models. One possibility for correlation and comparison of records is using chronology. Radiocarbon dating, which is commonly used in dating marine and terrestrial records, can be very useful in establishing such synchronising. Variations in the atmospheric ^{14}C content provide time markers. For example, the atmospheric $^{14}C/^{12}C$ ratio is known to increase dramatically around 11 kyr ^{14}C (a fast change from 11 kyr BP to the younger ca. 10.6 kyr BP radiocarbon ages) and then dropped during the following millennium creating radiocarbon age plateaux [1].

THE HUELMO AND MASCARDI CHRONOLOGIES

We have focused on chronologies of two sites from South America: the Huelmo (41 31S, 73 00W) mire and sediments of Lake Mascardi (41 08S, 71 34W). Both sites have been studied for paleoclimatic reconstruction of the last deglaciation. Vegetation history has been reconstructed using pollen from sediment cores of the Huelmo site [2]. Pollen data from the Chilean Lake District show that the warming, which began around 14.5 kyr BP, was punctuated by cold events. The last of the cold cycles appeared in Huelmo pollen record around 11 kyr BP.

Similarly, the changes observed in sediments of Mascardi show that warming was not uniform. This lake is located close to the Tronador ice cap. An expansion of the Tronador ice cap at the end of the Late Glacial as deduced from the proxy data was also dated to be close to the European YD [3].

When plotted versus sediment depth, both chronologies reconstruct characteristic features of the radiocarbon time scale such as plateaux and wiggles observed in data from tree rings, varves, lake sediments. Based on this dating the cooling at Huelmo and Mascardi occurred around 11,400 yr. BP and preceeded the European YD cold event by some 500 to 600 cal years (Fig 1).

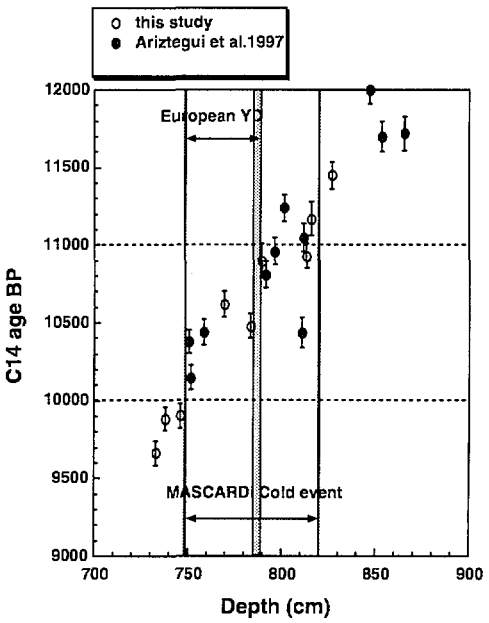

Fig. 1: Radiocarbon chronology of Lake Mascardi.

REFERENCES

[1] I. Hajdas et al., Geology **26**, 1047 (1998).

[2] P.I. Moreno, J. Quaternary Sci. **12**, 485 (1998).

[3] D. Ariztegui et al., Quaternary Sci. Rev. **12**, 333 (1997).

RADIOCARBON AGES FROM SEQUENTIAL LEACHES OF LACUSTRINE OSTRACODS, CARSON SINK AND MONO LAKE PLEISTOCENE SECTIONS

S.R. Hemming (Columbia University), I. Hajdas, G. Bonani (ETHZ)

Radiocarbon dating of ostracod samples from Great Basin of the United States provides independent chronology of climate and volcanic eruptions. Leaching of ostracods was applied in order to remove carbonate coating which might be a source of contamination.

One of the most important challenges to understanding the dynamics of Earth's past climate system is improvement of methods for correlation among archives. An essential goal in this endeavor is to establish consistent time scales. In the quest for correlation between marine and continental sedimentary successions, lacustrine carbonate samples are important targets due to their potential for dating by radiocarbon as well as U-series methods. However, radiocarbon compositions of lacustrine carbonates produce ages "too old" due to reservoir effects of unknown and sometimes large magnitude [1, 2]. Further complications result from addition of young carbon, significantly after the time of deposition, a problem well-documented for samples of the late-glacial high lake stand tufa deposits around Lake Lahonton in the western Great Basin of the United States [3, 4].

We have made a study of ostracod samples from two Great Basin lacustrine sections, Carson Sink, Nevada and the Wilson Creek exposures north of Mono Lake, California. Ostracods from the Carson Sink exposures were taken from thin layers of virtually pure ostracods, presumably lag deposits from storm events. Stratigraphic positions were measured relative to the Wono ash bed, a distinctive white layer. Nine layers were sampled from 74 cm below the ash to 19 cm above the ash. Residues remaining after 50% of the carbonate was removed yield uncorrected apparent ages between 31 and 25 ky, and they define a distinct minimum at about 11 cm below the ash. This apparent carbon excursion is matched by one found by Benson et al. [5] from organic carbon from a Pyramid Lake section, and ostracod results imply an age of approximately 28 ky for the Wono ash, consistent with the organic carbon-based estimate of 27.3 ky from Pyramid Lake. Apparent ages of leaches from three of the samples are 2950 - 3450 years younger than their associated residues. Three Wilson Creek samples have been measured. Stratigraphic positions were measured relative to the top of the underlying gravel deposit. Samples came from 0.5, 1.0, and 1.6 m above the contact, and residues yield uncorrected ages of 40, 36, and 34 ky, respectively. Ostracod shells from the Wilson Creek section tend to be filled with a lumpy carbonate cement and leaching does not preferentially remove this material. For the 0.5 m sample we compared the apparent ages of residues from picked shells that contained no visible precipitate and from picked shells that contained the precipitate, and the results were 41600 (± 900) years and 39700 (± 800) years, respectively. In the Wilson Creek samples, residues are 2150 - 4350 years older than leaches; however, leaches more closely match values reported from previous studies of the Wilson Creek section [6].

Uncertainties of the magnitude implied by our results (Fig.1) are impediments to assessing global correlations of climate change on millennial and shorter time scales. Extreme care is needed for radiocarbon dating of Great Basin Pleistocene carbonates, and age estimates from published carbonate data may be too young by several thousand years.

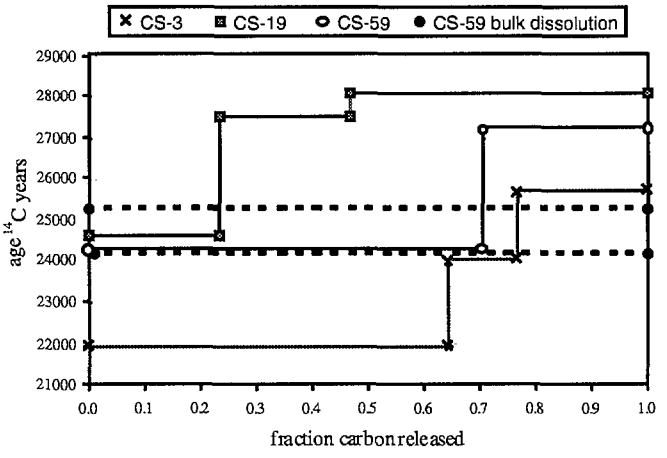

Fig. 1: Results of radiocarbon dating of ostracods shells. Sequence of leaching fractions released from one sample was dated.

REFERENCES

[1] W.S. Broecker and A. Walton, Geochim. Cosmochim. Acta **16,** 15 (1999).

[2] J.L. Bischoff et al., Geochim. Cosmochim. Acta **57,** 3855 (1993).

[3] L. Benson, Quat. Res. **39,** 163 (1993).

[4] J. Lin et al., Geochim. Cosmochim. Acta **60,** 2817 (1996).

[5] L. Benson et al., Quat. Res. **47,** (1997).

[6] L. Benson et al., Paleo-Geography -Climatology - Ecology **78,** 241 (1990).

^{41}Ca MEASUREMENTS WITH THE HIGH-CURRENT ION SOURCE AT THE ZURICH AMS FACILITY

C. Schnabel, M. Suter (ETHZ), H.-A Synal (PSI), A. Tarabischi, J. Kuhnhenn, U. Herpers (Univ. zu Köln), M. Gloris, R. Michel (Univ. Hannover)

New production cross sections for ^{41}Ca from Fe and Ni measured with the 6 MV tandem accelerator at ETH/PSI are presented. Drastic improvements have led to more stable measurement conditions for ^{41}Ca AMS.

^{41}Ca is a nuclide of interest for studies of the irradiation history of extraterrestrial material partly because its half-life of 104 ka fits in an excellent way to determine the terrestrial ages of Antarctic meteorites. Moreover, ^{41}Ca constitutes a potential neutron monitor in silicate phases of meteorites. In extraterrestrial material spallation of Fe and Ni nuclei by galactic cosmic ray protons are two of the main production channels of ^{41}Ca. Some energy points of the respective excitation functions have already been measured by Fink et al. [1], Schnabel et al. [2, 3] and Gartenmann [4]. Here we present new data to fill the gap between 200 and 600 MeV. This work is part of the effort to model the production of ^{41}Ca in meteoroids, what will be possible when the thick target production rates will have been determined.

In order to suppress the interference by K, CaH_2 is used as target material in the ion source. In an earlier report [2] typical low energy currents of 200 nA were reported. With the high-current ion source these currents have been more than doubled to 300 to 1400 nA with a transmission of 2.5 to 4%, when the charge state 5+ is being selected. Moreover, the storage of the moisture-sensitive CaH_2 has been improved resulting in shorter periods of outgassing before stable measurement conditions are established.

The proton induced production cross sections of ^{41}Ca from Fe obtained so far are shown in Fig. 1 and compared to the results of a model calculation (HETC).

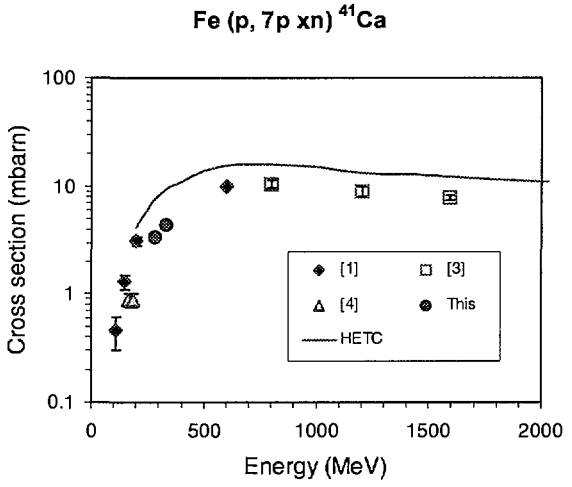

Fig. 1: Proton-induced production cross sections of ^{41}Ca from Fe

In the present work the gap between 200 and 600 MeV has been reduced. With some additional data e.g. at an energy above 1600 MeV the data set will be good enough – in combination with experimental thick target production rates – to model the production of ^{41}Ca in meteoroids.

In Fig.2 the respective data for Ni instead of Fe as target element are shown. The data of this work again substantially reduce the gap in proton energy between 200 and 600 MeV. Because Ni is not as an important target element for ^{41}Ca production in meteoroids as Fe, the existing excitation function is sufficient to model this production.

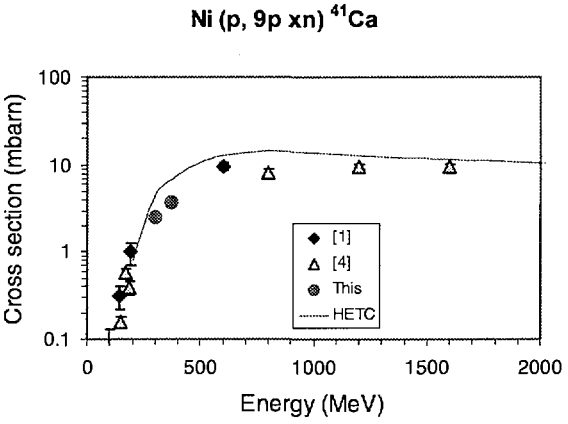

Fig. 2: Proton-induced production cross sections of ^{41}Ca from Ni

We have made another step forward towards the goal of modelling the production of ^{41}Ca in meteoroids. With the ion currents available now, measurements of ^{41}Ca activities in meteorites should have become more precise than in an earlier experiment [4]. Also, the preparation and storage of the target material in the ion source – CaH_2 – has been improved in a way that precise measurements of relatively large numbers of biomedical samples should be feasible with the Zurich AMS facility.

REFERENCES

[1] D. Fink et al., Nucl. Instr. and Meth. **B 29**, 275 (1987).

[2] C. Schnabel et al., PSI Annual Report **1996**, Annex **IIIA**, 39.

[3] C. Schnabel et al., Proceedings of the Italian Physical Society **59**, 1559 (1997).

[4] P. Gartenmann, Ph.D. Thesis, ETH Zürich No.13084 (1999).

AMS MEASUREMENTS OF IODINE-129 IN EUROPEAN ENVIRONMENTAL MATERIALS

S. Szidat, R. Michel, J. Handl, D. Jakob (ZSR, Univ. Hannover), H.-A. Synal (PSI), M. Suter (ETHZ)

Various European soils and precipitation from Lower Saxony/Germany from 1997/1998 were analyzed for ^{129}I by AMS and for ^{127}I by ICP-MS and ion chromatography. Deposition densities of ^{129}I are strongly inhomogeneous. $^{129}I/^{127}I$ ratios in precipitation and deposition rates of ^{129}I show ongoing deposition in Western Europe at a nearly constant rate since 1988 after an increase by three orders of magnitude since 1950.

The natural abundance of ^{129}I ($T_{1/2}$ = 15.7 Ma) has been dramatically changed as a consequence of civil and military use of nuclear fission, but its radioecology is still insufficiently known [1]. We therefore established reliable analytical protocols [1-3] for ^{129}I and ^{127}I analysis in environmental materials. Here, we report results from a project, in which ^{129}I and ^{127}I in soil samples and in precipitation, surface and ground waters are investigated.

From the analysis of soils, we determined the ^{129}I deposition densities at various places of Europe (Table 1). A soil profile from Lutovinovo taken in 1939 allowed us to determine the ^{129}I natural equilibrium deposition density. ^{129}I deposition densities for Moscow show the influence of global weapons fall-out. The significantly higher values for Ukraine are due to contamination by Chernobyl fall-out and provide a basis for retrospective dosimetry of the human radiation exposure due to the short-lived ^{131}I.

location	year	D [mBq m^{-2}]
Lutovinovo, RU	1939	0.084 ± 0.017
Moscow, RU	1996	37 ± 3
Moscow, RU	1996	64 ± 5
Nemirowka, UA	1995	186 ± 14
Nosdrischtsche, UA	1995	1390 ± 100
location	**year**	**$\dot{D}$ [mBq m^{-2} a^{-1}]**
Fiescherhorn, CH	1950	0.014 [5]
Fiescherhorn, CH	1983	0.92 [5]
Mappenberg, D	1988/89	5.2 ± 2.1 [6]
various, D	1995	7.4 ± 2.3 [7]
Lower Saxony (I), D	1997/98	12.7 ± 3.4
Lower Saxony (II), D	1997/98	7.2 ± 1.5
Lower Saxony (IIa), D	1997/98	17.1 ± 6.2
Lower Saxony (IV), D	1997/98	2.0 ± 0.8

Tab. 1: ^{129}I deposition densities D and deposition rates $\dot{D}$

In a systematic study of ^{129}I in rain, surface and ground waters in Lower Saxony [4], we determined ^{129}I annual deposition rates for 1997/98 in Lower Saxony (Table 1). ^{129}I deposition shows regional differences depending on the distance from the North Sea (regions I, II, and IV) as well as differences between open-field (II) and through-falling rain (IIa) [4]. Based on all available information for Switzerland and Germany we conclude that ^{129}I deposition rates increased by three orders of magnitude since 1950 and changed just little after 1988. This view is supported by the development of $^{129}I/^{127}I$ ratios in rain (Fig. 1). $^{129}I/^{127}I$ ratios stabilized after a decades-long increase and a local maximum due to the Chernobyl fall-out at a high level of ~10^{-6} which is more than one order of magnitude higher than recent ratios in the biosphere in Germany [9].

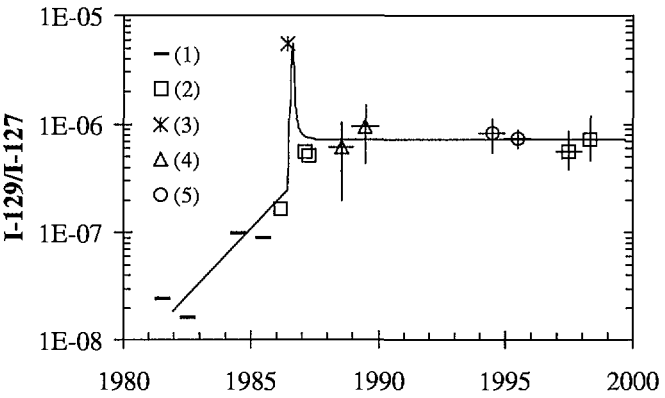

Fig.1: $^{129}I/^{127}I$ ratios in precipitation in Switzerland and Germany [4]. Data are from an ice core (1) from the Fiescherhorn/CH [5] and from precipitation from (2) Lower Saxony/D [4], (3) Munich/D [8], (4) Mappenberg/D [6] and (5) various locations in Germany [7].

REFERENCES

[1] A. Schmidt et al., Sci. Total Environ. **223,** 131 (1998).

[2] S. Szidat et al., J. Radioanl. Chem. (1999) in press.

[3] S. Szidat et al., Kerntechnik (1999) submitted.

[4] S. Szidat et al., Nucl. Instr. Meth. **B** (1999) submitted.

[5] M.J.M. Wagner et al., Nucl. Instr. Meth. **B 113,** 490 (1996).

[6] H. Bachhuber, K. Bunzl, J. Environm. Radioactivity **16,** 77 (1992).

[7] G. Krupp, D.C. Aumann, J. Environm. Radioactivity **46,** 287 (1999).

[8] M. Paul et al., Nucl. Instr. Meth. **B 29,** 341 (1987).

[9] J. Handl, Radiochimica Acta **72,** 33 (1996).

SUB-NANOMETER DEPTH RESOLUTION IN RBS DEPTH PROFILING

M. Döbeli (PSI)

Rutherford Backscattering Spectrometry with a Time-of-Flight spectrometer allows fully quantitative elemental depth profiling with a resolution of 0.5 nm in SiO_2. This is made possible by an ultrathin diamond-like carbon foil used in the start detector. Monolayer resolution in heavier sample materials is within reach.

INTRODUCTION

With the downscaling of electronic devices and the development of new gate dielectrics to replace the thermal SiO_2, the determination of the composition of thin insulating layers (1.5-3 nm) becomes more and more important in micro-electronics. At present, no physical characterization method has both the necessary depth resolution, sensitivity and the absolute quantification possibilities required to determine basic properties such as the detailed elemental distribution at the interface or the composition of the thin film. Elastic scattering of MeV ions (Rutherford Backscattering (RBS) or Elastic Recoil Detection Analysis (ERDA)) are fully quantitative due to the extremely well known interaction cross-sections. So far, the necessary depth resolution could only be obtained with relatively sophisticated magnetic spectrometers. We have used a simple Time-of-Flight (TOF) spectrometer to measure 1 MeV ^{4}He backscattering spectra of state-of-the-art dielectric layers.

EXPERIMENTAL DETAILS

The primary ^{4}He beam had an energy of 1 MeV with an energy spread less than 1 keV. The surface normal of the sample was tilted by 82° with respect to the incident beam and backscattered particles were measured under an angle of 175°. The TOF spectrometer is described in detail in [1]. The heart of the system is a 0.6 μg/cm^2 diamond-like carbon foil to produce secondary electrons in the start detector. For the measurements presented here the energy straggling in this foil is the main limiting factor for the energy resolution of the spectrometer which is 1.8 keV at 250 keV and 4 keV at 500 keV He energy. Due to the long flight path of 1.3 m the solid angle of the system is only 0.5 msr.

RESULTS

The depth resolution capability of the set-up was tested in an inter-laboratory comparison [2]. The test sample was a 2 nm thick oxynitride layer on silicon. Backscattering spectra were taken at different spots on the sample for about 2 hours each. In order to obtain the atomic concentrations of Si and O from the raw spectra, a linear background subtraction procedure was applied. For the silicon signal the contribution from ^{29}Si and ^{30}Si was subtracted as a constant background. In order to convert the silicon RBS yield into atomic concentration, the spectrum height was normalized to the substrate signal and corrected by the stopping power in the SiO_xN_y. For oxygen the concentration scale was normalized using RUMP simulations [3]. The depth scale was calculated with the stopping powers given by TRIM. The results shown in Fig. 1 clearly demonstrate an oxygen concentration close to the nominal value of 66% over a region of approximately 1 nm. Moreover, the data reveals an SiO_2/Si interface of more than 1 nm. The nitrogen signal is low and is not shown here for the sake of clearness.

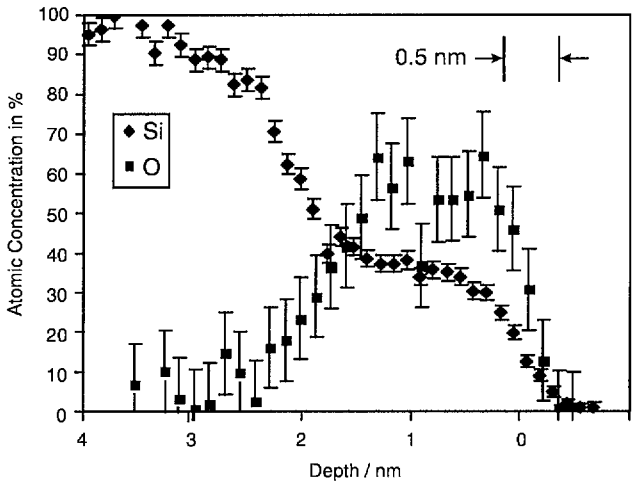

Fig. 1: Elemental depth profiles of a 2 nm thick oxynitride layer on silicon. The background has been subtracted and the RBS yield has been transformed into atomic concentration (see text). Depth resolution is approximately 0.5 nm.

Both the oxygen and the silicon signal display a flat-top region confirming true resolution of the layer. The right edges of both profiles have a width of about 0.5 nm. This corresponds to about twice the distance between silicon atoms in the material.

In compounds with heavier components such as PbSe or PbSb the energy loss per atom would be considerably higher than in SiO_2. With the same energy resolution of the spectrometer it should be possible to resolve single atomic layers in such a mono-crystalline material of high surface quality.

REFERENCES

[1] M. Döbeli et al.
Nucl. Instr. and Meth. **B 142**, 417 (1998).

[2] B. Brijs et al., Nucl. Instr. and Meth. **B**, in print.

[3] L.R. Doolittle,
Nucl. Instr. and Meth. **B 15**, 227 (1986).

SPONTANEOUS MULTILAYERED PHASE FORMATION IN HIGH FLUENCE NICKEL IMPLANTED ALUMINIUM

A. Hessler-Wyser, A. Cuenat and R. Gotthardt (Institut de Génie Atomique, EPFL), M. Döbeli (PSI)

The spontaneous formation of several distinct layers in high fluence Ni implanted aluminium crystals has been observed by TEM. Up to seven sub-layers of thickness of the order of 100 nm develop. The interfaces between the clearly separated phases are sharp within a few nm.

INTRODUCTION

Ion implantation is a common technique which allows an element to be incorporated into a bulk material at any chosen concentration. It can be used to synthesise layers of compounds that cannot be obtained under equilibrium conditions. In the case of nickel ion implantation into aluminium crystals, previous studies [1], [2] have shown that for Ni concentrations of only a few atomic percent, the implanted layer is inhomogeneous and is composed of small amorphous spherical zones containing 25 atomic percent of Ni in an Al(Ni) solid solution. For higher nickel concentrations, exceeding 20 atomic percent, amorphous and homogeneous layers have been observed**Fehler! Textmarke nicht definiert.**. High implantation fluences and high ion flux have not yet been investigated. This report is presenting completely unexpected results of such implantations.

EXPERIMENTAL DETAILS

The Al samples (5N purity) were cleaned and then annealed at 120 °C for 1 hour in vacuum. Ion implantation with 5 MeV Ni was performed at the PSI/ETH EN tandem accelerator. The average beam current was 400 nA, at a current density of 11 $\mu A/cm^2$. Two samples were implanted to fluences of about $7.5 \cdot 10^{17}$ cm^{-2} resulting in a maximum nickel concentration of approx. 25 atomic percent in the implanted layer, i.e. very close to the stoichiometric ratio of Al_3Ni. The samples were kept at a temperature of approximately 100 K during the whole implantation.

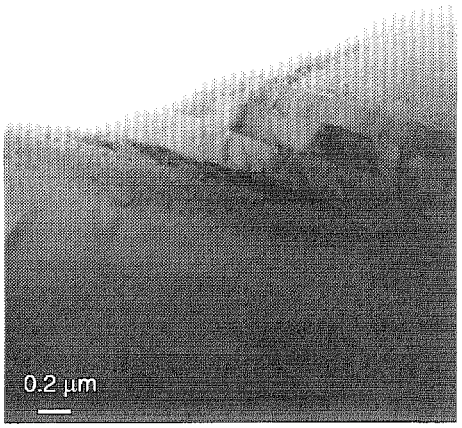

Fig. 1: TEM micrograph of the implanted region.

The implanted samples were prepared for cross-sectional transmission electron microscopy (TEM). TEM and EDS (Energy Dispersive X-ray Spectroscopy) measurements were performed at the Philips CM20 of the Centre Interdépartemental de Microscopie Electronique at EPFL.

RESULTS

The two samples gave very similar results. A view of one of the implanted layers is presented in Fig. 1. It shows distinct sub-layers, corresponding to different Ni concentrations in the implantation profile. As shown in detail in Fig. 2, the interfaces between the individual phases are extremely well defined within a few nm. The composition and structure of the sub-layers are symmetrical with respect to the central layer and clearly depend on the local Ni concentration. The diffraction patterns of the layer closest to the surface indicate the presence of small amorphous Al_3Ni zones in the Al matrix. The next layer contains incoherent crystalline Al_3Ni precipitates in Al. Finally, the central layers are made up of polycrystalline Al_3Ni with a grain size of about 200 nm.

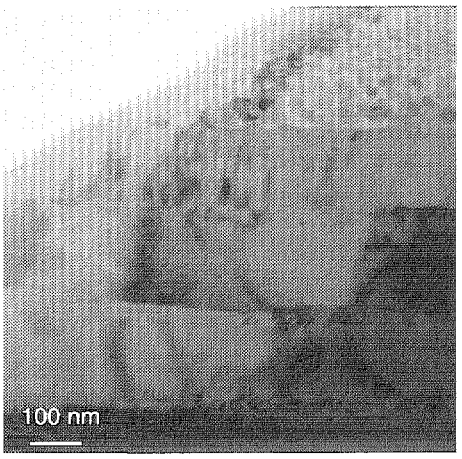

Fig. 2: Close view of the extremely sharp interfaces.

No similar behavior was ever found in any implantation experiment before. Not even a single layer with well defined borders has been observed in any of the previous irradiations. So far, the phenomenon cannot be explained in a satisfactory manner. The microstructure is, however, similar to the one expected from a heating treatment after implantation. Further investigations are being conducted to study the formation of these layers.

REFERENCES

[1] R. Schäublin and R. Gotthardt, Phil. Mag. **A 74**, 593 (1996).

[2] A. Wyser, R. Schäublin, and R. Gotthardt, Nucl. Instr. and Meth. **B 107**, 273 (1996).

THIN OXIDES ON PASSIVATED SILICON IRRADIATED BY FOCUSED ION BEAMS

H. Fuhrmann, M. Döbeli, R. Kötz, B. Schnyder (PSI), R. Mühle (ETHZ)

We investigate the influence of surface oxidation on a novel lithography process we have recently developed. It is shown that the oxides used in the process are a factor of 5 thinner than a typical native oxide. Nevertheless, our experiments indicate that oxidation is the dominant mechanism in our lithography process.

We have recently published a novel lithography technique for silicon surfaces [1]. It uses adsorbed hydrogen as a resist, which can be locally removed by irradiation with focused ion beams (FIB). Thus, the irradiated areas can be selectively oxidised, while all unirradiated parts of the sample remain passivated by the adsorbed hydrogen. The oxide is then used as a mask in anisotropic etchants such as KOH.

Other effects of the irradiation - such as damage or chemical reactions with components of the residual gas - can also affect the etch rate of silicon in KOH. Therefore, we have investigated the irradiation induced oxide and its role in the etching process [2].

ANALYSIS OF THE OXIDE

We analysed the oxide by means of x-ray photoelectron spectroscopy (XPS). For this experiment, an area of 450 µm by 450 µm was irradiated with 30 keV Si^+ ions at a fluence of $5 \cdot 10^{14}$ cm^{-2}, which is well above the fluence required for hydrogen desorption. The substrate was heated to 200 °C to minimize damage, and the surface was exposed to molecular oxygen from a gas inlet during the irradiation. After the irradiation, the sample was transferred into the UHV chamber of the XPS system within 10 minutes.

The integrated peak areas of the XPS-signals corresponding to oxidised silicon ($Si\ 2p_{oxide}$) and unoxidised silicon (Si 2p) were then measured. Their ratio is proportional to the thickness of the oxide (SiO_x) layer on the sample. The same measurement was performed for three reference samples. Two of them had been exposed to air for a certain time after removal of the native oxide by a HF dip. The third reference sample had a full-size native oxide. The results are compiled in Table 1.

Sample	$\frac{Si\ 2p_{oxide}}{Si\ 2p}$
# 1: 10 min after HF-dip	0.002
# 2: 4h after HF-dip	0.049
# 3: no HF-dip	0.251
irradiated with FIB	**0.054**

Tab. 1: Relative oxide thickness on an irradiated surface, compared to three reference samples (#1 - #3).

Comparison of the result of the irradiated sample with the three reference samples shows that the irradiation-induced oxide is about a factor of 5 thinner than a full-size native oxide (# 3), while it is comparable to a native oxide that has built up within 4 hours (# 2). Since the thickness of a native oxide is about 1-2 nm, a reasonable estimate for the absolute thickness of our oxide would be 2-4 Å.

THE OXIDE AS AN ETCH MASK

Considering the very small thickness of the oxide layer, the question arises, if this oxide can really be the dominating factor for the masking effect in KOH. We have investigated this problem experimentally.

Two samples were irradiated with 30 keV Si^+ ions at various fluences between 10^{12} cm^{-2} and 10^{16} cm^{-2}. While one of them ("sample") was etched in KOH directly after the irradiation, the other one ("dummy") was dipped into HF prior to the etch step in KOH. The "dummy" is therefore expected to have no oxide at all. Both samples were etched in KOH for 1 min. The resulting step heights were measured using a surface profiler. Fig. 1 shows the step heights, normalized to the saturation value of the "sample".

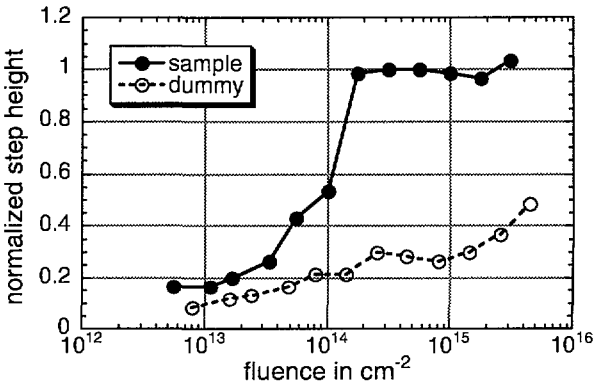

Fig. 1: Normalized step heights vs. ion fluence for "sample" and "dummy".

The result shows a striking difference between the "sample" and the "dummy". At a fluence of $2 \cdot 10^{14}$ cm^{-2}, the "dummy" exhibits only 25% of the step height that is measured for a normal sample. This can only be due to the removal of the oxide by the additional HF dip. Oxidation obviously is the dominating mechanism of our process.

REFERENCES

[1] H. Fuhrmann et al., J. Vac. Sci. Technol. **B 17 (3),** 945 (1999).
[2] H. Fuhrmann et al., J. Vac. Sci. Technol. **B 17 (6)**, 3068 (1999).

ANALYTICAL MODEL FOR IRRADIATION-INDUCED DESORPTION OF HYDROGEN FROM A SILICON SURFACE

H. Fuhrmann, M. Döbeli (PSI), R. Mühle (ETHZ)

For a deeper understanding of the novel lithography process we have recently investigated, a model for hydrogen desorption is developed. It calculates the number of desorbed hydrogen atoms per incident ion based on a thermal spike approach. The predicted critical fluence for desorption compares well with measured values.

We have recently shown that adsorbed hydrogen can be used as a resist in a new, focused ion beam based lithography technique [1]. A more profound analysis of this process requires a quantitative model that describes the desorption and allows to predict critical fluences. Thus, we have to calculate the properties of the thermal spike, the number of hydrogen atoms desorbed by it, and the critical fluence as a function of this number.

DESORPTION BY A THERMAL SPIKE

When a quantity Q of heat is instantaneously released at a certain point inside a solid, it causes a temperature peak of the form

$$T(r,t) = \frac{Q}{4\pi^{\frac{3}{2}} c_p \rho} \cdot \frac{1}{(Dt)^{\frac{3}{2}}} \exp\left(-\frac{r^2}{4Dt}\right)$$

where c_p is the heat capacity at constant pressure, ρ the density, D the thermal diffusivity, r the distance from the point where the heat is released, and t the time. Q depends on the ion species and energy. In our case, only the fraction of energy which is deposited very closely to the surface can contribute to the desorption, because the temperature only extends to some nm in space. We therefore calculated the mean energy δE that is transferred during the first collision between the ion and an atom of the substrate using the TRIM code [2]. In our calculations, Q was then set to δE; the values are given in Table 1.

The desorption process is described by the following differential equation for the areal density Θ of hydrogen at the silicon surface:

$$\dot{\Theta}(r,t) = -\nu_d \exp\left(-\frac{E_a}{k_B T(r,t)}\right) \cdot \Theta(r,t)$$

Here, ν_d is a constant with $\nu_d = 2.1 \cdot 10^{15}$ s^{-1} [3] and E_a is the activation energy for desorption. The two main phases of hydrogen adsorbed at a silicon surface are the monohydride and the dihydride phase. Their desorption temperatures are 530°C and 400°C, respectively [4]. Since E_a=2.48 eV for the dihydride [3], E_a=3.0 eV is a reasonable value for the monohydride. Both phases have to be desorbed for oxidation to occur [4], so that we substitute E_a=3.0 eV in our case.

The number of hydrogen atoms $N_{H,1}$ desorbed by a single thermal spike can then be calculated by numerically solving the differential equation for Θ and integration over t and r. The result is shown in Table 1.

Ion	Energy in keV	δE in eV	$N_{H,1}$	D_k in 10^{14} cm^{-2}	
				model	measured
Si^+	15	850	9.9	0.75	1.08±0.23
Si^+	30	1060	11.3	0.67	0.74±0.22
Si^{++}	60	1290	12.5	0.61	0.70±0.20

Tab. 1: mean amount of energy δE transferred in the first collision, number of thermally desorbed hydrogen atoms $N_{H,1}$ and critical fluences for hydrogen desorption for Si ions at various energies.

CALCULATION OF THE CRITICAL FLUENCE

In order compare the predictions of the model with experimental results, it is interesting to calculate the critical fluence D_k of the desorption process. D_k is defined as the fluence at which half of the hydrogen is desorbed and can be measured as the critical dose of the lithography process. The number of hydrogen atoms desorbed by several ions cannot be calculated by simply multiplying $N_{H,1}$ by the number of ions. This is due to the fact that the hit areas are randomly distributed over the surface and therefore overlap. Since the probability for an ion to hit an area, which is still covered with hydrogen, is proportional to the fraction of the surface that has not been hit, this leads to a simple linear differential equation for Θ. The solution of this equation is

$$\frac{\Theta(D)}{\Theta_0} = \exp\left(-\frac{N_{H,1} \cdot D}{\Theta_0}\right)$$

where D is the fluence and $\Theta_0 = 1.2 \cdot 10^{15}$ cm^{-2} the initial coverage with hydrogen [4]. The critical fluence D_k can then be computed via

$$D_k = \ln(2) \cdot \Theta_0 / N_{H,1}$$

Calculated and measured values of D_k are also compiled in Table 1. They agree reasonably well, so that the model of the desorption mechanism is confirmed.

REFERENCES

[1] H. Fuhrmann et al., this annual report, and references therein.

[2] J.F. Ziegler, J.P. Biersack, U. Littmark, TRIM, 1985.

[3] U. Hofer et al., Phys. Rev. **B 45**, 9485 (1992).

[4] N. Hirashita et al., Appl. Phys. Lett. **56**, 451 (1989).

INVESTIGATION OF PLATINUM GROUP ELEMENTS WITH ACCELERATOR SIMS

C. Maden (ETHZ), M. Döbeli (PSI), B. Hofmann (Nat. Hist. Museum, Berne)

Platinum Group Elements (PGE) have been examined with Accelerator SIMS in electrically insulating matrices at the PSI/ETH AMS facility in order to investigate the potential of the method for solving problems in the field of geology.

Platinum Group Elements are important trace elements in the field of geology and can be used to investigate major global events such as meteorite impacts. These events are manifested by anomalies in PGE concentrations in sedimentary layers. The excelent detection limits for trace elements in silicon together with a high latteral resolution of 100 µm of the PSI/ETH Accelerator SIMS facility [1, 2] lead to assume that profiles of PGE concentrations in sedimentary layers can be measured in-situ with the resolution and sensitivity required by geologists.

The investigation, whether this goal is achievable or not, requires developing a technique for measuring electrically insulating samples with Accelerator SIMS and measuring the sputter yields of PGEs in silicon dioxide, which is the main component of the rock matrices examined.

ELECTRICALLY INSULATING SAMPLES

The Natural History Museum in Berne provided a sample of sedimentary rock. It represents a continuous cross section through the sediment layers at the Cretaceous-Tertiary boundary.

For a stable extraction of secondary ions, charging of the electrically insulating sample surface through bombardment with the primary ion beam has to be prevented. This was achieved by coating the sample with a 50 nm thick carbon layer using a technique common in electron microscopy. This leads to a stable secondary ion beam as long as the sputtered area does not exceed a few hundred micrometers.

SPUTTER YIELDS OF PGE IN SILICON DIOXIDE

In order to get a good estimate of the detection limits of PGEs in quarz based sedimentary rock, their sputter yields in this matrix have to be measured. This was done by measuring the yields relative to those of a pure silicon matrix, for which the apparatus has been tested extensively. The following experiment is in progress to obtain these yields.

SIMOX wafers, consisting of a 200 nm thick suface layer of pure silicon followed by a 100 nm thick layer of silicon dioxide on a substrate of pure silicon, were prepared by implanting a specific PGE isotope into the wafer at two different energies, so that there is a concentration maximum of the PGE in both the silicon dioxide layer and the silicon substrate. The energies were chosen to be 600 keV and 2 MeV for the isotopes ^{103}Rh, ^{106}Pd and ^{107}Ag and 950 keV and 3.5 MeV for the isotopes ^{192}Os, ^{193}Ir, ^{195}Pt and ^{197}Au. Figure 1 shows an example of a SRIM 2000 simulation of the ^{195}Pt concentration as a function of depth in the SIMOX wafer. Depth profiles of the prepared SIMOX wafers were then measured with Accelerator SIMS. A typical depth profile is shown in figure 2.

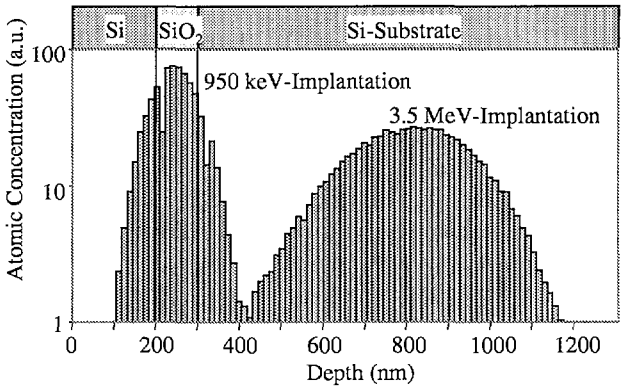

Fig. 1: SRIM simulation of the atomic concentration of ^{195}Pt as a function of depth in the SIMOX wafer.

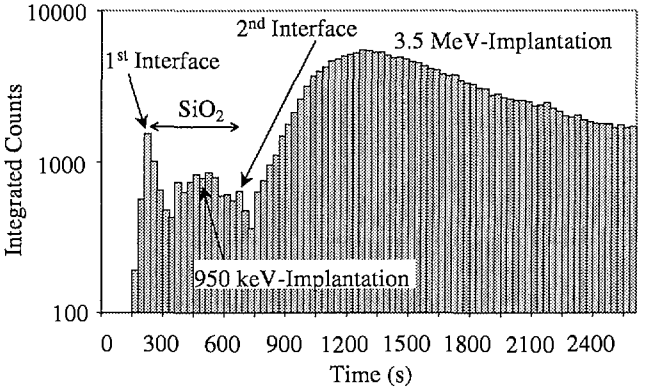

Fig. 2: Counting rate of ^{195}Pt from an implanted SIMOX wafer against measurement time.

From the ratio of the counting rates at the maximum of the two implantation peaks, the ratio of the corresponding concentrations from the SRIM simulations and the background counting rate of the detector the following preliminary bulk detection limits for a silicon dioxide matrix were obtained in units of atoms per matrix atom:

$1 \cdot 10^{-8}$ for Pt

$3 \cdot 10^{-6}$ for Au

$3 \cdot 10^{-8}$ for Ag

The measurements for the remaining PGEs are still in progress.

REFERENCES

[1] R.M. Ender et al., Nucl. Instr. and Meth. **B 123**, 575 (1997).

[2] C. Maden, Diploma Thesis, ETH Zürich, 1998.

FABRICATION OF SATURABLE ABSORBERS IN SEMICONDUCTOR LASER DIODES BY HEAVY ION BOMBARDMENT

M. Dülk, H. Melchior (ETHZ), M. Döbeli (PSI)

Saturable absorbers in bulk semiconductor laser diodes have been fabricated by bombardment with MeV phosphorus and oxygen ions. The dependence of various laser parameters, like lasing threshold, internal quantum efficiency, wavelength shift and others, on the ion dosage has been investigated.

INTRODUCTION

Semiconductor lasers are key components in optical fibre communication systems. Due to their small size the modulation bandwidth usually exceeds 10 GHz, which makes them attractive as optical pulse or clock sources. Mode-locked semiconductor lasers with saturable absorbers exhibit superior optical pulse quality like chirp-free narrow pulses with very good extinction ratio [1]. The aim of this experiment was to create saturable absorbers in bulk semiconductor laser diodes by MeV ion bombardment.

The semiconductor laser diodes (LD) used for this experiment were 250 µm long ridge semiconductor lasers with an InGaAsP bulk active layer of 110 nm thickness. Initial lasing threshold is 29 mA, the gain peaks at a wavelength of 1550 nm. Ion implantation allows to fabricate an absorbing section inside the active layer with a width of some tens of microns. The targeted ion range is five to ten microns from the laser facet whereas the damage to the facet should be kept as low as possible.

EXPERIMENTAL DETAILS

The TRIM code [2] was used to simulate the damage depth profile for various projectiles and energies. In the end, oxygen with an energy of 12 MeV and phosphorus ions with an energy of 26 MeV were chosen to be good candidates for producing optically absorbing layers with the appropriate width and depth. Several laser diodes with equal initial output characteristics have been bombarded by successive low fluences of P or O ions, respectively. Immediately after each irradiation, the output of the laser diodes was characterized.

RESULTS

The dependence of various laser parameters, like lasing threshold, internal quantum efficiency, wavelength shift and others, on the ion fluence has been investigated. The increase in the lasing threshold as a function of the fluence for the oxygen implantation is presented in Fig. 1. The results for the phosphorus implantation is given in Fig. 2.

For both ion species, the threshold increases with a functional dependence of the form $(1\text{-}e^{-F/Fo})$ as a function of the fluence F up to a certain dose F_o. For higher fluences a linear increase is observed. As expected from the simulated number of displaced atoms per implanted ion, the saturation takes place faster for the phosphorus bombardment.

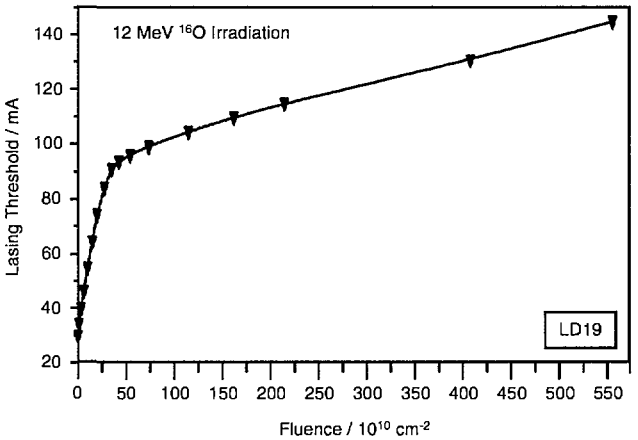

Fig. 1: Lasing threshold for laser diode LD19 versus irradiation fluence. The diode was irradiated with 12 MeV oxygen ions.

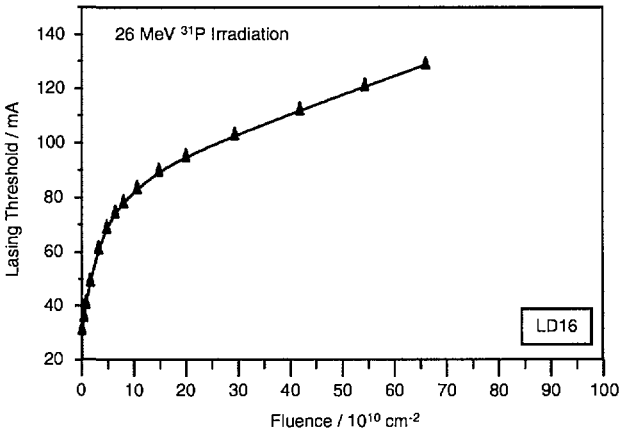

Fig. 2: Lasing threshold for laser diode LD16 versus irradiation fluence. The diode was irradiated with 26 MeV phosphorus ions.

In conclusion, ion implantation offers the possibility to successfully tailor laser parameters by the choice of the projectile, the implantation energy and fluence.

REFERENCES

[1] R. Ludwig, S. Diez, A. Ehrhardt, L. Küller, W. Pieper, and H.G. Weber, IEICE Trans. Electron., **E81-C**, 140 (1998).

[2] J.F. Ziegler, J.P. Biersack, and U. Littmark, *"The Stopping and Range of Ions in Solids"*, Pergamon Press, New York, 1985.

LIST OF PUBLICATIONS

LABORATORY FOR PARTICLE PHYSICS

R-86-05
H.-Ch. Schröder, A. Badertscher, P. F. A. Goudsmit, M. Janousch, H. J. Leise, E. Matsinos, D. Sigg, Z. G. Zhao, D. Chatellard, J.-P. Egger, E. Jeannet, K. Gabathuler, P. Hauser, L. M. Simons, A. J. Rusi El Hassani
Determination of the πN scattering lengths from pionic hydrogen
Phys. Lett. **B 469**, 25 (1999).

R-87-13
A. Lehmann, D. Androić, G. Backenstoss, D. Bosnar, T. Dooling, M. Furić, P. A. M. Gram, N. K. Gregory, A. Hoffart, C. H. Q. Ingram, A. Klein, K. Koch, J. Köhler, B. Kotliński, M. Kroedel, G. Kyle, A. O. Mateos, K. Michaelian, T. Petković, M. Planinić, R. P. Redwine, D. Rowntree, N. Šimičević, R. Trezeciak, H. Ullrich, H. J. Weyer, M. Wildi, K. E. Wilson
Total cross sections of the charge exchange reaction (π^+,π^0) on ^2H, ^3He and ^4He across the Δ (1232) resonance
Physical Review **C 60**, 024603 (1999).

D. Rowntree, D. Androić, G. Backenstoss, D. Bosnar, H. Breuer, H. Döbbeling, T. Dooling, M. Furić, P. A. M. Gram, N. K. Gregory, A. Hoffart, C. H. Q. Ingram, A. Klein, K. Koch, J. Köhler, B. Kotliński, M. Kroedel, G. Kyle, A. Lehmann, A. O. Mateos, K. Michaelian, T. Petković, M. Planinić, R. P. Redwine, N. Šimičević, R. Trezeciak, H. J. Weyer, M. Wildi, K. E. Wilson
π^+ absorption on N and Ar
Physical Review **C 60**, 054610 (1999).

R-88-03
T. Case, D. V. Balin, W. H. Breunlich, K. M. Crowe, H. Daniel, B. Gartner, F. J. Hartmann, P. Kammel, B. Lauss, E. M. Maev, V. E. Markushin, M. Mühlbauer, C. Petitjean, G. E. Petrov, W. Prymas, G. N. Schapkin, W. Schott, G. G. Semenchuk, Yu. V. Smirenin, A. A. Vasiliev, A. A. Vorobyov, N. I. Voropaev, J. Zmeskal
Insights on $d\mu t$ sticking from $d\mu d$ stripping and μ^3He capture
Hyperfine Interactions **118**, 197 (1999).

R-91-10
K. Kirch, D. Abbott, B. Bach, P. Hauser, P. Indelicato, F. Kottmann, J. Missimer, P. Patte, R. T. Siegel, L. M. Simons, D. Viel
Muonic cascades in isolated low Z atoms and molecules
Phys. Rev. **A 59**, 3357 (1998).

R-94-03
S. Tresch, R. Jacot-Guillarmod, F. Mulhauser, C. Piller, L. A. Schaller, L. Schellenberg, H. Schneuwly, Y.-A. Thalmann, A. Werthmüller, P. Ackerbauer, W. H. Breunlich, M. Cargnelli, B. Gartner, R. King, B. Lauss, J. Marton, W. Prymas, J. Zmeskal, C. Petitjean, D. Chatellard, J.-P. Egger, E. Jeannet, F. J. Hartmann, M. Mühlbauer
Muon transfer rates from hydrogen to ^3He and ^4He measured at low temperature
Phys. Rev. **A 57**, 2496 (1998).

S. Tresch, R. Jacot-Guillarmod, F. Mulhauser, L. A. Schaller, L. Schellenberg, H. Schneuwly, Y.-A. Thalmann, A. Werthmüller
Charge transfer from the ground state of muonic hydrogen to ^4He at room temperature
Eur. Phys. J. **D 2**, 93 (1998).

S. Tresch, M. Augsburger, D. Chatellard, F. Mulhauser, C. Piller, L. A. Schaller, L. Schellenberg, H. Schneuwly, Y.-A. Thalmann, A. Werthmüller, P. Ackerbauer, W. H. Breunlich, M. Cargnelli, B. Gartner, R. King, B. Lauss, J. Marton, W. Prymas, J. Zmeskal, C. Petitjean, J.-P. Egger, E. Jeannet, T. von Egidy, F. J. Hartmann, M. Mühlbauer, W. Schott
Measurement of the formation rate and the radiative decay of the muonic molecules $(p\mu^3He)^*$ AND $(p\mu^4He)^*$
Phys. Rev. **A 58**, 3528 (1998).

B. Gartner, P. Ackerbauer, M. Augsburger, W. H. Breunlich, M. Cargnelli, D. Chatellard, J.-P. Egger, T. von Egidy, F. J. Hartmann, R. Jacot-Guillarmod, E. Jeannet, P. Kammel, R. King, A. Kosak, B. Lauss, J. Marton, M. Mühlbauer, F. Mulhauser, C. Petitjean, C. Piller, W. Prymas, L. A. Schaller, L. Schellenberg, H. Schneuwly, W. Schott, Y.-A. Thalmann, S. Tresch, A. Werthmüller, J. Zmeskal
Muon transfer from ground state deuterium to helium nuclei and its temperature dependence
Hyperfine Interactions **119**, 103 (1999).

S. Tresch, P. Ackerbauer, M. Augsburger, W. H. Breunlich, M. Cargnelli, D. Chatellard, J.-P. Egger, T. von Egidy, B. Gartner, F. J. Hartmann, R. Jacot-Guillarmod, E. Jeannet, R. C. King, B. Lauss, J. Marton, M. Mühlbauer, F. Mulhauser, C. Petitjean, C. Piller, W. Prymas, L. A. Schaller, L. Schellenberg, H. Schneuwly, W. Schott, Y.-A. Thalmann, A. Werthmüller, J. Zmeskal
Muon transfer from protium to helium isotopes at low temperature
Hyperfine Interactions **119**, 109 (1999).

R-94-04
M. Mühlbauer, H. Daniel, F. J. Hartmann, P. Hauser, F. Kottmann, C. Petitjean, W. Schott, D. Taqqu, P. Wojchiechowsky
Frictional cooling: experimental results
Hyperfine Interactions **119**, 305 (1999).

R-94-05
B. Lauss, P. Ackerbauer, W. H. Breunlich, M. Cargnelli, D. Chatellard, H. Daniel, J.-P. Egger, B. Gartner, F. J. Hartmann, E. Jeannet, M. Jeitler, P. Kammel, A. Kosak, J. Marton, C. Petitjean, W. Prymas, J. Zmeskal
Hydrogen/deuterium-mixtures as a laboratory for the study of the muonic cascade and muon-catalyzed fusion
Hyperfine Interactions **118**, 79 (1999).

C. Petitjean, D. V. Balin, W. H. Beunlich, T. Case, K. M. Crowe, H. Daniel, M. P. Faifman, V. A. Ganzha, B. Gartner, F. J. Hartmann, P. Kammel, S. Kozlov, B. Lauss, E. M. Maev, V. E. Markushin, Yu. A. Misko, M. Mühlbauer, G. E. Petrov, W. Prymas, G. N. Schapkin, W. Schott, G. G. Semenchuk, Yu. V. Smirenin, V. A. Trofimov, A. A. Vasiliev, A. A. Vorobyov, N. I. Voropaev, J. Zmeskal
Muon catalyzed fusion in deuterium gas
Hyperfine Interactions **118**, 127 (1999).

N. I. Voropaev, D. V. Balin, W. H. Beunlich, T. Case, K. M. Crowe, H. Daniel, V. A. Ganzha, B. Gartner, F. J. Hartmann, P. Kammel, S. Kozlov, B. Lauss, E. M. Maev, V. E. Markushin, Yu. A. Misko, M. Mühlbauer, C. Petitjean, G. E. Petrov, W. Prymas, G. N. Schapkin, W. Schott, G. G. Semenchuk, Yu. V. Smirenin, V. A. Trofimov, A. A. Vasiliev, A. A. Vorobyov, J. Zmeskal
First observation of spin flip in $d\mu$-atoms via formation and back decay of $dd\mu$ molecules
Hyperfine Interactions **118**, 135 (1999).

G. G. Semenchuk, D. V. Balin, T. Case, K. M. Crowe, V. A. Ganzha, F. J. Hartmann, S. Kozlov, B. Lauss, E. M. Maev, M. Mühlbauer, C. Petitjean, G. E. Petrov, S. M. Sadetsky, G. N. Schapkin, W. Schott, Yu. V. Smirenin, M. A. Soroka, A. A. Vasiliev, A. A. Vorobyov, N. I. Voropaev, J. Zmeskal
Study of muon catalyzed dd-fusion in HD gas
Hyperfine Interactions **118**, 141 (1999).

E. M. Maev, D. V. Balin, T. Case, K. M. Crowe, A. Del Rosso, V. A. Ganzha, F. J. Hartmann, S. Kozlov, B. Lauss, O. E. Maev, M. Mühlbauer, F. Mulhauser, C. Petitjean, G. E. Petrov, S. M. Sadetsky, G. N. Schapkin, W. Schott, G. G. Semenchuk, Yu. V. Smirenin, M. A. Soroka, A. A. Vasiliev, A. A. Vorobyov, N. I. Voropaev, J. Zmeskal
Search for muon catalyzed d^3He fusion
Hyperfine Interactions **118**, 171 (1999).

E. M. Maev, D. V. Balin, T. Case, K. M. Crowe, A. Del Rosso, V. A. Ganzha, F. J. Hartmann, S. Kozlov, B. Lauss, O. E. Maev, M. Mühlbauer, F. Mulhauser, C. Petitjean, G. E. Petrov, S. M. Sadetsky, G. N. Schapkin, W. Schott, G. G. Semenchuk, Yu. V. Smirenin, M. A. Soroka, A. A. Vasiliev, A. A. Vorobyov, N. I. Voropaev, J. Zmeskal
Measurement of the muon transfer rate from deuterium to ^3He at low temperature
Hyperfine Interactions **119**, 121 (1999).

R-95-01
Y.-A. Thalmann, R. Jacot-Guillarmod, F Mulhauser, L. A. Schaller, L. Schellenberg, H. Schneuwly, S. Tresch A. Werthmüller
Muon transfer from excited states of hydrogen and deuterium to nitroten, neon, and argon
Phys. Rev. **A 57**, 1713 (1998).

A. Werthmüller, A. Adamczak, R. Jacot-Guillarmod, F. Mulhauser, L. A. Schaller, L. Schellenberg, H. Schneuwly, Y.-A. Thalmann and S. Tresch
Energy dependence of the charge exchange reaction from muonic hydrogen to oxygen
Hyperfine Interactions **116**,1 (1998).

R-95-03
J. Schottmüller, A. Badertscher, M. Daum, P. F. A. Goudsmit, M. Janousch, P.-R. Kettle, J. Koglin, V. E. Markushin, Z. G. Zhao
Kinetic energy of $\pi^- p$-atoms in liquid and gaseous hydrogen
Hyperfine Interactions **119**, 95 (1999).

R-96-04
J. Sromicki, K. Bodek, D. Conti, St. Kistryn, J. Lang, S. Navert, O. Naviliat-Cuncic, E. Stephan, C. Sys, J. Zejma, W. Haeberli, E. Reichert, M. Steigerwald
Polarization in Mott Scattering of Multi-MeV Electrons from Heavy Nuclei
Phys. Rev. Lett. **82**, 57 (1999).

J. Sromicki
Time Reversal Tests in Nuclear and Neutron Beta Decay
Nucl. Phys. **A 654**, 967c (1999).

J. Sromicki
Search for Time Reversal Violation with Nuclei and Neutrons
Physics Beyond the Standard Model, World Scientific Publishing Co., 1999, p. 562-578.

R-97-05
A. A. Vorobyov, P. Ackerbauer, A. Adamczak, V. A. Andreev, D. V. Balin, G. A. Beer, W. H. Breunlich, T. Case, K. M. Crowe, H. Daniel, J. Deutsch, P. U. Dick, A. Dijksman, J. Egger, T. von Egidy, M. P. Faifman, A. A. Fetisov, V. A. Ganzha, J. Govaerts, V. V. Gusev, F. J. Hartmann, W. D. Herold, P. Kammel, A. G. Krivschitz, B. Lauss, E. M. Maev, V. E. Markushin, J. Martino, J. Marton, L.I. Men'shikov, M. Mühlbauer, C. Petitjean, Th. Petitjean, G. E. Petrov, L. I. Ponomarev, R. Prieels, W. Prymas, G. N. Schapkin, W. Schöps, W. Schott, G. G. Semenchuk, Yu. V. Smirenin, N. I. Voropaev
Final results on the μ^3He capture experiment and perspectives for μp-capture studies
Hyperfine Interactions **118**, 13 (1999).

R-98-02
V. F. Boreiko, V. M. Bystritsky, V. I. Datskov, A. N. Fedorov, V. N. Pavlov, V. A. Stolupin, A. Del Rosso, R. Jacot-Guillarmod, F. Mulhauser, L. A. Rivkis
New target cryostat for experiments with negative muons
Nucl. Instrum. Methods **A 416**, 221 (1998).

A. Del Rosso, V. F. Boreiko, V. M. Bystritsky, M. Filipowicz, R. Jacot-Guillarmod, P. E. Knowles, F. Mulhauser, V. N. Pavlov, C. Petitjean, N. P. Popov, V. G. Sandukovsky, L. A. Schaller, H. Schneuwly, V.A. Stolupin, Y.-A. Thalmann, S. Tresch and J. Woźniak
Measurement of fusion rate in μd^3He
Hyperfine Interactions **118**, 177 (1999).

V. A. Stolupin, V. F. Boreiko, V. M. Bystritsky, V. I. Datskov, A. Del Rosso, A. N. Fedorov, R. Jacot-Guillarmod, F. Mulhauser, V. N. Pavlov and L. N. Rivkis
A cryogenic target to study charge nonsymmetric muonic molecules
Hyperfine Interactions **119**, 373 (1999).

R-98-03
F. Kottmann, H. Daniel, F. J. Hartmann, P. Hauser, C. Maierl, V. E. Markushin, M. Mühlbauer, C. Petitjean, R. Pohl, W. Schott, D. Taqqu
Kinetic energies of exotic H atoms at formation and cascade
Hyperfine Interactions **119**, 3 (1999).

R. Pohl, T. W. Hänsch, F. J. Hartmann, P. Hauser, F. Kottmann, G. Lloså, C. Petitjean, W. Schott, D. Taqqu
Long-lived population of the metastable 2s state in muonic hydrogen
Hyperfine Interactions **119**, 77 (1999).

D. Taqqu, F. Biraben, C. A. N. Conde, T. W. Hänsch, F. J. Hartmann, P. Hauser, P. Indelicato, P. Knowles, F. Kottmann, F. Mulhauser, C. Petitjean, R. Pohl, P. Rabinowtz, R. Rosenfelder, J. M. F. Santos, W. Schott, L. M. Simons, J. F. C. A. Veloso
Laser spectroscopy of the Lamb shift in muonic hydrogen
Hyperfine Interactions **119**, 311 (1999).

R-99-01
R. Bilger, K. Föhl, H. Clement, M. Cröni, A. Erhardt, R. Meier, J. Pätzold, G.J. Wagner
Search for Exotic Muon Decays
Phys. Lett. **B 446**, 363 (1999).

Z-91-01
P.E. Garrett, D.G. Burke, M. Délèze, S. Drissi, J. Jolie, J. Kern, H. Lehmann, S.J. Mannanal, N. Warr
States in ^{191}Os observed with the ^{192}Os$(p, pn\gamma)$ reaction.
Phys. Rev. **C 58**, 3734 (1998).

Z-92-02
M. Zeier, H. Anklin, S. Buttazzoni, W. Glöckle, J. Golak, A. Honegger, J. Jourdan, T. Petitjean, I. Sick, H. Witala, B. Zihlmann
Polarization Transfer in $^2H(\vec{p}, \vec{n})pp$
Nuclear Physics **A 654**, 541 (1999).

Z-95-10
D. Castella, D. Chmielewska, D. Corminboeuf, J-Cl. Dousse, B. Galley, Ch. Herren, J. Hoszowska, T. Ludziejewski, J. Kern, M. Pajek, M. Polasik, P. Rymuza, J. Rzadkiewicz, Z. Sujkowski
He-like hole states in mid-Z atoms studied by high resolution K X-ray spectroscopy
Phys. Lett.**A 264**, 186 (1999).

E-91-01
G.M. Marshall, T.A. Porcelli, A. Adamczak, J.M. Bailey, G.A. Beer, M.P. Faifman, M.C. Fujiwara, T.M. Huber, R. Jacot-Guillarmod, P. Kammel, S.K. Kim, P.E. Knowles, A.R. Kunselmann, M. Maier, V.E. Markushin, G.R. Mason, F. Mulhauser, A. Olin, C. Petitjean, J. Zmeskal
Resonant formation measurements of $dt\mu$ via time of flight
Hyperfine Interactions **118**, 89 (1999).

M.C. Fujiwara, A. Adamczak, J.M. Bailey, G.A. Beer, J.L. Beveridge, M.P. Faifman, T.M. Huber, R. Jacot-Guillarmod, P. Kammel, S.K. Kim, P.E. Knowles, A.R. Kunselmann, M. Maier, V.E. Markushin, G.M. Marshall, C.J. Martoff, G.R. Mason, F. Mulhauser, A. Olin, C. Petitjean, T.A. Porcelli, J. Wozniak, J. Zmeskal
Time-of-flight spectroscopy of muonic tritium
Hyperfine Interactions **118**, 151 (1999).

T.M. Huber, A. Adamczak, J.M. Bailey, G.A. Beer, J.L. Beveridge, B.P. Ellerbush, M.C. Fujiwara, R. Jacot-Guillarmod, P. Kammel, S.K. Kim, P.E. Knowles, A.R. Kunselmann, G.J. Lindquist, M. Maier, V.E. Markushin, G.M. Marshall, C.J. Martoff, G.R. Mason, F. Mulhauser, A. Olin, C. Petitjean, T.A. Porcelli, J. Wozniak, J. Zmeskal
Time-of-flight studies of emission of μt from frozen hydrogen films
Hyperfine Interactions **118**, 159 (1999).

A. Olin, A. Adamczak, G.A. Beer, V.M. Bystritsky, M. Filipowicz, M.C. Fujiwara, T.M. Huber, R. Jacot-Guillarmod, P. Kammel, S.K. Kim, P.E. Knowles, A.R. Kunselmann, M. Maier, V.E. Markushin, G.M. Marshall, F. Mulhauser, C. Petitjean, T.A. Porcelli, V.A. Stolupin, J. Wozniak, J. Zmeskal
Study of μ-catalyzed fusion in H-D mixtures
Hyperfine Interactions **118**, 163 (1999).

F. Mulhauser, A. Adamczak, G.A. Beer, V.M. Bystritsky, M. Filipowicz, M.C. Fujiwara, T.M. Huber, R. Jacot-Guillarmod, P. Kammel, S.K. Kim, P.E. Knowles, A.R. Kunselmann, M. Maier, V.E. Markushin, G.M. Marshall, A. Olin, C. Petitjean, T.A. Porcelli, V.A. Stolupin, J. Wozniak, J. Zmeskal
Scattering of muonic hydrogen atoms
Hyperfine Interactions **119**, 35 (1999).

J. Wozniak, A. Adamczak, G.A. Beer, V.M. Bystritsky, M. Filipowicz, M.C. Fujiwara, T.M. Huber, R. Jacot-Guillarmod, P. Kammel, S.K. Kim, P.E. Knowles, A.R. Kunselmann, M. Maier, V.E. Markushin, G.M. Marshall, F. Mulhauser, A. Olin, C. Petitjean, T.A. Porcelli, V.A. Stolupin, J. Zmeskal
New effects in low energy scattering of $p\mu$ atoms
Hyperfine Interactions **119**, 63 (1999).

BROOKHAVEN E865 COLLABORATION
R. Appel et al.,
J. Egger, W. Herold, H. Kaspar, H. Weyer
A new measurement of the properties of the rare decay $K^+ \to \pi^+ e^+ e^-$
Phys. Rev. Lett. **83**, 4482 (1999).

CERN, L3 COLLABORATION
M. Acciarri, *et al.*,
A. Barczyk, K. Deiters, M. Fabre
Search for extra dimensions in boson and fermion pair production in e^+e^- interactions at LEP
Phys. Lett. **B 470**, 281 (1999);

Search for neutral Higgs bosons of the minimal supersymmetric standard model in e^+e^- interactions at $\sqrt{s}$ = 189 GeV
Phys. Lett. **B 471**, 321 (1999);

Searches for scalar quarks in e^+e^- interactions at $\sqrt{s}$ = 189 GeV
Phys. Lett. **B 471**, 308 (1999);

Single and multi-photon events with missing energy in e^+e^- collisions at $\sqrt{s}$ = 189 GeV
Phys. Lett. **B 470**, 268 (1999);

Measurement of triple-gauge-boson couplings of the W boson at LEP
Phys. Lett. **B 467**, 171 (1999);

Search for scalar leptons in e^+e^- collisions at $\sqrt{s}$ = 189 GeV
Phys. Lett. **B 471**, 280 (1999);

Study of Z boson pair production in e^+e^- collisions at LEP at $\sqrt{s}$ = 189 GeV
Phys. Lett. **B 465**, 363 (1999);

Search for charged Higgs bosons in e^+e^- collisions at $\sqrt{s}$ = 189 GeV
Phys. Lett. **B 466**, 71 (1999);

Search for low scale gravity effects in e^+e^- collisions at LEP
Phys. Lett. **B 464**, 135 (1999);

Measurement of the spectroscopy of orbitally excited B mesons at LEP
Phys. Lett. **B 465**, 323 (1999);

Measurement of inclusive $D^{*\pm}$ production in two-photon collisions at LEP
Phys. Lett. **B 467**, 137 (1999);

Search for heavy isosinglet neutrinos in e^+e^- annihilation at 130 GeV < $\sqrt{s}$ <189 GeV
Phys. Lett. **B 461**, 397 (1999);

Search for standard model Higgs boson in e^+e^- interactions at $\sqrt{s}$ = 189 GeV
Phys. Lett. **B 461**, 376 (1999);

Search for heavy neutral and charged leptons in e^+e^- annihilation at $\sqrt{s}$ = 183 GeV and 189 GeV
Phys. Lett. **B 462**, 354 (1999);

Formation of the η_c in two-photon collisions at LEP
Phys. Lett. **B 461**, 155 (1999);

Measurement of an elongation of the pion source in Z decays
Phys. Lett. **B 458**, 517 (1999);

Search for R-parity violating chargino and neutralino decays in e^+e^- collisions up to $\sqrt{s}$ = 183 GeV
Phys. Lett. **B 459**, 354 (1999);

Search for scalar leptons in e^+e^- collisions at $\sqrt{s}$ = 183 GeV
Phys. Lett. **B 456**, 283 (1999);

Measurement of mass and width of the W boson at LEP
Phys. Lett. **B 454**, 386 (1999).

CERN, CPLEAR COLLABORATION
A. Apostolakis et al.,
P. Bargassa, F. Blanc, P.-R. Kettle, V. E. Markushin, M.P. Locher, T. Nakada, O. Wigger
Pion correlations and resonance effects in $\overline{p}p$ annihilation at rest to $2\pi^+2\pi^-\pi^0$
Eur. Phys. J. **C 6**, 437 (1999).

A. Angelopoulos et al.,
P. Bargassa, F. Blanc, P.-R. Kettle, V. E. Markushin, M. P. Locher, T. Nakada, O. Wigger
Dispersion relation analysis of the neutral kaon regeneration amplitude in carbon
Eur. Phys. J. **C 10**, 19 (1999).

A. Apostolakis et al.,
P. Bargassa, F. Blanc, P.-R. Kettle, T. Nakada, O. Wigger
A determination of the CP violation parameter η_{+-} from the decay of strangeness-tagged neutral kaons
Phys. Lett. **B 458**, 545 (1999);

Determination of the T- and CPT-violation parameters in the neutral kaon system using the Bell-Steinberger relation and data from CPLEAR
Phys. Lett. **B 456**, 297 (1999);

Tests of the equivalence principle with neutral kaons
Phys. Lett. **B 452**, 425 (1999).

CERN, EXPERIMENT PS207
M. Augsburger et al.,
P. Hauser, K. Kirch, L.M. Simons
Measurement of the strong interaction parameters in antiprotonic deuterium
Phys. Lett. **B 461**, 417 (1999);

Measurement of the strong interaction parameters in antiprotonic hydrogen and probable evidence for an interference with inner bremsstrahlung
Nucl. Phys. **A 658**, 339 (1999).

CERN, CMS COLLABORATION
S. Baccaro *et al.*,
K. Deiters, D. Renker
Radiation damage effect on avalanche photodiodes.
Nucl. Instrum. Meth. **A 426**, 206 (1999).

DESY, H1 COLLABORATION
C. Adloff et al.,
S. Egli, R. Eichler, K. Gabathuler, J. Gassner, R. Horisberger
Measurement of open beauty production at HERA
Phys. Lett. **B 467**, 156 (1999);

Forward π^0 meson production at HERA
Phys. Lett. **B 462**, 440 (1999);

A search for leptoquark bosons and lepton flavour violation in e^+ p collisions at HERA
Eur. Phys. J. **C 11**, 447 (1999);

Charmonium production in deep inelastic scattering at HERA
Eur. Phys. J. **C 10**, 373 (1999);

Measurement of internal jet structure in dijet production in deep inelastic scattering at HERA
Nucl. Phys. **B 545**, 3 (1999);

Measurement of D^* meson cross-sections at HERA and determination of the gluon density in the proton using NLO QCD
Nucl. Phys. **B 545**, 21 (1999);

Measurement of leading proton and neutron production in deep inelastic scattering at HERA
Eur. Phys. J. **C 6**, 587 (1999);

Charged particle cross-sections in photoproduction and extraction of the gluon density in the photon
Eur. Phys. J. **C 10**, 363 (1999);

Forward jet and particle production at HERA
Nucl. Phys. **B 538**, 3 (1999);

Diffractive dijet production at HERA
Eur. Phys. J. **C 6**, 421 (1999);

Multijet event rates in deep inelastic scattering and determination of the strong coupling constant
Eur. Phys. J. **C 6**, 575 (1999).

THEORY GROUP
C. Alexandrou, A. Boriçi, A. Feo, Ph. de Forcrand, A. Galli, F. Jegerlehner and T. Takaishi
The deconfinement phase transition in one flavor QCD
Phys. Rev. **D 60**, 034504 (1999).

C. Alexandrou, R. Rosenfelder and A. W. Schreiber
Worldline path integral for the massive Dirac propagator: a four-dimensional approach
Phys. Rev. **A 59**, 1762 (1999).

A. Angelopoulos *et al.* (CPLEAR Collaboration), M. P. Locher, V. E. Markushin and O. Wigger
Pion correlations and resonance effects in $p\bar{p}$ annihilation at rest to $2\pi^+2\pi^-\pi^0$
Eur. Phys. J. **C 6**, 437 (1999).

A. Angelopoulos *et al.* (CPLEAR Collaboration), M. P. Locher, V. E. Markushin and O. Wigger
Dispersion relation analysis of the neutral kaon regeneration amplitude in carbon
Eur. Phys. J. **C 10**, 1 (1999).

U. Baur, S. Keller, D. Wackeroth
Electroweak radiative corrections to W boson production in hadronic collisions
Phys. Rev. **D 59**, 013002 (1999).

A. Boriçi
On the Neuberger overlap operator
Phys. Lett. **B 453**, 46 (1999).

T. Case *et al.*, V. E. Markushin
Insights on $d\mu t$ sticking from $d\mu d$ stripping and μ^3He capture
Hyperfine Interactions **118**, 197 (1999).

A. Denner and S. Dittmaier
Complete $\mathcal{O}(\alpha)$ QED corrections to polarized Compton scattering
Nucl. Phys. **B 540**, 58 (1999).

A. Denner and S. Pozzorini
Electroweak radiative corrections to polarized Moeller scattering at high energies
Eur. Phys. J. **C 7**, 185 (1999).

A. Denner and S. Dittmaier
Production of light fermion-antifermion pairs in $\gamma\gamma$ collisions
Eur. Phys. J. **C 9**, 425 (1999).

A. Denner, S. Dittmaier, M. Roth and D. Wackeroth
Predictions for all processes $e^+e^- \to 4$ fermions $+ \gamma$
Nucl. Phys. **B 560**, 33 (1999).

M. C. Fujiwara *et al.*, V. E. Markushin
Time-of-flight spectroscopy of muonic tritium
Hyperfine Interactions **118**, 151 (1999).

D. Graudenz
Jets and fragmentation
J. Phys. **G 25**, 1289 (1999).

T.M. Huber *et al.*, V. E. Markushin
Time-of-flight studies of emission of μt from frozen hydrogen films
Hyperfine Interactions **118**, 159 (1999).

K. Junker, V. A. Kuz'min and T. V. Tetereva
Gamow-teller strength function in spherical nuclei
Eur. Phys. J. **A 5**, 37 (1999).

F. Kottmann *et al.*, V. E. Markushin
Kinetic energy of exotic H atoms at formation and cascade
Hyperfine Interaction **119**, 3 (1999).

V. E. Markushin
Few body problems in muon catalyzed fusion
Few-Body Syst. Suppl. **10**, 169 (1999).

V. E. Markushin
Loop calculations and OZI rule
Nucl. Phys. **A 655**, 185c (1999).

V. E. Markushin
Cascade in muonic and pionic atoms with $Z = 1$
Hyperfine Interactions **119**, 11 (1999).

V. E. Markushin and M. P. Locher
Structure of the light scalar mesons from a coupled channel analysis of the S-wave $\pi\pi - K\bar{K}$ *scattering*
Frascati Physics Series Vol.**XV**, 229 (1999).

G. M. Marshall *et al.*, V. E. Markushin
Resonant formation measurements of $dt\mu$ *via time of flight*
Hyperfine Interactions **118**, 89 (1999).

F. Mulhauser *et al.*, V. E. Markushin
Scattering of muonic hydrogen atoms
Hyperfine Interactions **119**, 35 (1999).

A. Olin *et al.*, V. E. Markushin
Study of μ*-catalyzed fusion in H-D mixtures*
Hyperfine Interactions **118**, 163 (1999).

C. Petitjean *et al.*, V. E. Markushin
Muon catalyzed fusion in deuterium gas
Hyperfine Interaction **118**, 127 (1999).

R. Rosenfelder
Proton polarization shifts in electronic and muonic hydrogen
Phys. Lett. **B 463**, 317 (1999).

D. Taqqu *et al.*, R. Rosenfelder
Laser spectroscopy of the Lamb shift in muonic hydrogen
Hyperfine Interactions **119**, 311 (1999).

A. A. Vorobyov *et al.*, V. E. Markushin
Final results on the $\mu^3 He$ *capture experiment and perspectives for* μp*-capture studies*
Hyperfine Interaction **118**, 13 (1999).

N. I. Voropaev *et al.*, V. E. Markushin
First observation of spin flip in $d\mu$*-atoms via formation and back decay of* $dd\mu$ *molecules*
Hyperfine Interaction **118**, 135 (1999).

J. Wozniak *et al.*, V. E. Markushin
New effects in low energy scattering of $p\mu$ *atoms*
Hyperfine Interactions **119**, 63 (1999).

LABORATORY FOR ASTROPHYSICS

M. Audard, M. Güdel, E. F. Guinan
Implications from Extreme-Ultraviolet Observations for Coronal Heating of Active Stars
Astrophys. J. **513**, L53 (1999).

T. R. Ayres, A. Brown, S. A. Drake, A. K. Dupree, M. Güdel, E. F. Guinan, G. M. Harper, C. Jordan, J. L. Linsky, D. Reimers, J. H. M. M. Schmitt, T. Simon
Origins, Structure, and Evolution of Magnetic Activity in the Cool Half of the H–R Diagram: an HST STIS Survey
Astron. Astrophys. Suppl. **195**, 5013A (1999).

M. Gagné, J. A. Valenti, J. L. Linsky, G. Tagliaferri, S. Covino, M. Güdel
The Active Corona of HD35850
Astrophys. J. **515**, 423 (1999).

M. Güdel, J. L. Linsky, A. Brown, F. Nagase
Flaring and Quiescent Coronae of UX Arietis: Results from ASCA and EUVE Campaigns
Astrophys. J. **511**, 405 (1999).

M. Güdel
Prospects for Cool Star Astronomy with the Square Kilometer Array
Chapters in *Science with the Square Kilometer Array - A Next Generation World Radio Observatory*,
Ed. A. R. Taylor, R. Braun (1999), 89ff and 112ff.

K. Smith, M. Güdel, A. O. Benz
Radio Counterparts to Extreme X-Ray YSOs
Astron. Astrophys. **349**, 475 (1999).

K. Smith, G. Lewis, I. Bonnell, P. Bunclark, J. Emerson
Rapid variations of T Tauri spectral features: clues to the morphology of the inner regions
MNRAS **304**, 367 (1999).

F. De Paolis, G. Ingrosso, Ph. Jetzer and M. Roncadelli
Baryonic dark matter
in proceedings of the "8th Marcel Grossmann Meeting on General Relativity"
(Jerusalem, June 1997), (World Scientific, Singapore 1999), p. 1426.

F. De Paolis, G. Ingrosso, Ph. Jetzer and M. Roncadelli
Microlensing implications for halo dark matter
in proceedings of the "8th Marcel Grossmann Meeting on General Relativity"
(Jerusalem, June 1997), (World Scientific, Singapore 1999), p. 1429.

F. De Paolis, G. Ingrosso, and Ph. Jetzer
Microlensing results and the Galactic models
in proceedings of the "8th Marcel Grossmann Meeting on General Relativity"
(Jerusalem, June 1997), (World Scientific, Singapore 1999), p. 1561.

F. De Paolis, G. Ingrosso, Ph. Jetzer and M. Roncadelli
Gamma ray astronomy and baryonic dark matter
Astrophys. J. **510**, L103 (1999).

L. Grenacher, Ph. Jetzer, M. Strässle and F. De Paolis
Microlensing towards different Galactic targets
Astron. Astrophys. **351**, 775 (1999).

Ph. Jetzer
Gravitational microlensing research
in proceedings of the "8th Marcel Grossmann Meeting on General Relativity"
(Jerusalem, June 1997), (World Scientific, Singapore 1999), p. 1543.

Ph. Jetzer and D. Scialom
On the stability of real scalar boson stars
in proceedings of the "8th Marcel Grossmann Meeting on General Relativity"
(Jerusalem, June 1997), (World Scientific, Singapore 1999), p. 1639.

Ph. Jetzer
Gravitational microlensing
Naturwissenschaften **86**, 201 (1999).

D. Puy, L. Grenacher and Ph. Jetzer
Thermal equilibrium of molecular clouds in cooling flow clusters
Astron. Astrophys. **345**, 723 (1999).

D. Puy and M. Signore
Primordial chemistry
New Astronomy Reviews **43**, 223 (1999).

M. Signore and D. Puy
Primordial nucleosynthesis
New Astronomy Reviews **43**, 185 (1999).

M. Strässle, M. Huser, Ph. Jetzer and F. De Paolis
Dark matter in the dwarf galaxy NGC247
Astron. Astrophys. **349**, 1 (1999).

G. Paesold, Arnold O. Benz
Electron Firehose instability and acceleration of electrons in solar flares
Astron. Astrophys. **351**, 741 (1999).

A. Zehnder, Ph. Lerch, S. P. Zhao, Th. Nussbaumer, E. Kirk and H. R. Ott
Proximity effect in $Nb/Al - AlO_x - Al/Nb$ superconducting tunneling junctions
Phys. Rev. **B 59**, 8875 (1999).

LABORATORY FOR MUON SPIN SPECTROSCOPY

RA-86-07
I. D. Reid and E. Roduner
Muon-Spin Resonance Spectroscopy
In J.L. Holmes, J.C. Lindon, G.E. Tranter, Eds., *Encyclopedia of Spectroscopy and Spectrometry,*
Academic Press, London, 1999.

U. Himmer, H. Dilger, E. Roduner, J. J. Pan, D. J. Arseneau, D. G. Fleming, M. Senba
Kinetic isotope effect in the gas phase reaction of muonium with molecular ox oxygen
J. Phys. Chem. **A 103**, 2076 (1999).

E. Roduner
Aspects of muon chemistry
In R. Cywinski, S. L. Lee, S. H. Kilcoyne, Eds., *Muon science - muons in physics, chemistry and materials,* pages 173-209,
Institute of Physics Publishing, London/Philadelphia, 1999.

RA-90-02
F. N. Gygax, G. Solt, A. Amato, I. S. Anderson, M. Pinkpank, A. Schenck, T. J. Udovic
Light hydrogen isotope μ^+ in Sc and α-ScH_x solid solutions
Phys. Rev. **B 61**, 168 (2000).

RA-90-07
A. Shengelaya, Guo-meng Zhao, C. M. Aegerter, K. Conder, I. M. Savić and H. Keller
Giant oxygen isotope effect on the spin glass transition in $La_{2-x}Sr_xCu_{1-z}Mn_zO_4$ as revealed by muon spin rotation
Phys. Rev. Lett. **83**, 5142 (1999).

RA-90-19
Ch. Niedermayer, C. Bernhard, T. Blasius, A. Golnik, A. Moodenbaugh, J. I. Budnick
Doping dependence of the antiferromagnetic correlations in $La_{2-x}Sr_xCuO_4$ and $Y_{1-x}Ca_xBa_2Cu_3O_6$
Advances in Solid State Physics **39**, 413 (1999).

RA-92-01
A. Lappas, K. Prassides, F. N. Gygax, A. Schenck
Spin glass magnetism in the oxygen-rich $La_2Co_xCu_{1-x}O_{4+\delta}$ layered oxides: magnetic susceptibility and muon spin relaxation studies
J. Solid State Chem. **145**, 471 (1999).

RA-92-06
G. Alexandrowicz, T. Tashma, M. Sokolovsky, A. Amato, A. Grayevsky, F. N. Gygax, M. Pinkpank, A. Schenck and N. Kaplan
μ^+ Hopping between magnetically labeled sites in $PrIn_3$: "Kinematic" simulation and analytic treatment
Phys. Rev. Lett. **82**, 1028 (1999).

RA-93-03
K. Prassides, S. Margadonna, D. Arcon, A. Lappas, H. Shimoda, Y. Iwasa
Magnetic ordering in the ammoniated fulleride $(ND_3)K_3C_{60}$
J. Am. Chem. Soc. **121**, 11227 (1999).

D. Arcon, A. Lappas, S. Margadonna, K. Prassides, E. Ribera, J. Veciana, C. Rovira, R. T. Henriques, M. Almeida
Magnetic behavior of a two-leg organic spin-ladder compound
Phys. Rev. **B 60**, 4191 (1999).

RA-93-06
S. J. Blundell, S. L. Lee, F. L. Pratt, C. M. Aegerter, Th. Jestadt, B. W. Lovett, C. Ager, T. Sasaki, V. N. Laukhin, E. Laukhina, E. M. Forgan and W. Hayes
Stability of the vortex lattice in ET superconductors studied by μSR
Synth. Met. **103**, 1925 (1999).

S. J. Blundell
μSR studies of organic magnets
Phil. Trans. R. Soc. Lond. **A 357**, 2923 (1999).

T. Sugano, S. J. Blundell, F. L. Pratt, Th. Jestadt, B. W. Lovett, W. Hayes and P. Day
Several kinds of aminoxyl radicals and their metal ion complexes
Mol. Cryst. Liq. Cryst. **334**, 477 (1999).

S. J. Blundell
Spin-polarized muons in condensed matter physics
Contemp. Phys. **40**, 175 (1999).

Th. Jestadt, M. Kurmoo, S. J. Blundell, B. W. Lovett, F. L. Pratt and W. Hayes
Layered transition metal molecular magnets studied with implanted muons
Synth. Met. **103**, 2325 (1999).

B. W. Lovett, S. J. Blundell, Th. Jestadt, F. L. Pratt, M. Kurmoo, S. Tagaki and W. Hayes
Muon study of the spin dynamics in the organic spin-Peierls compound MEM(TCNQ)$_2$
Synth. Met. **103**, 2034 (1999).

RA-93-10
M. Schefzik, R. Scheuermann, L. Schimmele, A. Seeger, D. Herlach, O. Kormann, J. Major, A. Röck
Oxygen-Related Anisotropic Muonium Centres in Crystalline Silicon
Philosophical Magazine **B 79**, 1561 (1999).

RA-93-12
F. L. Pratt, S. J. Blundell, B. W. Lovett, K. Nagamine, K. Ishida, W. Hayes, Th. Jestadt and A. P. Monkman
Anisotropic polaron motion in conducting polymers studied by muon spin relaxation
Synth. Met. **101**, 323 (1999).

RA-94-03
A. Schenck, D. Andreica, M. Pinkpank, F. N. Gygax, H. R. Ott, A. Amato, R. H. Heffner, D. E. MacLaughlin, G. J. Nieuwenhuys
New μSR results on the magnetic structure of $CeAl_2$
Physica **B 14**, 14 (1999).

RA-94-04
E. M. Forgan, P. G. Kealey, T. M. Riseman, S. L. Lee, D. McK.Paul, C. M. Aegerter, R. Cubitt, P. Schleger, A. Pautrat and Ch. Simon
Fluxoids and Neutron Polarisation Effects
Physica **B 267-268**, 115 (1999).

S. J. Bludell, S. L. Lee, F. L. Pratt, C. M. Aegerter, Th. Jestädt, B. W. Lovett, C. Ager, T. Sasaki, V. N. Laukhin, E. M. Forgan and W. Hayes
Stability of the vortex lattice in ET superconductors studied by μSR
Synth. Met. **103**, 1925 (1999).

S. T. Johnson, E. M. Forgan, S. H. Lloyd, C. M. Aegerter, S. L. Lee, R. Cubitt, P. G. Kealey, C. Ager, S. Tajima, A. Rykov and D. McK. Paul
Flux-line lattice structures in untwinned $YBa_2Cu_3O_{7-\delta}$
Phy. Rev. Lett. **29**, 2792 (1999).

RA-94-14
G. Solt, C. Baines, V. S. Egorov, D. Herlach, U. Zimmermann
Diamagnetic domains in beryllium observed by muon-spin-rotation spectroscopy
Phys. Rev. **B 59**, 6834 (1999).

RA-95-03
M. Pinkpank, A. Amato, D. Andreica, F. N. Gygax, H. R. Ott, A. Schenck
The effect of the oxygen reduction on the magnetic properties of RE $Ba_2Cu_3O_{6+x}$ *(RE=Gd, Ho)*
Physica **C 317-318**, 299-303 (1999).

RA-95-10
V. Yu. Pomjakushin, A. A. Zakharov, A. M. Balagurov, F. N. Gygax, A. Schenck, A. Amato, D. Herlach, A. I. Beskrovny, V. N. Duginov, Yu. V. Obukhov, A. N. Ponomarev, S. N. Barilo
Microscopic phase separation in La_2CuO_{4+x} *induced by the superconducting transition*
Phys. Rev **B 58**, 12350 (1998).

RA-95-18
R. J. Keizer, A. de Visser, A. A. Menovsky, J. J. M. Franse, A. Amato, F. N. Gygax, M. Pinkpank and A. Schenck
Magnetism in heavy-fermion $U(Pt, Pd)_3$ *studied by* μSR
J. Phys.: Condens. Matter **11**, 8591 (1999).

RA-96-01
Th. Jestadt, K. H. Chow, S. J. Blundell, W. Hayes, F. L. Pratt, B. W. Lovett, M. A. Green, J. E. Millburn and M. J. Rosseinsky
Temperature and doping-level dependence of magnetic order in $La_{2-x}Sr_xNiO_{4+\delta}$ *studied by muon spin rotation*
Phys. Rev. **B 59**, 3775 (1999).

RA-96-07
T. Blasius, Ch. Niedermayer, J. L. Tallon, D. M. Pooke, A. Golnik and C. Bernhard
Evidence for a two-stage melting transition in the vortex matter of $Bi_2Sr_2CaCu_2O_{8+\delta}$ *single crystals obtained by* μSR
Phys. Rev. Lett. **82**, 4926 (1999).

RA-97-19
R. I. Bewley, S. J. Blundell, B. W. Lovett, Th. Jestädt, F. L. Pratt, K. H. Chow, W. Hayes, P. D. Battle, M. A. Green, M. J. Rosseinsky, L. E. Spring and J. F. Vente
μSR studies of magnetic order and dynamics of the $n = 2$ Ruddlesden-Popper phases $Sr_2LnMn_2O_7$ *where Ln=Pr, Nd, Sm, Eu, Gd, Tb, Dy and Ho*
Phys. Rev. **B 60**, 12286 (1999).

RA-97-23
J. M. Gil, P. J. Mendes, L. P. Ferreira, H. V. Alberto, R. C. Vilão, N. Ayres de Campos, A. Weidinger, Y. Tomm, Ch. Niedermayer, M. V. Yakushev, R. D. Tomlinson, S. P. Cottrell, S. F. J. Cox
Modelling hydrogen in $CuInSe_2$ *and* $CuInS_2$ *solar cell materials using implanted muons*
Phys. Rev. **B 59**, 1912 (1999).

J. M. Gil, H. V. Alberto, R. C. Vilão, J. Piroto Duarte, P. J. Mendes, L. P. Ferreira, N. Ayres de Campos, A. Weidinger, J. Krauser, Ch. Niedermayer, S. F. J. Cox
Novel Muonium State in CdS
Phys. Rev. Lett. **83**, 5294 (1999).

RA-97-25
T. N. Mamedov, I. L. Chaplygin, V. N. Duginov, V. N. Gorelkin, D. Herlach, J. Major, A. V. Stoykov, M. Schefzik, U. Zimmermann
Shallow acceptor centres in silicon studied by means of spin rotation of negative muons
J. Phys.: Condens. Matter **11**, 2849 (1999).

RA-98-07
D. Andreica, K. Alami-Yadri, D. Jaccard, A. Amato, A. Schenck
Transport properties and μSR spectroscopy of $Yb(Ni_xCu_{1-x})_2Si_2$
Physica **B 259-261**, 144 (1999).

RA-99-11
C. Bernhard, J. L. Tallon, Ch. Niedermayer, T. Blasius, A. Golnik, E. Brcher, R. K. Kremer, D. R. Noakes, C. E. Stronach, E. J. Ansaldo
Coexistence of ferromagnetism and superconductivity in the hybrid ruthenate-cuprate compound $RuSr_2GdCu_2O_8$ studied by muon spin rotation (μSR) and DC-magnetization
Phys. Rev. **B 59**, 14099 (1999).

RA-99-15
Ch. J. Rhodes, I. D. Reid and R. M. Macrae
The first observation of a muonium-carbonyl adduct with a negative muon hyperfine coupling constant
J. Chem. Soc., Chem. Commun., 2157 (1999).

Ch. J. Rhodes,
Electron Spin Resonance
Ann. Rep. Prog. Chem., Sect. **C 95**, 3 (1999).

LOW ENERGY MUONS
E. Morenzoni
Physics and applications of low energy muons
in Muon Science, S. Lee et al. Eds., IOP Publishing (1999)

Ch. Niedermayer, E. M. Forgan, H. Glückler, A. Hofer, E. Morenzoni, M. Pleines, T. Prokscha, T. M. Riseman, M. Birke, T. J. Jackson, J. Litterst, M. W. Long, H. Luetkens, A. Schatz, and G. Schatz
Direct observation of a flux line lattice field distribution across an $YBa_2Cu_3O_{7-\delta}$ surface by low energy muons
Phys.Rev.Lett. **83**, 3932 (1999).

T. Prokscha, M. Birke, E. Forgan, H. Glückler, A. Hofer, T. Jackson, K. Küpfer, J. Litterst, E. Morenzoni, Ch. Niedermayer, M. Pleines, T. Riseman, A. Schatz, G. Schatz, H. P. Weber and C. Binns
First μSR studies on thin films with a new beam of low energy positive muons at energies below 20 keV
Hyperfine Interactions **120/121**, 569 (1999).

H. D. Mieskes, W. Assmann, M. Brodale, M. Dobler, H. Glückler, P. Hartung, P. Stenzel
Measuring sputtering yields of high energy heavy ions on metals
Nucl. Inst. and Meth. **B 146**, 162 (1998).

LABORATORY FOR MICRO AND NANO TECHNOLOGY

C. David, R. Hartmann, U. Gennser, E. Müller and D. Grützmacher
Pre-structuring of silicon substrates to investigate MBE-growth of SiGe layers
Microelectronic Engineering **46,** 274 (1999).

C. David and D. Hambach
Line width control using a defocused low voltage electron beam
Microelectronic Engineering **46,** 219 (1999).

C. David and A. Souvorov
High efficiency Bragg-Fresnel Lenses with 100 nm outermost zone width
Review of Scientific Instruments **70**, no. 11, 4168 (1999).

H. Elgamel and J. Gobrecht
Improving the quality of polycrystalline silicon string ribbon for fabricating high efficiency solar cells
Solid State Phenomena **67-68**, 521 (1999)

J.H. Fabian, L. Scandella, H. Fuhrmann, R. Berger, T. Mezzacasa, Ch. Musil, J. Gobrecht and E. Meyer,
Finite Element Calculations and Fabrication of Cantilever Sensors for Nanoscale Detection, Ultramicroscopy,
82, 69 (2000).

D. Grützmacher, R. Hartmann, O. Leifeld, U. Gennser, C. David, E. Müller and J.-C. Panitz
Optical properties of Si-Ge-C nanostructures deposited by MBE
in Proceedings of SPIE **3630**: Silicon-based Optoelectronics edited by D. C. Houghton and E. A. Fitzgerald,
The Society of Photo-Optical Instrumentation Engineers p. 171 (Bellingham, WA, 1999).

R. Hartmann, U. Gennser, H. Sigg, D. Grützmacher and G. Dehlinger
Si/SiGeC Heterostructures: A Path towards High-Mobility Channels
Future Trends in Microelectronics - The Road Ahead, ed. S. Luryi, J. Xu, and A. Zaslavsky p. 133 (John Wiley, 1999).

F. J. Himpsel, T. Jung, A. Kirakosian, J.L. Lin, D.Y. Petrovykh, H. Rauscher and J. Viernow
Nanowires by Step Decoration, Materials Research Society,
MRS Bulletin **24,** 20 (1999).

R.W. Jaszewski, H. Schift, B. Schnyder, A. Schneuwly and P. Gröning
The deposition on anti-adhesive ultra-thin teflon-like films and their interaction with polymers during hot embossing
Applied Surface Science **143,** 301 (1999).

S. Köppel, H. Schift, M. Gabriel and W. Kaiser
Spritzguss stösst in immer kleinere Dimensionen vor
Kunststoffe-Synthetics **2/99,** 11 (1999).

O. Leifeld, E. Müller, D. Grützmacher, B. Müller and K. Kern
In-situ scanning tunneling microscopy study of C induced Ge quantum-dot formation on Si(100)
Applied Physics Letters **74**, 994 (1999).

O. Leifeld, D. Grützmacher, B. Müller, and K. Kern, Efthimios Kaxiras and P. Kelires
Dimer-pairing on the C-alloyed Si(001) surface
Physical Review Letters **82**, 972 (1999).

O. Leifeld, R. Hartmann, E. Müller, E. Kaxiras, K. Kern and D. Grützmacher
Self organized growth of Ge quantum dots on Si(001) substrates induced by sub-monolayer C coverages
Nanotechnology **10**, 122 (1999).

E. Müller, R. Hartmann, and D. Grützmacher
TEM study of an anti-correlation relation in corrugated layers of Si1-xGex/Si superlattices
Proc. of 11th Int. Conf. on Microscopy of Semiconducting Materials, 22-25 March 1999,
University of Oxford, Vol. 164, p. 227, (1999).

E. Müller, R. Hartmann, C.David and D. Grützmacher
Structural characterization of SiGe step graded buffer layers grown on prestructured Si [001] substrates by molecular beam epitaxy
Thin Solid Films **336**, 92 (1999)

H. Rauscher, T. A. Jung, J.-L. Lin, A. Kirakosian, F.J. Himpsel, U. Rohr and K. Müllen
One-dimensional confinement of organic molecules via selective adsorption on CaF versus CaF_2
Chemical Physics Letters **303,** 363 (1999).

C. Schäfle, C. Bechinger, B. Rinn, C. David and P. Leiderer
Cooperative evaporation in ordered arrays of volatile droplets
Physical Review Letters, **83** (25), 5302 (1999)

H. Schift, R.W. Jaszewski, C. David and J. Gobrecht
Nanostructuring of polymers and fabrication of interdigitated electrodes by hot embossing lithography
Microelectronic Engineering **46,** 121 (1999).

V. Senz, U. Dötsch, U. Gennser, T. Ihn, T. Heinzel, K. Ensslin, R. Hartmann and D. Grützmacher
Metal-insulator transition in a 2-dimensional system with an easy spin axis
Ann. Phys. **8,** SI-237 (1999).

H. Sorribas, L. Leder, D. Fitzli, C. Padeste, T. Mezzacasa, P. Sonderegger and L. Tiefenauer
Neurite outgrowth on microstructured surfaces functionalized by a neural adhesion protein
J. Mat. Sci.: Materials in Medicine **10**, 787 (1999).

L. Tiefenauer and C. Padeste
Micro- and nanotechnology in biosensor research
Chimia **53**, 62 (1999).

LABORATORY FOR RADIO- AND ENVIRONMENTAL CHEMISTRY

HEAVY ELEMENTS

A. Türler, W. Brüchle, R. Dressler, B. Eichler, R. Eichler, H.W. Gäggeler, M. Gärtner, J-P. Glatz, K.E. Gregorich, S. Hübener, D.T. Jost, V.Ya. Lebedev, V.G. Pershina, M. Schädel, S. Taut, S.N. Timokhin, N. Trautmann, A. Vahle, A.B. Yakushev
Erste experimentelle Bestimmung einer thermochemischen Größe einer Seaborgiumverbindung
Angew. Chem. **111**, 2349 (1999).

A. Türler, W. Brüchle, R. Dressler, B. Eichler, R. Eichler, H.W. Gäggeler, M. Gärtner, J-P. Glatz, K.E. Gregorich, S. Hübener, D.T. Jost, V.Ya. Lebedev, V.G. Pershina, M. Schädel, S. Taut, S.N. Timokhin, N. Trautmann, A. Vahle, A.B. Yakushev
First measurement of a thermochemical property of a seaborgium compound
Angew. Chem. Int. Ed. **38**, 2212 (1999).

B. Eichler, A. Türler, H.W. Gäggeler
Thermochemical characterization of seaborgium compounds in gas adsorption chromatography
J. Phys. Chem. **A 103,** 9296 (1999).

B. Eichler, R. Dressler
Löslichkeit von Kernreaktions- und Korrosionsprodukten im Quecksilber-Spallationstarget - Bedeutung für das Betriebsverhalten und Möglichkeiten der Kalkulation
PSI-Bericht Nr. **99-02,** (1999).

R. Dressler, B. Eichler, D.T. Jost, D. Piguet, A. Türler, Ch. Düllmann, R. Eichler, H.W. Gäggeler, M. Gärtner, M. Schädel, S. Taut, N. Trautmann, A.B. Yakushev,
Production of ^{262}Db (Z=105) in the Reaction ^{248}Cm(^{19}F; 5n)
Phys. Rev. **C 59**, 3433 (1999).

A. Vahle, S. Hübener, H. Funke, B. Eichler, D.T. Jost, A. Türler, W. Brüchle, E. Jäger
Gas Chromatographic Studies of Oxide and Hydroxide Species of Tungsten - Model Experiments with Respect to the Physico-Chemical Characterization of Seaborgium (Element 106)
Radiochim. Acta **84**, 43 (1999).

A. Türler
Gas Phase Chemistry of the Transactinides
Czech. J. Phys. **49/S1**, 581 (1999).

SURFACE CHEMISTRY, AEROSOL CHEMISTRY, ANALYTICAL CHEMISTRY

M. Ammann, M. Stalder, M. Saurer, R. Siegwolf, F. Pichlmayer and C. Brunold
Estimating the uptake of traffic derived NO_2 from ^{15}N abundance in Norway spruce needles
Oecologia **118**, 124 (1999).

B. Aumont, S. Madronich, M. Ammann, U. Baltensperger, D. Hauglustaine, F. Brocheton
On the NO_2 + soot reaction in the atmosphere
J. Geophys. Res. **104**, 1729 (1999).

U. Baltensperger, M. Ammann, M. Schwikowski, H.W. Gäggeler
The Life Cycle of Atmospheric Aerosol Particles
EUROTRAC Newsletter **21**, 2 (1999).

M.A. Geyh, M. Grosjean, L. Nuñez, U. Schotterer
Radiocarbon reservoir effect and the timing of the late-glacial/early holocene humid phase in the Atacama Desert (Northern Chile)
Quaternary Res. **52**, 143 (1999).

M. Kalberer, M. Ammann, H.W. Gäggeler, U. Baltensperger
Adsorption of NO_2 on carbon aerosol particles in the low ppb range
Atmos. Environ. **33**, 2815 (1999).

M. Kalberer, M. Ammann, F. Arens, H.W. Gäggeler, U Baltensperger
Heterogeneous formation of nitrous acid (HONO) on soot aerosol particles
J. Geophys. Res. **104**, 13825 (1999).

V.M.H. Lavanchy, H.W. Gäggeler, S. Nyeki, U. Baltensperger
Elemental carbon (EC) and black carbon (BC) measurements with a thermal method and an aethalometer at the high-alpine research station Jungfraujoch
Atmos. Environ. **33**, 2759 (1999).

V.M.H. Lavanchy, H.W. Gäggeler, U. Schotterer, M. Schwikowski, and U. Baltensperger
Historical record of carbonaceous particle concentrations from a European high-alpine glacier (Colle Gnifetti, Switzerland)
J. Geophys. Res. **104**, 21'227 (1999).

S. Nussbaum, M. Ammann, J. Fuhrer
Foliar, absorption and use of airborne oxidised nitrogen by terrestrial plants
In: Modes of Nitrogen Nutrition (H.S. Srivastava, R.P. Singh, eds.), Oxford & IBH Publishing Co. Pvt. Ltd., New Delhi, Calcutta, 1999, p. 103.

S. Nyeki, M. Kalberer, M. Lugauer, E. Weingartner, A. Petzold, F. Schröder, I. Colbeck, U. Baltensperger
Condensation nuclei (CN) and ultrafine CN in the free troposphere to 12 km: a case study over the Jungfraujoch high-alpine research station
Geophys. Res. Lett., **26**, 2195 (1999).

M. Schwikowski, S. Brütsch, H.W. Gäggeler and U. Schotterer
A high resolution air chemistry record from an Alpine ice core (Fiescherhorn glacier, Swiss Alps)
J. Geophys. Res. **104**, 13'709 (1999).

M. Schwikowski, A. Döscher, H.W. Gäggeler and U. Schotterer
Anthropogenic versus natural sources of atmospheric sulphate from an Alpine ice core
Tellus **51 B**, 938 (1999).

G. Skillas, H. Burtscher, K. Siegmann, U. Baltensperger
The density and fractal-like dimension of particles from a laminar diffusion flame
J. Colloid Interface Sci. **217**, 269 (1999).

H.R. von Gunten, E. Rössler, R.T. Lowson, P.D. Reid, St.A. Short
Distribution of uranium- and thorium series radionuclides in mineral phases of a weathered lateritic transect of ore body
Chem. Geol. **160**, 225 (1999).

E. Weingartner, S. Nyeki, U. Baltensperger
Seasonal and diurnal variation of aerosol size distributions ($10 < D < 750$ nm) at a high-alpine site (Jungfraujoch 3580 m asl)
J. Geophys. Res. **104**, 26809 (1999).

P. Zanis, E. Schuepbach, H.W. Gäggeler, S. Hübener, L. Tobler
Factor controlling beryllium-7 at Jungfraujoch in Switzerland
Tellus **51 B**, 789 (1999).

C. Zellweger, M. Ammann, P. Hofer, U. Baltensperger
NO_y speciation with a combined wet effluent diffusion denuder - aerosol collector coupled to ion chromatography
Atmos. Environ. **33**, 1131 (1999).

PROJECT RADWASTE

J. Koziorowski, O. Lebeda, R. Weinreich
A cryotrap as flow reactor for synthesis of ^{211}At labelled compounds
Appl. Radiat. Isot. **50**, 527 (1999).

J.-E. Ryser, P. Bläuenstein, N. Rémy, R. Weinreich, P.H. Hasler, I. Novak-Hofer, P.A. Schubiger
[^{76}Br]Bromodeoxyuridine, a potential tracer for the measurement of cell proliferation by positron emission tomography, in vitro and in vivo studies in mice
Nucl. Med. Biol. **26**, 673 (1999).

LABORATORY FOR ION BEAM PHYSICS

G. Bonani
Radiocarbon Dating of Milligram Samples of Anatolian Kilims by Accelerator Mass Spectrometry
Anatolian Kilims & Radiocarbon Dating, Jürg Rageth (edt), Riehen, Switzerland, (1999).

W.S. Broecker, K. Matsumoto, E. Clark, I. Hajdas and G. Bonani
Radiocarbon age differences between coexisting forminiferal species
Paleoceanography **14**, 431 (1999).

W. S. Broecker, E. Clark, D. C. McCorkle, I. Hajdas and G. Bonani
Core top ^{14}C ages as function of latitude and water depth on the Ontong-Java plateau
Paleoceanography **14**, 13 (1999).

W.S. Broecker, E. Clark, D.C. McCorkle, T.-H. Peng, I. Hajdas, G. Bonani
Evidence for a reduction in the carbonate ion content of the deep sea during the course of the Holocene
Paleoceanography **14**, 744 (1999).

C. Degueldre, M. Pouchon, M. Döbeli, G. Ledergerber
Behaviour of Cs and I in Zirconia Based Fuel
Mat. Res. Soc. Symp. Proc. **540**, 337 (1999).

H. Fuhrmann, M. Döbeli, R. Mühle, M. Suter
Focused Ion-beam Structuring of Si and Si/$CoSi_2$ Heterostructures Using Adsorbed Hydrogen as a Resist
J. Vac. Sci. Technol. **B 17**, 945 (1999).

H. Fuhrmann, A. Candel, M. Döbeli, R. Mühle
Minimizing Damage During Focused-Ion-Beam Induced Desorption of Hydrogen
J. Vac. Sci. Technol. **B 17**, 2443 (1999).

H. Fuhrmann, M. Döbeli, R. Kötz, R. Mühle, B. Schnyder
Thin Oxides on Passivated Silicon irradiated by Focused Ion Beams
J. Vac. Sci. Technol. **B 17**, 3068 (1999).

S. Hausmann, L. Bischoff, M. Voelskow, J. Teichert, W. Möller, H. Fuhrmann
Dwell-time effects in focused ion beam synthesis of cobalt disilicide: reflectivity measurements
Nucl. Instr. and Meth. **B 148**, 610 (1999)

S. Ivy-Ochs, C. Schlüchter, P. W. Kubik and G. H. Denton
Moraine exposure dates imply synchronous Younger Dryas glacier advances in the European Alps and in the Southern Alps of New Zealand
Geografisika Annaler **81 A**, 313 (1999).

H. Kerschner, S. Ivy-Ochs and C. Schlüchter
Paleoclimatic interpretation of the early Late-gacial glacier in the Gschnitz valley, central Alps, Austria
Annals of Glaciology **28**, 135 (1999).

J. M. López-Gutiérrez, M. García-León, C. Schnabel, A. Schmidt, R. Michel, H.-A. Synal and M. Suter
Determination of ^{129}I in atmospheric samples by accelerator mass spectrometry
Appl. Radiat. Isotop. **51**, 315 (1999).

R. Mühle, M. Döbeli, C. Maden
A Time-of-Flight Spectrometer for investigations on Liquid Metal Ion Sources
J. Phys. **D 32**, 187 (1999).

F. Oberli, P. Gartenmann, M. Meier, W. Kutschera, M. Suter and G. Winkler
The half-life of ^{126}Sn refined by thermal ionization mass spectrometry measurements
Int. J. Mass Spectrometry **184,** 145 (1999).

D. Perruchoud, F. Joos, A. Fischlin, I. Hajdas and G. Bonani
Evaluating time scales of carbon turnover in temperate forest soils with radiocarbon data
Global Biochemical Cycles **13**, 555 (1999).

M. Pouchon, M. Döbeli, C. Degueldre, M. Burghartz
Behaviour of Cs Implanted in Zirconia Based Inert Matrix Fuel
J. Nucl. Mater. **274**, 61 (1999).

M. Pouchon, M. Döbeli, C. Degueldre
Retention of Iodine in Yttria Stabilized Zirconia
Nucl. Instr. and Meth. **B 148**, 783 (1999).

C. Scheffel, A. Blinov, S. Massonet, H. Sachsenhauser, C. Stan-Sion, J. Beer, H. A. Synal, P. W. Kubik, M. Kaba and E. Nolte
^{36}Cl in modern atmospheric precipitation
Geophysical Research Letters **26**, 1401 (1999).

A.N. Tiwari, M. Krejci, F.J. Haug, H. Zogg, M. Döbeli, V. Zelezny, V. Vorlicek
Heteroepitaxy of $CuIn_xSe_y$: Material for High Efficiency and Stable Thin Film Solar Cells
J. Cryst. Gr. **202**, 1057 (1999).

I. Stolichnov, A. Tagantsev, M. Döbeli, P. Schmuki
Pt-Ion-Implantation-Induced Suppression of Leakage Conduction in $Pt/Pb(Zr_xTi_{1-x})O_3/Pt$ Capacitors
Integrated Ferroelectrics **23**, 357 (1999).

CONTRIBUTIONS TO CONFERENCES AND WORKSHOPS

LABORATORY FOR PARTICLE PHYSICS

R. Baur - CMS Collaboration
The Readout Architecture of the CMS Pixel Detector
5th Workshop on Electronics for LHC Experiments, Snowmass (Colorado, USA), 20th-24th September 1999.

A. Barczyk - L3 Collaboration
Measurement of Trilinear Gauge Couplings of the W Boson at LEP
APS, Centennial Conference, Atlanta, 22nd March 1999.

A. Barczyk - L3 Collaboration
Status of the L3 Muon Detector
L3 General Meeting, Lyon, 8th June 1999.

A. Barczyk - L3 Collaboration
W Boson Properties at LEP
EPS-HEP'99, Tampere, 16th July 1999.

M. Daum - NewHeavns Collaboration
Search for a Particle of Mass 33.9 MeV in Pion Decay
17th Workshop on Weak Interactions, WIN'99, Cape Town, South Africa, 24th-28th January 1999.

M. Daum - UCN Collaboration
A Facility for the Production of Ultracold Neutrons at PSI
Second International UCN Workshop, Pushkin, Russia, 13th-18th June 1999.
Proceedings of the Second International UCN Workshop (1999).

M. Daum - NTOF Collaboration
Experimental Verification of Coulomb De-excitation in pionic Hydrogen
Mesons and Nuclei, MENU'99, Zuoz, Switzerland, 15th-21st August 1999.
Proceedings of Mesons and Nuclei, MENU'99.

K. Deiters - CMS Collaboration
Properties of Avalanche Photodiodes for the CMS Electromagnetic Calorimeter
7th Int. Conference on Instrumentation for Colliding Beam Physics Hamamatsu, Japan, 15th - 19th November 1999.

R. Eichler
Search for Lepton Number Violation at HERA and PSI
Invited talk at Physics with e^+e^- colliders at the Φ and J/Ψ, Novosibirsk, March 1999

R. Eichler
Search for Lepton Number Violation at HERA and PSI
Invited talk at HADORN 99, Beijing, August 1999.

R. Eichler
The future of Particle Physics at PSI
Meeting of German Intermediate Energy Community, Endingen, 5. Oktober 1999.

R. Eichler
Search for Lepton Number Violation at HERA and PSI
Celebration of 40 years collaboration ETHZ/PSI/Krakau, Krakau, Oktober 1999.

R. Kaufmann, B. Henrich
Lorentz-Angle Measurements in Irradiated Silicon
ENDEASED (European Network on Defect Engineering of Advanced Semiconductor Devices)
Workshop and Summer-School, Santorini, Greece, 17th-23rd April 1999.

P.-R. Kettle - NewHeavns Collaboration
The KARMEN Time Anomal, Search for a Neutral Particle of Mass 33.9 MeV in Pion Decay
Proceedings of XVIII International Conference on Neutrino Physics and Astophysics, Takayama, Japan
Nucl. Phys **B 77**, 527 (1999); **77**, 529 (1999).

J. Koglin - NewHeavns Collaboration
The KARMEN Time Anomaly: Search for a Neutral Particle of Mass 33.9 MeV in Pion Decay
University of Virginia, 19th January 1999.

J. Koglin - NewHeavns Collaboration
The KARMEN Time Anomaly: Search for a Neutral Particle of Mass 33.9 MeV in Pion Decay
Annual Meeting of the Swiss Physical Society, University of Bern, 26th February 1999.

J. Koglin - NewHeavns Collaboration
The KARMEN Time Anomaly: Search for a Neutral Particle of Mass 33.9 MeV in Pion Decay
1999 European School of High-Energy Physics
Casta-Pariernicka, Slovak Republic, 22nd August to 4th September 1999.

B. Kotlinski - LADS Collaboration
Pion Absorption on N, Ar and Xe Nuclei Measured with LADS
Proceedings of the 8th Symposium on Meson-Nucleon Physics MENU99, Zuoz, 1999 PiN Newsletter 15 (1999) 218.

B. Kotlinski - CMS Collaboration
The CMS Pixel Detector
Proceedings of the 5th Position Sensitive Detector Conference PSD5, London 1999.

T. Nakada - LHCb Collaboration
The LHCb Experiment
CNPq Workshop, Rio de Janeiro Brazil, 12th January 1999.

T. Nakada - LHCb Collaboration
The LHCb Experiment
Seminar, Saclay France, 18th January 1999.

T. Nakada - LHCb Collaboration,
The LHCb Experiment
International Meeting on Fundamental Physics, Sierra Nevada Spain, 1st-5th February 1999

T. Nakada - LHCb Collaboration,
The LHCb experiment
Seminar, Vienna Austria, 12th January 1999.

T. Nakada - LHCb Collaboration
Status of the LHCb experiment
CERN Russia Joint Working Group meeting, Moscow Russia, 22nd April 1999.

T. Nakada - LHCb Collaboration
The LHCb experiment
Seminar, Lisbon Portugal, 4th May 1999

T. Nakada
Discrete Symmetries in elementary particle physics
Colloquium, University of Fribourg Switzerland, 19th May 1999.

T. Nakada - LHCb Collaboration
The LHCb experiment
Seminar, Munich Germany, 22nd June 1999.

T. Nakada - LHCb Collaboration
The LHCb experiment
Hadron 99, Beijing China, 24th-28th August 1999.

T. Nakada - LHCb Collaboration
The LHCb experiment
Seminar, Rome Italy, 27th October 1999.

T. Nakada - LHCb Collaboration
The LHCb experiment
Seminar, Hamburg Germany, 2nd November 1999.

T. Nakada - LHCb Collaboration
The LHCb experiment
Seminar, Zeuthen Germany, 3rd November 1999.

T. Nakada - LHCb Collaboration
The LHCb experiment
CERN-China LHC workshop, Beijing China, 29th-30th November 1999.

T. Nakada
Experimental summary of the conference
Third international conference on B physics and CP violation, Taipei Taiwan, 3rd-4th December 1999.

T. Nakada - LHCb Collaboration
The LHCb experiment
Seminar, Ferrara Italy, 14th December 1999.

T. Nakada - CPLEAR Collaboration
Summary of the CPLEAR experiment
Seminar, Villigen Switzerland, 17th December 1999.

C. Petitjean, P. Kammel et al. - R-97-05 Collaboration
Precision Measurement of μp-Capture in a Hydrogen TPC
PANIC 99 (XVth Particle and Nuclei International Conference), June 10th-16th June 1999, Uppsala, Sweden.

R. Pohl - R98-03 Collaboration
Experiment to Measure the Lamb Shift in Muonic Hydrogen
APAC99: 1st Euroconference on Atomic Physics at Accelerators: Laser Spectroscopy and Applications
19th - 24th September 1999, Univ. Mainz and Schloss Waldthausen, Budenheim, Germany

D. Renker et al. - CMS Collaboration
Properties of the most recent avalanche photodiodes for the CMS electromagnetic calorimeter
2nd. International conference on New Developments in Photodetection, Beaune, June 1999.

S. Ritt
New components of the MIDAS DAQ system
11th IEEE NPSS Real Time Conference, Santa Fe, NM, USA, 14th-19th June 1999.

D. Taqqu
Intense slow positron production via radiative cooling
Workshop on the Positron Source at the TESLA Test Facility DESY, Hamburg,1st-3rd September 1999.

D. Zürcher - CMS Collaboration
Nuclear Counter Effect and pion -electron misidentification
2nd International Conference on New developments in Photodetection, Beaune, France 21st - 25th June 1999.

D. Zürcher - CMS Collaboration
Vector boson pair production: PYTHIA vs. NLO
1999 Workshop on SM Physics (and more) at the LHC, QCD working group meeting, CERN, 11th October 1999.

D. Zürcher - CMS Collaboration
Vector boson pair production: PYTHIA vs. NLO
1999 Workshop on SM Physics (and more) at the LHC, Plenary meeting, CERN, 14th October 1999.

THEORY GROUP

A. Borici
Truncated Overlap Fermions
Lattice 99, PISA/Italy, 29th June to 3rd July 1999.

A. Borici
Fast methods for computing the Neuberger Operator (Invited talk)
Interdisciplinary Workshop on Numerical Challenges to Lattice QCD'', Wuppertal, 22nd-24th August 1999.

A. Borici
Truncated Overlap Fermions: the link between Overlap and Domain Wall Fermions (Invited talk)
"Lattice Fermions and Structure of the Vacuum", 4th-9th October 1999 Dubna, Russia.

A. Denner
VV scattering in the Standard Model with radiative corrections (Invited talk)
LHC workshop: electro-weak physics working group meeting, CERN, Geneva, 14th April 1999.

A. Denner
Das Standardmodell der Teilchenphysik (Invited talk)
Physikschule fuer Lehrer zur "Teilchen- und Hochenergiephysik", Bad Honnef, 21st June 1999.

A. Denner, S. Dittmaier, M. Roth and D. Wackeroth
Radiative corrections on $e^+e^- \to W W \to 4$ fermions (Invited talk)
ECFA DESY Linear Collider workshop, Obernai, 16th-19th October 1999.

D. Graudenz:
Jet Production in DIS (Invited talk)
Workshop on New Trends in HERA Physics Ringberg/Germany, 30th May to 4th June 1999.

D. Graudenz and M. Weber
NLO programs for DIS and photoproduction: Report from working group 20
Monte Carlo Generators for HERA physics, DESY, Hamburg 1999.

V.E. Markushin
Structure of the Light Scalar Mesons from a Coupled Channel Analysis of the S-wave $\pi\pi$ – $K\bar{K}$ scattering
Workshop on Hadron Spectroscopy, Frascati, 8th-12th March 1999 Frascati Physics Series Vol. XV 1999.

M. Melles
Precise Measurment of $\Gamma(H\to\gamma\gamma)$ at the Photon Linear Collider
ECFA/DESY workshop in Obernai, France, 17th October 1999.

M. Melles, V.Fadin, L.Lipatov and A.Martin
Resummation of Sudakov logarithms in electroweak processes
ECFA/DESY workshop in Obernai, France, 18th October 1999.

D. Wackeroth
Non-QCD loop corrections to top pair production at the LHC
CERN LHC-TH 1999 workshop, Top subgroup meeting, CERN, January 1999.

D. Wackeroth
Electroweak corrections to Drell-Yan procceses
CERN LHC-TH 1999 workshop, EWK subgroup meeting, CERN, January 1999.

D. Wackeroth
Predictions for $e^+ e^- \to 4$ fermions$+\gamma$
2nd ECFA/DESY Study on Physics and Detectors for a Linear Electron - Positron Collider, Oxford, March 1999.

D. Wackeroth
Predictions for $e^+ e^- \to 4$ fermions$+\gamma$
Phenomenology Seminar at the University of Wisconsin, Madison, June 1999.

D. Wackeroth
Parity Violating Asymmetries in Top Pair Production at Hadron Colliders (Invited talk)
SUSY99 Conference at Fermilab, Batavia, June 1999.

D. Wackeroth
Predictions for $e^+ e^- \to 4$ fermions+γ
Theory Seminar at the Ludwig-Maximilians-University, Munich, July 1999.

LABORATORY FOR MUON SPIN SPECTROSCOPY

I.D. Reid, S.F.J. Cox, RA-97-28 Collaboration
Muons in sulphur
8th International Conference on Muon Spin Rotation, Relaxation and Resonance (Les Diablerets, Switzerland)
August 30 - September 3, 1999.

A. Amato, X. Donath, D. Herlach, I.D. Reid, G. Solt, U. Zimmermann, C. Baines, A.-R. Raselli, D. Renker - PSI
Muons on request: A unique tool for high time-resolution, low-background μSR at PSI
8th International Conference on Muon Spin Rotation, Relaxation and Resonance (Les Diablerets, Switzerland)
August 30 - September 3, 1999.

D. Herlach *et al.*, RA-95-17 Collaboration
μSR on Co_xPd_{1-x}, an alloy exhibiting ferromagnetism in the liquid phase
8th International Conference on Muon Spin Rotation, Relaxation and Resonance (Les Diablerets, Switzerland)
August 30 - September 3, 1999.

V.S. Egorov, G. Solt *et al.*, RA-99-09 Collaboration
Structure of the superconducting intermediate state near H_C: new results by μSR
8th International Conference on Muon Spin Rotation, Relaxation and Resonance (Les Diablerets, Switzerland)
August 30 - September 3, 1999.

G. Solt *et al.*, RA-94-14 Collaboration
Diamagnetic (Condon) domains in beryllium and white tin studied by μSR
8th International Conference on Muon Spin Rotation, Relaxation and Resonance (Les Diablerets, Switzerland)
August 30 - September 3, 1999.

G. Solt *et al.*, RA-94-13 Collaboration
Observation of dia- and paramagnetic domains in beryllium and white tin by muon spin rotation spectroscopy
44th Annual Conference on Magnetism and Magnetic Materials (San Jose, California) November 15-18, 1999.

A. Schenck, G. Solt *et al.*, RA-90-16 Collaboration
Muon tunneling along a ring-shaped orbit in UNi_2Al_3
8th International Conference on Muon Spin Rotation, Relaxation and Resonance (Les Diablerets, Switzerland)
August 30 - September 3, 1999.

D. Herlach, T. Wider, K. Maier - PSI-Bonn Collaboration
Hydrogen embrittlement of metals
8th International Conference on Muon Spin Rotation, Relaxation and Resonance (Les Diablerets, Switzerland)
August 30 - September 3, 1999.

A.-R. Raselli, A. Amato, D. Herlach, C. Baines - PSI
Integration of new data acquisition hardware at PSI
8th International Conference on Muon Spin Rotation, Relaxation and Resonance (Les Diablerets, Switzerland)
August 30 - September 3, 1999.

U. Staub, B. Roessli, A. Amato *et al.*, RA-98-20 Collaboration
Magnetic ordering in Li_2CuO_2 studied by μSR technique
8th International Conference on Muon Spin Rotation, Relaxation and Resonance (Les Diablerets, Switzerland)
August 30 - September 3, 1999.

D. Andreica, A. Amato *et al.* - RA-98-07 Collaboration
Chemical pressure effects in the $Yb(Cu_{1-x}Ni_x)_2Si_2$ system
8th International Conference on Muon Spin Rotation, Relaxation and Resonance (Les Diablerets, Switzerland) August 30 - September 3, 1999.

A. Schenck, A. de Visser, A. Amato *et al.* - RA-95-18 Collaboration
Muon localization site in $U(Pt,Pd)_3$
8th International Conference on Muon Spin Rotation, Relaxation and Resonance (Les Diablerets, Switzerland) August 30 - September 3, 1999.

LOW-ENERGY MUONS GROUP
T. Prokscha - PSI
μ^+SR studies on thin films with low-energy muons at energies between 0 and 30 keV
20th μSR seminar of PNPI winter school (Gatchina, Russia) March 22-28, 1999.

H. Luetkens - PSI
Magnetism of thin epitaxial chromium films studied with LE-μSR
XXXIV Zakopane School of Physics (Zakopane, PL) May 9-15, 1999.

M. Pleines - PSI
μSR studies on thin HT_C superconductor films with slow muons at energies between 0 and 30 keV
XXXIV Zakopane School of Physics (Zakopane, PL) May 9-15, 1999.

M. Pleines - PSI
Status des LE-μ Projektes und Experimente an dünnen supraleitenden Filmen
Treffen des Verbundes Wasserstoff und Myonen in niedrigdimensionalen Systemen (Berlin, D) March 12-13, 1999.

H. Glückler - PSI
Range studies of low energy muons in a thin Al film
8th International Conference on Muon Spin Rotation, Relaxation and Resonance (Les Diablerets, Switzerland) August 30 - September 3, 1999.

T. Prokscha - PSI
μSR studies on thin films with low-energy muons at energies between 0 and 30 keV
XX μSR-Seminar (St. Petersburg, Gatchina) March 22-28, 1999.

E. Morenzoni - PSI
Low-energy muons at PSI
Workshop on Applications of Low Energy Muons to Solid State Phenomena, PSI, February 17-19, 1999.

E. Morenzoni - PSI
Muon-solid collisions (invited)
International Conference on Atomic Collisions in Solids (Odense, DK) August 3-8, 1999.

E. Morenzoni - PSI
Low energy muons (invited)
Workshop on Next Generation US Muon Facility Workshop (Los Alamos, USA) September 23-24, 1999.

E. Morenzoni - PSI
New low energetic beams and their applications (invited)
International Workshop on Atomic Collisions and spectroscopy with slow antiprotons (Tsurumi, JP) July 19-21, 1999.

E. Morenzoni - PSI
Polarized low energy muons as probes of thin films
Seminar at DPMC, University of Geneva, June 16, 1999.

E. Morenzoni - PSI
New surface muon beam for LE- and HE-μSR
8th International Conference on Muon Spin Rotation, Relaxation and Resonance. (Les Diablerets, Switzerland) August 30 - September 3, 1999.

M. Pleines et al. - PSI-Birmingham-Braunschweig-Konstanz Collaboration
Low-energy μSR study of the field distribution of a flux line lattice crossing an $Yba_2Cu_3O_{7-d}$ surface
8th International Conference on Muon Spin Rotation, Relaxation and Resonance. (Les Diablerets, Switzerland)
August 30 - September 3, 1999.

H. Luetkens et al. - PSI-Birmingham-Braunschweig-Konstanz Collaboration
Magnetism of thin chromium films studied with low energy muon spin rotation
8th International Conference on Muon Spin Rotation, Relaxation and Resonance. (Les Diablerets, Switzerland)
August 30 - September 3, 1999.

M. Birke et al. - PSI-Birmingham-Braunschweig-Konstanz Collaboration
LE-μ_+ measurements on thin Ni-films
8th International Conference on Muon Spin Rotation, Relaxation and Resonance. (Les Diablerets, Switzerland)
August 30 - September 3, 1999.

E. Morenzoni et al. - PSI-Birmingham-Braunschweig-Konstanz Collaboration
Low energy μSR at PSI: present and future
8th International Conference on Muon Spin Rotation, Relaxation and Resonance. (Les Diablerets, Switzerland)
August 30 - September 3, 1999.

LABORATORY FOR ASTROPHYSICS

M. Audard
Coronal Heating of Active Stars
LAP Seminar, May 12, 1999.

M. Audard, M. Güdel, E. F. Guinan, J. J. Drake
Active Late-Type Stellar Coronae: Hints for Heating by Flares?
IAU Symposium 195, "Highly Energetic Physical Processes and Mechanisms for Emissions from Astrophysical Plasmas."
MSU, Bozeman, USA, July 5-10, 1999.

M. Audard, M. Güdel, J. J. Drake, V. Kashyap, E. F. Guinan
Flares as Heating Agents of Active Late-Type Stellar Coronae?
Eleventh Cambridge Workshop on Cool Stars, Stellar Systems, and the Sun, Puerto de la Cruz,
Tenerife, Spain, October 4-8, 1999.

L. Grenacher
Clusters of galaxies, cooling flows and cold molecular clouds
PSI LAP Seminar, May 5, 1999.

L. Grenacher, Ph. Jetzer and D. Puy
Molecular clouds in cooling flow clusters of galaxies
IGRAP International Conference, Clustering at high redshift Marseille (France), June 29 - July 2 1999.

L. Grenacher, Ph. Jetzer and D. Puy
Thermal equilibrium of cold clouds in PKS 0745-191
International Workshop NOA-NASA, Large scale structure in the X-ray Universe
Santorini Island (Greece), September 20-22, 1999.

L. Grenacher, Ph. Jetzer and D. Puy
Cold clouds in cooling flows
International Workshop NOA-NASA, Large scale structure in the X-ray Universe
Santorini Island (Greece), September 20-22, 1999.

L. Grenacher, Ph. Jetzer and D. Puy
H_2 molecules and cold clouds in the cooling flow cluster
International conference, H_2 in space Paris (France), September 28 - October 1, 1999.

M. Güdel
Koronale Physik auf kühlen Sternen
Final 'F3A Bereichskonferenz', PSI, January 1999.

M. Güdel
New Prospects for the Study of Thin Stellar Plasmas (Invited talk)
Annual Meeting of the Swiss Physical Society, University of Bern, February 5, 1999.

M. Güdel
Stellar and Solar Astrophysics
LAP/TEM Meeting, PSI, May 6, 1999.

M. Güdel
Astrophysics at PSI
XMM Get-Together
Meeting on the occasion of the visit of R. Lainé, M. C. E. Huber, and F. Jansen at PSI, May 21, 1999.

M. Güdel
X-Ray Radiation from Flare-Heated Coronal Plasma
IAU Symposium 195, "Highly Energetic Physical Processes and Mechanisms for Emissions from Astrophysical Plasmas." MSU, Bozeman, USA, July 5-10, 1999.

M. Güdel, A. Zucker
A Characterization of High-Energy Electron Populations in Active Stellar Coronae from Their Gyrosynchrotron Emission.
IAU Symposium 195, "Highly Energetic Physical Processes and Mechanisms for Emissions from Astrophysical Plasmas." MSU, Bozeman, USA, July 5-10, 1999.

M. Güdel, M. Audard, E. F. Guinan, R. Mewe, J. J. Drake, I. Y. Alekseev
The Ups and Downs of AD Leo
Eleventh Cambridge Workshop on Cool Stars, Stellar Systems, and the Sun, Puerto de la Cruz, Tenerife, Spain, October 4-8, 1999.

M. Güdel, M. Audard
Radio Characteristics of Cool Stars and the HRD
Eleventh Cambridge Workshop on Cool Stars, Stellar Systems, and the Sun, Puerto de la Cruz, Tenerife, Spain, October 4-8, 1999.

M. Güdel
Signatures of Flare Heating in Stellar Coronae
Eleventh Cambridge Workshop on Cool Stars, Stellar Systems, and the Sun, Puerto de la Cruz, Tenerife, Spain, October 4-8, 1999.

M. Güdel, E. Gaidos
Deep VLA Observation of a Young Solar Analog: Constraints on the Evolution of the Hadean Sun
Eleventh Cambridge Workshop on Cool Stars, Stellar Systems, and the Sun, Puerto de la Cruz, Tenerife, Spain, October 4-8, 1999.

M. Güdel
Heisse Plasmen auf kühlen Sternen
Plasmakolloquium des Instituts für Plasmaforschung, Universität Stuttgart, October 28, 1999.

M. Güdel
EPIC Calibration
RGS Consortium Meeting, Utrecht, December 6-7, 1999.

W. Hajdas, J. Bialkowski, A. Mchedlishvili, R. Henneck, K. Thomsen and A. Zehnder
Components Total Dose and Single Event Testing for the HESSI RAS and SAS Modules
Nuclear and Space Radiation Effects Conference NSREC'99, Nordfolk VA, USA

W. Hajdas, J. Bialkowski, L. Adams, A. Mohammadazdeh, R. Nickson and B. O'Connell
Sensitivity of the SREM RADFET Dosimeters for STRV-1c to Various Radiation Environments
5th European Conference on Radiation and its Effects on Components and Systems RADECS 99, Abbaye de Fonteraud, F.

R. Henneck
Die High Energy Solar Spectroscopic Imager (HESSI) Mission für das nächste Solar Maximum
Frühjahrstagung Extraterrestrische Physik der DPG, Giessen, March 15-17, 1999.

R. Henneck, J. Bialkowski, F. Burri, M. Fivian, W. Hajdas, A. Mchedlishvili, P. Ming, K. Thomsen, J. Welte, A. Zehnder, M. Dettwyler, F. Bürki, G. Hurford, D. Curtis, D. Pankow
The Roll Angle System (RAS) for the High Energy Solar Spectroscopic Imager HESSI
SPIE Proc. 3765, Denver, July 1999.

R. Henneck, J. Bialkowski, F. Burri, M. Fivian, W. Hajdas, A. Mchedlishvili, P. Ming, K. Thomsen, J. Welte, A. Zehnder, B.R. Dennis, G. Hurford, D. Curtis, D. Pankow
The Solar Aspect System (SAS) for the High Energy Solar Spectroscopic Imager HESSI
SPIE Proc. 3765, Denver, July 1999,

Ph. Jetzer
Gravitationslinsen und dunkle Materie
Seniorenuniversität Zürich, June 1, 1999.

Ph. Jetzer
Gamma rays from the Galactic halo
TAUP99 Meeting, Paris, September 1999.

Ph. Jetzer
Microlensing towards different Galactic targets
Capri Meeting on Gravitational Lensing, September 1999.

Ph. Jetzer
A review on microlensing
Capri Meeting on Gravitational Lensing, September 1999.

Ph. Jetzer
Gravitationslinsen und dunkle Materie
Kolloquium Universität Konstanz, December 10, 1999.

P. Koch
Cooling flows in galaxies
Seminar at the University of Zürich, December 7, 1999.

J. L. Linsky, A. Krishnamurthi, M. Gagné, M. Güdel
Are the Shapes of Coronal Emission Measure Distributions Controlled by Rotation and Convection Zone Parameters?
Stellar Clusters and Associations: Convection, Rotation, and Dynamos. Mondello (Palermo), Sicily, Italy,
May 25-28, 1999.

D. Puy
Evolution of primordial H_2 for different cosmological models
International conference, H_2 in space
Paris (France), September 28 - October 1, 1999.

D. Puy
Molecules et nuages aux grands redshifts
Seminar, Centre d'Etudes Saclay, CEA, March 23, 1999, Saclay (France)

G. Rauw, K.A. van der Hucht, R. Mewe, M. Güdel, J.-M. Vreux, E. Gosset, W. Schmutz, I.R. Stevens
On the Perspectives of Using XMM to Study Fundamental Paramenters of Early-Type Stars
Wolf-Rayet Phenomena in Massive Stars and Staburst Galaxies, IAU Symposium 193,
Eds. K.A. van der Hucht, G. Köningsberger, P.R.J. Enens, San Francisco, ASP, 1999.

K. Smith
Coronal activity of intermediate mass young stellar objects
PSI astrophysics colloquium.

K. Smith, I. Bonnell, J. Emerson, T. Jenness
NGC1333/IRAS4 is an unstable triple
Eleventh Cambridge Workshop on Cool Stars, Stellar Systems, and the Sun, Puerto de la Cruz, Tenerife, Spain, October 4-8, 1999.

K. Smith, G. Lewis, I. Bonnell, P. Bunclark, J. Emerson
Accretion structures of DR Tau
Contributed talk at the Second Three Islands Euroconference: Stellar Clusters and Associations: Convection, Rotation, and Dynamos. Mondello (Palermo), Sicily, Italy, May 25-28, 1999.

K. Smith
T Tauri accretion structures revealed by spectroscopic variations
Invited colloquium speaker at Astronomisches Rechen-Institut, Heidelberg, and Star formation colloquium at MPIA, Heidelberg.

A. Zehnder
The HESSI and XMM - Missions
SPG Frühjahrstagung, Bern, February 25, 1999.

A. Zender
The High Energy Solar Spectroscopic Imager (HESSI)
Jahrestagung SAG, Luzern, September 14, 1999.

LABORATORY FOR MICRO AND NANO TECHNOLOGY

J. A. Anna Selvan, D. Grützmacher, E. Müller,E. Ortell, A. Wokaun, H. Sigg, S.Stutz, C. Musil, D. Bächle and J. Gobrech
Building blocks for the development of Thin film Si Solar cells
National photovoltaic conference, November 10-11,. Zurich, Switzerland, 1999.

C. David
Herstellung von Bragg-Fresnel Linsen für harte Röntgenstrahlung
DESY, Hamburg, Germany, April 13, 1999.

C. David
Linienbreitensteuerung durch Defokussieren
EULE'99, Physikalisch Technische Bundesanstalt, Braunschweig, Germany, April 15, 1999.

C. David, C. Musil, A. Souvorov and B. Kaulich
Nanofabrication of Custom X-Ray Optical Components
X-Ray microscopy XRM'99, Berkeley, California, August 2-6, 1999.

C. David
Fabrication of stair-case profiles with high aspect ratios for blazed optical elements
Micro and Nanoengineering MNE'99, Rome, Italy, September 21-24, 1999.

C. David, C. Musil, A. Souvorov and B. Kaulich
Nanofabrication of Custom X-Ray Optical Components
SLS Workshop, Brunnen, Switzerland, October 26-30, 1999.

C. David
Hochauflösende Elektronenstrahllithographie
DFG Schwerpunktsprogramm Workshop: Methodenvergleich Erzeugung von Nanostrukturen & STM / SECM
Schloss Reisensburg, Germany, December 12-14, 1999.

H. Elgamel and J. Gobrecht
A Simple And Efficient Process For Fabricating High Efficiency Polycrystalline Silicon Ribbon Solar Cells
11th Int. PV Science and Engineering Conf. (PVSEC-11), Sapporo, Japan, September 20-24, 1999.

J.H. Fabian, L. Scandella, H. Fuhrmann, R. Berger, T. Mezzacasa, Ch. Musil, J. Gobrecht and E. Meyer
Finite Element Calculations and Fabrication of Cantilever Sensors for Nanoscale Detection
Seattle'99: Scanning Probe Microscopy, Cantilever Sensors and Nanostructures, Seattle, USA, May 30 - June 1, 1999.

U. Gennser
La transition métal - isolant à 2d dans un puis quantique de SiGe
L2M-CNRS Bagnieux, February, 1999.

U. Gennser
Expériences sur des structures de bandes dans des hétérostructures IV-IV: Une approche "hors piste" par rapport au Si ?
INSA - Toulose, March, 1999.

U. Gennser
Metal - Insulator Transitions in 2-Dimensional Systems
Solid State Physics Laboratory, ETH Zürich, April, 1999.

U. Gennser
La transition métal - isolant dans des systèmes bi-dimensionelles
Laboratoire de Physique Théorique et Modèles Statistiques, CNRS-Université Paris XI, Orsay, July, 1999.

U. Gennser
Using the constraints of a non-ideal heterostructure: From the 2D metal – insulator transition to tunnelling in SiGe
L2M-CNRS Bagnieux, December, 1999.

J. Gobrecht and H. Elgamel
High efficiency polycrystalline silicon sheet ribbon solar cells using a simple process
11th Workshop on quantum solar energy concersion „QUANTSOL 99", Wildhaus, Switzerland, March 14-19, 1999.
2 page extended abstract in the workshop's proceedings.

J. Gobrecht
Über Mikrostrukturen in die Nanowelt
Univ. of Würzburg, Germany, April 13, 1999.

J. Gobrecht
Mikrostrukturen für den Zugang zur Nanowelt
In the framework of „Probleme der Mechatronik, ETH Zürich, May 15, 1999.

J. Gobrecht and M. Gale
PSI and CSEM – competence centers for micro- and nanostructuring in Switzerland
TOP Nano 21 Information Meeting, Bern, September 9, 1999.

J. Gobrecht
EMINENT steps into the nano-world
final MINAST convention, Bern November 30, 1999.

D. Grützmacher, R. Hartmann, O. Leifeld, U. Gennser, C. David, E. Müller, J.-C. Panitz
Optical properties of Si-Ge-C nanostructures deposited by MBE (Invited talk)
SPIE Conferences on Silicon-based Optoelectronics, San Jose, California, January 1999.

D. Grützmacher
SiGeC Nanostrukturen: Jenseits des Si Horizontes
Seminar at Forschungszentrum Jülich, Institut für Schicht und Ionentechnik, April 15, 1999.

D. Grützmacher
Structure and optical properties of Si-Ge-C quantum systems
Seminar at Technische Universität Berlin, July 8, 1999.

D. Grützmacher
Si-Ge-C Nanostrukturen: Neue Wege in der Si Technologie,
Seminar at Universität Konstanz, November 24, 1999.

T. A. Jung, H. Rauscher, J. K. Gimzewski, F.J. Himpsel and K. Muellen
Key Elements of Molecular Nanotechnology. Lecture given at the Venture
Business Laboratory of Kyoto University, Japan, January 6, 1999.

T. A. Jung, H. Rauscher, J. K. Gimzewski, F.J. Himpsel and K. Muellen,
Molecular Nanotechnology. Invited Seminar at the Kansai Advanced
Research Institute, Nishi-Akashi, Japan, January 19, 1999.

T. A. Jung, H. Rauscher, J. K. Gimzewski, F.J. Himpsel and K. Muellen
Key Elements of Molecular Nanotechnology: Positioning, Switching and Adressing of Individual Molecules
Department of Materials Physics and Chemistry, Kyushu University, Hakata, Japan, January 21, 1999.

T. A. Jung, H. Rauscher, J. K. Gimzewski, F.J. Himpsel and K. Muellen,
Molecular Nanotechnology: A playground towards concepts for future integrated devices
Tohoku University, Surface Science Laboratory, Sendai, Japan, February 1, 1999.

T. A. Jung, H. Rauscher, J. K. Gimzewski, F.J. Himpsel and K. Muellen
Key Elements of Molecular Nanotechnology: Positioning, Switching and Adressing of Individual Molecules as a Playground towards concepts for future integrated Devices
University of Canterbury, Christchurch, New Zealand, February 8, 1999.

T. A. Jung, S. Berner, H. Rauscher, F. J. Himpsel and K. Muellen.
Chemical Information about Single Molecules using Scanning Probe Microscopy. Single Molecule Physics and Chemstry
Workshop, Grimentz, Switzerland, March 15-19, 1999.

T.A. Jung
Chemical Information from Scanning Probe Microscopy and Spectroscopy
Wayne State University, Detroit, March 30, 1999.

T.A. Jung, S. Berner and F. Meisinger
What we need to know about Single Interfaced Molecules before we can call it a Device
Castelen Seminar über Nanowissenschaften, Landgut Castelen, Augst, August 23, 1999.

T. A. Jung
Molecular Nanoscience: Will there be Molecular Devices after Microelectronics?
Symposium Scientia Europaea No 4, September 19–23, 1999.

T. A. Jung
Atomic and Molecular Positioning and Self Assembly towards the integration of future Molecular Devices on the Nanometer Scale.
Int. Symposium on Nanometer Scale Electronic and Electromagnetic fields, Tsukuba, Japan, October 27 – 29, 1999.

T. A. Jung, F.J. Himpsel and H. J. Guentherodt
Key Elements of Molecular Nanotechnology: Towards the integration of individual molecules
Institute for Solid State Physics, The University of Tokyo, November 1, 1999.

T. A. Jung, H. Rauscher and F. J. Himpsel
Using Surface Science and single molecules to explore new concepts for devices
Kobe University, Venture Business Laboratory, November 2, 1999.

O. Leifeld, A. Beyer, E. Müller, K. Kern, and D. Grützmacher
Formation and Ordering Effects of C-induced Ge Dots Grown on Si (100) by Molecular Beam Epitaxy
3rd Conference on Low Dimensional Structures and Devices (LDSD´99), Antalya, Turkey, September 1999.

O. Leifeld, D. Grützmacher and K. Kern
Ge Nukleation auf C-vorbelegtem Si(001)
MBE-Workshop 1999, Universität Würzburg, Germany, September 28-29, 1999.

O. Leifeld
Ge Quantum Dot Formation on the C-alloyed Si(001) Surface – a Scanning Tunneling Microscopy Study
Institut d'Electronique Fondamentale CNRS, Université Paris-Sud, Orsay, France, October 19, 1999.

C. Padeste
Mikrostrukturierung, Nanotechnologie und molekulare Architektur für die Biosensorik
Seminar, Frauenhofer Institut für Festkörpertechnologie, München, March 4, 1999.

C. Padeste, A. Grubelnik and L. Tiefenauer
Microperoxidase-antibody conjugates for automated amperometric immunosensing
Nanotech99, Montreux, November 28-29, 1999.

C. Padeste, A. Grubelnik, R. Ros, H. Sorribas and L. Tiefenauer
Microstructuring, nanotechnology and surface chemistry for biosensors and related applications
Nanotech 99, Montreux, November 30 - December 2, 1999.

R. Ros, C. Padeste, F. Schwesinger, A. Plückthun, H.-J. Güntherodt and L. Tiefenauer
SPM for functional identification of individual biomolecules
BIOS99, San Jose, January 23-29, 1999.

R. Ros, F. Schwesinger, A. Plückthun, D. Anselmetti, H.-J. Güntherodt and L. Tiefenauer
Force spectroscopy on individual single-chain Fv antibody fragments
RMS, Basel, October 4-6, 1999.

H. Schift
Recent advances in LIGA
Workshop on micro- and nanostructuring beamline at SLS, Bern, Switzerland, April 22, 1999.

H. Schift
Replication of micro- and nanostructures using molding techniques
Graduiertenkolleg workshop on micro- and nanostructures: development, characterization, application, Ulm, Germany, May 10-12, 1999.

H. Schift and L.J. Heyderman
Nanoembossing and nanomoulding
4th Workshop MEL-ARI /NID on Printing, Duisburg, Germany, July 7-9, 1999.

H. Schift, J. Gobrecht, L.J. Heyderman, R.W. Jaszewski and W. Kaiser
Replication of micro- and nanostructures using molding techniques
Nanoforum CH-US, Zürich, Switzerland, September 20-22, 1999.

H. Schift, C. David, M. Gabriel, J. Gobrecht, L.J. Heyderman, W. Kaiser, S. Köppel and L. Scandella
Nanoreplication in polymers using hot embossing and injection molding
Micro- and Nanoengineering (MNE'99), Rome, Italy, September 22-24, 1999.

H. Sorribas, L. Leder, D. Fitzli, C. Padeste, T. Mezzacasa, P. Sonderegger and L. Tiefenauer
Neurite outgrowth on microstructured surfaces functionalized by a neural adhesion protein
ESB99, 15th Int. Conf. on Biomaterials, , Bordeaux France, September 12-15, 1999.

H. Sorribas, L. Leder, C. Padeste, P. Sonderegger and L. Tiefenauer
Patterns of the adhesion protein axonin-1 for neurite guidance on glass
EMBL Workshop on „Axon guidance and neural plasticity" Varenna (I), September 30 - October 3, 1999.

H. Sorribas, L. Leder, C. Padeste, P. Sonderegger and L. Tiefenauer
Patterning adhesion proteins for neuron guidance on glass
USGEB, Basel October 14-15, 1999.

F. Schwesinger, R. Ros, L. Tiefenauer, D. Anselmetti, H.-J. Günterodt and A. Plückthun
Antigen binding forces of individually addressed single-chain Fv antibody molecules
Proc. *STM '99*, Seoul, Korea, July 19-23, 1999.

L. Tiefenauer
Molecular Nanotechnology: Molecules and structures
Regio Seminars, Biocenter, University of Basel, April 27, 1999.

L. Tiefenauer
Molecular Nanotechnology: From single molecules to functional devices
Seminar, Solid State Physics, University of Fribourg, December 6, 1999.

L. Tiefenauer
Designed surfaces for functional molecules
Seminar, Max-Planck-Institute for Biochemistry, München, December 22, 1999.

LABORATORY FOR RADIO- AND ENVIRONMENTAL CHEMISTRY

HEAVY ELEMENTS
Ch. Düllmann, A. Türler, B. Eichler, H.W. Gäggeler
Thermochromatographic investigation of ruthenium with oxygen as carrier-gas
1st Int. Conference on the Chemistry and Physics of Transactinide Elements, Seeheim, September 26-30, 1999.

B. Eichler, H.W. Gäggeler
Entropies of transactinides
1st Int. Conference of the Chemistry and Physics of the Transactinide Elements, Seeheim, Germany, September 26-30, 1999.

R. Eichler, B. Eichler, H.W. Gäggeler, A. Türler
Gas phase chemistry of the group 7 homologues of bohrium (element 107)
1st Int. Conference on the Chemistry and Physics of Transactinide Elements, Seeheim, September 26-30, 1999.

R. Eichler, B. Eichler, H.W. Gäggeler, A. Türler
Gaschemische Untersuchungen der Homologen des Elementes Bohrium (Element 107)
Seminar Radio- und Umweltchemie, PSI, December 17, 1999.

H.W. Gäggeler
Das Labor für Radio- und Umweltchemie: Auf dem Weg zur Nummer 1
Festveranstaltung Rückblick Bereich F3A, Paul Scherrer Institut, January 18, 1999.

H.W. Gäggeler
Wie entdeckt und untersucht man neue chemische Elemente?
Berner Chemische Gesellschaft, March 31, 1999.

H.W. Gäggeler
Chemie der superschweren Elemente
Seminar Radio- und Umweltchemie, PSI, April 30, 1999.

H.W. Gäggeler
Synthesis of the heaviest elements and study of their chemical properties at the PSI-PHILIPS cyclotron
3rd Int. Conf. On Modern Problems of Nuclear Physics, MPNP'99, Bukhara, Usbekistan, August 23-27, 1999.

H.W. Gäggeler
Gas Chemical Separations of Transactinides
224 WE-Heraeus Seminar, Int. Workshop on Ion Chemical Aspects in Ion Guide Systems, Mainz, Germany, September 30 - October 2., 1999.

H.W. Gäggeler
Schwerelementforschung am Paul Scherrer Institut
Physik Institut Universität Basel, October 28, 1999.

H.W. Gäggeler
Research activities of the PSI division TEM
2nd Int. SLS Workshop on Synchrotron Radiation, October 26-30, 1999.

M. Gärtner, R. Dressler, B. Eichler, R. Eichler, A. Türler, H.W. Gäggeler
Koppelung der in-situ Chemie von Polonium mit der on-line Gaschromatographie
ANAKON '99, Konstanz, Germany, April 7-10, 1999.

D.T. Jost
SINQ-Gas-jet, Miss Piggy and Kermit: Facilities to produce tracers for model-experiments in transactinide chemistry
1st Int. Conference on the Chemistry and Physics of Transactinide Elements, Seeheim, September 26-30, 1999.

A. Türler
Speaker for a Paul Scherrer Institute - Bern University - Gesellschaft für Schwerionenforschung - Forschungszentrum Rossendorf - Mainz University - Flerov Laboratory of Nuclear Reactions - Lawrence Berkeley National Laboratory collaboration
Identification of Heavy and Superheavy Nuclides Using Chemical Separator Systems
Experimental Nuclear Physics in Europe, ENPE 99, Facing the next Millennium, Sevilla, June 20-26, 1999, AIP Conference Proceedings **495**, edited by B. Rubio et al., 149 (1999).

A. Türler
Gas Phase Chemistry of the Transactinide Elements
1st International Conference on the Chemistry and Physics of Transactinide Elements, Seeheim, September 26-30, 1999.

A. Türler
Chemie und Physik der Transaktiniden
‚Kernphysikalisches Kolloquium der Ludwig-Maximilians-Universität und der Technischen Universität München, December 3, 1999.

SURFACE CHEMISTRY, AEROSOL CHEMISTRY, ANALYTICAL CHEMISTRY

M. Ammann
Die Nutzung von kurzlebigen Radionukliden in Laborexperimenten zur heterogenen Atmosphärenchemie
Seminarvortrag, Institut für Kernphysik, ETH Zürich, Juni 1, 1999.

M. Ammann, F. Arens, U. Baltensperger
Nanoparticles - Chemical Facts and Artefacts: 1. Effect of Sampling Procedures on Chemical Parameters of Soot Particles.
Third International ETH-Workshop on Nanoparticle Measurement, Zürich, August 9-10, 1999.

M. Ammann, F. Arens, E. Rössler, H.W. Gäggeler, U. Baltensperger
The reaction of NO_2 with solid anthracenetriol and naphthalenediol
In R. Vogt, G. Axelsdottir (ed.s) *EC/Eurotrac-2 Joint Workshop, Aachen, September 20-22, 1999*, ISBN 3-00-005414-6, pp 236-239.

M. Ammann, F. Arens, L. Gutzwiller, U. Baltensperger, H.W. Gäggeler
The HONO formation capacity of primary and aged diesel soot particles
In R. Vogt, G. Axelsdottir (ed.s) *EC/Eurotrac-2 Joint Workshop, Aachen, September 20-22, 1999*, ISBN 3-00-005414-6, pp 219-222.

F. Arens, M. Ammann, E. Rössler, H.W. Gäggeler, U. Baltensperger
Heterogeneous reaction of NO_2 with substituted PAH's adsorbed on aerosol particles
European Geophysical Society General Assembly, The Hague, April 18-23, 1999.

F. Arens, M. Ammann, M. Kalberer, H.W. Gäggeler, U. Baltensperger
The reaction of NO_2 with solid anthracenetriol - a model process for HONO formation on soot aerosol particles ?
International Conference 'Air Quality in Europe, Challenges for the 2000s', Venice, May 19-21, 1999.

F. Arens, M. Ammann, M. Kalberer, H.W. Gäggeler, U. Baltensperger
The effect of sampling conditions on the reactivity of diesel soot particles towards NO_2
European Aerosol Conference, Prague, September 6-10, J. Aerosol Sci. **30**, Suppl. 1, S873-S874 (1999).

F. Arens, M. Ammann, M. Kalberer, S. Nyeki, U. Baltensperger, H.W. Gäggeler
Formation of HONO from the reaction of NO_2 with diesel soot
American Association of Aerosol Research, Tacoma, October 11-15, 1999.

U. Baltensperger
Atmospheric Aerosol Chemistry
EPFL Lausanne, Cours de troisième cycle en sciences de l'environnement, February 5, 1999.

U. Baltensperger
Die Verwendung von Aerosol- und Radon-Daten auf dem Jungfraujoch zur Untersuchung vertikaler Tansportprozesse
Universität für Bodenkultur, Vienna, March 3, 1999.

U. Baltensperger
Klimarelevante Aerosolparameter an einem hochalpinen Standort (Jungfraujoch, 3580 m ü. M)
Experimentalphysik, Universität Wien, Vienna, March 4, 1999.

U. Baltensperger
Hochalpine Atmosphärenchemie am Jungfraujoch
Technische Universität Wien, Vienna, March 5, 1999.

U. Baltensperger
Overview on the activities of the scientific advisory group on Aerosols and optical depth
GAW Meeting SAG chairs, Zürich, March 12, 1999.

U. Baltensperger
Aerosolpartikel, winzige Teilchen in der Atmosphäre mit grossen Auswirkungen
ETH Zürich, Privatdozent-Antrittsvorlesung, May 10, 1999.

U. Baltensperger
Umweltforschung im Labor für Radio- und Umweltchemie
Hochrheinseminar, PSI, May 19, 1999.

U. Baltensperger
Session Chair
12th Int. Congress of the International Society for Aerosols in Medicine / GAeF Satellite Meeting, Aerosols for Medical Applications, Vienna, June , 1999.

U. Baltensperger, H.W. Gäggeler, M. Schwikowski
The Jungfraujoch as a Platform to Study the Life Cycle of Atmospheric Aerosol Particles
Audit on the Atmospheric Sciences at the Jungfraujoch, Grindelwald, June 24-25, 1999.

U. Baltensperger
Aerosol Research at the Jungfraujoch
HFSJG Board Meeting, Interlaken, October 8, 1999.

U. Baltensperger
Veränderung von Partikeln aus der Verbrennung in der Atmosphäre
Seminar Feinstpartikelemissionen von Verbrennungsmotoren, Haus der Technik, München, October 12-13, 1999.

U. Baltensperger
Aerosol measurements within the WMO Global Atmosphere Watch programme: providing data related to climate forcing and air quality (invited)
EMEP/WMO Workshop on Fine Particles, Interlaken, November 22-25, 1999.

U. Baltensperger, E. Weingartner, S. Henning, S. Nyeki
Aerosol measurements: providing the data for the quantification of aerosol impact on climate
EMEP/WMO Workshop on Fine Particles, Interlaken, November 22-25, 1999.

A. Eichler
Umwelt- und Klimaforschung - Informationen aus den kältesten Archiven Mitteleuropas
Seminar Radio- und Umweltchemie, Universität Bern, May 28, 1999.

A. Eichler, M. Schwikowski, H.W. Gäggeler
Bestimmung von Spurenstoffen mit hoher zeitlicher Auflösung in einem Alpinen Eisbohrkern
Jahrestreffen 1999 der AG Hochgebirgsökologie, Bern, June 3-6, 1999.

A. Eichler, M. Schwikowski, H.W. Gäggeler
Historical climate and environmental information preserved in an Alpine ice core
Swiss Climate Summerschool, Hasliberg, July 17-24, 1999.

A. Eichler, M. Schwikowski, H.W. Gäggeler
High resolution paleo atmospheric records from Alpine ice cores
6th Scientific Conference of the Int. Global Atmospheric Chemistry Project (IGAC), Bologna, Italy, September 13-17, 1999.

K. Eleftheriadis, A.G. Karydas, S. Nyeki, E. Weingartner, U. Baltensperger
Composition profile of a Saharan dust event over Central Europe
European Aerosol Conference, Prague, J. Aerosol Sci. **30**, Suppl. 1, S167-S168, September 6-10, 1999.

K. Eleftheriadis, S. Nyeki, H. Beine, E. Weingartner, I. Colbeck, U. Baltensperger
Arctic black carbon measurements at Ny Alesund, Svalbard
European Aerosol Conference, Prague, J. Aerosol Sci. **30**, Suppl. 1, S843-S844, September 6-10, 1999.

H.W. Gäggeler
Fachtagung Permafrost
Glaziologische Kommission der SANW, Kursaal Interlaken, January 14, 1999.

H.W. Gäggeler
Atmosphärische Aerosolteilchen als Informationsträger von Umweltprozessen
Festkolloquium Proffs. W. Dannecker und A. Reller, Universität Hamburg, May 6, 1999.

H.W. Gäggeler, M. Schwikowski, U. Schotterer, A. Döscher, T. Döring, V. Lavanchy
History of European air pollution from Alpine ice cores
AGU Spring Meeting, Boston, USA, June 1-4, 1999.

H.W. Gäggeler
Gletscherarchive erzählen die Geschichte von Luftinhaltstoffen
Tagung AG Hochgebirgsökologie, Bern, June3-6, 1999.

H.W. Gäggeler
HR-ICP-MS measurements of lead in an alpine glacier
Analytical Russian-German Ukrainian Symposia (ARGUS-99), Odessa Ukraine, August 29 - September 2, 1999.

Ch. George, M. Ammann, H. Berresheim, J.N. Crowley, T. Hoffmann
Tropospheric aerosols: formation and heterogeneous chemistry
Co-Convenor and session chair, European Geophysical Society General Assembly, The Hague, April 18-23, 1999.

P. Ginot, M. Funk, H.W. Gäggeler. Hübener, U. Schotterer, M. Schwikowski, W. Stichler
Environmental record preserved in an ice core from Cerro Tapado, Chile
Jahrestreffen 1999 der AG Hochgebirgsökologie, Bern, June 3-6, 1999.

P. Ginot, M. Funk, H.W. Gäggeler. Hübener, U. Schotterer, M. Schwikowski, W. Stichler
Environmental record preserved in an ice core from Cerro Tapado, Chile
Swiss Climate Summerschool, Hasliberg, July 17-24, 1999.

P. Ginot
Environmental records from Tropical and extra Tropical circulation regimes in Andean ice cores
Seminar Radio- und Umweltchemie, Universität Bern, November 26, 1999.

L. Gutzwiller, M. Ammann, U. Baltensperger
HONO measurements in the EUPHORE smog chamber in Valencia
DIFUSO Workshop, Wuppertal, July 27, 1999.

L. Gutzwiller, M. Ammann, U. Baltensperger, J. Kleffmann, M. Lackhoff, P. Wiesen, K. Wirz, V. Scheer
Assessing HONO formation on real diesel exhaust in a smog chamber experiment
In R. Vogt, G. Axelsdottir (eds) EC/Eurotrac-2 Joint Workshop, Aachen, September 20-22, 1999, ISBN 3-00-005414-6, p. 232.

L. Gutzwiller, N. Streit, M. Ammann, U. Baltensperger
Possible artefacts in the HONO determination by wet effluent diffusion denuders caused by a combination of NO_2 and additional interferents
Scientific results of the BERLIOZ and PIPAPO field campaigns, Varese, December 13-15, 1999.

S. Henning, E. Weingartner, S. Nyeki, M. Schwikowski, U. Baltensperger, H.W. Gäggeler
Size dependent activation of aerosol particles to cloud droplets at the high alpine site Jungfraujoch (3580 m asl)
Jahrestagung der Arbeitsgruppe Hochgebirgsökologie, Bern, June 3-6, 1999.

S. Henning, E. Weingartner, S. Nyeki, M. Schwikowski, U. Baltensperger, H.W. Gäggeler
Size dependent activation of aerosol particles to cloud droplets at the high alpine site Jungfraujoch (3580 m asl)
Swiss climate summer school, Hasliberg, July 17-24, 1999.

S. Henning, M. Lugauer, E. Weingartner, S. Nyeki, B. Buchmann, H.W. Gäggeler, U. Baltensperger
Influence of synoptic weather conditions on the aerosol size distribution at the high-Alpine site Jungfraujoch
European Aerosol Conference, Prague, September 6-10, J. Aerosol Sci. **30**, Suppl. 1, S579-S580, 1999.

S. Henning
Einfluss der synoptischen Situation auf die Aerosolgrössenverteilung auf dem Jungfraujoch
Seminar Radio- und Umweltchemie, Villigen, October 29, 1999.

T. Huber, M. Schwikowski, H.W. Gäggeler
Continuous Melting and Analyses of Ice Cores
Swiss Climate Summerschool, Hasliberg, July 17-24, 1999.

Z. Krivacsy, A. Hoffer, U. Baltensperger, S. Nyeki, E. Weingartner, A. Molnar, Gy. Kiss
Characterisation of carbonaceous fine aerosol at the Jungfraujoch
European Aerosol Conference, Prague, September 6-10, J. Aerosol Sci. **30**, Suppl. 1, S81-S82 (1999).

V.M.H. Lavanchy
Entwicklung der atmosphärischen Russpartikelkonzentrationen der letzten 200 Jahre in Westeuropa
Seminar Radio- und Umweltchemie, Universität Bern, May 28, 1999.

V.M.H. Lavanchy, H.W. Gäggeler, U. Schotterer, M. Schwikowski, U. Baltensperger
Historical record of carbonaceous particle concentrations from a European high-Alpine glacier (Colle Gnifetti, Switzerland)
European Aerosol Conference, Prague, September 6-10, J. Aerosol Sci. **30**, Suppl. 1, S611-S612 (1999).

S. Nyeki, S. De Wekker, D. Steyn, M. Kossmann, M. Kalberer, I. Colbeck, U. Baltensperger
Airborne lidar study of convective boundary layer development over pre-Alpine area
European Aerosol Conference, Prague, September 6-10, J. Aerosol Sci. **30**, Suppl. 1, S209-S210 (1999).

S. Nyeki, I. Colbeck, M. Kalberer, U. Baltensperger, M. Kossmann, S. DeWekker, D. Steyn
Development of the planetary boundary layer over complex mountainous terrain: a temporal and spatial lidar study
American Association for Aerosol Research Conference (AAAR), Seattle, October 11-15, 1999.

Zs. Sarvari, Z. Krivacsy, U. Baltensperger, S. Nyeki, E. Weingartner, S. Wessel, S.G. Jennings
Low-molecular weight carboxylic acids in atmospheric aerosol at different European sites
European Aerosol Conference, Prague, September 6-10, J. Aerosol Sci. **30**, Suppl. 1, S261-S262 (1999).

U. Schotterer
Isotopenklimatologie: Deuterium und Sauerstoff-18 im Niederschlag und in Eisbohrkernen der tropischen Anden
Seminar Radio- und Umweltchemie, Bern, May 28, 1999.

U. Schotterer, W. Stichler, H.W. Gäggeler, P. Ginot, M. Schwikowski, B. Francou, B. Pouyaud, K. Froehlich
Temperature, precipitation, seasonality: stable isotope climate information in shallow ice cores from the Alps and the Andes
AGU Spring Meeting, Boston, USA, June 1-4, 1999.

M. Schwikowski, S. Brütsch, T. Döring, A. Döscher, A. Eichler, H.W. Gäggeler, V. Lavanchy, U. Schotterer
The history of European air pollution in Alpine ice cores and other natural archives
Seminar Environment Institute, Commission of the European Communities, Ispra, January 14, 1999.

M. Schwikowski, U. Baltensperger, S. H. Ehrman, O. Poulida, B. Tenberken
Scavenging von aerosolgebundenen Spurenstoffen durch Wolkentröpfchen und Schnee
Seminar Institut für Meteorologie und Klimaforschung, Forschungszentrum Karlsruhe, January 19, 1999.

M. Schwikowski
European glaciating cloud experiment at the Jungfraujoch
Workshop on Atmospheric Ice Formation below the Cirrus Level, Leipzig, Germany, March 11-12, 1999.

M. Schwikowski, T. Döring, A. Döscher, S.H. Ehrman, A. Eichler, H.W. Gäggeler, P. Ginot, T. Huber, V. Lavanchy, U. Schotterer, B. Tenberken
Chemische Analyse von Spurenstoffen in Schnee und Eis
ANAKON '99, Konstanz, April 7-10, 1999.

M. Schwikowski, A. Döscher, A. Eichler, H.W. Gäggeler, P. Ginot, T. Huber, U. Schotterer, B. Tenberken-Pötzsch
Analyse ionischer Spurenstoffe in alpinen Schnee- und Eisproben zur Rekonstruktion der Geschichte der Luftverschmutzung
2. Fachtagung Ionenanalyse mit Chromatographie und Kapillarelektrophorese, Idstein, Germany, September 14-15, 1999,

M. Schwikowski, P. Ginot, M. Funk, H.W. Gäggeler, S. Hübener, B. Pouyaud, U. Schotterer, W. Stichler
Palaeo atmospheric chemistry and precipitation climatology from Cerro Tapado ice core, Chile
6th Scientific Conference of the Int. Global Atmospheric Chemistry Project (IGAC), Bologna, Italy, September 13-17, 1999.

M. Schwikowski
Hochalpine Gletscher als Archive für die Geschichte der Luftverschmutzung
Seminar AMI Heute, October 1, 1999, PSI.

M. Schwikowski
Chemische Analysen von Spurenstoffen in Schnee und Eis hochalpiner Gletscher
PSI-Herbstschule, October 6, 1999.

M. Schwikowski
Palaeo atmospheric chemistry from an Andean ice core (Cerro Tapado, Chile)
PACIFIC workshop, Bern, Switzerland, December 16, 1999.

G. Skillas, L. Tobler, C. Beeli, H. Burtscher, K. Siegmann, U. Baltensperger
On the density of silver nanoparticles. A comparison
European Aerosol Conference, Prague, September 6-10, J. Aerosol Sci. **30**, Suppl. 1, S493-S494 (1999).

N. Streit
Aerosolcharakterisierung während Sommer-Smoglagen in Mailand
Seminar Radio- und Umweltchemie, Bern, March 26, 1999.

N. Streit, E. Weingartner, S. Nyeki, U. Baltensperger, R. van Dingenen, J. Putaud, A. Even, H. ten Brink, A. Blatter, A. Neftel, H. W. Gäggeler
Aerosol measurements during summer smog events in the Milan area
Air Quality in Europe: Challenges for the 2000s, Venice, May 19-21, 1999.

N. Streit, E. Weingartner, S. Nyeki, S. Henning, U. Baltensperger, and H. W. Gäggeler
Global Atmosphere Watch: Measurements on the Jungfraujoch are providing data for the quantification of aerosol impact on climate
Jahrestagung der Arbeitsgruppe Hochgebirgsökologie, Bern, June 3-6, 1999.

N. Streit, E. Weingartner, S. Nyeki, U. Baltensperger, R. van Dingenen, J.-P. Putaud, A. Even, H. ten Brink, A. Blatter, A. Neftel, H.W. Gäggeler
Aerosol characterization during summer smog events in the greater Milan area
European Aerosol Conference, Prague, September 6-10, J. Aerosol Sci. **30**, Suppl. 1, S115-S116 (1999).

N. Streit, E. Weingartner, S. Nyeki, U. Baltensperger, R. van Dingenen, J.-P. Putaud, A. Even, H. ten Brink, A. Blatter, A. Neftel, H.W. Gäggeler
Primary and secondary aerosol measurements during summer smog events in the Milan area
Scientific results of the BERLIOZ and PIPAPO field campaigns, Varese, December 13-15, 1999.

B. Tenberken-Pötzsch, M. Schwikowski, H.W. Gäggeler
Analysis of size-classified ice crystals by capillary electrophoresis
23rd Int. Symposium on High Performance Liquid Phase Separations and Related Techniques HPLCH '99, Granada, Spain, May 30 - June 4 1999.

E. Weingartner, S. Nyeki, S. Henning, U. Baltensperger
Hygroscopic properties of aerosol particles in the temperature range -11°C < T < 20°C
Third International ETH-Workshop on Nanoparticle Measurement, Zürich, August 9-10, 1999.

E. Weingartner, S. Nyeki, S. Henning, U. Baltensperger
Hygroscopic properties of aerosol particles at low temperatures (T < 0°C)
European Aerosol Conference, Prague, September 6-10, J. Aerosol Sci. 30, Suppl. 1, S17-S18 (1999).

E. Weingartner, S. Nyeki, U. Baltensperger
Seasonal and diurnal variation of aerosol size distributions (10 < D < 750 nm) at a high-alpine site (Jungfraujoch 3580 m asl)
Sixth Scientific Conference of the International Global Atmospheric Chemistry Project (IGAC), Bologna, September 13-17, 1999.

E. Weingartner, U. Baltensperger, S. Nyeki
Seasonal and diurnal variation of aerosol size distributions (10 < D < 750 nm) at a high-alpine site (Jungfraujoch 3580 m asl)
American Association for Aerosol Research Conference (AAAR), Seattle, October 11-15, 1999.

E. Weingartner, S. Henning, S. Nyeki, U. Baltensperger
Seasonal and diurnal variation of aerosol size distributions (10 < D < 750 nm) at a high-alpine site (Jungfraujoch 3580 m asl)
EMEP/WMO Workshop on Fine Particles, Interlaken, November 22-25, 1999.

CEMENT CHEMISTRY
H.P. Zimmermann, M. Egloff, R. Gubler, M. Lips
Application of the parallel-plate squeezing-flow technique for quality control of bituminous samples
Radwaste Bituminization '99, Rez/Prague, Czech Republic, June 29 - July 2, 1999.

PROJECT RADWASTE
C. Salt
Benzimidazolic DTPA- and DOTA-based ^{157}Gd-Chelates for Gadolinium Neutron Capture Therapy (GdNCT)
1st Young Members Neutron Capture Therapy Meeting, Petten, Netherlands, September 8-11, 1999.

R. Weinreich
Radionuclide analysis of accelerator waste materials
Seminar, TIS Radiation Protection Group, CERN, Geneva, March 18, 1999.

R. Weinreich
Production of ^{211}At and labelling of DNA-seeking compounds
Workshop "^{211}Astatine in Anti-Cancer Therapy", Ispra, Italy, June 7-8, 1999.

R. Weinreich, M. Argentini
Bestimmung von Radionuklidvektoren in Beschleunigerabfällen
Workshop "Radiochemische Analytik beim Betrieb und Rückbau kerntechnischer Anlagen, der Deklaration von Abfällen und im Strahlenschutz", Dresden, Deutschland, September 6-7, 1999.

R. Weinreich, M. Argentini
Determination of radionuclide inventory in accelerator waste
8th International Conference SIS'99 "Separation of Ionic Solutes", Stará Lesná, High Tatras, Slovakia, September 11-16, 1999.

R. Weinreich
Analytical problems in the determination of radionuclides in accelerator waste
Seminar, Department of Radiopharmaceuticals and Radiation Protection, Atomic Research Institute, Debrecen, Hungary, September 17, 1999.

LABORATORY FOR ION BEAM PHYSICS

J. Beer, G. Wagner, R. Muscheler, P.W. Kubik, H.-A. Synal
$^{10}Be/^{36}Cl$ ratio in ice
8th International Conference on Accelerator Mass Spectrometry, Vienna, Austria, September 6–10, 1999.

A. Blinov, S. Massonet, C. Stan-Sion, V. Lazarev, J. Beer, H.-A. Synal, P.W. Kubik, M. Kaba, E. Nolte
An excess of ^{36}Cl in modern precipitation
8th International Conference on Accelerator Mass Spectrometry, Vienna, Austria, September 6–10, 1999.

G. Bonani
^{14}C-Altersbestimmungen von Milligrammproben: Möglichkeiten und Grenzen der Beschleunigermassenspektrometrie Mit zahlreichen Beispielen aus der Archäologie
Basler Zirkel für Ur- und Frühgeschichte, Universität Basel, Basel, Switzerland, January 12, 1999.

G. Bonani
Radiokarbondatierung von Milligrammproben mit der Beschleunigermassenspektrometrie-Methode (AMS) Anwendungen in der Archäologie
Archäologisches Institut, Universität Zürich, Zürich, Switzerland, January 18, 1999.

G. Bonani
Radiokarbondatierung von Milligrammproben mit der Beschleunigermassenspektrometrie-Methode (AMS)
Archäolischer Diest des Kantons Bern, Bern, Switzerland, January 19, 1999.

G. Bonani
Radiocarbon Dating of Milligram-Size Samples by Accelerator Mass Spectrometry (AMS)
International Symposium on Turkmen Carpets, Liestal, Switzerland, February 26–28, 1999.

M. Döbeli
Nachweis von Spurenelementen mit Beschleuniger-SIMS
Radio- und Umweltchemieseminar, Universität Bern, March 26, 1999.

M. Döbeli
High Depth Resolution He RBS with a Time-of-Flight Spectrometer
International Conference on Ion Beam Analysis IBA-14, Dresden, July 27, 1999.

A. Duhr, M. Suter
Betrieb einer Sputterquelle mit Rubidium
63. Physikertagung der Deutschen Physikalischen Gesellschaft, Heidelberg, Germany, March 15–19, 1999.

Duhr, P.W. Kubik, M. Döbeli
The high current source at the heavy-ion injector at Zürich AMS facility
8th International Conference on Accelerator Mass Spectrometry, Vienna, Austria, September 6–10, 1999.

H. Fuhrmann, M. Döbeli, R. Mühle
A focused ion beam lithography technique for silicon surfaces using adsorbed hydrogen as a resist
EIPBN '99 Conference, Marco Island, Florida, USA, June 4, 1999.

P. Gartenmann, M. Suter, H.-A. Synal
Investigation of ^{60}Fe with the ETH/PSI AMS facility
8th International Conference on Accelerator Mass Spectrometry, Vienna, Austria, September 6–10, 1999.

I. Hajdas
Radiocarbon chronologies and calendar time scales—the last 40,000 years
Laminated sediments (varves) meeting, Lammi, Finland, April 13–18, 1999.

I. Hajdas, G. Bonani, D. Ariztegui, P. Moreno
Radiocarbon chronologies and climatic records — the last 13 kyr
XV INQUA Congress, Durban, South Africa, August 3-11, 1999.

I. Hajdas, G. Bonani, D. Ariztegui, P. Moreno
Radiocarbon chronologies of South American climatic records kyr
8th International Conference on Accelerator Mass Spectrometry, Vienna, Austria, September 6–10, 1999.

Heisinger, S. Neumaier, F.J. Hartmann, S. Ivy-Ochs, P.W. Kubik, D. Lal, T. Jull, E. Nolte
Cosmic-muon induced in-situ production of radionuclides and exposure ages
8th International Conference on Accelerator Mass Spectrometry, Vienna, Austria, September 6–10, 1999.

F.-J. Haug, M. Krejci, A. N. Tiwari, H. Zogg, M. Döbeli, V. Zelezny, V. Vorlicek
Growth and Structural Characterisation of $CuGa_xSe_y$ Layers
Proc. 2. World Conf. on Photovoltaic Solar Energy Conversion, 696 1999.

S. Ivy-Ochs, C. Roth, H.-A. Synal, P.W. Kubik, G. Denton, C. Schlüchter
A test of north-south climate synchrony: surface exposure dating of moraines on the South Island of New Zealand
8th International Conference on Accelerator Mass Spectrometry, Vienna, Austria, September 6–10, 1999.

S.A.W. Jacob, M. Suter, H.-A. Synal
Neue Perspektiven in der Beschleunigermassenspektrometrie: Molekülzerstörung durch Stösse
63. Physikertagung der Deutschen Physikalischen Gesellschaft, Heidelberg, Germany, March 15–19, 1999.

S.A.W. Jacob, M. Suter, H.-A. Synal
Ion-beam interaction with stripper gas – the key for AMS at sub MeV
8th International Conference on Accelerator Mass Spectrometry, Vienna, Austria, September 6–10, 1999.

S.A.W. Jacob
Accelerator Mass Spectrometry (AMS): operating principles and a new generation of small facilities
Hitachi Ltd, Advanced Research Laboratories, Hatoyama, Japan, October 4, 1999.

S.A.W. Jacob
Accelerator Mass Spectrometry (AMS) at low energies and a new generation of small facilities
MALT, University of Tokyo, Tokyo, Japan, October 6, 1999.

S.A.W. Jacob
Accelerator Mass Spectrometry (AMS): operating principles and a new generation of small facilities
National Institute for Environmental Studies (NIES), Tsukuba, Japan, October 8, 1999.

S.A.W. Jacob
TANDY - Beschleunigermassenspektrometrie im Handy
Umweltphysikseminar, EAWAG, Dübendorf, Switzerland, November 19, 1999.

M. Krejci, A.N. Tiwari, F.-J. Haug, H. Zogg, and M. Döbeli
Investigations of the Interfaces Between Substrate and Epitaxial $CuIn_xSe_y$ Layers
Proc. 2. World Conf. on Photovoltaic Solar Energy Conversion, 585 1999.

P.W. Kubik, S. Ivy-Ochs, J. Schäfer, L. Bruno, R. Wieler, C. Schlüchter
Langzeitproduktionsraten von ^{10}Be, ^{26}Al und ^{21}Ne für Expositionsaltersbestimmungen
63. Physikertagung der Deutschen Physikalischen Gesellschaft, Heidelberg, Germany, March 15–19, 1999.

P.W. Kubik, S. Ivy-Ochs, J. Schäfer, L. Bruno, R. Wieler, C. Schlüchter
^{10}Be, ^{26}Al and ^{21}Ne production rates for exposure dating
XXIV General Assembly of the European Geophysical Society, The Hague, Netherlands, April 19-23, 1999.

P.W. Kubik, S. Ivy-Ochs, J. Schäfer, L. Bruno, R. Wieler, C. Schlüchter
A consistent set of long-term ^{10}Be, ^{26}Al and ^{21}Ne production rates for exposure dating
8th International Conference on Accelerator Mass Spectrometry, Vienna, Austria, September 6–10, 1999.

V.Kh. Liechtenstein, T.M. Ivkova, E.D. Olshanski, I. Feigenbaum R. Repnow, R. Hellborg, M. Döbeli, R.A. Weller
Advanced Targetry with Diamond-like Carbon Films for Tandem Accelerators and RBS TOF Spectrometers
International Conference on Ion Beam Analysis IBA-14, Dresden 1999.

C. Maden, M. Döbeli
Status der PSI/ETH-Beschleuniger-SIMS-Anlage
63. Physikertagung der Deutschen Physikalischen Gesellschaft, Heidelberg, Germany, March 15–19, 1999.

C. Maden, M. Döbeli
Detection of trace elements in electrically insulating samples with TEAMS (Trace Element AMS)
8th International Conference on Accelerator Mass Spectrometry, Vienna, Austria, September 6–10, 1999.

S. Merchel, M. Altmaier, T. Faestermann, U. Herpers, K. Knie, G. Korschinek,, P.W. Kubik, S. Neumann, R. Michel, M. Pätsch, L. Schultz, M. Suter
Saharan meteorites with short or complex exposure histories
Workshop on Extraterrestrial Materials from Hot and Cold Deserts, Pilanesberg, South Africa, July 6-8, 1999.

R. Muscheler, J. Beer, G. Wagner, P.W. Kubik
Vergleich von ^{10}Be- und ^{14}C-Datensätzen der letzten 10000 Jahre
63. Physikertagung der Deutschen Physikalischen Gesellschaft, Heidelberg, Germany, March 15–19, 1999.

R. Muscheler, J. Beer, G. Wagner, P.W. Kubik, J. Masarik
Changes in atmospheric circulation deduced from a comparison of ^{14}C and ^{10}Be data records
8th International Conference on Accelerator Mass Spectrometry, Vienna, Austria, September 6–10, 1999.

M. Schaller, F. von Blanckenburg, P.W. Kubik, J.D. Kramers
Catchment-wide denudation rates from cosmogenic nuclides in river sediment
10. Conference of the European Union of Geosciences, Strasbourg, France, March, 1999.

M. Schaller, F. von Blanckenburg, P.W. Kubik
Catchment-wide denudation rates from cosmogenic nuclides in river sediment
8th International Conference on Accelerator Mass Spectrometry, Vienna, Austria, September 6–10, 1999.

M. Schaller, F. von Blanckenburg, N. Hovius, P.W. Kubik
Denudation rates from in-situ ^{10}Be in European river sediments
Fall Meeting of the American Geophysical Union, San Francisco, USA, December, 1999.

J. Schäfer, I. Leya, R. Wieler, S. Ivy-Ochs, S. Tschudi, P.W. Kubik, C. Schlüchter
Consistency of long term cosmogenic ^{3}He and ^{21}Ne production rates and new findings concerning the nucleogenic production of neon
XXIV General Assembly of the European Geophysical Society, The Hague, Netherlands, April 19-23, 1999.

J. Schäfer, D. R. Marchant, G.H. Denton, S. Ivy-Ochs, R. Wieler, H. Baur, C. Schlüchter
Many million years old relict ice in Beacon Valley, Antarctica: new implications from a cosmogenic noble gas study
8th International Conference on Accelerator Mass Spectrometry, Vienna, Austria, September 6–10, 1999.

Strobl, M. Molnar, V. Schulz, C. Woda, D. Hoffmann, S. Schäper, P.W. Kubik, M.Suter, A. Mangini
High-resolution stratigraphy of two sediment cores from the central Arctic Ocean based on ^{10}Be, $^{230}Th_{excess}$ and ESR
AGU 1999 Fall Meeting, San Francisco, USA, December 13-17, 1999.

M. Suter
Eine neue kompakte Anlage für ^{14}C Datierungen
63. Physikertagung der Deutschen Physikalischen Gesellschaft, Heidelberg, Germany, March 15–19, 1999.

M. Suter
Eine neue Generation von ^{14}C-Datierungsanlagen - kleiner, einfacher und billiger
Seminar, Institut für Isotopengeologie und Mineralische Rohstoffe, ETHZ, Zürich, Switzerland, May 20, 1999.

M. Suter
Ein neuer Kleinbeschleuniger für ^{14}C-Datierungen
Seminar, Klima und Umweltphysik, Universität Bern, Bern, Switzerland, June 7,1999.

M. Suter
Eine neue ^{14}C-Datierungsanlage - einfacher, kleiner und billiger
Physik Kolloquium, Universität Erlangen, Erlangen, Germany, June 24, 1999.

M. Suter
Tandem AMS at sub-MeV energies – status and prospects
8th International Conference on Accelerator Mass Spectrometry, Vienna, Austria, September 6–10, 1999.

M. Suter
A new generation of accelerator mass spectrometers - smaller, simpler and cheaper
Annual Meeting of the Swiss Group for Mass Spectrometry, Rigi, Switzerland, October 28, 1999.

M. Suter
Beschleunigermassenspekrometrie - Blick in die Vergangenheit und Zukunft
Kernphysikalisches Kolloquium, TU-München, Garching, Germany, December 17, 1999.

M. Suter, R. Huber, S. A. W. Jacob, H.-A. Synal and J.B. Schroeder
A new small accelerator for radiocarbon dating
Proceedings of the Fifteenth International Conference on Application of Accelerators in Research and Industry, eds. J.L. Duggan and I.L.Morgan, Part Two 665, AIP Conference Proceedings 475, AIP, 1999.

H.-A. Synal
New concepts for radiocarbon detection systems
14th International Conference on Ion Beam Analysis (IBA-14), Dresden, Germany, July 26-30, 1999.

H.-A. Synal, S. Jacob, M. Suter, J.B. Schroeder
The PSI/ETH small radiocarbon dating system
8th International Conference on Accelerator Mass Spectrometry, Vienna, Austria, September 6–10, 1999.

H.-A. Synal
Radiocarbon Dating at Sub MeV Energies
8th International ISMAS Symposium on Mass Spectrometry, Hyderabad, India, December 7, 1999.

H.-A. Synal, S. Jacob and M. Suter
Radiocarbon dating at sub MeV energies
Proc. 8th ISMAS Symp. on Mass Spectrometry Vol. 1, 409, 1999.

A.N. Tiwari, M. Krejci, F.-J. Haug, H. Zogg, M. Döbeli, V. Zelezny and V. Vorlicek, G. Lippold
Structural Properties of In-rich Phases of $CuIn_xSe_y$
Proc. 2. World Conf. on Photovoltaic Solar Energy Conversion, 1999, p. 581.

S. Tschudi, S. Ivy-Ochs, C. Schlüchter, P.W. Kubik, H. Rainio
^{10}Be and ^{26}Al dating of Younger Dryas Salpausselkä I formation in Finland
8th International Conference on Accelerator Mass Spectrometry, Vienna, Austria, September 6–10, 1999.

F. von Blanckenburg, M. Schaller, P.W. Kubik
Eine neue Methode zur flächenhaften Quantifizierung langfristiger Bodenerosion
Umwelt 2000, Halle, Germany, September, 1999

D. Wagenbach, A. Stanzick, M. Auer, I. Levin, E. Lehrer, S. Kipfstuhl, P.W. Kubik
Radioisotopes Observed in Bipolar Aerosol Samples and Ice Cores
Int. Workshop on „Tracers in Global Circulation Studies", Uppsala, Sweden, November 4-6, 1999.

G. Wagner, J. Beer, R. Muscheler, P.W. Kubik, H.-A. Synal
Datierung von Eisbohrkernen anhand der kosmogenen Radionuklide Be-10 und Cl-36
63. Physikertagung der Deutschen Physikalischen Gesellschaft, Heidelberg, Germany, March 15–19, 1999.

PUBLICATIONS AND LECTURES FOR GENERAL PUBLIC

R. Eichler
Kindervorlesung: Physik für 5. Klasse Schule Villigen
Vorlesung, psi-forum, PSI Villigen, Switzerland, April 27, 1999.

R. Eichler
Kindervorlesung: Physik für 5. Klasse Schule Würenlingen
Vorlesung, psi-forum, PSI Villigen, Switzerland, April 27, 1999.

M. Güdel
Ein neues Kapitel der Rötgenastronomie - Erfolgreicher Abschluss der ROSAT-MISSION
Beitrag zu Forschung und Technik, Neue Zürich Zeitung, April 7,.1999, p.74.

Ph. Jetzer
XMM: Un satellite per lo studio della sorgenti X
Carriere de Ticino, December 10, 1999

M. Kalberer, M. Lugauer, S. Nyeki, U. Baltensperger
Partikel-Immissionen PM10, Literaturübersicht in englischer Sprache
Bundesamt für Umwelt, Wald und Landschaft (BUWAL), 1999.

H. Schift, J. Gobrecht and L.J. Heyderman, issued by SNF, Presse- und Informationsdienst
Der Fortschritt heisst drucken, Lösungen für die Massenproduktion von Nanobauteilen
Bild des Monats aus Wissenschaft und Forschung, Swiss National Foundation (SNF)
Swiss National Foundation (SNF), Priority Programme NFP36, Bern, Switzerland, May 1999.

LECTURES AND COURSES

Prof. Dr. R. Eichler
ETH Zürich, SS99:
- Ergänzendes physikalisches Praktikum für UNW
- Physikpraktikum für Vorgerückte
- Seminar in Physik der Elementarteilchen (with others)
- Teilchenphysik am PSI (with others)
- Physikalisches Kolloquium (with ohers)

ETH Zürich, WS99/00:
- Physik II
- Physikpraktikum für Vorgerückte
- Seminar in Physik der Elementarteilchen (with others)
- Teilchenphysik am PSI (with others)
- Physikalisches Kolloquium (with ohers)

LABORATORY FOR ASTROPHYSICS

Dr. M. Güdel
ETH Zürich und Universität Zürich, WS99/00:
- Hochenergie-Astrophysik (with Prof. A. Benz)

ETH Zürich und Universität Zürich, SS99:
- Physik der Stern- und Planetenentstehung

PD Dr. Ph. Jetzer
Universität Zürich, SS99:
- Weisse Zwerge, Neutronensterne und Schwarze Löcher II

Universität Zürich, WS99/00:
- Gravitationslinsen und Dunkle Materie

Universität Zürich:
- Mitwirkung an der Organisation des Theorie-Seminars (gemeinsam mit der ETH)

ETH Zürich, WS 99/00
- Mitwirkung am Proseminar in Theoret. Physik

LABORATORY FOR MICRO AND NANO TECHNOLOGY

Dr. J. Gobrecht
ETH Zürich, WS99/00:
- Vorlesung und Übungen „Grundlagen der Mikro- und Nanotechnik"

Dr. T.A. Jung
Universität Basel, SS99
- Einführung in die Nanowissenschaften (with others)

Dr. T.A. Jung
VSM Fachhochschule Rapperswil
- Zerstörungsfreie Materialpruefung mit Rastersensormethoden

LABORATORY FOR RADIO- AND ENVIRONMENTAL CHEMISTRY

PD Dr. U. Baltensperger
ETH Zürich, SS 1999:
- Aerosole II (with Prof. Dr. H. Burtscher)

ETH-Zürich, WS 1999/2000:
- Aerosole I (with Prof. Dr. H. Burtscher and Prof. Dr. T. Peter)
- Analytische Chemie V (with others)

Prof. Dr. H.W. Gäggeler

Universität Bern, SS99:

- Physikalische Chemie IV
- Instrumentalanalytik II
- Seminar in anorganischer und physikalischer Chemie (with others)
- Seminar in Radio- und Umweltchemie (with Dr. M. Ammann), in collaboration with Paul Scherrer Institut

Universität Bern, WS 1999/2000:

- Anwendung von Radioisotopen
- Radiochemiepraktikum (with PD Dr. A. Türler)
- Seminar in anorganischer und physikalischer Chemie (with others)
- Seminar in Radio- und Umweltchemie (with Dr. M. Ammann), in collaboration with Paul Scherrer Institut

Dr. M. Schwikowski

Universität Bern, SS99:

- Instrumentalanalytik II (with Prof. H.W. Gäggeler)

LABORATORY FOR ION BEAM PHYSICS

Dr. M. Suter

ETH Zürich, SS 99:

- Seminar Kernphysik mit Anwendungen (with others)
- Doktorierendenseminar über Kern- und Teilchenphysik (with others)

Dr. M. Suter

ETH Zürich, WS 99/00:

- Kernphysik II, Wahlfachvorlesung
- Seminar Kernphysik mit Anwendungen (with others)

Dr. M. Döbeli

EPF Lausanne, WS 99:

- Lecture course (3^{eme} cycle): Materials Analysis with MeV Ion Beams

PARTICLE PHYSICS

PD Dr. T. Nakada

DESY Academic Training Programme, Hamburg Germany, 14th April, 28th April, 12th, May 1999

- Physics of CP violation

NATO Advanced Institute Summer School, Cargese Corsica, 26th July to 8th August 1999

- Physics of CP violation and rare decays

ETH Zürich, SS 99:

- Statistische Methoden der Datenanalyse

THEORY GROUP

PD Dr. A. Denner

ETH Zürich, WS 98/99:

- Das Standardmodell der elektroschwachen Wechselwirkung und dessen Erweiterungen

ETH Zürich, SS99:

- Seminar über Physik der Elementarteilchen (with D. Graudenz) at PSI

ETH Zürich, WS99/00:

- Das Standardmodell der elektroschwachen Wechselwirkung und dessen Erweiterungen
- Seminar über Physik der Elementarteilchen (with D. Graudenz) at PSI

PD Dr. D. Graudenz

ETH Zürich, SS99:

- Einführung in die Quantenchromodynamik
- Seminar über Physik der Elementarteilchen (with A. Denner) at PSI

ETH Zürich, WS99/00:

- Seminar über Physik der Elementarteilchen (with A. Denner) at PSI

PD Dr. K. Junker

Technische Universität Wien, SS 99:

- Einführung in die theoretische Mittelenergiephysik

Prof. Dr. M. P. Locher

Universität Zürich, WS 98/99:

- Aktuelles aus der Teilchenphyik
  Theoretisch-Phyikalisches Seminar

Universität Zürich, SS 99:

- Aktuelles aus der Teilchenphyik
  Theoretisch-Phyikalisches Seminar

Universität Zürich, WS 99/00:

- Aktuelles aus der Teilchenphyik
  Theoretisch-Phyikalisches Seminar

PD Dr. R. Rosenfelder

ETH Zürich, WS99/00:

- Pfadintegrale in der Quantenphysik

LABORATORY FOR MUON SPIN SPECTROSCOPY

Dr. A. Amato

Tohoku University (Japan), April 1999:

- μSR technique: A complementary tool to study the strongly correlated electron systems

Hiroshima University (Japan), April 1999:

- New μSR studies on strongly correlated electron systems

Osaka University (Japan), April 1999:

- Heavy fermion systems studied by μSR technique

Kumamoto University (Japan), May 1999

- μSR technique: An introduction

AWARDS

Titles:

R. Eichler — Chairman of Scientific Council of DESY

T.A. Jung — President of the Swiss Physical Society

M. Suter — Titularprofessor at ETH Zürich

Habilitation:

A. Türler:

Title of thesis:
Gas Phase Chemistry of the Transactinide Elements Rutherfordium, Dubnium and Seaborgium
PSI & Universität Bern

Doctoral Thesis:

P. Bargassa

Title of Thesis:
A Measurement of K^0, $\overline{K}^0 \rightarrow 3\pi^0$
ETH Zürich / PSI

Thesis advisors:
Prof. H.-J. Gerber (ETH Zürich)
PD Dr. T. Nakada (PSI)
Dr. A. Schopper (CERN)

L. Desorgher

Title of thesis:
Variations of the Earth's Outer Electron Belt, REM Observations between 1995 and 1997, and Simulations of Magnetic Storm Effects
PSI

Thesis advisors:
Dr. P. Bühler (PSI)
Dr. A. Zehnder (PSI)
Prof. E. Flückiger (Uni Bern)

R. Dressler:

Title of thesis:
Synthese neutronenreicher Isotope schwerster Elemente in xn- and α-xn-Reaktionen
PSI

Thesis advisors:
Prof. Dr. H.W. Gäggeler (Universität Bern & PSI).

Th. Döring:

Title of thesis:
Rekonstruktion der atmosphärischen Kupfer-, Zink- und Bleigehalte sowie der Bleiisotopen-zusammensetzung aus einem hochalpinen Eisbohrkern unter Anwendung der hochauflösenden ICP-MS-Technik
PSI

Thesis advisors:
Prof. Dr. H.W. Gäggeler (Universität Bern & PSI).
Dr. M. Schwikowski (PSI)

T. Flügel

Title of Thesis:
The Pion Beta Decay Experiment and a Re-Measurement of the Panofsky Ratio
ETH Zürich / PSI

Thesis advisors:
Prof. H. Hofer (ETH Zürich)
Dr. D. Renker (PSI)

P. Gartenmann:

Title of thesis:
Untersuchung von anthropogenem ^{60}Fe und anderen mittel-schweren Radionukliden mit Beschleunigermassenspektrometrie
ETH

Thesis advisors:
Prof. Dr. J. Lang (ETH Zürich)
Prof. Dr. W. Kutschera (Universität Wien)
Prof. Dr. M. Suter (ETH Zürich)

B. Henrich:

Title of thesis:
Test and Evaluation of Silicon as Sensor Material for the CMS Pixel Detector
University of Basel / PSI

Thesis advisors:
Prof. L. Tauscher (University of Basel)
Dr. R. Horisberger (PSI)

V. Lavanchy:

Title of thesis:
Historical Evolution of the Atmospheric Particulate Carbon Concentration from a High-alpine Ice Core using an Optical and a Thermal Method
Universität Bern/PSI

Thesis advisors:
Prof. Dr. H.W. Gäggeler (Universität Bern & PSI)
PD Dr. U. Baltensperger (PSI).

O. Leifeld:

Title of thesis:
Ge Quantum Dot Formation on the C-alloyed Si(001) Surface – a Scanning Tunneling Microscopy Study
EPFL / PSI

Thesis advisors:
Prof. K. Kern (EPFL)
Dr. K. Eberl (Max-Planck-Institut, Stuttgart, Germany)
Dr. D. Grützmacher (PSI)
Prof. E. Kapon (EPFL)

M. Roth:

Title of thesis:
Precise Predictions for Four-Fermion Production in Electron-Positron Annihilation
ETH Zürich / PSI

Thesis advisors:
Prof. Z. Kunszt (ETH Zürich)
PD Dr. A. Denner (PSI)

J. Schottmüller:

Title of thesis:

Kinetische Energie von π^-p-Atomen in flüssigem und gasförmigem Wasserstoff

University of Zürich / PSI

Thesis advisors:

Prof. R. Engfer (University of Zürich)

Dr. M. Daum (PSI)

O. Wigger:

Title of thesis:

Bose-Einstein Correlation and Resonance Production of Pionic Final States in Antiproton Annihilation at Rest

ETH Zürich / PSI

Thesis advisors:

PD Dr. T. Nakada (PSI/ ETH Zürich)

Prof. H.-J. Gerber (ETH Zürich)

Dr. P. Weber (ETH Zürich)

P. Zanis:

Title of thesis:

In-situ photochemical control of ozone at Jungfraujoch in the Swiss Alps

Universität Bern

Thesis advisors:

Prof. Dr. H.W. Gäggeler (Universität Bern & PSI).

Prof. Dr. H. Wanner (Universität Bern)

PAUL SCHERRER INSTITUT

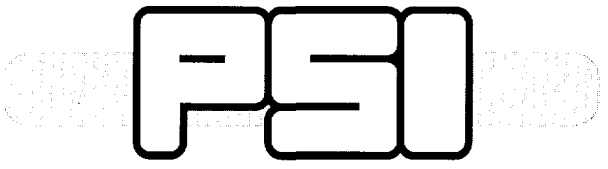

Paul Scherrer Institut
CH-5232 Villigen PSI
Internet

Phone +41 56 310 21 11
Fax +41 56 310 21 99
http://www.psi.ch